COMPUTATIONAL DISLOCATION DYNAMICS

N. M. Ghoniem

Contributors: X. Han, Z. Wang, J. Huang, M. Wen, Q. Hu, S. Banerjee, and S. Noronha

Mechanical and Aerospace Engineering Department
University of California, Los Angeles, CA 90095-1597, USA

Contents

Preface **xxix**

1 Introduction **1**

2 Experimental Observations **7**

2.1 Basic Dislocation Structures 7

2.2 Inhomogeneous Plastic Deformation 11

3 Geometry of Defects **21**

3.1 Topological Defects 21

3.1.1 Point defects 21

3.1.2 Dislocations 22

3.1.3 Surface defects 23

3.1.4 Volume defects 24

4 Mathematical Foundations **29**

4.1 Basic Vector and Tensor Operations 29

4.2 Infinitesimal Deformation and the Strain Tensor 37

4.3 The Stress Tensor 39

4.4 Thermodynamics of Deformation 40

4.5 Constitutive Relations 42

4.6 Anisotropic Crystals 44

4.7 Navier's Equation 46

4.8 Parametric Dislocations 48

4.8.1 Differential Geometry of Dislocation Loops 48
4.8.2 Circular, Elliptic and Helical Loops 49
4.8.3 Linear Parametric Segments 49
4.8.4 Cubic Spline Parametric Segments 50
4.8.5 Quintic Spline Parametric Segments 50

5 Two-dimensional Elastic Fields **53**
5.1 Infinite Isotropic Media 53
5.1.1 Edge Dislocations 53
5.1.2 Screw Dislocations 58
5.2 Infinite Anisotropic Media 59
5.3 Finite Media 63
5.3.1 Image Construction 63
5.3.2 Complex Variable Method 65
5.4 Interfacial Dislocation Networks 69
5.4.1 Single Dislocation Solution 70
5.4.2 Network Dislocation Solution 74
5.4.3 Results 75

6 Green's Tensor Functions **79**
6.1 Basic Equations 79
6.2 Differential Geometry 81
6.3 Green's Functions in Isotropic Materials 83
6.3.1 Full Space 83
6.3.2 Half Space 84
6.4 Green's Functions in Anisotropic Materials 86
6.5 Green's Functions in Layered Media 92
6.5.1 Basic formulas 93
6.5.2 Derivatives of the Green's functions 96
6.5.3 Green's Functions in Bimaterials 97

6.5.4 Application to infinitesimal dislocations 102

7 Three-dimensional Elastic Fields 123

7.1 Fundamental Principles & Theorems 123

7.1.1 Minimum Potential Energy Principle 123

7.1.2 The Reciprocity Theorem 124

7.1.3 The Volterra Formula 125

7.1.4 Eshelby's Methods 126

7.2 Infinite Isotropic Media 139

7.2.1 Dislocation Ensembles in Isotropic Crystals 140

7.2.2 Affine Covariant-contravariant Vector Forms 154

7.3 Line Integral Forms for Dislocations in Bi-materials 160

7.3.1 Objectives and Problem Setup 160

7.3.2 Fourier Transformation of The Governing Equations 161

7.3.3 Describing Equations 162

7.3.4 Fourier Transformation of Infinite Solutions 163

7.3.5 Determination of Solution Matrices 172

7.3.6 Fourier Transform Details 173

7.4 3D Dislocations in Infinite Anisotropic Media 177

7.4.1 Basic Procedure 177

7.4.2 Forces on a dislocation loop 181

7.4.3 Accuracy verification 182

7.4.4 Numerical results 183

7.5 Thin Films and Nanolayers 184

7.5.1 Introduction 184

7.5.2 Infinitesimal Dislocation Loop in Film-on-substrate 200

7.5.3 Dislocation Loop in Film-on-substrate 201

7.5.4 Dislocation-Interface Interaction 202

7.5.5 Film-on-substrate 203

7.5.6 Capped Film-on-substrate 203

7.5.7 Dislocation loop across an interface 204
7.5.8 Summary and Conclusions 205

8 Computational Methods **215**
8.1 2D Dislocation Dynamics - Noronha 215
8.1.1 Basic Procedure 215
8.1.2 Multipole expansions 215
8.1.3 Applications 215
8.2 Variational Equations of Motion 215
8.2.1 Irreversible Thermodynamics of Dislocation Motion 218
8.2.2 Variational Formulation 224
8.2.3 Computational Geometry of Dislocation Loops 228
8.2.4 Applications of Parametric Dislocation Dynamics 234
8.3 Numerical Accuracy & Convergence 244
8.3.1 Dimensionless Equations of Motion for PDD 245
8.3.2 Spatial and Temporal Resolution of Dislocation Mechanisms 247
8.4 O(N) Algorithms 256
8.4.1 Multipole Representation of Dislocation Fields 256
8.4.2 Rules for Combination of Moments 261
8.4.3 Applications to dislocation boundaries and walls 262
8.4.4 R and Its Derivatives 267
8.5 Coupling between the DD and FEM Computational Procedures 269
8.5.1 Loop Node Stress Tensor Estimation 270
8.5.2 Peierls Forces 271
8.5.3 A Shear Loop in a Finite Crystal 272
8.5.4 The Influence of Crystal Surfaces on the Deformation of Frank Reed Sources 273
8.5.5 Conclusions 274

9 Applications **287**
9.1 Fundamental Mechanisms 287

9.1.1 Finite-Size Dipole Formation and Destruction . . . 287
9.1.2 Dislocation interaction with defect clusters . . . 288
9.1.3 Dislocation Junctions . . . 300
9.2 Work Hardening in Single Crystals . . . 302
9.2.1 Introduction . . . 302
9.2.2 Simulation Procedure . . . 304
9.2.3 Simulation Results . . . 305
9.3 Thin Films & Nanolayers . . . 312
9.3.1 Experimental Procedure and Results . . . 322
9.3.2 Dislocation Dynamics in Thin Foils . . . 327
9.3.3 PDD Simulations for Experimental Analysis . . . 330
9.3.4 Basic Equations for Anisotropic Nanolayers . . . 335
9.3.5 Peach-Koehler Forces in Layered Materials . . . 342
9.3.6 Dislocation-Interface Interaction . . . 343
9.3.7 Dislocation Dynamics in Layered Materials . . . 346
9.3.8 Confined Layer Slip (CLS) . . . 348
9.3.9 Loss of Slip Confinement . . . 350
9.4 Ductile-to-Brittle Transition . . . 355
9.5 Plastic Flow Localization . . . 355
9.5.1 Introduction . . . 355
9.5.2 Interaction Between Dislocations & Defects . . . 356
9.5.3 Unlocking of Dislocations from Defect Clusters . . . 359
9.5.4 The Mechanism of Channel Formation . . . 363
9.5.5 Summary & Conclusions . . . 375
9.6 Persistent Slip Bands in Fatigue . . . 377
9.6.1 Dynamics of a Glide Dislocation and Dipolar Loops . . . 378
9.6.2 Results . . . 381
9.6.3 Conclusions . . . 388

10 Continuum Dislocation Theory 389

11 Kinetic Monte Carlo Simulation of Defects **391**

11.1 Experimental Observations of Nano-defects . . . 391

11.2 Description of Point Defects by Force Multipoles . . . 396

11.3 The Kinetic Monte Carlo (KMC) Method . . . 403

11.3.1 The n-fold way algorithm . . . 403

11.3.2 Simulation Procedure . . . 404

11.3.3 Elastic Interaction between Point Defects . . . 406

11.4 Comparison of KMC model with Experiments . . . 425

12 Dislocation Representation of Cracks **433**

12.1 Numerical Simulations of General 3-D Cracks . . . 435

12.1.1 Penny-shaped Crack . . . 435

12.1.2 Effect of a Non-uniform Stress Field . . . 439

12.1.3 2-D Straight Crack . . . 439

12.2 Three Dimensional Dislocation Interaction with Cracks . . . 443

12.3 Motion of Dislocations ahead of Crack Tips . . . 446

12.4 Conclusion . . . 450

13 The Dislocation Core **453**

13.1 The Peierls-Nabarro (PN) Model . . . 453

13.1.1 The Edge dislocation . . . 453

13.1.2 The Screw dislocation . . . 455

13.2 Modifications of the PN Model . . . 457

13.3 The Peierls Stress . . . 460

14 Surface Defects and Atom Clusters **463**

14.1 Surface Defects and Surface Atoms . . . 463

14.2 Bulk Point Defects . . . 464

14.3 Surface Atom Clusters . . . 465

14.3.1 Interaction between a line defect and a point defect . . . 466

14.3.2 Interaction between periodic line defects . . . 467

15 Computer Programs & Architecture **469**

15.1 Basic DD Program 469

15.2 2D Simulations - Noronha 491

15.3 Isotropic DD - Jianming 491

15.4 Anisotropic DD - Han 491

15.5 DD in Nanolayers - Han 491

15.6 Large-Scale DD - Zhiqiang 491

Acknowledgement **497**

Bibliography **499**

List of Figures

2.1 Frank-Read source in silicon. Courtesy of Dash 7

2.2 Frank-Read source in Si. Courtesy of Dash 8

2.3 Intense shear bands (ISBs) form preferentially at grain boundaries (G.B) and grow into the crystal. The ISBs are first observed at the onset of the cyclic softening. Tht picture shows Cu-30%Zn cycled to $\varepsilon = 3.4 \times 10^{-3}$. 8

2.4 Dislocation Spiral. Courtesy of Amelincx 9

2.5 Two apparently different types of dipole arrays are observed in Cu-30%Zn. (a) The array marked with A is a regularly spaced array of dipoles. (b) The array marked with B appears to be a stacking fault band (Courtesy Riso National Laboratory in Roskilde, Denmark). 9

2.6 Dislocation dipole arrays. Courtesy of Neuhauser 10

2.7 Considerable variations of the dipole spacing is found even within the same crystal grain. The figure shows a dipole array, marked with an A. The measured dipole spacing is approximately 650 Å. An interaction between two arrays is seen at B 10

2.8 Fatigue-tested Cu at a stress amplitude of 80 MPa (N(f) = 515928) showing bands of dislocations 11

2.9 A fairly uniform structure of planar dislocation arrays are seen after completion of cyclic softening. No dipole arrays were found at this stage. The picture shows Cu-30%Zn cycled to $\varepsilon = 3.4 \times 10^{-3}$. The polycrystal is found to contain a fairly uniform structure of planar dislocation arrays 12

2.10 Microstructure of the unirradiated copper and copper alloys.(a) OFHC-Cu (annealed at 550 degrees C for 2h), (b) CuCrZr (prime aged) and (c) CuAl-25 (as-wrought). 13

2.11 Dislocation cell structure in Iron. Picture adapted from the work of Reppich . . 14

2.12 Schematic of Dislocation cell structure evolution. Picture adapted from the work of Takeuchi and Argon. 14

2.13 Post-fatigue microstructure of unirradiated OFHC-Cu tested at room temperature showing formation of equiaxed and elongated cells: (a,b) 180 MPa, N(f) = 1121, (c) 120 MPa, N(f) = 21646.(Courtesy Riso National Laboratory in Roskilde, Denmark) 15

2.14 Transmission microscopy picture of Persistent Slip Bands (PSB's) in cyclically-deformed copper. Picture adapted from the work of Essman and Mughrabi . . . 16

2.15 Transmission microscopy picture of Persistent Slip Bands (PSB's) in cyclically-deformed copper. Picture adapted from the work of Essman and Mughrabi . . . 16

2.16 Self-interstitial Atom (SIA) decorations of dislocations in irradiated Cu. Courtesy of Singh 17

2.17 Dislocation channels in irradiated Cu. Courtesy of Singh 17

2.18 Dislocation channels in irradiated Cu. Courtesy of Singh. 18

2.19 Post-fatigue microstructure of the OFHC-Cu irradiated at 47 °C to 0.5 dpa and tested at room temperature at a stress amplitude of 250 MPa (N(f) = 32) showing significant area to area variations: (a) small cells with loose dislocation walls, (b) slip bands, and (c) "cleared" channels. Note the lack of dislocation generation in the regions away from the cleared channel (c). 19

3.1 Dislocation types in materials 22

3.2 Burgers circuit for an edge dislocation 22

3.3 Crystal distortion as a result of a dislocation slip event 24

3.4 Types of disclinations in materials 25

3.5 $< 100 >$-tilt boundary 25

3.6 Stable tilt boundary 26

3.7 Twist boundary between grains 26

3.8 Slip band geometry 26

3.9 Twin band geometry 27

3.10 Classification of cracks: (a) mode-I (opening); (b) mode-II (sliding); (c) mode-II (twisting) 27

4.1 Cartesian coordinate system before and after rotation of axes 29

4.2 Surface and bounding contour for Stokes' theorem 36

4.3 Representative volume for Gauss's theorem 37

4.4 A space dislocation loop discretized into a finite number of curved segments, N_s 48

4.5 Basic elements of a space curve representing one dislocation segment 49

5.1 Bonded layer structure with a single interfacial dislocation 70

5.2 Comparison of σ_{xx} between inhomogeneous system (Si/Ge) and homogeneous system(Si) with a single dislocation at the thickness of 8 nm 76

5.3 Surface stress map of 8 nm thin film structure 77

5.4 Surface stress map of 80 nm thin film structure 77

5.5 Surface displacement map of 8 nm thin film 78

5.6 Surface curvature map of 8 nm thin film 78

6.1 Representation of the solid angle, Ω, at a field point (Q) away from the dislocation loop line containing the set of points (P) 81

6.2 A concentrated force applied to an isotropic half space medium 85

6.3 Geometry of a multilayered thin film system. 93

6.4 Al or Ni film on Cu substrate. 105

6.5 The Green's displacements along $(0.5h, 0, z)$ due to a point force at $(0, 0, -0.5h)$ in the (a) x-direction; (b) y-direction; (c) z-direction. 106

6.6 The Green's out-plane stresses along $(0.5h, 0, z)$ due to a point force at $(0, 0, -0.5h)$ in the (a) x-direction; (b) y-direction; (c) z-direction. 107

6.7 The Green's in-plane stresses along $(0.5h, 0, z)$ due to a point force at $(0, 0, -0.5h)$ in the (a) x-direction; (b) y-direction; (c) z-direction. 108

6.8 Four-layer material. 109

6.9 The Green's displacements along $(0.5h, 0, z)$ due to a point force at $(0, 0, 0.5h)$ in the (a) x-direction; (b) y-direction; (c) z-direction. 110

6.10 The Green's out-plane stresses along $(0.5h, 0, z)$ due to a point force at $(0, 0, 0.5h)$ in the (a) x-direction; (b) y-direction; (c) z-direction. 111

6.11 The Green's in-plane stresses along $(0.5h, 0, z)$ due to a point force at $(0, 0, 0.5h)$ in the (a) x-direction; (b) y-direction; (c) z-direction. 112

6.12 An infinitesimal dislocation in a Al or Ni film on Cu substrate. 113

6.13 The in-plane stress σ_{12} on $y = 0$ plane due to a infinitesimal dislocation at $(0, 0, 0.5h)$ in the (a) Cu(substrate)-Al(film) solid; (b) Cu(substrate)-Ni(film) solid; (c) Cu half-space; (d) isotropic half-space. 115

6.14 The out-plane stress σ_{32} on $y = 0$ plane due to a infinitesimal dislocation at $(0, 0, 0.5h)$ in the (a) Cu(substrate)-Al(film) solid; (b) Cu(substrate)-Ni(film) solid; (c) Cu half-space; (d) isotropic half-space. 117

6.15 The strain energy on $y = 0$ plane due to a infinitesimal dislocation at $(0, 0, 0.5h)$ in the (a) Cu(substrate)-Al(film) solid; (b) Cu(substrate)-Ni(film) solid; (c) Cu half-space; (d) isotropic half-space. 119

6.16 The strain energy on the $z = h$ free surface due to a infinitesimal dislocation at $(0, 0, 0.5h)$ in the (a) Cu(substrate)-Al(film) solid; (b) Cu(substrate)-Ni(film) solid; (c) Cu half-space; (d) isotropic half-space. 121

7.1 Example of an eigenstrain in a domain Ω caused by thermal expansion inside a confining matrix 127

7.2 Representation of volume defects as either an inhomogeneity (left) or inclusion (right) 127

7.3 Illustration of the eigenstrain induced by a stress-free transformation of shape or size of an inclusion 131

7.4 Free expansion of an inclusion with the eigenstrain ε^*_{ij} 132

7.5 Applying tractions $-\sigma^*_{ij}n_j$ on the inclusion to fit it back in the original matrix cut 132

7.6 Applying an equal and opposite layer of body forces $+\sigma^*_{ij}n_j$ over the surface $\partial\Omega$ to remove unwanted tractions 133

7.7 Creation of a dislocation by a cut on the surface (S) 141

7.8 Normal stress iso-surface, σ_{11}, in the local loop coordinates, where the 1-axis is [010]-direction and the 3-axis is the [110]-direction. 146

7.9 Shear stress iso-surface, σ_{12}, in the local loop coordinates, where the 1-axis is [010]-direction and the 3-axis is the [110]-direction. 147

7.10 Shear stress iso-surface , σ_{23}, in the local loop coordinates, where the 1-axis is [010]-direction and the 3-axis is the [110]-direction. 147

7.11 A comparison between numerical (current method) and exact analytical (Kroupa) solutions for the normal stress component σ_{zz} of a circular prismatic loop. 148

7.12 Dependence of the error between numerical and analytical (Kroupa) normal stress results on the distance from loop center, for various number of segments. 149

7.13 A comparison between numerical (current method) and analytical (deWit) results for the interaction energy between two prismatic loops. 150

7.14 A comparison between numerical (current method) and analytical (Hirth and Lothe) results for the self energy of a slip loop. 151

7.15 Dependence of the error between numerical and analytical solutions in FIG. 10 above on the loop radius and number of cubic spline segments. 151

7.16 Normal stress iso-surface (186 MPa), σ_{11}, for a single Frank-Read source in Molybdenum 152

7.17 Normal stress distribution resulting from the interaction of the single FR source with the surface of a Molybdenum single crystal 153

7.18 Shear stress distribution resulting from the interaction of a single FR source with the surface of a Molybdenum single crystal 153

7.19 Normal stress iso-surface(-130 MPa), σ_{33}, for two interacting Frank-Read sources in Molybdenum 154

7.20 Shear stress iso-surface(170 MPa), σ_{13}, for two interacting Frank-Read sources in Molybdenum 155

7.21 Geometry and variables for infinitely-long screw and edge dislocations 158

7.22 Geometry and variables for circular shear and prismatic loops 158

7.23 Schematic diagram of a closed dislocation loop L. 177

7.24 A circular dislocation loop on the (111) plane, with **b** along $[\bar{1}10]$ direction (a) Global system, (b) Local coordinate system. 185

7.25 Stresses along x-axis (local coordinate system) (a)σ_{zx} and (b) σ_{xy}. With stresses divided by $0.5(C_{11} - C_{12})b/R$, $C_{11}/C_{12}/\mu = 5 : 3 : 1$. 186

7.26 Stress Iso-surface for σ_{zx}(=0.08), with (a) $A = 1$, (b) $A = 4$ and (c) $A = 0.25$. Stresses divided by $0.5(C_{11}-C_{12})b/R$, $C_{11}/C_{12}/\mu = 5 : 3 : 1$, and local coordinate system is used. 187

7.27 Stress Iso-surfaces for σ_{xx}(=-0.2), with (a) $A = 1$, (b) $A = 4$ and (c) $A = 0.25$. Stresses divided by $0.5(C_{11}-C_{12})b/R$, $C_{11}/C_{12}/\mu = 5 : 3 : 1$, and local coordinate system is used. 188

7.28 Stress Iso-surface for σ_{zx}(=0.2), dislocation loop in (a) Al ($A = 1.21$), (b) Cu ($A = 3.21$) and (c) Isotropic material ($A = 1$, with C_{11} and C_{12} choosing the values of Cu). Stresses divided by $10^{10}b/R$, and local coordinate system is used. 189

7.29 Stress Iso-surface for σ_{xx}(=-0.2), dislocation loop in (a) Al ($A = 1.21$), (b) Cu ($A = 3.21$) and (c) Isotropic material ($A = 1$, with C_{11} and C_{12} choosing the values of Cu). Stresses divided by $10^{10}b/R$, and local coordinate system is used. 190

7.30 Stress Iso-surface for σ_{yy}(=-0.2), dislocation loop in (a) Al ($A = 1.21$), (b) Cu ($A = 3.21$) and (c) Isotropic material ($A = 1$, with C_{11} and C_{12} choosing the values of Cu). Stresses divided by $10^{10}b/R$, and local coordinate system is used. 191

7.31 Stress Iso-surface for σ_{zz}(=-0.4), dislocation loop in (a) Al ($A = 1.21$), (b) Cu ($A = 3.21$) and (c) Isotropic material ($A = 1$, with C_{11} and C_{12} choosing the values of Cu). Stresses divided by $10^{10}b/R$, and local coordinate system is used. 192

7.32 A circular dislocation loop on the (110) plane, with **b** along [$\bar{1}$11] direction (a) Global system, (b) Local coordinate system. 193

7.33 Stress Iso-surface for σ_{zx}(=0.2), dislocation loop in (a) Fe ($A = 2.36$), (b) Nb ($A = 0.51$) and (c) Isotropic material ($A = 1$, with C_{11} and C_{12} choosing the values of Nb). Stresses divided by $10^{10}b/R$, and local coordinate system is used. 194

7.34 Stress Iso-surface for σ_{xx}(=-0.4), dislocation loop in (a) Fe ($A = 2.36$), (b) Nb ($A = 0.51$) and (c) Isotropic material ($A = 1$, with C_{11} and C_{12} choosing the values of Nb). Stresses divided by $10^{10}b/R$, and local coordinate system is used. 195

7.35 Stress Iso-surface for σ_{zz}(=-0.6), dislocation loop in (a) Fe ($A = 2.36$), (b) Nb ($A = 0.51$) and (c) Isotropic material ($A = 1$, with C_{11} and C_{12} choosing the values of Nb). Stresses divided by $10^{10}b/R$, and local coordinate system is used. 196

7.36 Peach-Koehler force (divided by $0.5(C_{11}-C_{12})bb_2/R$) of unit dislocation element on $z = 0$ plane and along y, with $d = 1.5R$, (a) glide component, (b) climb component 197

7.37 The self-force (divided by $0.5(C_{11} - C_{12})b^2/R$) along a slip circular loop, with $R = 100b$ 197

7.38 The self-force of a circular dislocation loop in different materials. (A) Al, (B) Cu, and (C) Ni. The self force is normalized to $b^2R^{-1} \times 10^{10}$. 198

7.39 Geometry of a multilayered thin film system. 201

7.40 Geometry and coordinate system for the film-on-substrate arrangement. 201

7.41 σ_{32} stress contours on the $y = 0$ plane due to an infinitesimal dislocation loop at $(0, 0, 0.5h)$ in (a) Al(film) on a Cu(substrate); (b) Ni(film) on a Cu(substrate). . 208

7.42 σ_{12} stress contours on the $y = 0$ plane due to an infinitesimal dislocation loop at $(0, 0, 0.5h)$ in (a) Al(film) on a Cu(substrate; (b) Ni(film) on a Cu(substrate). . . 209

7.43 σ_{23} stress Iso-Surface for a circular shear dislocation loop in (a) Al(film) on a Cu(substrate); (b) Al infinite space. 210

7.44 Free surface and interface image force distributions on a circular dislocation loop in (a) Al(film) on a Cu(substrate); (b) Ni(film) on a Cu(substrate). 211

7.45 Image force of an oblong dislocation loop in an Al film on a Cu substrate. The Al film is capped by a Cu layer of thickness $h_c = 0.1h$ (a), $0.2h$ (b) and $0.5h$. . . 212

7.46 Force distributions on a dislocation loop : (a) as it approaches the interface, but is contained in a softer material of small elastic anisotropy; (b) as it straddles the interface (c) the loop is totally contained in a harder material of large elastic anisotropy. 213

7.47 Dependence of force components on (a) the leading point A and (b) the trailing point B, as functions of their distance from the interface. Koehler's 2D solution is represented by dashed lines. 214

8.1 Discretization of a dislocation loop with linear segments leads to loss of connectivity when the equations of motion are developed only for mid-points. 216

8.2 Force distribution on the straight segment AB from neighboring segments shows singular behavior at sharp corners. Force averaging over linear segments diverges as its length is decreased. 217

8.3 Representation of loop motion in an infinitesimal transition, illustrating thermodynamic variables 218

8.4 3-D motion of a curved dislocation segment involving in-plane glide and out-of-plane climb. 223

8.5 Nodal displacements for the first time-step of an initially straight segment. . . . 236

8.6 Operation of the Frank-Read source for isotropic dislocation mobility on the glide plane. 236

8.7 Operation of the Frank-Read source for isotropic dislocation mobility on the glide plane. (a) 3-d , (b) projection on the glide plane 237

8.8 Details of nodal arrangements before annihilation of opposite-character segments. 238

8.9 Angular variation of the self force (units of $\frac{\sigma}{\mu a}$) in copper for the Frank-Read source after segment annihilation. The angle θ is defined in the insert. All distances on the figure are in units of the lattice constant. 239

8.10 Interaction between a Frank-Read source and discrete barriers in fcc metals. . . 240

8.11 Double-ended Frank-Read source in bcc metals. The straight segments are either screw or edge, while the curved corners are of mixed type. 240

8.12 Dislocation loop generation by the Frank-Read mechanism for anisotropic mobility of screw and edge components. 241

8.13 Dislocation generation in covalently-bonded silicon. The directions of the hexagon sides are along $< 111 >$-orientations for screw segments, and $\pm 60^o$ for mixed ones. 242

8.14 Coplanar dislocation loop interaction 242

8.15 Formation of a dislocation junction in bcc metals 243

8.16 Computer simulation of forest hardening in Cu. 244

8.17 Effects of gradually increasing the applied stress on the evolution of an F-R source with $\mathbf{b} = \frac{1}{2}[\bar{1}01]$. When the Orowan stress is reached, the source is unstable . . 249

8.18 The influence of number of segments on the shape convergence of an F-R source with Burgers vector $\frac{1}{2}[\bar{1}01]$ at different stress levels: (a) stable state ($\sigma_{11} = 80\ MPa$, $\tau/\mu = 0.064\%$), (b)unstable state - same time: ($\sigma_{11} = 200\ MPa$, $\tau/\mu = 0.16\%$). 250

8.19 The influence of the time integration scheme on the shape convergence of an F-R source. Same conditions as in FIG. 8.18 252

8.20 Expansion of an F-R source from an initially pure screw dislocation subjected to a step function stress $\sigma_{11} = 120$ MPa($\tau/\mu = 0.096\%$). The glide plane in Cu is (1 1 1), and the Burgers vector is $\mathbf{b} = \frac{1}{2}[0\bar{1}1]$. At the instant of annihilation the time is reset to $t_1^* = 0$. Subsequent dimensionless times are: $t_2^* = 1.0 \times 10^6$, $t_3^* = 1.5 \times 10^6$, $t_4^* = 2.0 \times 10^6$, $t_5^* = 3.0 \times 10^6$. 253

8.21 Expansion of an initially mixed dislocation segment in an F-R source under the step function stress of $\sigma_{22} = 140$ MPa($\tau/\mu = 0.112\%$). The F-R source is on the (1 1 1)-plane of a Cu crystal with Burgers vector $\mathbf{b} = \frac{1}{2}[0\bar{1}1]$. The time interval between different contours is $\Delta t^* = 5 \times 10^5$. 254

8.22 The effects of a rigid grain boundary in Cu on the evolution of a closed dislocation loop emanating from an F-R source. Conditions are the same as in FIG. 8.20, the time interval between successive positions $\Delta t^* = 1.5 \times 10^6$. 255

8.23 The effects of a rigid grain boundary of triangular cross-section in Cu on the evolution of a closed dislocation loop emanating from an F-R source. Conditions are the same as in FIG. 8.22. 257

8.24 Illustration of the geometries of (a) a single volume with center O containing dislocations, (b) a single volume (center O') containing many small volumes with centers O^m. 259

8.25 Relative error of the MEM vs (a) the expansion order, (b) the R/h value for a simulation volume with an edge length of 10 μm. 263

8.26 Illustration of a tilt boundary. A single dislocation from an F-R source lies on the [111] glide plane with Burgers vector $\frac{1}{2}[\bar{1}01]$ interacts with the tilt boundary. 264

8.27 (a)Dislocation configurations at different simulation time steps: t_1=0 ns, t_2=0.31 ns, t_3=0.62 ns, t_4=1.23 ns, (b)Relative error of the dislocation position along the line X in (a). 265

8.28 Dislocation wall structure with dislocation density 5×10^{10} cm/cm^3. A small dislocation segment S with Burgers vector $\frac{1}{2}[10\bar{1}]$ lies along x. 266

8.29 (a) P-K forces on a small dislocation segment at different positions along direction x, (b) Relative error of the P-K force from MEM with respect to that from full calculation. 266

8.30 Two views of the displacement field induced by a 4000 a-radius shear loop in the (101)-[111] slip system. Burgers vectors are represented at loop nodes. 276

8.31 Vector plot for the tractions produced by the elastic stress field of a 4000 a radius shear loop 277

8.32 $\sigma_{xx} = 2000$ MPa stress iso-surface for the total dislocation plus image elastic field 278

8.33 Force distributions on a 4000 a radius shear loop in the (101)-[111] slip system in Fe, applied stress $\sigma_{xx} = 100$ MPa. Vectors to scale except self and image with scale factors of 2 and 10, respectively 279

8.34 Two views of the image force distribution on a loop in the corner of the unit cell. The loop is 250 a from the edge of the cell. The Burgers vector direction is also represented. 280

8.35 The 500 a radius loop and the deformation that results under an applied stress of 350 MPa. 281

8.36 Image force distributions on a 2000 a radius shear loop in the (101)-[111] slip system, (A)1000 a, and (B) 10 a from z=10000 a surface. Vector scale factors: (A)100,(B) 1 282

8.37 Deformation of a 2000 a radius shear loop in the (101) -[111] slip system. The loop is initially 10 a from the surface with applied stress: $\sigma_{xx} = 50$ MPa. 283

8.38 Schematic of cross-slip of a screw dislocation adjacent to a surface in a crystal.(a) Initial configuration of an expanding F-R source, (b) emergence of an incipient surface step by penetration of the edge component through the surface, and (c) the deformation of the dislocation line following cross-slip 284

8.39 Isometric view of a crystal containing an FR-source, and a 2-d view of the deformed geometry as viewed normal to the (101)-plane. (1) Initial geometry, (2) Intermediate, and (3) Equilibrium. The applied stress $\sigma_{xx} = 125$ MPa. 285

8.40 Isometric (A), and 2-d (B, C, and D) views of the evolution of an FR-source near a crystal surface. View C depicts the "low screw/edge force" ratio case, while D depicts the "high" ratio case. 4000 time steps. 286

9.1 Two F-R source dislocations with the same Burgers vector($\mathbf{b} = \frac{1}{2}[\bar{1}01]$) but opposite tangent vectors gliding on two parallel (111)-planes (distance $h = 25\sqrt{3}a$ apart) form a short dipole in an unstressed state. The view is projected on the (111)-plane. Time intervals are: (1) 2.5×10^5, (2) 4.75×10^5, (3) 5×10^5 , (4) Equilibrium state 289

9.2 The relative shear stress(τ/μ) to break up a finite size dipole as a function of the relative inverse separation$1/h^*$, $h^* = h/a$. h is the distance between the two parallel planes. The distance between the pinning points of the two F-R sources $L = 1600a$, and they are originally separated by $350a$ horizontally. 290

9.3 Geometry representation of the relationship between one cluster and a dislocation on its glide plane. (a) Burgers vector of the cluster is parallel to that of the F-R source. (b) the two Burgers vectors are normal to each other. 292

9.4 Interaction between an F-R source ($\mathbf{b} = \frac{1}{2}[10\bar{1}]$) in Cu on the (1 1 1)-plane with a single sessile prismatic interstitial defect cluster($\mathbf{b} = \frac{1}{2}[111]$), d=50 a, subjected to a step function stress $\sigma_{11} = 120$ MPa ($\tau/\mu = 0.096\%$). The cluster center has the local coordinate: (a)=(0 -800 80); (b)=(0 -800 120). 294

9.5 Dynamics of the *asymmetric unlocking* mechanism from a cluster atmosphere of 15 equally spaced sessile interstitial clusters ($d = 40,\ y = 80$ and $l = 100$). (a)Equilibrium state with equal shear stress interval of 4 MPa ($\Delta\tau/\mu = 0.008\%$). (b)Unlocking state at a stress $\sigma_{11} = 140$ MPa ($\tau/\mu = 0.112\%$), with equal time interval $\Delta t^* = 2 \times 10^5$. 295

9.6 The influence of the number of segments on the resolution of the dislocation unlocking mechanism: (a) 6 segments; (b) 18 segments; (c) 30 segments. 297

9.7 Comparison between the results of PDD simulations and the analytical results of Trinkaus et al. for the dependence of CRSS (τ/μ) on the inter-cluster distance. 298

9.8 Comparison between the results of PDD simulations and the analytical results of Trinkaus et al.for the dependence of CRSS (τ/μ) on the inverse square stand-off distance. Case (1): Burgers vectors of clusters and the dislocation are parallel; Case(2): Burgers vectors of clusters is orthogonal to that of the dislocation. . . . 299

9.9 Dynamics of 2 unstressed F-R sources ($\frac{1}{2}[01\bar{1}](111)$ and $\frac{1}{2}[101](11\bar{1})$) forming a 3D junction along $(\bar{1}10)$, $\mathbf{b} = \frac{1}{2}[110]$. (a) 2D view for the motion of the F-R source ($\frac{1}{2}[01\bar{1}](111)\frac{1}{2}[\bar{1}01](1\bar{1}1)$) on its glide plane(111). Time intervals are (1) initial configuration, (2) 1.5×10^4, (3) 5.0×10^4, (4) 1.3×10^5, (5) Final configuration. (b) 3-D view of the junction 301

9.10 Dynamics of a *stressed* junction showing configurations at various stress levels: (a) Equilibrium, $\sigma_{11} = 100$ MPa (b) Equilibrium, $\sigma_{11} = 250$ MPa (c) Unstable, $\sigma_{11} = 300MPa$. 303

9.11 (a) Simulated strain-stress curve; (b) Dislocation density vs strain simulated.(Result 1) 305

9.12 (a) Initial simulated microstructure(Result 1); (b) Different colors represent different gliding systems. 306

9.13 Simulated microstructure at time step 450.(Result 1) 306

9.14 Simulated microstructure at time step 1200.(Result 1) 307

9.15 Simulated microstructure at time step 1800.(Result 1) 307

9.16 (a) Simulated strain-stress relation; (b) Dislocation density vs strain.(Result 2) . 308

9.17 Frequency of annihilation vs strain simulated.(Result 2) 308

9.18 Initial simulated microstructure.(Result 2) 309

9.19 Simulated microstructure at time step 500.(Result 2) 309

9.20 Simulated microstructure at time step 750.(Result 2) 310

9.21 Simulated microstructure at time step 1000.(Result 2) 310

9.22 Simulated microstructure at time step 100. Short range interactions of junctions and dipoles are illustrated.(Result 2) 311

9.23 Simulated microstructure at time step 1000. Dislocations are forming into cell structures.(Result 2) 311

9.24 Simulated microstructure at time step 1000. Dislocation tangles are shown in the figure.(Result 2) 312

9.25 (a) Simulated strain-stress relation; (b) dislocation density vs strain.(Result 3) . 313

9.26 Frequency of annihilation vs strain.(Result 3) 313

9.27 Initial simulated microstructure.(Result 3) 314

9.28 Simulated microstructure at time step 250.(Result 3) 314

9.29 Simulated microstructure at time step 500.(Result 3) 315

9.30 Simulated microstructure at time step 750.(Result 3) 315

9.31 Simulated microstructure at time step 1000.(Result 3) 316

9.32 Simulated microstructure at time step 1350.(Result 3) 316

9.33 Simulated microstructure at time step 1000, junctions and dipoles are shown.(Result 3) 317

9.34 Simulated microstructure at time step 1350, dislocations form complex 3D structures.(Result 3) 317

9.35 (a) Simulated strain-stress curve; (b) dislocation density vs strain. (Result 4) . . 318

9.36 Relation of stress to the square-root of the dislocation density, the dashed line is the linear fit from least-square method.(Result 4) 318

9.37 Initial simulated microstructure.(Result 4) 319

9.38 Simulated microstructure at time step 250.(Result 4) 319

9.39 Simulated microstructure at time step 500.(Result 4) 320

9.40 Simulated microstructure at time step 750.(Result 4) 320

9.41 Simulated microstructure at time step 840.(Result 4) 321

9.42 (a) The solid model of the sample, and (b) FEM mesh around the central hole. . 323

9.43 Stereo pair (top) and diffraction pattern demonstrating the modified stereo technique. 324

9.44 Time sequence of in-situ TEM measurements during straining. Time units are - min:sec:sec fraction 325

9.45 3D rendering of experimentally-observed dislocation configurations in the Cu thin foil - (a) before deformation, and (b) after deformation. 326

9.46 Illustration of Lothe's formula to calculate surface image force. 328

9.47 FEM results for normal stress distribution in the sample along the axial direction (y) and its normal (x). 330

9.48 FEM results for σ_{yy} contour around the central hole. 330

9.49 Initial and final dislocation configurations simulated by PDD 331

9.50 Dislocation 22 positions during cross-slip motion: (1) Final configuration without cross-slip, (2) Final configuration with cross-slip 332

9.51 Schematic for the geometry of a 3-D circular dislocation loop near an interface or free surface 342

9.52 Stress components along the z-axis for a circular dislocation loop (see Figure (9.51)) in (a) Al half-space and (b) Al-Ni bi-material. Solid lines represent surface integral results, small square symbols: line integral results, and dashed lines: infinite space solutions. 344

9.53 Image force distribution on an oblong dislocation loop in a thin Al layer on a Cu substrate with an additional aluminum oxide film on top (a) the layer is capped with an Al_2O_3 film of thickness h_c=0.1 h (b), and 1.0 h. 345

9.54 Dislocation motion in a thin layer with h=144 nm under different applied biaxial stress levels (a) $\sigma_a = 210$ MPa $< \sigma_c^{th} = 250$ MPa, and (b) $\sigma_a = 280$ MPa $> \sigma_c^{th} = 250$ MPa. Each line corresponds to a time increment of 0.1 ns. 349

9.55 Dislocation motion in a thin layer with h=10.8 nm under an applied stress $\sigma_a = 1.2$ GPa $> \sigma_c^{th} = 1$ GPa. Each line corresponds to a time increment of 2 ps. . . . 350

9.56 Yield strength of a Ni-Cu layered thin film as a function of the layer thickness. Solid line: Freund's formula , triangles: experimental results , and circles: current simulation results. 351

9.57 Plastic deformation mechanism and strength map for thin layered films. 353

9.58 Experimental stress-strain curves for irradiated and unirradiated Cu. Specimens were irradiated in DR-3 reactor at RISO at 320 K, and tensile tested at 295 and 320 K (Singh, Edwards & Toft 1996). 357

9.59 TEM picture of localized plastic flow emanating form internal inclusions in Cu-CrZr alloy, neutron-irradiated at 320 K to a dose level of 0.3 dpa and fatigue-tested at 320 K with a loading frequency of 0.5 Hz (Singh, Stubbins and Toft 2000a) 358

9.60 Dynamics of F-R source ($\mathbf{b} = \frac{1}{2}[\bar{1}01]$) interaction with a single sessile prismatic interstitial defect cluster very near the glide plane. The cluster has a radius of 50 a, and a Burgers vector of $\mathbf{b} = \frac{1}{2}[110]$ on the (111) glide plane. The cluster is located at (0, -1000 a, 40 a) in the local plane coordinates. Time intervals are: (1) 1 ps, (2) 2.5 ps, (3) 25 ps, (4) 50 ps, (5) 1200 ps. 360

9.61 Dynamics of F-R source interaction with a single sessile prismatic interstitial defect cluster at a farther *stand-off* distance. All conditions are the same as in Fig.9.60, except that the cluster is located at (0, -1000 a, 80 a) in the local plane coordinate, and time intervals are: (1) 1 ps, (2) 2.5 ps, (3) 25 ps, (4) 50 ps, (5) 75 ps. 361

9.62 Dynamics of F-R source interaction with an attractive interstitial defect cluster atmosphere at the *stand-off* distance of 100 a. Clusters have parallel and identical Burgers vectors to the F-R source of $\mathbf{b} = \frac{1}{2}[\bar{1}01]$. The apllied stress, σ_{11} is gradually increased to 200 MPa before the dislocation line breaks free from clusters. 362

9.63 Dynamics of the *symmetric unlocking* mechanism, initiated by small fluctuations in the dislocation line as it passes near the cluster atmosphere. Conditions are the same as in Fig.9.62, except that the clusters are repulsive, and of a Burgers vector $\mathbf{b} = \frac{1}{2}[110]$. 364

9.64 Scaling of the critical shear stress with the stand-off distance for a fixed inter-cluster spacing of 50 a 364

9.65 Scaling of the critical shear stress with the inter-cluster distance for a fixed stand-off distance of 40 a 365

9.66 Propagation of plastic slip emanating from a single Frank-Read source in copper irradiated and tested at 100 ^oC. Displacement damage dose=0.1 dpa, STF's density= $4.5 \times 10^{23} m^{-3}$, size=2.5 nm. Simulated crystal size=4500 a (1.62 μm). Initial F-R source length=1600 a (576 nm). Stress is applied along [100]. "Unzipping" of curved dislocation segments is clear during the initial stages of deformation, where long segments can get "stuck" till they are unzipped by increasing the applied stress. 366

9.67 Spread of plastic slip emanating from two interacting Frank-Read sources in copper irradiated and tested at 100 ^oC. While the simulation conditions are the same in Fig.9.66, the two F-R sources are separated by 20 a (7.2 nm). Significant deformation of the two loops is observed when corresponding segments meet, and a higher stress is required to overcome the additional forces generated by each F-R source on the other one. 368

9.68 The effects of inter-planar F-R source interactions on the flow stress in copper irradiated and tested at 100 ^oC, and a displacement damage dose of 0.1 dpa. Local strain is measured as the fractional area of swept glide planes. 369

9.69 Dose dependence of the increase in flow stress in copper irradiated and tested at 100 ^oC. The displacement damage dose varies in the range 0.001 - 0.1 dpa, and conditions correspond to the experimental data of Singh, Edwards and Toft (2000b). 370

9.70 Comparison between the dose dependence of computed increase in flow stress values and the experimental measurements of Singh, Edwards and Toft (2000b). 371

9.71 A front 3-D view of the glide/ climb mechanism of the jogged dislocation pileup. Note the gradual destruction of SFTs as the pileup develops. 372

9.72 $< 1\bar{1}0 >$ projection for glide/ climb motion of a dislocation loop pileup, consisting of three successive loops. SFT's have been removed for visualization clarity. . . . 373

9.73 3-D view for the formation of dislocation channels on glide planes which have low SFT density, for irradiated copper at a dose of 0.01 dpa. For clarity of visualization, the apparent SFT density has been reduced by a factor of 100. Note that other dislocation segments are inactive as a result of high density of surrounding clusters 374

9.74 Geometry and initial configuration of a dipolar loop and a glide dislocation. (a) relative positions in 3D geometry. (b) representation of the dipolar loop and dislocation in the local coordinate system. 379

9.75 Configuration of the dipolar loop describe in Figure 9.74 under an external shear stress $\tau = 4$ MPa, with full interaction between its segments. The coordinates of the dipolar loop center are (0,30,20). 380

9.76 Distribution of line force per unit length generated on an initially straight dislocation line by a dipolar loop situated at various stand-off distances. The coordinates of the dipolar loop are (0,30,D). (a) The direction of the dislocation is normal to the loop's major axis. (b) The direction of the dislocation is parallel to loop's major axis. 382

9.77 Interaction between a screw dislocation and a mobile dipolar loop under an external shear stress $\tau = 4$MPa. The initial condition of the dipolar loop is the same as that in Figure 9.76. Note that the scale on the axes is different. (a) Relative position of the dipolar loop and configuration of the dislocation at 0.88 ns and 2.83 ns, respectively. (b) Loop position and velocity as functions of time. 383

9.78 Change of position of the dipolar loop as a function of the number of stress cycles.384

9.79 The effect of mutual interaction between two parallel dipolar loops. The stand-off distances are 12 nm and 20 nm, respectively. Both loops have the same Burgers vector $\mathbf{b}=[10\bar{1}]$. (a) Driving force generated by the first dipolar loop on the second. x & y stand for their relative horizontal distance. (b) The same driving force for $y = 0$. The dashed and solid lines stand for the forces of dipolar loop 1 and 2, respectively. 385

9.80 Interaction between a Frank-Read source with an initial screw orientation and two mutually interactive dipolar loops, initially located at(-5,30,24) and (5,30,24), respectively. Both dislocation and dipolar loops have $\mathbf{b}=\frac{1}{2}[10\bar{1}]$. (a) Dislocation configuration at different times (time interval Δt=0.7 ns). (b) Change of position for the two loops as a function of time. 385

9.81 Comparison between the effects of including and excluding the mutual interaction of the two dipolar loops. The two dipolar loops are initially located at(-10,30,24) and (10,20,24) respectively. 386

9.82 The relative configuration of 20 dipolar loops at the end of different cycles: (a)-initial, (b)-5^{th} cycle, (c)-10^{th} cycle, (d)-15^{th} cycle 387

9.83 *trajectory* plot of the dynamics of 20 interacting dipolar loops, driven by an oscillating screw dislocation. 387

11.1 Idealized representation of an side view of prismatic edge dislocation loops comprising a raft 393

11.2 Dislocation structure in Nickel 270 irradiated to a fluence of $3.2\times10^{1}9$ neutron/cm^2 (Stiegler and Bloom 1971). 395

11.3 Primary damage state at 17 ps for a 100 KeV cascade: (◯) interstitials; (•) vacancies. 412

11.4 A close view of the structure of one single cascade at $t = 94$ ps. Small circular loops represent SIA clusters, and solid points represent vacancies. 412

11.5 (a) Center-of-mass trajectories of a SIA cluster migration for 10000 consecutive KMC steps at 300K with a reorientation activation energy ration $f = 0.8$. The unit are in lattice constant. All the straight line segments are oriented along the $\langle 111 \rangle$ directions. (b) Schematic view of the computational box for the KMC simulations. The small circles represent randomly distributed SIA clusters. The Burgers vector directions as well as the normal directions of loop planes are shown as small line segments. 415

11.6 KMC simulation of 200 SIA clusters diffusion in the stress field of a 3-D dislocation loop. SIA loops are clearly observed to accumulate along edge components of the loop. (a) 0 ns; (b) 0.1 ns; (3) 0.3 ns; (d) 0.4 ns. 416

11.7 A TEM micrograph of pure single crystal Mo irradiated with fission neutrons at 320 K to a displacement dose level of 0.16 dpa (Singh, Foreman and Trinkaus 1997). 417

11.8 KMC simulation of SIA cluster diffusion and agglomeration. SIA loops are self-pinned, and rafts are clearly observed as the simulation progresses. 418

11.9 KMC simulation of 200 SIA clusters diffusion and clustering in the stress field of a 3-D dislocation loop. Dislocation decoration and SIA loop $Rafts$ are clearly observed in the circled region in (d). (a) 0 ns; (b) 0.4 ns; (3) 0.7 ns; (d) 1.0 ns. . 420

11.10Centre-of-mass trajectories of a 6-SIA cluster migration for 10000 consecutive steps. 425

11.11SIA cluster densities as a fuction of accumulated dose for bcc iron irradiated at 300 K under cascade irradiation at 5×10^{-8} dpa/s. Simulation results are compared to experimental data from TEM observation of iron irradiated in HFIR ((Eldrup, Singh, Zinkle, Byun and Farrell 2002)). 427

11.12Size distribution of SIA clusters at a dose level of 5.21×10^{-3} dpa. The red slim bar is the number of clusters of a certain size, and the yellow thick bar are the total number of clusters within a certain range of sizes. 428

11.13(a) Local iso-energy contours for the interaction energy of an interstitial cluster of Burgers vector $a/2 < \bar{1}\ 1\ 1 >$ with an edge dislocation on the $< \bar{1}\ \bar{2}\ 1 >$ -plane in bcc iron; (b) local iso-energy contours of the interaction energy of an interstitial defect clusters of Burgers vector $a/2 < \bar{1}\ 1\ 1 >$ with a pre-existing same type cluster and an edge dislocation on the $< \bar{1}\ \bar{2}\ 1 >$ -plane. 429

11.14A snap-shot of the micro-structure of interstitial clusters at 1.3×10^{-3} dpa, where the decoration by interstitial clusters along dislocation line can be clearly seen. . 430

11.15A snap-shot of the micro-structure of interstitial clusters at 5.2×10^{-3} dpa, where the accumulation of glissile interstitial clusters near the dislocation is further intensified. 431

11.16A close view of the configuration of a raft of interstitial clusters formed at dose level of 1.8×10^{-3} dpa. 431

12.1 Illustration of the solution to general crack problem according to Bueckner's Principle. 433

12.2 Distribution of crack dislocation loops of penny-shaped crack under mode-II loading with $\tau/\mu = 0.004$. (a) illustration of local coordinate system. (b) Final distribution of crack dislocations. 436

12.3 Comparisons of the stress component σ_{xz} along y-direction from the final dislocation distribution between current numerical results and analytical results. All the other loading conditions are the same as that in Figure (12.2) (a) The distribution of σ_{xz}. (b) The relative error of σ_{xz}. 437

12.4 Comparisons of relative error of σ_{zz} for penny-shaped crack under external load $\sigma_{zz}/\mu = 0.004$. (a) along radial direction, (b) along the vertical direction from the center 437

12.5 Comparisons of crack opening displacement(COD) with the same condition as in Figure (12.4) except the density of crack dislocation n=18. (a) The COD along diameter. (b) Recover of the crack opening shape in three dimension. 438

12.6 A penny-shaped crack is subjected to a normal stress inside the crack surface with a decreasing gradient. (a) the applied stress. (b) correponding crack opening shape439

12.7 A penny-shaped crack is subjected to a normal stress inside the crack surface with an increasing gradient. (a) the applied stress. (b) crack opening shape . . . 440

12.8 Distribution of crack dislocations of a straight crack under mode-I loading with an applied tension of $\sigma_{zz}/\mu = 0.004$ along the z-direction. (a) the projection view of the crack. (b) Distribution of crack dislocations, the length of the Burgers vector is chosen as $b/r_0 = 7.5 \times 10^{-4}$. (c) The crack shape in three dimension . 441

12.9 Comparison of relative error of σ_{zz}. The same condition as in Figure (12.8) . . . 442

12.10Straight crack under mixed model I & II loading. (a) Crack dislocation distribution. (b) Comparison of the relative error of σ_{zx} with different inclination angle. 442

12.11Interaction of an edge dislocation and a straight crack in 2D. (a) relative position of crack and the edge dislocation, r_0 is the half width of the crack. (b) comparison of the numerical simulation in the stress intensity factor (solid line) with the analytical results (dashed line). 445

12.12Shielding effect of a shear dislocation loop ahead of crack tip. (a) contour of the σ_{33} generated by the loop when its radius R_0 is $0.5d$. (b) comparison of the stress intensity factor for different initial source sizes. 446

12.13Motion of dislocation a half loop ahead of a crack tip in Tungsten single crystal. The initial size of the loop is chosen as 400 a. (a) configuration of the dislocation at different times. (b) the corresponding shielding effects of the dislocation along the crack. 447

12.14Contour of the $\{11\}$ component of the stress tensor from crack tip due to the applied stress and image stress. (a) t=0, (b) t=0.29 ms, (c) t=0.58 ms, (d) t=1.58 ms, (e) t=2.58 ms, (f) t=3.58 ms 448

12.15Motion of dislocation half loop ahead of crack tip. The initial size of the loop is chosen as 40 a. (a) configuration of the dislocation at different times. (b) the corresponding shielding effects of the dislocation on the crack. 449

15.1 Self force calculation of a dislocation loop in anisotropic or isotropic materials. . 492

15.2 The stress field induced by dislocation loops and their interactions. 493

15.3 Image force calculation in multilayers, using line integration method. 494

15.4 Image force calculation in multilayers, using straight line approximation method. 495

15.5 Green's functions and dislocation image force calculation in multilayers, using Green's functions and surface integral method. 496

List of Tables

4.1 Elastic constants C_{11}, C_{12}, & C_{44}, and the anisotropy ratio $A = \frac{2C_{44}}{C_{11}-C12}$ for common metallic crystals 47

5.1 Elastic and lattice constants for Si, Ge, and $Si_{0.85}Ge_{0.15}$ 75

5.2 Comparison of σ_{xx} between Fourier Transform method and Complex Variable Method by averaging errors. 75

7.1 Variables for screw and edge dislocations 159

7.2 Variables for circular shear and prismatic loops 159

8.1 Error Estimation for the stable state of a Frank-Read source. 249

8.2 Error Estimation for an unstable Frank-Read source at $t^* = 5 \times 10^6$. 251

8.3 Error Estimation for Different Integration Schemes. The implicit scheme is chosen as the reference configuration. 251

9.1 Error Estimation for different nodal distributions during junction formation. The configuration with 12 segments for each dislocation is selected as reference. . . . 302

9.2 Schmid factors for the Cu thin foil under simple tension. 324

9.3 Nodal segment distributions on dislocations, with corresponding Burgers vectors ($\boldsymbol{b}$), glide plane Miller indices. All segments are in mixed characters. 329

9.4 Probabilities of cross-slip of screw segments at an applied stresses of 100MPa . . 331

9.5 Schmid factors for the common fcc systems under simple tension. 333

11.1 Migration Energy E_m, lattice constant a, initial cluster radius R, Temperature T, pre-exponential factor ω_0, ratio of migration energy of 1-D motion relative to reorientation energy f, shear modulus μ, and Poisson's ratio ν for BCC Fe. . . 414

11.2 Evolution time for Running 800,000 KMC Steps (in ns). 420

Preface

After a long and cold winter in Germany during the first few months of 1984, I left for England to spend three months working at the Theoretical Physics Division of Harwell, near Oxford. Harwell research laboratories were run by the UK Atomic Energy Authority, and I joined the research group of Ron Bullough as a part of my sabbatical leave from teaching at UCLA. I collaborated with Juan Matthews on the development of a dislocation-based creep model for structural steels. The model was based on rate equations for mobile and immobile dislocations, and growth or shrinkage of dislocation cells inside grains. During the course of this work, I was struck by the fact that dislocation creep is controlled by the average cell size (which is also true for the strength of the material), and that the cell size is inversely proportional to the applied stress with what is known as the Holt constant. Getting further into this story, I examined many TEM micrographs and discovered for myself what many others have already known: that the deformation microstructure is very inhomogeneous and that it is self-organized into dislocation cells, walls, etc. This observation started a long and unfinished journey in an attempt to answer the "why" question. It was strange for me at that time to realize that when an external stress is applied on a material, its dislocation microstructure re-organizes itself into cells with unique average size. It seemed to me that a piece of structural steel is alive in the sense that it changes its internal geometry to best respond to the applied stress just like changes in the geometry of a tree in response to light or gravity. There is something really mysterious about that. After several attempts in developing a statistical description of dislocation densities, I gave up this approach because the statistical mechanics of these objects was not well-understood. I started with Robert Amodeo, my former PhD student, on an entirely different idea to solve this problem, by attempting to develop direct numerical simulations of interacting dislocation ensembles. This led to the emergence of the field of Dislocation Dynamics in our early attempts by late 1986 and early 1987. Since then, tremendous progress has been achieved worldwide in the ability to understand the fundamental nature of plastic deformation in materials. Computer simulations of dislocation dynamics have contributed to a growing body of knowledge in plasticity and deformation at the nano- and micro-scales. Nevertheless, we are still a good distance away from reaching two significant goals: (1) a full understanding of self-organization phenomena in plasticity (e.g. the formation of well-organized dislocation cells, subgrains, Persistent Slip Bands (PSBs), dislocation dipole arrays, etc.), and (2) rigorous connections between microscopic and macroscopic theories of plasticity. In this report, we compile details of efforts, mainly at UCLA during the past 15 years or so, on the development of computational methods of dislocation dynamics. It is intended as a "practitioner's manual" rather than a succinct book. Thus, this report contains many details that miss the compact publication standards of scientific journals. It also contains details of

the computer programming that are in use in our group at UCLA in this area.

This report is based on the work of many of my former students and post doctoral fellows: Robert Amodeo, Anter Elazab, Lizhi Sun, Marco Baccaloni, Jianming Huang, Zhiqiang Wang, Ming Wen, Qiyang Hu, Xueli Han, Silvester Noronha, and Suavik Banerjee. I acknowledge their valuable contributions to the progress of research in this area over the years. The following is a list of publications from which I drew the majority of the contents for this manual.

1. R. J. Amodeo and N. M. Ghoniem, "Dynamical Computer Simulation of the Evolution of a One-Dimensional Dislocation Pileup," *Int. J. Eng. Sci.,* **26**:653-662, 1988.

2. R. J. Amodeo and N. M. Ghoniem, "A Review of Experimental Observations and Theoretical Models of Dislocation Cells and Subgrains," *Res Mechanica,* **23**:137-160, 1988.

3. N. M. Ghoniem, "Determination of the Bias Factor by the Moments Solution to to the Fokker-Planck Equation," *J. Nucl. Mater.,* **155-157**:1123-1127, 1988.

4. N. M. Ghoniem and R. Amodeo, "Computer Simulation of Dislocation Pattern Formation," *Solid State Phenomena*, **3&4**:377-388, 1988.

5. D. Walgraef and N. M. Ghoniem, "Spatial Instabilities and Dislocation Loop Ordering in Irradiated Materials," *Phys. Rev.* **B39**:8867-8872, 1989.

6. N. M. Ghoniem, "Stochastic Theory of Diffusional Planar Atomic Clustering and Its Application to Dislocation Loops," *Phys. Rev.* **B39**:11810-11819, 1989.

7. N. M. Ghoniem, J. R. Matthews, and R. J. Amodeo, "A Dislocation Model for Creep in Engineering Materials," *Res Mechanica,* **29**:197-219, 1990.

8. R. J. Amodeo and N. M. Ghoniem, "Dislocation Dynamics: Part I-A Proposed Methodology for Deformation Micromechanics," *Phys. Rev.*, **B41**:6958-6967, 1990.

9. R. J. Amodeo and N. M. Ghoniem, "Dislocation Dynamics: Part II-Applications to the Formation of Persistent Slip Bands, Planar Arrays, and Dislocation Cells," *Phys. Rev.*, **B41**:6968-6976, 1990.

10. N. M. Ghoniem and R. J. Amodeo, "Numerical Simulation of Dislocation Patterns During Plastic Deformation," in *Patterns, Defects and Materials Instabilities,* D. Walgraef and N. M. Ghoniem, Eds., Applied Sciences, Series E, **183**, NATO ASI Series (Kluwer, The Netherlands, 1990) pp. 303-329.

11. R.J. Amodeo, N.M. Ghoniem, "Rapid Algorithms for Dislocation Dynamics in Micromechanical Calculations," *Modeling of Deformation of Crystalline Solids,* T. Lowe, T. Rollett, P. Follansbee, and G. Daehn, Eds., TMS Press, 1991, pp. 125-143.

12. N.M. Ghoniem, "Non-Linear Dynamics of Shear Crack Interaction with Dislocations," *Non-Linear Phenomena in Material Science II,* L. Kubin and G. Martin, Eds., Kluwer Academic Publishers, 1992.

13. N.M. Ghoniem and D. Walgraef,"Evolution dynamics of 3-D Periodic Microstructures in Irradiated Materials,", *Modeling in Materials Science and Engineering*, 1, 1993, pp. 569-590.

14. A. Elazab and N.M. Ghoniem,"Green's function for the Elastic Field of an Edge Dislocation in a Finite Anisotropic Medium,"*Int. Journ. Fracture Mech.,* **61**, 1993, pp. 17-37.

15. D. Walgraef and N.M. Ghoniem, "Non-linear Dynamics of Self-organized Microstructures Under Irradiation,"*Phys. Rev. B,* **52,6** 3951-3962, 1995.

16. D. Walgraef, J. Lauzeral, and N.M. Ghoniem, "Theory and Simulations of Defect Ordering in Irradiated Materials,", *Phys. Rev. B*, 53,20: 14782-14794, 1996.

17. D. Walgraef, N.M. Ghoniem, and J. Lauzeral, "Deformation Patterns in Thin Films Under Uniform Laser Irradiation,"*Phys. Rev. B, 56,* **No. 23**: 15361-15377 (1997).

18. Lauzeral, D. Walgraef, and N.M. Ghoniem, "Rose Deformation Patterns in Thin films Irradiated By Focused Laser Beams,"*Phys. Rev. Lett.* **79, No. 14**: 2706-2709 (1997).

19. H. Huang, N.M. Ghoniem, T. Diaz de la Rubia, M. Rhee, H. Zbib and J. Hirth, "Stability Of Dislocation Short-Range Reactions In BCC Crystals,"*J. Eng. Mat. & Tech.,* **121(2)**: 143 (1999).

20. N.M. Ghoniem, "Curved Parametric Segments For The Stress Field Of 3-D Dislocation Loops,"*J. Eng. Mat. & Tech.,* **121(2)**: 136 (1999).

21. N. M. Ghoniem, L. Sun, "Fast Sum Method for the Elastic Field of 3-D Dislocation Ensembles,"*Phys. Rev. B,* **60(1)**: 128-140 (1999).

22. N.M. Ghoniem, B. N. Singh, L. Z. Sun, and T. Diaz de la Rubia, "Interaction and Accumulation of Glissile defect Clusters Near Dislocations,"*J. Nucl. Mater,* **276**: 166-177 (2000).

23. N.M. Ghoniem, S.- H. Tong, and L. Z. Sun , "Parametric Dislocation Dynamics: A Thermodynamics-based Approach to Investigations of Mesoscopic Plastic Deformation,"*Phys. Rev. B,* **139(1)**: 913-927 (2000).

24. L. Sun, N.M. Ghoniem, and B.N. Singh, "3-D Dislocation Dynamics Study of Plastic Instability In Irradiated Copper,"*J. Nucl. Mater.,* **283**:741(2000).

25. L.Z. Sun, N.M. Ghoniem, and Z.Q. Wang, "Analytical and Numerical Determination of the Elastic Interaction Energy between Glissile Dislocations and Stacking Fault Tetrahedra in FCC Metals", *J. Mat. Sci. & Engr.*, **A309-310**:178183 (2001).

26. N.M. Ghoniem, S.H. Tong, B.N. Singh, and L.Z. Sun, "On Dislocation Interaction with Radiation-induced Defect Clusters and Plastic Flow Localization in FCC Metals", *Phil. Mag. A*, **81 (11)**:, 2743-2764 (2001).

27. N.M. Ghoniem, J.M. Huang, and Z.Q. Wang, "Affine Covariant-contravariant Vector Forms for the Elastic Field of Parametric Dislocations in Isotropic Crystals," *Phil. Mag. Lett.*, **82(2)**: 55-63 (2002).

28. N.M. Ghoniem and J.M. Huang, "Computer Simulations of Mesoscopic Plastic Deformation with Differential Geometric Forms for the Elastic Field of Parametric Dislocations: Review of Recent Progress,"Invited Paper at the 5th Euro-Conference on Mechanics of Materials, Delft, Netherlands, March 6-9, 2001, Also *J. de Physique IV*, **11(5)**:53-60 (2001).

29. D. Walgraef and N.M. Ghoniem, "The Effects of Crystal Anisotropy and Adherence Forces on Laser Induced Deformation Patterns in Thin Films," *Phys. Rev. B*, **65** 1555304-1 to 1555304-10 (2001).

30. N.M. Ghoniem,D. Walgraef and S. J. Zinkle, "Theory and Experiment of Nanostructure Self-organization in Irradiated Materials,"Invited Perspective Article, *J. Comp. Aided Mat. Design*, **8**:1-38 (2002).

31. Jianming Huang and Nasr M. Ghoniem, "The Dynamics of Dislocation Interaction with Sessile Self-Interstitial Atom(SIA) Defect Cluster Atmospheres,", *J. Comp. Mat. Science*,**23**:225234 (2002).

32. R. Martinez and N. M. Ghoniem, "The Infuence of Crystal Surfaces on Dislocation Interactions in Mesoscopic Plasticity: A Combined Dislocation Dynamics- Finite Element Approach,", *J. Comp. Meth. Engr. Science, CMES*, **3(2)**:229-243 (2002).

33. Nasr M. Ghoniem and Kyeongjae Cho, "The Emerging Role of Multiscale Modeling in Nano- and Micro-mechanics of Materials," *J. Comp. Meth. Engr. Science, CMES,* **3(2)**:147-173 (2002).

34. N. M. Ghoniem, S.H. Tong, J. Huang, B.N. Singh, and M. Wen, "Mechanisms of Dislocation-Defect Interactions in Irradiated Metals Investigated by Computer Simulations," *J. Nucl. Mater.*, **307311**: 843851 (2002).

35. B.N. Singh, N.M. Ghoniem and H. Trinkaus, "Experiment-Based Modelling of Hardening and Localized Plasticity in Metals Irradiated Under Cascade Damage Conditions," *J. Nucl. Mater.*, **307311**:159170 (2002).

36. Jianming Huang and Nasr M. Ghoniem, "Accuracy & Convergence of Parametric Dislocation Dynamics (PDD)," *Mod. Sim. Mat. Sci. Engr.,* **10**:1-19 (2002).

37. X. Han, N.M. Ghoniem and Z. Wang, "Parametric Dislocation Dynamics of Anisotropic Crystalline Materials," *Phil. Mag. A.*, Vol. 83, Nos. 3134, 37053721, (2003).

38. D.Walgraef and N.M.Ghoniem, "The Effects of Glissile Interstitial Clusters on Microstructure Self-organization in Irradiated Materials," *Phys. Rev. B*, **67**, 0641XX (2003).

39. Nasr M. Ghoniem, Hanchen Huang, Esteban Busso, and Nicolas Kioussis, "Multiscale Modeling of Nano- and Micro-Mechanics: an Overview," *Phil. Mag.*, Vol. 83, Nos. 3134, 34753528, (2003).

40. J. Huang, N.M. Ghoniem, and J. Kratochvil "On the Sweeping Mechanism of Dipolar Dislocation Loops Under Fatigue Conditions,", *Mod. Sim. Mat. Sci. Engr.,* **in Press** (2004).

41. S.J. Noronha, J. Huang, and N.M. Ghoniem, "Multiscale modeling of the brittle to ductile transition," *J. Nucl. Mater.*, **in Press** (2004).

42. Z. Wang, Nasr m. Ghoniem, and Richard LeSar, "Multipole Representation of the Elastic Field of Dislocation Ensembles," *Phys. Rev. B,* **In Press** (2004).

43. Ming Wen, Nasr M. Ghoniem, and B. Singh, "Dislocation Decoration and Raft Formation in Irradiated Materials, " *Phys. Rev. B,* **Submitted** (2004).

44. Nasr M. Ghoniem and Xueli Han, "Plasticity and Strength of Anisotropic Nano-layered Materials," *Phys. Rev. B,* **Submitted** (2004).

45. Xueli Han and Nasr M. Ghoniem, "Stress Field and Interaction Forces of Dislocations in Anisotropic Multilayer Thin Films,",*Phil Mag.* **Submitted** (2004).

Nasr M. Ghoniem

University of California, Los Angeles
Los Angeles, California 90095
USA

Chapter 1

Introduction

A fundamental description of plastic deformation has been recently pursued in many parts of the world as a result of dissatisfaction with the limitations of continuum plasticity theory. Although continuum models of plastic deformation are extensively used in engineering practice, their range of application is limited by the underlying database. The reliability of continuum plasticity descriptions is dependent on the accuracy and range of available experimental data. Under complex loading situations, however, the database is often hard to establish. Moreover, the lack of a characteristic length scale in continuum plasticity makes it difficult to predict the occurrence of critical localized deformation zones. Although homogenization methods have played a significant role in determining the elastic properties of new materials from their constituents (e.g. composite materials), the same methods have failed to describe plasticity. It is widely appreciated that plastic strain is fundamentally heterogenous, displaying high strains concentrated in small material volumes, with virtually un-deformed regions in-between. Experimental observations consistently show that plastic deformation is heterogeneous at all length-scales. Depending on the deformation mode, heterogeneous dislocation structures appear with definitive wavelengths. A satisfactory description of realistic dislocation patterning and strain localization has been rather elusive. Attempts aimed at this question have been based on statistical mechanics, reaction-diffusion dynamics, or the theory of phase transitions. Much of the efforts have aimed at clarifying the fundamental origins of inhomogeneous plastic deformation. On the other hand, engineering descriptions of plasticity have relied on experimentally verified constitutive equations.

At the macroscopic level, shear bands are known to localize plastic strain, leading to material failure. At smaller length scales, dislocation distributions are mostly heterogeneous in deformed materials, leading to the formation of a number of strain patterns. Generally, dislocation patterns are thought to be associated with energy minimization of the deforming material, and manifest themselves as regions of high dislocation density separated by zones of virtually un-deformed material. Dislocation-rich regions are zones of facilitated deformation, while dislocation poor regions are hard spots in the material, where plastic deformation does not occur. Dislocation structures, such as Persistent slip Bands (PSB's), planar arrays, dislocation cells, and sub-grains, are experimentally observed in metals under both cyclic and steady deformation

conditions. Persistent slip bands are formed under cyclic deformation conditions, and have been mostly observed in copper and copper alloys. They appear as sets of parallel walls composed of dislocation dipoles, separated by dislocation-free regions. The length dimension of the wall is orthogonal to the direction of dislocation glide.

Dislocation planar arrays are formed under monotonic stress deformation conditions, and are composed of parallel sets of dislocation dipoles. While PSB's are found to be aligned in planes with normal parallel to the direction of the critical resolved shear stress, planar arrays are aligned in the perpendicular direction. Dislocation cell structures, on the other hand, are honeycomb configurations in which the walls have high dislocation density, while the cell interiors have low dislocation density. Cells can be formed under both monotonic and cyclic deformation conditions. However, dislocation cells under cyclic deformation tend to appear after many cycles. Direct experimental observations of these structures have been reported for many materials.

Two of the most fascinating features of micro-scale plasticity are the spontaneous formation of dislocation patterns, and the highly intermittent and spatially localized nature of plastic flow. Dislocation patterns consist of alternating dislocation rich and dislocation poor regions usually in the μm range (e.g. dislocation cells, sub-grains, bundles, veins, walls, and channels). On the other hand, the local values of strain rates associated with intermittent dislocation avalanches are estimated to be on the order of 1-10 million times greater than externally imposed strain rates. Understanding the collective behavior of defects is important because it provides a fundamental understanding of failure phenomena (e.g. fatigue and fracture). It will also shed light on the physics of elf-organization and the behavior of critical-state systems (e.g. avalanches, percolation, etc.)

Because the internal geometry of deforming crystals is very complex, a physically-based description of plastic deformation can be very challenging. The topological complexity is manifest in the existence of dislocation structures within otherwise perfect atomic arrangements. Dislocation loops delineate regions where large atomic displacements are encountered. As a result, long-range elastic fields are set up in response to such large, localized atomic displacements. As the external load is maintained, the material deforms plastically by generating more dislocations. Thus, macroscopically observed plastic deformation is a consequence of dislocation generation and motion. A closer examination of atomic positions associated with dislocations shows that large displacements are confined only to a small region around the dislocation line (i.e. *the dislocation core*). The majority of the displacement field can be conveniently described as elastic deformation. Even though one utilizes the concept of dislocation distributions to account for large displacements close to dislocation lines, a physically-based plasticity theory can paradoxically be based on the theory of elasticity!

Studies of the mechanical behavior of materials at a length scale larger than what can be handled by direct atomistic simulations, and smaller than what allows macroscopic continuum averaging represent particular difficulties. When the mechanical behavior is dominated by microstructure heterogeneity, the mechanics problem can be greatly simplified if all atomic degrees of freedom were adiabatically eliminated, and only those associated with defects are retained. Because the motion of all atoms in the material is not relevant, and only atoms

around defects determine the mechanical properties, one can just follow material regions around defects. Since the density of defects is many orders of magnitude smaller than the atomic density, two useful results emerge. First, defect interactions can be accurately described by long-range elastic forces transmitted through the atomic lattice. Second, the number of degrees of freedom required to describe their topological evolution is many orders of magnitude smaller than those associated with atoms. These observations have been instrumental in the emergence of meso-mechanics on the basis of defect interactions by Eshelby, Kröner, Kossevich, Mura and others. Thanks to many computational advances during the past two decades, the field has steadily moved from conceptual theory to practical applications. While early research in defect mechanics focused on the nature of the elastic field arising from defects in materials, recent computational modelling has shifted the emphasis on defect ensemble evolution.

Although the theoretical foundations of dislocation theory are well-established, efficient computational methods are still in a state of development. Other than a few cases of perfect symmetry and special conditions, the elastic field of 3-D dislocations of arbitrary geometry is not analytically available. The field of dislocation ensembles is likewise analytically unattainable. A relatively recent approach to investigating the fundamental aspects of plastic deformation is based on direct numerical simulation of the interaction and motion of dislocations. This approach, which is commonly known as Dislocation Dynamics (DD), was first introduced for 2-D straight, infinitely long dislocation distributions, and then later for complex 3-D microstructure. In DD simulations of plastic deformation, the computational effort per time-step is proportional to the square of the number of interacting segments, because of the long-range stress field associated with dislocation lines. The computational requirements for 3-D simulations of plastic deformation of even single crystals are thus very challenging.

The study of dislocation configurations at short-range can be quite complex, because of large deformations and reconfiguration of dislocation lines during their interaction. Thus, adaptive grid generation methods and more refined treatments of self-forces have been found to be necessary. In some special cases, however, simpler topological configurations are encountered. For example, long straight dislocation segments are experimentally observed in materials with high Peierls potential barriers (e.g. covalent materials), or when large mobility differences between screw and edge components exist (e.g. some bcc crystals at low temperature). Under conditions conducive to glide of small prismatic loops on glide cylinders, or the uniform expansion of nearly circular loops, changes in the loop *shape* is nearly minimal during its motion. Also, helical loops of nearly constant radius are sometimes observed in quenched or irradiated materials under the influence of point defect fluxes. It is clear that, depending on the particular application and physical situation, one would be interested in a flexible method which can capture the essential physics at a reasonable computational cost. A consequence of the long-range nature of the dislocation elastic field is that the computational effort per time step is proportional to the square of the number of interacting segments. It is therefore advantageous to reduce the number of interacting segments within a given computer simulation, or to develop more efficient approaches to computations of the long range field.

While continuum approaches to constitutive models are limited to the underlying experimental data-base, DD methods offer new directions for modeling microstructure evolution from

fundamental principles. The limitation to the method presented here is mainly computational, and much effort is needed to overcome several difficulties. First, the length and time scales represented by the present method are still short of many experimental observations, and methods of rigorous extensions are still needed. Second, the boundary conditions of real crystals are more complicated, especially when external and internal surfaces are to be accounted for. Thus, the present approach does not take into account large lattice rotations, and finite deformation of the underlying crystal, which may be important for explanation of certain scale effects on plastic deformation. And finally, a much expanded effort is needed to bridge the gap between atomistic calculations of dislocation properties on the one hand, and continuum mechanics formulations on the other. Nevertheless, with all of these limitations, the DD approach is worth pursuing, because it opens up new possibilities for linking the fundamental nature of the microstructure with realistic material deformation conditions. It can thus provide an additional tool to both theoretical and experimental investigations of plasticity and failure of materials.

Two main approaches have been advanced to model the mechanical behavior in this *meso* length scale. The first is based on statistical mechanics methods. In these developments, evolution equations for statistical averages (and possibly for higher moments) are to be solved for a complete description of the deformation problem. The main challenge in this regard is that, unlike the situation encountered in the development of the kinetic theory of gases, the topology of interacting dislocations within the system must be included. The second approach, commonly known as Dislocation Dynamics (DD), was initially motivated by the need to understand the origins of heterogeneous plasticity and pattern formation. An early variant of this approach (the cellular automata) was first developed by (Lepinoux and Kubin 1987), and that was followed by the proposal of DD (Ghoniem and Amodeo 1988, Amodeo and Ghoniem 1990b, Amodeo and Ghoniem 1990a). In these early efforts, dislocation ensembles were modelled as infinitely long and straight in an isotropic infinite elastic medium. The method was further expanded by a number of researchers, with applications demonstrating simplified features of deformation microstructure.

Since it was first introduced in the mid-eighties independently by Lepinoux and Kubin, and by Ghoniem and Amodeo, Dislocation Dynamics (DD) has now become an important computer simulation tool for the description of plastic deformation at the micro- and meso-scales (i.e. the size range of a fraction of a micron to tens of microns). The method is based on a hierarchy of approximations that enable the solution of relevant problems with today's computational resources.

In its early versions, the collective behavior of dislocation ensembles was determined by direct numerical simulations of the interactions between infinitely long, straight dislocations (Wang and LeSar 1995). Recently, several research groups extended the DD methodology to the more physical, yet considerably more complex 3-D simulations. The method can be traced back to the concepts of internal stress fields and configurational forces. The more recent development of 3-D lattice dislocation dynamics by Kubin and co-workers has resulted in greater confidence in the ability of DD to simulate more complex deformation microstructure (Kubin, Canova, Condat, Devincre, Pontikis and Brechet 1992, Canova, Brechet and Kubin 1992, Devincre and Kubin 1994a). More rigorous formulations of 3-D DD have contributed to its rapid development

and applications in many systems (Hirth, Rhee and Zbib 1996, Schwarz and Tersoff 1996, Zbib, Rhee and Hirth 1998, Rhee, Zbib, Hirth, Huang and Diaz de la Rubia 1998, Ghoniem and Sun 1999b, Ghoniem, Tong and Sun 2000a, Ghoniem, Huang and Wang 2001). We can classify the computational methods of DD into the following categories:

1. The Parametric Method: The dislocation loop can be geometrically represented as a continuous (to second derivative) composite space curve. This has two advantages: (1) there is no abrupt variation or singularities associated with the self-force at the joining nodes in between segments, (2) very drastic variations in dislocation curvature can be easily handled without excessive re-meshing. Other approximation methods have been developed by a number of groups. These approaches differ mainly in the representation of dislocation loop geometry, the manner by which the elastic field and self energies are calculated, and some additional details related to how boundary and interface conditions are handled. The suitability of each method is determined by the required level of accuracy and resolution in a given application. dislocation loops are divided into contiguous segments represented by parametric space curves.

2. The Lattice Method: Straight dislocation segments (either pure screw or edge in the earliest versions , or of a mixed character in more recent versions) are allowed to jump on specific lattice sites and orientations. The method is computationally fast, but gives coarse resolution of dislocation interactions.

3. The Force Method: Straight dislocation segments of mixed character in the are moved in a rigid body fashion along the normal to their mid-points, but they are not tied to an underlying spatial lattice or grid. The advantage of this method is that the explicit information on the elastic field is not necessary, since closed-form solutions for the interaction forces are directly used.

4. The Differential Stress Method: This is based on calculations of the stress field of a differential straight line element on the dislocation. Using numerical integration, Peach-Koehler forces on all other segments are determined . The Brown procedure (Brown 1967) is then utilized to remove the singularities associated with the self force calculation.

5. The Phase Field Microelasticity Method : This method is based on the reciprocal space theory of the strain in an arbitrary elastically homogeneous system of misfitting coherent inclusions embedded into the parent phase . Thus, consideration of individual segments of all dislocation lines is not required. Instead, the temporal and spatial evolution of several density function profiles (fields) are obtained by solving continuum equations in Fourier space (Wang, Jin, Cuitino and Khachaturyan 2001).

Chapter 2

Experimental Observations

2.1 Basic Dislocation Structures

One of the most important experimental observations is the direct experimental confirmation of the Frank-Read mechanism by Transmission Electron Microscopy (TEM). Figures 2.1 and 2.2 show TEM observations of the operation of Frank Read sources in Silicon, where several loops emitted from the source are shown. Frank-Read sources can result in a substantial increase in the local dislocation density, once activated. Activation of these sources requires a local region of high stress, for example, near a grain boundary, as can be seen in Figure 2.3.

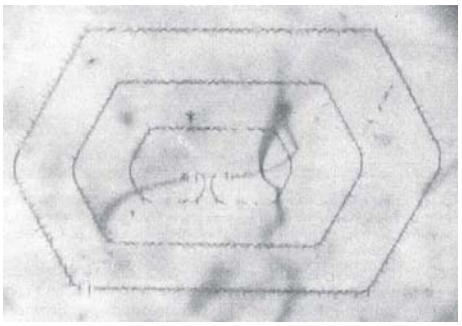

Figure 2.1: Frank-Read source in silicon. Courtesy of Dash

Amelincx has used etch-pit and crystal growth techniques to capture the helical operation of a dislocation spiral, as shown in Figure 2.4.

Dislocation planar arrays are formed under monotonic stress deformation conditions, and are composed of parallel sets of dislocation dipoles, as shown in Figures 2.5, 2.6, and 2.7. While PSB's are found to be aligned in planes with normal parallel to the direction of the critical resolved shear stress, planar arrays are aligned in the perpendicular direction.

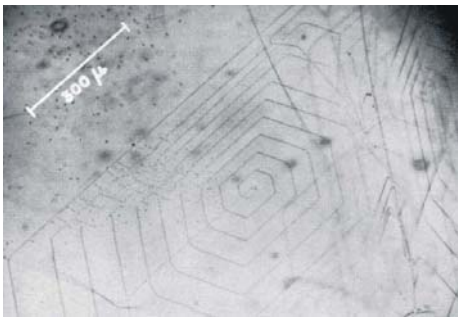

Figure 2.2: Frank-Read source in Si. Courtesy of Dash

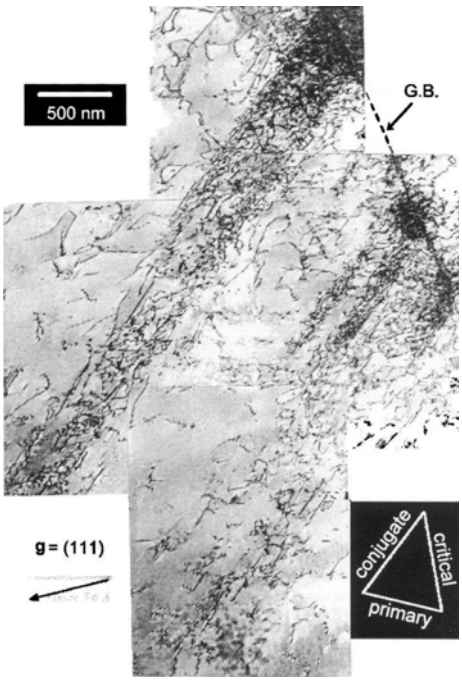

Figure 2.3: Intense shear bands (ISBs) form preferentially at grain boundaries (G.B) and grow into the crystal. The ISBs are first observed at the onset of the cyclic softening. Tht picture shows Cu-30%Zn cycled to $\varepsilon = 3.4 \times 10^{-3}$.

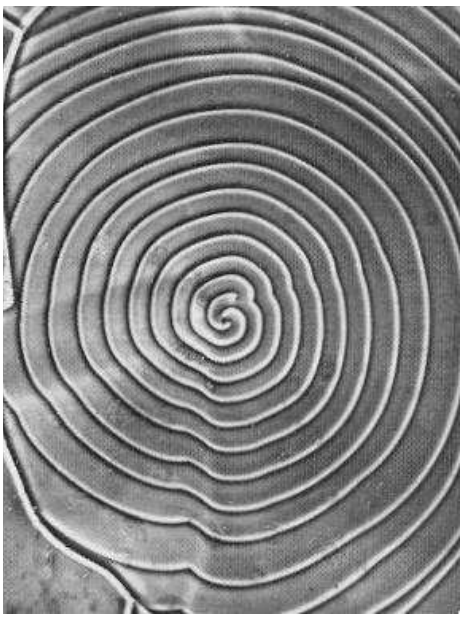

Figure 2.4: Dislocation Spiral. Courtesy of Amelincx

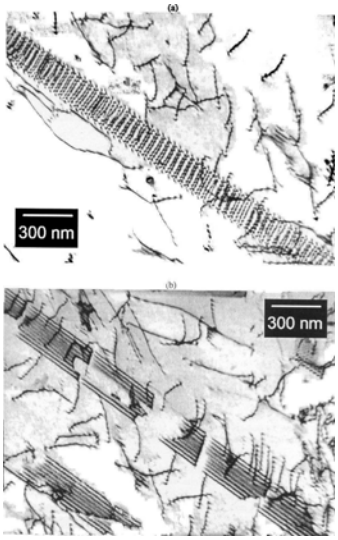

Figure 2.5: Two apparently different types of dipole arrays are observed in Cu-30%Zn. (a) The array marked with A is a regularly spaced array of dipoles. (b) The array marked with B appears to be a stacking fault band (Courtesy Riso National Laboratory in Roskilde, Denmark).

Figure 2.6: Dislocation dipole arrays. Courtesy of Neuhauser

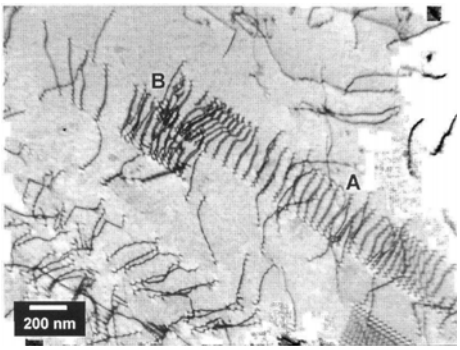

Figure 2.7: Considerable variations of the dipole spacing is found even within the same crystal grain. The figure shows a dipole array, marked with an A. The measured dipole spacing is approximately 650 Å. An interaction between two arrays is seen at B

2.2 Inhomogeneous Plastic Deformation

Plastic deformation of materials has been observed to be heterogeneous at several length scales. At the macroscopic level, shear bands are known to localize plastic strain, leading to material failure. At smaller length scales, dislocation distributions are mostly heterogeneous in deformed materials, leading to the formation of a number of strain patterns ((?), (?) - (?)). Generally, dislocation patterns are thought to be associated with energy minimization of the deforming material, and manifest themselves as regions of high dislocation density separated by zones of virtually un-deformed material. Dislocation-rich regions are zones of facilitated deformation, while dislocation poor regions are hard spots in the material, where plastic deformation does not occur. Typical microstructure under fatigue conditions of Cu is shown in Figure 2.8, where bands of dislocations are shown separated by regions of low dislocation densities. During early stages of deformation, plastic slip is localized in "planar" regions, separated by dislocation-free zones, as can be seen in Figure 2.9. Dislocation structures, such as Persistent slip Bands (PSB's), planar arrays, dislocation cells, and sub-grains, are experimentally observed in metals under both cyclic and steady deformation conditions (?). Observed at lower magnification, dislocation structures form inside grains of the material, and are distributed as shown in Figure 2.10.

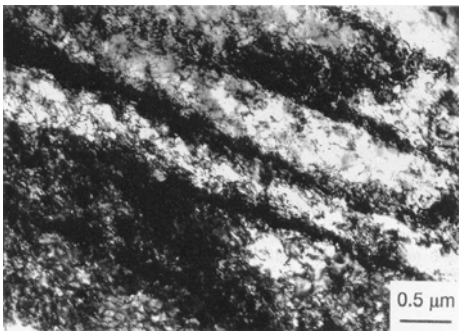

Figure 2.8: Fatigue-tested Cu at a stress amplitude of 80 MPa (N(f) = 515928) showing bands of dislocations

Dislocation cell structures, are honycomb configurations in which the walls have high dislocation density, while the cell interiors have low dislocation density. An example of the experimental observations of dislocation cells is shown in Figure 2.11, while a schematic illustration of cell evolution from the work of Takeuchi and Argon (?) is illustrated in Figure 2.12. Cells can be formed under both monotonic (?), (?) and cyclic (?) deformation conditions. However, dislocation cells under cyclic deformation tend to appear after many cycles, as shown in Figure ??.

Persistent slip bands are formed under cyclic deformation conditions, and have been mostly observed in copper and copper alloys (?), (?), (?). They appear as sets of parallel walls composed of dislocation dipoles, separated by dislocation-free regions. The length dimension

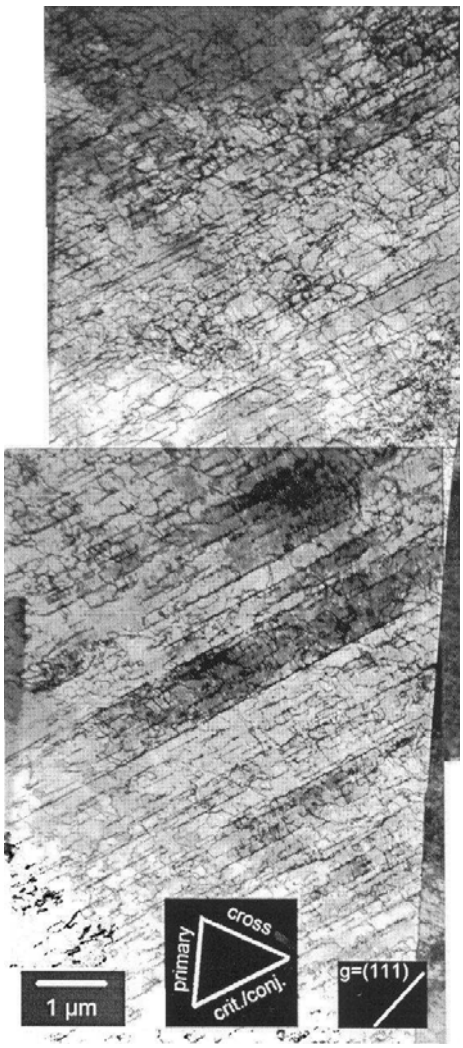

Figure 2.9: A fairly uniform structure of planar dislocation arrays are seen after completion of cyclic softening. No dipole arrays were found at this stage. The picture shows Cu-30%Zn cycled to $\varepsilon = 3.4 \times 10^{-3}$. The polycrystal is found to contain a fairly uniform structure of planar dislocation arrays

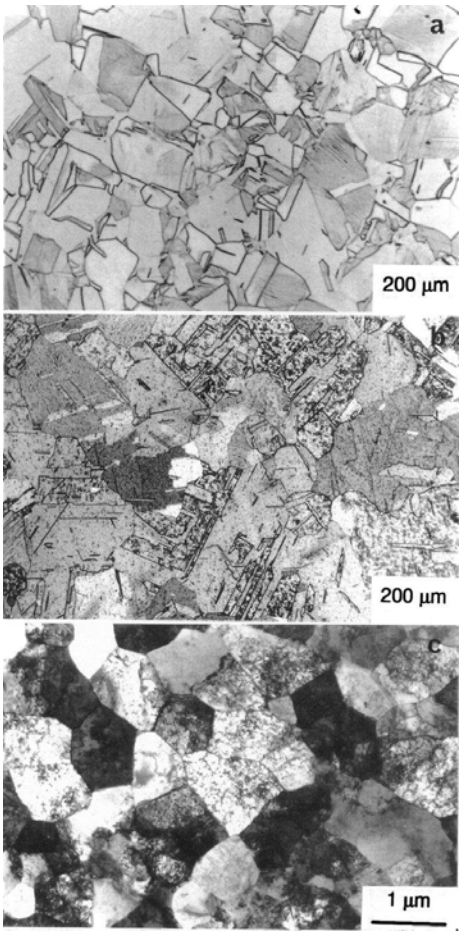

Figure 2.10: Microstructure of the unirradiated copper and copper alloys.(a) OFHC-Cu (annealed at 550 degrees C for 2h), (b) CuCrZr (prime aged) and (c) CuAl-25 (as-wrought).

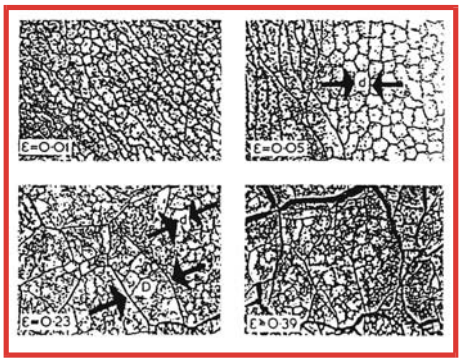

Figure 2.11: Dislocation cell structure in Iron. Picture adapted from the work of Reppich (?)

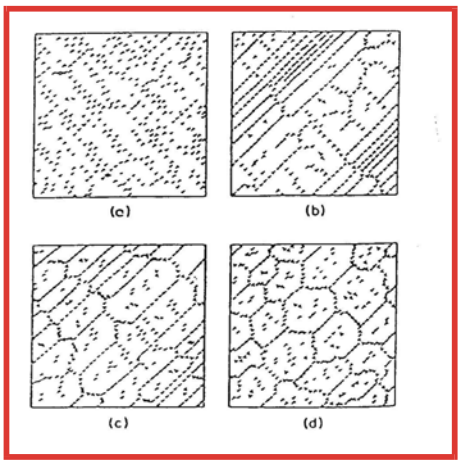

Figure 2.12: Schematic of Dislocation cell structure evolution. Picture adapted from the work of Takeuchi and Argon.

(?)

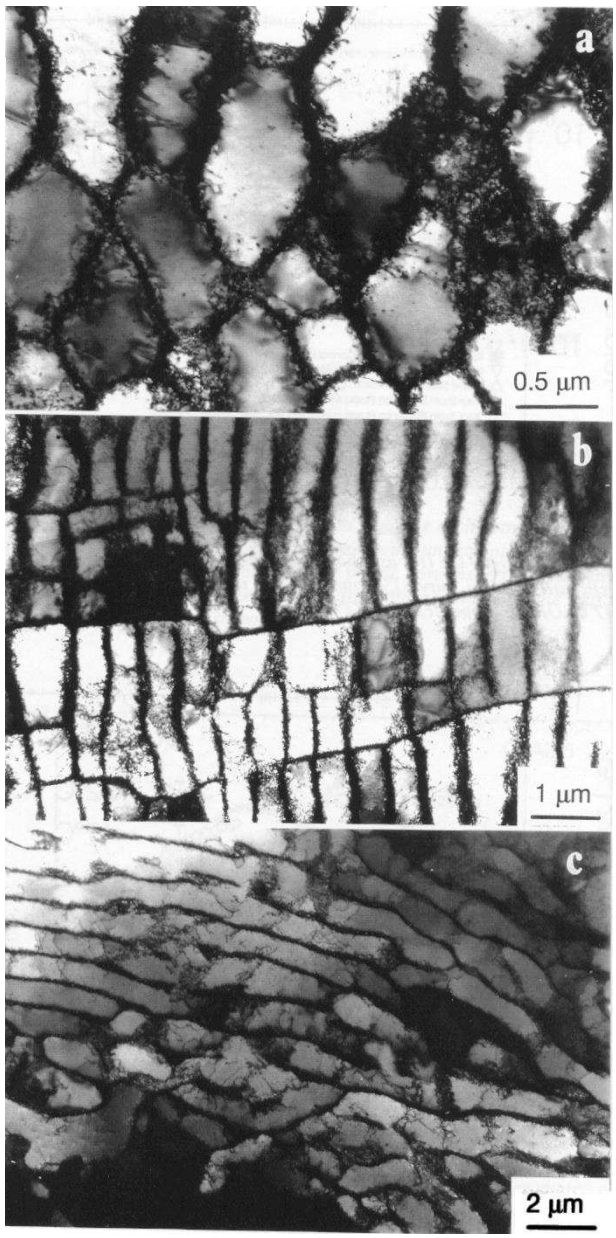

Figure 2.13: Post-fatigue microstructure of unirradiated OFHC-Cu tested at room temperature showing formation of equiaxed and elongated cells: (a,b) 180 MPa, N(f) = 1121, (c) 120 MPa, N(f) = 21646.(Courtesy Riso National Laboratory in Roskilde, Denmark)

of the wall is orthogonal to the direction of dislocation glide. Figures 2.14 and 2.15 show TEM picture of experimental observations of PSB's.

Figure 2.14: Transmission microscopy picture of Persistent Slip Bands (PSB's) in cyclically-deformed copper. Picture adapted from the work of Essman and Mughrabi (?)

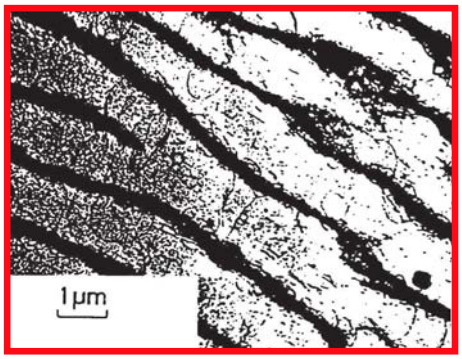

Figure 2.15: Transmission microscopy picture of Persistent Slip Bands (PSB's) in cyclically-deformed copper. Picture adapted from the work of Essman and Mughrabi (?)

In irradiated materials, the interaction of energetic neutrons with lattice atoms produces small interstitial atom clusters that migrate rapidly in response to the internal stress field of dislocations. They form what is known as "decorations" around dislocations, as shown in Figure 2.16, with the effect that dislocations become locked-in with reduced mobility or they become totally immobile. Once an external stress is applied, areas of stress concentrations or where dislocations can move start to respond to the stress. The strain is thus very localized, and confined only to what is known as dislocation channels, as can be seen in Figures 2.17 and 2.18.

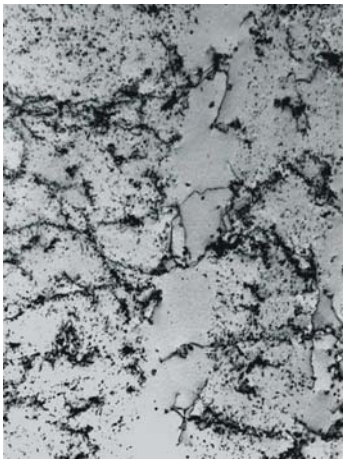

Figure 2.16: Self-interstitial Atom (SIA) decorations of dislocations in irradiated Cu. Courtesy of Singh

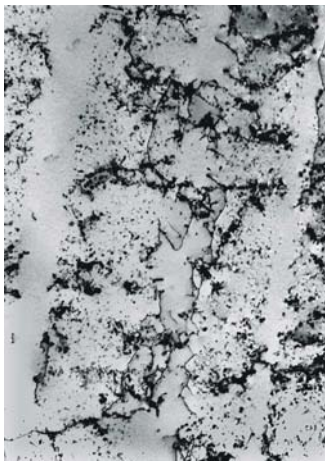

Figure 2.17: Dislocation channels in irradiated Cu. Courtesy of Singh

Figure 2.18: Dislocation channels in irradiated Cu. Courtesy of Singh.

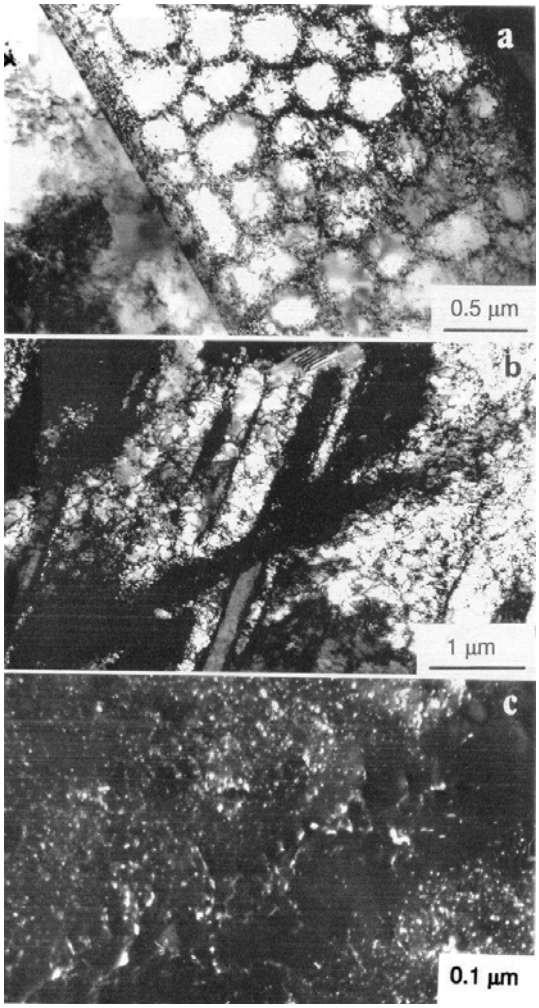

Figure 2.19: Post-fatigue microstructure of the OFHC-Cu irradiated at 47 °C to 0.5 dpa and tested at room temperature at a stress amplitude of 250 MPa (N(f) = 32) showing significant area to area variations: (a) small cells with loose dislocation walls, (b) slip bands, and (c) "cleared" channels. Note the lack of dislocation generation in the regions away from the cleared channel (c).

Chapter 3

Geometry of Defects

3.1 Topological Defects

Defects in crystals may usually be related to the local lack of atomic ordering. Let us describe the various types of defects encountered in crystalline materials, and, when possible, relate them to the general concept of topological defect.

3.1.1 Point defects

If one neglects thermal vibrations, all atoms of a perfect crystal occupy specific lattice sites. In such a lattice, two types of intrinsic point defects are possible. One corresponds to a vacant lattice site, or vacancy. The other one corresponds to an extra atom at a non-lattice site, or interstitial. Vacancies and interstitials may be produced by plastic deformation and high-energy particle irradiation, which is particularly important in nuclear materials. However, intrinsic point defects may simply be produced by thermal effects, and there is thus a thermodynamically stable concentration of point defects. The equilibrium fraction of defects of each type is given by

$$N_{eq}^{i} = N_a \exp\Big(-\frac{E_f^d}{k_B T}\Big) \tag{3.1}$$

where $d = v, i$ stands for defect type i for interstitial, v for vacancy), n_a is the total number of lattice sites, E_f^i is the formation energy of a single defect, k_B is the Boltzmann constant and T the temperature.

For vacancies, the formation energy is the energy required to remove an atom from a lattice site and put it on the surface of the crystal. It varies from about 1 eV for fcc metals to about 3 eV for bcc metals. For example, in Copper $E_f^v \simeq 1.3$ eV, and the fraction of vacant sites is of the order of 10^{-22} at a temperature of 300 K, but of the order of 10^{-5} at 1300 K. Interstitial formation energy is typically from two to four times larger then vacancy formation energy.

Hence, in metals in thermal equilibrium interstitial concentration is negligible versus vacancy concentration.

Another important property of point defects is the rate at which they move from one site to another. It is proportional to $\exp(-E_m^d/k_BT)$, where E_m^d is the migration energy, which varies typically from 0.1 eV to 1.0 eV. This rate is important for defect recombination, since, when an interstitial meets a vacancy, they annihilate by recombination. On the other hand this rate decreases exponentially with temperature. Hence point defects are nearly immobile at room temperature. Besides their formation by thermal effects, point defects may also be created by mechanical or ballistic effects, where equilibrium atoms are kicked off from their lattice site, generating vacancy-interstitial pairs. or Frenkel pairs.

One also has to consider extrinsic point defects, such as impurity atoms, which play an important role in physical and mechanical properties of crystals. They may be divided in two types: substitutional impurity atoms, where an atom of the underlying lattice is replaced by an impurity atom, and interstitials, where an impurity atom occupies a non-lattice site, similarly to the self-interstitials described previously.

3.1.2 Dislocations

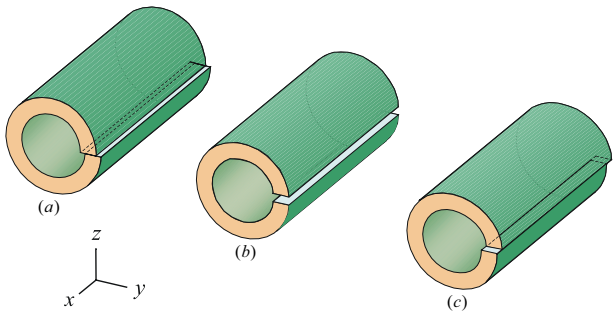

Figure 3.1: Dislocation types in materials

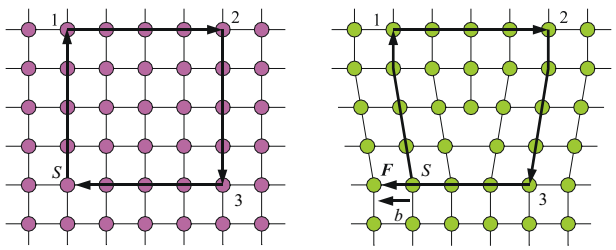

Figure 3.2: Burgers circuit for an edge dislocation

The existence of dislocations has been deduced theoretically, before any direct observation of these typical line defects. In fact, it appeared as the only way to reconcile theoretical and experimental values of applied shear stresses required to plastically deform single crystals. Plastic deformation is known to be induced by atomic plans sliding over each other. In 1934, G. I. Taylor, E. Orowan, and M. Polyani independently proposed that lattice imperfections must exist in materials, and that they can be moved with the application of small levels of stress. In a perfect crystal, i.e. in the absence of dislocations, the sliding of one atomic plane over an adjacent one requires the rigid motion of all the atoms in the plane, from one position to another one. The shear stress required for this process was first calculated by Frenkel in 1926. He assumed that the shearing force required to translate one row of atoms over another one by a distance x is sinusoidally periodic in x, with a period equal to the interatomic distance b. His result is then that the corresponding applied shear stress τ is given by

$$\tau = \frac{Gb}{2\pi a} \sin \frac{2\pi x}{b} \tag{3.2}$$

where G is the shear modulus and a the spacing between rows. For small strains ($x << b$), one recovers Hooke's law, while the maximum value of τ, or theoretical critical shear stress is

$$\tau_{th} = \frac{G}{2\pi} \frac{b}{a} \tag{3.3}$$

Since b and a are of the same order of magnitude, τ_{th} is only a fraction of the shear modulus. More realistic expressions for the shear dependence of the force lead to values of τ_{th} of the order of $\tau_{th} \simeq G/30$, in striking disagreement with measured values of shear stresses required for slip in real, well annealed crystals, and which vary from 10^{-8} G to 10^{-4} G. Before considering the role of dislocations in plastic deformation, let us first describe edge and screw dislocations, and their basic properties. If one considers a cylinder cut along the axial direction, as shown in Figure 3.1, then allows one part of the cylinder to slide either radially (a), azimuthally (b), or axially (c), provided that the two parts are glued again together and prevented from sliding back, a state of self-stress is created in the cylinder. The topological configuration of the line imperfection is called a dislocation. The dislocation is described by two vectors, one along the displacement direction, while the other is along the cut direction. The first vector is the Burgers vector, $\mathbf{b}$, while the second is the dislocation sense vector, $\boldsymbol{\xi}$. If the two vectors are parallel, the dislocation is termed a screw, as depicted in Figure 3.1-(a)&(b). On the other hand, it is called edge when the two vectors are perpendicular to one another, as seen in Figure 3.1-(c). An illustration of a Burgers circuit that is often used to define the geometry of a dislocated crystal is shown in Figure 3.2, from Start (S) to Finish (F). The resulting crystal distortion upon the passage of a dislocation from one surface to the other end is shown in Figure 3.3.

3.1.3 Surface defects

Surface defects are generated in materials by similar processes to what we described for dislocations. For example, if the displacement on the two cuts of the cylinder described above are

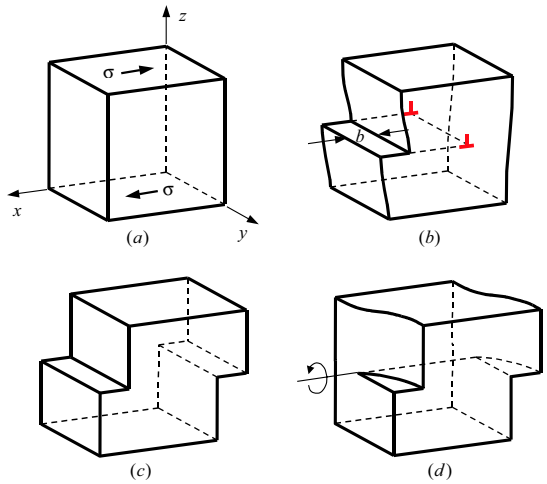

Figure 3.3: Crystal distortion as a result of a dislocation slip event

replaced by rotations, followed by a process of welding and release, a *disclination* is created, as can be seen in Figure fig:disclinations. Because of the rotation of one surface with repeat to another, a surface rather than a line defect is produced. Like a dislocation, a disclination can be described by two basic vectors (or a single dyadic tensor) representing the cut direction and the rotation vector direction. Grain boundaries can be described either as collections of dislocations on meeting surfaces, or as a result of surface disclinations. Examples of grain boundaries are shown in Figures 3.5 and 3.6 for a low-angle tilt boundary, and in Figure 3.7 for a twist boundary between two adjacent grains.

When single crystals are subjected to external shearing forces, they accommodate the necessary deformation in one of two possible ways. If shear deformation propagates to the crystal surface and localize the strain in a adjacent packets of slip planes, a *slip band* is formed a s surface defect between two virgin volumes, as can be seen in Figure 3.8. On the other hand, atomic planes may locally buckle without slip on one another forming mirror images of atomic plane stacking across two interfaces, a *twin-band* is thus formed. In this latter case, the strain accommodated by twinning is totally recoverable because it is elastic. This gives rise to the non-linear elastic response of materials undergoing martensitic transformations, such as shape-memory alloys. This type of surface defect is shown in Figure 3.9.

3.1.4 Volume defects

Typical volume defects such as precipitates, voids and bubbles, may appear under different circumstances and have important effects on physico-chemical properties of crystalline solids. The presence of a volume that is distinctly different in phase (e.g. atomic arrangement, lattice

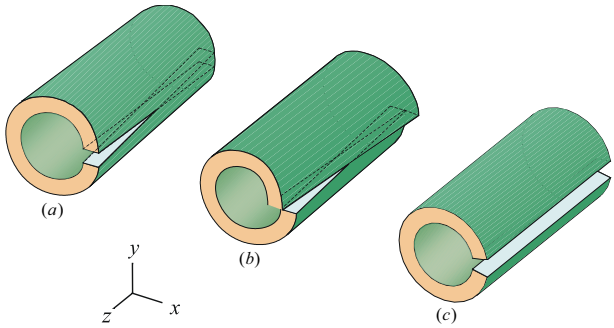

Figure 3.4: Types of disclinations in materials

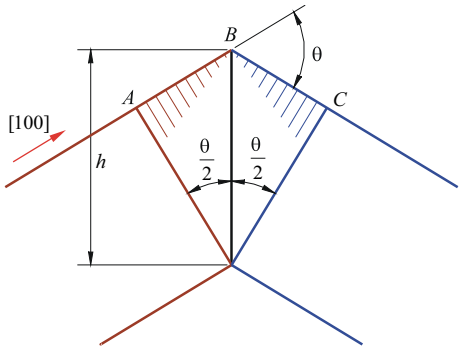

Figure 3.5: $< 100 >$-tilt boundary

constant, etc.) from the otherwise homogeneous crystal lattice can be considered as a volume defect. Internal volume inhomogeneities of this type also result in self-stress fields, and have been considered by Eshelby in what is known as the inclusion problem. The most significant type of volume defect is the three-dimensional crack that forms a volume bounded by crack surfaces that cannot support traction. Three basic types of crack deformation are identified, as shown in Figure 3.10. The crack opening mode, or mode I, is associated with with local displacements in which the crack surfaces move directly apart, as shown in (a). The sliding mode, or mode II, is characterized by crack surfaces sliding over each other in a direction perpendicular to the leading edge of the crack, as shown in Figure 3.10-(b). The tearing, twisting mode, or mode III, is developed when the crack surfaces slide with respect to each other in a direction parallel to the leading edge of the crack, as illustrated in Figure 3.10-(c).

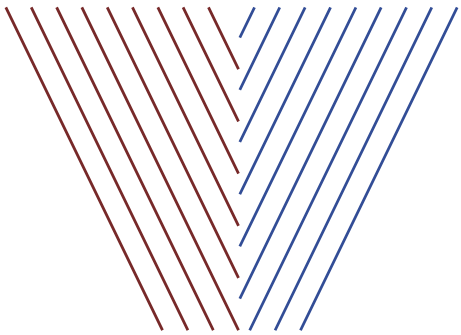

Figure 3.6: Stable tilt boundary

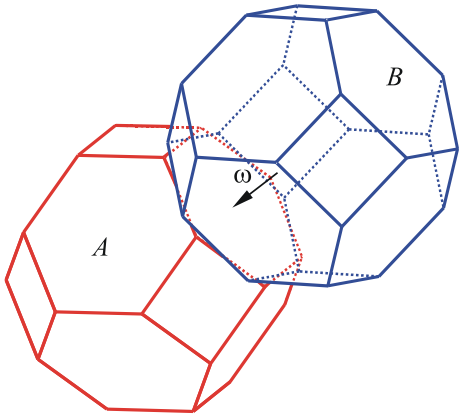

Figure 3.7: Twist boundary between grains

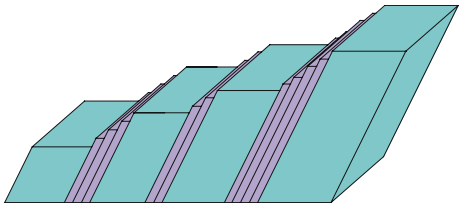

Figure 3.8: Slip band geometry

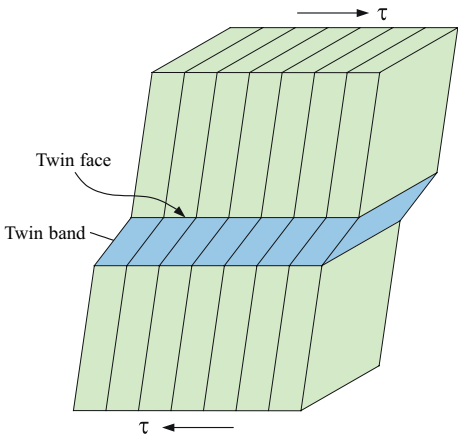

Figure 3.9: Twin band geometry

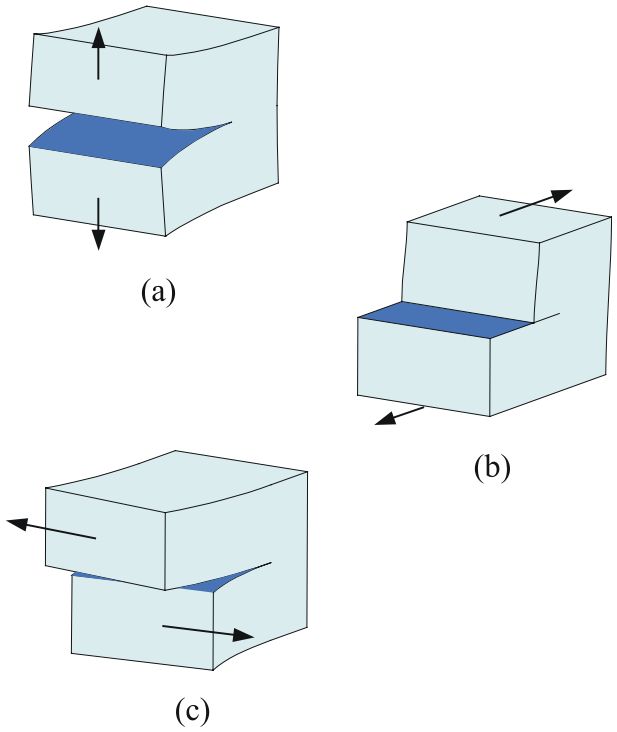

Figure 3.10: Classification of cracks: (a) mode-I (opening); (b) mode-II (sliding); (c) mode-II (twisting)

Chapter 4

Mathematical Foundations

4.1 Basic Vector and Tensor Operations

Consider the representation of a material point $\mathbf{P}$, described by the triplet coordinates (x_1, x_2, x_3), along the direction of the basis unit vectors $\mathbf{e_1}$, $\mathbf{e_2}$ and $\mathbf{e_3}$, as shown in Fig. (4.1).

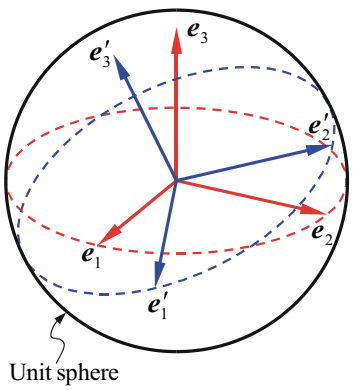

Figure 4.1: Cartesian coordinate system before and after rotation of axes

The vector $\mathbf{R}$ can be represented in terms of the triplet coordinates and the base vectors as:

$$\mathbf{R} = \sum_{j=1}^{3} x_j \mathbf{e}_j \tag{4.1}$$

where the base vectors $\{\mathbf{e}_i\}$ posses the properties:

$$\mathbf{e}_i \cdot \mathbf{e}_j = \mathbf{e}_j \cdot \mathbf{e}_i = \delta_{ij} \tag{4.2}$$

where the Kronecker delta

$$\delta_{ij} = \begin{cases} 1 \text{ for } i = j, \\ 0 \text{ for } i \neq j. \end{cases} \tag{4.3}$$

Performing the dot product $\mathbf{R} \cdot \mathbf{R}$, we obtain the length of a vector as:

$$|\mathbf{R}| = \sqrt{\mathbf{R} \cdot \mathbf{R}} = \sqrt{x_1^2 + x_2^2 + x_3^2} \tag{4.4}$$

If we now choose another basis set of vectors $\{\mathbf{e}'_j\}$, with a corresponding triplet coordinate set $\{x'_j\}$, as shown in Fig. (4.1), the vector $\mathbf{R}$ can be equally represented in the two coordinate systems:

$$\mathbf{R} = \sum_{j=1}^{3} x_j \mathbf{e}_j = \sum_{j=1}^{3} x'_j \mathbf{e}'_j \tag{4.5}$$

Taking the dot product:$\mathbf{e}'_j \cdot \mathbf{R}$, and using the orthogonality property, we obtain a set of three equations for the coordinate triplet in the "prime" system:

$$x'_j = \mathbf{e}'_j \cdot \mathbf{R} = (\mathbf{e}'_j \cdot \mathbf{e}_1)x_1 + (\mathbf{e}'_j \cdot \mathbf{e}_2)x_2 + (\mathbf{e}'_j \cdot \mathbf{e}_3)x_3, \qquad j = 1, 2, 3 \tag{4.6}$$

The dot products $l_{ij} = \mathbf{e}'_j \cdot \mathbf{e}_i$ (i,j=1,2,3) represent the direction cosines between the original and rotated (prime) coordinate axis. There are (3×3) direction cosines can be organized in a (3×3) matrix, $\mathbf{L}$. Thus, we may write:

$$\{x'_j\} = \mathbf{L}\{x_j\} \tag{4.7}$$

or

$$\mathbf{R}' = \mathbf{L}\,\mathbf{R} \tag{4.8}$$

as the coordinate transformation rule. It is easily verified that the matrix $\mathbf{L}$ is orthogonal, with the following properties:

$$\mathbf{L^{-1}} = \mathbf{L^T} \quad \& \quad |\mathbf{L}|^2 = 1 \tag{4.9}$$

Several important conventions will now be discussed, as they become essential in compact formulations including vectors and tensors in later sections. We will first introduce the index notation and summation convention for second order tensors, and define various elementary operations with vectors and tensors.

- *The range convention*:

  It states that every subscript (or index) takes on the values 1,2,3, unless otherwise stated. Thus x_j stands for the three coordinate numbers x_1, x_2, x_3, and α_{ij} stands for numbers: $\alpha_{11}, \alpha_{12}, \cdots$ etc.

- *The summation convention*:

It states that if an index i appears twice in a given expression, a summation over i must be performed. The repeated index is called a *"dummy index"*, and cannot occur more than twice in an equation. Thus, the previous coordinate transformation equation can simply be written as:

$$\mathbf{R} = x_j \mathbf{e}_j = x'_j \mathbf{e}'_j \tag{4.10}$$

and

$$x'_j = \mathbf{e}'_j \cdot (x_i \cdot \mathbf{e}_i) = (\mathbf{e}'_j \cdot \mathbf{e}_i) x_i \tag{4.11}$$

- *The Kronecker delta*:

  δ_{ij}, can now be used fore a number of properties, as listed below.

  We note that $x_i \delta_{ij} = x_j$, $a_{ik}\delta_{ij} = a_{jk}$. Thus, the presence of the dummy index i and δ_{ij} results in the replacement of i with j. This is known as the substitution property. Also, the orthogonality of the vector basis $\{\mathbf{e}_i\}$ can be easily represented as:

$$\mathbf{e}_i \cdot \mathbf{e}_j = \delta_{NJ} \tag{4.12}$$

- *The Permutation Symbol*:

  To express cross products between vectors, we introduce the permutation symbol ϵ_{ijk}, as:

$$\epsilon_{ijk} = \frac{1}{2}(i-j)(j-k)(k-i) \tag{4.13}$$

  giving

$$\epsilon_{ijk} = \begin{cases} 1 & \text{if } ijk \text{ are in cyclic order, i.e. 123, 231 and 312,} \\ -1 & \text{if } ijk \text{ are not in cyclic order, i.e. 132, 213 and 321,} \\ 0 & \text{if any two indices are equal.} \end{cases} \tag{4.14}$$

  Thus,

$$\mathbf{e}_i \times \mathbf{e}_j = \epsilon_{ijk} \mathbf{e}_k \tag{4.15}$$

$$(\mathbf{e}_i \times \mathbf{e}_j) \cdot \mathbf{e}_k = \epsilon_{ijk} \tag{4.16}$$

$$\mathbf{u} \times \mathbf{v} = \epsilon_{ijk} u_i v_j \mathbf{e}_k \tag{4.17}$$

  and

$$(\mathbf{u} \times \mathbf{v}) \cdot \mathbf{w} = \epsilon_{ijk} u_i v_j w_k = \begin{vmatrix} u_1 & v_1 & w_1 \\ u_2 & v_2 & w_2 \\ u_3 & v_3 & w_3 \end{vmatrix} \tag{4.18}$$

  is the volume spanned by the three vectors $\mathbf{u}$, $\mathbf{v}$ and $\mathbf{w}$.

- *Cartesian Tensors*:

  As a generalization of vectors, Cartesian tensors are defined as follows. In 3-dimensional Euclidean space, and for a given vector basis set $\{\mathbf{e}_i\}$, a collection of an ordered set of 3^n

numbers denoted by $a_{ijk\cdots}$ containing n indices. The numbers $a_{ijk\cdots}$ are the components of an n-th order tensor $\mathbf{A}$ or $\mathbf{a}$. Furthermore, if upon rotation of axes, the components of $\mathbf{A}$ in the new vector basis $\{\mathbf{e}'_i\}$ become $a'_{ijk\cdots}$, such that

$$a'_{ijk\cdots} = l_{i\alpha} l_{j\beta} l_{k\gamma} \cdots a_{\alpha\beta\gamma\cdots} \tag{4.19}$$

Note that l_{ij} is the direction cosine between the $\{\mathbf{e}'_i\}$ and $\{\mathbf{e}_j\}$ axes. Here $\mathbf{A}$ is called a Cartesian tensor of order n.

- *Vector and Tensor Products*:

Let us consider second order tensors $\mathbf{S}$ and $\mathbf{A}$, vectors $\mathbf{u}$, $\mathbf{v}$, and $\mathbf{w}$, and basis vector sets $\{\mathbf{e}_i\}$ and $\{\mathbf{e}'_i\}$, with direction cosines of axes rotation $l_{ij} = \mathbf{e}_i \cdot \mathbf{e}'_j$. We will now consider operations as inner (or dot) products, which lead to *contraction* of the tensor to lower order, and operations as outer, dyad or tensor products, which lead to successive increase in the tensor order.

Tensor products

The **tensor** product or **dyad** of the two vectors $\mathbf{u}$ and $\mathbf{v}$, which is denoted $\mathbf{u} \otimes \mathbf{v}$, is a second order tensor that transforms a vector $\mathbf{w}$ into a vector with the direction of $\mathbf{u}$, as follows:

$$(\mathbf{u} \otimes \mathbf{v})\mathbf{w} = \mathbf{u}(\mathbf{v} \cdot \mathbf{w}) = (\mathbf{v} \cdot \mathbf{w})\mathbf{u} \tag{4.20}$$

In general, the dyad is not commutative: $\mathbf{u} \otimes \mathbf{v} \neq \mathbf{v} \otimes \mathbf{u}$. A **dyadic** is a linear combination of dyads with scalar coefficients. For example, the linear combination: $(a\mathbf{u} \otimes \mathbf{v} + b\mathbf{w} \otimes \mathbf{v})$, where a and b are scalars, is a dyadic. Thus, any second order tensor $\mathbf{S}$ can be expressed as a dyadic (i.e. linear combination of *basis* dyads):

$$\mathbf{S} = S_{ij} \mathbf{e}_i \otimes \mathbf{e}_j \tag{4.21}$$

The dyadic corresponding to the unit tensor $\mathbf{I}$ is the unit dyadic or idemfactor:

$$\mathbf{I} = \delta_{ij} \mathbf{e}_i \otimes \mathbf{e}_j = \mathbf{e}_j \otimes \mathbf{e}_j = \mathbf{e}_1\mathbf{e}_1 + \mathbf{e}_2\mathbf{e}_2 + \mathbf{e}_3\mathbf{e}_3 \tag{4.22}$$

This notation is useful, for example, in obtaining individual components, as:

$$\mathbf{e}_k \cdot \mathbf{S} \cdot \mathbf{e}_m = \mathbf{e}_k \cdot S_{ij} \mathbf{e}_i \mathbf{e}_j \cdot \mathbf{e}_m = \delta_{ki} \delta_{jm} S_{ij} = S_{km} \tag{4.23}$$

likewise,

$$S_{mk} = \mathbf{e}_m \cdot \mathbf{S} \cdot \mathbf{e}_k \tag{4.24}$$

Dot products

The **dot product** of two second order tensors $\mathbf{A}$ and $\mathbf{B}$ is also a second order tensor, denoted by $\mathbf{A} \cdot \mathbf{B}$, and defined by:

$$(\mathbf{A} \cdot \mathbf{B})\mathbf{u} = \mathbf{A}(\mathbf{B} \cdot \mathbf{u}) \tag{4.25}$$

In general, the dot product is not commutative: $\mathbf{A} \cdot \mathbf{B} \neq \mathbf{B} \cdot \mathbf{A}$. The components of the dot product are obtained by summation over one single index: $(\mathbf{A} \cdot \mathbf{B})_{ij} = A_{ik}B_{kj}$.

Trace and contraction

The trace of a tenor $\mathbf{S}$ is a scalar, denoted by $tr\mathbf{S}$. Thus, the trace of the dyad $\mathbf{u} \otimes \mathbf{v}$ is just the dot product of the two vectors, i.e. $tr(\mathbf{u} \otimes \mathbf{v}) = \mathbf{u} \cdot \mathbf{v} = u_i v_i$. Also, the trace of a tensor $\mathbf{S}$ with respect to the orthonormal basis $\{\mathbf{e}_i\}$ is given by:

$$tr\mathbf{S} = tr(S_{ij}\mathbf{e}_i \otimes \mathbf{e}_j) = S_{ij}tr(\mathbf{e}_i \otimes \mathbf{e}_j) = S_{ij}(\mathbf{e}_i \cdot \mathbf{e}_j) = S_{ij}\delta_{ij} = S_{ii} \tag{4.26}$$

A **double contraction** operation is defined by summing the dot product of two second order tensors over *two* indices, and is symbolically characterized by two dots, and yields a scalar as shown below.

$$\mathbf{A} : \mathbf{B} = tr(\mathbf{A}^T\mathbf{B}) = tr(\mathbf{B}^T\mathbf{A}) = \mathbf{B} : \mathbf{A} \tag{4.27}$$

Double contraction is very useful in tensor operations. Consider, for example, the following identities:

$$\begin{aligned} \mathbf{I} : \mathbf{S} &= tr\mathbf{S} = \mathbf{S} : \mathbf{I} \\ (\mathbf{u} \otimes \mathbf{w}) : (\mathbf{v} \otimes \mathbf{x}) &= (\mathbf{u} \cdot \mathbf{v})(\mathbf{w} \cdot \mathbf{x}) \\ (\mathbf{e}_i \otimes \mathbf{e}_j) : (\mathbf{e}_k \otimes \mathbf{e}_l) &= (\mathbf{e}_i \cdot \mathbf{e}_k) : (\mathbf{e}_j \cdot \mathbf{e}_l) = \delta_{ik}\delta_{jl} \end{aligned} \tag{4.28}$$

Symmetric and skew tensors

Any tensor $\mathbf{W}$ can be uniquely decomposed into a symmetric tensor $\mathbf{S}$, and a skew (or antisymmetric) tensor $\mathbf{A}$, such that : $\mathbf{W} = \mathbf{S} + \mathbf{A}$, where:

$$\mathbf{S} = \frac{1}{2}(\mathbf{W} + \mathbf{W}^T) \quad , \qquad \mathbf{A} = \frac{1}{2}(\mathbf{W} - \mathbf{W}^T) \tag{4.29}$$

The notation: $sym\mathbf{W}$ for $\mathbf{S}$ and $skew\mathbf{W}$ for $\mathbf{A}$ is also used. Hence:

$$S_{ij} = S_{ji} \quad , \qquad A_{ij} = -A_{ji} \tag{4.30}$$

Projection, spherical and deviatoric tensors

Consider the vector $\mathbf{w}$ and the unit vector $\mathbf{e}$. We can decompose the vector $\mathbf{w}$ into a component along $\mathbf{e}$, and another for the projection of $\mathbf{w}$ on the plane normal to $\mathbf{e}$, thus: $\mathbf{w} = \mathbf{w}_{\parallel} + \mathbf{w}_{\perp}$. With the tensor product rules, we have:

$$\mathbf{u}_{\parallel} = (\mathbf{w} \cdot \mathbf{e})\mathbf{e} = (\mathbf{e} \otimes \mathbf{e})\mathbf{w} = \mathbf{P}_e^{\parallel}\mathbf{w} \tag{4.31}$$

Similarly, we have for the normal component of $\mathbf{w}$:

$$\mathbf{w}_{\perp} = \mathbf{w} - \mathbf{w}_{\parallel} = \mathbf{w} - (\mathbf{e} \otimes \mathbf{e})\mathbf{w} = (\mathbf{I} - \mathbf{e} \otimes \mathbf{e})\mathbf{w} = \mathbf{P}_e^{\perp}\mathbf{w} \tag{4.32}$$

Therefore, the projection tensors, $\mathbf{P}_e^{\parallel}$ and $\mathbf{P}_e^{\perp}$ are defined by the relationships:

$$\mathbf{P}_e^{\parallel} = (\mathbf{e} \otimes \mathbf{e}) \quad , \qquad \mathbf{P}_e^{\perp} = (\mathbf{I} - \mathbf{e} \otimes \mathbf{e}) \tag{4.33}$$

Every tensor can be decomposed into a *spherical* and a *deviatoric* part, as follows:

$$\mathbf{S} = \alpha\mathbf{I} + dev\mathbf{S}, \quad or \quad S_{ij} = \alpha\delta_{ij} + devS_{ij} \tag{4.34}$$

Where, $\alpha = \frac{1}{3}tr\mathbf{S} = \frac{1}{3}(\mathbf{I} : \mathbf{S}) = \frac{1}{3}S_{ii}$, and $dev\mathbf{S} = \mathbf{S} - \frac{1}{3}tr\mathbf{S}\mathbf{I}$.

Higher order tensors

A tensor of order three may be expressed as:

$$\mathcal{S} = \mathcal{S}_{ijk}\mathbf{e}_i \otimes \mathbf{e}_j \otimes \mathbf{e}_k \tag{4.35}$$

Where S_{ijk} are $3^3 = 27$ components of the tensor $\mathcal{S}$. A special third order tensor is the triadic product: $\mathbf{u} \otimes \mathbf{v} \otimes \mathbf{w} = (\mathbf{u} \otimes \mathbf{v}) \otimes \mathbf{w}$. A few useful identities for third order tensors are given below:

$$\begin{aligned} (\mathbf{u} \otimes \mathbf{v} \otimes \mathbf{w}) \cdot \mathbf{x} &= (\mathbf{w} \cdot \mathbf{x})\mathbf{u} \otimes \mathbf{v} \\ (\mathbf{u} \otimes \mathbf{v} \otimes \mathbf{w}) : (\mathbf{m} \otimes \mathbf{n}) &= (\mathbf{v} \cdot \mathbf{m})(\mathbf{w} \cdot \mathbf{n})\mathbf{u} \\ (\mathbf{u} \otimes \mathbf{v} \otimes \mathbf{w}) : \mathbf{I} &= (\mathbf{v} \cdot \mathbf{w})\mathbf{u} \end{aligned} \tag{4.36}$$

The components of the third order tensor can be obtained by double contraction as:

$$\mathcal{S}_{ijk} = (\mathbf{e}_i \otimes \mathbf{e}_j) : \mathcal{S} \cdot \mathbf{e}_k = \mathbf{e}_i \otimes \mathbf{e}_j : \mathcal{S}_{ijk}\mathbf{e}_i \otimes \mathbf{e}_j \otimes \mathbf{e}_k \cdot \mathbf{e}_k \tag{4.37}$$

Similar operations can be defined for tensors of higher order. For example, a fourth order tensor can be written as vector products in the form:

$$\mathbf{C} = C_{ijkl}\mathbf{e}_i \otimes \mathbf{e}_j \otimes \mathbf{e}_k \otimes \mathbf{e}_l \tag{4.38}$$

- <u>*Vector and Tensor Calculus*</u>:

If the components of vectors or tensors are functions of space or time, they are termed tensor (or vector) fields. We outline here a few useful differential and integral operation with such fields. The first partial derivative of a scalar function of space and time $\phi(\mathbf{R}, t)$ is denoted by:

$$\frac{\partial \phi(\mathbf{R}, t)}{\partial x_k} = \phi_{,k} \ , \qquad k = 1, 2, 3 \tag{4.39}$$

where the "," in $\phi_{,k}$ stands for differentiation. We can now generalize to any tensor and differentiation order. For example,

$$\frac{\partial^2 s_{ij}}{\partial x_k \partial x_l} = s_{ij,kl} \tag{4.40}$$

Partial derivatives with respect to time are denoted as: $\frac{\partial \phi}{\partial t} = \dot{\phi} = \phi_{,t}$, etc.

It is easy to see that one can form three components of a vector from a scalar function by differentiation as:

$$v_i = \phi_{,i}$$

and that the vector $\mathbf{v}$, transforms as:

$$v_i' = \phi_{,j} \frac{\partial x_j}{\partial x_i'} = l_{ij} \phi_{,j} = l_{ij} v_j \tag{4.41}$$

This vector is called the *gradient* of ϕ. Thus a vector field is generated from a scalar field as:

$$\text{grad } \phi = \nabla \phi = \phi_{,i} \, \mathbf{e_i} \tag{4.42}$$

similarly, a second order, symmetric tensor field can be generated by double differentiation, as:

$$\phi_{,ij} = \frac{\partial^2 \phi}{\partial x_i \partial x_j} \tag{4.43}$$

The scalar $\phi_{,ii}$ is denoted by $\nabla^2 \phi$, where ∇^2 is the Laplace operator:

$$\nabla^2 \phi = \phi_{,ii} = \frac{\partial^2 \phi}{\partial x_1^2} + \frac{\partial^2 \phi}{\partial x_2^2} + \frac{\partial^2 \phi}{\partial x_3^2} \tag{4.44}$$

If we consider a vector field $\mathbf{v}$, we can generate a non-symmetric second order tensor field by differentiation as:

$$a_{ij} = v_{i,j} \tag{4.45}$$

which can be shown to transform as a second order tensor. The particular condition $a_{ii} = v_{i,i}$ is a scalar, and is denoted by the divergence of $\mathbf{v}$:

$$\text{div } \mathbf{v} = \nabla \cdot \mathbf{v} = v_{i,i} \tag{4.46}$$

In general, then, if $\mathbf{S}$ is a tensor of order n, then the components $s_{ijk\cdots,m}$ are the components of a tensor of order (n+1), and is termed the *gradient* of $\mathbf{S}$.

The *curl* of a vector $\mathbf{v}$ is denoted by $\nabla \times \mathbf{v}$, and in index notation is given by:

$$\nabla \times \mathbf{v} = \epsilon_{ijk} v_{j,i}\, \mathbf{e_k} \tag{4.47}$$

The following identities, which can be easily verified, will be useful:

$$\begin{aligned} \nabla \times \nabla\phi &= 0 && (4.48)\\ \nabla \cdot \nabla\phi &= \nabla^2\phi && (4.49)\\ \nabla \cdot \nabla \times \mathbf{v} &= 0 && (4.50)\\ \nabla \times \nabla \times \mathbf{v} &= \nabla(\nabla \cdot \mathbf{v}) - \nabla^2\mathbf{v} && (4.51) \end{aligned}$$

Thus a gradient vector field is irrotational, while the curl of a vector field is divergence free. Note that any operation that are written in direct vector notation are valid in any coordinate system, and not only Cartesian.

The integration of vector and tensor fields over volumes, surfaces and lines can usefully be manipulated through the divergence (Gauss) theorem and Stokes's theorem as follows.

- *Stokes' (Circulation) Theorem*:

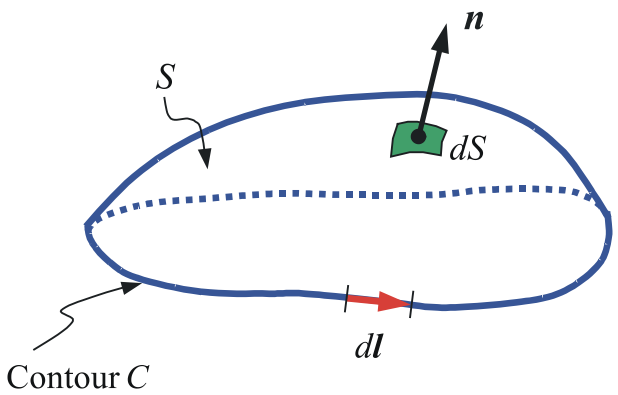

Figure 4.2: Surface and bounding contour for Stokes' theorem

For an open piece-wise smooth surface S, bounded by a simple closed curve C, for any vector field $\mathbf{v}$, we can show:

$$\oint_C \mathbf{v} \cdot \mathrm{d}\mathbf{l} = \int_S (\nabla \times \mathbf{v}) \cdot \mathbf{n} \mathrm{d}S \tag{4.52}$$

where $\mathrm{d}\mathbf{l}$ is a line element (tangent to C), $\mathrm{d}S$ is an area element and $\mathbf{n}$ is an outward surface normal, as can be seen in Fig. (4.2). This can be put in index notation as:

$$\oint_C v_i \cdot \mathrm{d}l_i = \int_S \epsilon_{ijk} v_{j,i}\, n_k \mathrm{d}S \tag{4.53}$$

The theorem can be extended to any order tensor as:

$$\oint_C \alpha_{ijk\ldots} \mathrm{d}l_i = \int_S \epsilon_{ijk} \alpha_{jk\ldots,i}\, n_k \mathrm{d}S \tag{4.54}$$

- *The Divergence (Gauss') Theorem*:

Consider the volume Ω of a region in space bounded by a piece-wise smooth and closed surface S, depicted in Fig. (4.3). It can be shown that:

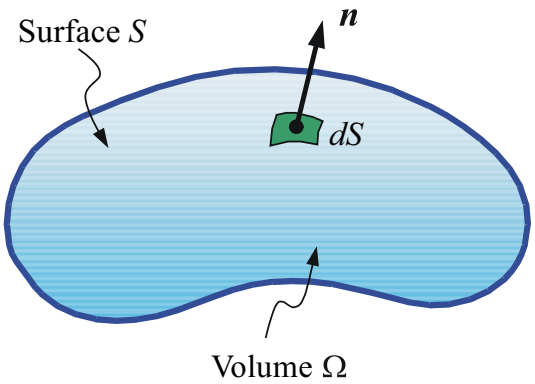

Figure 4.3: Representative volume for Gauss's theorem

$$\int_S \mathbf{v} \cdot \mathbf{n}\, \mathrm{d}S = \int_\Omega \nabla \cdot \mathbf{v}\, \mathrm{d}\Omega \tag{4.55}$$

In index notation, it can be re-written as:

$$\int_S v_i \cdot n_i \mathrm{d}S = \int_\Omega v_{i,i}\, \mathrm{d}\Omega \tag{4.56}$$

which can now be extended to any order tensor as:

$$\int_S \alpha_{ijk\ldots} n_i \mathrm{d}S = \int_\Omega \alpha_{ijk\ldots,i}\, \mathrm{d}\Omega \tag{4.57}$$

4.2 Infinitesimal Deformation and the Strain Tensor

Under the action of applied forces, solids exhibit deformation and change in shape. The position of any point in the body is defined by its radius vector $\mathbf{r}$ (with components $x_1 = x, x_2 = y, x_3 = z$) in some coordinate system. When the body is deformed, every point in it is in displaced. Consider some particular point, let its radius vector before the deformation be $\mathbf{R}$, and after the

deformation have a different value $\mathbf{R}'$ (with components x_i'). The displacement of this point due to the deformation is then given by the vector $\mathbf{u} = \mathbf{R}' - \mathbf{R}$:

$$u_i = x_i' - x_i \tag{4.58}$$

The vector $\mathbf{u}$ is called the *displacement vector*. The coordinates x_i' of the displaced point are functions of the coordinates x_i of the point before displacement. The displacement vector u_i is therefore also a function of the coordinates x_i. If the vector $\mathbf{u}$ is given as a function of x_i, the deformation of the body is entirely determined.

When a body is deformed, the distances between its points change. Consider two points very close together. If the radius vector joining them before the deformation is $\mathrm{d}x_i' = \mathrm{d}x_i + \mathrm{d}u_i$. The distance between the points is $\mathrm{d}l = \sqrt{\mathrm{d}x_1^2 + \mathrm{d}x_2^2 + \mathrm{d}x_3^2}$ before the deformation, and $\mathrm{d}l' = \sqrt{\mathrm{d}x_1'^2 + \mathrm{d}x_2'^2 + \mathrm{d}x_3'^2}$ after it. Using the summation rule, we can write $\mathrm{d}l^2 = \mathrm{d}x_i^2$, $\mathrm{d}l'^2 = \mathrm{d}x_i'^2 = (\mathrm{d}x_i + \mathrm{d}u_i)^2$. Substituting $\mathrm{d}u_i = u_{i,k}\,\mathrm{d}x_k$, we can write

$$\mathrm{d}l'^2 = \mathrm{d}l^2 + 2u_{i,k}\,\mathrm{d}x_i\mathrm{d}x_k + u_{i,k}\,u_{i,l}\,\mathrm{d}x_k\mathrm{d}x_l.$$

We note that $u_{i,k}\,\mathrm{d}x_i\mathrm{d}x_k = u_{k,i}\,\mathrm{d}x_i\mathrm{d}x_k$, then $\mathrm{d}l'^2$ takes the form

$$\mathrm{d}l'^2 = \mathrm{d}l^2 + 2u_{ik}\mathrm{d}x_i\mathrm{d}x_k, \tag{4.59}$$

the tensor u_{ik} is defined as

$$u_{ik} = \frac{1}{2}(u_{i,k} + u_{k,i} + u_{l,i}\,u_{l,k}\,). \tag{4.60}$$

The tensor u_{ik} is called the *strain tensor*, which is symmetric.

For small (infinitesimal) deformations, the strain tensor can be taken as:

$$u_{ik} = \frac{1}{2}(u_{i,k} + u_{k,i}\,) \tag{4.61}$$

which is evidently symmetric, and can thus be diagonalized. This means that, at any given point, we can choose coordinate axes (the *principal axes* of the tensor) in such a way that only the diagonal components u_{11}, u_{22}, u_{33} of the tensor u_{ik} are different from zero. These components, the *principal values* of the strain tensor, and will be denoted by $u^{(1)}$, $u^{(2)}$, $u^{(3)}$.

If the strain tensor is diagonalized at a given point, the element of length square near it becomes:

$$\begin{aligned} \mathrm{d}l'^2 &= (\delta_{ik} + 2u_{ik})\mathrm{d}x_i\mathrm{d}x_k && (4.62)\\ &= (1 + 2u^{(1)})\mathrm{d}x_1^2 + (1 + 2u^{(2)})\mathrm{d}x_2^2 + (1 + 2u^{(3)})\mathrm{d}x_3^2 && (4.63) \end{aligned}$$

We can see that the expression is the sum of three independent terms. This means that the strain in any volume element may be regarded as composed of independent strains in three mutually perpendicular directions, namely three of the principal axes of the strain tensor. Each of these strains is a simple extension (or compression) in the corresponding direction: the

length element along the first principal axes becomes $\mathrm{d}x_1' = \sqrt{1+2u^{(1)}}\mathrm{d}x_1$, and similar for the other two axes. The quantity $\sqrt{1+2u^{(i)}}-1$ is the relative extension $(\mathrm{d}x_i' - \mathrm{d}x_i)/\mathrm{d}x_i$ along the ith principal axis. The relative extensions of the elements of length along the principal axes of the strain tensor are, to within higher-order terms, $\sqrt{1+2u^{(i)}} - 1 \approx u^{(i)}$, i.e. they are the principal values of the tensor u_{ik}.

Let us consider an infinitesimal volume element $\mathrm{d}V$, and find its volume $\mathrm{d}V'$ after the deformation. In this case, we take the principal axes of the strain tensor at the point considered, as the coordinate axes. Then the elements of length $\mathrm{d}x_1$, $\mathrm{d}x_2$, $\mathrm{d}x_3$ along these axes become, after the deformation, $\mathrm{d}x_1' = (1+u^{(1)})\mathrm{d}x_1$, etc. The volume $\mathrm{d}V$ is the product $\mathrm{d}x_1\mathrm{d}x_2\mathrm{d}x_3$, while $\mathrm{d}V'$ is $\mathrm{d}x_1'\mathrm{d}x_2'\mathrm{d}x_3'$. Thus $\mathrm{d}V' = \mathrm{d}V(1+u^{(1)})(1+u^{(2)})(1+u^{(3)})$. Neglecting higher-order terms, we would have $\mathrm{d}V' = \mathrm{d}V(1+u^{(1)}+u^{(2)}+u^{(3)})$. The sum $u^{(1)}+u^{(2)}+u^{(3)}$ of the principal values of a tensor can be shown to be invariant, and is equal to the sum of the diagonal components $u_{ii} = u_{11} = u_{22} = u_{33}$ in any coordinate system. Thus

$$\mathrm{d}V' = \mathrm{d}V(1+u_{ii}) \tag{4.64}$$

It is clear that the sum of the diagonal components of the strain tensor is the relative volume change $(\mathrm{d}V' - \mathrm{d}V)/\mathrm{d}V$.

4.3 The Stress Tensor

The theory of elasticity is based on the assumption that the range of internal forces between atoms is very localized (i.e. short-range). As we will see later, lattice incompatibilities (e.g. dislocations) can result in long range internal forces, and will therefore require careful consideration. It follows from the basic assumption of elasticity that the force exerted on any part of the body by surrounding parts can only exist at the surface. Consider the total force on some portion of the body. First, this total force is equal to the sum of all the forces on all the volume elements in that portion of the body, i.e. it can be written as the volume integral $\int \mathbf{F}\mathrm{d}\Omega$, where $\mathbf{F}$ is the force per unit volume and $\mathbf{F}\mathrm{d}\Omega$ the force on the volume element $\mathrm{d}\Omega$. Second, the forces with which various parts of the portion considered act on one another cannot give anything but zero in the total resultant force. Thus, each of the three components $\int F_i\mathrm{d}\Omega$ of the resultant of all internal stresses can be transformed into a surface integral. By the divergence theorem (eq. (4.57) of Section (**??**)), we conclude that the force vector $\mathbf{F}$ must be the divergence of a tensor of rank two. Thus:

$$F_i = \sigma_{ik,k} \tag{4.65}$$

or

$$\mathbf{F} = \nabla \cdot \underline{\underline{\sigma}} \tag{4.66}$$

The force on any volume can be written as:

$$\int_\Omega F_i \mathrm{d}\Omega = \int_\Omega \sigma_{ik,k}\,\mathrm{d}\Omega = \int_S \sigma_{ik}\mathrm{d}S_k \tag{4.67}$$

The tensor σ_{ik} is called the *stress tensor*. It is clear from eq.(4.67) that $\sigma_{ik}\mathrm{d}S_k$ is the ith component of the force on the surface element $\mathrm{d}\mathbf{S}$. If we just consider element of area in the planes of xy, yz, zx, the component σ_{ik} will be the ith component of the force per unit area perpendicular to the x_k-axis. Thus, the force per unit area parallel to the x-axis and normal to the yz-plane is σ_{xx}.

By considering internal moment equilibrium, it can be easily shown that the stress tensor must be symmetric, i.e., we must have:

$$\sigma_{ik} = \sigma_{ki} \tag{4.68}$$

The equation of equilibrium can be formed if we realize that the internal force at every volume element must balance, i.e. $F_i = 0$. If there are additional body force per unit volume (e.g. gravitational, centrifugal, etc.) with value f_i, we must have $F_i + f_i = 0$. Thus:

$$\sigma_{ij,j} + f_i = 0 \tag{4.69}$$

Solution of this set of equilibrium equations is subject to boundary conditions. Let $\mathbf{P}$ be the external force per unit surface area, thus the equilibrium of a surface element $\mathrm{d}S$ implies that the sum of the internal $(-\sigma_{ik}\mathrm{d}S_k)$ and external $P_i\mathrm{d}S$ must vanish. Since $\mathrm{d}S_k = n_k\mathrm{d}S$, where $\mathbf{n}$ is a unit normal, then, the condition of boundary equilibrium is expressed as:

$$\sigma_{ij}n_j = P_i \tag{4.70}$$

4.4 Thermodynamics of Deformation

Let's assume that the deformation of a body changes the displacement vector $\mathbf{u}$ by a small amount $\delta\mathbf{u}$, and we wish to determine the work done by internal stresses. We will adopt here the sign convention that input work or heat to the body is positive. Thus, the work integrated over the body is:

$$\int \delta W \ \mathrm{d}\Omega = \int_S \mathbf{t} \cdot \delta\mathbf{u} \ \mathrm{d}S + \int_\Omega \mathbf{F} \cdot \delta\mathbf{u} \ \mathrm{d}\Omega \tag{4.71}$$

where $\mathbf{t}$ is the surface traction vector, $t_i = \sigma_{ik}n_k$, δW is the incremental amount of work done per unit volume. The negative sign is for work done *by* the body. Input heat or work to the body are positive by convention. Equation(4.71) can be re-written as:

$$\int_\Omega \delta W \ \mathrm{d}\Omega = \int_S \delta u_i \sigma_{ik} \mathrm{d}S_k + \int_\Omega f_i \delta u_i \ \mathrm{d}\Omega \tag{4.72}$$

Using the divergence theorem for the first integral, we obtain:

$$\int \delta W \ \mathrm{d}\Omega = \int_\Omega (\sigma_{ik}\delta u_i)_{,k} \ \mathrm{d}\Omega + \int_\Omega f_i \delta u_i \ \mathrm{d}\Omega \tag{4.73}$$

$$= \int_\Omega (f_i + \sigma_{ik,k})\delta u_i \ \mathrm{d}\Omega + \int_\Omega \sigma_{ik}\delta u_{i,k} \ \mathrm{d}\Omega \tag{4.74}$$

As a result of mechanical equilibrium (7.207), the first term is zero. Also, because the stress tensor is symmetric, we have:

$$\begin{aligned} \int \delta W \, \mathrm{d}\Omega &= \frac{1}{2}\int (\sigma_{ik}\delta u_{i,k} + \sigma_{ki}\delta u_{k,i}) \, \mathrm{d}\Omega \\ &= \frac{1}{2}\int \sigma_{ik}\varepsilon_{ik} \, \mathrm{d}\Omega \end{aligned} \tag{4.75}$$

This finally gives the work done on the body per unit volume as:

$$\delta W = \sigma_{ik}\varepsilon_{ik} \tag{4.76}$$

We will assume that the deformation is slow enough such that thermodynamic equilibrium is established, and that the deformation is elastic and reversible. The thermodynamic functions: internal energy U, entropy S, Gibbs free energy G, and Helmholz free energy A are all taken per unit volume. The first law of thermodynamics can be stated as:

$$\mathrm{d}U = \delta Q + \delta W \tag{4.77}$$

And since $A = U - TS$, we have:

$$\mathrm{d}U = T\mathrm{d}S + \sigma_{ik}\mathrm{d}\varepsilon_{ik} \tag{4.78}$$

$$\mathrm{d}A = -S\mathrm{d}T + \sigma_{ik}\mathrm{d}\varepsilon_{ik} \tag{4.79}$$

Also, we may generalize the standard form of the enthalpy for a P-V-T system ($H = U + PV$) to ($H = U - \sigma_{ik}\varepsilon_{ik}$), and because $G = H - TS$, we would have:

$$G = U - TS - \sigma_{ik}\varepsilon_{ik} = A - \sigma_{ik}\varepsilon_{ik} \tag{4.80}$$

Taking the differentials of the enthalpy and Gibbs free energy, we get:

$$\mathrm{d}G = -S\mathrm{d}T - \varepsilon_{ik}\mathrm{d}\sigma_{ik} \tag{4.81}$$

$$\mathrm{d}H = T\mathrm{d}S - \varepsilon_{ik}\mathrm{d}\sigma_{ik} \tag{4.82}$$

It is clear that the components of stress or strain tensors can be obtained from the previous equations (4.78- 4.82) by differentiation as:

$$\sigma_{ik} = \left[\frac{\partial U}{\partial \varepsilon_{ik}}\right]_S = \left[\frac{\partial A}{\partial \varepsilon_{ik}}\right]_T \tag{4.83}$$

and,

$$\varepsilon_{ik} = -\left[\frac{\partial G}{\partial \sigma_{ik}}\right]_T = -\left[\frac{\partial H}{\partial \sigma_{ik}}\right]_S \tag{4.84}$$

4.5 Constitutive Relations

The stress and strain tensors have been introduced as far without any connection between them. When a body deforms, atoms move apart, and the forces are non-linearly dependent on the distance between atoms via the inter atomic potential. For small deviations from equilibrium, the interatomic potential can be approximated as a quadratic function of displacement, and interatomic forcs become approximately linear functions of atomic displacements, with the proportionality constant determined only by the curvature of the potential near equilibrium. This microscopic picture can be extended to the macroscopic domain, if one ignores material incompatibilities due to dislocations and other defects. An analog to this microscopic relationship is the situation encountered in dealing with the classical mass-spring system, when the force $\mathbf{F}$ is linear with the displacement x ($F = Kx$), and the potential is quadratic (i.e. $U = -\frac{1}{2}Kx^2$), where K is the spring stiffness. Now, let's generalize this to the case of elastic deformation involving stress and strain tensors.

Consider a body in equilibrium. Then, for $u_{ik} = 0$, the internal stresses are zero also, i.e. $\sigma_{ik} = 0$. For an isothermal thermodynamic process, $\sigma_{ik} = \left[\frac{\partial A}{\partial \varepsilon_{ik}}\right]_T$. It follows that there is no linear terms in the expansion of A in powers ε_{ik}, otherwise we would have a constant force at equilibrium. Next, since the Helmholtz free energy is a scalar, each term in the expansion of A must be a scalar also. Two independent scalars of the second degree can be formed from the components of the symmetrical tensor ε_{ik}, they can be taken as the squared sum of the diagonal components ε_{ii}^2 and the sum of the squares of all the components ε_{ik}^2. Expanding A in powers of ε_{ik}, we therefore have, up to second order terms:

$$A = A_0 + \frac{1}{2}\lambda\varepsilon_{ii}^2 + \mu\varepsilon_{ik}^2 \tag{4.85}$$

This is the general expression for the Helmholtz free energy of an isotropic body, deformed isothermally. The quantities λ and μ are called *Lamé coefficients*.

The change in volume in the deformation is given by the sum ε_{ii}. If this sum is zero, then the volume of the body is unchanged by the deformation, only its shape being altered. Such deformation is called a *pure shear*. The opposite case is that of deformation which causes a change in the volume of the body but no change in its shape. Each volume element of the body retains its shape also. The tensor of such deformation is $\varepsilon_{ik} =$constant$\times\delta_{ik}$. This type of deformation is called *hydrostatic compression*.

Any deformation can be represented as the sum of a pure shear and a hydrostatic compression. To do so, we need only the identity:

$$\varepsilon_{ik} = (\varepsilon_{ik} - \frac{1}{3}\delta_{ik}\varepsilon_{ll}) + \frac{1}{3}\delta_{ik}\varepsilon_{ll} \tag{4.86}$$

The first term on the right is obviously a pure shear, since the sum of its diagonal terms is zero ($\delta_{ii} = 3$). The second term is a hydrostatic compression. As a general expression for the Helmholtz free energy of a deformed isotropic body, it is convenient to replace eq. (4.85) by another formula, using this decomposition of an arbitrary deformation into pure shear and

hydrostatic compression. We take as the two independent scalars of the second degree the sums of the squared components of the two terms in eq. (4.85). Then A becomes

$$A = \mu(\varepsilon_{ik} - \frac{1}{3}\delta_{ik}\varepsilon_{ll})^2 + \frac{1}{2}K\varepsilon_{ll}^2. \tag{4.87}$$

The quantities K and μ are called the *bulk modulus* and the *shear modulus*, respectively. K is related to the Laméconstants by:

$$K = \lambda + \frac{2}{3}\mu. \tag{4.88}$$

To calculate the derivatives $\partial A/\partial\varepsilon_{ik}$, we write the total differential $\mathrm{d}A$ (for constant temperature):

$$\mathrm{d}A = K\varepsilon_{ll}\mathrm{d}\varepsilon_{ll} + 2\mu(\varepsilon_{ik} - \frac{1}{3}\delta_{ik}\varepsilon_{ll})\mathrm{d}(\varepsilon_{ik} - \frac{1}{3}\delta_{ik}\varepsilon_{ll}) \tag{4.89}$$

In the second term, multiplication of the first parenthesis by δ_{ik} gives zero, resulting in:

$$dA = [K\varepsilon_{ll}\mathrm{d}\varepsilon_{ll} + 2\mu(\varepsilon_{ik} - \frac{1}{3}\delta_{ik}\varepsilon_{ll})\mathrm{d}\varepsilon_{ik} \tag{4.90}$$

or writing $\mathrm{d}\varepsilon_{ll} = \delta_{ik}\mathrm{d}\varepsilon_{ik}$, we have:

$$\mathrm{d}A = [K\varepsilon_{ll}\delta_{ik} + 2\mu(\varepsilon_{ik} - \frac{1}{3}\delta_{ik}\varepsilon_{ll})]\mathrm{d}(\varepsilon_{ik} \tag{4.91}$$

The stress tensor is therefore given by:

$$\sigma_{ik} = K\varepsilon_{ll}\delta_{ik} + 2\mu(\varepsilon_{ik} - \frac{1}{3}\delta_{ik}\varepsilon_{ll}). \tag{4.92}$$

This constitutive relationship between the stress and strain tensors shows that, if the deformation is a pure shear or a pure hydrostatic compression, the relation between σ_{ik} and ε_{ik} is determined only by the shear modulus or the bulk modulus, respectively. If we now use eq. (4.92) to find $\sigma_{ii} = 3K\varepsilon_{ii}$, and substitute each into the same equation, we obtain the inverse relationship between strain and stress.

$$\varepsilon_{ik} = \delta_{ik}\sigma_{ll}/9K + (\sigma_{ik} - \frac{1}{3}\delta_{ik}\sigma_{ll})/2\mu. \tag{4.93}$$

Equations (4.92) and (4.93) are valid for small deformation, and represent Hooke's law for isotropic solids. It is clear that only two elastic constants are required to describe the stress-strain relationship of isotropic solids. It is common to use Young's modulus (E) and Poisson's ratio (ν) instead. We have:

$$\mu = \frac{E}{2(1+\nu)},\ K = \frac{E}{3(1-2\nu)}$$

Thus, Equations (4.92) and (4.93) become:

$$\sigma_{ik} = \frac{E}{1+\nu}(\varepsilon_{ik} + \frac{\nu}{1-2\nu}\varepsilon_{ll}\delta_{ik}) \tag{4.94}$$

and

$$\varepsilon_{ik} = \frac{1}{E}[(1+\nu)\sigma_{ik} - \nu\sigma_{ll}\delta_{ik}]. \tag{4.95}$$

This procedure can be extended to anisotropic crystals, as will be discussed briefly here.

4.6 Anisotropic Crystals

In most crystalline materials, the elastic properties are dependent on specific directions as a result of unique atomic arrangement. In addition, when certain regions of a parent phase transform into another phase of a different crystal structure, the elastic properties change when the phase boundary is crossed. Materials with macroscopic degrees of symmetry (e.g. natural wood, fiber-reinforced composites, etc.) have elastic properties that are dependent on specific directions. Under the most general conditions, the constitutive equation of a crystal undergoing elastic deformation can be expressed in the form:

$$\sigma_{ij} = C_{ijkl}\varepsilon_{kl} \tag{4.96}$$

In eq. (4.96, the fourth-order tensor for the elastic constants, C_{ijkl} has 81 independent components. However, most of these components are redundant, as is shown in the following arguments. For general anisotropic materials, both the stress and strain tensors are symmetric, thus:

$$\sigma_{ij} = \sigma_{ji}; \qquad \varepsilon_{ij} = \varepsilon_{ji} \tag{4.97}$$

Hence one can write:

$$C_{ijkl} = C_{jikl} = C_{ijlk} \tag{4.98}$$

This symmetry leaves only 36 independent components of C_{ijkl}. Moreover, assuming that there exists a strain energy from which the stress can be derived as:

$$\sigma_{ij} = \frac{\partial U}{\partial \varepsilon_{ij}} \tag{4.99}$$

where;

$$U = \frac{1}{2} C_{ijkl}\varepsilon_{ij}\varepsilon_{kl} \tag{4.100}$$

One can conclude that the index symmetry of $C_{ijkl} = C_{klij}$ results in only 21 independent components. This most general condition is applicable to *triclinic materials*, or hyperelastic materials. Several special cases will be outlined next. Let us now adopt a simpler notation, as follows:

$$\{\sigma\}^T = [\sigma_1, \sigma_2, \sigma_3, \sigma_4, \sigma_5, \sigma_6] = [\sigma_{11}, \sigma_{22}, \sigma_{33}, \sigma_{23}, \sigma_{13}, \sigma_{12}] \tag{4.101}$$

and;

$$\{\varepsilon\}^T = [\varepsilon_1, \varepsilon_2, \varepsilon_3, \varepsilon_4, \varepsilon_5, \varepsilon_6] = [\varepsilon_{11}, \varepsilon_{22}, \varepsilon_{33}, 2\varepsilon_{23}, 2\varepsilon_{13}, 2\varepsilon_{12}] \tag{4.102}$$

The general constitutive elasticity relationship $\sigma_{ij} = C_{ijkl}\varepsilon_{kl}$ can thus be re-written as:

$$\begin{Bmatrix} \sigma_1 \\ \sigma_2 \\ \sigma_3 \\ \sigma_4 \\ \sigma_5 \\ \sigma_6 \end{Bmatrix} = \begin{bmatrix} C_{11} & C_{12} & C_{13} & C_{14} & C_{15} & C_{16} \\ C_{21} & C_{22} & C_{23} & C_{24} & C_{25} & C_{26} \\ C_{31} & C_{32} & C_{33} & C_{34} & C_{35} & C_{36} \\ C_{41} & C_{42} & C_{43} & C_{44} & C_{45} & C_{46} \\ C_{51} & C_{52} & C_{53} & C_{54} & C_{55} & C_{56} \\ C_{61} & C_{62} & C_{63} & C_{64} & C_{65} & C_{66} \end{bmatrix} \begin{Bmatrix} \varepsilon_1 \\ \varepsilon_2 \\ \varepsilon_3 \\ \varepsilon_4 \\ \varepsilon_5 \\ \varepsilon_6 \end{Bmatrix} \tag{4.103}$$

In the following, we discuss the special cases of symmetry that are usually encountered in anisotropic materials:

- *Monoclinic (Monotropic) Materials*

  If one plane of elastic symmetry exists, the material is said to be monoclinic or monotropic, and this condition leaves only 13 independent components of C_{ijkl}. For example, let the 2-3 plane (y-z plane) be the symmetry plane, then:

$$C_{14} = C_{16} = C_{25} = C_{26} = C_{35} = C_{36} = C_{45} = C_{46} = 0 \tag{4.104}$$

- *Orthotropic Materials*

  If three mutually orthogonal planes of symmetry exist, the material is said to be orthotropic, which leaves 9 independent components of C_{ijkl}. Wood is a common example of orthotropic materials. Thus,

$$[C] = \begin{bmatrix} C_{11} & C_{12} & C_{13} & 0 & 0 & 0 \\ C_{12} & C_{22} & C_{23} & 0 & 0 & 0 \\ C_{13} & C_{23} & C_{33} & 0 & 0 & 0 \\ 0 & 0 & 0 & C_{44} & 0 & 0 \\ 0 & 0 & 0 & 0 & C_{55} & 0 \\ 0 & 0 & 0 & 0 & 0 & C_{66} \end{bmatrix} \tag{4.105}$$

- *Transversely Isotropic Materials*

  If an orthotropic solid exhibits symmetry with respect to arbitrary rotations about one of the axes, it is then called transversely isotropic, which reduces the independent components of C_{ijkl} to only 5. For example, let x3-axis be the symmetric axis. Then,

$$[C] = \begin{bmatrix} C_{11} & C_{12} & C_{13} & 0 & 0 & 0 \\ C_{12} & C_{11} & C_{13} & 0 & 0 & 0 \\ C_{13} & C_{13} & C_{33} & 0 & 0 & 0 \\ 0 & 0 & 0 & C_{44} & 0 & 0 \\ 0 & 0 & 0 & 0 & C_{44} & 0 \\ 0 & 0 & 0 & 0 & 0 & C_{66} \end{bmatrix} \tag{4.106}$$

  With $C_{66} = \frac{1}{2}(C_{11} - C_{12})$. A unidirectional fiber-reinforced composite is a common example of a transversely isotropic material.

- *Cubic Materials*

Cubic materials have similar symmetry about three mutually orthogonal planes, and thus only 3 independent components of C_{ijkl} are needed. Therefore, for materials of cubic symmetry (e.g. FCC and BCC metals, cf. table 4.6), we have:

$$[C] = \begin{bmatrix} C_{11} & C_{12} & C_{12} & 0 & 0 & 0 \\ C_{12} & C_{11} & C_{12} & 0 & 0 & 0 \\ C_{12} & C_{12} & C_{11} & 0 & 0 & 0 \\ 0 & 0 & 0 & C_{44} & 0 & 0 \\ 0 & 0 & 0 & 0 & C_{44} & 0 \\ 0 & 0 & 0 & 0 & 0 & C_{44} \end{bmatrix} \tag{4.107}$$

- *Isotropic Materials*

A material with point symmetry or an infinite number of material symmetry planes is said to be isotropic, which leaves only 2 independent components of C_{ijkl}. In this case, we have:

$$[C] = \begin{bmatrix} C_{11} & C_{12} & C_{12} & 0 & 0 & 0 \\ C_{12} & C_{11} & C_{12} & 0 & 0 & 0 \\ C_{12} & C_{12} & C_{11} & 0 & 0 & 0 \\ 0 & 0 & 0 & C_{44} & 0 & 0 \\ 0 & 0 & 0 & 0 & C_{44} & 0 \\ 0 & 0 & 0 & 0 & 0 & C_{44} \end{bmatrix} \tag{4.108}$$

With $C_{44} = \frac{1}{2}(C_{11} - C_{12})$. In this very special case, the elasticity constants tensor has only two components, and one can write:

$$C_{ijkl} = \lambda \delta_{ij} \delta_{kl} + \mu(\delta_{ik}\delta_{jl} + \delta_{il}\delta_{jk}) \tag{4.109}$$

4.7 Navier's Equation

Determination of the distribution of stress, strain and displacements everywhere within the elastic body requires satisfying the equations of equilibrium, the constitutive equations and the boundary conditions, which can be specified in terms of known surface traction, displacements, or both. We will not concern ourselves here with boundary value problems, but we will rather focus our attention on elasticity problems that involve internal defects of material inhomogeneities. As such, we describe here the fundamental equation of elasticity that can be derived from both equilibrium and stress-strain relationships (Navier's equation), and then dedicate the remainder of this chapter to problems of microstructure evolution, as described by internal displacement discontinuities associated with dislocation loops, or internal sources of stress as a result of phase transitions. If we substitute the stress-strain relationship into the equilibrium equation:

$$\sigma_{ik,k} + f_i = C_{ijkl} u_{k,lj} + f_i = 0 \tag{4.110}$$

Table 4.1: Elastic constants $C_{11},\ C_{12},\ \&\ C_{44}$, and the anisotropy ratio $A = \frac{2C_{44}}{C_{11}-C12}$ for common metallic crystals

((?))

Metal	Crystal Structure	C_{11}	C_{12}	C_{44}	A
Au	fcc	18.6	15.7	4.20	2.9
Ag	fcc	12.40	9.34	4.61	3.01
Al	fcc	10.82	6.13	2.85	1.21
Cu	fcc	16.84	12.14	7.54	3.21
Ni	fcc	24.65	14.73	12.47	2.52
Mo	bcc	46.0	17.6	11.0	0.775
Nb	bcc	24.6	13.4	2.87	0.51
Cr	bcc	35.0	5.78	10.1	0.69
Fe	bcc	24.2	14.65	11.2	2.36
Ta	bcc	26.7	16.1	8.25	1.56
V	bcc	22.8	11.9	4.26	0.78

For isotropic materials, substituting eq. (4.109) into the equation of equilibrium (4.110), we obtain:

$$(\lambda + \mu)u_{j,ji} + \mu\, u_{i,jj} + f_i = 0 \tag{4.111}$$

In vector form, this last equation can be written as:

$$(\lambda + \mu)\nabla(\nabla \cdot \mathbf{u}) + \mu\nabla^2\mathbf{u} + \mathbf{f} = 0 \tag{4.112}$$

Equation (4.112) is known as Navier's equation, which describe the displacement vector field anywhere in a body in elastic equilibrium. In the absence of body forces, the Navier's equation of equilibrium becomes:

$$\nabla^2\mathbf{u} + \frac{1}{1-2\nu}\nabla(\nabla \cdot \mathbf{u}) = 0. \tag{4.113}$$

General solutions for Navier's equation without body forces have been obtained by Boussinesq in 1878 and by Galerkin in 1930, as follows.

$$\mathbf{u} = \nabla^2\mathbf{a} - \frac{1}{2(1-\nu)}\nabla(\nabla \cdot \mathbf{a}) \tag{4.114}$$

where the vector function $\mathbf{a}$ satisfies the biharmonic equation: $\nabla^2\nabla^2\mathbf{a} = 0$. On the other hand, Papkovitch (1932)and Neuber (1934) presented solutions of the form:

$$\mathbf{u} = \mathbf{b} - \frac{1}{4(1-\nu)}\nabla(b_0 + \mathbf{r} \cdot \mathbf{b}) \tag{4.115}$$

Where: the scalar function b_0, and the vector function $\mathbf{b}$ satisfy the harmonic equations: $\nabla^2 b_0 = 0$, $\nabla^2\mathbf{b} = 0$, $\mathbf{r} = x_i\mathbf{e}_i$, respectively.

4.8 Parametric Dislocations

4.8.1 Differential Geometry of Dislocation Loops

The core of an arbitrary-shape, 3-D dislocation loop can be reduced to a continuous line. Assume that the dislocation line is segmented into (n_s) arbitrary curved segments, labelled $(1 \leq i \leq n_s)$., as shown in Figure 4.4. For each segment, we define $\hat{\mathbf{r}}(u) = \mathbf{P}(u)$ as the position vector for any point on the segment, $\mathbf{T}(u) = T\mathbf{t}$ as the tangent vector to the dislocation line, and $\mathbf{N}(u) = N\mathbf{n}$ as the normal vector at any point (See Figure 4.5)). The space curve is then completely described by the parameter u, if one defines certain relationships which determine $\hat{\mathbf{r}}(u)$. Note that the position of any other point in the medium (Q) is denoted by its vector $\mathbf{r}$, and that the vector connecting the source point $\mathbf{P}$ to the field point is $\mathbf{R}$, thus $\mathbf{R} = \mathbf{r} - \hat{\mathbf{r}}$. In the following developments, we restrict the parameter $0 \leq u \leq 1$, although we map it later on the interval $-1 \leq \hat{u} \leq 1$, and $\hat{u} = 2u - 1$ in the numerical quadrature implementation of the method.

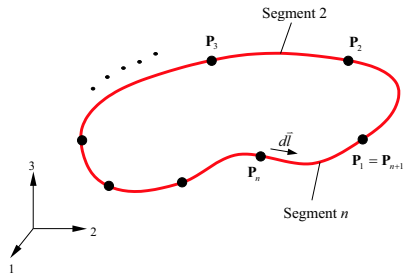

Figure 4.4: A space dislocation loop discretized into a finite number of curved segments, N_s

To specify a parametric form for $\hat{\mathbf{r}}(u)$, we will now choose a set of generalized coordinates $\mathbf{q}_i^{(j)}$ for each segment (j), which can be quite general. If one defines a set of basis functions $\mathcal{N}_i(u)$, where u is a parameter, and allows for index sums to extend also over the basis set $(i = 1, 2, .., I)$, the equation of the segment can be written as:

$$\hat{\mathbf{r}}^{(j)}(u) = \mathbf{q}_i^{(j)} \mathcal{N}_i(u) \tag{4.116}$$

Or, in compact component (k) form, this can be put as:

$$\hat{x}_k^{(j)}(u) = q_{ik}^{(j)} \mathcal{N}_i(u) \tag{4.117}$$

Thus, the components of the displacement vector are given by:

$$\delta\hat{x}_k^{(j)}(u) = \delta q_{ik}^{(j)} \mathcal{N}_i(u) \tag{4.118}$$

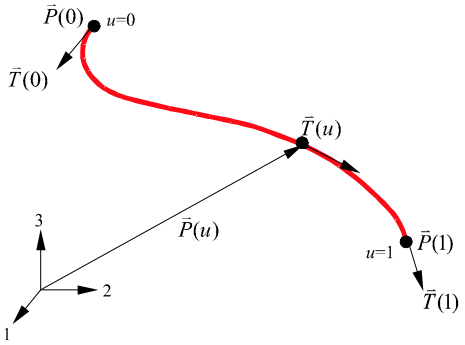

Figure 4.5: Basic elements of a space curve representing one dislocation segment

At this point, we must specify the form of parametric description for the dislocation line. Although this step is open to pure computational convenience, we present here those parametric forms which we use later in this work. Parametric dislocation representation discussed below are also sufficient to describe the majority of experimentally observed dislocation line geometry.

4.8.2 Circular, Elliptic and Helical Loops

Small prismatic loops of circular (or nearly elliptic) shapes are observed in many materials under deformation, irradiation and quenching conditions(?). Helical loops of unusual regularity have also been experimentally observed under large vacancy supersaturation (?). Therefore, it seems natural to use a simple representation for such loops, where the shape functions are given by:

$$\mathcal{N}_1 = cos(2\pi u), \qquad \mathcal{N}_2 = sin(2\pi u), \qquad \mathcal{N}_3 = u \tag{4.119}$$

And their parametric derivatives, which we use later in determining the arc length, are simply given by:

$$\mathcal{N}_{1,u} = -2\pi\mathcal{N}_2, \qquad \mathcal{N}_{1,u} = 2\pi\mathcal{N}_1, \qquad \mathcal{N}_{3,u} = 1 \tag{4.120}$$

Note that in this case, the description is not in Cartesian coordinates, and that the generalized degrees of freedom are given by:

$$q_1 = a, \qquad q_2 = b, \qquad ,\& \qquad q_3 = c \tag{4.121}$$

Loop motion is described in terms of the time variations of the generalized coordinates, a, b, and c.

4.8.3 Linear Parametric Segments

The majority of 3-D dislocation dynamics developments are based on analytic solutions to the elastic field of linear segments(?)-(?). Sometimes it is just as convenient to use a purely numer-

ical method, without any loss of computational speed or accuracy(**?**). Under these conditions, the *shape functions* $\mathcal{N}_i(u)$ and their derivatives $\mathcal{N}_{i,u}$ take the form:

$$\mathcal{N}_1 = 1 - u \qquad \mathcal{N}_2 = u \tag{4.122}$$

$$\mathcal{N}_{1,u} = -1 \qquad \mathcal{N}_{2,u} = 1 \tag{4.123}$$

The available degrees of freedom for a *free, or unconnected* linear segment (j) are just the position vectors of the beginning(j) and end $(j+1)$ nodes. Thus:

$$q_{1k}^{(j)} = P_k^{(j)}, \qquad \& \qquad q_{2k}^{(j)} = P_k^{(j+1)} \tag{4.124}$$

4.8.4 Cubic Spline Parametric Segments

The self-force on a dislocation segment can be approximated as a simple function of its curvature ((**?**),(**?**),(**?**)). To allow for continuity of the self-force along the entire dislocation loop, and to capture non-linear deformations of the dislocation line itself during, a higher order parametric representation is desired. For cubic spline segments, we use the following set of shape functions, their parametric derivatives, and their associated degrees of freedom, respectively:

$$\begin{aligned}
\mathcal{N}_1 &= 2u^3 - 3u^2 + 1, \quad \mathcal{N}_2 = -2u^3 + 3u^2, \quad \mathcal{N}_3 = u^3 - 2u^2 + u, \quad \& \quad \mathcal{N}_4 = u^3 - u^2 \\
\mathcal{N}_{1,u} &= 6u^2 - 6u, \quad \mathcal{N}_{2,u} = -6u^2 + 6u2, \quad \mathcal{N}_{3,u} = 3u^2 - 4u + 1, \quad \& \quad \mathcal{N}_{4,u} = 3u^2 - 2u \\
q_{1k}^{(j)} &= P_k^{(j)}, \qquad q_{2k}^{(j)} = P_k^{(j+1)}, \qquad q_{3k}^{(j)} = T_k^{(j)}, \qquad \& q_{4k}^{(j)} = T_k^{(j+1)}
\end{aligned} \tag{4.125}$$

4.8.5 Quintic Spline Parametric Segments

A greater degree of flexibility can be achieved if one considers even higher order representation. The special case of continuous quintic splines is rather interesting. The available degrees of freedom can be increased to include variations in the normal vector, $\mathbf{N}$, as well as the position $\mathbf{P}$ and tangent $\mathbf{T}$ vectors. So, in passing from linear to cubic and then to quintic representation, one has $\{\mathbf{P}\}, \{\mathbf{P}\&\mathbf{T}\}$, and $\{\mathbf{P}, \mathbf{T}\&\mathbf{N}\}$, respectively. With that, line curvature can be smoothly controlled and out-of-plane dislocation motion can be simultaneously followed with glide events. The equations for shape functions, their parametric derivatives, and available degrees of freedom for quintic splines are given by:

$$\begin{aligned}
\mathcal{N}_1 &= -6u^5 + 15u^4 - 10u^3 + 1, \quad \mathcal{N}_2 = 6u^5 - 15u^4 + 10u^3, \quad \mathcal{N}_3 = -3u^5 + 8u^4 - 6u^3 + u, \\
\mathcal{N}_4 &= -3u^5 + 7u^4 - 4u^3, \quad \mathcal{N}_5 = \frac{1}{2}(-u^5 + 3u^4 - 3u^3 + u^2), \quad \& \quad \mathcal{N}_6 = \frac{1}{2}(u^5 - 2u^4 + u^3) \\
\mathcal{N}_{1,u} &= 30(-u^4 + 2u^3 - u^2), \quad \mathcal{N}_{2,u} = -\mathcal{N}_{1,u}, \quad \mathcal{N}_{3,u} = -15u^4 + 32u^3 - 18u^2 + 1, \\
\mathcal{N}_{4,u} &= -15u^4 + 28u^3 - 12u^2, \quad \mathcal{N}_{5,u} = \frac{1}{2}(-5u^4 + 12u^3 - 9u^2 + 2u), \quad \mathcal{N}_{6,u} = \frac{1}{2}(5u^4 - 8u^3 + 3u^2) \\
q_{1k}^{(j)} &= P_k^{(j)}, \quad q_{2k}^{(j)} = P_k^{(j+1)}, \quad q_{3k}^{(j)} = T_k^{(j)}, \quad q_{4k}^{(j)} = T_k^{(j+1)}, q_{5k}^{(j)} = N_k^{(j)}, \quad \& q_{6k}^{(j)} = N_k^{(j+1)}
\end{aligned} \tag{4.126}$$

The total number of available degrees of freedom for a dislocation segment requires careful consideration. Even though more flexibility, and hence accuracy, is achieved by higher order

splines, it is still desirable to reduce the number of degrees (N_{DF}) of freedom from a computational standpoint. For a *free, or discrete* segment, N_{DF} is thus equal to the number of components in the Cartesian vector $\mathbf{q}^{(\mathrm{j})}{}_i$; i.e. $N_{DF} = 6, 12$, and 18, for linear, cubic and quintic splines, respectively. However, N_{DF} can be greatly reduced on physical and geometric grounds. Since all segments must be connected on the loop, only one node is associated with each segment instead of two. Loop boundary conditions can be used to define (or fix) specific DF's on certain nodes. Thus, for a *continuous* representation, N_{DF} is reduced by a factor of 2. Moreover, if the motion is that of pure glide on the slip plane, appropriate coordinate transformations can be used to assign *local* DF's in two dimensions. Thus, planar loop motion can be described by $N_{DF}^{local} = 2, 4, \&6$ for the three parametric cases we consider here. Additional physical and geometric constraints can still be imposed to reduce N_{DF} even further.

Forces and energies of dislocation segments are given per unit length of the curved dislocation line. Also, line integrals of the elastic field variables are carried over differential line elements. Thus, if we express the Cartesian differential in the parametric form:

$$d\ell_k^{(j)} = \hat{x}_{k,\,u}^{(j)} du = q_{sk}^{(j)} \mathcal{N}_{s,\,u} du \tag{4.127}$$

The arc length differential for segment j is then given by:

$$\begin{aligned} \mid d\ell^{(j)} \mid &= \left(d\ell_k^{(j)} d\ell_k^{(j)} \right)^{\frac{1}{2}} = \left(\hat{x}_{k,\,u}^{(j)} \hat{x}_{k,\,u}^{(j)} \right)^{\frac{1}{2}} du \\ &= \left(q_{pk}^{(j)} \mathcal{N}_{p,\,u} \;\; q_{sk}^{(j)} \mathcal{N}_{s,\,u} \right)^{\frac{1}{2}} du \end{aligned} \tag{4.128}$$

Chapter 5

Two-dimensional Elastic Fields

5.1 Infinite Isotropic Media

5.1.1 Edge Dislocations

Consider an edge dislocation with the Burgers vector as x_1-axis of a rectangular Cartesian co-ordinate system and the dislocation line as x_3-axis of an isotropic elastic cylinder of infinite length L and radius R. We apply the linear theory of elasticity in the region $r_0 < r < R$, where r_0 is the core radius (usually 5 to 10 atomic spacings) and assume that the surface tractions acting at the inner and outer boundary are known and independent of x_3. Therefore, the straight edge dislocation described above produces displacement field that do not depend on x_3. The deformation induced is known as *plane strain* and is given by

$$u_1 = u_1(x_1, x_2), \qquad u_2 = u_2(x_1, x_2), \qquad u_3 = 0 \tag{5.1}$$

Consequently, $\varepsilon_{13} = \varepsilon_{23} = \varepsilon_{33} = 0$, and $\varepsilon_{11}, \varepsilon_{22}$, and ε_{12} are independent of x_3. The stresses are given by

$$\begin{aligned} \sigma_{11} &= (\lambda + 2\mu)\varepsilon_{11} + \lambda\varepsilon_{22} \\ \sigma_{22} &= \lambda\varepsilon_{11} + (\lambda + 2\mu)\varepsilon_{22} \\ \sigma_{33} &= \lambda(\varepsilon_{11} + \varepsilon_{22}) = \nu(\sigma_{11} + \sigma_{22}) \\ \sigma_{12} &= 2\mu\varepsilon_{12}, \qquad \sigma_{13} = \sigma_{23} = 0 \end{aligned} \tag{5.2a}$$

Assuming the body force to be zero, the first two equilibrium equations become

$$\begin{aligned} \sigma_{11,1} + \sigma_{12,2} &= 0 \\ \sigma_{12,1} + \sigma_{22,2} &= 0 \end{aligned} \tag{5.3a}$$

and the third one is identically satisfied.

We consider that $\mathbf{u}$ is single-valued in the region $\triangle$ between the inner and outer boundary. Then, it is clear that u_2 will be continuous across the cut $x_2 = 0$, $-R \leq r \leq -r_0$, while the

component u_1 will have jump across this cut, given by

$$u_1(x_1, 0^+) - u_1(x_1, 0^-) = -b, \qquad -R \leq r \leq -r_0 \tag{5.4}$$

where, b is the magnitude of the true Burger vector. Since it was assumed that the traction, $t_z^* = 0$, for $r = r_0$ and $r = R$, the components of the surface tractions acting on the elastic boundary are t_r^* and t_θ^*. Assuming that these components may be expressed in complex Fourier series of the polar angle θ, we write

$$t_r^* + it_\theta^* \;=\; \begin{cases} \sum\limits_{k=-\infty}^{\infty} t_k^{(1)} e^{ik\theta} & for\ \ r = r_0 \\ \sum\limits_{k=-\infty}^{\infty} t_k^{(2)} e^{ik\theta} & for\ \ r = R \end{cases} \tag{5.5}$$

However, we can set $\boldsymbol{t^* = 0}$ on the external boundary of the cylinder, if we are interested only in calculating the self-stresses produced by dislocations. On the contrary, the inner boundary used to isolate the dislocation line is acted on by forces arising from the dislocation core, which can be determined only by a combined continuum and atomistic calculation. It can be shown, that the contributions of these forces toward the stress field are negligible with increasing distance from the dislocation line compared to those arising from the effect of L and b that characterize the long range stress field of the dislocation. Thus, we can set $\boldsymbol{t^* = 0}$ at $r = r_0$.

It may be shown that

$$\sigma_{rr} + i\sigma_{r\theta} = \frac{1}{2}[\sigma_{11} + \sigma_{22} + (\sigma_{11} - \sigma_{22} + 2i\sigma_{12})e^{-2i\theta}] \tag{5.6}$$

and hence the boundary conditions given by Equations 5.5 can be written in the equivalent complex form

$$\frac{1}{2}[\sigma_{11} + \sigma_{22} + (\sigma_{11} - \sigma_{22} + 2i\sigma_{12})e^{-2i\theta}] \;=\; t_r^* + it_\theta^* \tag{5.7}$$

for $r = r_0$ and for $r = R$. The above formulated boundary value problem can be solved using complex variable method. It is well known that the general solution to the two-dimensional equations of elastostatics can be expressed in terms of two analytic but otherwise arbitrary functions of a complex variable. A detailed discussion can be found in Sokolnikoff (1956) and England (1971). We summarize the results as follows.

$$\begin{aligned} \sigma_{11} + \sigma_{22} &= 2[F'(z) + \overline{F'(z)}] = 4Re[F'(z)] \\ \sigma_{11} - \sigma_{22} + 2i\sigma_{12} &= -2[z\overline{F"(z)} + \overline{G'(z)}] \\ 2\mu U(z, \overline{z}) &= (3 - 4\nu)F(z) - z\overline{F'(z)} - \overline{G(z)} \end{aligned} \tag{5.8}$$

where, F(z) and G(z) are analytic functions of complex number z in $\triangle$ and U is the complex displacement. Equations 5.8 give the Kolosov's representation of the solution of the plane strain

problem of linear elasticity in terms of complex potentials F(z) and G(z). The jump condition given by Equation 5.1 and boundary conditions (Equations 5.5) can then be restated as:

$$\begin{array}{rcl} U(x_1,0^+)-U(x_1,0^-) & = & -b \\ F'(z)+\overline{F'(z)}-e^{-2i\theta}\ \{z\overline{F''(z)}+\overline{G'(z)}\} & = & 0\ \ for\ \ z=r_0e^{i\theta}, Re^{i\theta} \end{array} \tag{5.9}$$

The boundary value problem can now be solved by finding the functions F(z) and G(z) that are analytic in $\triangle$ and that satisfy the jump condition Equation 5.1-(a) and the boundary conditions of Equation 5.5-(b).

Since the stress components are continuous across the negative x_1 axis, equations 5.8(a),(b) imply that the analytic functions $F'(z)$ and $G'(z)$ must be continuous and single valued in $\triangle$ and hence they can be expanded in Laurent power series of z

$$F'(z)=\sum_{k=-\infty}^{\infty} a_k z^k \quad G'(z)=\sum_{k=-\infty}^{\infty} b_k z^k \tag{5.10}$$

Integrating (5.11) gives

$$F(z)=a_{-1}\ln(z)+\sum_{k=-\infty,k\neq-1}^{\infty}\frac{a_k z^{k+1}}{k+1} \quad G(z)=b_{-1}\ln(z)+\sum_{k=-\infty,k\neq-1}^{\infty}\frac{b_k z^{k+1}}{k+1} \tag{5.11}$$

We set the constants of integration to zero in order to suppress the translational components of the rigid body displacements in 5.8(c). This impose the supplementary conditions $F(0)=0$ and $G(0)=0$. In order to avoid the rigid body rotation we need to enforce the condition $Im\ F'(0)=0$ which gives $Im\ a_0=0$. The multiple valued function $\ln(z)$ may be determined as single valued by introducing a suitable cut in the z-plane. As an example, by choosing a cut $x_2=0$, $x_1\leq 0$, we can take

$$\ln(z)=\ln|z|+iarg(z), \tag{5.12}$$

where

$$|z| \ = \ r=\sqrt{x_1^2+x_2^2} \tag{5.13a}$$

$$\arg(z) \ = \ \theta=\begin{cases} \text{cotan}^{-1}\frac{x_1}{x_2} & \text{for} \quad x_2{=}0 \\ 0 \quad \text{for} & x_2{=}0,\ x_1{=}0 \\ \text{cotan}^{-1}\frac{x_1}{x_2}-\pi & \text{for} \quad x_2{=}0 \end{cases} \tag{5.13b}$$

Thus, the limiting values of arg(z) on the upper and lower faces of the cut are π and $-\pi$, respectively. Introducing 5.10 and 5.11 into 5.8(c), and using the jump condition 5.9(a), we find

$$(3-4\nu)a_{-1}+\overline{b}_{-1}=-\frac{i\mu b}{\pi} \tag{5.14}$$

By substituting 5.10 into 5.9(b) and equating coefficients of $e^{ik\theta}$ for $k=0,\pm1,\pm1.....$, we obtain for $k=0$:

$$2a_0-\overline{b}_{-2}r_0{-}2=0, \quad 2a_0-\overline{b}_{-2}R^{-2}=0 \tag{5.15}$$

for $k = -1$:

$$a_{-1} - \overline{b}_{-1} = 0 \tag{5.16}$$

for k=1:

$$a_1 r_0 + 2\overline{a}_{-1} r_0^{-1} - \overline{b}_{-3} r_0^{-3} = 0, \quad a_1 R + 2\overline{a}_{-1} R^{-1} - \overline{b}_{-3} R^{-3} = 0 \tag{5.17}$$

Solving 5.14-5.17, we obtain

$$a_0 = 0, \;\; a_{-1} = \overline{b}_{-1} = \frac{i\mu b}{4\pi(1-\nu)}, \;\; a_1 = \frac{i\mu b}{2\pi(1-\nu)(R^2 + r_0^2)}, \;\; b_{-2} = 0, \;\; b_{-3} = \frac{i\mu b R^2 r_0^2}{2\pi(1-\nu)(R^2 + r_0^2)} \tag{5.18}$$

and all other coefficients a_k, b_k vanish if we solve all equations obtained by equating coefficients for $k = \pm 2, \pm 3, \ldots$. Thus, the boundary problem formulated above is completely solved. We can now obtain the stress and displacements realizing that

$$F(z) = a_{-1} \ln(z) + \frac{a_1 z^2}{2}, \;\; G(z) = b_{-1} \ln(z) - \frac{b_{-3}}{2z^2}. \tag{5.19}$$

Using 5.18, 5.19 and 5.8(a)-(c), and taking into account that

$$\begin{aligned} \sigma_{rr} + \sigma_{\theta\theta} &= \sigma_{11} + \sigma_{22} \\ \sigma_{rr} - \sigma_{\theta\theta} + 2i\sigma_{r\theta} &= (\sigma_{11} - \sigma_{22} + 2i\sigma_{12}) e^{-2i\theta} \end{aligned}$$

we obtain,

$$u_1 = -\frac{b}{2\pi}\{\theta + \frac{1}{4(1-\nu)}[1 + \frac{(3-4\nu)r^2}{R^2 + r_0^2} - \frac{R^2 r_0^2}{(R^2 + r_0^2) r^2}] \sin(2\theta)\} \tag{5.20a}$$

$$u_2 = \frac{b}{8\pi(1-\nu)}\{2(1-2\nu)\ln r + \frac{2r^2}{R^2 + r_0^2} + [1 + \frac{(3-4\nu)r^2}{R^2 + r_0^2} - \frac{R^2 r_0^2}{(R^2 + r_0^2) r^2}] \cos(2\theta)\} \tag{5.20b}$$

$$\sigma_{rr} = \frac{\mu b}{2\pi(1-\nu)}(\frac{1}{r} - \frac{r}{R^2 + r_0^2} - \frac{R^2 r_0^2}{(R^2 + r_0^2) r^2}) \sin\theta \tag{5.20c}$$

$$\sigma_{\theta\theta} = \frac{\mu b}{2\pi(1-\nu)}(\frac{1}{r} - 3\frac{r}{R^2 + r_0^2} + \frac{R^2 r_0^2}{(R^2 + r_0^2) r^2}) \sin\theta \tag{5.20d}$$

$$\sigma_{r\theta} = \frac{\mu b}{2\pi(1-\nu)}(-\frac{1}{r} + \frac{r}{R^2 + r_0^2} - \frac{R^2 r_0^2}{(R^2 + r_0^2) r^2}) \cos\theta \tag{5.20e}$$

$$\sigma_{zz} = \nu(\sigma_{rr} + \sigma_{\theta\theta}), \quad \sigma_{rz} = 0 \tag{5.20f}$$

The displacement and stress components in (5.19,20) can be simplified extensively under certain assumptions as follows: (a) it is assumed that the body containing the dislocations are much larger than the range of elastic field produced, hence, we can set $R \longrightarrow \infty$ in (5.20), (b) the terms of order $O(r^{-3})$ in the stress and $O(r^{-2})$ in the displacement components are often ignored as $r \longrightarrow \infty$, since the boundary conditions on the dislocation core are unknown without a simultaneous atomic calculations. With these assumptions, (5.19) and (5.20) yield

the simplified relations

$$u_1 = -\frac{b}{2\pi}\{\theta + \frac{1}{4(1-\nu)}\sin(2\theta)\} \quad (5.21a)$$

$$u_2 = \frac{b}{8\pi(1-\nu)}\{2(1-2\nu)\ln r + \cos(2\theta)\} \quad (5.21b)$$

$$\sigma_{rr} = \sigma_{\theta\theta} = \frac{\mu b}{2\pi(1-\nu)}\frac{\sin\theta}{r} \quad (5.21c)$$

$$\sigma_{r\theta} = -\frac{\nu\mu b}{\pi(1-\nu)}\frac{\cos\theta}{r} \quad (5.21d)$$

$$\sigma_{zz} = \frac{\nu\mu b}{\pi(1-\nu)}\frac{\sin\theta}{r} \qquad \sigma_{rz} = 0 \quad (5.21e)$$

In cartesian coordinates the stresses are given by

$$\sigma_{11}(x,y) = \frac{\mu b}{2\pi(1-\nu)}\frac{y(3x^2+y^2)}{(x^2+y^2)^2} \quad (5.22a)$$

$$\sigma_{22}(x,y) = -\frac{\mu b}{2\pi(1-\nu)}\frac{y(x^2-y^2)}{(x^2+y^2)^2} \quad (5.22b)$$

$$\sigma_{12}(x,y) = -\frac{\mu b}{2\pi(1-\nu)}\frac{x(x^2-y^2)}{(x^2+y^2)^2} \quad (5.22c)$$

For a linear elastic solid, the strain energy density may be written as

$$W = \frac{1}{2}C_{ijkl}\varepsilon_{ij}\varepsilon_{kl} \quad (5.23)$$

If the material is isotropic, (5.23) takes the simple form

$$W = \frac{\lambda}{2}\varepsilon_{mm}^2 + \mu\varepsilon_{km}\varepsilon_{mk} \quad (5.24)$$

where, $\lambda = \frac{\nu E}{(1+\nu)(1-2\nu)}$ and $\mu = \frac{E}{2(1+\nu)}$. From (5.24), the strain energy density produced by the edge dislocation is

$$W = \frac{\mu b^2}{8\pi^2(1-\nu)^2}\frac{1-2\nu\sin^2\theta}{r^2} \quad (5.25)$$

The strain energy stored per unit length of the dislocation line can then be given by

$$E = \int_{r_0}^{R}\rho d\rho\int_0^{2\pi}W d\theta\int_0^1 dz = \frac{\mu b^2}{4\pi(1-\nu)}\ln\frac{R}{r_0} \quad (5.26)$$

If the energy per unit length of the dislocation core, say E_0 is taken into account, (5.26) can be rewritten in terms of total energy per unit length as

$$E_t = \int_{r_0}^{R}\rho d\rho\int_0^{2\pi}W d\theta\int_0^1 dz = \frac{\mu b^2}{4\pi(1-\nu)}\ln\frac{R}{r_0} + E_0 \quad (5.27)$$

5.1.2 Screw Dislocations

We now consider a screw dislocation with burgers vector parallel to the dislocation line that coincides with the axis x_3 of an isotropic elastic circular cylinder of radius R. Making use of the cylindrical co-ordinates r, θ, z and the symmetry of the problem, it is clear that the strain and stress components are independent of θ and z, and the displacement vector must be parallel to the dislocation line and independent of z, i.e.

$$u_z = u_z(r, \theta), \qquad u_r = u_\theta = 0 \tag{5.28}$$

Thus, in contrast to the case of edge dislocation, u_r and u_θ are now continuous across the cut $x_2 = 0$, $-R \leq r \leq -r_0$, but, u_z is discontinuous across this cut, given by

$$u_z(r, \pi) - u_z(r, -\pi) = -b, \qquad -R \leq r \leq -r_0 \tag{5.29}$$

We also assume that both cylindrical surfaces $r = r_0$ and $r = R$ are free of tractions, i.e.

$$\sigma_{rr} = \sigma_{r\theta} = \sigma_{rz} = 0 \qquad -R \leq r \leq -r_0 \tag{5.30}$$

The condition (5.29) yields the solution for u_z as

$$u_z = -\frac{b\theta}{2\pi} \qquad \theta \in [-\pi, \pi] \tag{5.31}$$

Using the constitutive equations in cylindrical co-ordinates, the stress components are given by

$$\sigma_{\theta z} = \sigma_{z\theta} = -\frac{\mu b}{2\pi r} \tag{5.32}$$

In cartesian coordinates, they are given by

$$\sigma_{13} = \frac{\mu b x_2}{2\pi(x_1^2 + x_2^2)} \tag{5.33a}$$

$$\sigma_{23} = -\frac{\mu b x_1}{2\pi(x_1^2 + x_2^2)} \tag{5.33b}$$

$$\sigma_{11} = \sigma_{22} = \sigma_{12} = 0, \quad \sigma_{33} = \nu(\sigma_{11} + \sigma_{22}) \tag{5.33c}$$

Using (5.23), the strain energy density for a screw dislocation is given by

$$W = \frac{\mu b^2}{8\pi^2 r^2} \tag{5.34}$$

Hence, the strain energy stored per unit length of screw dislocation can be obtained from (5.27) as

$$E = \frac{\mu b^2}{4\pi} \ln \frac{R}{r_0} \tag{5.35}$$

while the total energy per unit length of screw dislocation is $E_t = E + E_0$. Comparing (5.26) and (5.35), it is seen that the strain energy of a screw dislocation is smaller than that of an edge dislocation for $0 < \nu < 0.5$.

It can be noticed further that the elastic field corresponding to edge and screw dislocations in an infinite isotropic medium are 'uncoupled'. This allows us to calculate the elastic field produce by a 'mixed dislocation' whose Burgers vector makes an α with the dislocation line, by replacing b with $b\sin\alpha$ in the elastic field produced by an edge dislocation (eqs. 5.21), with $b\cos\alpha$ in that by an screw dislocation(eqs. 5.32) and summing up the results. The strain energy stored per unit length of a mixed dislocation can thus be expressed as

$$w = \frac{\mu b^2}{4\pi}(\cos^2\alpha + \frac{\sin^2\alpha}{1-\nu})\ln\frac{R}{r_0} \tag{5.36}$$

5.2 Infinite Anisotropic Media

The elastic field of infinite straight dislocations under a *state of generalized plane strain* was developed by Eshelby et al.(1953) and was extended by Foreman, Stroh, Seeger, Shoeck, Chou and others. Consider an anisotropic elastic body, B, referred to a rectangular cartesian coordinate system, x_k, with the x_3 axis parallel to the dislocation line. The material properties, c_{ijkl}, are also referred to this system. The elastic field, i.e, stresses, strains and displacements can now be assumed to be independent of x_3, and the corresponding state is called after Lekhnitski a *state of generalized plane strain*. Thus

$$u_k = u_k(x_1, x_2), k = 1, 2, 3 \tag{5.37}$$

The equations of equilibrium take the reduced form

$$\frac{\partial\sigma_{i\alpha}}{\partial x_\alpha} = 0 \tag{5.38}$$

and the stress-displacement relationships become

$$\sigma_{i\alpha} = c_{i\alpha k\beta}\frac{\partial u_k}{\partial x_\beta} \tag{5.39}$$

where, the pair of Greek letters α and β are taken to be one of the numbers 1 and 2, and in deriving Eq. (6.3), the general symmetries in c_{ijkl} are used.

On substituting (6.3) into (6.2), we obtain

$$c_{i\alpha k\beta}\frac{\partial u_k}{\partial x_\alpha \partial x_\beta} = 0 \tag{5.40}$$

Following Eshelby et al., the solutions of the partial deferential equations in (6.4) take the standard forms

$$u_k = A_k f(z), \tag{5.41}$$

where *f(z)* is an analytic function of the complex variable $z = x_1 + px_2$, and A_k and p are constants. (6.5) is a solution of Eqs. (6.4) provided the constant vector A_k satisfies the equations

$$(c_{i1k1} + pc_{i1k2} + pc_{i2k1} + p^2 c_{i2k2})A_k = 0 \tag{5.42}$$

The nonzero values of A_k can be found to satisfy these equations if p is a root of the sextic equation

$$|c_{i1k1} + pc_{i1k2} + pc_{i2k1} + p^2 c_{i2k2}| = 0 \tag{5.43}$$

It is often convenient to replace the pairs of suffices (i,j) and (k,l) by single suffices M and N according to the scheme that 11 corresponds to 1, 22 to 2, 33 to 3, 23 to 4, 31 to 5, and 12 to 6. Then the sextic equation (6.7) can be written in explicit form in terms of the elastic compliances S_{KM} as

$$l(p) = l_2(p)l_4(p) - l_3^2(p) = 0 \tag{5.44}$$

where,

$$l_2(p) = S_{55}p^2 - 2S_{45}p + S_{44} \tag{5.45}$$
$$l_3(p) = S_{15}p^3 - (S_{14} + S_{56})p^2 + (S_{25} + S_{46})p - S_{24} \tag{5.46}$$
$$l_4(p) = S_{11}p^4 - 2S_{16}p^3 + (2S_{12} + S_{66})p^2 - S_{26}p + S_{22} \tag{5.47}$$

For each root p_n, $n = 1...6$, there is a set A_{kn} which satisfies Eqn. (6.6). Eshelby et al. have proved that in order for the strain energy to be positive Eqn. (6.7) has no real roots, so that the roots occur in complex conjugate pairs. A general expression for the the displacement can then be written as

$$u_k = \sum_{n=1}^{3} A_{kn} f_n(z_n) + \sum_{n=1}^{3} \overline{A}_{kn} \overline{f_n(z_n)} \tag{5.48}$$

where, overbar denotes the complex conjugate and $z_n = x_1 + p_n x_2$. Since u_k is real, expression (6.8) can be written in an alternate form as

$$u_k = Re[\sum_{n=1}^{3} A_{kn} f_n(z_n)] \tag{5.49}$$

where Re means "the real part of". Thus one need only consider three roots p_1, p_2, p_3 $(Im[p] > 0)$ and the corresponding sets A_{k1}, A_{k2}, A_{k3}. The coefficients A_{kn} can be calculated by the formulae:

$$A_{1\alpha} = S_{11}p_\alpha^2 - S_{16}p_\alpha + S_{12} + \lambda_\alpha(S_{15}p_\alpha - S_{14}) \quad (5.50a)$$
$$A_{2\alpha} = S_{12}p_\alpha^2 - S_{26}p_\alpha + S_{22} + \lambda_\alpha(S_{25}p_\alpha - S_{24})/p_\alpha \quad (5.50b)$$
$$A_{3\alpha} = S_{14}p_\alpha^2 - S_{46}p_\alpha + S_{24} + \lambda_\alpha(S_{45}p_\alpha - S_{44})/p_\alpha \quad (5.50c)$$

for $\alpha = 1, 2$ and

$$A_{13} = \lambda_3(S_{11}p_\alpha^3 - S_{16}p_3 + S_{12}) + S_{15}p_3 - S_{14}) \quad (5.51a)$$
$$A_{23} = \{\lambda_3(S_{12}p_3^2 - S_{26}p_3 + S_{22}) + S_{25}p_3 - S_{24}\}/p_3 \quad (5.51b)$$
$$A_{33} = \{\lambda_3(S_{14}p_3^2 - S_{46}p_3 + S_{24}) + S_{45}p_3 - S_{44}\}/p_3 \quad (5.51c)$$

where

$$\lambda_1 = -\frac{l_3(p_1)}{l_2(p_1)} \quad \lambda_2 = -\frac{l_3(p_2)}{l_2(p_2)} \quad \lambda_3 = -\frac{l_3(p_3)}{l_4(p_3)} \tag{5.52}$$

The f_n are arbitrary analytic functions and need to be solved from the boundary conditions of the problem as follows.

The displacements u_k are multiple-valued if we make a cut encircling the dislocation lying along the x_3 axis. The boundary conditions require that the displacement vector,u_k, is single valued and of class C^3 outside the cut, and is discontinuous across the cut $x_2 = 0$, $x_1 > 0$; its jump across the cut is given by

$$u_k(x_1, 0^+) - u_k(x_1, 0^-) = b_k, \qquad x_1 > 0 \tag{5.53}$$

where b_k is the k^{th} component true burgers vector $\mathbf{b}$ of the dislocation.

The stress boundary conditions suggest that the function $f'(z)$ is single valued and continuous except at the origin and it can be expressed in a Laurent series,

$$f'(z) = \sum_{s=-\infty}^{\infty} a_n^{'} z^n \tag{5.54}$$

Integration of this relation gives the most general form of the function $f(z)$

$$f(z) = -\frac{D}{2\pi i}\ln(z) + \sum_{s=-\infty}^{\infty} a_n z^s \tag{5.55}$$

Since all the power-series terms are continuous across the cut, from (6.12),

$$\triangle f = +D. \tag{5.56}$$

It is due to the fact that the we have considered imaginary part of p to be positive; then a counterclockwise path around the dislocation corresponds to a counterclockwise path in the z plane. Thus across the cut $\triangle \ln(z) = -2\pi i$.

From the previous studies on the straight dislocation in finite media, we have seen that the terms involving $s \geq 1$ and $s \leq 1$ are not the characteristics of the straight dislocation in infinite media. They only correspond to the image effects and the core effects. For brevity, we only retain the logarithmic term. Hence,

$$f_n(z_n) = -\frac{D_n}{2\pi i}\ln(z_n) \tag{5.57}$$

Using the boundary condition (6.17) along with (6.13) and (6.20) we obtain the following expression for D_n

$$Re[\sum_{n=1}^{3} A_{kn} D_n] = b_k \qquad k = 1, 2, 3 \tag{5.58}$$

It is clear that Eq. (6.22) gives a set of three equations containing six unknowns, the real and imaginary parts of the D_n for $n = 1, 2, 3$. Thus we need three additional equations to completely solve the current boundary-value problem. The supplementary condition that brings three more equations is given by the requirement that there be no force on the dislocation core.

The resultant force per unit length, L, on the surface of a cylinder enclosing the dislocation and parallel to it is

$$\frac{\mathbf{F}}{L} = \oint \Sigma \cdot (d\mathbf{l} \times e_3) \tag{5.59}$$

where Σ is the stress tensor and $d\mathbf{l} = e_1 dx_1 + e_2 dx_2$. Setting $\mathbf{F}$=0 we obtain

$$\oint (\sigma_{i1} dx_2 - \sigma_{i2} dx_1) = 0 \qquad i = 1, 2, 3 \tag{5.60}$$

The integral over dx_2 vanishes if we choose the integration path as a rectangle, infinitely narrow in the limit (in the x_2 direction) and containing the dislocation. Hence, using (6.3), 6.24 becomes

$$\oint (c_{i2k1} \frac{\partial u_k}{\partial x_1} + c_{i2k2} \frac{\partial u_k}{\partial x_2}) dx_1 = 0 \tag{5.61}$$

Introducing (6.13) into (6.25) we obtain

$$Re[\oint (c_{i2k1} + c_{i2k2} p_n) A_{kn} \frac{\partial f_n(z_n)}{\partial x_1} dx_1] = 0 \tag{5.62}$$

The integral in (6.26) can be evaluated directly for the integration path chosen, since we know

$$\oint \frac{\partial f_n(z_n)}{\partial x_1} dx_1 = -\Delta f_n(z_n) = -D_n \tag{5.63}$$

Eq. (6.22) is then

$$Re[\sum_{n=1}^{3} (c_{i2k1} + c_{i2k2} p_n) A_{kn} D_n] = 0 \qquad i = 1, 2, 3 \tag{5.64}$$

Eqns. (6.22) and (6.28) give six equations to determine D_n completely. The final form of u_k can then be given by

$$u_k = Re[\frac{-1}{2\pi i} \sum_{n=1}^{3} A_{kn} D_n \ln(z_n)] \tag{5.65}$$

The stresses are given by

$$\sigma_{ij} = Re[\frac{-1}{2\pi i} \sum_{n=1}^{3} L_{ijkn} A_{kn} D_n \frac{1}{(z_n)}] \tag{5.66}$$

where, $L_{ijkn} = c_{ijk1} + c_{ijk2} p_n$

The strain energy stored per unit dislocation length can be calculated using work-energy principle. The energy stored is equal to the work done in forming the dislocation by cutting and displacing the plane $x_2 = 0$. In this plane $z_n = x_1$ so that

$$\sigma_{ij} = Im[-\frac{1}{2\pi x_1} \sum_{n=1}^{3} L_{ijkn} A_{kn} D_n] \tag{5.67}$$

Applying the theorem of work and energy, the work done per unit length on the plane cut $x_2 = 0$, $r_0 \leq x_1 \leq R$ is

$$\frac{W}{L} = -\frac{1}{2}\int_{r_0}^{R} \sigma_{i2} b_i dx_1 \quad (5.68a)$$

$$= \frac{b_i}{4\pi} \ln \frac{R}{r_0} Im[\sum_{n=1}^{3} L_{ijkn} A_{kn} D_n] \quad (5.68b)$$

Introducing an energy factor K, Eq. (6.32b) becomes

$$E = \frac{W}{L} = \frac{Kb^2}{4\pi} \ln(\frac{R}{r_0}) \quad (5.69)$$

where,

$$Kb^2 = b_i Im[\sum_{n=1}^{3} L_{ijkn} A_{kn} D_n] \quad (5.70)$$

For an isotropic media, the energy factor, K, replaces the isotropic parameter μ for a screw dislocation, $\mu/(1-\nu)$ for an edge dislocation.

5.3 Finite Media

In presence of free surfaces the solutions for the dislocations in infinite media need to be modified. This is due to the fact that the dislocations interact with the free surfaces due the traction free boundary conditions imposed on the free surfaces. Several approaches have been undertaken over the last century. Here, we briefly review several simple approaches in a systematic manner.

5.3.1 Image Construction

a. Screw dislocation

Let us consider a screw dislocation parallel to a planar free surface and located at a distance l from the free surface as shown. The boundary condition requires that $\sigma_{13} = 0$ at the free surface. This can be achieved through the superposition of the stress field of the original screw dislocation with that of an imaginary (image) screw dislocation of the same strength and opposite sign located at the mirror position outside the solid. The superposed stress field induced can be written as

$$\sigma_{13} = -\frac{\mu b}{2\pi} \frac{x_2}{((x_1+l)^2 + x_2^2)} + \frac{\mu b}{2\pi} \frac{x_2}{((x_1-l)^2 + x_2^2)} \quad (5.71a)$$

$$\sigma_{23} = \frac{\mu b}{2\pi} \frac{x_1+l}{((x_1+l)^2 + x_2^2)} - \frac{\mu b}{2\pi} \frac{x_1-l}{((x_1-l)^2 + x_2^2)} \quad (5.71b)$$

It is now clear that $\sigma_{13} = 0$ at the free surface ($x_1 = l$) and the image stress at the core of the dislocation ($x_1 = -l$) is given by

$$\sigma_{23} = \frac{\mu b}{4\pi l} \tag{5.72}$$

b. Edge dislocation

Following the same procedure as that of an screw dislocation, it is clear that if the stresses from the dislocation and its image are added together, all stresses acting on the surface vanish except σ_{12}, given by

$$\sigma_{12}(0, x_2) = \frac{\mu b}{\pi(1-\nu)} \frac{l(l^2 - x_2^2)}{(l^2 + x_2^2)^2} \tag{5.73}$$

Hence the simple image construction doesn't give correct solution. In order to enforce the stress free boundary condition, we must introduce a function, namely Airy's stress function, ϕ, which produces

$$\sigma_{12}(0, x_2) = -\frac{\mu b}{\pi(1-\nu)} \frac{l(l^2 - x_2^2)}{(l^2 + x_2^2)^2} \tag{5.74}$$

and $\sigma_{11} = \sigma_{13} = 0$ at the boundary and vanishing stress at $x_1 = -\infty$. The stress function must satisfy the equation

$$\nabla^4 \phi = 0 \tag{5.75}$$

if the stresses are expressed in the form

$$\sigma_{11} = \frac{\partial^2 \phi}{\partial x_2^2}, \qquad \sigma_{22} = \frac{\partial^2 \phi}{\partial x_1^2}, \qquad \sigma_{12} = -\frac{\partial^2 \phi}{\partial x_1 \partial x_2} \tag{5.76}$$

The solution of ϕ subject to the aforementioned conditions can be obtained using the method of 'separation of variables' as follows:

Assume ϕ of the form

$$\phi = A(x_1)B(x_2) \tag{5.77}$$

The solutions of A and B can readily be obtained after substituting (5.7) into (5.5) and are given by

$$A(x_1) = (a_0 + a_1 x_1)e^{kx_1} + (a_2 + a_3 x_1)e^{-kx_1} \tag{5.78a}$$

$$B(x_2) = b_0 \sin(kx_2) + b_1 \cos(kx_1) \tag{5.78b}$$

Since $A(x_1)$ needs to be zero as $x \to -\infty$, a_2 and a_3 must be zero. Also, the traction free boundary condition $\sigma_{11}(0, x_2) = 0$ for $A(0, x_2) = 0$ is satisfied if $a_0 = 0$. It is also clear that the term involving $\cos(kx_2)$ is dropped since $\sigma_{12}(0, x_2) = 0$ is even function in x_2. Hence, the final form of the solution is

$$\phi = \int_0^\infty b_0(k) x e^{kx_1} \sin(kx_2) dk \tag{5.79}$$

The solution of $b_0(k)$ can be obtained satisfying the boundary condition for σ_{12}.

$$\sigma_{12}(0,x_2) = -\left(\frac{\partial^2\phi}{\partial x_1 \partial x_2}\right)_{x_1=0} = -\int_0^\infty b_0(k)k\cos(kx_2)dk = -\frac{\mu b}{\pi(1-\nu)}\frac{l(l^2-x_2^2)}{(l^2+x_2^2)^2} \tag{5.80}$$

so that the fourier inversion after some manipulation yields

$$b_0(k) = \frac{\mu b l}{\pi(1-\nu)}e^{-kl}. \tag{5.81}$$

Therefore,

$$\phi = \frac{\mu b l}{\pi(1-\nu)}\int_0^\infty x_1 e^{k(x_1-l)}\sin(kx_2)dk = \frac{\mu b l x_1 x_2}{\pi(1-\nu)\left[(x_1-l)^2+x_2^2\right]} \tag{5.82}$$

The complete stress distribution for the edge dislocation can then be written in explicit form, after superposing the stress fields of the dislocation itself, the image dislocation, and the stresses derived from (5.12), as

$$\sigma_{11} = -\frac{2\mu b l x_1 x_2}{\pi(1-\nu)(l^2+x_2^2)^3}\left[3(l-x_1)^2 - x_2^2\right] \tag{5.83}$$

$$\sigma_{22} = \frac{\mu b l}{\pi(1-\nu)(l^2+x_2^2)^3}\left[4(l-x_1)^3x_2 + 6(l-x_1)^2x_1x_2 + 4(l-x_1)x_2^3 - 2x_1x_2^3\right] \tag{5.84}$$

$$\sigma_{12} = -\frac{\mu b l}{\pi(1-\nu)(l^2+x_2^2)^3}\left[(l-x_1)^4 + 2x_1(l-x_1)^3 - 6x_1x_2^2(l-x_1) - x_2^4\right] \tag{5.85}$$

$$\sigma_{33} = \frac{4\mu b l\nu}{\pi(1-\nu)(l^2+x_2^2)^3}\left[(l-x_1)^3x_2 + (l-x_1)x_2^3\right] \tag{5.86}$$

5.3.2 Complex Variable Method

A closed-form Green's function for the elastic field of an edge dislocation of arbitrary Burger's vector at an arbitrary point in an orthotropic finite elastic medium, that is free of traction, was developed by El-Azab and Ghoniem N.M (1993). The method is based on the classical theory of potential fields, with an additional distribution of surface dislocations to satisfy the free traction boundary condition. A solution is first developed for a dislocation in a semi-infinite half plane. The resulting field is composed of two parts: a singular contribution from the original dislocation, and a regular component associated with the surface distribution. The Schwarz-Christoffel transformation is then utilized to map the field quantities to a finite, polygonal domain. The method is described here briefly. For a detailed discussion the reader is referred to El-Azab and Ghoniem N.M (1993).

a. Infinite domain solution

The elastic field of a two dimensional continuum under plane stress are written in terms of complex potentials, $\phi_1(z_1)$ and $\phi_2(z_2)$ as follows

$$\begin{aligned}
\sigma_x &= 2Re[\lambda_1^2\phi_1^{'}(z_1) + \lambda_2^2\phi_2^{'}(z_2)] && (5.87a)\\
\sigma_y &= 2Re[\phi_1^{'}(z_1) + \phi_2^{'}(z_2)] && (5.87b)\\
\sigma_{xy} &= -2Re[\lambda_1\phi_1^{'}(z_1) + \lambda_2\phi_2^{'}(z_2)] && (5.87c)\\
u &= p(\lambda_1)\phi_1(z_1) + p(\lambda_2)\phi_2(z_2) + p(\overline{\lambda_1})\overline{\phi_1}(\overline{z_1}) + p(\overline{\lambda_2})\phi_2(\overline{z_2}) && (5.87d)
\end{aligned}$$

where the overbar denotes the complex conjugate and prime represents the derivative. The constants λ_1 and λ_2 and their complex conjugates are the roots of the following characteristic equation

$$S_{11}\lambda^4 - 2S_{16}\lambda^3 + (2S_{12} + S_{66})\lambda^2 - 2S_{26}\lambda + S_{22} = 0 \tag{5.88}$$

where, S_{mn} are the elastic constants requiring Hooke's law and z_1 and z_2 are complex variables defined as

$$\begin{aligned}
z_1 &= x + \lambda_1 y = (\gamma_1 z + \delta_1\overline{z})/2 && (5.89a)\\
z_2 &= x + \lambda_2 y = (\gamma_2 z + \delta_2\overline{z})/2 && (5.89b)
\end{aligned}$$

in which, $z = x + iy$, $\gamma_j = 1 - i\lambda_j$ and $\delta_j = 1 + i\lambda_j$, j=1,2. The polynomial $p(\lambda)$ is given by

$$p(\lambda) = (S_{12} - S_{16}\lambda + S_{11}\lambda^2) + \frac{i}{\lambda}(S_{22} - S_{26}\lambda + S_{12}\lambda^2) \tag{5.90}$$

Assuming that the complex potentials,$\phi_1(z_1)$ and $\phi_2(z_2)$ of the dislocation are analytic except at the core of the dislocation z_o, they can be expressed as

$$\begin{aligned}
\phi_{1s}(z_1) &= A_1 log(z_1 - z_{10}) && (5.91a)\\
\phi_{2s}(z_2) &= A_2 log(z_2 - z_{20}) && (5.91b)
\end{aligned}$$

where, z_{10} and z_{20} are related to z_0 by the set of equations (5.16). The subscript s is used to indicate that the infinite domain potentials are singular at the location of the dislocation z_0. The complex constants $A_{1,2}$ are determined by the conditions:
(a) the deformation due to a single dislocation is non single valued, i.e.

$$b = [u]_L = \oint_L du(z_1, z_2, \overline{z}_1, \overline{z}_2) \tag{5.92}$$

where du is the exact differential of the complex displacement u, and L is any contour in the z plane which encircles the dislocation with burgers vector $b = |b|e^{i\theta}$. Equation (5.19) after some manipulation gives

$$b = 2\pi i\left[A_1 p(\lambda_1) - \overline{A_1}p(\overline{\lambda}_1) + A_2 p(\lambda_2) - \overline{A_2}p(\overline{\lambda}_2)\right] \tag{5.93}$$

(b) the traction integral along any arbitrary contour surrounding the dislocation vanishes (self-equilibrium), the stress resultant $X + iY$ around a contour is written as

$$X + iY = \oint_L (\sigma_x + i\sigma_{xy})dy - (i\sigma_y + \sigma_{xy})dx = 0 \tag{5.94}$$

This condition yields the following equation

$$\delta_1 A_1 - \overline{\gamma_1}\overline{A_1} + \delta_2 A_2 - \overline{\gamma_2}\overline{A_2} = 0 \tag{5.95}$$

By taking the complex conjugate of (5.20) and (5.22), two additional equations are obtained. The four equations can now be solved for A_1, $\overline{A}_1$, A_2, $\overline{A}_2$. For the case of an orthotropic domain, where $S_{16} = S_{26} = 0$, A_1 and A_2 are written as

$$A_1 = c_{11} Im(b) + ic_{12} Re(b) \tag{5.96a}$$
$$A_2 = c_{21} Im(b) + ic_{22} Re(b) \tag{5.96b}$$

where,

$$c_{11} = -\frac{\beta_2}{2\pi(\beta_1\alpha_2 - \beta_2\alpha_1)}; \quad \alpha_1 = \frac{2}{\beta_1}(S_{22} - S_{12}\beta_1^2); \quad \beta_1^2 = |-r_1 + \sqrt{r_1^2 - r_2}|$$
$$c_{12} = -\frac{1}{2\pi(\alpha_3 - \alpha_4)}; \quad \alpha_2 = \frac{2}{\beta_2}(S_{22} - S_{12}\beta_2^2); \quad \beta_2^2 = |-r_1 - \sqrt{r_1^2 - r_2}|$$
$$c_{21} = \frac{\beta_1}{2\pi(\beta_1\alpha_2 - \beta_2\alpha_1)}; \quad \alpha_3 = 2(S_{12} - S_{11}\beta_1^2); \quad r_1 = \left(\frac{2s_{12} + s_{66}}{2s_11}\right)$$
$$c_{22} = \frac{1}{2\pi(\alpha_3 - \alpha_4)}; \quad \alpha_4 = 2(S_{12} - S_{11}\beta_2^2); \quad r_2 = \left(\frac{s_{22}}{s_11}\right)$$

b. Semi-infinite domain solution

The Green's function in an unbounded medium automatically satisfies the governing field equations. Any linear combination of the infinite domain Green's functions, which also satisfies specified boundary conditions for a finite domain, must be the Green's function in that finite domain. The solution, therefore, will be constructed as a linear combination of the singular, infinite domain solution, and an additional distribution of surface dislocations, such that the boundary is free of forces (i.e. zero surface tractions).

Let $F(t)$ be a distribution function of surface dislocation, which is complex, and written as

$$F(t) = f_1(t) + if_2(t) \tag{5.97}$$

where, t is a complex variable describing the domain boundary L, and $f_1(t)$, $f_2(t)$ are real functions of complex variable t. It is now clear that the traction caused by the original dislocation

and the surface distribution, evaluated at any arbitrary point along the boundary, must be equal to any prescribed boundary tractions. Assuming the boundary is traction free, this condition is written as

$$X_d(t) + iY_d(t) + \oint_L [X_s(t_0,t) + iY_s(t_0,t)]ds_0 = 0 \tag{5.98}$$

where $s_0 = s(t_0)$ and $X_d(t)+iY_d(t)$ is the residual complex traction at t on L due to the original dislocation at z_0 inside the finite domain D^+ bounded by the contour L. $X_s(t_0,t) + iY_s(t_0,t)$ is the complex traction at t on L due to a surface dislocation of Burger's vector $F(t_0)$ at t_0 on L. Equations (5.14), (5.18) and (5.23) should be used to calculate both $X_d(t) + iY_d(t)$ and $X_s(t_0,t) + iY_s(t_0,t)$ with the exception that $Re(b)$ and $Im(b)$ in (5.23) need to be replaced by $f_1(t_0)$ and $f_2(t_0)$ while calculating the second one. This means that the complex quantities A_1 and A_2 are no longer constant when dealing with surface dislocations. Let these quantities be denoted by B_1 and B_2, and be written as

$$B_1 = c_{11}f_2(t) + ic_{12}f_1(t) \tag{5.99a}$$
$$A_2 = c_{21}f_2(t) + ic_{22}f_1(t) \tag{5.99b}$$

Equation (5.25) can now be utilized to determine $f_1(t)$ and $f_2(t)$ and the total stress field can then be calculated.

Mathematics to find the distribution functions is somewhat laborious and is omitted here for brevity. The reader is referred to the article mentioned before. Choosing the domain of the solution $D+$ is the upper half plane, $Im(z) \geq 0$, so that the contour L is taken to be the x axis from $-\infty$ to $+\infty$ and assuming that the dislocation of an arbitrary Burger's vector $b = |b|e^{i\theta}$ is located at the point $z_0 = x_0 + iy_0$, the distribution functions for the surface dislocations of the semi-infinite domain can be found as

$$f_1(x) = -\frac{i}{\pi a_1}\left[\frac{\lambda_1 A_1}{x - z_{10}} - \frac{\overline{\lambda}_1\overline{A}_1}{x - \overline{z}_{10}} + \frac{\lambda_2 A_2}{x - z_{20}} - \frac{\overline{\lambda}_2\overline{A}_2}{x - \overline{z}_{20}}\right] \tag{5.100a}$$

$$f_2(x) = \frac{i}{\pi a_2}\left[\frac{A_1}{x - z_{10}} - \frac{\overline{A}_1}{x - \overline{z}_{10}} + \frac{A_2}{x - z_{20}} - \frac{\overline{A}_2}{x - \overline{z}_{20}}\right] \tag{5.100b}$$

The potentials for the total stress field for the semi-infinite domain is now constructed as the superposition of the singular (infinite domain) and regular (surface dislocations) fields as

$$\phi_j(z_j) = \phi_{js}(z_j) + \phi_{jr}(z_j) \tag{5.101}$$

c. Rectangular finite domain solution: Schwarz-Christoffel transformation

Schwarz-Christoffel transformation, which maps the upper half-plane onto a polygon, is applied to the semi-infinite domain solution to obtain the solution in a rectangular domain. The boundaries of the rectangular domain are assumed to be traction free. The general form of the

transformation is written as

$$w = f(z) = C_1 \int_0^z \prod_{j=1}^{n} (z - a_j)^{\alpha_j - 1} dz + C_2 \tag{5.102}$$

This transformation maps the upper half of the z-plane onto a polygon on n vertices in the w-plane. $C_{1,2}$ are complex constants which adjust the size, orientation and location of the polygon. The points a_j on the x-axis (z plane) transform to vertices of the polygon, and $\alpha_j \pi$ are the interior angles of the polygon. With thsi transformation, solutions in polygonal domains can be obtained from the semi-infinite domain solution. In case of a rectangle, $\alpha_j = 0.5$, and $n = 4$. Equation (5.29) can now be written as

$$w = f(z) = \int_0^z \frac{d\xi}{\sqrt{(1-\xi^2)(1-k^2\xi^2)}} = F(z,k); \quad 0 < k < 1 \tag{5.103}$$

where, $F(z,k)$ is the elliptical integral of the first kind. The integral (5.30) maps the upper half of the z-plane onto a rectangle in the w plane for any k. The vertices of the rectangle in the w plane (where $w = u + iv$) are $\pm K(k)$ and $+iK(k')$; $k^2 + k'^2 = 1$, where $K(k)$ is a complete elliptic integral of the first kind given by (5.30) with the integration limit $0 \rightarrow 1$ and $K(k')$ is the complementary complete elliptic integral of the first kind replacing k by k'. The vertices of the rectangle are mapped to the points ± 1 and $\pm 1/k$, on the x-axis in the z plane.

If the actual rectangular domain which contains the dislocation is defined in the w^*-plane (where, $w^* = u^* + iv^*$) with the vertices $\pm H_1$ and $\pm H_1 + iH_2$, then the mapping from w^* plane to w plane and hence to the z plane can be obtained through

$$u* = \frac{H_1}{K(k)} u \tag{5.104a}$$

$$v* = \frac{H_2}{K(k')} v \tag{5.104b}$$

$$w* = u* + iv* = \frac{H_1}{K(k)} u + i \frac{H_2}{K(k')} v \tag{5.104c}$$

Assuming a linear mapping of the form $w* = cw$ where c is a constant; it follows that $H_1/K(k) = H_2/K(k') = c$. Once the parameter k is determined by solving the transcendental equation

$$\frac{H_2}{H_1} = \frac{K(k')}{K(k)}; \quad k^2 + k'^2 = 1, \tag{5.105}$$

the constant c will be determined and hence all the field quantities can be obtained completely as explained by El-Azab and Ghoniem N.M (1993).

5.4 Interfacial Dislocation Networks

In the present work, the elastic field of the surface is obtained in two steps. The first step is to simplify the model to a thin film and substrate system, as shown in Figure 5.1, in which

the Si capping layer is ignored. In this step, the basic elastic field solution is set up using the the Fourier transform approach, (**?**, **?**). Ignoring the interactions between dislocations, a 2-dimensional field solution can be obtained by superposing the basic dislocation solution at different location. The surface curvature can also be obtained from the displacement field. The second step is to consider the stretching of the Si capping layer as a result of lattice mismatch. A simple model based on the analysis of 2-D stress state is developed for this purpose. The curvature effects and chemical potential terms will be discussed based on the analytical solution. Results will be presented at the end of this section.

5.4.1 Sing' Di .t.. S.l.t..

The stress field ure is a plane problem, which plane first, as illustrated in fig

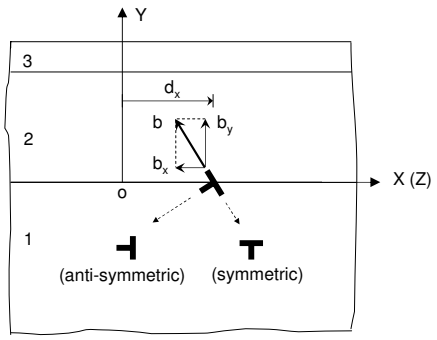

Figure 5.1: Bonded layer structure with a single interfacial dislocation

The solution can be obtained by the Fourier transform with respect to x:

$$U^{(i)}(x,y) = \frac{1}{\sqrt{2\pi}} \int_{-\infty}^{+\infty} \Psi^{(i)}(\alpha, y)\, e^{-i\alpha x} d\alpha \tag{5.106}$$

where i denotes i^{th} layer ($i = 1, ...n$) and the dislocation lies at the interface between layers (i)

and $(i+1)$.

$U^{(i)}$ is the displacement vector of the i^{th} layer and:

$$U^{(i)} = \left(u^{(i)}(x,y), v^{(i)}(x,y)\right)^T \tag{5.107}$$

$\Psi^{(1)}$ is the complex transformed displacement vector of the i^{th} layer in Fourier space and:

$$\Psi^{(i)} = \left(\phi^{(i)}(\alpha,y), \psi^{(i)}(\alpha,y)\right)^T \tag{5.108}$$

The displacement and transformed displacement can be decomposed to symmetric and anti-symmetric parts.

$$U^{(i)} = U_s^{(i)} + U_a^{(i)}, \qquad \Psi^{(i)} = \Psi_s^{(i)} + \Psi_a^{(i)} \tag{5.109}$$

Consider the solution for the symmetric case,

$$\begin{aligned} u_s^{(i)}(x,y) &= \frac{2}{\pi}\int_0^\infty \phi_s^{(i)}(\alpha,y)\sin\alpha x d\alpha \\ v_s^{(i)}(x,y) &= \frac{2}{\pi}\int_0^\infty \psi_s^{(i)}(\alpha,y)\cos\alpha x d\alpha \end{aligned} \tag{5.110}$$

Using the Navier's equations for an isotropic, homogeneous medium, i.e.

$$\left(\lambda^{(i)}+\mu^{(i)}\right)\nabla\left(\nabla\cdot U_s^{(i)}\right) + \mu^{(i)}\nabla^2 U_s^{(i)} = 0 \tag{5.111}$$

The displacement vector can be obtained with unknown A_{sj}, which are the functions of α:

$$\begin{aligned} u_s^{(i)}(x,y) &= \frac{2}{\pi}\int_0^{+\infty}\left[\left(A_{s1}^{(i)}+A_{s2}^{(i)}y\right)e^{-\alpha y} + \left(A_{s3}^{(i)}+A_{s4}^{(i)}y\right)e^{\alpha y}\right]\sin\alpha x d\alpha \\ v_s^{(i)}(x,y) &= \frac{2}{\pi}\int_{-\infty}^{+\infty}\left\{\left[A_{s1}^{(i)}+\left(\frac{\kappa^{(i)}}{\alpha}+y\right)A_{s2}^{(i)}\right]e^{-\alpha y}\right. \\ &\qquad \left. + \left[-A_{s3}^{(i)}+\left(\frac{\kappa^{(i)}}{\alpha}-y\right)A_{s4}^{(i)}\right]e^{\alpha y}\right\}\cos\alpha x d\alpha \end{aligned} \tag{5.112}$$

where $\kappa^{(i)} = 3-4\nu^{(i)}$ for plane strain and $\left(3-\nu^{(i)}\right)\Big/\left(1+\nu^{(i)}\right)$ for plane stress. and $A_{sj}^{(i)}$ are functions of α , which will be determined from the boundary and the continuity conditions by the following:

$$
\begin{aligned}
\alpha A_{s1}^{(1)} + \alpha A_{s3}^{(1)} - \alpha A_{s3}^{(2)} &= b_x \cos \alpha t \\
-\alpha A_{s1}^{(1)} - \kappa^{(1)} + \alpha A_{s3}^{(1)} - \kappa^{(1)} A_{s4}^{(1)} - \alpha A_{s3}^{(2)} + \kappa^{(2)} A_{s4}^{(2)} &= 0 \\
-\alpha \mu^{(1)} A_{s1}^{(1)} - 2\mu^{(1)} \left(1 - \nu^{(1)}\right) A_{s2}^{(1)} - \alpha \mu^{(1)} A_{s3}^{(1)} & \\
+2\mu^{(1)} \left(1 - \nu^{(1)}\right) A_{s4}^{(1)} + \alpha \mu^{(2)} A_{s3}^{(2)} - 2\mu^{(2)} \left(1 - \nu^{(2)}\right) A_{s4}^{(2)} &= 0 \\
-\alpha \mu^{(1)} A_{s1}^{(1)} - \mu^{(1)} \left(1 - 2\nu^{(1)}\right) A_{s2}^{(1)} + \alpha \mu^{(1)} A_{s3}^{(1)} & \\
-\mu^{(1)} \left(1 - 2\nu^{(1)}\right) A_{s4}^{(1)} - \alpha \mu^{(2)} A_{s3}^{(2)} + \mu^{(2)} \left(1 - 2\nu^{(2)}\right) A_{s4}^{(2)} &= 0 \\
-\alpha e^{2\alpha h} A_{s1}^{(1)} - \left[\alpha h + 2\left(1 - \nu^{(1)}\right)\right] e^{-2\alpha h} A_{s2}^{(1)} & \\
-\alpha A_{s3}^{(1)} - \left[\alpha h - 2\left(1 - \nu^{(1)}\right)\right] A_{s4}^{(1)} &= 0 \\
-\alpha e^{2\alpha h} A_{s1}^{(1)} - \left[\alpha h + \left(1 - 2\nu^{(1)}\right)\right] e^{-2\alpha h} A_{s2}^{(1)} & \\
+\alpha A_{s3}^{(1)} + \left[\alpha h - \left(1 - 2\nu^{(1)}\right)\right] A_{s4}^{(1)} &= 0
\end{aligned}
\tag{5.113}
$$

Using 2-D stress-strain relations, the stresses can be evaluated as follows:

$$
\begin{aligned}
\sigma_{sxx}^{(i)} &= \frac{4\mu^{(i)}}{\pi} \int_0^\infty \left\{ \left[\alpha \left(A_{s1}^{(i)} + A_{s2}^{(i)} y\right) - 2\nu^{(i)} A_{s2}^{(i)}\right] e^{-\alpha y} \right. \\
&\qquad \left. + \left[\alpha \left(A_{s3}^{(i)} + A_{s4}^{(i)} y\right) + 2\nu^{(i)} A_{s4}^{(i)}\right] e^{\alpha y} \right\} \cos \alpha x d\alpha \\
\sigma_{syy}^{(i)} &= \frac{4\mu^{(i)}}{\pi} \int_0^\infty \left\{ -\left[\alpha \left(A_{s1}^{(i)} + A_{s2}^{(i)} y\right) + 2\left(1 - \nu^{(i)}\right) A_{s2}^{(i)}\right] e^{-\alpha y} \right. \\
&\qquad \left. + \left[-\alpha \left(A_{s3}^{(i)} + A_{s4}^{(i)} y\right) + 2\left(1 - \nu^{(i)}\right) A_{s4}^{(i)}\right] e^{\alpha y} \right\} \cos \alpha x d\alpha \\
\sigma_{sxy}^{(i)} &= \frac{4\mu^{(i)}}{\pi} \int_0^\infty \left\{ -\left[\alpha \left(A_{s1}^{(i)} + A_{s2}^{(i)} y\right) + \left(1 - 2\nu^{(i)}\right) A_{s2}^{(i)}\right] e^{-\alpha y} \right. \\
&\qquad \left. + \left[\alpha \left(A_{s3}^{(i)} + A_{s4}^{(i)} y\right) - \left(1 - 2\nu^{(i)}\right) A_{s4}^{(i)}\right] e^{\alpha y} \right\} \sin \alpha x d\alpha
\end{aligned}
\tag{5.114}
$$

For the anti-symmetric case:

$$
\begin{aligned}
u_a^{(i)}(x, y) &= \frac{2}{\pi} \int_0^\infty \phi_a^{(i)}(\alpha, y) \cos \alpha x d\alpha \\
v_a^{(i)}(x, y) &= \frac{2}{\pi} \int_0^\infty \psi_a^{(i)}(\alpha, y) \sin \alpha x d\alpha
\end{aligned}
\tag{5.115}
$$

By the same procedure as the symmetric case, we have the equations for solving $A_{aj}^{(i)}$:

$$
\alpha A_{a1}^{(1)} + \alpha A_{a3}^{(1)} - \alpha A_{a3}^{(2)} = 0
$$

$$\begin{aligned}
-\alpha A_{a1}^{(1)} - \kappa^{(1)} + \alpha A_{a3}^{(1)} - \kappa^{(1)} A_{a4}^{(1)} - \alpha A_{a3}^{(2)} + \kappa^{(2)} A_{a4}^{(2)} &= b_y \sin \alpha t \\
-\alpha\mu^{(1)} A_{a1}^{(1)} - 2\mu^{(1)} \left(1-\nu^{(1)}\right) A_{a2}^{(1)} - \alpha\mu^{(1)} A_{a3}^{(1)} & \\
+2\mu^{(1)} \left(1-\nu^{(1)}\right) A_{a4}^{(1)} + \alpha\mu^{(2)} A_{a3}^{(2)} - 2\mu^{(2)} \left(1-\nu^{(2)}\right) A_{a4}^{(2)} &= 0 \\
-\alpha\mu^{(1)} A_{a1}^{(1)} - \mu^{(1)} \left(1-2\nu^{(1)}\right) A_{a2}^{(1)} + \alpha\mu^{(1)} A_{a3}^{(1)} & \\
-\mu^{(1)} \left(1-2\nu^{(1)}\right) A_{a4}^{(1)} - \alpha\mu^{(2)} A_{a3}^{(2)} + \mu^{(2)} \left(1-2\nu^{(2)}\right) A_{a4}^{(2)} &= 0 \\
-\alpha e^{2\alpha h} A_{a1}^{(1)} - \left[\alpha h + 2\left(1-\nu^{(1)}\right)\right] e^{-2\alpha h} A_{a2}^{(1)} & \\
-\alpha A_{a3}^{(1)} - \left[\alpha h - 2\left(1-\nu^{(1)}\right)\right] A_{a4}^{(1)} &= 0 \\
-\alpha e^{2\alpha h} A_{a1}^{(1)} - \left[\alpha h + \left(1-2\nu^{(1)}\right)\right] e^{-2\alpha h} A_{a2}^{(1)} & \\
+\alpha A_{a3}^{(1)} + \left[\alpha h - \left(1-2\nu^{(1)}\right)\right] A_{a4}^{(1)} &= 0
\end{aligned} \tag{5.116}$$

The displacement and stress solutions are as following:

$$\begin{aligned}
u_a^{(i)}(x,y) &= \frac{2}{\pi} \int_0^{+\infty} \left[\left(A_{a1}^{(i)} + A_{a2}^{(i)} y\right) e^{-\alpha y} + \left(A_{a3}^{(i)} + A_{a4}^{(i)} y\right) e^{\alpha y}\right] \cos \alpha x d\alpha \\
v_a^{(i)}(x,y) &= \frac{1}{\pi} \int_{-\infty}^{+\infty} \left\{ \left[A_1^{(i)} + \left(\frac{\kappa^{(i)}}{\alpha} + y\right) A_2^{(i)}\right] e^{-\alpha y} \right. \\
&\qquad \left. + \left[-A_3^{(i)} + \left(\frac{\kappa^{(i)}}{\alpha} - y\right) A_4^{(i)}\right] e^{\alpha y} \right\} \cos \alpha x d\alpha
\end{aligned} \tag{5.117}$$

$$\begin{aligned}
\sigma_{axx}^{(i)} &= \frac{4\mu^{(i)}}{\pi} \int_0^{\infty} \left\{ \left[-\alpha \left(A_{a1}^{(i)} + A_{a2}^{(i)} y\right) + 2\nu^{(i)} A_{a2}^{(i)}\right] e^{-\alpha y} \right. \\
&\qquad \left. - \left[\alpha \left(A_{a3}^{(i)} + A_{a4}^{(i)} y\right) + 2\nu^{(i)} A_{a4}^{(i)}\right] e^{\alpha y} \right\} \sin \alpha x d\alpha \\
\sigma_{ayy}^{(i)} &= \frac{4\mu^{(i)}}{\pi} \int_0^{\infty} \left\{ \left[\alpha \left(A_{a1}^{(i)} + A_{a2}^{(i)} y\right) + 2\left(1-\nu^{(i)}\right) A_{a2}^{(i)}\right] e^{-\alpha y} \right. \\
&\qquad \left. + \left[\alpha \left(A_{a3}^{(i)} + A_{a4}^{(i)} y\right) - 2\left(1-\nu^{(i)}\right) A_{a4}^{(i)}\right] e^{\alpha y} \right\} \sin \alpha x d\alpha \\
\sigma_{axy}^{(i)} &= \frac{4\mu^{(i)}}{\pi} \int_0^{\infty} \left\{ -\left[\alpha \left(A_{a1}^{(i)} + A_{a2}^{(i)} y\right) + \left(1-2\nu^{(i)}\right) A_{a2}^{(i)}\right] e^{-\alpha y} \right. \\
&\qquad \left. + \left[\alpha \left(A_{a3}^{(i)} + A_{a4}^{(i)} y\right) - \left(1-2\nu^{(i)}\right) A_{a4}^{(i)}\right] e^{\alpha y} \right\} \cos \alpha x d\alpha
\end{aligned} \tag{5.118}$$

The medium is assumed to be traction-free at the top surface such that:

$$\begin{aligned}
\sigma_{syy}^{(n)} &= \sigma_{ayy}^{(n)} = 0 \\
\sigma_{sxy}^{(n)} &= \sigma_{axy}^{(n)} = 0
\end{aligned} \tag{5.119}$$

While at the interfaces, continuity is required in adjacent layers, such that:

$$\begin{aligned} u_s^{(i+1)} - u_s^{(i)} = u_a^{(i+1)} - u_a^{(i)} &= 0 \\ v_s^{(i+1)} - v_s^{(i)} = v_a^{(i+1)} - v_a^{(i)} &= 0 \\ \sigma_{syy}^{(i+1)} - \sigma_{syy}^{(i)} = \sigma_{ayy}^{(i+1)} - \sigma_{ayy}^{(i)} &= 0 \\ \sigma_{sxy}^{(i+1)} - \sigma_{sxy}^{(i)} = \sigma_{asxy}^{(i+1)} - \sigma_{axy}^{(i)} &= 0 \end{aligned} \tag{5.120}$$

For an interface with a dislocation at $x = d_x$, we have:

$$\begin{aligned} \frac{\partial}{\partial x}\left(u_s^{(1)} - u_s^{(2)}\right) &= b_x^e \delta\left(x - d_x\right) \\ \frac{\partial}{\partial x}\left(u_a^{(1)} - u_a^{(2)}\right) &= 0 \\ \frac{\partial}{\partial x}\left(v_s^{(1)} - v_s^{(2)}\right) &= 0 \\ \frac{\partial}{\partial x}\left(v_a^{(1)} - v_a^{(2)}\right) &= b_y^e \delta\left(x - d_x\right) \end{aligned} \tag{5.121}$$

where $\delta(x - d_x)$ is the Dirac Delta function.

By numerical methods, the solutions for displacement and stress expressions can be obtained by substituting Equation (5.114, 5.112) into Equations (5.119, 5.120, 5.121). The final displacement and stress field are the sum of the symmetric and anti-symmetric parts.

5.4.2 Network Dislocation Solution

If the solution is applied in $z - y$ plane, which means making the coordinate substitutes: $x \to z$ and $y \to y$, the elastic field is obtained for $w^{(i)}$, $v^{(i)}\sigma_{yy}^{(i)}$, $\sigma_{zz}^{(i)}$, $\sigma_{yz}^{(i)}$ according to the dislocation array in $z - y$ plane.

Solutions for dislocation networks can be constructed by the superposing single dislocation solutions given above. Assuming $d_x^{(k_x)}$ and $d_z^{(k_z)}$ are the k^{th} dislocations' location along the x and z directions respectively, the solution becomes:

$$\begin{aligned} u_{xi} &= \sum_{k=1}^{n_x} u_{xi}\left(x - d_x^k, y\right) \\ u_{yi} &= \sum_{k_x=1}^{n_x}\sum_{k_z=1}^{n_y}\left[u_{yi}\left(x - d_x^{k_x}, y\right) + u_{yi}\left(z - d_z^{k_z}, y\right)\right] \\ u_{zi} &= \sum_{k=1}^{n_z} u_{zi}\left(z - d_z^k, y\right) \end{aligned} \tag{5.122}$$

In the $x-y$ plane problem, since an edge dislocation line is along the z-direction, the deformation along the z direction is zero, which implies a plain strain state. It is the same for the $z-y$ plane. Hence, we have:

$$\begin{aligned}
\sigma_{xx} &= \sum_{k_x=1}^{n_x}\sum_{k_z=1}^{n_y}\left[\sigma_{xx}\left(x-d_x^{k_x},y\right)+\nu\sigma_{zz}\left(z-d_z^{k_z},y\right)\right] \\
\sigma_{yy} &= \sum_{k_x=1}^{n_x}\sum_{k_z=1}^{n_z}\left[\sigma_{yy}\left(x-d_x^{k_x},y\right)+\sigma_{yy}\left(z-d_z^{k_z},y\right)\right] \\
\sigma_{zz} &= \sum_{k_x=1}^{n_x}\sum_{k_z=1}^{n_y}\left[\sigma_{zz}\left(x-d_x^{k_x},y\right)+\nu\sigma_{xx}\left(z-d_z^{k_z},y\right)\right]
\end{aligned} \tag{5.123}$$

5.4.3 Results

During the following calculations, the material constants used in the present simulation are selected as shown in Table 5.1:

Material	***Shear Modulus***	***Poisson Ratio***	***Lattice Constant***	***Burger's Vector***
Si	79.9 GPa	0.266	5.43095 $\mathring{A}$	3.84026 $\mathring{A}$
Ge	67.0 GPa	0.280	5.64613 $\mathring{A}$	3.99241 $\mathring{A}$
$Si_{0.85}Ge_{0.15}$	77.965 GPa	0.268	5.46322 $\mathring{A}$	3.86308 $\mathring{A}$

Table 5.1: Elastic and lattice constants for Si, Ge, and $Si_{0.85}Ge_{0.15}$

The accuracy of the Fourier transform method is tested by a simple 1-D case which has a single dislocation at the interface of a bi-layer structure as illustrated in Figure 5.1 without 3^{rd} layer. The comparison is first made between Fourier transform method and Complex variable method in the case that the substrate and the film are the same material, say Si. The Burger's vector is assumed to be: $\mathbf{b} = 0.1\mathbf{x} + 0.1\mathbf{y}$(nm). Table 5.2 shows the error estimation of two methods with different thickness of thin film, in which, the normal stress along x direction (σ_{xx}) is calculated and averaged along the same length of a specimen.

Method	***Absolute Error*** ϵ_a	***Relative Error*** ϵ_r
Complex Variable	0	0
Fourier Transform (h=8nm)	7.94×10^{-5}GPa	0.017%
Fourier Transform (h=80nm)	3.55×10^{-6}GPa	0.020%

Table 5.2: Comparison of σ_{xx} between Fourier Transform method and Complex Variable Method by averaging errors.

The effect of inhc rence of the values of homogenous mate ole methods is very small, as can be seer

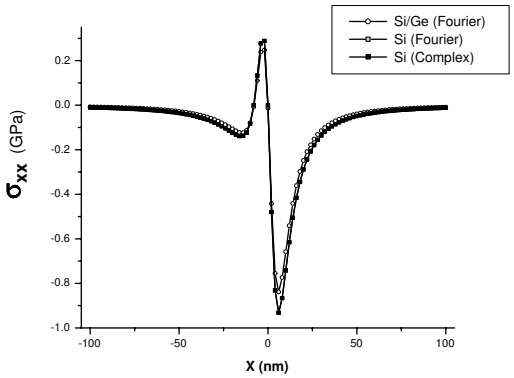

Figure 5.2: Comparison of σ_{xx} between inhomogeneous system (Si/Ge) and homogeneous system(Si) with a single dislocation at the thickness of 8 nm

In the following calculations, we focus on two different thicknesses of Si/Ge buffer layer: 8nm and 80nm. In 8nm thickness case, a 2×2 interfacial dislocation network is considered. The dislocations exist at x(z)=25 and 75nm. In 80nm thickness, due to the computational reasons, only a 1×1 dislocation network is considered. The dislocations exist at x(z)=250nm. The Burger's vector is selected as shown in Table 5.1.

The calculated stress maps with capping layer of thin film and thick film are shown in Figure 5.3 and Figure 5.6. Figure shows the displacement and curvature maps of the film with the thin case.

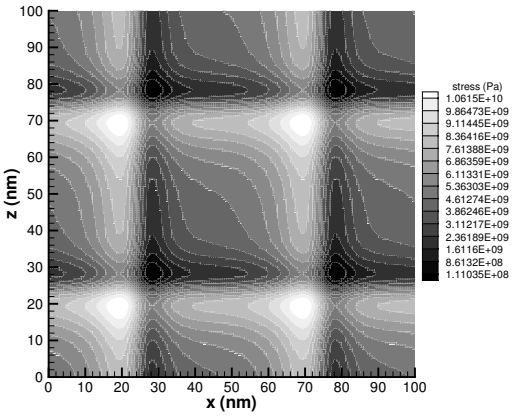

Figure 5.3: Surface stress map of 8 nm thin film structure

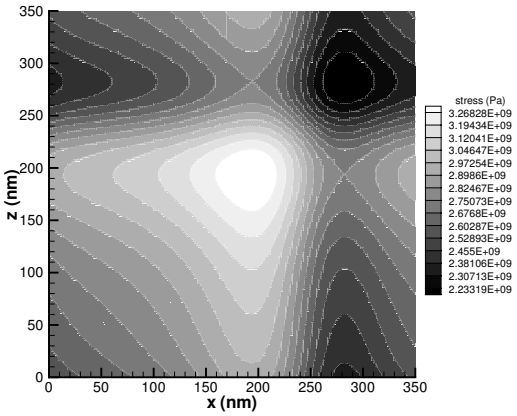

Figure 5.4: Surface stress map of 80 nm thin film structure

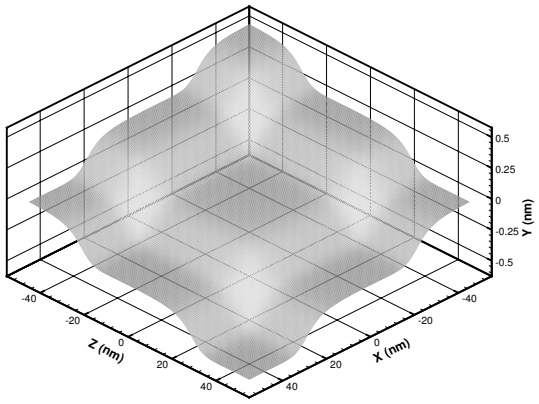

Figure 5.5: Surface displacement map of 8 nm thin film

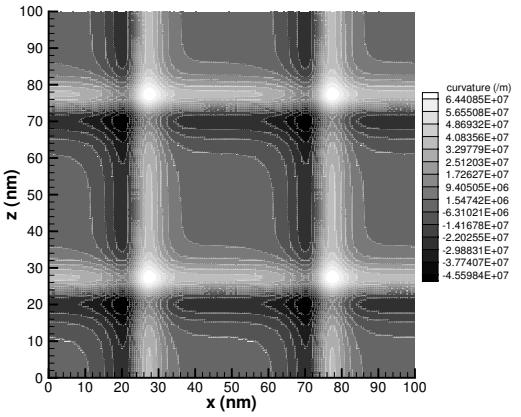

Figure 5.6: Surface curvature map of 8 nm thin film

Chapter 6

Green's Tensor Functions

6.1 Basic Equations

Define Green's function: $U_{ij}(\mathbf{R})$, as the displacement component $U_i(\mathbf{r})$ at position $(\mathbf{R})$ due to point force in the R_j-direction at the origin. It can be obtained by considering the equation of translational equilibrium, that is:

$$C_{ijkl}u_{k,lj} + f_i = 0 \tag{6.1}$$

If the point force is in the m-direction, it can be represented by:

$$f_i = \delta_{im}\delta(\mathbf{r}) \tag{6.2}$$

Where the Dirac-delta function is $\delta(\mathbf{r}) = \delta(r_1)\delta(r_2)\delta(r_3)$, with the property:

$$\int_V \delta(\mathbf{r} - \hat{\mathbf{r}})f(\hat{\mathbf{r}})\ dV = f(\mathbf{r})$$

Translational equilibrium is satisfied by:

$$C_{ijkl}U_{k,lj} + \delta_{im}\delta(\mathbf{r}) = 0 \tag{6.3}$$

Given a point force distribution $f_m(\mathbf{r})$, the corresponding displacement vector distribution is obtained as:

$$u_i(\mathbf{r}) = \int_{allspace} U_{km}(\mathbf{r} - \hat{\mathbf{r}})f_m(\hat{\mathbf{r}})\ d\hat{V} \tag{6.4}$$

However, for a finite region of space, we use the divergence theorem for any rank tensor $\mathbf{T}$ is expressed as:

$$\int_V \nabla \bullet \mathbf{T}\ dV = \int_S \mathbf{T}\bullet\ d\mathbf{S} = \int_V \mathbf{T}_{,i} dV = \int_S \mathbf{T} dS_i$$

Now consider the following equation:

$$\begin{aligned}
\int_{\hat{V}} C_{ijkl}\left[u_i(\hat{\mathbf{r}})U_{km,\hat{l}\hat{j}} - U_{im}(\mathbf{r}-\hat{\mathbf{r}})u_{k,\hat{l}\hat{j}}(\hat{\mathbf{r}})\right]\ d\hat{V} = \\
= \int_{\hat{S}} C_{ijkl}\left[u_i(\hat{\mathbf{r}})U_{km,\hat{l}} - U_{im}u_{k,\hat{l}}(\hat{\mathbf{r}})\right]\ dS_{\hat{j}} \\
= \int_{\hat{V}} \left[-u_i(\hat{\mathbf{r}})\delta_{ij}\delta(\mathbf{r}-\hat{\mathbf{r}}) + U_{im}f_i\right]\ d\hat{V} \\
= \int_{\hat{S}} \left[u_i(\hat{\mathbf{r}})C_{ijkl}U_{km,\hat{l}} - U_{im}\sigma_{ij}(\hat{\mathbf{r}})\right]\ dS_{\hat{j}}
\end{aligned} \tag{6.5}$$

Re-arranging terms, we can easily determine the displacement vector anywhere, given that a distributed force system is specified in the volume, and that stress and displacement conditions are prescribed at the boundary. Hence, we have:

$$\begin{aligned}
u_m(\mathbf{r}) &= \int_{\hat{V}} U_{im}(\mathbf{r}-\hat{\mathbf{r}})\, f_i(\hat{\mathbf{r}})\, d\hat{V} - \int_{\hat{S}} u_i(\hat{\mathbf{r}})\, C_{ijkl}U_{km,\hat{l}}(\mathbf{r}-\hat{\mathbf{r}})\, d\hat{S}_j \\
&+ \int_{\hat{S}} U_{im}(\mathbf{r}-\hat{\mathbf{r}})\, \sigma_{ij}(\hat{\mathbf{r}})\, d\hat{S}_j
\end{aligned} \tag{6.6}$$

The second and third terms in Equation 7.84 account for displacement and traction boundary conditions on the surface $\hat{S}$, respectively. The specific case of a dislocation loop is characterized by the absence of body forces within the volume (i.e. $f_i = 0$), zero tract ions on the boundary (i.e. $\sigma_{ij} = 0$) on $\hat{S}$, and a rigid displacement vector b_i across the surface $\hat{S}$. The displacement equation is finally given by:

$$u_m(\mathbf{r}) = -b_i \int_{\hat{S}} C_{ijkl}U_{km,\hat{l}}(\mathbf{r}-\hat{\mathbf{r}})\, d\hat{S}_j = b_i \int_{\hat{S}} C_{ijkl}U_{km,l}(\mathbf{r}-\hat{\mathbf{r}})\, d\hat{S}_j \tag{6.7}$$

To complete determination of the displacement field, we need to evaluate Green's functions of isotropic elasticity, as given below. We use the method of Fourier transform, defined as:

$$\tilde{U}_{km}(\mathbf{k}) = \int_V U_{km}(\mathbf{r})\, e^{-i\mathbf{k}\cdot\mathbf{r}} dV \tag{6.8}$$

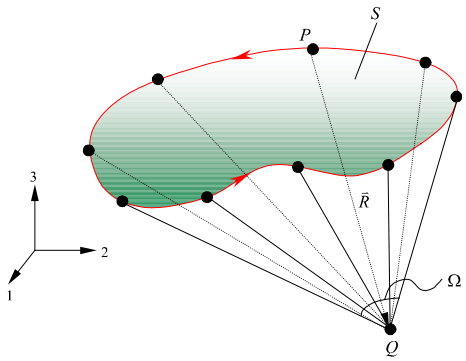

Figure 6.1: Representation of the solid angle, Ω, at a field point (Q) away from the dislocation loop line containing the set of points (P)

with its inverse:

$$U_{km}(\mathbf{r}) = \frac{1}{(2\pi)^3}\int_{V_k} \tilde{U}_{km}(\mathbf{k})\, e^{i\mathbf{k}\cdot\mathbf{r}} dV_k \tag{6.9}$$

and the associated differentiation rules:

$$k_l \tilde{U}_{km} = \int_V U_{km,l}(\mathbf{r}) e^{-i\mathbf{k}\cdot\mathbf{r}} dV \tag{6.10}$$

$$-k_l k_j \tilde{U}_{km} = \int_V U_{km,lj}(\mathbf{r}) e^{-i\mathbf{k}\cdot\mathbf{r}} dV \tag{6.11}$$

We start now from the equilibrium equation, and take its Fourier transform:

$$\begin{aligned} C_{ijkl} U_{km,lj} &= -\delta_{im}\delta(\mathbf{r}) \\ -C_{ijkl} k_l k_j \tilde{U}_{km}(\mathbf{k}) &= -\delta_{im} \end{aligned} \tag{6.12}$$

6.2 Differential Geometry

As will be clear later in this section, Green's tensor functions are used to obtain the elastic fields in inhomogeneous materials, in which compatibilities are described along internal lines or surfaces. Differential geometry of closed lines will then be essential to further development of the theory of internal elastic fields. We consider here differential geometric aspects of a closed space curve bounding an internal surface within the material. As shown in Figure 6.1, the solid angle differential $d\Omega$ is the ratio of the projected area element $d\mathbf{S}$ to the square of R. Thus:

$$\Omega = \int d\Omega = \int_S \frac{\mathbf{e} \bullet d\mathbf{S}}{R^2} = \int_S \frac{X_i dS_i}{R^3} = -\frac{1}{2}\int_S R_{,ppi} dS_i \tag{6.13}$$

where $\mathbf{e} = \mathbf{R}/R = set\{e_i\}$ is a unit vector along $\mathbf{R} = set\{X_i\}$, and $R_{,ppi} = -2X_i/R^3$. The solid angle can be computed as a line integral, by virtue of Stokes theorem. A vector potential $\mathbf{A}\ (\mathbf{R})$ is introduced by deWit to satisfy the differential equation: $\in_{pik} A_{k,p}(\mathbf{R}) = X_i R^{-3}$. The solution is given by (**?**): $A_k(\mathbf{R}) = \in_{ijk} X_i s_j/[R(R + \mathbf{R} \bullet \mathbf{s})]$, where $\mathbf{s}$ is an arbitrary unit vector. This results in non-uniqueness of the displacement field, although it can be arbitrarily symmetrized (**?**). The solid angle is then given as a line integral: $\Omega(\mathbf{R}) = \oint_C A_k(\mathbf{R}) d\ell_k$. Taking the derivatives of Ω in Equation 6.13, and applying Equation 7.87, we obtain:

$$\Omega_{,j} = \frac{1}{2}\int_S (R_{,ppll} dS_j - R_{,pplj} dS_l) = \frac{1}{2}\oint_C \in_{jkl} R_{,ppl} dl_k \tag{6.14}$$

Successive derivatives of the vector $\mathbf{R}$ are given by the following set of equations:

$$\begin{aligned}
R_{,i} &= \frac{X_i}{(X_q X_q)^{\frac{1}{2}}} = \frac{X_i}{R} = e_i \\
R_{,ij} &= \frac{\delta_{ij}}{(X_q X_q)^{\frac{1}{2}}} - \frac{X_i X_j}{(X_q X_q)^{\frac{3}{2}}} = \frac{\delta_{ij}}{R} - \frac{X_i X_j}{R^3} = (\delta_{ij} - e_i e_j)/R \\
R_{,ijk} &= -\frac{\delta_{jk} X_i + \delta_{ik} X_j + \delta_{ij} X_k}{(X_q X_q)^{\frac{3}{2}}} + \frac{3 X_i X_j X_k}{(X_q X_q)^{\frac{5}{2}}} \\
&= -\frac{\delta_{jk} X_i + \delta_{ik} X_j + \delta_{ij} X_k}{R^3} + \frac{3 X_i X_j X_k}{R^5} \\
&= (3 e_i e_j e_k - [\delta_{ij} e_k + \delta_{jk} e_i + \delta_{ki} e_j])/R^2
\end{aligned} \tag{6.15}$$

The third rank tensor R_{ijk} has only 10 non-vanishing terms, and these are given below for convenience.

$$\begin{aligned}
R_{,111} &= 3e_1({e_1}^2 - 1)/R^2, & R_{,112} &= e_2(3e_1^2 - 1)/R^2 \\
R_{,113} &= e_3(3e_1^2 - 1)/R^2, & R_{,221} &= e_1(3e_2^2 - 1)/R^2 \\
R_{,222} &= 3e_2(e_2^2 - 1)/R^2, & R_{,223} &= e_3(3e_2^2 - 1)/R^2 \\
R_{,331} &= e_1(3e_3^2 - 1)/R^2, & R_{,332} &= 3e_2(3e_3^2 - 1)/R^2 \\
R_{,333} &= 3e_3(e_3^2 - 1)/R^2, & R_{,123} &= 3e_1 e_2 e_3/R^2
\end{aligned} \tag{6.16}$$

One can also write the vector $R_{,i} \equiv \mathbf{R1}$ and the second order tensor $R_{,ij} \equiv \mathbf{R2}$ in dyadic notation as (see eq. (4.33)):

$$\begin{aligned}
\mathbf{R1} &= \mathbf{e} \\
\mathbf{R2} &= (\mathbf{I} - \mathbf{e} \otimes \mathbf{e})/R = \mathbf{P}_e^{\perp}/R
\end{aligned} \tag{6.17}$$

6.3 Green's Functions in Isotropic Materials

6.3.1 Full Space

For an isotropic elastic solid, we have:

$$\begin{aligned} \mu\left(\delta_{ik}\delta_{jl}+\delta_{il}\delta_{jk}\right)k_l k_j \tilde{U}_{km}(\mathbf{k}) + \lambda\delta_{ij}\delta_{kl}k_l k_j \tilde{U}_{km}(\mathbf{k}) &= \delta_{im} \\ \mu\delta_{ik}\delta_{jl}k_l k_j \tilde{U}_{km}(\mathbf{k}) + \mu\delta_{il}\delta_{jk}k_l k_j \tilde{U}_{km}(\mathbf{k}) + \lambda\delta_{ij}\delta_{kl}k_l k_j \tilde{U}_{km}(\mathbf{k}) &= \delta_{im} \end{aligned} \tag{6.18}$$

Using the substitution property of the delta function, we obtain:

$$\begin{aligned} \mu\delta_{ik}\delta_{jl}k_l k_j \tilde{U}_{km}(\mathbf{k}) &= \mu k_l k_l \tilde{U}_{im}(\mathbf{k}) \\ \mu\delta_{il}\delta_{jk}k_l k_j \tilde{U}_{km}(\mathbf{k}) = \mu k_i k_j \tilde{U}_{jm}(\mathbf{k}) &= \mu k_i k_k \tilde{U}_{km}(\mathbf{k}) \end{aligned} \tag{6.19}$$

Now, exchange $j \rightarrow k$:

$$\lambda\delta_{ij}\delta_{kl}k_l k_j \tilde{U}_{km}(\mathbf{k}) = \lambda k_l k_i \tilde{U}_{lm}(\mathbf{k}) = \lambda k_i k_k \tilde{U}_{km}\mathbf{k}) \tag{6.20}$$

And exchange $l \rightarrow k$:

$$(\mu+\lambda)k_k k_i \tilde{U}_{km} + \mu k^2 \tilde{U}_{im} = \delta_{im} \tag{6.21}$$

Then, multiply by k_i and sum over i:

$$\begin{aligned} (\mu+\lambda)k_k k_i k_i \tilde{U}_{km} + \mu k^2 k_i \tilde{U}_{im} &= \delta_{im}k_i \\ (\mu+\lambda)k_k k^2 \tilde{U}_{km} + \mu k^2 k_i \tilde{U}_{im} &= k_m \end{aligned} \tag{6.22}$$

Exchange $i \leftarrow k$, and re-arrange:

$$\begin{aligned} (\mu+\lambda)k_k k^2 \tilde{U}_{km} + \mu k^2 k_k \tilde{U}_{km} &= k_m \\ (2\mu+\lambda)k_k k^2 \tilde{U}_{km} &= k_m \qquad \text{or,} \\ k_k \tilde{U}_{km} &= \frac{k_m}{(2\mu+\lambda)k^2} \end{aligned} \tag{6.23}$$

This result can now be substituted back into Equation 6.21 above. The elastic Green's functions are readily obtained in Fourier space as:

$$\begin{aligned}\left(\frac{\mu+\lambda}{2\mu+\lambda}\right)\frac{k_i k_m}{k^2}+\mu k^2\tilde{U}_{im} &= \delta_{im} \\ \tilde{U}_{im}(\mathbf{k}) &= \frac{1}{\mu}\left[\frac{\delta_{kim}}{k^2}-\left(\frac{\mu+\lambda}{2\mu+\lambda}\right)\frac{k_k k_m}{k^4}\right]\end{aligned} \tag{6.24}$$

To obtain the elastic Green's functions in Cartesian space, we use the following properties of the inverse Fourier transform:

$$\frac{1}{\pi^2}\int_{V_k}\frac{e^{i\mathbf{k}\cdot\mathbf{r}}}{k^4}dV_k=-r \tag{6.25}$$

And its second derivative:

$$\frac{1}{\pi^2}\int_{V_k}\frac{k_m k_m e^{i\mathbf{k}\cdot\mathbf{r}}}{k^4}dV_k=r_{,km} \tag{6.26}$$

While for $k=m=p$, we have:

$$\frac{1}{\pi^2}\int_{V_k}\frac{e^{i\mathbf{k}\cdot\mathbf{r}}}{k^2}dV_k=r_{,pp} \tag{6.27}$$

Finally, we can now use Equations 6.26 and 6.55, and take the inverse Fourier transform of Equation 6.24 to obtain the explicit form of the isotropic elastic Green's functions:

$$U_{km}(\mathbf{r})=\frac{1}{8\pi\mu}\left[\delta_{km}r_{,pp}-\left(\frac{\lambda+\mu}{\lambda+2\mu}\right)r_{,km}\right] \tag{6.28}$$

Similarly, the Green's functions $U_{km}(\mathbf{r}-\hat{\mathbf{r}})=U_{km}(\mathbf{R})$, and their derivative with respect to l are given by:

$$\begin{aligned}U_{km}(\mathbf{R}) &= \frac{1}{8\pi\mu}\left[\delta_{km}R_{,pp}-\left(\frac{\lambda+\mu}{\lambda+2\mu}\right)R_{,km}\right] \\ U_{km,l}(\mathbf{R}) &= \frac{1}{8\pi\mu}\left[\delta_{km}R_{,ppl}-\left(\frac{\lambda+\mu}{\lambda+2\mu}\right)R_{,kml}\right]\end{aligned} \tag{6.29}$$

6.3.2 Half Space

For an isotropic case, the complete solution of the displacement induced by a concentrated force on the surface is a classical elasticity problem, which is known as Boussinesq's problem

for a normal concentrated force and Cerruti's problem for a tangential concentrated force. The most direct and regular method of solving the Navier's equation is to use Fourier's method as Rob Philips did in his book. But in that case we always have to meet some fairly complicated integrals. On the other hand, by some artificial stress functions, the calculations are simpler. Here I will not reproduce the well-known but laborious procedure and just give the final results of the problem.

The physical problem is illustrated in the figure 6.2

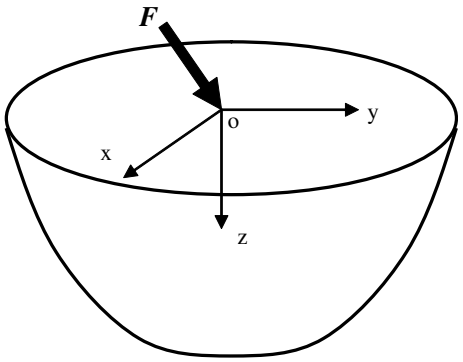

Figure 6.2: A concentrated force applied to an isotropic half space medium

The displacement field are determined by the following formulae (Landau and Lifshitz 1959):

$$\begin{aligned}
u_x &= \frac{1+\nu}{2\pi E}\left\{\left[\frac{xz}{r^3}-\frac{(1-2\nu)\,x}{r\,(r+z)}\right]F_z+\frac{2\,(1-\nu)\,r+z}{r\,(r+z)}F_x+\frac{\left[2r\,(\nu r+z)+z^2\right]x}{r^3\,(r+z)^2}\,(xF_x+yF_y)\right\}\\
u_y &= \frac{1+\nu}{2\pi E}\left\{\left[\frac{yz}{r^3}-\frac{(1-2\nu)\,y}{r\,(r+z)}\right]F_z+\frac{2\,(1-\nu)\,r+z}{r\,(r+z)}F_y+\frac{\left[2r\,(\nu r+z)+z^2\right]y}{r^3\,(r+z)^2}\,(xF_x+yF_y)\right\}\\
u_z &= \frac{1+\nu}{2\pi E}\left\{\left[\frac{2\,(1-\nu)}{r}+\frac{z^2}{r^3}\right]F_z+\left[\frac{1-2\nu}{r\,(r+z)}+\frac{z}{r^3}\right](xF_x+yF_y)\right\}
\end{aligned}\tag{6.30}$$

where E is Young's modulus and ν is Poisson's ratio.

In particular, the displacement of points on the surface of the medium is given by putting $z=0$:

$$\begin{aligned}
u_x &= \frac{1+\nu}{2\pi E}\frac{1}{r}\left\{-\frac{(1-2\nu)\,x}{r}F_z+2\,(1-\nu)\,F_x+\frac{2\nu x}{r^2}\,(xF_x+yF_y)\right\}\\
u_y &= \frac{1+\nu}{2\pi E}\frac{1}{r}\left\{-\frac{(1-2\nu)\,y}{r}F_z+2\,(1-\nu)\,F_y+\frac{2\nu y}{r^2}\,(xF_x+yF_y)\right\}
\end{aligned}\tag{6.31}$$

$$u_z = \frac{1+\nu}{2\pi E}\frac{1}{r}\left\{2\left(1-\nu\right)F_z + \left(1-2\nu\right)\frac{1}{r}\left(xF_x + yF_y\right)\right\}$$

Considering the solution on the surface $z = 0$ and using the 2-D position vector $\vec{R} = \vec{\rho} - \vec{\rho}'$, $i, j = 1, 2$, we can obtain the surface Green's tensor as:

$$U_{ij}\left(\vec{R}, 0\right) = \frac{1+\nu}{\pi E}\left[\left(1-\nu\right)\frac{\delta_{ij}}{R} + \nu\frac{R_i R_j}{R^3}\right] \tag{6.32}$$

6.4 Green's Functions in Anisotropic Materials

It is well known that the Green's functions (which is the elastic displacement response of a linear elastic solid to a point force), are foundations of many numerical methods when analyzing an engineering or physical problem. They are essential to various integral equation methods and numerical element methods. Furthermore, they can be applied directly to some modern physical problems, such as elastic fields in quantum-dot semiconductors and atomistic simulations of point defects in crystals. Though they are basic and important, unfortunately, there is no unique universal Green's functions. Generally, they can be classified by isotropic or (monoclinic, transversely isotropic or general) anisotropic elastic media, by two-dimensional (2-D) or three-dimensional (3-D) deformation, and by infinite space, half-space, bi-materials or multi-layers. They are listed as following:

1. Isotropic, Two-dimensional Deformations.
   (a) Infinite space (Fredholm 1900)
   (b) Half-Space (Dundurs 1969, Head 1953)
   (c) Bimaterials (Dundurs 1969, Dundurs and Hetenyi 1965, Dundurs and Sendeckyj 1965a).
2. Isotropic, Three-dimensional Deformations.
   (a) Infinite space (Boussinesq 1885, Synge 1885)
   (b) Half-Space (Mindlin 1953)
   (c) Bimaterials (Rongved 1955b, Dundurs 1969, Dundurs and Hetenyi 1965, Dundurs and Sendeckyj 1965b).
3. Anisotropic, Two-dimensional Deformation.
   (a) Infinite space (Asaro, Hirth, Barnett and Lothe 1973, Barnett 1972, Barnett and Lothe 1973, Barnett and Swanger 1971, Chadwick and Smith 1977, Eshelby, Read and Shockley 1953, Kirchner and Alshits 1987, Malen 1971, Stroh 1958, Ting 1992a, Willis 1970)

(b) Half-Space (Barnett and Lothe 1975, Head 1953, Head 1965, Tewary, Wagoner and Hirth 1989a, Ting 1992b, Ting and Barnett 1993, Tucker 1969, Willis 1970)

(c) Bimaterials (Barnett and Lothe 1974, Barnett and Lothe 1995, Qu 1991, Tewary et al. 1989a, Tewary, Wagoner and Hirth 1989b, Ting 1992b, Tucker 1969)

4. Anisotropic, Three-dimensional Deformations.

(a) Infinite space (Dederichs and G. 1969, Dikici 1986, Dunn and Wienecke 1996, Elliott 1948, Hanson and Wong 1997, Indenbom and Orlov 1968, Kroner 1953, Lejcek 1969, Lie and Koehler 1968, Lifshitz and Rozenzweig 1947, Mura and Kinoshita 1971, Pan and Chou 1971, Tewary 1995, Ting and Lee 1997, Willis 1966, Wu 1999, Yu and Sanday 1994, Wang 1997, Tonon, Pan and Amadei 2001)

(b) Half-Space (Dunn and Wienecke 1999, Hanson and Wong 1997, Lee 1979, Barnett and Lothe 1975, Pan and Chou 1979b, Rongved 1955a, Wu 1999)

(c) Bimaterials (Pan and Chou 1979a, Rongved 1955b, Ting 1996, Pan and Yuan 1999).

(d) Three and multilayer (Yang and Pan 2002a, Yang and Pan 2002b, Yuan, Yang and Yang 2003).

For anisotropic elastic solids, the Green's functions can be obtained by the Fourier transform method as well. In the transformed domain, the Green's functions $\tilde{G}_{km}(\mathbf{k})$ satisfy the equilibrium equations:

$$C_{ijkl}k_l k_j \tilde{G}_{km}(\mathbf{k}) = \delta_{im}$$

Using the notation:

$$K_{ik}(\mathbf{k}) = C_{ijkl}k_l k_j \tag{6.33}$$

The equation can be written as

$$K_{ik}(\mathbf{k})\tilde{G}_{km}(\mathbf{k}) = \delta_{im} \tag{6.34}$$

Then $\tilde{G}_{ij}(\mathbf{k})$ can be obtained as:

$$\tilde{G}_{ij}(\mathbf{k}) = K_{ij}^{-1}(\mathbf{k}) = \frac{N_{ij}(\mathbf{k})}{D(\mathbf{k})} \tag{6.35}$$

where $K_{ij}^{-1}(\mathbf{k})$, $N_{ij}(\mathbf{k})$ and $D(\mathbf{k})$ are the inverse matrix, adjoint matrix and the determinant of $K_{ij}(\mathbf{k})$, respectively.

The Green's functions then can be obtained by the inverse Fourier transformation:

$$\begin{aligned} G_{ij}(\mathbf{r}) &= \frac{1}{(2\pi)^3}\int_{V_k} \tilde{G}_{ij}(\mathbf{k})\, e^{i\mathbf{k}\cdot\mathbf{r}} dV_k \\ &= \frac{1}{(2\pi)^3}\int_{V_k} \frac{N_{ij}(\mathbf{k})}{D(\mathbf{k})} e^{i\mathbf{k}\cdot\mathbf{r}} dV_k \end{aligned} \tag{6.36}$$

Now the main problem is to carry out the triple integrations. First, the volume element dV_k is expressed as

$$dV_k = k^2 dk dS_k \tag{6.37}$$

where $k = |\mathbf{k}|$ and dS_k is the surface element on the unit sphere $|\mathbf{k}| = 1$. By denoting

$$\bar{\mathbf{k}} = \mathbf{k}/k, \tag{6.38}$$

Eq.(6.36) can be written as

$$G_{ij}(\mathbf{r}) = \frac{1}{(2\pi)^3} \int_0^\infty dk \int_{S_k} \frac{N_{ij}(\bar{\mathbf{k}})}{D(\bar{\mathbf{k}})} e^{ik\bar{\mathbf{k}}\cdot\mathbf{r}} dS_k \tag{6.39}$$

Since $N_{ij}(\mathbf{k})$ and $D(\mathbf{k})$ are polynomials with degrees four and six, respectively, $N_{ij}(\mathbf{k})/D(\mathbf{k}) = k^{-2} N_{ij}(\bar{\mathbf{k}})/D(\bar{\mathbf{k}})$ is used.
Noticing that $N_{ij}(-\bar{\mathbf{k}})/D(-\bar{\mathbf{k}}) = N_{ij}(\bar{\mathbf{k}})/D(\bar{\mathbf{k}})$, The integral can be further expressed as:

$$G_{ij}(\mathbf{r}) = \frac{1}{2(2\pi)^3} \int_{-\infty}^\infty dk \int_{S_k} \frac{N_{ij}(\bar{\mathbf{k}})}{D(\bar{\mathbf{k}})} e^{ik\bar{\mathbf{k}}\cdot\mathbf{r}} dS_k \tag{6.40}$$

Noticing that the delta function $\delta(x) = \frac{1}{2\pi}\int_{-\infty}^{\infty} e^{ikx} dk$, the integration with respect to k leads to

$$G_{ij}(\mathbf{r}) = \frac{1}{8\pi^2} \int_{S_k} \delta(\bar{\mathbf{k}}\cdot\mathbf{r}) \frac{N_{ij}(\bar{\mathbf{k}})}{D(\bar{\mathbf{k}})} dS_k \tag{6.41}$$

Denoting the angle between $\bar{\mathbf{k}}$ and $\mathbf{r}$ by θ, we have

$$\bar{\mathbf{k}}\cdot\mathbf{r} = r\cos\theta, \quad dS_k = \sin\theta d\theta d\phi = -r^{-1} d(\bar{\mathbf{k}}\cdot\mathbf{r}) d\phi \tag{6.42}$$

where $r = |\mathbf{r}|$, and ϕ is an angle staring arbitrary on the plane perpendicular to $\mathbf{r}$, and the integration becomes

$$G_{ij}(\mathbf{r}) = \frac{1}{8\pi^2 r} \int_{-r}^{r} \delta(\bar{\mathbf{k}}\cdot\mathbf{r}) d(\bar{\mathbf{k}}\cdot\mathbf{r}) \int_0^{2\pi} d\phi \frac{N_{ij}(\bar{\mathbf{k}})}{D(\bar{\mathbf{k}})} \tag{6.43}$$

Using the property of delta function $\int_{-\infty}^{\infty} \delta(x) f(x) dx = f(0)$, we have

$$G_{ij}(\mathbf{r}) = \frac{1}{8\pi^2 r} \oint_{C_k} \frac{N_{ij}(\bar{\mathbf{k}})}{D(\bar{\mathbf{k}})} d\phi \tag{6.44}$$

where the integral is taken around the unit circle C_k ($|\bar{\mathbf{k}}| = 1$) on the plane normal to $\mathbf{r}$, and $\bar{\mathbf{k}}\cdot\mathbf{r} = 0$ in the equation. This integration can be calculated by numerical method.

The Fourier transform method is used by Mura (1987). Other methods can be used to obtain the Green's functions also, such as the Radon transform method by Bacon, Barnett and Scattergodd (1980). Their result is written in another form as:

$$G_{ij}(\mathbf{r}) = \frac{1}{8\pi^2 r} \oint_{|z|=1} (zz)^{-1}_{ij} ds, \tag{6.45}$$

where the notation $(zz)_{ij} = C_{mijp} z_m z_p$ is used, $(zz)_{ij}^{-1}$ is the inverse of $(zz)_{ij}$, and the integration contour is the unit circle $|z| = 1$ lying in the plane normal to $\mathbf{r}$.

The Green's functions can be written in other integral expressions. Let n and m be any two orthogonal unit vectors on the normal to $\mathbf{r}$. The unit vector $\bar{\mathbf{k}}$ on the plane can be represented by

$$\bar{\mathbf{k}} = \mathbf{n}\cos\phi + \mathbf{m}\sin\phi$$

and the equation can be expressed as

$$\begin{aligned} G_{ij}(\mathbf{r}) &= \frac{1}{8\pi^2 r}\int_0^{2\pi} \frac{N_{ij}(\mathbf{n}\cos\phi + \mathbf{m}\sin\phi)}{D(\mathbf{n}\cos\phi + \mathbf{m}\sin\phi)} d\phi \\ &= \frac{1}{4\pi^2 r}\int_0^{\pi} \frac{N_{ij}(\mathbf{n}\cos\phi + \mathbf{m}\sin\phi)}{D(\mathbf{n}\cos\phi + \mathbf{m}\sin\phi)} d\phi \end{aligned} \tag{6.46}$$

The second equality follows from the fact that $N_{ij}(\mathbf{n}\cos\phi + \mathbf{m}\sin\phi)/D(\mathbf{n}\cos\phi + \mathbf{m}\sin\phi)$ is periodic in ϕ with periodicity π.

Now introducing the substitution $\zeta = \tan\phi$, and considering the fact that $N_{ij}(\mathbf{k})/D(\mathbf{k})$ is a function of $\mathbf{k}$ of degree -2, we can write the equation (6.46) as

$$G_{ij}(\mathbf{r}) = \frac{1}{4\pi^2 r}\int_{-\infty}^{\infty} \frac{N_{ij}(\mathbf{n} + \mathbf{m}\zeta)}{D(\mathbf{n} + \mathbf{m}\zeta)} d\zeta \tag{6.47}$$

The integral in the equation (6.47) can be expressed in terms of residues in the complex ζ-plane by Cauchy's theorem. Then, eq.(6.47) becomes

$$G_{ij}(\mathbf{r}) = \frac{i}{2\pi r}\sum_N^3 \frac{N_{ij}(\mathbf{n} + \mathbf{m}\zeta^N)}{\frac{\partial D}{\partial \zeta}(\mathbf{n} + \mathbf{m}\zeta^N)} \tag{6.48}$$

where ζ^N are the three roots, with positive imaginary parts, of the equation

$$D(\mathbf{n} + \mathbf{m}\zeta^N) = 0 \tag{6.49}$$

Since $D(\mathbf{n} + \mathbf{m}\zeta^N) = 0$ is the sextic equation in ζ^N, for its roots, which has no closed-form solution exits for general anisotropy, and considerable computation is required. For the degenerate case of multiple roots, the solution base on the sextic equation method need to be treated specially, and cannot pass smoothly to the isotropic limit. While the integral expressions can be evaluated directly by numerical method, and they can pass smoothly into degenerate cases.

In many cases, the derivatives of Green's functions are needed, and should be considered specially. Differentiating the expression (6.41) of Green's functions with respect to coordinate r_k, leads to

$$G_{ij,k}(\mathbf{r}) = \frac{1}{8\pi^2}\int_{S_k} \delta'(\bar{\mathbf{k}}\cdot\mathbf{r})\bar{k}_k N_{ij}(\bar{\mathbf{k}}) D^{-1}(\bar{\mathbf{k}}) dS_k, \tag{6.50}$$

Since $\int_{S_k} dS_k = r^{-1}\oint_{C_k} d\phi \int_{-r}^{r} d(\bar{\mathbf{k}}\cdot\mathbf{r})$, and $\delta(\bar{\mathbf{k}}\cdot\mathbf{r})k_k N_{ij}(\bar{\mathbf{k}})D^{-1}(\bar{\mathbf{k}}) = 0$ at $\bar{\mathbf{k}}\cdot\mathbf{r} = \pm r$, integration by parts of equation () yields

$$\begin{aligned} G_{ij,k}(\mathbf{r}) &= \frac{-1}{8\pi^2 r}\oint_{C_k} d\phi \int_{-r}^{r} \delta(\bar{\mathbf{k}}\cdot\mathbf{r})\partial[\bar{k}_k N_{ij}(\bar{\mathbf{k}})D^{-1}(\bar{\mathbf{k}})]/\partial(\bar{\mathbf{k}}\cdot\mathbf{r}) d(\bar{\mathbf{k}}\cdot\mathbf{r}) \\ &= \frac{-1}{8\pi^2 r}\oint_{C_k} \partial[\bar{k}_k N_{ij}(\bar{\mathbf{k}})D^{-1}(\bar{\mathbf{k}})]/\partial(\bar{\mathbf{k}}\cdot\mathbf{r}) d\phi. \end{aligned} \tag{6.51}$$

where C_k is the unit circle normal to $\mathbf{r}$. On the plane, $\bar{\mathbf{k}} \cdot \mathbf{r} = 0$. Let n and m be any two orthogonal unit vectors on the plane. The unit vector $\bar{\mathbf{k}}$ can be write as

$$\bar{\mathbf{k}} = \cos\theta\bar{\mathbf{r}} + \sin\theta\cos\phi\mathbf{n} + \sin\theta\sin\phi\mathbf{m}$$

where $\bar{\mathbf{r}} = \mathbf{r}/r$, θ is the angle between $\bar{\mathbf{k}}$ and $\mathbf{r}$. On the C_k plane, $\theta = \pi/2$, and we have

$$\partial\bar{k}_k/\partial\theta = -\bar{x}_k,\ \partial(\bar{\mathbf{k}} \cdot \mathbf{r}) = -rd\theta \tag{6.52}$$

On the other hand, differentiating $K_{lm}N_{mj}D^{-1} = \delta_{lj}$ and $K_{lm} = C_{lpmq}\bar{k}_p\bar{k}_q$ with respect to θ, we obtain

$$\partial(N_{ij}D^{-1}/\partial\theta) = N_{il}N_{jm}D^{-2}C_{lpmq}(\bar{r}_p\bar{k}_q + \bar{k}_p\bar{r}_q) \tag{6.53}$$

Thus, the first derivatives of Green's functions can be expressed as

$$\begin{aligned} G_{ij,k}(\mathbf{r}) &= \frac{1}{8\pi^2 r^2}\oint_{C_k}[-\bar{r}_k N_{ij}(\bar{\mathbf{k}})D^{-1}(\bar{\mathbf{k}}) \\ &\quad +\bar{k}_k C_{lpmq}(\bar{r}_p\bar{k}_q + \bar{k}_p\bar{r}_q)N_{il}(\bar{\mathbf{k}})N_{jm}(\bar{\mathbf{k}})D^{-2}(\bar{\mathbf{k}})]d\phi \end{aligned} \tag{6.54}$$

Higher derivatives can be obtained in a similar manner. Such as, the second derivatives of Green's functions can be expressed as

$$\begin{aligned} G_{ij,kl}(\mathbf{r}) &= \frac{1}{8\pi^2 r^3}\oint_{C_k}\Big\{2\bar{r}_k\bar{r}_l N_{ij}(\bar{\mathbf{k}})D^{-1}(\bar{\mathbf{k}}) \\ &\quad -2[(\bar{r}_k\bar{k}_l + \bar{r}_l\bar{k}_k)(\bar{r}_p\bar{k}_q + \bar{r}_q\bar{k}_p) + \bar{r}_p\bar{r}_q\bar{k}_k\bar{k}_l]C_{hpmq}N_{ih}(\bar{\mathbf{k}})N_{jm}(\bar{\mathbf{k}})D^{-2}(\bar{\mathbf{k}}) \\ &\quad +\bar{k}_k\bar{k}_l C_{hpmq}(\bar{r}_p\bar{k}_q + \bar{r}_q\bar{k}_p)C_{satb}(\bar{r}_a\bar{k}_b + \bar{r}_b\bar{k}_a) \\ &\quad \times[N_{jm}(\bar{\mathbf{k}})N_{is}(\bar{\mathbf{k}})N_{ht}(\bar{\mathbf{k}}) + N_{js}(\bar{\mathbf{k}})N_{ih}(\bar{\mathbf{k}})N_{mt}(\bar{\mathbf{k}})]D^{-3}(\bar{\mathbf{k}})\Big\}\,d\phi \end{aligned} \tag{6.55}$$

Accuracy verification

Since the derivatives of Green's functions are the key functions in the evaluation of elastic field of dislocation loop, the calculating accuracy and computational efficiency to them will play a important role and effect the final results. We will first we compare the results of Green's functions and their derivatives by our direct integral method with other available ones. There is no closed form solution for the Green's functions and their derivatives in a generalized anisotropic elastic medium. To validate the direct numerical integration method we used here, our results are compared, for the case of transversely isotropic material, which a closed form solution is available (Pan and Chou 1971), and an example was given by Tonon et al. (2001).

In the example, the plane of transverse isotropy is parallel to the x_1x_2 plane, the material constants are $C_{1111} = C_{11} = 88$, $C_{3333} = C_{33} = 24$, $C_{1122} = C_{12} = 72$, $C_{1133} = C_{13} = 40$, $C_{2323} = C_{44} = 1.6$, the source point is at $\mathbf{x}' = (0, 0, 0)$ and the field point at $\mathbf{x} = (-1, 0.8, 1.5)$. The elastic constants are in the unit of 10^4kN/m^2 and distances in m.

The Green's functions (displacements) are listed in Table 1, with the results calculated by present Gaussian numerical methods and those given in the reference by Tonon et al. (2001).

When the number N_{max} of Gaussian quadrature is 16, the results have high accuracy with 9 significant digits, i.e., the relative errors are less than 10^{-9}. With the quadrature number N_{max} increasing, the accuracy of the present results increases also, and they convergent to the closed form solutions till the last (11th) digital figures when N_{max} is great than 16×5.

The Green's functions (displacements) are calculated first, and the results by the present (numerical Gaussian integration) method agree very well with those given in the reference by Tonon et al. (2001). When the number N_{max} of Gaussian quadrature is 16, the results have high accuracy with 9 significant digits, i.e., the relative errors are less than $10^{-7}\%$. With the quadrature number N_{max} increasing, the accuracy of the present results increases also, and they convergent to the closed form solutions till $11th$ numerical figures when N_{max} is greater than 80.

Table 1 Green's functions (

$\times 10^{-4}$

m) calculated by present method and compared with those given in the Reference (Tonon et al. 2001)

ij	G_{ij} Ref.	G_{ij} present		
		$N_{max} = 8$	$N_{max} = 16$	$N_{max} = 32$
11	$4.0141588610\times10^{-3}$	$4.0145152760\times10^{-3}$	$4.0141588605\times10^{-3}$	$4.0141588610\times10^{-3}$
22	$3.8822389799\times10^{-3}$	$3.8818535196\times10^{-3}$	$3.8822389804\times10^{-3}$	$3.8822389806\times10^{-3}$
33	$1.9003220284\times10^{-2}$	$1.9002795095\times10^{-2}$	$1.9003220276\times10^{-2}$	$1.9003220287\times10^{-2}$
12	$-2.9315529143\times10^{-4}$	$-2.9318417701\times10^{-4}$	$-2.9315529058\times10^{-4}$	$-2.9315529032\times10^{-4}$
23	$1.7214308137\times10^{-3}$	$1.7216123966\times10^{-3}$	$1.7214308070\times10^{-3}$	$1.7214308138\times10^{-3}$
31	$-2.1517885172\times10^{-3}$	$-2.1516822418\times10^{-3}$	$-2.1517885241\times10^{-3}$	$-2.1517885173\times10^{-3}$

The derivatives of Green's functions were not shown in the reference (Tonon et al. 2001), in stead the Green's stresses were given, which can be used to check the results of the derivatives of Green's functions. The Green's stress vector $\sigma_k = (\sigma_{11k}, \sigma_{22k}, \sigma_{33k}, \sigma_{23k}, \sigma_{31k}, \sigma_{12k})$ is related to Green's strain vector $\varepsilon_k = (\varepsilon_{11k}, \varepsilon_{22k}, \varepsilon_{33k}, \varepsilon_{23k}, \varepsilon_{31k}, \varepsilon_{12k})$ according to the constitutive, and the Green's strain is related to the derivatives of Green's functions by $\varepsilon_{ijk} = (G_{ik,j} + G_{jk,i})/2$. The Green's stresses are calculated, they (some components) are listed and compared in Table 2. When the number N_{max} of Guassain quadrature is 16, the results have high accuracy with 6 significant digits, i.e., the relative errors are less than $10^{-4}\%$. With N_{max} increasing, the accuracy of the present results increases also. When $N_{max} = 32$, the relative errors decrease to within $10^{-6}\%$. Even if $N_{max} = 8$ only, the relative errors are less than 1%.

Table 2 Green's stresses (kN/m^2) calculated by present method and compared with those given in the Reference (Tonon et al. 2001)

ijk	σ_{ijk} Ref.	σ_{ijk} present		
		$N_{max} = 8$	$N_{max} = 16$	$N_{max} = 32$
111	3.05346453×10^{-3}	3.035337×10^{-3}	3.053463×10^{-3}	3.05346449×10^{-3}
221	5.55165324×10^{-3}	5.574246×10^{-3}	5.551655×10^{-3}	5.55165325×10^{-3}
331	6.95945427×10^{-3}	6.958346×10^{-3}	6.959454×10^{-3}	6.95945424×10^{-3}
121	-1.80336282×10^{-3}	-1.789644×10^{-3}	-1.803363×10^{-3}	$-1.803362831\times10^{-3}$
231	2.51603056×10^{-3}	2.515036×10^{-3}	2.516030×10^{-3}	2.51603054×10^{-3}
311	-3.39333301×10^{-3}	-3.397382×10^{-3}	-3.393333×10^{-3}	-3.39333298×10^{-3}

From this example it can be seen that the derivatives of Green's functions (and including Green's functions) evaluated by present direct numerical integral method have high accuracy and computational efficiency.

6.5 Green's Functions in Layered Media

Introduction

Real solids are most often heterogeneous rather than homogenous ones. There are many problems in physical and material areas, can be modeled as a layered system, such as composite laminates, coatings and thin films on substrates, sandwiched interphases etc. For this system, since there are usually many laminates and interfaces, they pose great difficulty for existing numerical methods, such as the domain-discretizing finite element method (FEM) or the surface/interface-discretizing boundary element method (BEM). An reasonable approach with a computational efficiency and accuracy is to apply numerical formulations to the layered system with the Green's functions being those in the layered system instead of being those in a homogeneous and infinite domain. By doing so, no discretization along each interface is necessary, and the boundary condition along all interfaces are satisfied strictly. Therefore the key point in the modeling of layered systems is to provide the Green's functions for such systems.

There are several approaches for calculating the Green's functions in layered system. The most strict approach towards a horizontal layered system, is the transformation method in which some kinds (such as Fourier or Hankel) transformation is used to suppress the horizontal variables (Willis 1966, Singh 1970, Ting 1996, Pan 1989, Pan and Yuan 1999). A general solution for each layer in the transformed field can be found with coefficients to be undetermined, by solving the constitutive equation. The exact forms of those general solutions are often combinations of exponential terms of vertical variable Z. To avoid the numerical inversion transformation, series expansion can be used to approximate the exact general solutions to certain extents (Seale and Kausel 1989, Kausel and Roesset 1981, Choi and Earmme 2002). For a multilayered medium, the unknown transformed coefficients in each layers can be determined according to the boundary conditions of all surfaces and interfaces by forming a global algebraic linear system directly (Mal 1988, Lin and Keer 1989, Kuo and Keer 1995), or by a local system method, such as the propagator matrix method (Singh 1970, Singh 1986, Pan 1989, Pan 1997). After the transformed coefficients are determined, one need to perform the correspondent in-

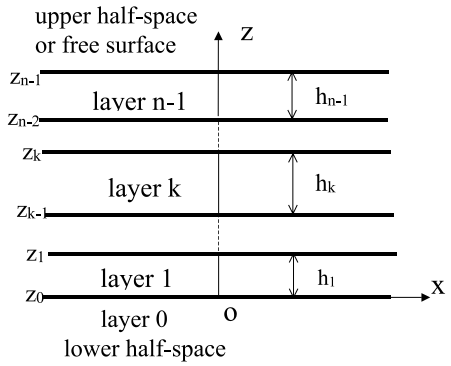

Figure 6.3: Geometry of a multilayered thin film system.

verse transformation to obtain the Green's functions in the physical domain. The elastostatic solutions of a layered system were derived by Singh (1970) and Kuo and Keer (1995) for the isotropic media, and by Singh (1986), Pan (1989) and Pan (1997) for the transverse isotropic media. For general anisotropic media, recently, the 3-D Green's functions have been derived by Ting (1996) and Pan and Yuan (1999) for bimaterials and Yang and Pan (2002b) for trimaterials. In this paper we will derive the 3-D Green's functions for a general anisotropic multilayered media.

6.5.1 Basic formulas

Consider a multilayered medium consisting of a stack of N layers bonded with uniform thickness and perfect bonded along the interfaces. We assume that each layer is homogeneous, anisotropic and with distinct material property in general.

Define Greens function: $G_{ij}(\mathbf{x}, \mathbf{x}')$, as the displacement component u_i at position $\mathbf{x}$ due to a unit point force in the x_j-direction applied at point $\mathbf{x}'$. The equilibrium equation should be satisfied as

$$C_{ijkl} u_{k,lj} + f_i = 0 \tag{6.56}$$

With $f_i = \delta_{im}\delta(\mathbf{x}, \mathbf{x}')$, the equilibrium equation for Green's functions is

$$C_{ijkl}(\mathbf{x}) G_{km,lj}(\mathbf{x}) + \delta_{im}\delta(\mathbf{x}, \mathbf{x}') = 0 \tag{6.57}$$

Now, introduce the two dimensional spatial Fourier transforms applied to the in-plane coordinates (x_1, x_2) of the displacement and the stress components defined by the pair:

$$\tilde{f}(\xi_1, \xi_2, x_3) = \int_{-\infty}^{\infty}\int_{-\infty}^{\infty} f(x_1, x_2, x_3) e^{\mathbf{i}\xi_\alpha x_\alpha} \mathrm{d}x_1 \mathrm{d}x_2,$$

$$f(x_1,x_2,x_3)=\frac{1}{(2\pi)^2}\int_{-\infty}^{\infty}\int_{-\infty}^{\infty}\tilde{f}(\xi_1,\xi_2,x_3)e^{-\mathbf{i}\xi_\alpha x_\alpha}\mathrm{d}\xi_1\mathrm{d}\xi_2. \tag{6.58}$$

where $\alpha=1,2$, and $\mathbf{i}=\sqrt{-1}$.

Applying the 2D Fourier transform to the governing eq.(6.57), it becomes a ordinary differential equation as

$$C_{i\alpha k\beta}\xi_\alpha\xi_\beta\tilde{G}_{km}+\mathbf{i}(C_{i\alpha k3}+C_{i3k\alpha})\xi_\alpha\tilde{G}_{km,3}-C_{i3k3}\tilde{G}_{km,33}=e^{\mathbf{i}\xi_\alpha x'_\alpha}\delta_{im}\delta(x_3,x'_3) \tag{6.59}$$

Solving it yields the general solution in the transformed field for the Green's function $\tilde{G}_{ji}$ (displacement in the jth direction due to a unit point force in the ith direction), as (Ting 1996, Pan and Yuan 1999, Yang and Pan 2002b):

$$\tilde{\mathbf{G}}(\xi_1,\xi_2,x_3;\mathbf{x}')=e^{\mathbf{i}\xi_\alpha x'_\alpha}\left[\tilde{\mathbf{G}}^{\infty}(\xi_1,\xi_2,x_3;x'_3)+\mathbf{i}\eta^{-1}(\bar{\mathbf{A}}<e^{-\mathbf{i}\bar{\mathbf{p}}\eta x_3}>\mathbf{V}+\mathbf{A}<e^{-\mathbf{i}\mathbf{p}\eta x_3}>\mathbf{W})\right] \tag{6.60}$$

where the over bar denotes complex conjugate, (η,θ) are the polar coordinates related to (ξ_1,ξ_2) by $\xi_1=\eta\cos\theta$ and $\xi_2=\eta\sin\theta$, $\mathbf{V}$ and $\mathbf{W}$ are unknown functions of η, θ and x'_3, $<e^{-\mathbf{i}\mathbf{p}\eta x_3}>=\mathrm{diag}[e^{-\mathbf{i}p_1\eta x_3},e^{-\mathbf{i}p_2\eta x_3},e^{-\mathbf{i}p_3\eta x_3}]$, with p_i and $\mathbf{A}=(\mathbf{a}_1,\mathbf{a}_2,\mathbf{a}_3)$ being (chosen to be the three independent pairs with $\mathrm{Im}p_i>0$) the eigenvalues and eigenmatrix of the generalized Stroh eigenproblem (Ting 1996, Pan and Yuan 1999, Yang and Pan 2002b)

$$[\mathbf{Q}+p_i\mathbf{R}+\mathbf{R}^T)+p_i^2\mathbf{T}]\mathbf{a}_i=0 \tag{6.61}$$

$$Q_{ik}=C_{ijks}n_jn_s,\ R_{ik}=C_{ijks}n_jm_s,\ T_{ik}=C_{ijks}m_jm_s$$

with $\mathbf{n}=[\cos\theta,\sin\theta,0]^T$ and $\mathbf{m}=[0,0,1]^T$, In this solution (9.23), the Green's displacement is separated as two part: the full-space solution $\tilde{\mathbf{G}}^{\infty}$ (with elastic properties being those where the field point $\mathbf{x}$ is located and the point force is applied at $\mathbf{x'}=(0,0,x'_3)$), and the complementary part (the other terms) which involves only regular functions. Separating the solution into an infinite-space solution and a complementary part has the advantage of avoiding numerical integral of singular function involved in the infinite-space solution. The full space Green's functions, in the transformed field, are

$$\tilde{\mathbf{G}}^{\infty}(\xi_1,\xi_2,x_3;x'_3)=\mathbf{i}\eta^{-1}\begin{cases}\mathbf{A}<e^{-\mathbf{i}\mathbf{p}\eta(x_3-x'_3)}>\mathbf{A}^T, & x_3<x'_3\\ -\bar{\mathbf{A}}<e^{-\mathbf{i}\bar{\mathbf{p}}\eta(x_3-x'_3)}>\bar{\mathbf{A}}^T, & x_3>x'_3\end{cases} \tag{6.62}$$

The full-space Green's functions in the physical-domain, have been derived explicitly by Ting and Lee (1997) and Tonon et al. (2001) based on the sextic equations. In our calculations, the integral expressions (including the Green's functions and their derivatives in the physical domain) derived by Barnett (1972), Willis (1975), Mura (1987), and given in the former chapter.

Using the elastic constitutive equation and the general solution for the Green's displacement, the Green's stress $\sigma_{jki}(\mathbf{x};\mathbf{x}')$ (the last subscript i indicates the direction of the unit point force) can be derived out. The out-of plane stress $\mathbf{t}=(\sigma_{31i},\sigma_{32i},\sigma_{33i})$ and in-plane stress $\mathbf{t}=(\sigma_{11i},\sigma_{12i},\sigma_{22i})$ can be expressed (in the transformed field) as

$$\tilde{\mathbf{t}}(\xi_1,\xi_2,x_3;\mathbf{x}')=e^{\mathbf{i}\xi_\alpha x'_\alpha}\left[\tilde{\mathbf{t}}^{\infty}(\xi_1,\xi_2,x_3;x'_3)+(\bar{\mathbf{B}}<e^{-\mathbf{i}\bar{\mathbf{p}}\eta x_3}>\mathbf{V}+\mathbf{B}<e^{-\mathbf{i}\mathbf{p}\eta x_3}>\mathbf{W})\right] \tag{6.63}$$

$$\tilde{\mathbf{s}}(\xi_1,\xi_2,x_3;\mathbf{x}') = e^{\mathbf{i}\xi_\alpha x'_\alpha}\left[\tilde{\mathbf{s}}^\infty(\xi_1,\xi_2,x_3;x'_3) + (\bar{\mathbf{C}} < e^{-\mathbf{i}\bar{\mathbf{p}}\eta x_3} > \mathbf{V} + \mathbf{C} < e^{-\mathbf{i}\mathbf{p}\eta x_3} > \mathbf{W})\right] \quad (6.64)$$

with $\tilde{\mathbf{t}}^\infty$ and $\tilde{\mathbf{s}}^\infty$ derived from $\tilde{\mathbf{u}}^\infty$ being the full-space Green's stresses, and in the transformed domain they are

$$\tilde{\mathbf{t}}^\infty(\xi_1,\xi_2,x_3;x'_3) = \begin{cases} \mathbf{B} < e^{-\mathbf{i}\mathbf{p}\eta(x_3-x'_3)} > \mathbf{A}^T, & x_3 < x'_3 \\ -\bar{\mathbf{B}} < e^{-\mathbf{i}\bar{\mathbf{p}}\eta(x_3-x'_3)} > \bar{\mathbf{A}}^T, & x_3 > x'_3 \end{cases} \quad (6.65)$$

$$\tilde{\mathbf{s}}^\infty(\xi_1,\xi_2,x_3;x'_3) = \begin{cases} \mathbf{C} < e^{-\mathbf{i}\mathbf{p}\eta(x_3-x'_3)} > \mathbf{A}^T, & x_3 < x'_3 \\ -\bar{\mathbf{C}} < e^{-\mathbf{i}\bar{\mathbf{p}}\eta(x_3-x'_3)} > \bar{\mathbf{A}}^T, & x_3 > x'_3 \end{cases} \quad (6.66)$$

The matrix $\mathbf{B} = (\mathbf{b}_1, \mathbf{b}_2, \mathbf{b}_3)$ and $\mathbf{C} = (\mathbf{c}_1, \mathbf{c}_2, \mathbf{c}_3)$ are related to $\mathbf{A}$ by

$$\mathbf{b}_i = (\mathbf{R}^T + p_i\mathbf{T})\mathbf{a}_i, \qquad \mathbf{c}_i = \mathbf{D}_i\mathbf{a}_i \quad (6.67)$$

with

$$D_{kli} = C_{1kl\alpha}n_\alpha + p_i C_{1kl3} \text{ for } k = 1,2, \text{ and } D_{3li} = C_{22l\alpha}n_\alpha + p_i C_{22l3}.$$

Noticing that the general solutions (9.23), (9.26) and (9.27) remain valid if x_3 (in $< e^{-\mathbf{i}\bar{\mathbf{p}}\eta x_3} >$ and $< e^{-\mathbf{i}\mathbf{p}\eta x_3} >$) is replaced by $(x_3 - \gamma)$ with γ being an arbitrary real constant. The displacements and stresses for kth layer, $z_{k-1} < x_3 < z_k$ can be rewriten in forms as

$$\begin{pmatrix} \tilde{\mathbf{u}} \\ \tilde{\mathbf{t}} \end{pmatrix}_k (x_3) = e^{\mathbf{i}\xi_\alpha x'_\alpha}\left[\begin{pmatrix} \tilde{\mathbf{u}} \\ \tilde{\mathbf{t}} \end{pmatrix}_k^\infty (x_3) + \mathbf{Z}_k(x_3)\begin{pmatrix} \mathbf{V} \\ \mathbf{W} \end{pmatrix}_k\right] \quad (6.68)$$

$$\tilde{\mathbf{s}}_k(x_3) = e^{\mathbf{i}\xi_\alpha x'_\alpha}\left[\tilde{\mathbf{s}}_k^\infty(x_3) + (\bar{\mathbf{C}}_k < e^{-\mathbf{i}\bar{\mathbf{p}}_k\eta(x_3-z_{k-1})} > \mathbf{V}_k + \mathbf{C}_k < e^{-\mathbf{i}\mathbf{p}_k\eta(x_3-z_k)} > \mathbf{W}_k)\right] \quad (6.69)$$

with

$$\mathbf{Z}_k(x_3) = \begin{pmatrix} \mathbf{i}\eta^{-1}\bar{\mathbf{A}}_k & \mathbf{i}\eta^{-1}\mathbf{A}_k \\ \bar{\mathbf{B}}_k & \mathbf{B}_k \end{pmatrix}\begin{pmatrix} < e^{-\mathbf{i}\bar{\mathbf{p}}_k\eta(x_3-z_{k-1})} > & 0 \\ 0 & < e^{-\mathbf{i}\mathbf{p}_k\eta(x_3-z_k)} > \end{pmatrix} \quad (6.70)$$

If the 0th layer, is a half-space, the finite solution requirmence as $|x_3| \to \infty$ gives $\mathbf{V}_0 = \mathbf{0}$ in it's general solution. Similarly, if nth layer is a half-space, $\mathbf{W}_n = \mathbf{0}$ in it's general solution.

The boundary conditions (perfectly bonded) along the interfaces ($k = 0, ...n-1$), are

$$(\,\mathbf{Z}_k(z_k) \quad -\mathbf{Z}_{k+1}(z_k)\,)\begin{pmatrix} \mathbf{V}_k \\ \mathbf{W}_k \\ \mathbf{V}_{k+1} \\ \mathbf{W}_{k+1} \end{pmatrix} = \begin{pmatrix} \tilde{\mathbf{u}} \\ \tilde{\mathbf{t}} \end{pmatrix}_{k+1}^\infty (z_k) - \begin{pmatrix} \tilde{\mathbf{u}} \\ \tilde{\mathbf{t}} \end{pmatrix}_k^\infty (z_k), \quad k = 0, ...n-1 \quad (6.71)$$

If nth layer has a free surface along $x_3 = z_n$, the boundary condition along it gives another equation as

$$(\,\bar{\mathbf{B}}_n < e^{-\mathbf{i}\bar{\mathbf{p}}_n\eta h_n} > \qquad \mathbf{B_n}\,)\begin{pmatrix} \mathbf{V}_n \\ \mathbf{W}_n \end{pmatrix} = -\tilde{\mathbf{t}}_n^\infty(z_n) \quad (6.72)$$

These boundary condition equations (6.71) (and (6.72) when the layer n has a finite free surface) form a banded (with width 12) linear algebraic equation system. In this system, all

elements of the coefficients matrix are regular and finite ones (including terms as $\mathbf{A}_k$, $\mathbf{B}_k$, $\bar{\mathbf{A}}_k$, $\bar{\mathbf{B}}_k$and combinations with exponentials terms $< e^{-\mathbf{i}\bar{\mathbf{p}}_k\eta h_k} >$ and $< e^{\mathbf{i}\mathbf{p}_k\eta h_k} >$, see equation (6.70)). The banded linear equation system can be solved easily. Then the unknowns $\mathbf{V}_k$ and $\mathbf{W}_k$ $(k = 0, ...n)$ are determined, and the solutions for every layers in the transformed domain are obtained.

Having obtained the transformed-domain solutions, the corresponding physical-domain solutions can be derived by the inverse Fourier transform. The inverse transform can be taken in the polar coordinates (η, θ) instead of (ξ_1, ξ_2) as

$$f(x_1, x_2, x_3) = \frac{1}{(2\pi)^2}\int_0^\infty \int_0^{2\pi} \eta \tilde{f}(\eta, \theta, x_3) e^{-\mathbf{i}\eta(x_1\cos\theta + x_2\sin\theta)} \mathrm{d}\theta \mathrm{d}\eta. \tag{6.73}$$

When applying the inverse transform to the Green's functions (6.68) and stresses (6.69) solutions, since the full-space solutions are available, only need to carry out the 2-D transform to the regular complementary parts by a standard numerical integral method.

6.5.2 Derivatives of the Green's functions

When the Green's functions are know, the elastic field of a dislocation loop (or inclusion etc.) can be constructed by integration. But the derivatives of the Green's functions (with respect to the field point or source point) are needed. In last section, we calculate the Green's functions and Green's stresses (including the derivatives of Green's functions with respect the field point). We need to calculate their derivatives with respect to the source point now.

From equation (6.68), the derivatives with respect to x_1' and x_2' in the transform-domain, can be obtained by

$$\partial\tilde{\mathbf{G}}_k/\partial x_\alpha' = \mathbf{i}\xi_\alpha\tilde{\mathbf{G}}_k\ , \qquad \alpha = 1, 2 \tag{6.74}$$

where $\tilde{\mathbf{G}}_k$ denotes the Green's functions (can be the Green's stresses or the Green's derivatives with respect to $\mathbf{x}$ also) of the k-th layer in the transform domain. From equation (6.68), the the derivatives of Green's functions with respect to x_3' can be expressed as

$$\partial\tilde{\mathbf{G}}_k/\partial x_3' = e^{\mathbf{i}\xi_\alpha x_\alpha'}\left[\frac{\partial\tilde{\mathbf{G}}_k^\infty}{\partial x_3'} + i\eta^{-1}(\bar{\mathbf{A}}_k < e^{-\mathbf{i}\bar{\mathbf{p}}_k\eta(x_3 - z_{k-1})} > \frac{\partial\mathbf{V}_k}{\partial x_3'} + \mathbf{A}_k < e^{-\mathbf{i}\mathbf{p}_k\eta(x_3 - z_k)} > \frac{\partial\mathbf{W}_k}{\partial x_3'})\right] \tag{6.75}$$

The the derivatives of Green's stresses can be expressed in the same way and won't be shown here.

When we calculate the Green's functions, $\mathbf{V}_k$ and $\mathbf{W}_k$ can be determined. But their derivatives $\partial\mathbf{V}_k/\partial x_3'$ and $\partial\mathbf{W}_k/\partial x_3'$ are not available, and we need to calculate them separately, as follow. Performing derivatives to the boundary condition equations (6.71) (and (6.72) if nth

layer has a free surface), we obtain

$$\left(\mathbf{Z}_k(z_k) \quad -\mathbf{Z}_{k+1}(z_k) \right) \begin{pmatrix} \partial \mathbf{V}_k/\partial x_3' \\ \partial \mathbf{W}_k/\partial x_3' \\ \partial \mathbf{V}_{k+1}/\partial x_3' \\ \partial \mathbf{W}_{k+1}/\partial x_3' \end{pmatrix} = \begin{pmatrix} \frac{\partial \tilde{\mathbf{u}}_{k+1}^{\infty}}{\partial x_3'} \\ \frac{\partial \tilde{\mathbf{t}}_{k+1}^{\infty}}{\partial x_3'} \end{pmatrix} (z_k) - \begin{pmatrix} \frac{\partial \tilde{\mathbf{u}}_{k}^{\infty}}{\partial x_3'} \\ \frac{\partial \tilde{\mathbf{t}}_{k}^{\infty}}{\partial x_3'} \end{pmatrix} (z_k), \ k = 0, ...n-1 \tag{6.76}$$

$$\left(\bar{\mathbf{B}}_n < e^{-\mathbf{i}\bar{\mathbf{p}}_n \eta h_n} > \qquad \mathbf{B_n} \right) \begin{pmatrix} \partial \mathbf{V}_n/\partial x_3' \\ \partial \mathbf{W}_n/\partial x_3' \end{pmatrix} = -\frac{\partial \tilde{\mathbf{t}}_n^{\infty}(z_n)}{\partial x_3'} \tag{6.77}$$

Solving these linear algebric equations (6.76) (and (6.77) when needed), $\partial \mathbf{V}_k/\partial x_3'$ and $\partial \mathbf{V}_k/\partial x_3'$ $(k = 0, ...n)$ can be determined. Taking inverse Fourier transforms to corresponding equations (6.74) and (6.75), the derivatives with respect to $\mathbf{x}'$ can be obtained.

6.5.3 Green's Functions in Bimaterials

In this section, for the special case of bimaterials, we give the formulae of the Green's functions, stresses and their derivatives stresses, using the method derived by Pan and Yuan (1999), and Yang and Pan (2002b).

The low half-space $z < 0$ and upper one $z > 0$ are denoted as 0-th layer and 1-th layer respectively, and quantities in different materials are denoted by corresponding subscripts. The Green's functions (displacement) $\mathbf{u}$, stresses $\mathbf{t}$, $\mathbf{s}$, and their derivaties with respect to the source point $\mathbf{x}'$ are listed below.

For the case of the source point $\mathbf{x}$ located in material 1

$$\mathbf{u}_1(\mathbf{x}, \mathbf{x}') = \mathbf{u}_1^{\infty}(\mathbf{x}, \mathbf{x}') + \frac{1}{4\pi^2} \int_0^{2\pi} \bar{A}_1 G_u^{(1)} A_1^T \mathrm{d}\theta$$

$$\mathbf{t}_1(\mathbf{x}, \mathbf{x}') = \mathbf{t}_1^{\infty}(\mathbf{x}, \mathbf{x}') + \frac{1}{4\pi^2} \int_0^{2\pi} \bar{B}_1 G_t^{(1)} A_1^T \mathrm{d}\theta$$

$$\mathbf{s}_1(\mathbf{x}, \mathbf{x}') = \mathbf{s}_1^{\infty}(\mathbf{x}, \mathbf{x}') + \frac{1}{4\pi^2} \int_0^{2\pi} \bar{C}_1 G_t^{(1)} A_1^T \mathrm{d}\theta$$

$$\mathbf{u}_0(\mathbf{x}, \mathbf{x}') = -\frac{1}{4\pi^2} \int_0^{2\pi} \bar{A}_0 G_u^{(0)} A_1^T \mathrm{d}\theta$$

$$\mathbf{t}_0(\mathbf{x}, \mathbf{x}') = -\frac{1}{4\pi^2} \int_0^{2\pi} \bar{B}_0 G_t^{(0)} A_1^T \mathrm{d}\theta$$

$$\mathbf{s}_0(\mathbf{x}, \mathbf{x}') = -\frac{1}{4\pi^2} \int_0^{2\pi} \bar{C}_0 G_t^{(0)} A_1^T \mathrm{d}\theta$$

$$\frac{\partial \mathbf{u}_1(\mathbf{x}, \mathbf{x}')}{\partial x_j'} = \frac{\partial \mathbf{u}_1^{\infty}(\mathbf{x}, \mathbf{x}')}{\partial x_j'} - \frac{1}{4\pi^2} \int_0^{2\pi} \bar{A}_1 G_t^{(1)} < g_j > A_1^T \mathrm{d}\theta$$

$$\frac{\partial \mathbf{t}_1(\mathbf{x}, \mathbf{x}')}{\partial x_j'} = \frac{\partial \mathbf{t}_1^{\infty}(\mathbf{x}, \mathbf{x}')}{\partial x_j'} - \frac{1}{2\pi^2} \int_0^{2\pi} \bar{B}_1 G_{td}^{(1)} < g_j > A_1^T \mathrm{d}\theta$$

$$\frac{\partial \mathbf{s}_1(\mathbf{x},\mathbf{x}')}{\partial x_j'} = \frac{\partial \mathbf{s}_1^{\infty}(\mathbf{x},\mathbf{x}')}{\partial x_j'} - \frac{1}{2\pi^2}\int_0^{2\pi} \bar{C}_1 G_{td}^{(1)} < g_j > A_1^T \mathrm{d}\theta$$

$$\frac{\partial \mathbf{u}_0(\mathbf{x},\mathbf{x}')}{\partial x_j'} = \frac{1}{4\pi^2}\int_0^{2\pi} \bar{A}_0 G_t^{(0)} < g_j > A_1^T \mathrm{d}\theta$$

$$\frac{\partial \mathbf{t}_0(\mathbf{x},\mathbf{x}')}{\partial x_j'} = \frac{1}{2\pi^2}\int_0^{2\pi} \bar{B}_0 G_{td}^{(0)} < g_j > A_1^T \mathrm{d}\theta$$

$$\frac{\partial \mathbf{s}_0(\mathbf{x},\mathbf{x}')}{\partial x_j'} = \frac{1}{2\pi^2}\int_0^{2\pi} \bar{C}_0 G_{td}^{(0)} < g_j > A_1^T \mathrm{d}\theta$$

with A, B and C being the same as in the text (see eq.(5) and (11)) which obtained from the generalized Stroth eigenproblem, and

$$(G_u^{(1)})_{ij} = \frac{(G_1)_{ij}}{-\bar{p}_i^{(1)} x_3 + p_j^{(1)} x_3' - [(x_1 - x_1')\cos\theta + (x_2 - x_2')\sin\theta]}$$

$$(G_t^{(1)})_{ij} = \frac{(G_1)_{ij}}{\{-\bar{p}_i^{(1)} x_3 + p_j^{(1)} x_3' - [(x_1 - x_1')\cos\theta + (x_2 - x_2')\sin\theta]\}^2}$$

$$(G_{td}^{(1)})_{ij} = \frac{(G_1)_{ij}}{\{-\bar{p}_i^{(1)} x_3 + p_j^{(1)} x_3' - [(x_1 - x_1')\cos\theta + (x_2 - x_2')\sin\theta]\}^3}$$

$$(G_u^{(0)})_{ij} = \frac{(G_0)_{ij}}{-p_i^{(0)} x_3 + p_j^{(1)} x_3' - [(x_1 - x_1')\cos\theta + (x_2 - x_2')\sin\theta]}$$

$$(G_t^{(0)})_{ij} = \frac{(G_0)_{ij}}{\{-p_i^{(0)} x_3 + p_j^{(1)} x_3' - [(x_1 - x_1')\cos\theta + (x_2 - x_2')\sin\theta]\}^2}$$

$$(G_{td}^{(0)})_{ij} = \frac{(G_0)_{ij}}{\{-p_i^{(0)} x_3 + p_j^{(1)} x_3' - [(x_1 - x_1')\cos\theta + (x_2 - x_2')\sin\theta]\}^3}$$

where $p_i^{(0)}$ and $p_i^{(1)}$ are the eigenvalues (see eq. (5)) for material 0 and 1, $< g_1 >= \mathrm{diag}[\cos\theta, \cos\theta, \cos\theta]$, $< g_2 >= \mathrm{diag}[\sin\theta, \sin\theta, \sin\theta]$, $< g_3 >= \mathrm{diag}[p_1^{(1)}, p_2^{(1)}, p_3^{(1)}]$ and

$$G_1 = -\bar{A}_1^{-1}(\bar{M}_1 + M_0)^{-1}(M_1 - M_0)A_1, \quad G_0 = A_0^{-1}(\bar{M}_1 + M_0)^{-1}(M_1 + \bar{M}_1)A_1, \quad M = -\mathbf{i}BA^{-1}$$

For the case of the source point $\mathbf{x}$ located in material 0

$$\mathbf{u}_1(\mathbf{x},\mathbf{x}') = \frac{1}{4\pi^2}\int_0^{2\pi} \bar{A}_1 G_u^{(1)} \bar{A}_0^T \mathrm{d}\theta$$

$$\mathbf{t}_1(\mathbf{x},\mathbf{x}') = \frac{1}{4\pi^2}\int_0^{2\pi} \bar{B}_1 G_t^{(1)} \bar{A}_0^T \mathrm{d}\theta$$

$$\mathbf{s}_1(\mathbf{x},\mathbf{x}') = \frac{1}{4\pi^2}\int_0^{2\pi} \bar{C}_1 G_t^{(1)} \bar{A}_0^T \mathrm{d}\theta$$

$$\mathbf{u}_0(\mathbf{x},\mathbf{x}') = \mathbf{u}_0^{\infty}(\mathbf{x},\mathbf{x}') - \frac{1}{4\pi^2}\int_0^{2\pi} A_0 G_u^{(0)} \bar{A}_0^T \mathrm{d}\theta$$

$$\mathbf{t}_0(\mathbf{x},\mathbf{x}') = \mathbf{t}_0^{\infty}(\mathbf{x},\mathbf{x}') - \frac{1}{4\pi^2}\int_0^{2\pi} B_0 G_t^{(0)} \bar{A}_0^T \mathrm{d}\theta$$

$$\mathbf{s}_0(\mathbf{x},\mathbf{x}') = \mathbf{s}_0^{\infty}(\mathbf{x},\mathbf{x}') - \frac{1}{4\pi^2}\int_0^{2\pi} C_0 G_t^{(0)} \bar{A}_0^T \mathrm{d}\theta$$

$$\frac{\partial \mathbf{u}_1(\mathbf{x},\mathbf{x}')}{\partial x_j'} = -\frac{1}{4\pi^2}\int_0^{2\pi} \bar{A}_1 G_t^{(1)} < g_j > \bar{A}_0^T \mathrm{d}\theta$$

$$\frac{\partial \mathbf{t}_1(\mathbf{x},\mathbf{x}')}{\partial x_j'} = -\frac{1}{2\pi^2}\int_0^{2\pi} \bar{B}_1 G_{td}^{(1)} < g_j > \bar{A}_0^T \mathrm{d}\theta$$

$$\frac{\partial \mathbf{s}_1(\mathbf{x},\mathbf{x}')}{\partial x_j'} = -\frac{1}{2\pi^2}\int_0^{2\pi} \bar{C}_1 G_{td}^{(1)} < g_j > \bar{A}_0^T \mathrm{d}\theta$$

$$\frac{\partial \mathbf{u}_0(\mathbf{x},\mathbf{x}')}{\partial x_j'} = \frac{\partial \mathbf{u}_0^{\infty}(\mathbf{x},\mathbf{x}')}{\partial x_j'} + \frac{1}{4\pi^2}\int_0^{2\pi} A_0 G_t^{(0)} < g_j > \bar{A}_0^T \mathrm{d}\theta$$

$$\frac{\partial \mathbf{t}_0(\mathbf{x},\mathbf{x}')}{\partial x_j'} = \frac{\partial \mathbf{t}_0^{\infty}(\mathbf{x},\mathbf{x}')}{\partial x_j'} + \frac{1}{2\pi^2}\int_0^{2\pi} B_0 G_{td}^{(0)} < g_j > \bar{A}_0^T \mathrm{d}\theta$$

$$\frac{\partial \mathbf{s}_0(\mathbf{x},\mathbf{x}')}{\partial x_j'} = \frac{\partial \mathbf{s}_0^{\infty}(\mathbf{x},\mathbf{x}')}{\partial x_j'} + \frac{1}{2\pi^2}\int_0^{2\pi} C_0 G_{td}^{(0)} < g_j > \bar{A}_0^T \mathrm{d}\theta$$

where

$$(G_u^{(1)})_{ij} = \frac{(G_1)_{ij}}{-\bar{p}_i^{(1)} x_3 + \bar{p}_j^{(0)} x_3' - [(x_1 - x_1')\cos\theta + (x_2 - x_2')\sin\theta]}$$

$$(G_t^{(1)})_{ij} = \frac{(G_1)_{ij}}{\{-\bar{p}_i^{(1)} x_3 + \bar{p}_j^{(0)} x_3' - [(x_1 - x_1')\cos\theta + (x_2 - x_2')\sin\theta]\}^2}$$

$$(G_{td}^{(1)})_{ij} = \frac{(G_1)_{ij}}{\{-\bar{p}_i^{(1)} x_3 + \bar{p}_j^{(0)} x_3' - [(x_1 - x_1')\cos\theta + (x_2 - x_2')\sin\theta]\}^3}$$

$$(G_u^{(0)})_{ij} = \frac{(G_0)_{ij}}{-p_i^{(0)} x_3 + \bar{p}_j^{(0)} x_3' - [(x_1 - x_1')\cos\theta + (x_2 - x_2')\sin\theta]}$$

$$(G_t^{(0)})_{ij} = \frac{(G_0)_{ij}}{\{-p_i^{(0)} x_3 + \bar{p}_j^{(0)} x_3' - [(x_1 - x_1')\cos\theta + (x_2 - x_2')\sin\theta]\}^2}$$

$$(G_{td}^{(0)})_{ij} = \frac{(G_0)_{ij}}{\{-p_i^{(0)} x_3 + \bar{p}_j^{(0)} x_3' - [(x_1 - x_1')\cos\theta + (x_2 - x_2')\sin\theta]\}^3}$$

with $< g_1 >= \mathrm{diag}[\cos\theta, \cos\theta, \cos\theta]$, $< g_2 >= \mathrm{diag}[\sin\theta, \sin\theta, \sin\theta]$, $< g_3 >= \mathrm{diag}[\bar{p}_1^{(0)}, \bar{p}_2^{(0)}, \bar{p}_3^{(0)}]$ and

$$G_1 = \bar{A}_1^{-1}(\bar{M}_1 + M_0)^{-1}(\bar{M}_0 + M_0)\bar{A}_0, \quad G_0 = A_0^{-1}(\bar{M}_1 + M_0)^{-1}(\bar{M}_1 - \bar{M}_0)\bar{A}_0, \quad M = -\mathbf{i}BA^{-1}$$

Numerical accuracy

In this section, several numerical examples are carried out to compare the present results and the existing ones, for reduced cases. These include Green's functions (and stresees) in an infinte ansiotropic space where the infinite space is divided artificially into two identical materials, a transversely isotropic half-space and in an isotropic multilayers. It is found that for these reduced cases, the present 2D Fourier transform method predict the same results as those obtained by Tonon et al. (2001) and Han, Ghoniem and Wang (2002) for the infinite space, and Pan and Yuan (1999) for anisotropic half/bi-half space, and Pan (1997) for isotropic/transverse isotropic multilayers. Since for bi-half space system, 1D Fourier transform results are available for Green's functions (and stresses) (Pan and Yuan 1999), they are given in the appendix B together with their derivatives with respect with the source point, and used to check present 2D solutions also.

Transversely isotropic half-space

The properties of the transversely isotropic ($x_1 - x_2$ is isotropic plane) material are $E_1 = 1$, $E_3 = 10$, $G_{13} = 1$, $\nu_{12} = \nu_{31} = 0.3$. The numerical results of the half-space ($x_3 \leq 0$) Green's functions and stresses are presented in Table 1, and compared with the known ones (Pan and Yuan 1999), with the source and field point at $(0, 0, -1)$ and $(0, 0, -0.75)$ respectively. It can be seen from the table, that the present results agree very well with the existing ones.

Table 1 Green's functions and stresses in a transversely isotropic half-space

u_{ij}	Present	Pan & Yuan (2000)
(11)=(22)	0.64233731	0.64233732
(33)	0.39504885	0.39504886
σ_{ijk}		
(131)=(232)	-1.34601662	-1.34601664
(113)=(223)	0.65825907	0.65825908
(333)	-11.9102534	-11.9102536

Isotropic multilayers

We choose a three layer isotropic materials as an example. The properties of the three layers are $E(0) = 4$, $E(1) = 2$, $E(2) = 1$, $\nu(0) = \nu(1) = \nu(2) = 0.3$. Layer 0 is a half-space and layer 2 has a free surface, with $z_0 = 0$ $z_1 = 1.0$ and $z_2 = 2.5$ (see figure 1). The source point and the field point are located at $(0, 0, 0.5)$ and $(0, 0, 0.6)$ respectively. The numerical results are presented in Table 2, and compared with the known ones (Pan 1997). It can be seen from the table, that the present results agree well with the existing ones. In our calculation for isotropic cases, the material properties are perturbed slightly so that all the roots of the sextic equations are distinct, and this result in tiny errors in the computed results.

Table 2 Green's functions and stresses in a transversely isotropic half-space

u_{ij}	Present	Pan (1997)
(11)=(22)	0.6694	0.6696070
(33)	1.0467	1.047322
σ_{ijk}		
(113)=(223)	2.3111	2.310295
(333)	-19.088	-19.10030

Derivatives of Green's functions and stresses in bimaterials

To check the rightness and accuracy of the Green's functions and their derivatives by the present 2D Fourier transform method, we use the transformed expressions (6), (9) and (10) of the Green's functions and stresses (and their first derivatives) in an infinite space, and perform the inverse transform. The results agree well with those obtained by the integral formulae.

For bimaterials (including half-space), 1D integral expressions of the Green's functions and stresses have been derived by Pan and Yuan (1999). For the bimaterial case, we use the 1D formulae of the Green's functions, stresses and their derivatives also (see Appendix B), and compare the results with those by the present 2D transform method. The results agree very well. In the example, the low half-space $z < 0$ is Copper, and up, Aluminum. They are cubic anisotropic crystals, with their crystallographic axes [100],[010] and [001] along the x, y and z coordinates axes, respectively, and their elastic constants (in units of 10^{10} Pa), together with anisotropic ratios $A = 0.5(C_{11} - C_{12})/C_{44})$ being listed in Table 3. The numerical results of some components of the Green's functions, stresses and their derivatives are presented and compared in Table 4, with the source point $\mathbf{x}$ located at $(0, 0, 0.5)$ (in Al), and field points $\mathbf{x}'$ at $(1, -0.5, 1)$ (in Al) and $(1, -0.5, -0.5)$ (in Cu), respectively, and G_{ij}, $G_{ij,k'}$ in units of 10^{-10}.

Table 3 Elastic constants of some cubic crystals

	C_{11}	C_{12}	C_{44}	A
Cu	16.84	12.14	7.54	3.21
Al	10.82	6.13	2.85	1.21
Ni	24.65	14.73	12.47	2.52
Isotropy	16.84	12.14	2.35	1.0

Table 4 Green's functions, stresses and their derivatives in Cu-Al bimaterilas

	$\mathbf{x}=(0,0,0.5)$, $\mathbf{x}'=(1,-0.2,1)$		$\mathbf{x}=(0,0,0.5)$, $\mathbf{x}'=(1,-0.2,-0.5)$	
	Present	1D formulae	Present	1D formulae
G_{11}	$1.95384557581\times10^{-2}$	$1.95384557533\times10^{-2}$	$1.21296191840\times10^{-2}$	$1.21296191770\times10^{-2}$
G_{12}	$-1.61140414276\times10^{-3}$	$-1.61140414282\times10^{-3}$	$9.59625004458\times10^{-4}$	$9.59624977115\times10^{-4}$
G_{33}	$1.44011129949\times10^{-2}$	$1.44011129933\times10^{-2}$	$1.27002385472\times10^{-2}$	$1.27002385459\times10^{-2}$
$\partial G_{11}/\partial x'_1$	$1.55441441718\times10^{-2}$	$1.55441441723\times10^{-2}$	$4.67278893468\times10^{-3}$	$4.67278892083\times10^{-3}$
$\partial G_{13}/\partial x'_2$	$-1.33814164191\times10^{-3}$	$-1.33814164185\times10^{-3}$	$3.13711240665\times10^{-4}$	$3.13711249267\times10^{-4}$
$\partial G_{33}/\partial x'_3$	$1.51434493595\times10^{-3}$	$1.51434493495\times10^{-3}$	$-4.62792119563\times10^{-3}$	$-4.62792115332\times10^{-3}$
σ_{111}	-1.00407315956E-1	-1.00407315960E-1	$-4.91883171614\times10^{-2}$	$-4.91883163435\times10^{-2}$
σ_{132}	$1.06384293746\times10^{-2}$	$1.06384293745\times10^{-2}$	$-1.07747701122\times10^{-2}$	$-1.07747706699\times10^{-2}$
σ_{333}	$-9.12125675695\times10^{-3}$	$-9.12125677138\times10^{-3}$	$5.43572079822\times10^{-2}$	$5.43572085312\times10^{-2}$
$\partial\sigma_{111}/\partial x'_2$	$5.86732661296\times10^{-2}$	$5.86732661295\times10^{-2}$	$7.22120675245\times10^{-3}$	$7.22120630742\times10^{-3}$
$\partial\sigma_{132}/\partial x'_1$	$3.28928262254\times10^{-2}$	$3.28928262253\times10^{-2}$	$-1.73017885558\times10^{-2}$	$-1.73017880366\times10^{-2}$
$\partial\sigma_{333}/\partial x'_3$	$5.87165788662\times10^{-2}$	$5.87165788667\times10^{-2}$	$6.14433699513\times10^{-3}$	$6.14433720238\times10^{-3}$

6.5.4 Application to infinitesimal dislocations

When the Green's functions are know, the elastic field of a dislocation loop can be constructed by integration. The displacement of a dislocation loop in a solid (no matter homogeneous medium or not) can be expressed as (Volterra 1907, Mura 1968)

$$u_i(\mathbf{x}) = -\int_S C_{jlmn} b_m \frac{\partial}{\partial x'_l} G_{ij}(\mathbf{x},\mathbf{x}') n_n \mathrm{d}S(\mathbf{x}') \tag{6.78}$$

where $G_{ij}(\mathbf{x},\mathbf{x}')$ are the Green's functions at $\mathbf{x}$ due to a point force applied at $\mathbf{x}'$, S is the surface capping the loop, n_n is a unit normal to S and b_m is the Burgers vector.

When the field point is far from a dislocation loop, the loop can be considered as infinitesimal one, and the finite loop can be generated by integrating the capping surface with infinitesimal loops. Here we only consider the infinitesimal loop. The displacement of a infinitesimal dislocation loop with surface $\mathrm{d}S$ and located at $\mathbf{x}'$can be obtained directly from equation (9.13) as

$$u_i(\mathbf{x}) = -C_{jlmn}(\mathbf{x}') b_m \frac{\partial}{\partial x'_l} G_{ij}(\mathbf{x},\mathbf{x}') n_n \mathrm{d}S \tag{6.79}$$

And the stress field can be expressed as

$$\sigma_{ij}(\mathbf{x}) = -C_{ijkl}(\mathbf{x}) C_{pqmn}(\mathbf{x}') b_m \frac{\partial^2}{\partial x_l \partial x'_q} G_{kp}(\mathbf{x},\mathbf{x}') n_n \mathrm{d}S \tag{6.80}$$

From the Betti's reciprocal theorem and the definition of Green's function, we have

$$G_{ij}(\mathbf{x},\mathbf{x}') = G_{ji}(\mathbf{x}',\mathbf{x}) \tag{6.81}$$

Using this relation, the equations (6.79) and (9.16) can be rewriten in other convenient forms as

$$\begin{aligned} u_i(\mathbf{x}) &= -C_{jlmn}(\mathbf{x}') b_m \tfrac{\partial}{\partial x'_l} G_{ji}(\mathbf{x}',\mathbf{x}) n_n \mathrm{d}S \\ &= -\sigma_{mni}(\mathbf{x}',\mathbf{x}) b_m n_n \mathrm{d}S \end{aligned} \tag{6.82}$$

$$\begin{aligned}\sigma_{ij}(\mathbf{x}) &= -C_{ijkl}(\mathbf{x})C_{pqmn}(\mathbf{x}')b_m\tfrac{\partial^2}{\partial x_l\partial x'_q}G_{pk}(\mathbf{x}',\mathbf{x})n_n\mathrm{d}S \\ &= -C_{ijkl}(\mathbf{x})\tfrac{\partial}{\partial x_l}\sigma_{mnk}(\mathbf{x}',\mathbf{x})b_m n_n\mathrm{d}S\end{aligned} \tag{6.83}$$

where $\sigma_{mni}(\mathbf{x}',\mathbf{x})$ are the mn-th Green's stress components at the field point $\mathbf{x}'$ due to a unit point force in the i-th direction applied at the source point $\mathbf{x}$.

For the special case of an infinitesimal dislocation loop in an isotropic infinite space, there is a analytical solution. The displacement of an infinitesimal dislocation in an infinite space can be written as

$$u_i(\mathbf{x}) = C_{jlmn}b_m G_{ij,l}(\mathbf{r})n_n\mathrm{d}S$$

with $\mathbf{r} = \mathbf{x} - \mathbf{x}'$, $G_{ij,l}(\mathbf{r}) = \partial G_{ij}(\mathbf{r})/\partial x_l$. For isotropic media, there are

$$C_{jlmn} = \lambda\delta_{jl}\delta_{mn} + \mu(\delta_{jm}\delta_{ln} + \delta_{jn}\delta_{lm})$$

$$G_{ij}(\mathbf{r}) = \frac{1}{16\pi\mu(1-\nu)r}[(3-4\nu)\delta_{ij} + \bar{r}_i\bar{r}_j]$$

with $r = |\mathbf{r}|$ and $\bar{\mathbf{r}} = \mathbf{r}/r$. Finally, we have

$$u_i(\mathbf{x}) = \frac{-b_m n_n\mathrm{d}S}{8\pi(1-\nu)}\frac{g_{mni}}{r^2}$$

with $g_{mni} = (1-2\nu)(\delta_{mi}\bar{r}_n + \delta_{ni}\bar{r}_m - \delta_{mn}\bar{r}_i) + 3\bar{r}_m\bar{r}_n\bar{r}_i$.

For a slip dislocation loop with $\mathbf{b} = b(1,0,0)$ and $\mathbf{n} = (0,0,1)$, the displacements are

$$\begin{aligned}u_1(\mathbf{x}) &= f_u[(1-2\nu)\bar{r}_3 + 3\bar{r}_1^2\bar{r}_3] \\ u_2(\mathbf{x}) &= f_u(3\bar{r}_1\bar{r}_2\bar{r}_3) \\ u_1(\mathbf{x}) &= f_u[(1-2\nu)\bar{r}_1 + 3\bar{r}_1\bar{r}_3^2]\end{aligned}$$

with $f_u = -b\mathrm{d}S/[8\pi(1-\nu)r^2]$, and the stresses are

$$\begin{aligned}\sigma_{11}(\mathbf{x}) &= f_\sigma\bar{r}_1\bar{r}_3(1-5\bar{r}_1^2) \\ \sigma_{22}(\mathbf{x}) &= f_\sigma\bar{r}_1\bar{r}_3(1-2\nu-5\bar{r}_2^2) \\ \sigma_{33}(\mathbf{x}) &= f_\sigma\bar{r}_1\bar{r}_3(1-5\bar{r}_3^2) \\ \sigma_{23}(\mathbf{x}) &= f_\sigma\bar{r}_1\bar{r}_2(\nu-5\bar{r}_3^2) \\ \sigma_{31}(\mathbf{x}) &= f_\sigma\bar{r}_1\bar{r}_3[(1+\nu)/3 - \nu\bar{r}_2^2 - 5\bar{r}_1^2\bar{r}_3^2] \\ \sigma_{12}(\mathbf{x}) &= f_\sigma\bar{r}_2\bar{r}_3(\nu-5\bar{r}_1^2)\end{aligned}$$

with $f_\sigma = -3\mu b\mathrm{d}S/[4\pi(1-\nu)r^3]$.

The stresses of a slip infinitesimal dislocation in an infinite isotropic medium calculated by the present method are shown in a table, and compared with known analytical formulae. In this example, the material constants are: $E = 1$, $\nu = 0.3$, the dislocation is located at $(0,0,0)$ with the Burgers vector $b(1,0,0)$ and a surface S on the plane $(0,0,1)$, and the field point is $(1,-0.5,0.1)$. In the table, the stress is normalized (divided) by bS. It can be seen the results agree very well.

The stresses of an infinitesimal dislocation in an infinite space

	Present	Analytical
σ_{11}	$2.184815141968856\times10^{-2}$	$2.184815141768209\times10^{-2}$
σ_{12}	$-1.350028820685802\times10^{-2}$	$-1.350028821557843\times10^{-2}$
σ_{13}	$-3.174758385200676\times10^{-2}$	$-3.174758387554415\times10^{-2}$
σ_{22}	$4.357946805850190\times10^{-3}$	$4.357946780104503\times10^{-3}$
σ_{23}	$9.580472855695101\times10^{-3}$	$9.580472814170755\times10^{-3}$
σ_{33}	$-7.068519604061059\times10^{-3}$	$-7.068519576308913\times10^{-3}$

Numerical results

Green's functions and stresses

In this section, the Green's functions in layered materials.

First example, a thin film (Al or Ni) (height being h) on a (Cu) half space ($z < 0$), see fig. 6.4. The two materials are bonded well, and their crystallographic axes [100],[010] and [001] are along the x, y and z coordinates axes, respectively, and the film has a free upper surface (at $z = h$).

Figure 6.5 show the variations of the Green's displacements (normalized/divided ones by $10^{-10}/h$) along the field point $(x/h, y/h, z/h) = (0.5, 0, z/h)$, with the applied source point being $(0, 0, -0.5h)$. Figure 6.6 and 6.7 show the corresponding Green's stresses (out-plane ones and in-plane ones respectively). The stresses are normalized by $1/h^2$. In these figures, also show the results of Cu half-space (with the moduli of all films being that of Cu) and Cu infinite-space.

We give another example of a multilayered material, a half-space system of four layers, see fig. 6.8. The lower substrate ($z < 0$) is Cu. The 1^{st}, 2^{nd} and 3^{rd} layer is Al, Ni and Al film, respectively, and the height of each film is h. All layers are bonded well, and their crystallographic axes [100],[010] and [001] are along the x, y and z coordinates axes, respectively, and the 3^{rd} film has a free upper surface (at $z = 3h$).

Figure 6.9 show the variations of the Green's displacements (normalized/divided by $10^{-10}/h$) along the field point $(x/h, y/h, z/h) = (0.5, 0, z/h)$, with the applied source point being $(0, 0, 0.5h)$. Figure 6.10 and 6.11 show the corresponding Green's stresses (out-plane ones and in-plane ones respectively). The stresses are normalized by $1/h^2$. In these figures, also show the results of Cu half-space and Cu infinite-space.

Infinitesimal dislocations

The field of a infinitesimal dislocation in an Al or Ni film system is considered. The film height is h ($0 < z < h$), it has a free upper surface and is bounded perfectly with a copper half-space, see Figure 9.51. Their crystallographic axes [100],[010] and [001] are along the x, y and z coordinates axes, respectively. A infinitesimal dislocation is assumed to be a slip one with normal direction $(1, 1, 1)$, surface dS and Burger's vector $\mathbf{b}$ along $[\bar{1}, 1, 0]$ and located at $(0, 0, 0.5h)$.

Figure 6.13 shows the in-plane stress σ_{12} on the $y = 0$ plane due to the infinitesimal disloca-

tion at $(0, 0, 0.5h)$ in different material systems: Cu(substrate)-Al(film), Cu(substrate)-Ni(film), Cu half-space and isotropic half-space (with modulus given in table 4), respectively. The stress field is normalized/divided by $b\mathrm{d}S\times10^{10}/h^3$. Figure 6.14 shows the out-plane stress σ_{32} on the $y = 0$ plane, correspondingly. The strain energy $E = \frac{1}{2}\sigma_{ij}\epsilon_{ij}$ is also calculated in the corresponding systems. Figure 6.15 and 6.16 show the strain energy in the $y = 0$ plane and $z = h$ plane respectively. The strain energy is normalized by $(b\mathrm{d}S/h^3)^2 \times 10^{10}$.

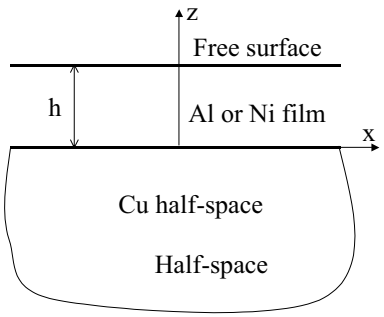

Figure 6.4: Al or Ni film on Cu substrate.

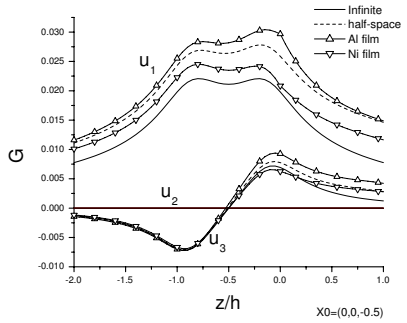

(a)

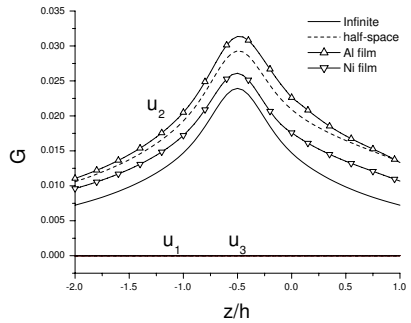

(b)

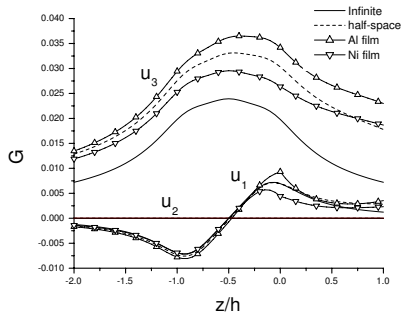

(c)

Figure 6.5: The Green's displacements along $(0.5h, 0, z)$ due to a point force at $(0, 0, -0.5h)$ in the (a) x-direction; (b) y-direction; (c) z-direction.

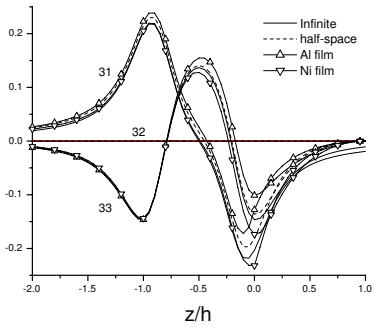

(a)

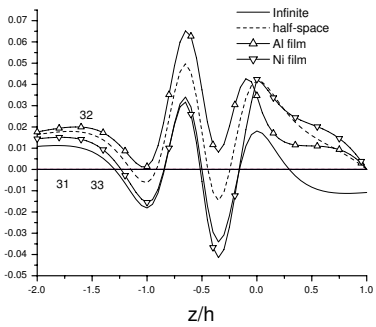

(b)

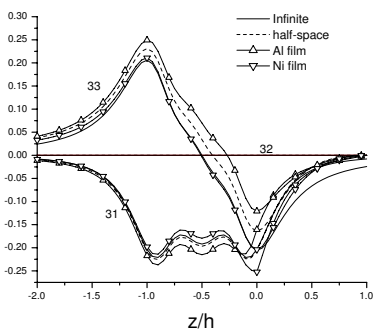

(c)

Figure 6.6: The Green's out-plane stresses along $(0.5h, 0, z)$ due to a point force at $(0, 0, -0.5h)$ in the (a) x-direction; (b) y-direction; (c) z-direction.

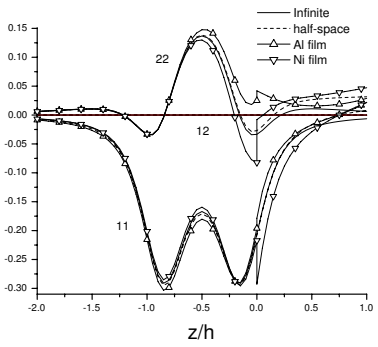

(a)

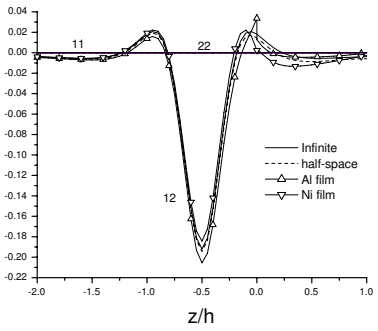

(b)

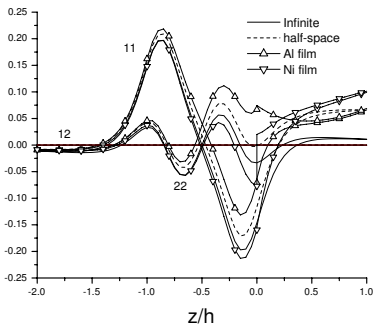

(c)

Figure 6.7: The Green's in-plane stresses along $(0.5h, 0, z)$ due to a point force at $(0, 0, -0.5h)$ in the (a) x-direction; (b) y-direction; (c) z-direction.

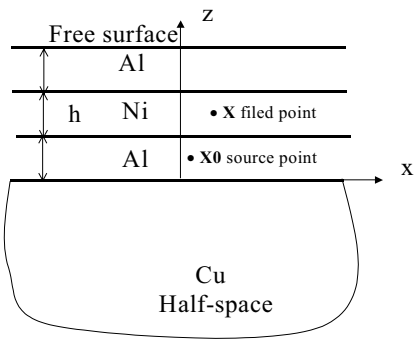

Figure 6.8: Four-layer material.

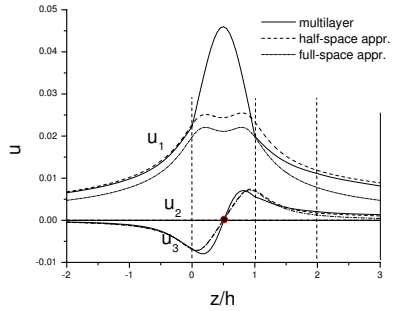

(a)

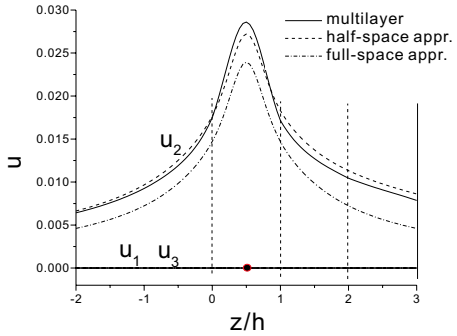

(b)

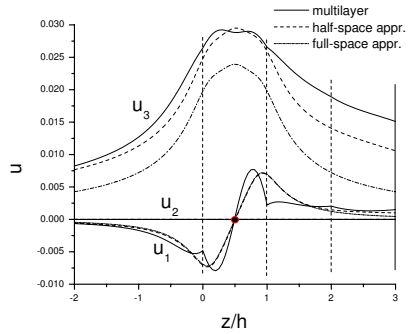

(c)

Figure 6.9: The Green's displacements along $(0.5h, 0, z)$ due to a point force at $(0, 0, 0.5h)$ in the (a) x-direction; (b) y-direction; (c) z-direction.

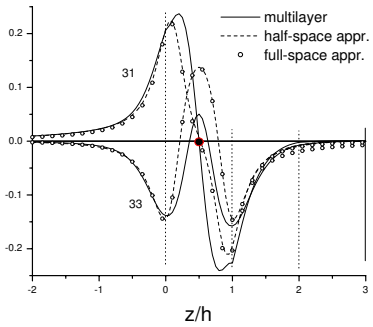

(a)

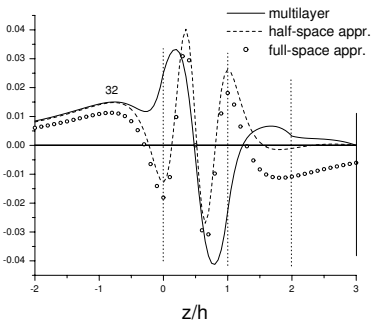

(b)

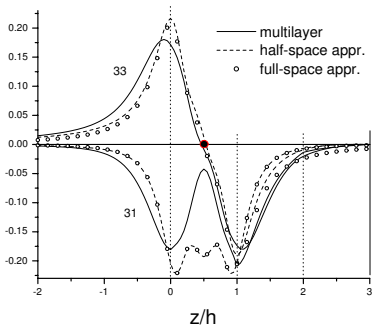

(c)

Figure 6.10: The Green's out-plane stresses along $(0.5h, 0, z)$ due to a point force at $(0, 0, 0.5h)$ in the (a) x-direction; (b) y-direction; (c) z-direction.

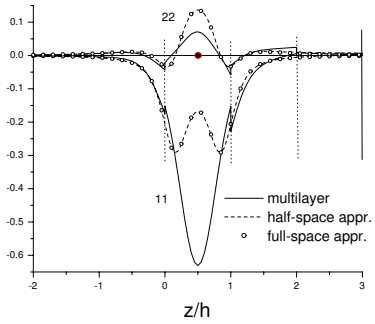

(a)

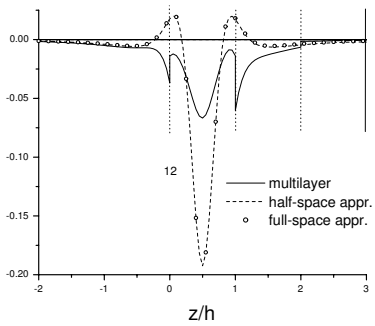

(b)

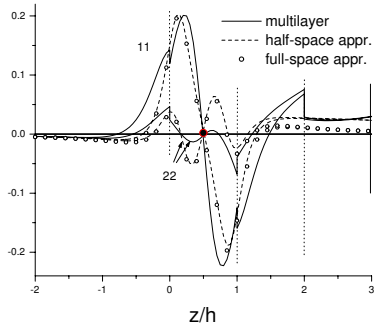

(c)

Figure 6.11: The Green's in-plane stresses along $(0.5h, 0, z)$ due to a point force at $(0, 0, 0.5h)$ in the (a) x-direction; (b) y-direction; (c) z-direction.

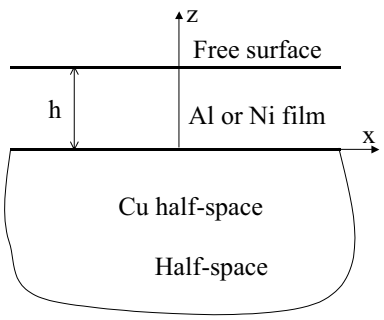

Figure 6.12: An infinitesimal dislocation in a Al or Ni film on Cu substrate.

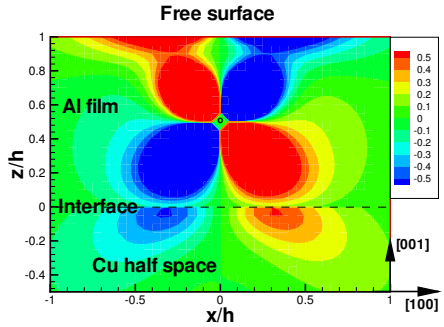
Free surface
Al film
Interface
Cu half space
[001]
[100]
z/h
x/h
1
0.8
0.6
0.4
0.2
0
-0.2
-0.4
-1
-0.5
0
0.5
1
0.5
0.4
0.3
0.2
0.1
0
-0.1
-0.2
-0.3
-0.4
-0.5

(a)

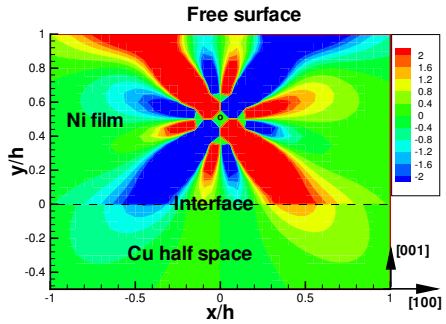
Free surface
Ni film
Interface
Cu half space
[001]
[100]
y/h
x/h
1
0.8
0.6
0.4
0.2
0
-0.2
-0.4
-1
-0.5
0
0.5
1
2
1.6
1.2
0.8
0.4
0
-0.4
-0.8
-1.2
-1.6
-2

(b)

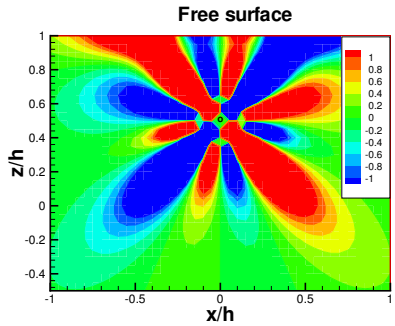

(c)

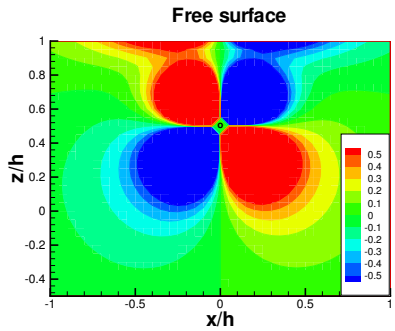

(d)

Figure 6.13: The in-plane stress σ_{12} on $y = 0$ plane due to a infinitesimal dislocation at $(0, 0, 0.5h)$ in the (a) Cu(substrate)-Al(film) solid; (b) Cu(substrate)-Ni(film) solid; (c) Cu half-space; (d) isotropic half-space.

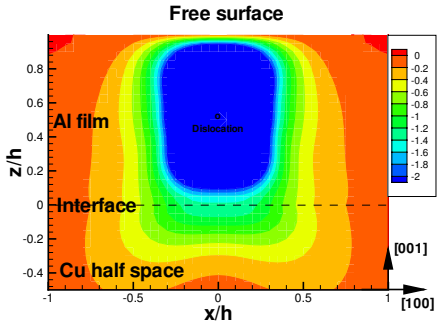
Free surface
Al film
Dislocation
Interface
Cu half space
z/h
x/h
[001]
[100]
0
-0.2
-0.4
-0.6
-0.8
-1
-1.2
-1.4
-1.6
-1.8
-2

(a)

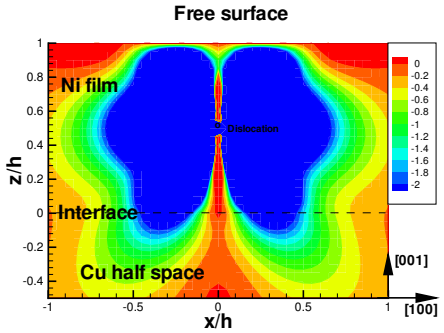
Free surface
Ni film
Dislocation
Interface
Cu half space
z/h
x/h
[001]
[100]
0
-0.2
-0.4
-0.6
-0.8
-1
-1.2
-1.4
-1.6
-1.8
-2

(b)

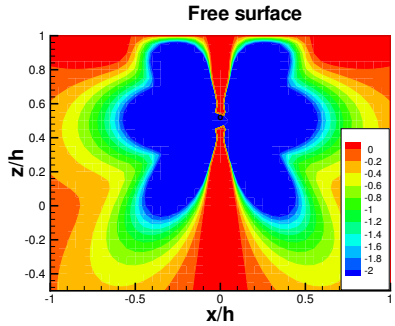

(c)

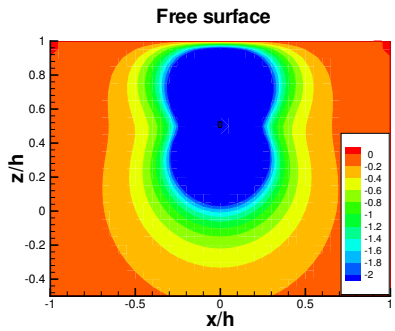

(d)

Figure 6.14: The out-plane stress σ_{32} on $y = 0$ plane due to a infinitesimal dislocation at $(0, 0, 0.5h)$ in the (a) Cu(substrate)-Al(film) solid; (b) Cu(substrate)-Ni(film) solid; (c) Cu half-space; (d) isotropic half-space.

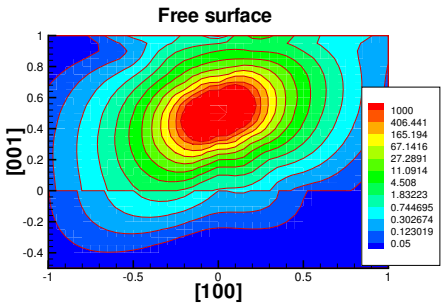
Free surface
[001]
[100]
1000
406.441
165.194
67.1416
27.2891
11.0914
4.508
1.83223
0.744695
0.302674
0.123019
0.05

(a)

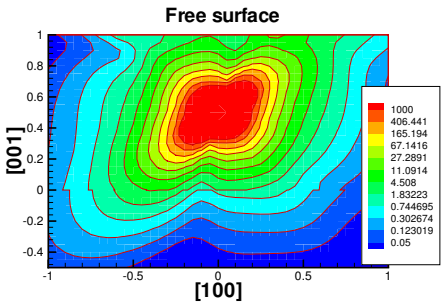
Free surface
[001]
[100]
1000
406.441
165.194
67.1416
27.2891
11.0914
4.508
1.83223
0.744695
0.302674
0.123019
0.05

(b)

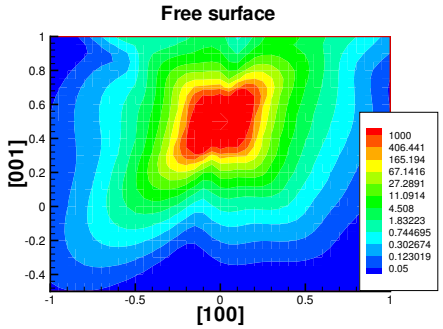

(c)

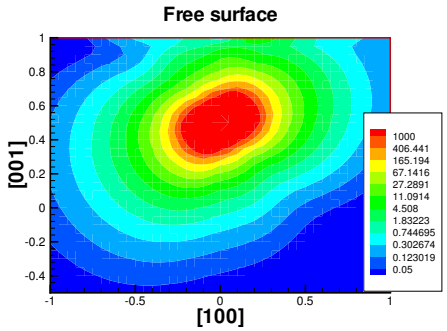

(d)

Figure 6.15: The strain energy on $y = 0$ plane due to a infinitesimal dislocation at $(0, 0, 0.5h)$ in the (a) Cu(substrate)-Al(film) solid; (b) Cu(substrate)-Ni(film) solid; (c) Cu half-space; (d) isotropic half-space.

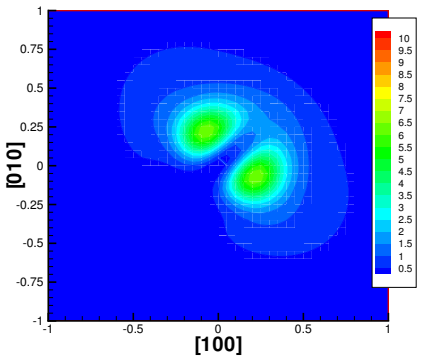
[010]
[100]
1
0.75
0.5
0.25
0
-0.25
-0.5
-0.75
-1
-1
-0.5
0
0.5
1
10
9.5
9
8.5
8
7.5
7
6.5
6
5.5
5
4.5
4
3.5
3
2.5
2
1.5
1
0.5

(a)

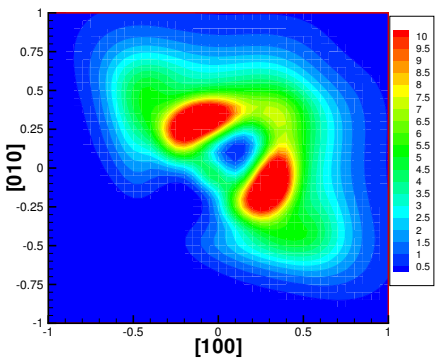
[010]
[100]
1
0.75
0.5
0.25
0
-0.25
-0.5
-0.75
-1
-1
-0.5
0
0.5
1
10
9.5
9
8.5
8
7.5
7
6.5
6
5.5
5
4.5
4
3.5
3
2.5
2
1.5
1
0.5

(b)

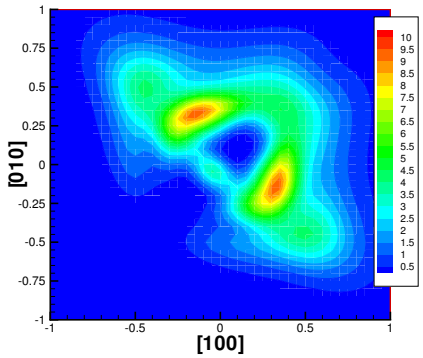

(c)

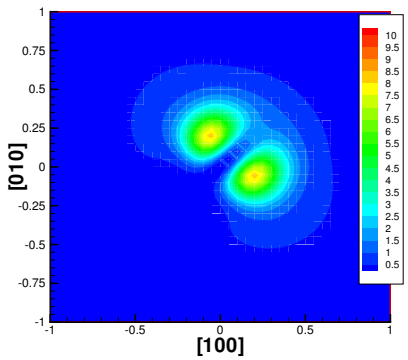

(d)

Figure 6.16: The strain energy on the $z = h$ free surface due to a infinitesimal dislocation at $(0, 0, 0.5h)$ in the (a) Cu(substrate)-Al(film) solid; (b) Cu(substrate)-Ni(film) solid; (c) Cu half-space; (d) isotropic half-space.

Chapter 7

Three-dimensional Elastic Fields

7.1 Fundamental Principles & Theorems

7.1.1 Minimum Potential Energy Principle

An equilibrium state of the solid is obtained when the potential energy functional is minimized. In particular, the equilibrium displacement field is that that minimizes the functional Π given by:

$$\Pi\{\mathbf{u}(x)\} = \frac{1}{2}\int_{\Omega} C_{ijkl}\varepsilon_{ij}\varepsilon_{kl}dV - \int_{\partial\Omega} \mathbf{t}\cdot\mathbf{u}dA - \int_{\Omega} \mathbf{f}\cdot\mathbf{u}dV \tag{7.1}$$

The first term on the left is for the elastic energy stored in the solid, the second stands for the work done on the body by external forces at its surface, and the last term is associated with the work of body forces. The principle of minimum potential energy stated above will be useful in finding approximate solutions to elasticity boundary value problems, for example, through the application of the Finite Element Method (FEM). It is formally equivalent to the equation of elastic equilibrium, as shown next.

Let's take the total variation of Equation 7.1. Using index notation, we obtain

$$\delta\Pi = \frac{1}{2}\int_{\Omega} C_{ijkl}\delta\varepsilon_{ij}\varepsilon_{kl}dV + \frac{1}{2}\int_{\Omega} C_{ijkl}\varepsilon_{ij}\delta\varepsilon_{kl}dV - \int_{\partial\Omega} t_i\delta u_i dA - \int_{\Omega} f_i\delta u_i dV \tag{7.2}$$

As a consequence of the symmetries of the elastic compliance tensor and the strain tensors, the first two terms may be combined together:

$$\frac{1}{2}\int_{\Omega} C_{ijkl}\delta\varepsilon_{ij}\varepsilon_{kl}dV + \frac{1}{2}\int_{\Omega} C_{ijkl}\varepsilon_{ij}\delta\varepsilon_{kl}dV \;\; = \;\; \int_{\Omega} \sigma_{ij}\delta\varepsilon_{ij}dV$$

$$
\begin{aligned}
&= \int_{\Omega} \sigma_{ij} \frac{\partial}{\partial x_j}(\delta u_i) dV \\
&= \int_{\Omega} \left[\frac{\partial}{\partial x_j}(\sigma_{ij} \delta u_i) - \sigma_{ij,j} \delta u_i \right] dV \qquad (7.3)
\end{aligned}
$$

Plugging this result back into Equation 7.2, and utilizing the divergence theorem, we obtain the following form for energy variation:

$$\delta \Pi = \int_{\Omega} \left[(\sigma_{ij,j} + f_i) \delta u_i \right] dV + \int_{\partial \Omega} \left[(\sigma_{ij} n_i - t_i) \delta u_i \right] dA = 0 \qquad (7.4)$$

Since the variation in the displacement vector δ_i is arbitrary, the first and second integrands must be independently zero. The first integrand is just the condition of equilibrium within the elastic body, while the second is representative of boundary equilibrium. Therefore, the variational principle of minimum potential is equivalent to the conditions of equilibrium.

7.1.2 The Reciprocity Theorem

This theorem considers two elastic states $(\mathbf{u}^{(1)}, \boldsymbol{\varepsilon}^{(1)}, \boldsymbol{\sigma}^{(1)})$ and $(\mathbf{u}^{(2)}, \boldsymbol{\varepsilon}^{(2)}, \boldsymbol{\sigma}^{(2)})$, where each state satisfies the condition of elastic equilibrium and the boundary conditions associated with body forces $\mathbf{f}_1$ and $\mathbf{f}_2$, respectively. The reciprocity theorem is stated as:

> *The work done by the external forces of system 1 on the displacement field of system 2 is equal to the work done by the external forces of system 2 on the displacement field of system 1.*

Proof

The work done by body forces and surface tractions of system 1 during the virtual displacements $\mathbf{u}^{(2)}$ is stored as elastic strain energy, thus:

$$\int_{\partial \Omega} \mathbf{t}^{(1)} \cdot \mathbf{u}^{(2)} dA + \int_{\Omega} \mathbf{f}^{(1)} \cdot \mathbf{u}^{(2)} dV = \int_{\Omega} \boldsymbol{\varepsilon}^{(2)} : \boldsymbol{\sigma}^{(1)} dV = \int_{\Omega} \boldsymbol{\varepsilon}^{(2)} : \mathbf{C} \boldsymbol{\varepsilon}^{(1)} dV \qquad (7.5)$$

Utilizing the symmetry of the elastic constants tensor, we can write:

$$\int_{\Omega} \boldsymbol{\varepsilon}^{(2)} : \mathbf{C} \boldsymbol{\varepsilon}^{(1)} dV = \int_{\Omega} \boldsymbol{\varepsilon}^{(1)} : \mathbf{C} \boldsymbol{\varepsilon}^{(2)} dV = \int_{\partial \Omega} \mathbf{t}^{(2)} \cdot \mathbf{u}^{(1)} dA + \int_{\Omega} \mathbf{f}^{(2)} \cdot \mathbf{u}^{(1)} dV \qquad (7.6)$$

which proves the theorem, mathematically stated as:

$$\int_{\partial \Omega} \mathbf{t}^{(1)} \cdot \mathbf{u}^{(2)} dA + \int_{\Omega} \mathbf{f}^{(1)} \cdot \mathbf{u}^{(2)} dV = \int_{\partial \Omega} \mathbf{t}^{(2)} \cdot \mathbf{u}^{(1)} dA + \int_{\Omega} \mathbf{f}^{(2)} \cdot \mathbf{u}^{(1)} dV \qquad (7.7)$$

7.1.3 The Volterra Formula

Consider a solid that has two different configurations. In the first configuration, the solid contains a dislocation with fields labelled with the superscript (d) and no body forces (i.e. $\mathbf{f}^{(d)} = 0$), while the solid in the second configuration contains a point force with associated fields labelled by the superscript (p). Applying the reciprocity theorem given by Equation 7.7 above, we have

$$\int_{\partial\Omega} \mathbf{t}^{(d)} \cdot \mathbf{u}^{(p)} dA = \int_{\partial\Omega} \mathbf{t}^{(p)} \cdot \mathbf{u}^{(d)} dA + \int_{\Omega} \mathbf{f}^{(p)} \cdot \mathbf{u}^{(d)} dV \tag{7.8}$$

Since the displacements associated with a dislocation loop are prescribed on the slip plane, we will re-write the surface integral that spans the slipped region as

$$\begin{aligned} \int_{\partial\Omega} \mathbf{t}^{(d)} \cdot \mathbf{u}^{(p)} dA &= \int_{\partial\Omega} \mathbf{t}^{(d)}(-) \cdot \mathbf{u}^{(p)}(-) dA + \int_{\partial\Omega} \mathbf{t}^{(d)}(+) \cdot \mathbf{u}^{(p)}(+) dA \\ &= \int_{\partial\Omega} \mathbf{t}^{(d)}(+) \cdot \mathbf{u}^{(p)}(+) dA - \int_{\partial\Omega} \mathbf{t}^{(d)}(+) \cdot \mathbf{u}^{(p)}(+) dA \\ &= 0 \end{aligned} \tag{7.9}$$

In re-writing the last equation, we used the notation (+) for quantities above the slip plane and (-) for below. We also note that the displacements must be continuous across the slip plane (i.e $\mathbf{u}^{(p)}(+) = \mathbf{u}^{(p)}(-)$), and that equilibrium dictates that the tractions must be equal and opposite (i.e. $\mathbf{t}^{(d)}(+) = -\mathbf{t}^{(d)}(-)$)).

Thus, we are left with a simple form of the reciprocity theorem

$$\int_{\partial\Omega} \mathbf{t}^{(p)} \cdot \mathbf{u}^{(d)} dA = -\int_{\Omega} \mathbf{f}^{(p)} \cdot \mathbf{u}^{(d)} dV \tag{7.10}$$

Again, utilizing equilibrium of tractions and continuity of displacements across the slip plane, the left hand side of Equation 7.10 can be re-written as

$$\int_{\partial\Omega} \mathbf{t}^{(p)} \cdot \mathbf{u}^{(d)} dA = \int_{\partial\Omega} \mathbf{t}^{(p)}(+) \cdot [\mathbf{u}^{(d)}(+) - \mathbf{u}^{(d)}(-)] dA = \int_{\partial\Omega} \mathbf{t}^{(p)}(+) \cdot \mathbf{b} dA \tag{7.11}$$

and since the traction vector is related to the stress tensor as $\mathbf{t} = \boldsymbol{\sigma} \cdot \mathbf{n}$, and $\mathbf{n}$ is the slip plane normal, then we have for the left hand side

$$\begin{aligned} \int_{\partial\Omega} \mathbf{t}^{(p)} \cdot \mathbf{u}^{(d)} dA &= \int_{\partial\Omega} \sigma_{ij}^{(p)} n_j b_i \, dA \\ &= \int_{\partial\Omega} C_{ijkl}^{(p)} u_{m,n}^{(p)} n_j b_i \, dA \\ &= \int_{\partial\Omega} C_{ijkl}^{(p)} G_{mk,n} f_k n_j b_i \, dA \end{aligned} \tag{7.12}$$

Noting that the right hand side of Equation 7.10 is just

$$\int_{\Omega} \mathbf{f}^{(p)} \cdot \mathbf{u}^{(d)} dV = u_k^{(d)} f_k \tag{7.13}$$

because of the point force property $f_j^{(p)}(\mathbf{r}') = f_j \delta(\mathbf{r} - \mathbf{r}')$. As a result of Equations 7.12 and 7.13, the following form of Volterra's formula is obtained

$$u_k(\mathbf{r}) = -\int_{\partial\Omega} C_{ijkl} G_{mk,n}(\mathbf{r} - \mathbf{r}') n_j b_i \; dA \tag{7.14}$$

7.1.4 Eshelby's Methods

Basic Definitions

The idea of eigenstrain was introduced t solve a variety of internal stress problems, with most of the initial developments carried out by Eshelby and Mura. An **eigenstrain** is defined as any nonelastic strain from sources such as from thermal expansion, phase transformations, initial residual strains, plastic strains, and misfit strains. Eigenstrains are free from external force and surface constraints, and are sometimes called *stress free strains*. Eshelby referred to the eigenstrain as stress-free transformation strain.

An **eigenstress** is defined as an internal stress caused by the incompatibility of eigenstrains when they remain constrained in materials. Let's take an example first. Consider a domain Ω, where temperature is raised by ΔT above the rest of the confining material, as shown in Figure 7.1. The eigenstrain here is the thermal expansion strain, when Ω can expand freely without any surrounding constraints, that is

$$\varepsilon_{ij}^* = \alpha T \delta_{ij} \tag{7.15}$$

Inclusion: When the eigenstrain ε_{ij}^* is prescribed in a finite sub-domain Ω in a homogeneous material $\mathcal{D}$, and is zero in the matrix $\mathcal{D} - \Omega$, then Ω is called an inclusion.

Inhomogeneity: If the sub-domain Ω in a material $\mathcal{D}$ has elastic constants different from those of the matrix, then the domain ω is called an inhomogeneity. An illustration to show the differences between an inclusion and an inhomogeneity is shown in Figure 7.2.

Solution Methods for the Eigenstrain Problem

The basic equations of elasticity are

$$\begin{aligned} e_{ij} &= \frac{1}{2}(u_{i,j} + u_{j,i}) && \text{Kinematics} \\ \sigma_{ij} &= C_{ijkl} e_{kl} = C_{ijkl} u_{k,l} && \text{Constitutive} \end{aligned}$$

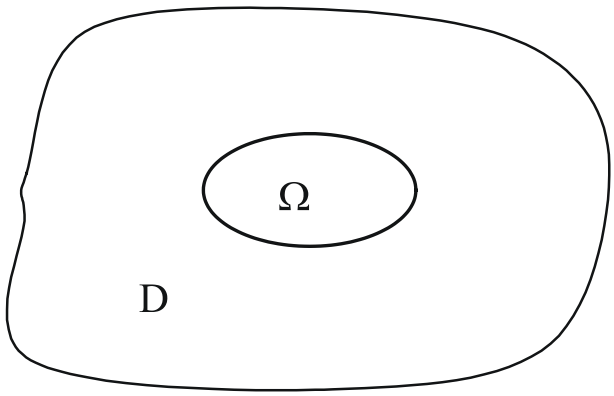

Figure 7.1: Example of an eigenstrain in a domain Ω caused by thermal expansion inside a confining matrix

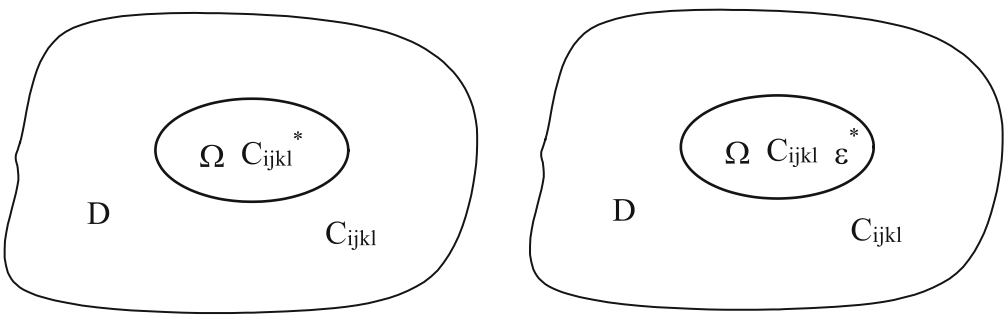

Figure 7.2: Representation of volume defects as either an inhomogeneity (left) or inclusion (right)

$$\begin{array}{rcll} \sigma_{ij,j} & = & 0\ (-f_i)\ \ (C_{ijkl}u_{k,lj} = 0\ (-f_i)) & \text{Equilibrium} \\ \sigma_{ij}n_j & = & 0\ (T_i)\ \ (C_{ijkl}u_{k,l}n_j = 0\ (T_i)) & \text{Boundary conditions} \end{array} \tag{7.16}$$

The basic equations that describe the eigenstrain problem are

$$\begin{array}{rcll} \varepsilon_{ij} & = & e_{ij} + \varepsilon^*_{ij} & \text{Eigenstrain} \\ \varepsilon_{ij} & = & \dfrac{1}{2}(u_{i,j} + u_{j,i}) & \text{Kinematics} \\ \sigma_{ij} & = & C_{ijkl}e_{kl} = C_{ijkl}(\varepsilon_{kl} - \varepsilon^*_{kl}) = C_{ijkl}(u_{k,l} - \varepsilon^*_{kl}) & \text{Constitutive} \\ \sigma_{ij,j} & = & 0\ \ (C_{ijkl}u_{k,lj} = C_{ijkl}\varepsilon^*_{kl,j}) & \text{Equilibrium} \\ \sigma_{ij}n_j & = & 0\ \ (C_{ijkl}u_{k,l}n_j = C_{ijkl}\varepsilon^*_{kl}n_j) & \text{Boundary conditions} \end{array} \tag{7.17}$$

It is seen that the displacement vector u_i caused by the eigenstrain ε^*_{ij} is equivalent to a body force $-C_{ijkl}\varepsilon^*_{kl,j}$ and a surface force $C_{ijkl}\varepsilon^*_{kl}n_j$.

Solution Method I– Green's Functions

The *Green's function* $G_{km}(\mathbf{x}, \mathbf{x}')$–$x_k$ is the displacement component at point $\mathbf{x}$ when a unit force in the x_m direction is applied at the point $\mathbf{x}'$. The unit force in the x_m-direction point $\mathbf{x}'$ can be represented by: $f_i = \delta_{im}\delta(\mathbf{x}, \mathbf{x}')$, where the Dirac-delta function is $\delta(\mathbf{x}, \mathbf{x}') = \delta(x_1, x_1')\delta(x_2, x_2')\delta(x_3, x_3')$, has the property: $\int\limits_V \delta(\mathbf{x}, \mathbf{x}')f(\mathbf{x}')\ dV = f(\mathbf{x})$. G_{km} should obey the equilibrium equation ($C_{ijkl}u_{k,lj} + f_i = 0$), that is G_{ij} satisfies the condition:

$$C_{ijkl}G_{km,lj}(\mathbf{x}, \mathbf{x}') + \delta_{im}\delta(\mathbf{x}, \mathbf{x}') = 0 \tag{7.18}$$

For a body force distribution $f_m(\mathbf{x}')$, the corresponding displacement can be obtained as:

$$u_i(\mathbf{x}) = \int\limits_\Omega G_{ij}(\mathbf{x}, \mathbf{x}')f_j(\mathbf{x}')dV' \tag{7.19}$$

The displacement vector u_i caused by ε^*_{ij} satisfying $C_{ijkl}u_{k,lj} = C_{ijkl}\varepsilon^*_{kl,j}$, can be considered as a displacement caused by the body force $-C_{ilmn}\varepsilon^*_{mn,l}$ in the x_i direction, so the solution for the eigenstrain problem can be presented by the product of G_{ij} and the body force $-C_{jlmn}\varepsilon^*_{mn,l}$, i.e.

$$u_i(\mathbf{x}) = -\int\limits_\Omega G_{ij}(\mathbf{x}, \mathbf{x}')C_{jlmn}\varepsilon^*_{mn,l}(\mathbf{x}')dV' \tag{7.20}$$

Integrating by parts and assuming that boundary terms vanish, then

$$u_i(\mathbf{x}) = \int\limits_\Omega C_{jlmn}\varepsilon^*_{mn}(\mathbf{x}')\frac{\partial}{\partial x_l'}G_{ij}(\mathbf{x}, \mathbf{x}')dV' \tag{7.21}$$

For a homogeneous infinite body, we can utilize the symmetry properties

$$G_{ij}(\mathbf{x}, \mathbf{x}') = G_{ij}(\mathbf{x} - \mathbf{x}'),\ \ \frac{\partial}{\partial x_l'}G_{ij}(\mathbf{x} - \mathbf{x}') = -\frac{\partial}{\partial x_l}G_{ij}(\mathbf{x} - \mathbf{x}') = -G_{ij,l}(\mathbf{x} - \mathbf{x}') \tag{7.22}$$

Therefore, the displacement induced by the eigenstrain can be written as

$$u_i(\mathbf{x}) = -\int_{\Omega} C_{jlmn}\varepsilon^*_{mn}(\mathbf{x}')G_{ij,l}(\mathbf{x}-\mathbf{x}')dV' \tag{7.23}$$

and the corresponding expressions for the strain and stress become

$$\varepsilon_{ij}(\mathbf{x}) = -\frac{1}{2}\int_{\Omega} C_{klmn}\varepsilon^*_{mn}(\mathbf{x}')[G_{ik,lj}(\mathbf{x}-\mathbf{x}') + G_{jk,li}(\mathbf{x}-\mathbf{x}')]dV' \tag{7.24}$$

$$\sigma_{ij}(\mathbf{x}) = -C_{ijkl}\left[\int_{\Omega} C_{pqmn}\varepsilon^*_{mn}(\mathbf{x}')G_{kp,ql}(\mathbf{x}-\mathbf{x}')dV' + \varepsilon^*_{kl}(\mathbf{x})\right] \tag{7.25}$$

When the eigenstrain $\varepsilon_{ij}(\mathbf{x})^*$ is given in the inclusion domain Ω, and is zero in the matrix domain $\mathcal{D}-\Omega$, the elastic field due to the inclusion can be written as:

$$u_i(\mathbf{x}) = -\int_{\Omega} C_{jlmn}\varepsilon^*_{mn}(\mathbf{x}')G_{ij,l}(\mathbf{x}-\mathbf{x}')dV' \tag{7.26}$$

$$\varepsilon_{ij}(\mathbf{x}) = -\frac{1}{2}\int_{\Omega} C_{klmn}\varepsilon^*_{mn}(\mathbf{x}')[G_{ik,lj}(\mathbf{x}-\mathbf{x}') + G_{jk,li}(\mathbf{x}-\mathbf{x}')]dV' \tag{7.27}$$

$$\sigma_{ij}(\mathbf{x}) = -C_{ijkl}\left[\int_{\Omega} C_{pqmn}\varepsilon^*_{mn}(\mathbf{x}')G_{kp,ql}(\mathbf{x}-\mathbf{x}')dV' + \varepsilon^*_{kl}(\mathbf{x})\right] \tag{7.28}$$

When the eigenstrain ε^*_{mn} is uniform in Ω, the volume integrations can be rewritten as surface integrals, i.e.

$$u_i(\mathbf{x}) = \int_{|\Omega|} C_{jlmn}\varepsilon^*_{mn}G_{ij}(\mathbf{x}-\mathbf{x}')n_l dS' \tag{7.29}$$

$$\varepsilon_{ij}(\mathbf{x}) = \frac{1}{2}\int_{|\Omega|} C_{klmn}\varepsilon^*_{mn}[G_{ik,j}(\mathbf{x}-\mathbf{x}') + G_{jk,i}(\mathbf{x}-\mathbf{x}')]n_l dS' \tag{7.30}$$

$$\sigma_{ij}(\mathbf{x}) = C_{ijkl}\left[\int_{|\Omega|} C_{pqmn}\varepsilon^*_{mn}G_{kp,l}(\mathbf{x}-\mathbf{x}')n_q dS' + \varepsilon^*_{kl}(\mathbf{x})\right] \tag{7.31}$$

Solution Method II– Fourier Integrals

The Fourier transform and its inverse are given by

$$\bar{f}(\xi) = (2\pi)^{-3}\int_{-\infty}^{\infty} f(\mathbf{x})\exp(-i\xi\mathbf{x})\mathrm{d}\mathbf{x}\,; \quad f(\mathbf{x}) = \int_{-\infty}^{\infty} \bar{f}(\xi)\exp(i\xi\mathbf{x})\mathrm{d}\xi \tag{7.32}$$

where

$$\int_{-\infty}^{\infty}\mathrm{d}\xi = \int_{-\infty}^{\infty}\mathrm{d}\xi_1\int_{-\infty}^{\infty}\mathrm{d}\xi_2\int_{-\infty}^{\infty}\mathrm{d}\xi_3\,; \quad \int_{-\infty}^{\infty}\mathrm{d}\mathbf{x} = \int_{-\infty}^{\infty}\mathrm{d}x_1\int_{-\infty}^{\infty}\mathrm{d}x_2\int_{-\infty}^{\infty}\mathrm{d}x_3 \tag{7.33}$$

In the Fourier integral method, we take the Fourier transform of the governing equation $C_{ijkl}u_{k,lj} = C_{ijkl}\varepsilon^*_{kl,j}$, to obtain:

$$C_{ijkl}\bar{u}_k\xi_l\xi_j = -iC_{ijkl}\bar{\varepsilon}^*_{kl}\xi_j \tag{7.34}$$

Using the notation $K_{ik}(\mathbf{x}) = C_{ijkl}\xi_l\xi_j$, the displacement $\bar{u}_i$, can be obtained as:

$$\bar{u}_i(\xi) = -iC_{ijkl}\bar{\varepsilon}^*_{kl}\xi_i N_{ij}(\xi)/D(\xi) \tag{7.35}$$

where $N_{im}(\mathbf{x})$ and $D(\xi)$ are co-factors and determinant of the matrix: $[K_{ik}]$. That is:

$$D(\xi) = \in_{ijk} K_{i1}K_{j2}K_{k3}\ ;\ \ N_{ij}(\xi) = \frac{1}{2}\in_{ikl}\in_{jmn} K_{km}K_{ln} \tag{7.36}$$

and $\in_{ijk}$ is the permutation tensor.

Substituting $\bar{\varepsilon}^*_{ij}(\xi) = (2\pi)^{-3}\int\limits_{-\infty}^{\infty}\varepsilon^*_{ij}(\mathbf{x}')\exp(-i\xi\mathbf{x}')\mathrm{d}\mathbf{x}'$ and taking the inverse Fourier transform to $\bar{u}_i$, we have

$$u_i(\mathbf{x}) = -i(2\pi)^{-3}\int\limits_{-\infty}^{\infty}\mathrm{d}\xi\int\limits_{-\infty}^{\infty}C_{jlmn}\varepsilon^*_{mn}(\mathbf{x}')\xi_l N_{ij}(\xi)D^{-1}(\xi)\exp[i\xi\cdot(\mathbf{x}-\mathbf{x}')]\mathrm{d}\mathbf{x}' \tag{7.37}$$

$$u_i(\mathbf{x}) = -(2\pi)^{-3}\frac{\partial}{\partial x_l}\int\limits_{-\infty}^{\infty}\mathrm{d}\xi\int\limits_{-\infty}^{\infty}C_{jlmn}\varepsilon^*_{mn}(\mathbf{x}')N_{ij}(\xi)D^{-1}(\xi)\exp[i\xi\cdot(\mathbf{x}-\mathbf{x}')]\mathrm{d}\mathbf{x}' \tag{7.38}$$

and

$$\varepsilon_{ij}(\mathbf{x}) = (2\pi)^{-3}\int\limits_{-\infty}^{\infty}\mathrm{d}\xi\int\limits_{-\infty}^{\infty}\frac{1}{2}C_{klmn}\varepsilon^*_{mn}(\mathbf{x}')\xi_l[\xi_j N_{ik}(\xi)+\xi_i N_{jk}(\xi)]D^{-1}(\xi)\exp[i\xi\cdot(\mathbf{x}-\mathbf{x}')]\mathrm{d}\mathbf{x}' \tag{7.39}$$

$$\sigma_{ij}(\mathbf{x}) = C_{ijkl}\left[(2\pi)^{-3}\int\limits_{-\infty}^{\infty}\mathrm{d}\xi\int\limits_{-\infty}^{\infty}C_{pqmn}\varepsilon^*_{mn}(\mathbf{x}')\xi_q\xi_l N_{kp}(\xi)D^{-1}(\xi)\exp[i\xi\cdot(\mathbf{x}-\mathbf{x}')]\mathrm{d}\mathbf{x}' - \varepsilon^*_{kl}(\mathbf{x})\right] \tag{7.40}$$

To show that the two methods are equivalent, let's take the Fourier transform of equilibrium equation of Green's functions:

$$C_{ijkl}G_{km,lj}(\mathbf{x}-\mathbf{x}') + \delta_{im}\delta(\mathbf{x}-\mathbf{x}') = 0 \tag{7.41}$$

resulting in

$$C_{ijkl}\bar{G}_{km}\xi_l\xi_j = \delta_{im} \tag{7.42}$$

From which the Green's functions in the Fourier domain can be obtained as

$$\bar{G}_{ij}(\xi) = N_{ij}(\xi)D^{-1}(\xi) \tag{7.43}$$

where $N_{im}(\mathbf{x})$ and $D(\xi)$ are co-factors and determinant of the matrix: $K_{ik}(\mathbf{x}) = C_{ijkl}\xi_l\xi_j$.

Taking the inverse transform, we obtain

$$G_{ij}(\mathbf{x}-\mathbf{x}') = (2\pi)^{-3} \int_{-\infty}^{\infty} N_{ij}(\xi) D^{-1}(\xi) \exp[i\xi \cdot (\mathbf{x}-\mathbf{x}')] \mathrm{d}\mathbf{xi} \tag{7.44}$$

Substituting it into Eqns. (7.38-7.40), we find that they are reduced to Eqns. (7.23-7.25).

Solution Method III–Eshelby's Theory

Consider an inclusion region Ω embedded in an isotropic infinite body $\mathcal{D}$. The region undergoes a change of shape and size (transformation eigenstrain). As a result of the constraint imposed by the surrounding material matrix, internal stresses will be induced. This is illustrated in Figure 7.3.

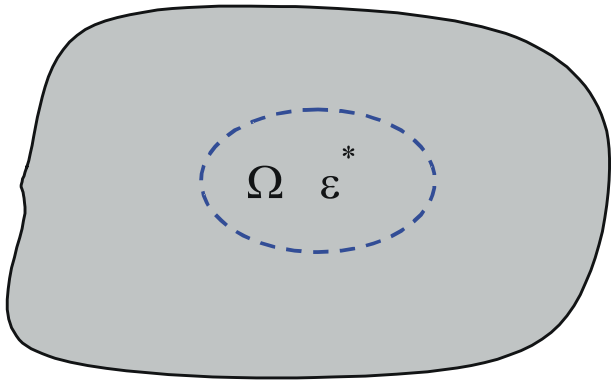

Figure 7.3: Illustration of the eigenstrain induced by a stress-free transformation of shape or size of an inclusion

To solve this problem, imagine the following cutting, straining and welding operations:

1. Cut around the inclusion region Ω; remove it from the matrix; allow the unconstrained inclusion to undergo the (eigenstrain ε^*_{ij}) transformation freely, as shown in Figure 7.4.

   At this stage, the stresses in the inclusion and matrix are zero. Let $\sigma^*_{ij} = C_{ijkl}\varepsilon^*_{kl}$ be the stress derived from ε^*_{ij} by general Hooke's law.

2. Now, apply surface tractions $-\sigma^*_{ij}n_j$ to the inclusion boundary $\partial\Omega$. This brings it back to the original form (shape and size) before the transformation took place. Put it back in the matrix hole and reweld the material across the cut boundary surface, as shown in Figure 7.5.

   The applied surface tractions $-\sigma^*_{ij}n_j$ now become a layer of body forces spread over the surface $\partial\Omega$. The stress is zero in the matrix and has the known value $(-\sigma^*_{ij} = -C_{ijkl}\varepsilon^*_{kl})$ in the inclusion.

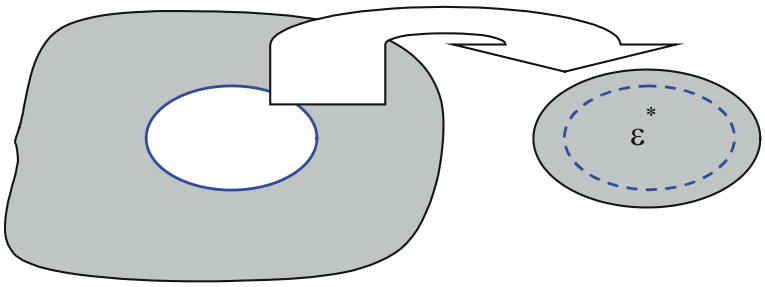

Figure 7.4: Free expansion of an inclusion with the eigenstrain ε^*_{ij}

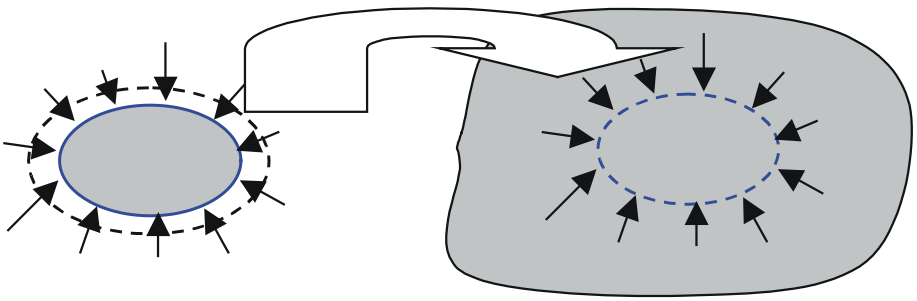

Figure 7.5: Applying tractions $-\sigma^*_{ij}n_j$ on the inclusion to fit it back in the original matrix cut

3. To remove the unwanted layer of surface tractions, we now apply an equal and opposite layer of body forces $+\sigma^*_{ij}n_j$ over the surface $\partial\Omega$, as shown in Figure 7.6.

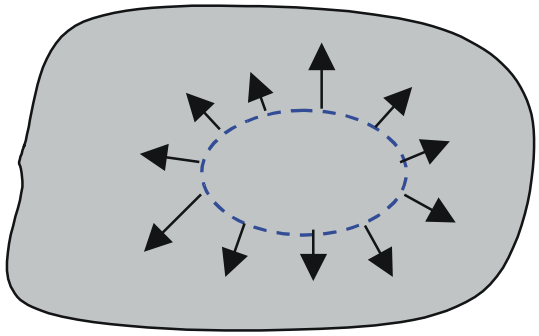

Figure 7.6: Applying an equal and opposite layer of body forces $+\sigma^*_{ij}n_j$ over the surface $\partial\Omega$ to remove unwanted tractions

The body is now free of any external forces, but is in a state of internal self-stress due to the eigenstrain of the inclusion. The additional elastic field induced by the body force $+\sigma^*_{ij}n_j$ over the inclusion surface $\partial\Omega$ can be found by integration of the point force solution (Green's functions) as

$$u_i(\mathbf{x}) = \int_{\partial\Omega} \sigma^*_{jk} n_k G_{ij}(\mathbf{x}-\mathbf{x}')\mathrm{d}S' = \int_S C_{jlmn}\varepsilon^*_{mn} G_{ij}(\mathbf{x}-\mathbf{x}')n_l \mathrm{d}S' \tag{7.45}$$

The strain in matrix and inclusion is $e_{ij} = \frac{1}{2}(u_{i,j} + u_{j,i})$, while the stress in the matrix is derived from e_{ij} by Hooke's law: $\sigma_{ij} = C_{ijkl}e_{kl} = C_{ijkl}u_{k,l}$, The inclusion has now the stress $-\sigma^*_{ij}$, so the total stress in the inclusion is

$$\sigma_{ij} = C_{ijkl}(e_{kl} - \varepsilon^*_{kl}) \tag{7.46}$$

Isotropic Ellipsoidal inclusions

Consider an ellipsoidal inclusion Ω in an isotropic infinite body. The eigenstrain in the ellipsoidal domain Ω is assumed to be uniform (constant). Eshelby derived explicit analytical expressions for the induced elastic field. For this ellipsoidal inclusion problem, the displacement takes the form

$$u_i(\mathbf{x}) = -C_{jkmn}\varepsilon^*_{mn} \int_\Omega G_{ij,k}(\mathbf{x}-\mathbf{x}')\mathrm{d}\mathbf{x}' \tag{7.47}$$

where the ellipsoid Ω satisfies

$$\frac{x_1^2}{a_1^2} + \frac{x_2^2}{a_2^2} + \frac{x_3^2}{a_3^2} \le 1, \quad or \quad \frac{x_i x_i}{a_I^2} \le 1 \tag{7.48}$$

For isotropic materials, we have $C_{ijkl} = \lambda\delta_{ij}\delta_{kl} + \mu(\delta_{ik}\delta_{jl} + \delta_{il}\delta_{jk})$, and the isotropic Green's function is given by:

$$G_{ij}(\mathbf{x}-\mathbf{x}') = \frac{1}{16\pi\mu(1-\nu)|\mathbf{x}-\mathbf{x}'|}\left[(3-4\nu)\delta_{ij} + \frac{(x_i - x_i')(x_j - x_j')}{|\mathbf{x}-\mathbf{x}'|^2}\right] \tag{7.49}$$

Solution for Interior Points

When the point $\mathbf{x}$ is located inside the inclusion, the integral can be explicitly performed. After some manipulation, the strain field inside the domain Ω is found to be constant, independent of $\mathbf{x}$, given by:

$$\begin{aligned}\varepsilon_{ij}(\mathbf{x}) &= \varepsilon_{ij} = -\frac{1}{2}C_{klmn}\varepsilon^*_{mn}\int_\Omega [G_{ik,lj}(\mathbf{x}-\mathbf{x}') + G_{jk,li}(\mathbf{x}-\mathbf{x}')]d\mathbf{x}' \\ &= S_{ijmn}\varepsilon^*_{mn}\end{aligned}$$

where S_{ijmn} is called Eshelby's tensor, and is defined as:

$$S_{ijmn} \equiv -\frac{1}{2}C_{klmn}\int_\Omega [G_{ik,lj}(\mathbf{x}-\mathbf{x}') + G_{jk,li}(\mathbf{x}-\mathbf{x}')]d\mathbf{x}',\ \mathbf{x}\in\Omega \tag{7.50}$$

The stress field inside the domain ($\mathbf{x}\in\Omega$) is given by

$$\sigma_{ij} = C_{ijkl}(S_{klmn} - I_{klmn})\varepsilon^*_{mn} \tag{7.51}$$

where the Eshelby tensor is given by:

$$S_{ijkl} = S^{(1)}_{IK}(0)\,\delta_{ij}\delta_{kl} + S^{(2)}_{IJ}(0)\,(\delta_{ik}\delta_{jl} + \delta_{il}\delta_{jk}) \tag{7.52}$$

where:

$$\begin{aligned}S^{(1)}_{IK}(0) &= -\frac{\nu}{2(1-\nu)}J_I(0) + \frac{1}{4(1-\nu)}\left[\frac{a_I^2}{a_I^2-a_K^2}J_I(0) + \frac{a_K^2}{a_K^2-a_I^2}J_K(0)\right] \\ S^{(2)}_{IJ}(0) &= -\frac{1}{4}[J_I(0)+J_J(0)] + \frac{1}{4(1-\nu)}\left[\frac{a_I^2}{a_I^2-a_J^2}J_I(0) + \frac{a_J^2}{a_J^2-a_I^2}J_J(0)\right]\end{aligned} \tag{7.53}$$

with:

$$J_I(0) = J_I(\lambda)|_{\lambda=0},\ J_I(\lambda) = \int_\infty^\lambda \frac{\rho^3(\lambda)}{a_I^2+\lambda}d\lambda,\ \rho(\lambda) = [\rho_1(\lambda)\rho_2(\lambda)\rho_3(\lambda)]^{1/3},\ \rho_I(\lambda) = \frac{a_I}{\sqrt{a_I^2+\lambda}} \tag{7.54}$$

Note that: $S_{ijkl} = S_{jikl} = S_{ijlk} \neq S_{klij}$. For the special case of a spherical inclusion, we have

$$S_{ijkl} = \frac{1}{15(1-\nu)}[(5\nu-1)\,\delta_{ij}\delta_{kl} + (4-5\nu)\,(\delta_{ik}\delta_{jl} + \delta_{il}\delta_{jk})] \tag{7.55}$$

Solution for Exterior Points

When point $\mathbf{x}$ is located outside the inclusion Ω, the field depend on $\mathbf{x}$. The strain field is expressed as

$$\begin{aligned}\varepsilon_{ij}(\mathbf{x}) &= -\frac{1}{2}C_{klmn}\varepsilon^*_{mn}\int_{\Omega}[G_{ik,lj}(\mathbf{x}-\mathbf{x}')+G_{jk,li}(\mathbf{x}-\mathbf{x}')]d\mathbf{x}' \\ &= \bar{G}_{ijmn}(\mathbf{x})\varepsilon^*_{mn}\end{aligned}$$

where $\bar{G}_{ijmn}$ is called the exterior-point Eshelby's tensor and is defined as

$$\bar{G}_{ijmn}(\mathbf{x}) \equiv -\frac{1}{2}C_{klmn}\int_{\Omega}[G_{ik,lj}(\mathbf{x}-\mathbf{x}')+G_{jk,li}(\mathbf{x}-\mathbf{x}')]d\mathbf{x}',\ \mathbf{x}\in\mathcal{D}-\Omega \tag{7.56}$$

The stress field outside the matrix $(\mathcal{D}-\Omega)$ is given by

$$\sigma_{ij}(\mathbf{x}) = C_{ijkl}\bar{G}_{klmn}(\mathbf{x})\varepsilon^*_{mn} \tag{7.57}$$

While the exterior Eshelby Tensor is given by:

$$\begin{aligned}\bar{G}_{ijkl}(x) &= S^{(1)}_{IK}(\lambda)\,\delta_{ij}\delta_{kl} + S^{(2)}_{IJ}(\lambda)\,(\delta_{ik}\delta_{jl}+\delta_{il}\delta_{jk}) + S^{(3)}_{I}(\lambda)\delta_{ij}\hat{n}_k\hat{n}_l + S^{(4)}_{K}(\lambda)\delta_{kl}\hat{n}_i\hat{n}_j \\ &+ S^{(5)}_{I}(\lambda)(\delta_{ik}\hat{n}_j\hat{n}_l+\delta_{il}\hat{n}_j\hat{n}_k) + S^{(6)}_{J}(\lambda)(\delta_{jk}\hat{n}_i\hat{n}_l+\delta_{jl}\hat{n}_i\hat{n}_k) + S^{(7)}_{IJKL}(\lambda)\hat{n}_i\hat{n}_j\hat{n}_k\hat{n}_l\end{aligned}$$

where

$$\begin{aligned}S^{(1)}_{IK}(\lambda) &= -\frac{\nu}{2(1-\nu)}J_I(\lambda) + \frac{1}{4(1-\nu)}\left[\frac{a_I^2}{a_I^2-a_K^2}J_I(\lambda)+\frac{a_K^2}{a_K^2-a_I^2}J_K(\lambda)\right] \\ S^{(2)}_{IJ}(\lambda) &= -\frac{1}{4}[J_I(\lambda)+J_J(\lambda)] + \frac{1}{4(1-\nu)}\left[\frac{a_I^2}{a_I^2-a_J^2}J_I(\lambda)+\frac{a_J^2}{a_J^2-a_I^2}J_K(\lambda)\right] \\ S^{(3)}_{I}(\lambda) &= \frac{\rho^3(\lambda)}{2(1-\nu)}[1-\rho_I^2(\lambda)] \\ S^{(4)}_{K}(\lambda) &= \frac{\rho^3(\lambda)}{2(1-\nu)}[1-2\nu-\rho_K^2(\lambda)] \\ S^{(5)}_{I}(\lambda) &= \frac{\rho^3(\lambda)}{2(1-\nu)}[\nu-\rho_I^2(\lambda)] \\ S^{(6)}_{J}(\lambda) &= \frac{\rho^3(\lambda)}{2(1-\nu)}[\nu-\rho_J^2(\lambda)]\end{aligned}$$

and

$$S^{(7)}_{IJKL}(\lambda) = \frac{\rho^3(\lambda)}{2(1-\nu)}\left[2[\rho_I^2(\lambda)+\rho_J^2(\lambda)+\rho_K^2(\lambda)+\rho_L^2(\lambda)]+\rho_m(\lambda)\rho_m(\lambda)-\frac{4\rho_M^2(\lambda)\Theta_m(\lambda)\Theta_m(\lambda)}{\Theta(\lambda)}-5\right] \tag{7.58}$$

and$\hat{n}_i$ is the outward unit normal vector at the matrix point on an imaginary ellipsoidal surface $\frac{x_i x_i}{a_I^2+\lambda}=1$, as: $\hat{n}_i = \frac{x_i}{(a_I^2+\lambda)\sqrt{\Theta(\lambda)}}$. In which: $\Theta(\lambda)=\Theta_i(\lambda)\Theta_i(\lambda)$, *and* $\Theta_i(\lambda)=\frac{x_i}{a_I^2+\lambda}$.

Discontinuities in Eshelby's Tensors over the Interface

The exterior-point Eshelby tensor $\bar{G}$ does not generally reduce to the interior point Eshelby tensor $\mathbf{S}$ when the material point $\mathbf{x}$ moves across the interface between the inclusion and the matrix. The difference can be expressed as

$$\bar{G}_{ijkl}(x) - S_{ijkl} = \frac{1}{1-\nu}\hat{n}_i\hat{n}_j\hat{n}_k\hat{n}_l - \frac{\nu}{1-\nu}\delta_{kl}\hat{n}_i\hat{n}_j - \frac{1}{2}(\delta_{ik}\hat{n}_j\hat{n}_l + \delta_{il}\hat{n}_j\hat{n}_k + \delta_{jk}\hat{n}_i\hat{n}_l + \delta_{jl}\hat{n}_i\hat{n}_k) \quad (7.59)$$

where $\hat{\mathbf{n}}_k$ recovers the outward unit normal vector to the inclusion.

Anisotropic inclusions

The Fourier Transform Method

Since explicit expressions for anisotropic Green's functions are not available, the Fourier transform method will be used

$$u_i(\mathbf{x}) = -(2\pi)^{-3}\frac{\partial}{\partial x_l}\int_{-\infty}^{\infty} \mathrm{d}\xi \int_{-\infty}^{\infty} C_{jlmn}\varepsilon^*_{mn}(\mathbf{x}')N_{ij}(\xi)D^{-1}(\xi)\exp[i\xi\cdot(\mathbf{x}-\mathbf{x}')]\mathrm{d}\mathbf{x}' \quad (7.60)$$

After some manipulation, for interior points of an ellipsoid, we have

$$\varepsilon_{ij} = S_{ijmn}\varepsilon^*_{mn} \quad (7.61)$$

where

$$S_{ijmn} = (1/8\pi)C_{pqmn}\int_{-1}^{1}\mathrm{d}\bar{\zeta}_3\int_0^{2\pi}[G_{ipjq}(\bar{\xi}) + G_{jpiq}(\bar{\xi})]\mathrm{d}\theta \quad (7.62)$$

The strain fields for interior points of an ellipsoid are constant when the eigenstrain ε^*_{ij} is uniform. For some special cases, such as spheroid, there are expressions including one fold integrals. For outside points, the final expression of the displacement gradient takes a complex form

$$u_{i,j}(\mathbf{x}) = \int_0^{2\pi}\mathrm{d}\phi\int_0^R r\mathrm{d}r\int_{\partial\Omega} F\mathrm{d}S \quad (7.63)$$

The Green's function's Method (Mura 1987)

The strain field is expressed as

$$\begin{aligned}\varepsilon_{ij}(\mathbf{x}) &= -\frac{1}{2}C_{klmn}\varepsilon^*_{mn}\int_\Omega [G_{ik,lj}(\mathbf{x}-\mathbf{x}') + G_{jk,li}(\mathbf{x}-\mathbf{x}')]d\mathbf{x}' \\ &= \bar{G}_{ijmn}(\mathbf{x})\varepsilon^*_{mn}\end{aligned}$$

while the Eshelby's tensor for both interior and exterior points is given by

$$\bar{G}_{ijmn}(\mathbf{x}) \equiv -\frac{1}{2}C_{klmn}\int_{\Omega}[G_{ik,lj}(\mathbf{x}-\mathbf{x}')+G_{jk,li}(\mathbf{x}-\mathbf{x}')]\mathrm{d}\mathbf{x}' \tag{7.64}$$

The final result can be calculated directly by numerical surface integration:

$$\bar{G}_{ijmn}(\mathbf{x}) = -\frac{1}{2}C_{klmn}\int_{|\Omega|}[G_{ik,j}(\mathbf{x}-\mathbf{x}')+G_{jk,i}(\mathbf{x}-\mathbf{x}')]n_l\mathrm{d}S \tag{7.65}$$

Ellipsoidal Inhomogeneities

When the elastic moduli of an ellipsoidal domain Ω of a material differ from those of the remainder (matrix), Ω is called an *inhomogeneity* (see Figure 7.2). Eshelby (1957) first pointed out that the stress disturbance in an applied stress due to the presence of an inhomogeneity can be simulated by an eigenstress caused by an inclusion when the eigenstrain is chosen properly. This equivalency is called the *equivalent inclusion method*. Consider an infinitely extended material with the elastic moduli C_{ijkl}, containing an ellipsoidal domain Ω with the elastic moduli C^*_{ijkl}. The far-field stress σ^0_{ij} is applied at infinity. The corresponding strain is: $\varepsilon^0_{ij} = C^{-1}_{ijkl}\sigma^0_{kl}$, and the stress disturbance and the strain disturbance are denoted by σ_{ij} and ε_{ij}, respectively. Now, Hooke's law states:

$$\begin{aligned}\sigma^0_{ij}+\sigma_{ij} &= C^*_{ijkl}(\varepsilon^0_{kl}+\varepsilon_{kl}) \quad \text{in } \Omega\\ \sigma^0_{ij}+\sigma_{ij} &= C_{ijkl}(\varepsilon^0_{kl}+\varepsilon_{kl}) \quad \text{in } D-\Omega\end{aligned}$$

The equivalent eigenstrain ε^*_{ij} is given by

$$\sigma^0_{ij}+\sigma_{ij} = C^*_{ijkl}(\varepsilon^0_{kl}+\varepsilon_{kl}) = C_{ijkl}(\varepsilon^0_{kl}+\varepsilon_{kl}-\varepsilon^*_{kl}) \quad \text{in } \Omega \tag{7.66}$$

The disturbing strain ε_{ij} can be obtained as a function of the eigenstrain ε^*_{ij} when the eigenstrain problem in the homogeneous material is solved. That is

$$\varepsilon_{kl} = S_{klmn}\varepsilon^*_{mn} \tag{7.67}$$

where S_{klmn} is the (interior-point) Eshelby's tensor, given by

$$C^*_{ijkl}(\varepsilon^0_{kl}+S_{klmn}\varepsilon^*_{mn}) = C_{ijkl}(\varepsilon^0_{kl}+S_{klmn}\varepsilon^*_{mn}-\varepsilon^*_{kl}) \quad \text{in } \Omega \tag{7.68}$$

From which the equivalent eigenstrain ε^*_{ij} is determined as

$$\varepsilon^*_{ij} = -(S_{ijkl}+A_{ijkl})^{-1}\varepsilon^0_{kl} \tag{7.69}$$

where the elastic mismatch tensor is: $A_{ijkl} = (C^*_{ijmn}-C_{ijmn})^{-1}C_{mnkl}$. For an **inhomogeneous inclusion**, the inhomogeneity Ω involves its own eigenstrain ϵ^p_{ij}. The stress fields are:

$$\begin{aligned}\sigma^0_{ij}+\sigma_{ij} &= C^*_{ijkl}(\varepsilon^0_{kl}+\varepsilon_{kl}-\varepsilon^p_{kl}) \quad \text{in } \Omega\\ \sigma^0_{ij}+\sigma_{ij} &= C_{ijkl}(\varepsilon^0_{kl}+\varepsilon_{kl}) \quad \text{in } \mathcal{D}-\Omega\end{aligned}$$

The inhomogeneous inclusion is simulated by an inclusion in the homogeneous material with an eigenstrain ε^p_{ij} plus an equivalent eigenstrain ε^*_{ij},

$$\begin{aligned} \sigma^0_{ij} + \sigma_{ij} &= C_{ijkl}(\varepsilon^0_{kl} + \varepsilon_{kl} - \varepsilon^p_{kl} - \varepsilon^*_{kl}) \quad \text{in } \Omega \\ \sigma^0_{ij} + \sigma_{ij} &= C_{ijkl}(\varepsilon^0_{kl} + \varepsilon_{kl}) \quad \text{in } \mathcal{D} - \Omega \end{aligned}$$

The (fictitious) equivalent eigenstrain ε^*_{ij} is given by:

$$\sigma^0_{ij} + \sigma_{ij} = C^*_{ijkl}(\varepsilon^0_{kl} + \varepsilon_{kl} - \varepsilon^p_{kl}) = C_{ijkl}(\varepsilon^0_{kl} + \varepsilon_{kl} - \varepsilon^p_{kl} - \varepsilon^*_{kl}) \text{ in } \Omega \tag{7.70}$$

The disturbing strain ε_{ij} can be taken as the solution of the inclusion problem with a uniform eigenstrain $\varepsilon^p_{ij} + \varepsilon^*_{ij}$, that is

$$\varepsilon_{kl} = S_{klmn}(\varepsilon^p_{mn} + \varepsilon^*_{mn}) \equiv S_{klmn}\varepsilon^{**}_{mn} \tag{7.71}$$

Therefore, the equivalent equation to determine ε^{**}_{ij} becomes

$$C^*_{ijkl}(\varepsilon^0_{kl} + S_{klmn}\varepsilon^{**}_{mn} - \varepsilon^p_{mn}) = C_{ijkl}(\varepsilon^0_{kl} + S_{klmn}\varepsilon^{**}_{mn} - \varepsilon^{**}_{kl}) \tag{7.72}$$

from which the equivalent eigenstrain ε^{**}_{ij} is determined as

$$\varepsilon^{**}_{ij} = -(S_{ijkl} + A_{ijkl})^{-1}(\varepsilon^0_{kl} - B_{klmn}\varepsilon^p_{mn}) \tag{7.73}$$

where the elastic mismatch tensors are:

$$A_{ijkl} = (C^*_{ijmn} - C_{ijmn})^{-1}C_{mnkl}, \quad B_{ijkl} = (C^*_{ijmn} - C_{ijmn})^{-1}C^*_{mnkl} \tag{7.74}$$

The Non-uniform Eigenstrain Problem

Non-uniform Eigenstrain

Assume that the eigenstrain is given in the form of polynomials of coordinates as:

$$\varepsilon^*_{ij}(x) = B_{ij} + B_{ijk}x_k + B_{ijkl}x_k x_l + \cdots \tag{7.75}$$

where B_{ij}, B_{ijk}, B_{ijkl}, are symmetric constants tensors. The disturbing strain can be shown to be given by

$$\varepsilon_{ij}(x) = \bar{G}_{ijkl}(x)B_{kl} + \bar{G}_{ijklm}(x)B_{klm} + \bar{G}_{ijklmn}(x)B_{klmn} + \cdots \tag{7.76}$$

It is noted here that, if $\mathbf{x}$ is inside the domain Ω, then:

$$\begin{aligned} \bar{G}_{ijkl}(x) &\rightarrow S_{ijkl} \\ \bar{G}_{ijklm}(x) &\rightarrow S_{ijkl,m}x_m \\ \bar{G}_{ijklmn}(x) &\rightarrow S_{ijklmn} + \frac{1}{2}S_{ijklmn,pq}x_p x_q \end{aligned} \tag{7.77}$$

Non-uniform Inhomogeneity

If an applied stress is linear with respect to the coordinates, the equivalent eigenstrain is also linear. In general, when the applied stress is a polynomial of degree n, the equivalent eigenstrain is also chosen as a polynomial of degree n. When an applied strain (or stress) is given as

$$\varepsilon^0_{ij}(x) = E_{ij} + E_{ijk}x_k + E_{ijkl}x_k x_l + . \cdots \tag{7.78}$$

The eigenstrain can correspondingly be written as:

$$\varepsilon^*_{ij}(x) = B_{ij} + B_{ijk}x_k + B_{ijkl}x_k x_l + \cdots \tag{7.79}$$

The coefficients B_{ij}, B_{ijk}, B_{ijkl}, ... can be determined by comparing coefficients in the power series from the Eshelby's equivalent equation:

$$C^*_{ijkl}(\varepsilon^0_{kl} + \varepsilon_{kl}) = C_{ijkl}(\varepsilon^0_{kl} + \varepsilon_{kl} - \varepsilon^*_{kl}) \quad \text{in } \Omega \tag{7.80}$$

For a finite region of space, the displacement field satisfies

$$\begin{aligned} u_m(\mathbf{x}) &= \int_V G_{im}(\mathbf{x}, \mathbf{x}') f_i(\mathbf{x}') dV' \\ &- \int_{\partial\Omega} [u_i(\mathbf{x}') C_{ijkl} G_{km,l'}(\mathbf{x}, \mathbf{x}') - G_{im}(\mathbf{x}, \mathbf{x}')\sigma_{ij}(\mathbf{x}')] dS'_j \end{aligned} \tag{7.81}$$

7.2 Infinite Isotropic Media

In this section, we present a numerical method for determination of a key ingredient in DD computer simulations; that is the elastic field of topologically complex dislocation ensembles. The main impetus for the present work is the need to describe the complex 3-D topology of dislocation loops in the most flexible way. A wide spectrum of dislocation line deformations, ranging from highly curved to rigid body translations arise within the same computational simulation. Existing methods are based on differential equations of motion for *straight* segments, where the elastic field variables affecting segment motion are computed at its center. When each segment moves under the influence of the stress field, the *connectivity* of the segments must be re-established, resulting in a number of possible complications. The increase in the self-energy of the dislocation line has to be accounted for(**?**). Additionally, when we consider forces on straight segments, we must necessarily deal with singular values of these forces at connectivity nodes (**?**). Thus, problems of convergence as the segment length is decreased would naturally arise, because of the inherent numerical errors of computations. Computations of the self-force on a straight dislocation segment is also difficult, because of the need to describe local curvature, even though the segment is straight to begin with(**?**). A modification of the Brown procedure (**?**) has been suggested to deal with this difficulty. Thus, the motivation behind the current work can be stated as follows:

1. To reduce the computational burden by providing a high degree of flexibility in the selection of *both length and shape* of a dislocation segment.

2. To avoid numerical problems arising from singularities at intersecting straight segments.

3. To calculate the self-force on dislocation segments with a high degree of accuracy.

4. To provide a flexible tool which sheds more light on the physics of close-range interactions involving in-plane high curvature variations.

5. To effectively deal with the physics of climb and cross-slip, which require out-of-plane dislocation line curvature.

Although the theoretical foundations of dislocation theory are well-established (e.g. (**?**),(**?**),(**?**)-(**?**)), efficient computational methods are still in a state of development (e.g. (**?**),(**?**),(**?**)). Other than a few cases of perfect symmetry and special conditions ((**?**),(**?**),(**?**),), the elastic field of 3-D dislocations of arbitrary geometry is not analytically available. The field of dislocation ensembles is likewise analytically unattainable. We plan, therefore, to present the main elements of 3-D dislocation theory such that the restrictions and limitations of the present computational method are clarified. The main steps in deriving equations for all field variables will thus be given, while the interested reader can find more helpful details in references ((**?**),(**?**),(**?**)).

7.2.1 Dislocation Ensembles in Isotropic Crystals

Elastic Field Variables as Fast Sums

As our main objective is to develop a computational method for numerical simulation of complex dislocation interactions, we need first to outline relevant theoretical foundations. In this section, we present a reasonably self-consistent discussion of isotropic elastic theory which leads to the present fast sum computational implementation. A number of equivalent formulations are available in the literature(**?**)-(**?**). However, because the present development is mainly computational, we follow the tensor index formulation of deWit(**?**), Kröner(**?**), and Kroupa(**?**). For detailed derivations related to this section and its appendices, the reader may consult reference(**?**).

The Displacement Field

The dislocation is formed by cutting over an arbitrary surface S, followed by *rigid* translation of the negative side of (S^-), while holding the positive side (S^+) fixed, as illustrated in FIG. 3. Define the dislocation line vector, $\mathbf{t}$, as the tangent to the dislocation line. The Burgers vector $\mathbf{b}$ is prescribed as the displacement jump condition across the surface (S). The elastic field is based on Burgers equation (**?**), which defines the distribution of elastic displacements around dislocation loops. The strain tensor can be obtained from deformation gradients, while the stress tensor is readily accessible through linear constitutive relations. Once the stress and strain tensors are found, elastic self and interaction energies can be obtained. Referring to FIG. 3, we define the dislocation loop by cutting over the surface S, translating the negative side by

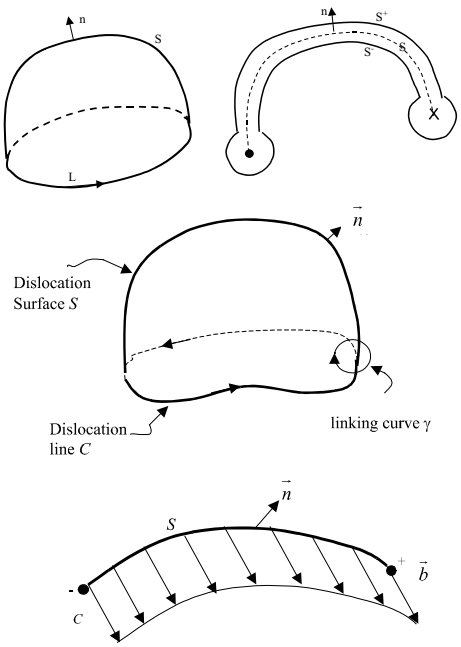

Figure 7.7: Creation of a dislocation by a cut on the surface (S)

the vector **b**, while holding the positive side fixed. Along any *linking curve* Γ, the closed line integral of the displacement vector is **b**. Thus:

$$\mathbf{b} = \oint_{\Gamma} d\mathbf{u} \quad , \quad or \quad b_i = \oint_{\Gamma} u_{i,j} dx_j \tag{7.82}$$

For a given force distribution $f_m(\hat{\mathbf{r}})$ in the medium, the displacement vector is given by:

$$u_k(\mathbf{r}) = \int_{allspace} U_{km}(\mathbf{r} - \hat{\mathbf{r}}) f_m(\hat{\mathbf{r}}) d^3\hat{\mathbf{r}} \tag{7.83}$$

where $U_{km}(\mathbf{r} - \hat{\mathbf{r}})$ are the isotropic elastic Green's functions, given by: $U_{km}(\mathbf{R}) = \frac{1}{8\pi\mu}\left[\delta_{km} R_{,pp} - \frac{\lambda+\mu}{\lambda+2\mu} R_{,}\right.$ Here μ and λ are Lamé constants. For the volume $\hat{V}$, bounded by the surface $\hat{S}$, and upon utilization of the divergence theorem for any rank tensor $\mathbf{T}: \int_V \mathbf{T}_{,i} dV = \int_S \mathbf{T} dS_i$, we obtain:

$$u_m(\mathbf{r}) = \int_{\hat{V}} U_{im}(\mathbf{r} - \hat{\mathbf{r}}) f_i(\hat{\mathbf{r}}) d\hat{V} - \int_{\hat{S}} u_i(\hat{\mathbf{r}}) C_{ijkl} U_{km,l}(\mathbf{r} - \hat{\mathbf{r}}) d\hat{S}_j + \int_{\hat{S}} U_{im}(\mathbf{r} - \hat{\mathbf{r}}) \sigma_{ij}(\hat{\mathbf{r}}) d\hat{S}_j \tag{7.84}$$

The second and third terms in EQUATION7.84 account for displacement and traction boundary conditions on the surface $\hat{S}$, respectively. Assuming that body forces are absent in the medium, as well as any zero traction and rigid displacements b_i across the surface $\hat{S}$, we obtain:

$$u_m(\mathbf{r}) = -b_i \int_{\hat{S}} C_{ijkl} U_{km,l}(\mathbf{r} - \hat{\mathbf{r}}) dS_j \tag{7.85}$$

For an elastic isotropic medium, the fourth rank elastic constants tensor is given in terms of Lamé's constants; μ and λ, thus:$C_{ijkl} = \lambda\delta_{ij}\delta_{kl} + \mu(\delta_{ik}\delta_{jl} + \delta_{il}\delta_{jk})$. Substituting in EQUATION7.85, and re-arranging terms, the displacement vector is given by:

$$u_m(\mathbf{r}) = \frac{1}{8\pi}\int_{\hat{S}} b_m R_{,ppj} d\hat{S}_j + \frac{1}{8\pi}\int_{\hat{S}} \left(b_l R_{,ppl} d\hat{S}_m - b_j R_{,ppm} d\hat{S}_j\right) + \frac{1}{4\pi}\frac{\lambda+\mu}{\lambda+2\mu}\int_{\hat{S}} \left(b_j R_{,ppm} d\hat{S}_j - b_k R_{,kmj} d\hat{S}_j\right) \tag{7.86}$$

EQUATION 7.86 can be converted to a line integral, if one recalls Stokes Theorem, extended to any rank tensor T, expressed as: $\int_S \in_{ijk} T_{abc\bullet\bullet,i} dS_k = \oint_C T_{abc\bullet\bullet} dl_j$. Noting the relationship between the Kronecker and permutation tensors, i.e. $\in_{ijk}\in_{klm} = \delta_{il}\delta_{jm} - \delta_{im}\delta_{jl}$, allows us to write Stokes theorem as: $\int_S (\delta_{il}\delta_{jm} - \delta_{im}\delta_{jl}) T_{abc\bullet\bullet,j} dS_i = \oint_C \in_{lmj} T_{abc\bullet\bullet} dl_j$. Using the substitution property of the Kronecker delta, Stokes' theorem can also be expressed in the *hat* coordinates in the following form:

$$\int_{\hat{S}} \left(T_{abc\bullet\bullet,m} d\hat{S}_l - T_{abc\bullet\bullet,l} d\hat{S}_m\right) = \oint_C \in_{klm} T_{abc\bullet\bullet} dl_k \tag{7.87}$$

The first integral in EQUATION 7.86 is the solid angle fraction subtended by the loop times the burgers vector (see Appendix **??**), while utilization of EQUATION 7.87 can reduce the second and third terms to their line integral form. Therefore, a convenient form for the displacement vector components is given by:

$$u_i = -\frac{b_i \Omega}{4\pi} + \frac{1}{8\pi} \oint_C \left[\in_{ikl} b_l R_{,pp} + \frac{1}{1-\nu} \in_{kmn} b_n R_{,mi} \right] dl_k \tag{7.88}$$

EQUATION7.88 determines the displacement field of a single dislocation loop. For a loop ensemble, one can use the property of linear superposition. Thus, the line integral in EQUATION 7.88 can be converted into a fast numerical sum over the following set: quadrature points ($1 \leq \alpha \leq Q_{max}$) associated with weighting factors (w_α), loop segments ($1 \leq \beta \leq N_s$), and number of ensemble loops ($1 \leq \gamma \leq N_{loop}$). Therefore, a computational form for the displacement vector is:

$$u_i = \frac{1}{4\pi} \sum_{\gamma=1}^{N_{loop}} \left\{ -b_i \Omega + \frac{1}{2} \sum_{\beta=1}^{N_s} \sum_{\alpha=1}^{Q_{max}} w_\alpha \left(\in_{ikl} b_l R_{,pp} + \frac{\in_{kmn} b_n R_{,mij}}{1-\nu} \right) \hat{x}_{k,u} \right\} \tag{7.89}$$

Strain and Stress Fields

Once the displacement field is determined, the strain and stress fields can be readily obtained. If we denote the deformation gradient tensor by u_{ij}, the strain tensor e_{ij} in infinitesimal elasticity is its symmetric decomposition: $u_{ij} = \frac{1}{2}(u_{i,j} + u_{j,i}) + \frac{1}{2}(u_{i,j} - u_{j,i}) = e_{ij} + \omega_{ij}$, where ω_{ij} is the rotation tensor. Taking the derivatives of EQUATION 7.88 yields the deformation gradient tensor:

$$u_{i,j} = -\frac{b_j \Omega_{,i}}{4\pi} + \frac{1}{8\pi} \oint_C \left[\in_{jkl} b_l R_{,ppi} + \frac{1}{1-\nu} \in_{kmn} b_n R_{,mij} \right] dl_k \tag{7.90}$$

From which the following strain tensor is obtained:

$$e_{ij} = -\frac{b_i \Omega_{,j} + b_j \Omega_{,i}}{8\pi} + \frac{1}{8\pi} \oint_C \left[\frac{1}{2} \left(\in_{jkl} b_l R_{,i} + \in_{ikl} b_l R_{,j} \right)_{,pp} + \frac{\in_{kmn} b_n R_{,mij}}{1-\nu} \right] dl_k \tag{7.91}$$

The derivatives of the solid angle Ω are given by EQUATION 6.14 in Appendix **??**, which can now be used to derive the strain tensor components as line integrals.

$$e_{ij} = \frac{1}{8\pi} \oint_C \left[-\frac{1}{2} \left(\in_{jkl} b_i R_{,l} + \in_{ikl} b_j R_{,l} - \in_{ikl} b_l R_{,j} - \in_{jkl} b_l R_{,i} \right)_{,pp} + \frac{\in_{kmn} b_n R_{,mij}}{1-\nu} \right] dl_k \tag{7.92}$$

Similar to EQUATION 7.89, the fast sum equivalent of EQUATION 7.110 is now given by:

$$e_{ij} = \frac{1}{8\pi} \sum_{\gamma=1}^{N_{loop}} \sum_{\beta=1}^{N_s} \sum_{\alpha=1}^{Q_{max}} w_\alpha \left(-\frac{1}{2} \left(\in_{jkl} b_i R_{,l} + \in_{ikl} b_j R_{,l} - \in_{ikl} b_l R_{,j} - \in_{jkl} b_l R_{,i} \right)_{,pp} + \frac{\in_{kmn} b_n R_{,mij}}{1-\nu} \right) \hat{x}_{k,u} \tag{7.93}$$

To deduce the stress tensor, we use the isotropic stress-strain relations of linear elasticity. First, the dilatation is obtained by letting both $i\&j = r$ in EQUATION 7.110 above: $e_{rr} = -\frac{1}{8\pi}\frac{1-2\nu}{1-\nu}\oint\limits_C \in_{kmn} b_n R_{,mrr} dl_k$. Using the stress-strain relations: $\sigma_{ij} = 2\mu e_{ij} + \lambda e_{rr}\delta_{ij}$, we can readily obtain the stress tensor.

$$\sigma_{ij} = \frac{\mu b_n}{4\pi}\oint\limits_C \left[\frac{1}{2}R_{,mpp}\left(\in_{jmn} dl_i + \in_{imn} dl_j\right) + \frac{1}{1-\nu}\in_{kmn}\left(R_{,ijm} - \delta_{ij}R_{,ppm}\right) dl_k\right] \tag{7.94}$$

The *computational* fast sum for the stress tensor is given below in compact form, while explicit representation are listed in appendix 8.68.

$$\sigma_{ij} = \frac{\mu}{4\pi}\sum_{\gamma=1}^{N_{loop}}\sum_{\beta=1}^{N_s}\sum_{\alpha=1}^{Q_{max}} b_n w_\alpha \left[\frac{1}{2}R_{,mpp}\left(\in_{jmn}\hat{x}_{i,u} + \in_{imn}\hat{x}_{j,u}\right) + \frac{1}{1-\nu}\in_{kmn}\left(R_{,ijm} - \delta_{ij}R_{,ppm}\right)\hat{x}_{k,u}\right] \tag{7.95}$$

Stress tensor components

For one loop, explicit fast sum forms of the 3-dimensional stress tensor components are given below. The inner sum is extended over the number of quadrature points assigned in the interval $-1 \leq \hat{u}l0$. Q_{max} is typically 8-16 for accurate results, although cases with Q_{max} up to 300 have been tested. The outer sum is over the number of loop segments, which is typically in the range 10-30. For an arbitrary number of loops of defined parametric geometry, a third sum over the loop number must additionally be included.

$$\sigma_{11} = \frac{\mu}{8\pi}\sum_{\gamma=1}^{N_{loop}}\sum_{\beta=1}^{N_s}\sum_{\alpha=1}^{Q_{max}} w_\alpha \left\{\begin{array}{l} \left[b_2\left(-2R_{,113} + \frac{2\nu}{1-\nu}\left(R_{,223} + R_{,333}\right)\right) + b_3\left(2R_{,112} - \frac{2\nu}{1-\nu}\left(R_{,222} + R_{,332}\right)\right)\right]\hat{x}_{1,u} + \\ \left[-b_1\frac{2}{1-\nu}\left(R_{,223} + R_{,333}\right) + b_3\frac{2}{1-\nu}\left(R_{,221} + R_{,331}\right)\right]\hat{x}_{2,u} + \\ \left[+b_1\frac{2}{1-\nu}\left(R_{,222} + R_{,332}\right) - b_2\frac{2}{1-\nu}\left(R_{,221} + R_{,331}\right)\right]\hat{x}_{3,u} \end{array}\right\}_\alpha \tag{7.96}$$

$$\sigma_{12} = \frac{\mu}{8\pi}\sum_{\gamma=1}^{N_{loop}}\sum_{\beta=1}^{N_s}\sum_{\alpha=1}^{Q_{max}} w_\alpha \left\{\begin{array}{l} \left[b_1\left(R_{,113} + R_{,223} + R_{,333}\right) - b_2\left(\frac{2}{1-\nu}R_{,123}\right) + b_3\left(\frac{1+\nu}{1-\nu}R_{,221} - R_{,111} - R_{,331}\right)\right]\hat{x}_{1,u} + \\ \left[b_1\left(\frac{2}{1-\nu}R_{,123}\right) - b_2\left(R_{,113} + R_{,223} + R_{,333}\right) + b_3\left(-\frac{1+\nu}{1-\nu}R_{,112} + R_{,222} + R_{,332}\right)\right]\hat{x}_{2,u} + \\ \frac{2}{1-\nu}\left(-b_1R_{,221} + b_2R_{,112}\right)\hat{x}_{3,u} \end{array}\right. \tag{7.97}$$

$$\sigma_{13} = \frac{\mu}{8\pi}\sum_{\gamma=1}^{N_{loop}}\sum_{\beta=1}^{N_s}\sum_{\alpha=1}^{Q_{max}} w_\alpha \left\{\begin{array}{l} \left[-b_1\left(R_{,112} + R_{,222} + R_{,332}\right) + b_2\left(R_{,111} + R_{,221} - \frac{1+\nu}{1-\nu}R_{,331}\right) + b_3\left(\frac{2}{1-\nu}R_{,123}\right)\right]\hat{x}_{1,u} + \\ \frac{2}{1-\nu}\left(b_1R_{,331} - b_3R_{,113}\right)\hat{x}_{2,u} + \\ \left[-b_1\left(\frac{2}{1-\nu}R_{,123}\right) - b_2\left(-\frac{1+v}{1-\nu}R_{,113} + R_{,223} + R_{,333}\right) + b_3\left(R_{,112} + R_{,222} + R_{,332}\right)\right]\hat{x}_{3,u} \end{array}\right. \tag{7.98}$$

$$\sigma_{22}=\frac{\mu}{8\pi}\sum_{\gamma=1}^{N_{loop}}\sum_{\beta=1}^{N_s}\sum_{\alpha=1}^{Q_{max}}w_\alpha\left\{\begin{array}{l}\left[b_2\frac{2}{1-\nu}\left(R_{,113}+R_{,333}\right)-b_3\frac{2}{1-\nu}\left(R_{,112}+R_{,332}\right)\right]\hat{x}_{1,u}+\\ \left[b_1\left[-\frac{2\nu}{1-\nu}\left(R_{,113}+R_{,333}\right)+2R_{,223}\right]+b_3\left[\frac{2\nu}{1-\nu}\left(R_{,111}+R_{,331}\right)-2R_{,221}\right]\right]\hat{x}_{2,u}+\\ \left[b_1\frac{2}{1-\nu}\left(R_{,112}+R_{,332}\right)-b_2\frac{2}{1-\nu}\left(R_{,111}+R_{,331}\right)\right]\hat{x}_{3,u}\end{array}\right\}_\alpha \tag{7.99}$$

$$\sigma_{23}=\frac{\mu}{8\pi}\sum_{\gamma=1}^{N_{loop}}\sum_{\beta=1}^{N_s}\sum_{\alpha=1}^{Q_{max}}w_\alpha\left\{\begin{array}{l}\left[-b_2\frac{2}{1-\nu}R_{,332}+b_3\frac{2}{1-\nu}R_{,223}\right]\hat{x}_{1,u}+\\ \left[b_1\left(-R_{,112}-R_{,222}+\frac{1+\nu}{1-\nu}R_{,332}\right)+b_2\left(R_{,111}+R_{,221}+R_{,331}\right)-b_3\left(\frac{2}{1-\nu}R_{,123}\right)\right]\hat{x}_{2,u}+\\ \left[b_1\left(R_{,113}+R_{,333}-\frac{1+\nu}{1-\nu}R_{,223}\right)+b_2\left(\frac{2}{1-\nu}R_{,123}\right)-b_3\left(R_{,111}+R_{,221}+R_{,331}\right)\right]\hat{x}_{3,u}\end{array}\right. \tag{7.100}$$

$$\sigma_{33}=\frac{\mu}{8\pi}\sum_{\gamma=1}^{N_{loop}}\sum_{\beta=1}^{N_s}\sum_{\alpha=1}^{Q_{max}}w_\alpha\left\{\begin{array}{l}\left[+b_2\frac{2}{1-\nu}\left(R_{,113}+R_{,223}\right)-b_3\frac{2}{1-\nu}\left(R_{,112}+R_{,222}\right)\right]\hat{x}_{1,u}+\\ \left[-b_1\frac{2}{1-\nu}\left(R_{,113}+R_{,223}\right)+b_3\frac{2}{1-\nu}\left(R_{,111}+R_{,221}\right)\right]\hat{x}_{2,u}+\\ \left[+b_1\left[\frac{2\nu}{1-\nu}\left(R_{,112}+R_{,222}\right)-2R_{,332}\right]+b_2\left[-\frac{2\nu}{1-\nu}\left(R_{,111}+R_{,221}\right)+2R_{,331}\right]\right]\hat{x}_{3,u}\end{array}\right\}_\alpha \tag{7.101}$$

Interaction and Self Energies

The mutual interaction between two dislocation loops can be obtained by a volume integration of the energy density resulting from the stress field of one loop, acting on the strain field of the other, as given below.

$$E_I=\int_V\sigma_{ij}^{(1)}e_{ij}^{(2)}dV \tag{7.102}$$

where $\sigma_{ij}^{(1)}$ is the elastic stress field from the first dislocation loop and $e_{ij}^{(2)}$ is the elastic strain tensor originating from the second one. After a lengthy derivation, deWit(**?**) provided a simple double line integral formulation for the interaction energy as:

$$E_I=-\frac{\mu b_i^{(1)}b_j^{(2)}}{8\pi}\oint_{C^{(1)}}\oint_{C^{(2)}}\left[R_{,kk}\left(dl_j^{(2)}dl_i^{(1)}+\frac{2\nu}{1-\nu}dl_i^{(2)}dl_j^{(1)}\right)+\frac{2}{1-\nu}\left(R_{,ij}-\delta_{ij}R_{,ll}\right)dl_k^{(2)}dl_k^{(1)}\right] \tag{7.103}$$

In EQUATION(7.103), the line integral is carried over the two space curves $C^{(1)}\&C^{(2)}$. Thus, the corresponding fast sum for the interaction energy reads:

$$E_I=-\frac{\mu b_i^{(1)}b_j^{(2)}}{8\pi}\sum_{\beta^{(1)}=1}^{N_s^{(1)}}\sum_{\beta^{(2)}=1}^{N_s^{(2)}}\sum_{\alpha^{(1)}=1}^{Q_{max}^{(1)}}\sum_{\alpha^{(2)}=1}^{Q_{max}^{(2)}}w_{\alpha^{(1)}}w_{\alpha^{(2)}}\left[R_{,kk}\left(\hat{x}_{j,u}^{(2)}\hat{x}_{i,u}^{(1)}+\frac{2\nu}{1-\nu}\hat{x}_{i,u}^{(2)}\hat{x}_{j,u}^{(1)}\right)+\frac{2}{1-\nu}\left(R_{,ij}-\delta_{ij}R_{,ll}\right)\hat{x}_{k,u}^{(2)}\right. \tag{7.104}$$

The self-energy of a single dislocation loop can be calculated as $\frac{1}{2}$ the interaction energy between two identical dislocation loops separated by a distance r_0. The contribution to the self energy from the dislocation core can be estimated from atomistic calculations, and is usually on the order of 5-10%

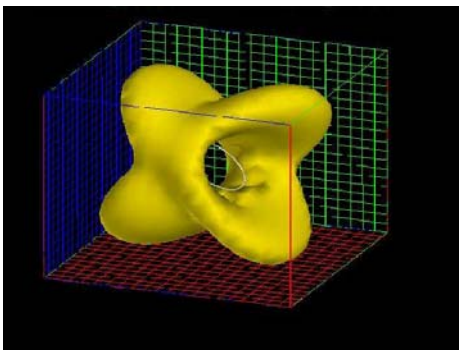

Figure 7.8: Normal stress iso-surface, σ_{11}, in the local loop coordinates, where the 1-axis is [010]-direction and the 3-axis is the [110]-direction.

of the self energy (**?**). However, the core contribution can be incorporated by adjusting the value of r_0. In a fairly rough evaluation, we may take the core energy into account by setting $r_0 = \frac{b}{2}$. (cf. (**?**))

Results and Method Validation

In this section, we discuss several test cases which both illustrate the utility of the fast sum method, and validate its accuracy. We will first present results of computations for the elastic field of isolated circular shear and prismatic dislocation loops. Since some analytical solutions are available for these cases, we will compare the results of the fast sum method to analytical results. The issues of numerical convergence and accuracy are also discussed. In the latter part of this section, we present results of calculations of the elastic field of typical complex-shape loops, representing familiar Frank-Read dislocation sources in crystalline materials.

Stress Field of Simple Loops

Circular Slip Loop

We consider here the stress distribution in the vicinity of a shear (slip) loop in a BCC crystal. The circular loop has a radius of 200 $|\mathbf{b}|$. The loop is oriented for primary slip (i.e. $(110)/\frac{1}{2}\{111\}$). In the figures shown in this section, all distances are given in units of $|\mathbf{b}|$,while stress values are relative to μ. In the local coordinates of the (110)-plane, FIG. 4 shows an iso surface for the normal stress around the dislocation loop. It is clear that the stress surface has an orientational dependence on the $< 111 >$-slip direction. On the glide plane itself, the normal stress vanishes, while the stress surface is symmetric with respect to the loop center. The shear stress components σ_{12} and σ_{23} are displayed in FIGS. 5 and 6. While σ_{12} shows a characteristic "lope" structure of the iso-surface, σ_{23} displays a crescent shape, where the maximum width is for pure edge, while the stress vanishes for the screw component of the loop.

The convergence and computational speed of the fast sum method is demonstrated in reference(**?**). The dependence of the numerical results on the number of segments, segment spline type, and quadra-

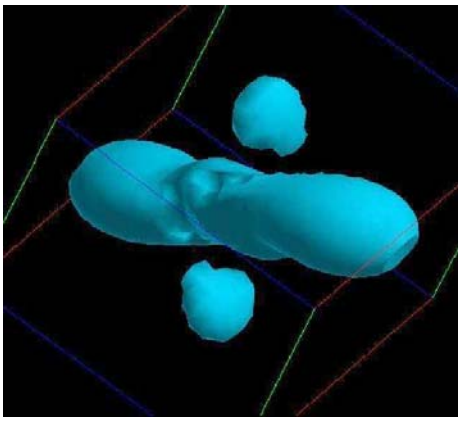

Figure 7.9: Shear stress iso-surface, σ_{12}, in the local loop coordinates, where the 1-axis is [010]-direction and the 3-axis is the [110]-direction.

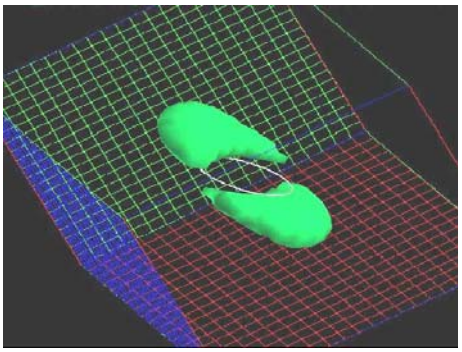

Figure 7.10: Shear stress iso-surface , σ_{23}, in the local loop coordinates, where the 1-axis is [010]-direction and the 3-axis is the [110]-direction.

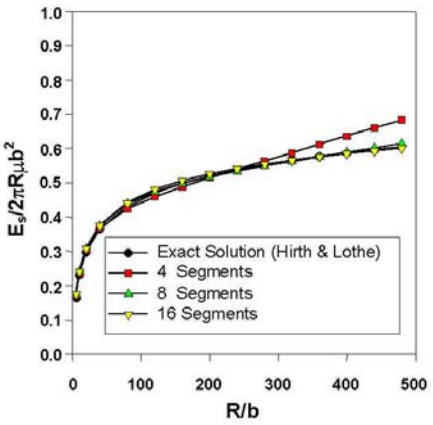

Figure 7.11: A comparison between numerical (current method) and exact analytical (Kroupa) solutions for the normal stress component σ_{zz} of a circular prismatic loop.

ture indicate that the method is numerically convergent, as the number of segments and/or quadrature integration points is increased (**?**). The issue of numerical accuracy of the method is addressed next, by comparison to one of the few available analytical solutions in the literature.

Circular Prismatic Loop

Kroupa(**?**) derived analytical solution for the stress field of a prismatic circular dislocation loop in an infinite isotropic medium. His explicit out-of-plane normal stress in the loop plane (i.e., $z = 0$) σ_z reads:

$$\frac{\sigma_z}{\frac{\mu b}{2\pi R(1-\nu)}} = \frac{2}{1-(\frac{x}{R})^2}E(\frac{x}{R}) \qquad (0 \le \frac{x}{R} < 1), \tag{7.105}$$

$$\frac{\sigma_z}{\frac{\mu b}{2\pi R(1-\nu)}} = 2\frac{R}{x}\left[K(\frac{R}{x}) - \frac{1}{1-(\frac{R}{x})^2}E(\frac{R}{x})\right] \qquad (\frac{x}{R} > 1) \tag{7.106}$$

where K and E are the complete elliptic integrals of the first and second kind, respectively, x is the distance from loop center, and R the loop radius.

In order to evaluate the accuracy of the present fast sum method, a comparison between Kroupa's analytical solution for the normal stress component, σ_{zz}, of a circular prismatic loop and our numerical calculations is shown in FIG. 7. It can be seen that the error in the value of the normal stress depends on the number of segments and on the distance between the field point and the dislocation core. The normal stress shows the characteristic asymmetric singularity at the dislocation line, where the stress field decays to zero at large distances from the core, while it remains finite at the loop center. A more quantitative measure of the error is shown in FIG. 8, where the percent error between the numerical and analytical solutions is shown as a function of distance along the x-axis on the loop

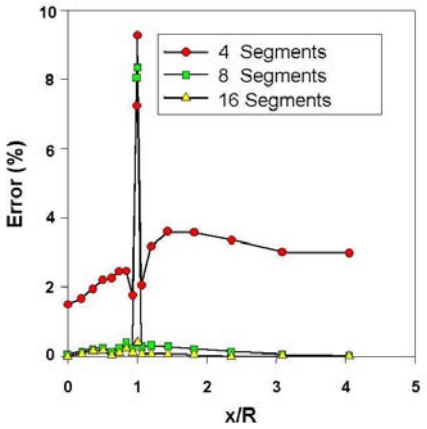

Figure 7.12: Dependence of the error between numerical and analytical (Kroupa) normal stress results on the distance from loop center, for various number of segments.

plane. It is seen that the numerical accuracy is below 4% for only four cubic spline segments, except very close to the dislocation core. The number of quadrature integration points is kept at 16 for all cases studied in the figure. The highest error (below 9%) is manifest at distances less than 1.5 $|\mathbf{b}|$ from the dislocation core, when the number of segments is less than 8. However, the maximum error is less than 0.3% at such close distances, when the number of segments is increased to 16. It is important to note that such high accuracy is needed in calculations of the self-force via the Brown formula(**?**), or its variants(**?**),(**?**). When the stress field is averaged at distances of $\pm\epsilon$ from the dislocation core, the singularity is removed and a convergent, finite self-force is obtained. Thus, the accuracy of field evaluation is apparent.

Interaction and Self Energies

To demonstrate the capability of our fast sum calculation of the interaction energy(E_I), we specify the two dislocations to be pure prismatic coaxial circular loops of equal radius and of the same Burgers vector. In such case, the exact analytical result is available from (**?**) as:

$$\frac{E_I}{2\pi R\mu b^2} = \frac{\kappa}{2\pi(1-\nu)}(K(\kappa) - E(\kappa)) \tag{7.107}$$

in which $\kappa = \left[\frac{1}{1+(d/2R)^2}\right]^{1/2}$ and d is the normal distance between the two parallel loop planes. FIG. 9 shows the results of our calculations, as compared with exact analytical results. The interaction energy is shown as a function of distance between the two loop planes. While the number of quadrature integration points in these calculations is kept at 128, the interaction energy is convergent as the number of segments is increased. This is particularly important at close distances, as can be seen from the figure.

Furthermore, Hirth and Lothe (**?**) provided an explicit expression for the self-energy of a circular slip loop as:

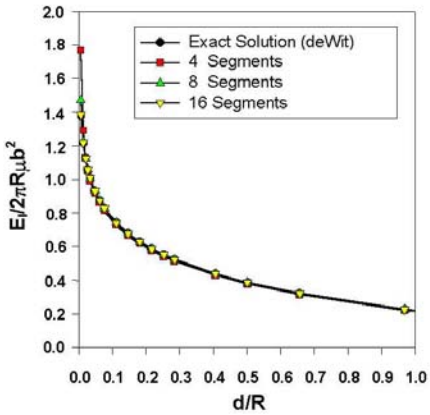

Figure 7.13: A comparison between numerical (current method) and analytical (deWit) results for the interaction energy between two prismatic loops.

$$\frac{E_s}{2\pi R\mu b^2} = \frac{2-\nu}{8\pi(1-\nu)}\left[-ln\left(tan\frac{\rho}{4R}\right) - 2cos\frac{\rho}{2R}\right] \tag{7.108}$$

where ρ is the dislocation core size and is taken as $\frac{1}{2|\mathbf{b}|}$, as suggested by deWit(**?**). FIG. 10 shows the dependence of the self-energy on the loop radius, computed numerically, and compared to the analytical solutions(**?**). The percent error between the numerical and analytical results is shown in FIG. 11. It is interesting to note that, even for four cubic spline segments, the error is rather small (a few percent), when the loop radius is in the tens-to-hundreds of $|\mathbf{b}|$. However, it is clearly demonstrated that more spline segments is necessary for larger size loops, and that the error can generally be brought down below 1%.

Complex Loop Geometries

Single Frank-Read Source

In typical Dislocation Dynamics computer simulations, heavy initial dislocation microstructure is introduced, and its subsequent evolution is followed by solving appropriate equations of motion. Visualization of the stress field associated with the evolving microstructure requires additional techniques to mask specific features, otherwise the 3-D computer image is hopelessly complicated to be useful. Nonetheless, it is instructive to investigate the nature of the elastic field resulting from reasonably complex loop configurations. In this section, we present results for two common dislocation problems: an isolated Frank-Read (FR) dislocation loop, and two interacting such sources in a Molybdenum single crystal. An initial straight edge dislocation segment, lying on the $(1\bar{1}1)$-plane is subjected to an applied stress. The pinned ends of the segment are located at $x = \pm 100|\mathbf{b}|$ from the plane center of the crystal. The expansion of the dislocation segment results in the dislocation loop, shown in FIG. 12, before annihilation of the two opposite screw components takes place. The pinned ends of the source are connected to the crystal surface by two rigid threading dislocations. FIG. 12 shows the normal stress iso-surface of (186 MPa)associated with the FR loop. The iso-surface shows orientational

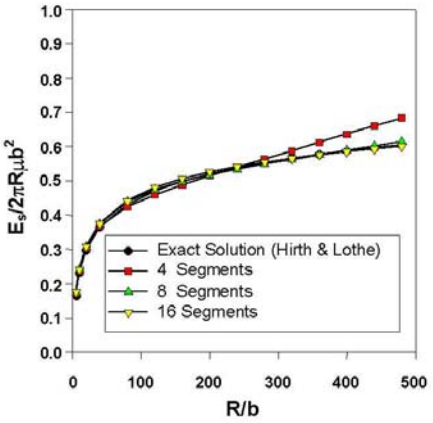

Figure 7.14: A comparison between numerical (current method) and analytical (Hirth and Lothe) results for the self energy of a slip loop.

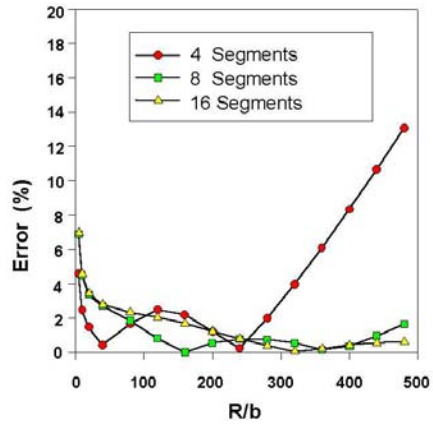

Figure 7.15: Dependence of the error between numerical and analytical solutions in FIG. 10 above on the loop radius and number of cubic spline segments.

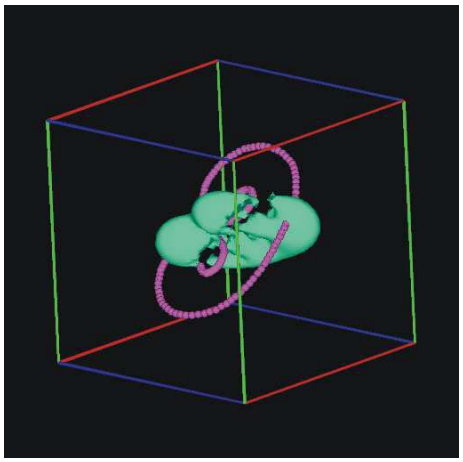

Figure 7.16: Normal stress iso-surface (186 MPa), σ_{11}, for a single Frank-Read source in Molybdenum

dependence on the Burgers vector, as well as symmetry with respect to the (111)-plane. Note the "dimples" in the stress surface which result from the deviation of the FR loop from perfect circular symmetry, as investigated in the earlier section.

So far, we have assumed that the crystal is elastically isotropic and of infinite dimensions. The solution method relies on the existence of analytic forms for the elastic Greens functions, and those are not available for finite media. Recently, Cleveringa, Needleman and Van der Giessen(**?**) have proposed a superposition method to satisfy the boundary conditions of crystals under external constraints. First, the surface traction resulting from the interaction of the dislocation loop with the crystal surface are computed. Once this is achieved, a Finite Element Method (FEM) is used to calculate the stress field resulting from the same traction, with a reversed sign (so- called image traction, in addition to other externally applied forces. The case of a free crystal is somewhat special, because only image traction boundary conditions can be imposed at the surface. Thus, and since a full dislocation loop is mechanically balanced, only rigid body displacements need to be carefully eliminated. We choose here to use the threading dislocation arms, which intersect the surface at two points, to eliminate rigid body rotation and translation. To show the effects of crystal boundaries, we follow the FEM approach, as suggested by Cleveringa et al. (**?**). FIG. 13 shows the results of FEM calculations for the normal stress component on the crystal surface, resulting from image traction. It is clear that the FR source is pulling on the upper surface, and that additional stress concentrations on the $x - z$ surface are associated with the rigid arms of the threading dislocation. The image shear stress σ_{13} is also shown in FIG. 14, where the surface displacements of the crystal are scaled to show the shape of a free crystal which contains an FR source. Note the symmetry with respect to the (111)-plane of positive and negative shear, and the high shear stress around the end points of the threading dislocation.

Interacting FR Dislocation Loops

When FR sources are activated on the same or neighboring slip planes, very complex patterns can emerge (**?**). Interaction of FR sources appears to be one of the main mechanisms which control

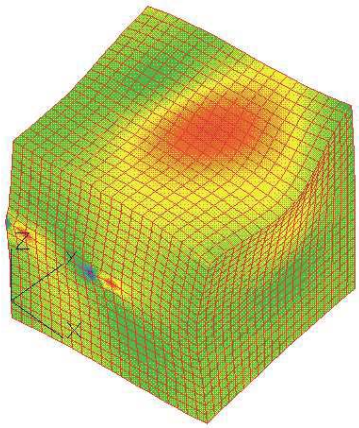

Figure 7.17: Normal stress distribution resulting from the interaction of the single FR source with the surface of a Molybdenum single crystal

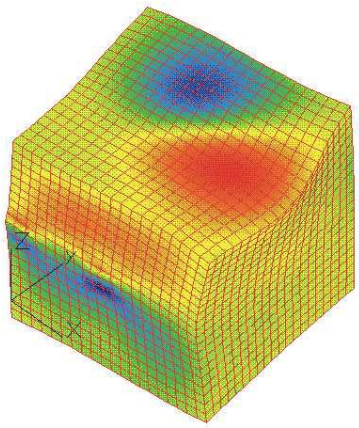

Figure 7.18: Shear stress distribution resulting from the interaction of a single FR source with the surface of a Molybdenum single crystal

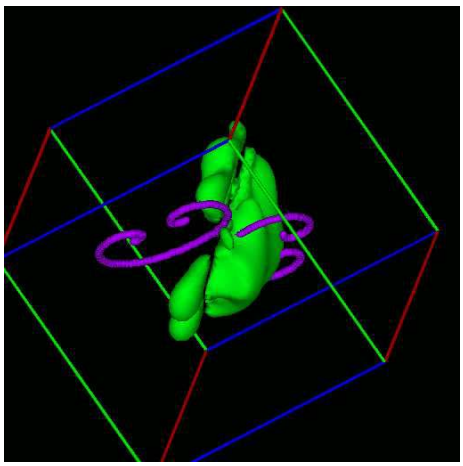

Figure 7.19: Normal stress iso-surface(-130 MPa), σ_{33}, for two interacting Frank-Read sources in Molybdenum

complex dislocation patterns. For this reason, we study the stress field of two such FR sources, which are both located on the $(1\bar{1}1)$-plane. The length of each initial straight edge segment is taken as $150|\mathbf{b}|$. one pinned end of the first FR source is located at $x = 225|\mathbf{b}|$, and at $x = -225|\mathbf{b}|$ for the second source. The other end is located by rotating the initial segment (i.e. $length = 150|\mathbf{b}|$ with an angle of $\theta = 220^o$, and $\theta = 100^o$ for the first and second FR source, respectively.

The normal stress $\sigma_{33} = -130$ MPa is shown in FIG. 15, while the shear stress iso-surface $\sigma_{13} = 170$ MPa is shown in FIG. 16. The normal stress iso-surface shows a split about the (111)-plane, but because of the initial lack of symmetry of the dislocation loop lines, the stress surface is likewise un symmetric. However, FIG. 16 shows an interesting mirror-like symmetry of the stress iso-surface and the original geometry of the FR-sources. This observation is only seen at high levels of stress, where there is nearly no overlap between the stress fields of various segments of the dislocation microstructure. In any event, going beyond the configurations presented here would introduce additional complexities, which are best utilized in computations of Peach-Kohler forces on dislocation segments.

7.2.2 Affine Covariant-contravariant Vector Forms

The displacement vector $\mathbf{u}$, strain ε and stress σ tensor fields of a closed dislocation loop are given by deWit (1960):

$$u_i = -\frac{b_i}{4\pi}\oint_C A_k dl_k + \frac{1}{8\pi}\oint_C \left[\epsilon_{ikl} b_l R_{,pp} + \frac{1}{1-\nu}\epsilon_{kmn} b_n R_{,mi}\right] dl_k \tag{7.109}$$

$$\varepsilon_{ij} = \frac{1}{8\pi}\oint_C \left[-\frac{1}{2}\left(\epsilon_{jkl} b_i R_{,l} + \epsilon_{ikl} b_j R_{,l} - \epsilon_{ikl} b_l R_{,j} - \epsilon_{jkl} b_l R_{,i}\right)_{,pp} \frac{\epsilon_{kmn} b_n R_{,mij}}{1-\nu}\right] dl_k \tag{7.110}$$

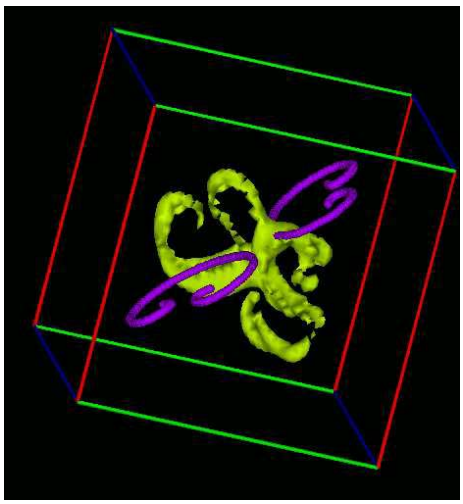

Figure 7.20: Shear stress iso-surface(170 MPa), σ_{13}, for two interacting Frank-Read sources in Molybdenum

$$\sigma_{ij} = \frac{\mu}{4\pi} \oint_C \left[\frac{1}{2} R_{,mpp} \left(\epsilon_{jmn} dl_i + \epsilon_{imn} dl_j \right) + \frac{1}{1-\nu} \epsilon_{kmn} \left(R_{,ijm} - \delta_{ij} R_{,ppm} \right) dl_k \right] \tag{7.111}$$

Where μ & ν are the shear modulus and Poisson's ratio, respectively, $\mathbf{b}$ is Burgers vector of Cartesian components b_i, and the vector potential $A_k(\mathbf{R}) = \epsilon_{ijk} X_i s_j / [R(R + \mathbf{R} \cdot \mathbf{s})]$ satisfies the differential equation: $\epsilon_{pik} A_{k,p}(\mathbf{R}) = X_i R^{-3}$, where $\mathbf{s}$ is an arbitrary unit vector. The radius vector $\mathbf{R}$ connects a source point on the loop to a field point, as shown in Fig.9.51, with Cartesian components R_i, successive partial derivatives $R_{,ijk....}$, and magnitude R. The line integrals are carried along the closed contour C defining the dislocation loop, of differential arc length $d\mathbf{l}$ of components dl_k. Also, the interaction energy between two closed loops with Burgers vectors $\mathbf{b}_1$ and $\mathbf{b}_2$, respectively, can be written as:

$$E_I = -\frac{\mu b_{1i} b_{2j}}{8\pi} \oint_{C^{(1)}} \oint_{C^{(2)}} \left[R_{,kk} \left(dl_{2j} dl_{1i} + \frac{2\nu}{1-\nu} dl_{2i} dl_{1j} \right) + \frac{2}{1-\nu} (R_{,ij} - \delta_{ij} R_{,ll}) dl_{2k} dl_{1k} \right] \tag{7.112}$$

The higher order derivatives of the radius vector, $R_{,ij}$ & $R_{,ijk}$ are components of second and third order Cartesian tensors, respectively, which can be cast in the form:

$$\begin{aligned} R_{,ij} &= \left(\delta_{ij} - \frac{X_i}{R} \frac{X_j}{R} \right) / R \\ R_{,ijk} &= \left(3 \frac{X_i}{R} \frac{X_j}{R} \frac{X_k}{R} - \left[\delta_{ij} \frac{X_k}{R} + \delta_{jk} \frac{X_i}{R} + \delta_{ki} \frac{X_j}{R} \right] \right) / R^2 \end{aligned} \tag{7.113}$$

Where X_i are Cartesian components of $\mathbf{R}$. Substituting $R_{,ij}$ and $R_{,ijk}$ in Equations7.109-7.112,

and considering the contributions only due to a differential vector element $d\mathbf{l}$, we obtain the differential relationships:

$$du_i = -\frac{b_i A_k dl_k}{4\pi} + \frac{1}{8\pi R(1-\nu)}\left[(1-2\nu)\epsilon_{ikl}b_l dl_k - \frac{1}{R^2}\epsilon_{kmn}b_n X_m X_i dl_k\right] \tag{7.114}$$

$$\begin{aligned} d\varepsilon_{ij} &= \frac{1}{8\pi}\left[\frac{1}{R^3}\left(\epsilon_{jkl}b_i X_l + \epsilon_{ikl}b_j X_l\right)dl_k + \frac{3}{R^5(1-\nu)}\epsilon_{kmn}b_n X_i X_j X_m dl_k\right. \\ &\left. -\frac{1}{R^3(1-\nu)}\epsilon_{kmn}b_n X_m \delta_{ij} dl_k + \frac{\nu}{R^3(1-\nu)}\epsilon_{jkl}b_l X_i dl_k + \frac{\nu}{R^3(1-\nu)}\epsilon_{ikn}b_n X_j dl_k\right] \end{aligned} \tag{7.115}$$

$$\begin{aligned} d\sigma_{ij} &= \frac{\mu}{4\pi}\frac{1}{R^3}\left[-\epsilon_{jmn}X_m b_n dl_i - \epsilon_{imn}X_m b_n dl_j\right. \\ &\left. +\frac{1}{1-\nu}\left(\frac{3}{R^2}\epsilon_{kmn}X_m b_n X_i X_j - \epsilon_{kjn}X_i b_n - \epsilon_{kin}X_j b_n + \epsilon_{kmn}X_m b_n \delta_{ij}\right)dl_k\right] \end{aligned} \tag{7.116}$$

Fig.9.51 shows a parametric representation of a general curved dislocation line segment, which can be described by a parameter ω that varies, for example, from 0 to 1 at end nodes of the segment. The segment is fully determined as an affine mapping on the scalar interval $\in [0,1]$, if we introduce the tangent vector $\mathbf{T}$, the unit tangent vector $\mathbf{t}$, the unit radius vector $\mathbf{e}$, and the vector potential $\mathbf{A}$, as follows:

$$\mathbf{T} = \frac{\mathbf{dl}}{d\omega},\ \mathbf{t} = \frac{\mathbf{T}}{|\mathbf{T}|},\ \mathbf{e} = \frac{\mathbf{R}}{R},\quad \mathbf{A} = \frac{\mathbf{e}\times\mathbf{s}}{R(1+\mathbf{e}\cdot\mathbf{s})}$$

The following relations can be readily verified:

$$\begin{aligned} A_k dl_k &= \mathbf{A}\cdot\mathbf{T}d\omega = Td\omega(\mathbf{A}\cdot\mathbf{t}) = \frac{Td\omega}{R}\cdot\frac{(\mathbf{e}\times\mathbf{s})\cdot\mathbf{t}}{1+\mathbf{e}\cdot\mathbf{s}} \\ \epsilon_{ikl}b_l dl_k \mathbf{e}_i &= -\mathbf{b}\times\mathbf{t} \\ \frac{1}{R^2}\epsilon_{kmn}b_n X_m X_i dl_k \mathbf{e}_i &= -\frac{1}{R^2}\epsilon_{knm}b_n X_m X_i dl_k \mathbf{e}_i \\ &= -\frac{d\omega}{R^2}[(\mathbf{T}\times\mathbf{b})\cdot\mathbf{R}]\ \mathbf{R} = -d\omega[(\mathbf{T}\times\mathbf{b})\cdot\mathbf{e}]\ \mathbf{e} \\ (\epsilon_{jkl}b_i X_l + \epsilon_{ikl}b_j X_l)dl_k \mathbf{e}_i\mathbf{e}_j &= \mathbf{b}\otimes(\mathbf{T}d\omega\times\mathbf{R}) + (\mathbf{T}d\omega\times\mathbf{R})\otimes\mathbf{b} \\ &= RTd\omega\ [\mathbf{b}\otimes(\mathbf{t}\times\mathbf{e}) + (\mathbf{t}\times\mathbf{e})\otimes\mathbf{b}] \\ \epsilon_{kmn}b_n X_i X_j X_m dl_k \mathbf{e}_i\mathbf{e}_j &= [(\mathbf{T}d\omega\times\mathbf{R})\cdot\mathbf{b}]\ \mathbf{R}\otimes\mathbf{R} = R^3 Td\omega[(\mathbf{t}\times\mathbf{e})\cdot\mathbf{b}]\ \mathbf{e}\otimes\mathbf{e} \\ \epsilon_{kmn}b_n X_m \delta_{ij} dl_k \mathbf{e}_i\mathbf{e}_j &= [(\mathbf{T}d\omega\times\mathbf{R})\cdot\mathbf{b}]\ \mathbf{I} = RTd\omega\ [(\mathbf{t}\times\mathbf{e})\cdot\mathbf{b}]\ \mathbf{I} \end{aligned}$$

Let the Cartesian orthonormal basis set be denoted by $\mathbf{1} \equiv \{\mathbf{1}_x, \mathbf{1}_y, \mathbf{1}_z\}$, $\mathbf{I} = \mathbf{1}\otimes\mathbf{1}$ as the second order unit tensor, and $\otimes$ denotes tensor product. Now define the three vectors ($\mathbf{g}_1 = \mathbf{e},\ \mathbf{g}_2 = \mathbf{t},\ \mathbf{g}_3 = \mathbf{b}/|\mathbf{b}|$) as a covariant basis set for the curvilinear segment, and their contravariant reciprocals as: $\mathbf{g}^i \cdot \mathbf{g}_j = \delta^i_j$, where δ^i_j is the mixed Kronecker delta and $V = (\mathbf{g}_1\times\mathbf{g}_2)\cdot\mathbf{g}_3$ the volume spanned by the vector basis, as shown in Fig. 9.51 (Holzapfel 2000). When the previous relationships are substituted back into Equations 9.23-7.116, with $V_1 = (\mathbf{s}\times\mathbf{g}_1)\cdot\mathbf{g}_2$, and $\mathbf{s}$ an arbitrary unit vector, we obtain:

$$
\begin{aligned}
\frac{d\mathbf{u}}{d\omega} &= \frac{|\mathbf{b}||\mathbf{T}|V}{8\pi(1-\nu)R}\left\{\left[\frac{(1-\nu)V_1/V}{1+\mathbf{s}\cdot\mathbf{g}_1}\right]\mathbf{g}_3+(1-2\nu)\mathbf{g}^1+\mathbf{g}_1\right\}\\
\frac{d\varepsilon}{d\omega} &= -\frac{V|\mathbf{T}|}{8\pi(1-\nu)R^2}\left\{-\nu\left(\mathbf{g}^1\otimes\mathbf{g}_1+\mathbf{g}_1\otimes\mathbf{g}^1\right)+(1-\nu)\left(\mathbf{g}^3\otimes\mathbf{g}_3+\mathbf{g}_3\otimes\mathbf{g}^3\right)+(3\mathbf{g}_1\otimes\mathbf{g}_1-\mathbf{I})\right\}\\
\frac{d\sigma}{d\omega} &= \frac{\mu V|\mathbf{T}|}{4\pi(1-\nu)R^2}\left\{\left(\mathbf{g}^1\otimes\mathbf{g}_1+\mathbf{g}_1\otimes\mathbf{g}^1\right)+(1-\nu)\left(\mathbf{g}^2\otimes\mathbf{g}_2+\mathbf{g}_2\otimes\mathbf{g}^2\right)-(3\mathbf{g}_1\otimes\mathbf{g}_1+\mathbf{I})\right\}\\
\frac{d^2E_I}{d\omega_1 d\omega_2} &= -\frac{\mu|\mathbf{T}_1||\mathbf{b}_1||\mathbf{T}_2||\mathbf{b}_2|}{4\pi(1-\nu)R}\left\{(1-\nu)\left(\mathbf{g}_2^I\cdot\mathbf{g}_3^I\right)\left(\mathbf{g}_2^{II}\cdot\mathbf{g}_3^{II}\right)+2\nu\left(\mathbf{g}_2^{II}\cdot\mathbf{g}_3^I\right)\left(\mathbf{g}_2^I\cdot\mathbf{g}_3^{II}\right)\right.\\
&\quad\left.-\left(\mathbf{g}_2^I\cdot\mathbf{g}_2^{II}\right)\left[\left(\mathbf{g}_3^I\cdot\mathbf{g}_3^{II}\right)+\left(\mathbf{g}_3^I\cdot\mathbf{g}_1\right)\left(\mathbf{g}_3^{II}\cdot\mathbf{g}_1\right)\right]\right\}\\
\frac{d^2E_S}{d\omega_1 d\omega_2} &= -\frac{\mu|\mathbf{T}_1||\mathbf{T}_2||\mathbf{b}|^2}{8\pi R\,(1-\nu)}\left\{(1+\nu)\left(\mathbf{g}_3\cdot\mathbf{g}_2^I\right)\left(\mathbf{g}_3\cdot\mathbf{g}_2^{II}\right)-\left[1+(\mathbf{g}_3\cdot\mathbf{g}_1)^2\right]\left(\mathbf{g}_2^I\cdot\mathbf{g}_2^{II}\right)\right\}
\end{aligned}
\tag{7.117}
$$

The superscripts $I\&II$ in the energy equations are for loops $I\&II$, respectively, and $\mathbf{g}_1$ is the unit vector along the line connecting two interacting points on the loops. The self energy is obtained by taking the limit of $\frac{1}{2}$ the interaction energy of two identical loops, separated by the core distance. Note that the interaction energy of prismatic loops would be simple, because $\mathbf{g}_3\cdot\mathbf{g_2}=0$. The field equations are affine transformation mappings of the scalar interval neighborhood $d\omega$ to the vector ($d\mathbf{u}$) and second order tensor ($d\varepsilon,\ d\sigma$) neighborhoods, respectively, such that $d\mathbf{u}=\mathbf{U}d\omega,\ d\sigma=\mathbf{S}d\omega,\ d\varepsilon=\mathbf{E}d\omega$. The maps are given by the covariant, contravariant and mixed vector and tensor functions:

$$
\begin{aligned}
\mathbf{U} &= u^i\mathbf{g}_i+u_i\mathbf{g}^i\\
\mathbf{S} &= sym[tr(A^i_{\ .j}\mathbf{g}_i\otimes\mathbf{g}^j)]+A^{11}(3\mathbf{g}_1\otimes\mathbf{g}_1-\mathbf{1}\otimes\mathbf{1})\\
\mathbf{E} &= sym[tr(B^i_{\ .j}\mathbf{g}_i\otimes\mathbf{g}^j)]+B^{11}(3\mathbf{g}_1\otimes\mathbf{g}_1+\mathbf{1}\otimes\mathbf{1})
\end{aligned}
\tag{7.118}
$$

The scalar metric coefficients $u_i, u^i, A^i_{\ .j}, B^i_{\ .j}, A^{11}, B^{11}$ are obtained by direct reduction of Equation7.117 into Equation7.118.

Applications

In some simple geometry of Volterra-type dislocations, special relations between $\mathbf{b}$, $\mathbf{e}$ and $\mathbf{t}$ can be obtained, and the entire dislocation line can also be described by one single parameter. In such cases, one can obtain the elastic field by proper choice of the coordinate system, followed by straightforward integration. Solution variables for the stress fields of infinitely-long pure and edge dislocations are given in Table 1, while those for the stress field along the $\mathbf{1}_z$-direction for circular prismatic and shear loops are shown in Table 2. The corresponding variables are defined in Fig. (7.21) for infinitely straight dislocations, and Fig. (7.22) for circular dislocation loops. Note that for the case of a pure screw dislocation, one has to consider the product of V and the contravariant vectors together, since $V=0$. When the parametric equations are integrated over z from $(-\infty$ to $+\infty)$ for the straight dislocations, and over θ from $(0\ -\ 2\pi)$ for circular dislocations, one obtains the entire stress field in dyadic notation as:

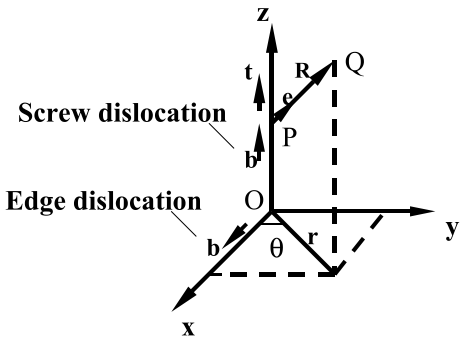

Figure 7.21: Geometry and variables for infinitely-long screw and edge dislocations

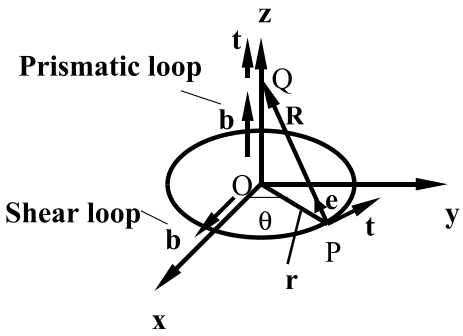

Figure 7.22: Geometry and variables for circular shear and prismatic loops

1. Infinitely-long screw dislocation:

$$\sigma = \frac{\mu b}{2\pi r}\left\{-\sin\theta\ \mathbf{1}_x\otimes\mathbf{1}_z + \cos\theta\ \mathbf{1}_y\otimes\mathbf{1}_z + \cos\theta\ \mathbf{1}_z\otimes\mathbf{1}_y - \sin\theta\ \mathbf{1}_z\otimes\mathbf{1}_x\right\} \tag{7.119}$$

2. Infinitely-long edge dislocation:

$$\begin{aligned}\sigma = \ &- \ \frac{\mu b}{2\pi(1-\nu)r}\left\{\sin\theta(2+\cos 2\theta)\mathbf{1}_x\otimes\mathbf{1}_x - (\sin\theta\cos 2\theta)\mathbf{1}_y\otimes\mathbf{1}_y\right.\\ &+ \ \left.(2\nu\sin\theta)\mathbf{1}_z\otimes\mathbf{1}_z - (\cos\theta\cos 2\theta)(\mathbf{1}_x\otimes\mathbf{1}_y + \mathbf{1}_y\otimes\mathbf{1}_x)\right\}\end{aligned} \tag{7.120}$$

3. Circular shear loop (evaluated on the $\mathbf{1}_z$-axis):

$$\sigma = \frac{\mu b r^2}{4(1-\nu)(r^2+z^2)^{\frac{5}{2}}}\left[(\nu-2)(r^2+z^2)+3z^2\right]\left[\mathbf{1}_x\otimes\mathbf{1}_z + \mathbf{1}_z\otimes\mathbf{1}_x\right] \tag{7.121}$$

4. Circular prismatic loop (evaluated on the $\mathbf{1}_z$-axis):

$$\sigma = \frac{\mu b r^2}{4(1-\nu)(r^2+z^2)^{\frac{5}{2}}} \left\{ (2(1-\nu)(r^2+z^2) - 3r^2) \left[\mathbf{1}_x \otimes \mathbf{1}_x + \mathbf{1}_y \otimes \mathbf{1}_y \right] - 2(4z^2+r^2) \left[\mathbf{1}_z \otimes \mathbf{1}_z \right] \right\} \tag{7.122}$$

Table 7.1: Variables for screw and edge dislocations

	screw dislocation	edge dislocation
$\mathbf{g}_1$	$\frac{1}{R}(r\cos\theta\mathbf{1}_x + r\sin\theta\mathbf{1}_y + z\mathbf{1}_z)$	$\frac{1}{R}(r\cos\theta\mathbf{1}_x + r\sin\theta\mathbf{1}_y + z\mathbf{1}_z)$
$\mathbf{g}_2$	$\mathbf{1}_z$	$\mathbf{1}_z$
$\mathbf{g}_3$	$\mathbf{1}_z$	$\mathbf{1}_x$
$\mathbf{g}^1$	0	$\frac{1}{V}\mathbf{1}_y$
$\mathbf{g}^2$	$\frac{r}{V\sqrt{r^2+z^2}}(-\sin\theta\mathbf{1}_x + \cos\theta\mathbf{1}_y)$	$\frac{1}{V\sqrt{r^2+z^2}}(-z\mathbf{1}_y + r\sin\theta\mathbf{1}_z)$
$\mathbf{g}^3$	$\frac{r}{V\sqrt{r^2+z^2}}(\sin\theta\mathbf{1}_x - \cos\theta\mathbf{1}_y)$	$\frac{r}{V\sqrt{r^2+z^2}}(\sin\theta\mathbf{1}_x - \cos\theta\mathbf{1}_y)$
$\mathbf{T}$	$\frac{dz}{d\omega}\mathbf{1}_z$	$\frac{dz}{d\omega}\mathbf{1}_z$
R	$\sqrt{r^2+z^2}$	$\sqrt{r^2+z^2}$
V	0	$\frac{r\sin\theta}{\sqrt{r^2+z^2}}$

Table 7.2: Variables for circular shear and prismatic loops

	shear loop	prismatic loop
$\mathbf{g}_1$	$\frac{1}{\sqrt{r^2+z^2}}(r\cos\theta\mathbf{1}_x + r\sin\theta\mathbf{1}_y + z\mathbf{1}_z)$	$\frac{1}{\sqrt{r^2+z^2}}(r\cos\theta\mathbf{1}_x + r\sin\theta\mathbf{1}_y + z\mathbf{1}_z)$
$\mathbf{g}_2$	$-\sin\theta\mathbf{1}_x + \cos\theta\mathbf{1}_y$	$-\sin\theta\mathbf{1}_x + \cos\theta\mathbf{1}_y$
$\mathbf{g}_3$	$\mathbf{1}_x$	$\mathbf{1}_z$
$\mathbf{g}^1$	$-\frac{\cos\theta}{V}\mathbf{1}_y$	$\frac{1}{V}(\cos\theta\mathbf{1}_x + \sin\theta\mathbf{1}_y)$
$\mathbf{g}^2$	$\frac{1}{V\sqrt{r^2+z^2}}(-z\mathbf{1}_y + r\sin\theta\mathbf{1}_z)$	$\frac{r}{V\sqrt{r^2+z^2}}(-\sin\theta\mathbf{1}_x + \cos\theta\mathbf{1}_y)$
$\mathbf{g}^3$	$\frac{1}{V\sqrt{r^2+z^2}}(-z\cos\theta\mathbf{1}_x - z\sin\theta\mathbf{1}_y + r\mathbf{1}_z)$	$\frac{1}{V\sqrt{r^2+z^2}}(-z\cos\theta\mathbf{1}_x - z\sin\theta\mathbf{1}_y + r\mathbf{1}_z)$
$\mathbf{T}$	$-r\sin\theta\frac{d\theta}{d\omega}\mathbf{1}_x + r\cos\theta\frac{d\theta}{d\omega}\mathbf{1}_y$	$-r\sin\theta\frac{d\theta}{d\omega}\mathbf{1}_x + r\cos\theta\frac{d\theta}{d\omega}\mathbf{1}_y$
R	$\sqrt{r^2+z^2}$	$\sqrt{r^2+z^2}$
V	$-\frac{z\cos\theta}{\sqrt{r^2+z^2}}$	$\frac{r}{\sqrt{r^2+z^2}}$

As an application of the method in calculations of self- and interaction energy between dislocations, we consider here two simple cases. First, the interaction energy between two parallel screw dislocations of length L and with a minimum distance ρ between them is obtained by making the following substitutions in Equation(7.117):

$$\mathbf{g}_2^I = \mathbf{g}_2^{II} = \mathbf{g}_3^I = \mathbf{g}_3^{II} = \mathbf{1}_z, \quad |\mathbf{T}| = \frac{dl}{dz} = 1, \ \mathbf{1}_z \cdot \mathbf{g}_1 = \frac{z_2 - z_1}{\sqrt{\rho^2 + (z_2 - z_1)^2}}$$

Where z_1 and z_2 are distances along $\mathbf{1}_z$ on dislocations 1 and 2, respectively, connected along the unit vector $\mathbf{g}_1$. The resulting scalar differential equation for the interaction energy is:

$$\frac{d^2E_I}{dz_1dz_2} = -\frac{\mu b^2}{4\pi(1-\nu)}\left\{\frac{\nu}{\sqrt{\rho^2+(z_2-z_1)^2}} - \frac{(z_2-z_1)^2}{[\rho^2+(z_2-z_1)^2]^{\ 3/2}}\right\} \tag{7.123}$$

Integration of Equation (7.123) over a finite length L yields identical results to those obtained by DeWit (1960), and by application of the more standard Blin formula (Hirth 1982). Second, the interaction energy between two coaxial prismatic circular dislocations with equal radius can be easily obtained by the following substitutions:

$$\mathbf{g}_3^I = \mathbf{g}_3^{II} = \mathbf{1}_z,\ \ \mathbf{g}_2^I = -\sin\varphi_1\mathbf{1}_x + \cos\varphi_1\mathbf{1}_y,\ \ \mathbf{g}_2^{II} = -\sin\varphi_2\mathbf{1}_x + \cos\varphi_2\mathbf{1}_y$$

$$\mathbf{1}_z\cdot\mathbf{g}_2^I = 0,\ \ R^2 = z^2 + (2\rho\ \sin\frac{\varphi_1-\varphi_2}{2})^2,\ \ \mathbf{1}_z\cdot\mathbf{g}_1 = \frac{z}{R}$$

Integration over the variables φ_1 & φ_2 from $(0-2\pi)$ yields the interaction energy, which can be verified to be identical to the form obtained by DeWit (1960), and by application of Blin's formula (Hirth 1982). Details of all integrations in this note can be readily verified, or checked in reference (Walgraef and Ghoniem 2002).

7.3 Line Integral Forms for Dislocations in Bi-materials

7.3.1 Objectives and Problem Setup

In many problems, boundary conditions of free surfaces and interfaces need to be considered. For these cases, in direct numerical simulations of dislocation dynamics, the forces acting on the dislocations have an additional term that come out to satisfy the boundary conditions. These forces are called images forces from the boundaries. There are different ways to solve the image forces, including finite element method, boundary element method. However, if there is a direct line integral formulation, it will be much easier to implement these images force into current dislocation dynamics simulations without much loss of computation speed. In this report, we try to formulate such a expression of the image forces in line-integral forms that can be used in our simulations.

Stress field of dislocation line in form of line integral for infinite material:

$$\sigma_{ij}^{\infty}(\mathbf{x}) = \oint_C S_{ijmn}^{\infty}(\mathbf{x}-\mathbf{x}')dl_m \tag{7.124}$$

where

$$S_{ijmn}^{\infty} = -b_n c_{ijpq}c_{nskl}\epsilon_{sqm}G_{sk,l} \tag{7.125}$$

For bi-material, we want to express the filed in form of line integral too. That is:

$$\sigma_{ij}^{\infty}(\mathbf{x}) = \oint_C \left[S_{ijmn}^{\infty}(\mathbf{x}-\mathbf{x}') + S_{ijmn}^{I}(\mathbf{x},\mathbf{x}')\right]dl_m \tag{7.126}$$

To get S_{ijmn}^I, we need to solve the following problem:

1. Equilibrium equation:

$$c^q_{ijkl} u^q_{k,lj}(\mathbf{x}, \mathbf{x}^{'}) = 0 \tag{7.127}$$

where $q = 1, 2$ for two materials.

2. Displacement boundary condition:

$$\triangle[\mathbf{u}]|_{x_3=0} = \mathbf{u}^1|_{x_3=0} - \mathbf{u}^2|_{x_3=0} = 0 \tag{7.128}$$

where,$\mathbf{u}^q = \mathbf{u}^{q\infty} + \mathbf{u}^{qI}$.

3. Traction boundary condition:

$$\triangle[S_{i3}]|_{x_3=0} = S^1_{i3}|_{x_3=0} - S^2_{i3}|_{x_3=0} = 0 \tag{7.129}$$

where $S^q_{i3} = S^{q\infty}_{i3} + S^{qI}_{i3}$.

For isotropic case, we have:

$$c_{ijkl} = \lambda\delta_{ij}\delta_{kl} + \mu(\delta_{ik}\delta jl + \delta_{il}\delta_{jk}) \tag{7.130}$$

7.3.2 Fourier Transformation of The Governing Equations

To solve above problem by Fourier transformation.

$$\tilde{\mathbf{u}}(\xi, x_3, x_3^{'}) = \int\int \mathbf{u}(\mathbf{x}, (0, 0, x_3^{'}))e^{i(\xi_1 x_1 + \xi_2 x_2)} dx_1 dx_2 \tag{7.131}$$

The inverse transformation is:

$$\mathbf{u} = \frac{1}{4\pi^2}\int\int \tilde{\mathbf{u}} e^{-i(\xi_1 x_1 + \xi_2 x_2)} d\xi_1 d\xi_2 \tag{7.132}$$

The transformed equilibrium equation is:

$$c_{i3k3}\tilde{u}_{k,33} - i\xi_\alpha(c_{i\alpha k3} + c_{i3k\alpha})\tilde{u}_{k,3} - \xi_\alpha\xi_\beta c_{i\alpha k\beta}\tilde{u}_k = 0 \tag{7.133}$$

where α and β range over 1, 2.

The transformed displacement boundary conditions are:

$$\triangle[\tilde{\mathbf{u}}]|_{x_3=0} = \tilde{\mathbf{u}}^1|_{x_3=0} - \tilde{\mathbf{u}}^2|_{x_3=0} = 0 \tag{7.134}$$

where $\tilde{\mathbf{u}}^q = \tilde{\mathbf{u}}^{q\infty} + \tilde{\mathbf{u}}^{qI}$. And the transformed traction boundary conditions are:

$$\triangle[\tilde{S}_{i3}]|_{x_3=0} = \tilde{S}^1_{i3}|_{x_3=0} - \tilde{S}^2_{i3}|_{x_3=0} = 0 \tag{7.135}$$

where $\tilde{S}^q_{i3} = \tilde{S}^{q\infty}_{i3} + \tilde{S}^{qI}_{i3}$.

We have the general solution of the transformed equilibrium equation as:

$$\tilde{u}(\xi, x_3) = \begin{bmatrix} \eta_1 & \eta_2 & \eta_1 x_3 \\ \eta_2 & -\eta_1 & \eta_2 x_3 \\ -i & 0 & -ix_3 + \frac{-i}{|\xi|}\frac{\lambda+3\mu}{\lambda+\mu} \end{bmatrix} \begin{bmatrix} A_1 \\ A_2 \\ A_3 \end{bmatrix} e^{-|\xi|x_3} \tag{7.136}$$

where A_1, A_2, A_3 are unknowns and

$$\eta = \xi/|\xi| \tag{7.137}$$

7.3.3 Describing Equations

To determine the unknown coefficient in the general solution (Equation (7.136)), we need to satisfy the boundary conditions (Equation (7.134) and (7.135)). What we need now is the transformed displacement field and stress field for the infinite media.

Displacement field is:

$$u_i = -\frac{b_i}{4\pi}\oint_C A_k dl_k + \frac{1}{8\pi}\oint_C \left(\epsilon_{ikl} b_l R_{,pp} + \frac{1}{1-\nu}\epsilon_{kmn} b_n R_{,mi}\right) dl_k \tag{7.138}$$

The derivative of the displacement field is:

$$\begin{aligned} u_{i,j} &= \frac{b_i \Omega_{,j}}{4\pi} + \frac{1}{8\pi}\oint_C \left[\epsilon_{ikl} b_l R_{,ppj} + \frac{1}{1-\nu}\epsilon_{kmn} b_n R_{,mij}\right] dl_k \\ &= -\frac{b_i}{8\pi}\oint_C \epsilon_{jkl} R_{,ppl} dl_k \\ &\quad + \frac{1}{8\pi}\oint_C \left[\epsilon_{ikl} b_l R_{,ppj} + \frac{1}{1-\nu}\epsilon_{kmn} b_n R_{,mij}\right] dl_k \\ &= \frac{1}{8\pi}\oint_C \left[-\epsilon_{jkl} b_i R_{,ppl} + \epsilon_{ikl} b_l R_{,ppj} + \frac{1}{1-\nu}\epsilon_{kmn} b_n R_{,mij}\right] dl_k \end{aligned} \tag{7.139}$$

So, we write:

$$u_i^{\infty} = -\frac{b_i}{4\pi} A_k + \frac{1}{8\pi}\epsilon_{ikl} b_l R_{,pp} + \frac{1}{8\pi}\frac{1}{1-\nu}\epsilon_{kmn} b_n R_{,mi} \tag{7.140}$$

and

$$u_{i,j}^{\infty} = \frac{1}{8\pi}\left[-\epsilon_{jkl} b_i R_{,ppl} + \epsilon_{ikl} b_l R_{,ppj} + \frac{1}{1-\nu}\epsilon_{kmn} b_n R_{,mij}\right] \tag{7.141}$$

Noticing that the first two terms in equation (7.140) are not related to material properties, i.e., they are continuous at the boundary, we can eliminate them from the boundary conditions. Define

$$u_i^{R\infty} = \frac{1}{8\pi}\frac{1}{1-\nu}\epsilon_{kmn} b_n R_{,mi} \tag{7.142}$$

and

$$u_i^{NR\infty} = u_i^{\infty} - u_i^{R\infty} \tag{7.143}$$

Now, the displacement boundary condition becomes as:

$$\triangle[\mathbf{u}^R]|_{x_3=0} = \mathbf{u}^{1R}|_{x_3=0} - \mathbf{u}^{2R}|_{x_3=0} = 0 \tag{7.144}$$

where $\mathbf{u}^{qR} = \mathbf{u}^{qI} + \mathbf{u}^{qR\infty}$. In the Fourier space, the B.C. is: The transformed displacement boundary conditions are:

$$\triangle[\tilde{\mathbf{u}}^R]|_{x_3=0} = \tilde{\mathbf{u}}^{1R}|_{x_3=0} - \tilde{\mathbf{u}}^{2R}|_{x_3=0} = 0 \tag{7.145}$$

where $\tilde{\mathbf{u}}^{qR} = \tilde{\mathbf{u}}^{qR\infty} + \tilde{\mathbf{u}}^{qI}$.

Relist the boundary conditions at $x_3 = 0$:

$$\begin{aligned} \triangle[\tilde{\mathbf{u}}^R] &= \tilde{\mathbf{u}}^{1R} - \tilde{\mathbf{u}}^{2R} \\ &= \tilde{\mathbf{u}}^{1R\infty} + \tilde{\mathbf{u}}^{1I} - \tilde{\mathbf{u}}^{2R\infty} - \tilde{\mathbf{u}}^{2I} = 0 \\ \triangle[\tilde{S}_{i3}] &= \tilde{S}^1_{i3} - \tilde{S}^2_{i3} \\ &= \tilde{S}^{1\infty}_{i3} + \tilde{S}^{1I}_{i3} - \tilde{S}^{2\infty}_{i3} - \tilde{S}^{2I}_{i3} = 0 \end{aligned} \tag{7.146}$$

i.e.,

$$\begin{aligned} \tilde{\mathbf{u}}^{1I} - \tilde{\mathbf{u}}^{2I} &= \tilde{\mathbf{u}}^{2R\infty} - \tilde{\mathbf{u}}^{1R\infty} = \triangle\tilde{\mathbf{u}}^{R\infty} \\ \tilde{S}^{1I}_{i3} - \tilde{S}^{2I}_{i3} &= \tilde{S}^{2\infty}_{i3} - \tilde{S}^{1\infty}_{i3} = \triangle\tilde{S}^{\infty}_{i3} \end{aligned} \tag{7.147}$$

Stress fourier transformation:

$$\begin{aligned} \tilde{S}_{i3} &= \int\int c_{i3kl} u_{k,l} e^{i(\xi_1 x_1 + \xi_2 x_2)} dx_1 dx_2 \\ &= c_{i3k3}\tilde{u}_{k,3} - i\xi_1 c_{i3k1}\tilde{u}_k - i\xi_2 c_{i3k2}\tilde{u}_k \end{aligned} \tag{7.148}$$

Substitute the general solution (equation (7.136)) and equation (7.148) into equation (7.147), we can finally get:

$$M_1 \cdot A = M_2 \tag{7.149}$$

where M_1 is a 6×6 matrix, $A = [A^1_1, A^1_2, A^1_3, A^2_1, A^2_2, A^2_3]^T$ is the unknown, and M_2 is 6×1 matrix as $[\triangle\tilde{u}^{R\infty}_1, \triangle\tilde{u}^{R\infty}_2, \triangle\tilde{u}^{R\infty}_3, \triangle\tilde{S}^{\infty}_{13}, \triangle\tilde{S}^{\infty}_{23}, \triangle\tilde{S}^{\infty}_{33}]^T$.

Thus, the solution of unknown is:

$$A = M_1^{-1} \cdot M_2 \tag{7.150}$$

So, we can express $\tilde{S}^i_{ij}$ by substitute A back to general solution. By applying inverse Fourier transformation, we can get the image stress field in the normal space.

7.3.4 Fourier Transformation of Infinite Solutions

To solve equation (7.150), we need to know the Fourier transformation of the infinite solution of displacement and stress fields.

Displacement fourier transformation:

$$\begin{aligned} \tilde{u}^{R\infty}_i &= \frac{1}{8\pi}\frac{1}{1-\nu}\epsilon_{kmn} b_n \int\int R_{,mi} e^{i(\xi_1 x_1 + \xi_2 x_2)} dx_1 dx_2 \\ &= \frac{1}{8\pi}\frac{1}{1-\nu}\epsilon_{kmn} b_n \tilde{R}_{mi} \end{aligned} \tag{7.151}$$

For infinite stress transformation:

$$\begin{aligned} \tilde{S}^{\infty}_{i3} &= \int\int c_{i3kl} u_{k,l} e^{i(\xi_1 x_1 + \xi_2 x_2)} dx_1 dx_2 \\ &= \frac{1}{8\pi}\int\int c_{i3kl}\left(-\epsilon_{lrs} b_k R_{,pps}\right. \end{aligned}$$

$$
\begin{aligned}
&+\epsilon_{krs}b_s R_{,ppl} + \frac{1}{1-\nu}\epsilon_{rmn}b_n R_{,mkl}\Big) e^{i(\xi_1 x_1+\xi_2 x_2)} dx_1 dx_2 \\
= \;& \frac{-c_{i3kl}\epsilon_{lrs}b_k}{8\pi}\int\int R_{,pps} e^{i(\xi_1 x_1+\xi_2 x_2)} dx_1 dx_2 + \frac{c_{i3kl}\epsilon_{krs}b_s}{8\pi}\int\int R_{,ppl} e^{i(\xi_1 x_1+\xi_2 x_2)} dx_1 dx_2 \\
& \frac{c_{i3kl}\epsilon_{rmn}b_n}{8\pi}\frac{1}{1-\nu}\int\int R_{,mkl} e^{i(\xi_1 x_1+\xi_2 x_2)} dx_1 dx_2 \\
= \;& \frac{-c_{i3kl}\epsilon_{lrs}b_k}{8\pi}\tilde{R}_{,pps} + \frac{c_{i3kl}\epsilon_{krs}b_s}{8\pi}\tilde{R}_{,ppl} + \frac{c_{i3kl}\epsilon_{rmn}b_n}{8\pi}\frac{1}{1-\nu}\tilde{R}_{,mkl}
\end{aligned} \tag{7.152}
$$

We have the following 3D Fourier transformation:

$$
\begin{aligned}
R &= \frac{1}{\pi^2}\int_V \frac{1}{\xi^4} e^{-i\xi\cdot\mathbf{R}} dV_\xi \\
&= \frac{1}{(2\pi)^3}\int_V \frac{-8\pi}{\xi^4} e^{-i\xi\cdot\mathbf{R}} dV_\xi \\
&= \frac{1}{(2\pi)^3}\int_V \tilde{r}(\xi) e^{-i\xi\cdot\mathbf{R}} dV_\xi \\
R_{,ij} &= \frac{1}{(2\pi)^3}\int_V -\xi_i\xi_j \frac{-8\pi}{\xi^4} e^{-i\xi\cdot\mathbf{R}} dV_\xi \\
&= \frac{1}{(2\pi)^3}\int_V \tilde{r}_{,ij}(\xi) e^{-i\xi\cdot\mathbf{R}} dV_\xi \\
R_{,ijk} &= \frac{1}{(2\pi)^3}\int_V \xi_i\xi_j\xi_k \frac{-8\pi}{\xi^4} e^{-i\xi\cdot\mathbf{R}} dV_\xi \\
&= \frac{1}{(2\pi)^3}\int_V \tilde{r}_{,ijk}(\xi) e^{-i\xi\cdot\mathbf{R}} dV_\xi
\end{aligned} \tag{7.153}
$$

A set of equations of Fourier transformation is needed and can be checked from the appendix. By integration w.r.t. ξ_3, we can get the 2D Fourier transformation of R as:

$$
\begin{aligned}
\tilde{R} &= \frac{1}{2\pi}\int_{-\infty}^{\infty} \tilde{r}(\xi) e^{-i\xi_3 x_3} d\xi_3 \\
\tilde{R}_{,ij} &= \frac{1}{2\pi}\int_{-\infty}^{\infty} \tilde{r}_{ij}(\xi) e^{-i\xi_3 x_3} d\xi_3 \\
\tilde{R}_{,ijk} &= \frac{1}{2\pi}\int_{-\infty}^{\infty} \tilde{r}_{ijk}(\xi) e^{-i\xi_3 x_3} d\xi_3
\end{aligned} \tag{7.154}
$$

By substitution of equation (7.154) into equation (7.151) and (7.152), we can get the Fourier transformation of the infinite solution of displacement and stress.

The 2D Fourier transformed residue displacement fields are:

$$
\begin{aligned}
\tilde{u}_1^{qR\infty} &= \frac{1}{8\pi}\frac{1}{1-\nu^q}\epsilon_{kmn}b_n\tilde{R}_{,m1} \\
&= \frac{1}{4}\frac{b_n}{1-\nu^q}\xi_1\Big[\epsilon_{k1n}\cdot\xi_1\Big[1-|\xi|(x_3-x_3^{'})\Big]\cdot\frac{1}{|\xi|^2} \\
&\quad +\epsilon_{k2n}\cdot\xi_2\Big[1-|\xi|(x_3-x_3^{'})\Big]\cdot\frac{1}{|\xi|^2} \\
&\quad +\epsilon_{k3n}\cdot\Big[-i(x_3-x_3^{'})\Big]\Big]\cdot\frac{e^{|\xi|(x_3-x_3^{'})}}{|\xi|}
\end{aligned} \tag{7.155}
$$

$$\begin{aligned}
\tilde{u}_2^{qR\infty} &= \frac{1}{8\pi}\frac{1}{1-\nu^q}\epsilon_{kmn}b_n\tilde{R}_{,m2} \\
&= \frac{1}{4}\frac{b_n}{1-\nu^q}\xi_2\Big[\epsilon_{k1n}\cdot\xi_1\Big[1-|\xi|(x_3-x_3^{'})\Big]\cdot\frac{1}{|\xi|^2} \\
&\quad +\epsilon_{k2n}\cdot\xi_2\Big[1-|\xi|(x_3-x_3^{'})\Big]\cdot\frac{1}{|\xi|^2} \\
&\quad +\epsilon_{k3n}\cdot\Big[-i(x_3-x_3^{'})\Big]\Big]\cdot\frac{e^{|\xi|(x_3-x_3^{'})}}{|\xi|} \qquad (7.156) \\
\tilde{u}_3^{qR\infty} &= \frac{1}{8\pi}\frac{1}{1-\nu^q}\epsilon_{kmn}b_n\tilde{R}_{,m3} \\
&= \frac{1}{4\pi}\frac{1}{1-\nu^q}b_n\Big[\epsilon_{k1n}\cdot\xi_1\Big[-i(x_3-x_3^{'})\Big]+\epsilon_{k2n}\cdot\xi_2\Big[-i(x_3-x_3^{'})\Big] \\
&\quad +\epsilon_{k3n}\Big[1+|\xi|(x_3-x_3^{'})\Big]\Big]\cdot\frac{e^{|\xi|(x_3-x_3^{'})}}{|\xi|} \qquad (7.157)
\end{aligned}$$

At $x_3=0$, we have:

$$\begin{aligned}
\tilde{u}_1^{qR\infty}(0) &= \frac{1}{4(1-\nu^q)}\xi_1\frac{e^{-|\xi|x_3^{'}}}{|\xi|}\Big[\xi_1(1+|\xi|x_3^{'})\cdot\frac{1}{|\xi|^2}(b2-b3) \\
&\quad +\xi_2(1+|\xi|x_3^{'})\cdot\frac{1}{|\xi|^2}(b3-b1)+x_3^{'}i(b1-b2)\Big] \\
&= \frac{e^{-|\xi|x_3^{'}}}{4(1-\nu^q)}\eta_1\Big[\eta_1(\frac{1}{|\xi|}+x_3^{'})(b2-b3) \\
&\quad +\eta_2(\frac{1}{|\xi|}+x_3^{'})(b3-b1)+x_3^{'}i(b1-b2)\Big] \qquad (7.158) \\
\tilde{u}_2^{qR\infty}(0) &= \frac{1}{4(1-\nu^q)}\xi_2\frac{e^{-|\xi|x_3^{'}}}{|\xi|}\Big[\xi_1(1+|\xi|x_3^{'})\cdot\frac{1}{|\xi|^2}(b2-b3) \\
&\quad +\xi_2(1+|\xi|x_3^{'})\cdot\frac{1}{|\xi|^2}(b3-b1)+x_3^{'}i(b1-b2)\Big] \\
&= \frac{e^{-|\xi|x_3^{'}}}{4(1-\nu^q)}\eta_2\Big[\eta_1(\frac{1}{|\xi|}+x_3^{'})(b2-b3) \\
&\quad +\eta_2(\frac{1}{|\xi|}+x_3^{'})(b3-b1)+x_3^{'}i(b1-b2)\Big] \qquad (7.159) \\
\tilde{u}_3^{qR\infty}(0) &= \frac{1}{4(1-\nu^q)}\frac{e^{-|\xi|x_3^{'}}}{|\xi|} \\
&\quad \Big[\xi_1x_3^{'}i(b_2-b_3)+\xi_2x_3^{'}i(b_3-b_1)+(1-|\xi|x_3^{'})(b_1-b_2)\Big] \\
&= \frac{e^{-|\xi|x_3^{'}}}{4(1-\nu^q)}\Big[\eta_1x_3^{'}i(b_2-b_3)+\eta_2x_3^{'}i(b_3-b_1)+(\frac{1}{|\xi|}-x_3^{'})(b_1-b_2)\Big] \qquad (7.160)
\end{aligned}$$

The 2D Fourier transformed stress fields are:

$$\tilde{S}_{13}^{q\infty} = \frac{1}{8\pi}\Big[-c_{13kl}^q\epsilon_{lrs}b_k\tilde{R}_{,pps}+c_{13kl}^q\epsilon_{krs}b_s\tilde{R}_{,ppl}+c_{13kl}^q\epsilon_{rmn}b_n\frac{1}{1-\nu^q}\tilde{R}_{,mkl}\Big]$$

$$
\begin{aligned}
&= \frac{\mu^q}{8\pi}\Big\{b_2\tilde{R}_{,pp1}+b_3\tilde{R}_{,pp2}-b_1\tilde{R}_{,pp2}-b_2\tilde{R}_{,pp3} \\
&\quad +\frac{2b_n}{1-\nu^q}(\epsilon_{r1n}\tilde{R}_{,131}+\epsilon_{r2n}\tilde{R}_{,231}+\epsilon_{r3n}\tilde{R}_{,331})\Big\} \qquad (7.161)\\
\tilde{S}^{q\infty}_{23} &= \frac{1}{8\pi}\left[-c^q_{13kl}\epsilon_{lrs}b_k\tilde{R}_{,pps}+c^q_{23kl}\epsilon_{krs}b_s\tilde{R}_{,ppl}+c^q_{23kl}\epsilon_{rmn}b_n\frac{1}{1-\nu^q}\tilde{R}_{,mkl}\right] \\
&= \frac{\mu^q}{8\pi}\Big\{b_2\tilde{R}_{,pp1}+b_1\tilde{R}_{,pp3}-b_3\tilde{R}_{,pp1}-b_1\tilde{R}_{,pp2} \\
&\quad +\frac{2b_n}{1-\nu^q}(\epsilon_{r1n}\tilde{R}_{,123}+\epsilon_{r2n}\tilde{R}_{,223}+\epsilon_{r3n}\tilde{R}_{,323})\Big\} \qquad (7.162)\\
\tilde{S}^{q\infty}_{33} &= \frac{1}{8\pi}\Big\{\tilde{R}_{,pp1}\left[2(\lambda+\mu)b_3-2\lambda b_2+\frac{\lambda}{1-\nu}(b_2-b_3)\right] \\
&\quad +\tilde{R}_{,pp2}\left[2\lambda b_1-2(\lambda+\mu)b_3+\frac{\lambda}{1-\nu}(b_3-b_1)\right] \\
&\quad +\tilde{R}_{,pp3}\left[-2(\lambda+\mu)b_1+2(\lambda+\mu)b_2+\frac{\lambda}{1-\nu}(b_1-b_2)\right] \\
&\quad +\frac{2\mu}{1-\nu}\left[\tilde{R}_{,133}(b_2-b_3)+\tilde{R}_{,233}(b_3-b_1)+\tilde{R}_{,333}(b_1-b_2)\right]\Big\} \qquad (7.163)
\end{aligned}
$$

At $x_3=0$, we have:

$$
\begin{aligned}
\tilde{S}^{q\infty}_{13}(0) &= \frac{\mu^q}{8\pi}e^{-|\xi|x_3^{'}}|\xi|\left\{\frac{1}{|\xi|}(-4\pi ib_2\eta_1-4\pi ib_3\eta_2+4\pi ib_1\eta_2-4\pi b_2)\right. \\
&\quad \left.+\frac{2\eta_1}{1-\nu^q}\left[2\pi\eta_2x_3^{'}(b_3-b_1)+2\pi\eta_1x_3^{'}(b_2-b_3)-2\pi i(\frac{1}{|\xi|}-x_3^{'})(b_1-b_2)\right]\right\} \qquad (7.164)\\
\tilde{S}^{q\infty}_{23}(0) &= \frac{\mu^q}{8\pi}e^{-|\xi|x_3^{'}}|\xi|\left\{\frac{1}{|\xi|}(-4\pi ib_2\eta_1+4\pi b_1+4\pi ib_3\eta_1+4\pi ib_1\eta_2)\right. \\
&\quad \left.+\frac{2\eta_2}{1-\nu^q}\left[2\pi\eta_1x_3^{'}(b_2-b_3)+2\pi\eta_2x_3^{'}(b_3-b_1)-2\pi i(\frac{1}{|\xi|}-x_3^{'})(b_1-b_2)\right]\right\} \qquad (7.165)\\
\tilde{S}^{q\infty}_{33}(0) &= \frac{e^{-|\xi|x_3^{'}}}{2}|\xi|\left\{\frac{1}{|\xi|}\left(-i\eta_1\left[2(\lambda+\mu)b_3-2\lambda b_2+\frac{\lambda}{1-\nu}(b_2-b_3)\right]\right.\right. \\
&\quad -i\eta_2\left[2\lambda b_1-2(\lambda+\mu)b_2+\frac{\lambda}{1-\nu}(b_3-b_1)\right] \\
&\quad \left.\left.+\left[-2(\lambda+\mu)b_1+2(\lambda+\mu)b_2+\frac{\lambda}{1-\nu}(b_1-b_2)\right]\right) \\
&\quad +\frac{\mu}{1-\nu}\left[-i\eta_1(\frac{1}{|\xi|}-x_3^{'})(b_2-b_3)-i\eta_2(\frac{1}{|\xi|}-x_3^{'})(b_3-b_1)\right. \\
&\quad \left.+(\frac{2}{|\xi|}-x_3^{'})(b_1-b_2)\right]\Big\} \qquad (7.166)
\end{aligned}
$$

Determination of The Unknowns in General Solution

In previous, we have formulated the equation from which we can determine the unknowns in the general solution. We need two matrix, which are called $[M_1]$ and $[M_2]$.

By substitute the general solution and the Fourier transformation of the infinite solution into the boundary conditions, we have following matrix equations from equation (7.150):

$$\begin{bmatrix} \eta_1 & \eta_2 & 0 & -\eta_1 & -\eta_2 & 0 \\ \eta_2 & -\eta_1 & 0 & -\eta_2 & \eta_1 & 0 \\ -i & 0 & -i\chi_3^1 & i & 0 & i\chi_3^2 \\ -2\mu^1\eta_1 & -\mu^1\eta_2 & -2\chi_1^1\eta_1\frac{1}{|\xi|} & 2\mu^2\eta_1 & \mu^2\eta_2 & 2\chi_1^2\eta_1\frac{1}{|\xi|} \\ -2\mu^1\eta_2 & \mu^1\eta_1 & -2\chi_1^1\eta_2\frac{1}{|\xi|} & 2\mu^2\eta_2 & -\mu^2\eta_1 & 2\chi_1^2\eta_2\frac{1}{|\xi|} \\ 2\mu^1 i & 0 & -2\chi_2^1 i\frac{1}{|\xi|} & -2\mu^2 i & 0 & 2\chi_2^2 i\frac{1}{|\xi|} \end{bmatrix} \begin{bmatrix} A_1^1 \\ A_2^1 \\ A_3^1 \\ A_1^2 \\ A_2^2 \\ A_3^2 \end{bmatrix} = \begin{bmatrix} \Delta\tilde{u}_1^{\infty R}(0) \\ \Delta\tilde{u}_2^{\infty R}(0) \\ \Delta\tilde{u}_3^{\infty R}(0) \\ \frac{1}{|\xi|}\Delta\tilde{S}_{13}^{\infty}(0) \\ \frac{1}{|\xi|}\Delta\tilde{S}_{23}^{\infty}(0) \\ \frac{1}{|\xi|}\Delta\tilde{S}_{33}^{\infty}(0) \end{bmatrix} \tag{7.167}$$

Where super-index means index of material. And χ_1, χ_2, and χ_3 are defined as:

$$\begin{aligned} \chi_1^q &= \frac{(\mu^q)^2}{\lambda^q + \mu^q} \\ \chi_2^q &= \frac{2\mu^q(\lambda^q + 2\mu^q)}{\lambda^q + \mu^q} \\ \chi_3^q &= \frac{\lambda^q + 3\mu^q}{\lambda^q + \mu^q} \end{aligned} \tag{7.168}$$

Here, $[M_1]$ is the 6×6 matrix, and $[M_2]$ is the right-side matrix. We found that $[M_1]$ can be written as the product of two matrixes, one is $[M_{11}]$ which is a function of η_1 and η_2, i.e., the angle if we use polar coordinates; and the other is $[M_{12}]$ which is a function of $|\xi|$. The two matrixes can be expressed as:

$$[M_{11}] = \begin{bmatrix} \eta_1 & \eta_2 & 0 & -\eta_1 & -\eta_2 & 0 \\ \eta_2 & -\eta_1 & 0 & -\eta_2 & \eta_1 & 0 \\ -i & 0 & -i\chi_3^1 & i & 0 & i\chi_3^2 \\ -2\mu^1\eta_1 & -\mu^1\eta_2 & -2\chi_1^1\eta_1 & 2\mu^2\eta_1 & \mu^2\eta_2 & 2\chi_1^2\eta_1 \\ -2\mu^1\eta_2 & \mu^1\eta_1 & -2\chi_1^1\eta_2 & 2\mu^2\eta_2 & -\mu^2\eta_1 & 2\chi_1^2\eta_2 \\ 2\mu^1 i & 0 & -2\chi_2^1 i & -2\mu^2 i & 0 & 2\chi_2^2 i \end{bmatrix} \tag{7.169}$$

And

$$[M_{12}] = \begin{bmatrix} 1 & 0 & 0 & 0 & 0 & 0 \\ 0 & 1 & 0 & 0 & 0 & 0 \\ 0 & 0 & \frac{1}{|\xi|} & 0 & 0 & 0 \\ 0 & 0 & 0 & 1 & 0 & 0 \\ 0 & 0 & 0 & 0 & 1 & 0 \\ 0 & 0 & 0 & 0 & 0 & \frac{1}{|\xi|} \end{bmatrix} \tag{7.170}$$

Also, we found $[M_2]$ can be written as:

$$[M_2] = e^{-|\xi|x_3^{'}}[M_2^{'}] \tag{7.171}$$

Thus,We have:

$$\begin{aligned} [A] &= [M_1]^{-1}[M_2] = \left([M_{11}] \cdot [M_{12}]\right)^{-1}[M_2] \\ &= [M_{12}]^{-1} \cdot [M_{11}]^{-1} \cdot [M_2] \end{aligned} \tag{7.172}$$

We have:

$$[M_{12}]^{-1} = \begin{bmatrix} 1 & 0 & 0 & 0 & 0 & 0 \\ 0 & 1 & 0 & 0 & 0 & 0 \\ 0 & 0 & |\xi| & 0 & 0 & 0 \\ 0 & 0 & 0 & 1 & 0 & 0 \\ 0 & 0 & 0 & 0 & 1 & 0 \\ 0 & 0 & 0 & 0 & 0 & |\xi| \end{bmatrix} = [I] + \begin{bmatrix} 0 & 0 & 0 & 0 & 0 & 0 \\ 0 & 0 & 0 & 0 & 0 & 0 \\ 0 & 0 & |\xi|-1 & 0 & 0 & 0 \\ 0 & 0 & 0 & 0 & 0 & 0 \\ 0 & 0 & 0 & 0 & 0 & 0 \\ 0 & 0 & 0 & 0 & 0 & |\xi|-1 \end{bmatrix} \tag{7.173}$$

where $[I]$ is the unit matrix. Define

$$[M_{12}^{'}] = \begin{bmatrix} 0 & 0 & 0 & 0 & 0 & 0 \\ 0 & 0 & 0 & 0 & 0 & 0 \\ 0 & 0 & 1 & 0 & 0 & 0 \\ 0 & 0 & 0 & 0 & 0 & 0 \\ 0 & 0 & 0 & 0 & 0 & 0 \\ 0 & 0 & 0 & 0 & 0 & 1 \end{bmatrix} \tag{7.174}$$

We have

$$[M_{12}]^{-1} = [I] + (|\xi| - 1)[M_{12}^{'}] \tag{7.175}$$

and we can write $[A]$ as:

$$\begin{aligned} [A] &= [M_1]^{-1}[M_2] = [M_{12}]^{-1}[M_{11}]^{-1}[M_2] = ([I] + (|\xi| - 1)[M_{12}^{'}])[M_{11}]^{-1}[M_2] \\ &= [M_{11}]^{-1}[M_2] + (|\xi| - 1)[M_{12}^{'}][M_{11}]^{-1}[M_2] \\ &= e^{-|\xi|x_3^{'}}\left\{[M_{11}]^{-1}[M_2^{'}] + (|\xi| - 1)[M_{12}^{'}][M_{11}]^{-1}[M_2^{'}]\right\} \end{aligned} \tag{7.176}$$

Image Stress in Fourier Space

In the Fourier space, the image stress can be expressed as:

$$\begin{aligned}
\tilde{S}^I_{ij} &= C_{ijkl}\tilde{u}^I_{k,l} \\
&= C_{ijk1}\tilde{u}^I_{k,1} + C_{ijk2}\tilde{u}^I_{k,2} + C_{ijk3}\tilde{u}^I_{k,3} \\
&= -i\xi_1 C_{ijk1}\tilde{u}^I_k - i\xi_2 C_{ijk2}\tilde{u}^I_k + C_{ijk3}\tilde{u}^I_{k,3} \\
&= C_{ijk3}\tilde{u}^I_{k,3} - (i\xi_1 C_{ijk1} + i\xi_2 C_{ijk2})\tilde{u}^I_k \\
&= C_{ijk3}\left(-|\xi|\tilde{u}^I_k + A_3\begin{pmatrix}\eta_1\\ \eta_2\\ -i\end{pmatrix}e^{-|\xi|x_3}\right) - (i\xi_1 C_{ijk1} + i\xi_2 C_{ijk2})\tilde{u}^I_k \\
&= -\left(C_{ijk3}|\xi| + i\xi_1 C_{ijk1} + i\xi_2 C_{ijk2}\right)\tilde{u}^I_k + C_{ijk3}A_3\begin{pmatrix}\eta_1\\ \eta_2\\ -i\end{pmatrix}e^{-|\xi|x_3} \\
&= -\left(C_{ijk3}|\xi| + i\xi_1 C_{ijk1} + i\xi_2 C_{ijk2}\right)A_1\begin{pmatrix}\eta_1\\ \eta_2\\ -i\end{pmatrix}e^{-|\xi|x_3} \\
&\quad -\left(C_{ijk3}|\xi| + i\xi_1 C_{ijk1} + i\xi_2 C_{ijk2}\right)A_2\begin{pmatrix}\eta_2\\ -\eta_1\\ 0\end{pmatrix}e^{-|\xi|x_3} \\
&\quad -\left(C_{ijk3}|\xi| + i\xi_1 C_{ijk1} + i\xi_2 C_{ijk2}\right)A_3\left[\begin{pmatrix}\eta_1\\ \eta_2\\ -i\end{pmatrix}x_3 + \frac{1}{|\xi|}\chi_3\begin{pmatrix}0\\ 0\\ -i\end{pmatrix}\right]e^{-|\xi|x_3} \\
&\quad +C_{ijk3}A_3\begin{pmatrix}\eta_1\\ \eta_2\\ -i\end{pmatrix}e^{-|\xi|x_3}
\end{aligned} \tag{7.177}$$

If we define:

$$\begin{aligned}
P_k &= C_{ijk3}|\xi| + i\xi_1 C_{ijk1} + i\xi_2 C_{ijk2} \\
&= |\xi|\left(C_{ijk3} + i\eta_1 C_{ijk1} + i\eta_2 C_{ijk2}\right) \\
&= |\xi| Q_k
\end{aligned} \tag{7.178}$$

Then:

$$\begin{aligned}
\tilde{S}^I_{ij} &= -P_k\begin{pmatrix}\eta_1\\ \eta_2\\ -i\end{pmatrix}A_1 e^{-|\xi|x_3} - P_k\begin{pmatrix}\eta_2\\ -\eta_1\\ 0\end{pmatrix}A_2 e^{-|\xi|x_3} \\
&\quad -P_k\left[\begin{pmatrix}\eta_1\\ \eta_2\\ i\end{pmatrix}x_3 + \frac{1}{|\xi|}\chi_3\begin{pmatrix}0\\ 0\\ -i\end{pmatrix}\right]A_3 e^{-|\xi|x_3} + C_{ijk3}\begin{pmatrix}\eta_1\\ \eta_2\\ -i\end{pmatrix}A_3 e^{-|\xi|x_3} \\
&= \left\{-P_k\begin{pmatrix}\eta_1\\ \eta_2\\ -i\end{pmatrix}A_1 - P_k\begin{pmatrix}\eta_2\\ -\eta_1\\ 0\end{pmatrix}A_2\right. \\
&\quad \left. -A_3\left[P_k\left[\begin{pmatrix}\eta_1\\ \eta_2\\ -i\end{pmatrix}x_3 + \frac{1}{|\xi|}\chi_3\begin{pmatrix}0\\ 0\\ -i\end{pmatrix}\right] - C_{ijk3}\begin{pmatrix}\eta_1\\ \eta_2\\ -i\end{pmatrix}\right]\right\}e^{-|\xi|x_3}
\end{aligned}$$

$$
\begin{aligned}
&= e^{-|\xi|x_3}\begin{bmatrix} -P_k\begin{pmatrix}\eta_1\\ \eta_2\\ -i\end{pmatrix} \\ -P_k\begin{pmatrix}\eta_2\\ -\eta_1\\ 0\end{pmatrix} \\ -\left(P_k x_3 - C_{ijk3}\right)\begin{pmatrix}\eta_1\\ \eta_2\\ -i\end{pmatrix} - \frac{\chi_3 P_k}{|\xi|}\begin{pmatrix}0\\ 0\\ -i\end{pmatrix}\end{bmatrix}^T \begin{bmatrix}A_1\\ A_2\\ A_3\end{bmatrix} \\
&= e^{-|\xi|x_3}\left(\begin{bmatrix} -P_k\begin{pmatrix}\eta_1\\ \eta_2\\ -i\end{pmatrix} \\ -P_k\begin{pmatrix}\eta_2\\ -\eta_1\\ 0\end{pmatrix} \\ -P_k x_3\begin{pmatrix}\eta_1\\ \eta_2\\ -i\end{pmatrix}\end{bmatrix}^T + \begin{bmatrix} 0\\ 0\\ C_{ijk3}\begin{pmatrix}\eta_1\\ \eta_2\\ -i\end{pmatrix} - \frac{\chi_3 P_k}{|\xi|}\begin{pmatrix}0\\ 0\\ -i\end{pmatrix}\end{bmatrix}^T\right)\begin{bmatrix}A_1\\ A_2\\ A_3\end{bmatrix} \\
&= e^{-|\xi|x_3}\left(\begin{bmatrix} -Q_k\begin{pmatrix}\eta_1\\ \eta_2\\ -i\end{pmatrix} \\ -Q_k\begin{pmatrix}\eta_2\\ -\eta_1\\ 0\end{pmatrix} \\ -Q_k x_3\begin{pmatrix}\eta_1\\ \eta_2\\ -i\end{pmatrix}\end{bmatrix}^T + \begin{bmatrix} 0\\ 0\\ C_{ijk3}\begin{pmatrix}\eta_1\\ \eta_2\\ -i\end{pmatrix} - \chi_3 Q_k\begin{pmatrix}0\\ 0\\ -i\end{pmatrix}\end{bmatrix}^T\right)\begin{bmatrix}A_1\\ A_2\\ A_3\end{bmatrix} \\
&= e^{-|\xi|x_3}\left(|\xi|[M_3] + [M_4]\right)[A] \qquad (7.179)
\end{aligned}
$$

where

$$
[M_3] = \begin{bmatrix} -Q_k\begin{pmatrix}\eta_1\\ \eta_2\\ -i\end{pmatrix} \\ -Q_k\begin{pmatrix}\eta_2\\ -\eta_1\\ 0\end{pmatrix} \\ -Q_k x_3\begin{pmatrix}\eta_1\\ \eta_2\\ -i\end{pmatrix}\end{bmatrix}^T \qquad (7.180)
$$

and

$$[M_4] = \begin{bmatrix} 0 \\ 0 \\ C_{ijk3}\begin{pmatrix}\eta_1\\ \eta_2\\ -i\end{pmatrix} - \chi_3 Q_k \begin{pmatrix}0\\0\\-i\end{pmatrix} \end{bmatrix}^T \tag{7.181}$$

Recall equation (7.176) and substitute it into equation (7.179), we have:

$$\begin{aligned}
\tilde{S}^I_{ij} &= e^{-|\xi|x_3}\left(|\xi|[M_3]+[M_4]\right)[A] \\
&= e^{-|\xi|(x_3+x_3^{'})}\left(|\xi|[M_3]+[M_4]\right)\left([M_{11}]^{-1}[M_2^{'}]+(|\xi|-1)[M_{12}^{'}][M_{11}]^{-1}[M_2^{'}]\right) \\
&= e^{-|\xi|(x_3+x_3^{'})}\Big\{[M_3][M_{11}]^{-1}[M_2^{'}]|\xi|+[M_3][M_{12}^{'}][M_{11}]^{-1}[M_2^{'}]|\xi|(|\xi|-1) \\
&\quad +[M_4][M_{11}]^{-1}[M_2^{'}]+[M_4][M_{12}^{'}][M_{11}]^{-1}[M_2^{'}](|\xi|-1)\Big\}
\end{aligned} \tag{7.182}$$

Image Stress From Inverse Fourier Transformation

In equation (7.182), $[M_3]$, $[M_4]$, and $[M_{11}]^{-1}$ are functions of angle related variables(η_1 and η_2), $[M_{12}^{'}]$ is a constant matrix, $[M_2^{'}]$ depends on both angle and length (i.e., η_1, η_2, and $|\xi|$). Thus we can obtain the image stress expression by inverse Fourier transformation as:

$$\begin{aligned}
S^I_{ij} &= \frac{1}{4\pi^2}\int\int \tilde{S}^I_{ij}e^{-i(\xi_1x_1+\xi_2x_2)}d\xi_1 d\xi_2 \\
&= \frac{1}{4\pi^2}\int_0^{2\pi}\int_0^{\infty}\tilde{S}^I_{ij}e^{-|\xi|(ix_1\cos\theta+ix_2\sin\theta)}|\xi|d|\xi|d\theta \\
&= \frac{1}{4\pi^2}\int_0^{2\pi}\int_0^{\infty}\Big\{[M_3][M_{11}]^{-1}[M_2^{'}]|\xi|+[M_3][M_{12}^{'}][M_{11}]^{-1}[M_2^{'}]|\xi|(|\xi|-1) \\
&\quad +[M_4][M_{11}]^{-1}[M_2^{'}]+[M_4][M_{12}^{'}][M_{11}]^{-1}[M_2^{'}](|\xi|-1)\Big\}e^{-|\xi|a}|\xi|d|\xi|d\theta \\
&= \frac{1}{4\pi^2}\int_0^{2\pi}\left\{[M_3][M_{11}]^{-1}\int_0^{\infty}[M_2^{'}]|\xi|^2e^{-|\xi|a}d|\xi|\right\}d\theta \\
&\quad +\frac{1}{4\pi^2}\int_0^{2\pi}\left\{[M_3][M_{12}^{'}][M_{11}]^{-1}\int_0^{\infty}[M_2^{'}]|\xi|^2(|\xi|-1)e^{-|\xi|a}d|\xi|\right\}d\theta \\
&\quad +\frac{1}{4\pi^2}\int_0^{2\pi}\left\{[M_4][M_{11}]^{-1}\int_0^{\infty}[M_2^{'}]|\xi|e^{-|\xi|a}d|\xi|\right\}d\theta \\
&\quad +\frac{1}{4\pi^2}\int_0^{2\pi}\left\{[M_4][M_{12}^{'}][M_{11}]^{-1}\int_0^{\infty}[M_2^{'}]|\xi|(|\xi|-1)e^{-|\xi|a}d|\xi|\right\}d\theta
\end{aligned} \tag{7.183}$$

where $a = x_3 + x_3^{'} + i\cos\theta x_1 + i\sin\theta x_2$, $\cos\theta = \eta_1 = \frac{\xi_1}{|\xi|}$, and $\sin\theta = \eta_2 = \frac{\xi_2}{|\xi|}$.

Thus, by integrating from 0 to ∞ over $|\xi|$ out, we have only one integration left for θ, this integration can be done by numerical method very easily and it is not time consuming. So, finally, we get a line integration for the image stresses from the surface.

If we define some new matrixes as:

$$\begin{aligned}
[M_{21}] &= \int_0^\infty [M_2^{'}]|\xi|^2 e^{-|\xi|a} d|\xi| \\
[M_{22}] &= \int_0^\infty [M_2^{'}]|\xi|^2 (|\xi|-1) e^{-|\xi|a} d|\xi| \\
[M_{23}] &= \int_0^\infty [M_2^{'}]|\xi| e^{-|\xi|a} d|\xi| \\
[M_{24}] &= \int_0^\infty [M_2^{'}]|\xi| (|\xi|-1) e^{-|\xi|a} d|\xi|
\end{aligned} \tag{7.184}$$

Then, we can write equation (7.183) as:

$$\begin{aligned}
S_{ij}^I &= \frac{1}{4\pi^2}\int_0^{2\pi} \left\{[M_3][M_{11}]^{-1}[M_{21}]\right\} d\theta \\
&\quad + \frac{1}{4\pi^2}\int_0^{2\pi} \left\{[M_3][M_{12}^{'}][M_{11}]^{-1}[M_{22}]\right\} d\theta \\
&\quad + \frac{1}{4\pi^2}\int_0^{2\pi} \left\{[M_4][M_{11}]^{-1}[M_{23}]\right\} d\theta \\
&\quad + \frac{1}{4\pi^2}\int_0^{2\pi} \left\{[M_4][M_{12}^{'}][M_{11}]^{-1}[M_{24}]\right\} d\theta
\end{aligned} \tag{7.185}$$

7.3.5 Determination of Solution Matrices

In above section, we have got the expression of the image stresses. Now the only thing that we need for the complete final expression is to determine the four new defined matrixes, M_{21}, M_{22}, M_{23}, M_{24}. Following we will begin to derive the exact forms of these matrixes.

As derived before, we have:

$$[M_2] = e^{-|\xi|x_3^{'}}[M_2^{'}] \tag{7.186}$$

If we define the six elements of matrix $[M_2^{'}]$ as $[M_2^{'}]_1$ to $[M_2^{'}]_6$, we find they are in the form as following:

$$\begin{aligned}
\left[M_2^{'}\right]_1 &= \delta\left(\frac{1}{4(1-\nu)}\right)\left\{\eta_1\left[\eta_1\left(\frac{1}{|\xi|}+x_3^{'}\right)(b_2-b_3)\right.\right. \\
&\quad \left.\left. +\eta_2\left(\frac{1}{|\xi|}+x_3^{'}\right)(b_3-b_1)+x_3^{'}i(b_1-b_2)\right]\right\} \\
\left[M_2^{'}\right]_2 &= \delta\left(\frac{1}{4(1-\nu)}\right)\left\{\eta_2\left[\eta_1\left(\frac{1}{|\xi|}+x_3^{'}\right)(b_2-b_3)\right.\right.
\end{aligned}$$

$$
\begin{aligned}
&+\eta_2\left(\frac{1}{|\xi|}+x_3^{'}\right)(b_3-b_1)+x_3^{'}i(b_1-b_2)\Big]\Big\}\\
\left[M_2^{'}\right]_3 &= \delta\left(\frac{1}{4(1-\nu)}\right)\left[\eta_1 x_3^{'}i(b_2-b_3)+\eta_2 x_3^{'}i(b_3-b_1)+\left(\frac{1}{|\xi|}-x_3^{'}\right)(b_1-b_2)\right]\\
\left[M_2^{'}\right]_4 &= \frac{1}{2}\left\{\frac{\delta(\mu)}{|\xi|}(-ib_2\eta_1-ib_3\eta_2+ib_1\eta_2-b_2)+\delta\left(\frac{\mu}{1-\nu}\right)\eta_1\Big[\eta_2 x_3^{'}(b_3-b_1)\right.\\
&\left.+\eta_1 x_3^{'}(b_2-b_3)-i\left(\frac{1}{|\xi|}-x_3^{'}\right)(b_1-b_2)\Big]\right\}\\
\left[M_2^{'}\right]_5 &= \frac{1}{2}\left\{\frac{\delta(\mu)}{|\xi|}(-ib_2\eta_1+ib_3\eta_1+ib_1\eta_2+b_1)+\delta\left(\frac{\mu}{1-\nu}\right)\eta_2\Big[\eta_2 x_3^{'}(b_3-b_1)\right.\\
&\left.+\eta_1 x_3^{'}(b_2-b_3)-i\left(\frac{1}{|\xi|}-x_3^{'}\right)(b_1-b_2)\Big]\right\}\\
\left[M_2^{'}\right]_6 &= \frac{1}{2}\frac{1}{|\xi|}\left\{-i\eta_1\left[\delta\left(\frac{2\nu-1}{1-\nu}\lambda\right)(b_2-b_3)+2\delta(\mu)\,b_3\right]\right.\\
&-i\eta_2\left[\delta\left(\frac{2\nu-1}{1-\nu}\lambda\right)(b_3-b_1)-2\delta(\mu)\,b_3\right]\\
&\left.+\left[\delta\left(\frac{2\nu-1}{1-\nu}\lambda\right)(b_1-b_2)+2\delta(\mu)\,(b_2-b_1)\right]\right\}\\
&-\frac{i}{2}\delta\left(\frac{\mu}{1-\nu}\right)\left[\eta_1\left(\frac{1}{|\xi|}-x_3^{'}\right)(b_2-b_3)+\eta_2\left(\frac{1}{|\xi|}-x_3^{'}\right)(b_3-b_1)\right.\\
&\left.-i\left(\frac{2}{|\xi|}-x_3^{'}\right)(b_1-b_2)\right]
\end{aligned}
\tag{7.187}
$$

where items like $\delta(\mu)$ means it is a difference value of this item between two materials, defined as $\delta(\mu)=\mu^1-\mu^2$.

As defined in equation (7.184), the integrations we need to perform over $|\xi|$ can be easily done because they are all in forms like:

$$\int_0^\infty |\xi|^n e^{-a|\xi|}d|\xi|=\frac{n!}{a^{n+1}} \tag{7.188}$$

Thus, we have obtained $[M_{21}]$, $[M_{22}]$, $[M_{23}]$, and $[M_{24}]$ (for exact forms of these matrixes, please see the appendix). By doing another numerical integration over θ, we finally obtained the line integration expression for the image stresses from a bi-material interface.

7.3.6 Fourier Transform Details

Lists of Several Fourier Transformations

During the Fourier transformation of infinite solutions in section (7.3.4), we used several of the following formulations:

$$\frac{1}{2\pi}\int_{-\infty}^{\infty}\frac{e^{-i\varsigma z}}{|\xi|^2+\varsigma^2}d\varsigma = \frac{e^{|\xi|z}}{2|\xi|}=\frac{e^{|\xi|(x_3-x_3^{'})}}{2|\xi|} \tag{7.189}$$

$$\frac{1}{2\pi}\int_{-\infty}^{\infty}\frac{e^{-i\varsigma z}}{(|\xi|^2+\varsigma^2)^2}d\varsigma = (1-|\xi|z)\frac{e^{|\xi|z}}{4|\xi|^3} = \left[1-|\xi|(x_3-x_3^{'})\right]\frac{e^{|\xi|(x_3-x_3^{'})}}{4|\xi|^3} \tag{7.190}$$

$$\frac{1}{2\pi}\int_{-\infty}^{\infty}\frac{\varsigma e^{-i\varsigma z}}{(|\xi|^2+\varsigma^2)^2}d\varsigma = -iz\frac{e^{|\xi|z}}{4|\xi|} = -i(x_3-x_3^{'})\frac{e^{|\xi|(x_3-x_3^{'})}}{4|\xi|} \tag{7.191}$$

$$\frac{1}{2\pi}\int_{-\infty}^{\infty}\frac{\varsigma^2 e^{-i\varsigma z}}{(|\xi|^2+\varsigma^2)^2}d\varsigma = (1+|\xi|z)\frac{e^{|\xi|z}}{4|\xi|} = \left[1+|\xi|(x_3-x_3^{'})\right]\frac{e^{|\xi|(x_3-x_3^{'})}}{4|\xi|} \tag{7.192}$$

$$\frac{1}{2\pi}\int_{-\infty}^{\infty}\frac{\varsigma e^{-i\varsigma z}}{|\xi|^2+\varsigma^2}d\varsigma = i\frac{e^{|\xi|z}}{2} = i\frac{e^{|\xi|(x_3-x_3^{'})}}{2} \tag{7.193}$$

$$\frac{1}{2\pi}\int_{-\infty}^{\infty}\frac{\varsigma^3 e^{-i\varsigma z}}{(|\xi|^2+\varsigma^2)^2}d\varsigma = i\left[\frac{1}{2}+\frac{|\xi|z}{4}\right]e^{|\xi|z} = i\left[\frac{1}{2}+\frac{|\xi|(x_3-x_3^{'})}{4}\right]e^{|\xi|(x_3-x_3^{'})} \tag{7.194}$$

Exact forms of Four Matrices

The four integrated out matrixes can be obtained through the method described in above section. Here we give the exact forms. Define the element of the matrix as $[M]_j$, where $j = 1, 6$.

For $[M_{21}]$, we have:

$$\begin{aligned}
[M_{21}]_1 &= \delta\left(\frac{1}{4(1-\nu)}\right)\left\{\eta_1\left[\eta_1\left(\frac{1}{a^2}+x_3^{'}\frac{2}{a^3}\right)(b_2-b_3)\right.\right.\\
&\quad\left.\left.+\eta_2\left(\frac{1}{a^2}+x_3^{'}\frac{2}{a^3}\right)(b_3-b_1)+x_3^{'}i(b_1-b_2)\frac{2}{a^3}\right]\right\}\\
[M_{21}]_2 &= \delta\left(\frac{1}{4(1-\nu)}\right)\left\{\eta_2\left[\eta_1\left(\frac{1}{a^2}+x_3^{'}\frac{2}{a^3}\right)(b_2-b_3)\right.\right.\\
&\quad\left.\left.+\eta_2\left(\frac{1}{a^2}+x_3^{'}\frac{2}{a^3}\right)(b_3-b_1)+x_3^{'}i(b_1-b_2)\frac{2}{a^3}\right]\right\}\\
[M_{21}]_3 &= \delta\left(\frac{1}{4(1-\nu)}\right)\left[\eta_1 x_3^{'}i(b_2-b_3)\frac{2}{a^3}+\eta_2 x_3^{'}i(b_3-b_1)\frac{2}{a^3}+\left(\frac{1}{a^2}-x_3^{'}\frac{2}{a^3}\right)(b_1-b_2)\right]\\
[M_{21}]_4 &= \frac{1}{2}\left\{\frac{\delta(\mu)}{a^2}(-ib_2\eta_1-ib_3\eta_2+ib_1\eta_2-b_2)+\delta\left(\frac{\mu}{1-\nu}\right)\eta_1\left[\eta_2 x_3^{'}(b_3-b_1)\frac{2}{a^3}\right.\right.\\
&\quad\left.\left.+\eta_1 x_3^{'}(b_2-b_3)\frac{2}{a^3}-i\left(\frac{1}{a^2}-x_3^{'}\frac{2}{a^3}\right)(b_1-b_2)\right]\right\}\\
[M_{21}]_5 &= \frac{1}{2}\left\{\frac{\delta(\mu)}{a^2}(-ib_2\eta_1+ib_3\eta_1+ib_1\eta_2+b_1)+\delta\left(\frac{\mu}{1-\nu}\right)\eta_2\left[\eta_2 x_3^{'}(b_3-b_1)\frac{2}{a^3}\right.\right.\\
&\quad\left.\left.+\eta_1 x_3^{'}(b_2-b_3)\frac{2}{a^3}-i\left(\frac{1}{a^2}-x_3^{'}\frac{2}{a^3}\right)(b_1-b_2)\right]\right\}\\
[M_{21}]_6 &= \frac{1}{2}\frac{1}{a^2}\left\{-i\eta_1\left[\delta\left(\frac{2\nu-1}{1-\nu}\lambda\right)(b_2-b_3)+2\delta(\mu)b_3\right]\right.\\
&\quad -i\eta_2\left[\delta\left(\frac{2\nu-1}{1-\nu}\lambda\right)(b_3-b_1)-2\delta(\mu)b_3\right]\\
&\quad \left.+\left[\delta\left(\frac{2\nu-1}{1-\nu}\lambda\right)(b_1-b_2)+2\delta(\mu)(b_2-b_1)\right]\right\}\\
&\quad -\frac{i}{2}\delta\left(\frac{\mu}{1-\nu}\right)\left[\eta_1\left(\frac{1}{a^2}-x_3^{'}\frac{2}{a^3}\right)(b_2-b_3)+\eta_2\left(\frac{1}{a^2}-x_3^{'}\frac{2}{a^3}\right)(b_3-b_1)\right.
\end{aligned}$$

$$-i\left(\frac{2}{a^2}-x_3^{'}\frac{2}{a^3}\right)(b_1-b_2)\Big] \tag{7.195}$$

For $[M_{22}]$, we have:

$$\begin{aligned}
[M_{22}]_1 &= \delta\left(\frac{1}{4(1-\nu)}\right)\Big\{\eta_1\Big[\eta_1\left(\frac{2}{a^3}-\frac{1}{a^2}+x_3^{'}\frac{6}{a^4}-x_3^{'}\frac{2}{a^3}\right)(b_2-b_3)\\
&\quad +\eta_2\left(\frac{2}{a^3}-\frac{1}{a^2}+x_3^{'}\frac{6}{a^4}-x_3^{'}\frac{2}{a^3}\right)(b_3-b_1)+x_3^{'}i(b_1-b_2)\left(\frac{6}{a^4}-\frac{2}{a^3}\right)\Big]\Big\}\\
[M_{22}]_2 &= \delta\left(\frac{1}{4(1-\nu)}\right)\Big\{\eta_2\Big[\eta_1\left(\frac{2}{a^3}-\frac{1}{a^2}+x_3^{'}\frac{6}{a^4}-x_3^{'}\frac{2}{a^3}\right)(b_2-b_3)\\
&\quad +\eta_2\left(\frac{2}{a^3}-\frac{1}{a^2}+x_3^{'}\frac{6}{a^4}-x_3^{'}\frac{2}{a^3}\right)(b_3-b_1)+x_3^{'}i(b_1-b_2)\left(\frac{6}{a^4}-\frac{2}{a^3}\right)\Big]\Big\}\\
[M_{22}]_3 &= \delta\left(\frac{1}{4(1-\nu)}\right)\Big[\eta_1x_3^{'}i(b_2-b_3)\left(\frac{6}{a^4}-\frac{2}{a^3}\right)+\eta_2x_3^{'}i(b_3-b_1)\left(\frac{6}{a^4}-\frac{2}{a^3}\right)\\
&\quad +\left(\frac{2}{a^3}-\frac{1}{a^2}-x_3^{'}\frac{6}{a^4}+x_3^{'}\frac{2}{a^3}\right)(b_1-b_2)\Big]\\
[M_{22}]_4 &= \frac{1}{2}\Big\{\delta(\mu)\left(\frac{2}{a^3}-\frac{1}{a^2}\right)(-ib_2\eta_1-ib_3\eta_2+ib_1\eta_2-b_2)\\
&\quad +\delta\left(\frac{\mu}{1-\nu}\right)\eta_1\Big[\eta_2x_3^{'}(b_3-b_1)\left(\frac{6}{a^4}-\frac{2}{a^3}\right)+\eta_1x_3^{'}(b_2-b_3)\left(\frac{6}{a^4}-\frac{2}{a^3}\right)\\
&\quad -i\left(\frac{2}{a^3}-\frac{1}{a^2}-x_3^{'}\frac{6}{a^4}+x_3^{'}\frac{2}{a^3}\right)(b_1-b_2)\Big]\Big\}\\
[M_{22}]_5 &= \frac{1}{2}\Big\{\delta(\mu)\left(\frac{2}{a^3}-\frac{1}{a^2}\right)(-ib_2\eta_1+ib_3\eta_1+ib_1\eta_2+b_1)\\
&\quad +\delta\left(\frac{\mu}{1-\nu}\right)\eta_2\Big[\eta_2x_3^{'}(b_3-b_1)\left(\frac{6}{a^4}-\frac{2}{a^3}\right)+\eta_1x_3^{'}(b_2-b_3)\left(\frac{6}{a^4}-\frac{2}{a^3}\right)\\
&\quad +\eta_1x_3^{'}(b_2-b_3)\left(\frac{6}{a^4}-\frac{2}{a^3}\right)-i\left(\frac{2}{a^3}-\frac{1}{a^2}-x_3^{'}\frac{6}{a^4}+x_3^{'}\frac{2}{a^3}\right)(b_1-b_2)\Big]\Big\}\\
[M_{22}]_6 &= \frac{1}{2}\left(\frac{2}{a^3}-\frac{1}{a^2}\right)\Big\{-i\eta_1\Big[\delta\left(\frac{2\nu-1}{1-\nu}\lambda\right)(b_2-b_3)+2\delta(\mu)b_3\Big]\\
&\quad -i\eta_2\Big[\delta\left(\frac{2\nu-1}{1-\nu}\lambda\right)(b_3-b_1)-2\delta(\mu)b_3\Big]\\
&\quad +\Big[\delta\left(\frac{2\nu-1}{1-\nu}\lambda\right)(b_1-b_2)+2\delta(\mu)(b_2-b_1)\Big]\Big\}\\
&\quad -\frac{i}{2}\delta\left(\frac{\mu}{1-\nu}\right)\Big[\eta_1\left(\frac{2}{a^3}-\frac{1}{a^2}-x_3^{'}\frac{6}{a^4}+x_3^{'}\frac{2}{a^3}\right)(b_2-b_3)\\
&\quad +\eta_2\left(\frac{2}{a^3}-\frac{1}{a^2}-x_3^{'}\frac{6}{a^4}+x_3^{'}\frac{2}{a^3}\right)(b_3-b_1)\\
&\quad -i\left(\frac{4}{a^3}-\frac{2}{a^2}-x_3^{'}\frac{6}{a^4}+x_3^{'}\frac{2}{a^3}\right)(b_1-b_2)\Big]
\end{aligned} \tag{7.196}$$

For $[M_{23}]$, we have:

$$[M_{23}]_1 = \delta\left(\frac{1}{4(1-\nu)}\right)\Big\{\eta_1\Big[\eta_1\left(\frac{1}{a}+x_3^{'}\frac{1}{a^2}\right)(b_2-b_3)$$

$$
\begin{aligned}
&+\eta_2\left(\frac{1}{a}+x_3^{'}\frac{1}{a^2}\right)(b_3-b_1)+x_3^{'}i(b_1-b_2)\frac{1}{a^2}\Big]\Big\}\\
[M_{23}]_2 &= \delta\left(\frac{1}{4(1-\nu)}\right)\Big\{\eta_2\Big[\eta_1\left(\frac{1}{a}+x_3^{'}\frac{1}{a^2}\right)(b_2-b_3)\\
&+\eta_2\left(\frac{1}{a}+x_3^{'}\frac{1}{a^2}\right)(b_3-b_1)+x_3^{'}i(b_1-b_2)\frac{1}{a^2}\Big]\Big\}\\
[M_{23}]_3 &= \delta\left(\frac{1}{4(1-\nu)}\right)\Big[\eta_1 x_3^{'}i(b_2-b_3)\frac{1}{a^2}+\eta_2 x_3^{'}i(b_3-b_1)\frac{1}{a^2}+\left(\frac{1}{a}-x_3^{'}\frac{1}{a^2}\right)(b_1-b_2)\Big]\\
[M_{23}]_4 &= \frac{1}{2}\Big\{\frac{\delta(\mu)}{a}(-ib_2\eta_1-ib_3\eta_2+ib_1\eta_2-b_2)+\delta\left(\frac{\mu}{1-\nu}\right)\eta_1\Big[\eta_2 x_3^{'}(b_3-b_1)\frac{1}{a^2}\\
&+\eta_1 x_3^{'}(b_2-b_3)\frac{1}{a^2}-i\left(\frac{1}{a}-x_3^{'}\frac{1}{a^2}\right)(b_1-b_2)\Big]\Big\}\\
[M_{23}]_5 &= \frac{1}{2}\Big\{\frac{\delta(\mu)}{a}(-ib_2\eta_1+ib_3\eta_1+ib_1\eta_2+b_1)+\delta\left(\frac{\mu}{1-\nu}\right)\eta_2\Big[\eta_2 x_3^{'}(b_3-b_1)\frac{1}{a^2}\\
&+\eta_1 x_3^{'}(b_2-b_3)\frac{1}{a^2}-i\left(\frac{1}{a}-x_3^{'}\frac{1}{a^2}\right)(b_1-b_2)\Big]\Big\}\\
[M_{23}]_6 &= \frac{1}{2}\frac{1}{a}\Big\{-i\eta_1\Big[\delta\left(\frac{2\nu-1}{1-\nu}\lambda\right)(b_2-b_3)+2\delta(\mu)b_3\Big]\\
&-i\eta_2\Big[\delta\left(\frac{2\nu-1}{1-\nu}\lambda\right)(b_3-b_1)-2\delta(\mu)b_3\Big]\\
&+\Big[\delta\left(\frac{2\nu-1}{1-\nu}\lambda\right)(b_1-b_2)+2\delta(\mu)(b_2-b_1)\Big]\Big\}\\
&-\frac{i}{2}\delta\left(\frac{\mu}{1-\nu}\right)\Big[\eta_1\left(\frac{1}{a}-x_3^{'}\frac{1}{a^2}\right)(b_2-b_3)+\eta_2\left(\frac{1}{a}-x_3^{'}\frac{1}{a^2}\right)(b_3-b_1)\\
&-i\left(\frac{2}{a}-x_3^{'}\frac{1}{a^2}\right)(b_1-b_2)\Big] \qquad (7.197)
\end{aligned}
$$

For $[M_{24}]$, we have:

$$
\begin{aligned}
[M_{24}]_1 &= \delta\left(\frac{1}{4(1-\nu)}\right)\Big\{\eta_1\Big[\eta_1\left(\frac{2}{a^3}-\frac{1}{a^2}+x_3^{'}\frac{6}{a^4}-x_3^{'}\frac{2}{a^3}\right)(b_2-b_3)\\
&+\eta_2\left(\frac{2}{a^3}-\frac{1}{a^2}+x_3^{'}\frac{6}{a^4}-x_3^{'}\frac{2}{a^3}\right)(b_3-b_1)+x_3^{'}i(b_1-b_2)\left(\frac{6}{a^4}-\frac{2}{a^3}\right)\Big]\Big\}\\
[M_{24}]_2 &= \delta\left(\frac{1}{4(1-\nu)}\right)\Big\{\eta_2\Big[\eta_1\left(\frac{2}{a^3}-\frac{1}{a^2}+x_3^{'}\frac{6}{a^4}-x_3^{'}\frac{2}{a^3}\right)(b_2-b_3)\\
&+\eta_2\left(\frac{2}{a^3}-\frac{1}{a^2}+x_3^{'}\frac{6}{a^4}-x_3^{'}\frac{2}{a^3}\right)(b_3-b_1)+x_3^{'}i(b_1-b_2)\left(\frac{6}{a^4}-\frac{2}{a^3}\right)\Big]\Big\}\\
[M_{24}]_3 &= \delta\left(\frac{1}{4(1-\nu)}\right)\Big[\eta_1 x_3^{'}i(b_2-b_3)\left(\frac{6}{a^4}-\frac{2}{a^3}\right)+\eta_2 x_3^{'}i(b_3-b_1)\left(\frac{6}{a^4}-\frac{2}{a^3}\right)\\
&+\left(\frac{2}{a^3}-\frac{1}{a^2}-x_3^{'}\frac{6}{a^4}+x_3^{'}\frac{2}{a^3}\right)(b_1-b_2)\Big]\\
[M_{24}]_4 &= \frac{1}{2}\Big\{\delta(\mu)\left(\frac{1}{a^2}-\frac{1}{a}\right)(-ib_2\eta_1-ib_3\eta_2+ib_1\eta_2-b_2)\\
&+\delta\left(\frac{\mu}{1-\nu}\right)\eta_1\Big[\eta_2 x_3^{'}(b_3-b_1)\left(\frac{2}{a^3}-\frac{1}{a^2}\right)+\eta_1 x_3^{'}(b_2-b_3)\left(\frac{2}{a^3}-\frac{1}{a^2}\right)
\end{aligned}
$$

$$
\begin{aligned}
& -i\left(\frac{1}{a^2}-\frac{1}{a}-x_3^{'}\frac{2}{a^3}+x_3^{'}\frac{1}{a^2}\right)(b_1-b_2)\Big]\Big\} \\
[M_{24}]_5 &= \frac{1}{2}\Big\{\delta(\mu)\left(\frac{1}{a^2}-\frac{1}{a}\right)(-ib_2\eta_1+ib_3\eta_1+ib_1\eta_2+b_1) \\
& +\delta\left(\frac{\mu}{1-\nu}\right)\eta_2\left[\eta_2 x_3^{'}(b_3-b_1)\left(\frac{2}{a^3}-\frac{1}{a^2}\right)+\eta_1 x_3^{'}(b_2-b_3)\left(\frac{2}{a^3}-\frac{1}{a^2}\right)\right. \\
& \left.+\eta_1 x_3^{'}(b_2-b_3)\left(\frac{2}{a^3}-\frac{1}{a^2}\right)-i\left(\frac{1}{a^2}-\frac{1}{a}-x_3^{'}\frac{2}{a^3}+x_3^{'}\frac{1}{a^2}\right)(b_1-b_2)\right]\Big\} \\
[M_{24}]_6 &= \frac{1}{2}\left(\frac{1}{a^2}-\frac{1}{a}\right)\Big\{-i\eta_1\left[\delta\left(\frac{2\nu-1}{1-\nu}\lambda\right)(b_2-b_3)+2\delta(\mu)b_3\right] \\
& -i\eta_2\left[\delta\left(\frac{2\nu-1}{1-\nu}\lambda\right)(b_3-b_1)-2\delta(\mu)b_3\right] \\
& +\left[\delta\left(\frac{2\nu-1}{1-\nu}\lambda\right)(b_1-b_2)+2\delta(\mu)(b_2-b_1)\right]\Big\} \\
& -\frac{i}{2}\delta\left(\frac{\mu}{1-\nu}\right)\left[\eta_1\left(\frac{1}{a^2}-\frac{1}{a}-x_3^{'}\frac{2}{a^3}+x_3^{'}\frac{1}{a^2}\right)(b_2-b_3)\right. \\
& +\eta_2\left(\frac{1}{a^2}-\frac{1}{a}-x_3^{'}\frac{2}{a^3}+x_3^{'}\frac{1}{a^2}\right)(b_3-b_1) \\
& \left.-i\left(\frac{2}{a^2}-\frac{2}{a}-x_3^{'}\frac{2}{a^3}+x_3^{'}\frac{1}{a^2}\right)(b_1-b_2)\right]
\end{aligned}
\tag{7.198}
$$

7.4 3D Dislocations in Infinite Anisotropic Media

7.4.1 Basic Procedure

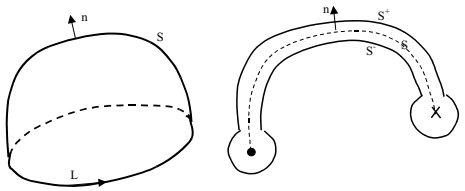

Figure 7.23: Schematic diagram of a closed dislocation loop L.

A dislocation can be visualized by imagining that it is made as follows. Make a cut in the material over a surface S bounded by a closed curve L. The positive direction of the normal n to the surface S is related to the positive direction of the curve L by the right-hand rule. The displacement $\mathbf{u}$ is considered to change discontinuously by a constant amount $\mathbf{b}$ when traversing opposite sides of S. If the negative side of the surface S, S^-, is displaced by $\mathbf{b}$ while the positive side S^+ is held fixed. Or alternatively, we could translate the positive side S^+ through a distance $-\mathbf{b}$ and keep the negative side S^- fixed. Operationally, we may produce the dislocation L by slitting the medium over the surface S, displacing the slit faces by the constant translation vector $\mathbf{b}$ and then welding the faces together again, adding or removing material as required.

Consider an infinitely extended materials V which contains an arbitrary shaped dislocation. The dislocation line L is boundary of a surface S where the displacement u_i has a jump $\mathbf{b}$ (Burgers vector) as,

$$[u_i] = u_i|_{S^+} - u_i|_{S^-} = -b_i \tag{7.199}$$

where S^+ and S^- denote the upper and lower plane of the slip plane S. The outward unit normal on surface S^+ is $-\mathbf{n}$ and on S^- is $\mathbf{n}$ where $\mathbf{n}$ is the unit normal to S.

We want to find the displacement solution of a dislocation using Green's functions. For an infinite continuous space, with a distribution of point force $f_m(\mathbf{x}')$, the corresponding displacement is obtained as,

$$u_i(\mathbf{x}) = \int_V G_{km}(\mathbf{x}, \mathbf{x}') f_m(\mathbf{x}') dV' \tag{7.200}$$

For a dislocation field, there is discontinuity on the dislocation surface S, the surface must be considered. For a finite region of space, we use the divergence theorem for any rank tensor $\mathbf{T}$ as,

$$\int_V \mathbf{T}_{,i} dV = \int_S \mathbf{T} dS_i$$

By means of the divergence theorem, we have

$$\begin{aligned} &\int_V C_{ijkl}[u_i(\mathbf{x}')G_{km,l'j'}(\mathbf{x}', \mathbf{x}) - u_{k,l'j'}(\mathbf{x}')G_{im}(\mathbf{x}', \mathbf{x})]dV' \\ &= \int_V C_{ijkl}[u_{k,l'}(\mathbf{x}')G_{im,j'}(\mathbf{x}', \mathbf{x}) - u_{i,j'}(\mathbf{x}')G_{km,l'}(\mathbf{x}', \mathbf{x})]dV' \\ &\quad + \int_S C_{ijkl}[u_i(\mathbf{x}')G_{km,l'}(\mathbf{x}', \mathbf{x}) - u_{k,l'}(\mathbf{x}')G_{im}(\mathbf{x}', \mathbf{x})]dS'_j \end{aligned} \tag{7.201}$$

with $V_{,i} = \partial V/\partial x_i$, and $V_{,i'} = \partial V/\partial x_{i'}$.

Changing the repeated indices and noting that $C_{ijkl} = C_{klij}$, we have

$$C_{ijkl}[u_{k,l'}(\mathbf{x}')G_{im,j'}(\mathbf{x}', \mathbf{x}) - u_{i,j'}(\mathbf{x}')G_{km,l'}(\mathbf{x}', \mathbf{x})] = 0$$

Considering the equilibrium equations

$$C_{ijkl}G_{km,l'j'}(\mathbf{x}', \mathbf{x}) = -\delta_{im}\delta(\mathbf{x}', \mathbf{x}) \ , \quad C_{ijkl}u_{k,l'j'}(\mathbf{x}') = -f_i(\mathbf{x}')$$

and the traction equation

$$C_{ijkl}u_{k,l'}(\mathbf{x}')n_j = \sigma_{ij}(\mathbf{x}')n_j$$

Finally, eq.(7.201) gives,

$$\begin{aligned} u_m(\mathbf{x}) \quad = \quad & \int_V G_{im}(\mathbf{x}', \mathbf{x}) f_i(\mathbf{x}') dV' + \int_S G_{im}(\mathbf{x}', \mathbf{x})\sigma_{ij}(\mathbf{x}')dS'_j \\ & - \int_S C_{ijkl}u_i(\mathbf{x}')G_{km,l'}(\mathbf{x}', \mathbf{x})dS'_j \end{aligned} \tag{7.202}$$

For the special case of a dislocation loop, the body force is zero ($f_i = 0$), the traction is continuous on the surface S: $(\sigma_{ij}n_j)|_{S^+} + (\sigma_{ij}n_j)|_{S^-} = 0$, and the displacement has a jump on S: $u_i|_{S^+} - u_i|_{S^-} = -b_i$, finally, the displacement induced by a dislocation loop is expressed as,

$$\begin{aligned} u_m(\mathbf{x}) &= -\int_{S^+} C_{ijkl}u_i(\mathbf{x}')G_{km,l'}(\mathbf{x}',\mathbf{x})dS'_j - \int_{S^-} C_{ijkl}u_i(\mathbf{x}')G_{km,l'}(\mathbf{x}',\mathbf{x})dS'_j \\ &= -b_i \int_{S^-} C_{ijkl}G_{km,l'}(\mathbf{x}',\mathbf{x})dS'_j \\ &= -b_i \int_{S} C_{ijkl}G_{km,l'}(\mathbf{x}',\mathbf{x})dS'_j \end{aligned} \tag{7.203}$$

Since $dS'_j = n_j dS'$, it can be rewritten as

$$u_i(\mathbf{x}) = -\int_S C_{jlmn}(\mathbf{x})b_m \frac{\partial}{\partial x'_l} G_{ji}(\mathbf{x}',\mathbf{x})n_n(\mathbf{x}')\mathrm{d}S'(\mathbf{x}') \tag{7.204}$$

where $G_{ji}(\mathbf{x}',\mathbf{x})$ are the Green's functions at $\mathbf{x}'$ due to a point force applied at $\mathbf{x}$, S is the surface capping the loop, n_n is a unit normal to S and b_m is the Burgers vector.

For infinite space, the Green's functions have the following properties:

$$G_{ji}(\mathbf{x}',\mathbf{x}) = G_{ji}(\mathbf{x}'-\mathbf{x}) = G_{ji}(\mathbf{x}-\mathbf{x}') = G_{ij}(\mathbf{x}-\mathbf{x}')$$

$$G_{ki,j}(\mathbf{x}',\mathbf{x}) = G_{ki,j}(\mathbf{x}'-\mathbf{x}) = -G_{ki,j}(\mathbf{x}-\mathbf{x}') = -G_{ki,j'}(\mathbf{x}'-\mathbf{x})$$

$$G_{ki,js}(\mathbf{x}',\mathbf{x}) = G_{ki,js}(\mathbf{x}'-\mathbf{x}) = G_{ki,js}(\mathbf{x}-\mathbf{x}') = G_{ki,j's'}(\mathbf{x}'-\mathbf{x})$$

The displacement gradient is

$$u_{i,j}(\mathbf{x}) = -\int_S C_{klmn}b_m \frac{\partial^2}{\partial x_j \partial x'_l} G_{ki}(\mathbf{x}',\mathbf{x})n_n(\mathbf{x}')\mathrm{d}S(\mathbf{x}') \tag{7.205}$$

For infinite homogeneous space

$$u_{i,j}(\mathbf{x}) = C_{klmn}\int_S b_m \frac{\partial^2}{\partial x'_j \partial x'_l} G_{ki}(\mathbf{x}'-\mathbf{x})n_n(\mathbf{x}')\mathrm{d}S(\mathbf{x}') \tag{7.206}$$

The equilibrium condition with body force at $\mathbf{x}'-\mathbf{x}$ gives:

$$C_{klmn}\frac{\partial^2}{\partial x'_n \partial x'_l} G_{ki}(\mathbf{x}'-\mathbf{x}) = 0 \tag{7.207}$$

Combining eq.(7.206) and (7.207), we have

$$u_{i,j}(\mathbf{x}) = C_{klmn}b_m \int_S \left[\frac{\partial^2}{\partial x'_j \partial x'_l} G_{ki}(\mathbf{x}'-\mathbf{x})\mathrm{d}S_n(\mathbf{x}') - \frac{\partial^2}{\partial x'_n \partial x'_l} G_{ki}(\mathbf{x}'-\mathbf{x})(\mathbf{x}')\mathrm{d}S_j(\mathbf{x}')\right] \tag{7.208}$$

Using Stokes theorem:

$$\int_S \left[\frac{\partial T}{\partial x'_j}\mathrm{d}S_n(\mathbf{x}') - \frac{\partial T}{\partial x'_n}\mathrm{d}S_j(\mathbf{x}')\right] = \epsilon_{njh}\oint_L T\mathrm{d}l_h(\mathbf{x}')$$

with ϵ_{njh} being the permutation tensor. Finally, the displacement gradient field is expressed as a line integral along the dislocation loop L as

$$u_{i,j}(\mathbf{x}) = C_{klmn}b_m\epsilon_{njh}\oint_L \frac{\partial}{\partial x'_l}G_{ki}(\mathbf{x}'-\mathbf{x})\mathrm{d}l_h(\mathbf{x}') = C_{klmn}b_m\epsilon_{jnh}\oint_L G_{ik,l}(\mathbf{x}-\mathbf{x}')\mathrm{d}l_h(\mathbf{x}') \tag{7.209}$$

where $\mathrm{d}l_h(\mathbf{x}') = \nu_h \mathrm{d}l(\mathbf{x}')$, ν_h is the unit tangent vector of the dislocation loop line at point $\mathbf{x}'$.

Or written as

$$u_{i,j}(\mathbf{x}) = \oint_L \beta_{jih}(\mathbf{x}-\mathbf{x}')\mathrm{d}l_h(\mathbf{x}') \tag{7.210}$$

with

$$\beta_{jih}(\mathbf{x}-\mathbf{x}') = C_{klmn}b_m\epsilon_{jnh}G_{ik,l}(\mathbf{x}-\mathbf{x}') \tag{7.211}$$

The stress field produced by the dislocation can be expressed as

$$\sigma_{ij}(\mathbf{x}) = C_{ijkl}\oint_L C_{pqmn}\epsilon_{lnh}b_m G_{kp,q}(\mathbf{x}-\mathbf{x}')\mathrm{d}l_h(\mathbf{x}') \tag{7.212}$$

Or written as

$$\sigma_{ij}(\mathbf{x}) = \oint_L S_{ijh}(\mathbf{x}-\mathbf{x}')\mathrm{d}l_h(\mathbf{x}') \tag{7.213}$$

with

$$S_{ijh}(\mathbf{x}-\mathbf{x}') = C_{ijkl}C_{pqmn}\epsilon_{lnh}b_m G_{kp,q}(\mathbf{x}-\mathbf{x}') \tag{7.214}$$

The kernel $S_{ijh}(\mathbf{x}-\mathbf{x}')$ can be considered as the ij-stress component at $\mathbf{x}$ produced by a line element of dislocation lying in the h-direction at $\mathbf{x}$', in an infinite space with Burgers vector $\mathbf{b}$. While $\beta_{jih}(\mathbf{x}-\mathbf{x}')$ can be considered as the corresponding elastic distortion.

In this Green's functions method, the elastic field (strain and stress) formulae involve derivatives of the Green's functions $G_{kp,q}(\mathbf{x}-\mathbf{x}')$. For general infinite anisotropic solids, analytical expressions are not available. However, these functions can be expressed in an integral form as (see former chapter):

$$\begin{aligned} G_{ij,k}(\mathbf{x}-\mathbf{x}') &= \frac{1}{8\pi^2|\mathbf{r}|^2}\oint_{C_k}[-\bar{r}_k N_{ij}(\bar{\mathbf{k}})D^{-1}(\bar{\mathbf{k}}) \\ &\quad +\bar{k}_k C_{lpmq}(\bar{r}_p\bar{k}_q + \bar{k}_p\bar{r}_q)N_{il}(\bar{\mathbf{k}})N_{jm}(\bar{\mathbf{k}})D^{-2}(\bar{\mathbf{k}})]d\phi \end{aligned} \tag{7.215}$$

where $\mathbf{r} = \mathbf{x}-\mathbf{x}'$, $\bar{\mathbf{r}} = \mathbf{r}/|\mathbf{r}|$, $\bar{\mathbf{k}}$ is the unit vector on the plane normal to $\mathbf{r}$, the integral is taken around the unit circle C_k on the plane normal to $\mathbf{r}$, $N_{ij}(\mathbf{k})$ and $D(\mathbf{k})$ are the adjoint matrix and the determinant of the second order tensor $C_{ikjl}k_k k_l$, respectively.

7.4.2 Forces on a dislocation loop

Dislocations will induce strain and stress field in materials. On the other hand, dislocations in stress fields will undergo forces and moving. The stress fields can be induced by external applied ones, or internal ones due to other dislocations, inclusions, and the dislocation itself. Under stress field, at a point such as P on a dislocation line L, the force per unit length on it is obtained by the Peach-Koehler formula: $\mathbf{F}^A = (\mathbf{b} \cdot \sigma^A) \times \mathbf{t}$, where σ^A is the sum of the stress from an applied load and that arising from internal sources at P, $\mathbf{b}$ is the Burgers vector of the dislocation, and $\mathbf{t}$ is the unit tangent vector of the element d$\mathbf{l}$. For the special, yet important case of a planar dislocation loop lying on a glide plane with unit normal $\mathbf{n}$, the glide force acts along the in-plane normal to L at P: $\mathbf{m} = \mathbf{n} \times \mathbf{t}$. The glide component F_g^A of the external force can be obtained by resolving $\mathbf{F}^A$ along $\mathbf{m}$ as:

$$F_g^A = \mathbf{F}^A \cdot \mathbf{m} = \mathbf{b} \cdot \sigma^A \cdot \mathbf{n} \tag{7.216}$$

The in-plane self-force at the point P on the loop is also obtained in a manner similar to the external Peach-Kohler force, with an additional contribution from *stretching* the dislocation line upon a virtual infinitesimal motion (Barnett 1976):

$$F^S = \kappa E(\mathbf{t}) - \mathbf{b} \cdot \tilde{\sigma}^S \cdot \mathbf{n} \tag{7.217}$$

where $E(\mathbf{t})$ is the pre-logarithmic energy factor for an infinite straight dislocation parallel to $\mathbf{t}$: $E(\mathbf{t}) = \frac{1}{2}\mathbf{b}\cdot\Sigma(\mathbf{t})\cdot\mathbf{n}$, with $\Sigma(\mathbf{t})$ being the stress tensor of an infinite straight dislocation along the loop's tangent at $\mathbf{P}$. σ^S is self stress tensor due to the dislocation L, and $\tilde{\sigma} = \frac{1}{2}[\sigma^S(\mathbf{P} + \epsilon\mathbf{m}) + \sigma^S(\mathbf{P} - \epsilon\mathbf{m})]$ is the *average* self-stress at P, κ is the in-plane curvature at $\mathbf{P}$, and $\epsilon = |\mathbf{b}|/2$.

Barnett (1976) and Gavazza and Barnett (1976) analyzed the structure of the self-force as a sum:

$$F^S = \kappa E(\mathbf{t}) - \kappa[E(\mathbf{t}) + E''(\mathbf{t})\ln(\frac{8}{\epsilon\kappa})] - J(L, \mathbf{P}) + F_{core} \tag{7.218}$$

where the second and third terms are line tension contributions, which usually account for the main part of the self-force, while $J(L, \mathbf{P})$ is a non-local contribution from other parts of the loop, and F_{core} is due to the contribution to the self-energy from the dislocation core. Generally, a dislocation loop is complex and irregular, there is no analytical expression for the non-local term. So, for exact self-force evaluation of a general dislocation loop, we can only use the method (7.217). In dislocation dynamics simulation, we may either ignore the non-local term or express it approximately (such as using a circular loop instead).

For the calculation of $E(\mathbf{t})$, the dislocation pre-logarithmic energy factor, and it's derivatives, can see the reference by Bacon et al. (1980) for details. For convenient, we listed below the formulae needed here.

$$E = B_{ij} b_i b_j$$

with $\mathbf{b}$ being the Burger's vector, and $\mathbf{B}$ depending on the dislocation direction $\mathbf{t}$ (for curved dislocation, $\mathbf{t}$ is the tangent vector at the concerned point).

Choose two orthogonal unit vectors $\mathbf{N}$ and $\mathbf{M}$ normal to dislocation direction $\mathbf{t}$. $\mathbf{N}$ can be the glide plane direction of the dislocation loop, and $\mathbf{M} = \mathbf{N} \times \mathbf{t}$. In the plane containing $\mathbf{M}$ and $\mathbf{N}$, we define another orthogonal unit vectors $\mathbf{m}$ and $\mathbf{n}$ by

$$\mathbf{m} = \mathbf{M}\cos\omega + \mathbf{N}\sin\omega\ , \quad \mathbf{n} = -\mathbf{M}\sin\omega + \mathbf{N}\cos\omega.$$

ω is an arbitrary angle. $\mathbf{B}(\mathbf{t})$ can be obtained by integration, as:

$$B_{ij} = B_{ji} = \frac{1}{4\pi^2}\int_0^\pi \{(mm)_{ij} - (mn)_{ir}(nn)^{-1}_{rk}(nm)_{kj}\}\mathrm{d}\omega$$

where $(ab)_{ik}$ is second-rank tensor defined by the contraction operation

$$(ab)_{jk} = a_i C_{ijkm} b_m$$

$E(\mathbf{t}) + E''(\mathbf{t})$ can be written as integral

$$E + E'' = A_{jsir}\left\{-(2M_j t_s + t_j M_s)\int_0^\pi (nn)^{-1}_{ir}\mathrm{d}\omega + 2\int_0^\pi (M_j n_s + t_j t_s \sin\omega)\, F_{ir}\mathrm{d}\omega + t_j\int_0^\pi n_s H_{ir}\mathrm{d}\omega\right\}$$

where

$$A_{jsir} = \frac{1}{4\pi^2} b_m b_g N_n \epsilon_{pjw} C_{ngip} C_{wmrs}$$

$$F_{rk} = F_{kr} = (nn)^{-1}_{rs}\left\{(nt)_{sp} + (tn)_{sp}\right\}(nn)^{-1}_{pk}$$

$$H_{rk} = F'_{rk} = -F_{rs}\{(nt)_{sp} + (tn)_{sp}\}(nn)^{-1}_{pk}\sin\omega - (nn)^{-1}_{rs}\{(nt)_{sp} + (tn)_{sp}\}F_{pk}\sin\omega$$
$$+(nn)^{-1}_{rs}\{(nM)_{sp} + (Mn)_{sp} + 2(tt)_{sp}\sin\omega\}(nn)^{-1}_{pk}.$$

For isotropic materials, with the x_1-axis along $\mathbf{t}$ and x_3-axis along $\mathbf{N}$,

$$B_{11} = \frac{\mu}{4\pi}\ , \quad B_{22} = B_{33} = \frac{\mu}{4\pi(1-\nu)}$$

So

$$E = \frac{\mu b^2}{4\pi(1-\nu)}(1 - \nu\cos^2\alpha)$$

with α being the angle between the Burgers vector and the tangent direction $\mathbf{t}$ as $\cos\alpha = b_1/b = \mathbf{t}\cdot\mathbf{b}/b$. And

$$E'' = \frac{\mu b^2 \nu}{4\pi(1-\nu)}\cos 2\alpha$$

For a circular loop (with radius R) in isotropic materials, there is analytical solution for the non-local part of the self-force as

$$J = -\frac{\mu b^2 \nu}{\pi(1-\nu)R}\cos 2\alpha.$$

7.4.3 Accuracy verification

To validate the accuracy of the present parametric dislocation method, we will present the elastic stresses of a circular dislocation loop, in the special case of an isotropic material, since analytical solutions are available (Kroupa 1960). In this example, the elastic constants are $C_{11}/C_{12}/C_{44} = 5:3:1$, and the stresses are normalized (divided) by $\mu b/[R(1-\nu)]$. μ, ν, b and R are Young's modulus, Possion's ratio, magnitude of Burger's vector and the radius of the circular dislocation loop, respectively.

Table Stresses in a prismatic circular loop with $\mathbf{b} = b(0, 0, 1)$

		σ analytical	σ present (relative error) $N_s = 8$	$N_s = 16$	$N_s = 24$
x/R		σ_{zz}	for points in the $z = 0$ plane		
0.5		0.622810	0.623383 (9×10^{-4})	0.622843 (5×10^{-5})	0.622817 (9×10^{-6})
0.9		1.962962	1.966650 (2×10^{-3})	1.963345 (2×10^{-4})	1.963055 (5×10^{-5})
0.99		16.45096	17.23815 (5×10^{-2})	16.38179 (4×10^{-3})	16.43815 (8×10^{-4})
1.01		-15.38702	-16.17236 (5×10^{-2})	-15.31418 (5×10^{-3})	-15.37140 (1×10^{-3})
1.1		-1.262697	-1.259719 (2×10^{-3})	-1.262375 (3×10^{-4})	-1.262617 (6×10^{-5})
2.0		-0.0431096	-0.0430383 (2×10^{-3})	-0.0431056 (9×10^{-5})	-0.0431089 (2×10^{-5})
z/R		σ_{zz}& σ_{rr}	for points along z-axis		
0.0	σ_{zz}	0.500000	0.500306 (6×10^{-4})	0.500017 (3×10^{-5})	0.500003 (6×10^{-6})
0.0	σ_{rr}	0.472222	0.472511 (6×10^{-4})	0.472238 (3×10^{-5})	0.472225 (7×10^{-6})
0.5	σ_{zz}	0.572433	0.572783 (6×10^{-4})	0.572453 (3×10^{-5})	0.572437 (6×10^{-6})
0.5	σ_{rr}	0.230563	0.230514 (2×10^{-4})	0.230561 (1×10^{-5})	0.230563 (2×10^{-6})

The stresses, calculated by the present method are compared to analytical solutions (Kroupa 1960) for a prismatic circular loop in the Table. In our calculations, the Guassian quadrature points N_{max} for $G_{ij,k}$ and the integration of parametric dislocation segments are both 16, and different segment numbers N_s are used. It can be seen that the accuracy of stress components increases with N_s, and decreases as the point approaches the dislocation core ($x/R \to 1$).

We have also calculated the stress field of a circular shear loop, and compared the results with analytical solutions (Kroupa 1960). The accuracy and tendency with N_s are found to be similar to the case of a prismatic loop.

7.4.4 Numerical results

In the following, the effects of elastic anisotropy on the behavior of dislocations will be examined. To measure the degree of deviation from elastic isotropy, we use the *anisotropy ratio* A, defined in the usual manner: $A = 2C_{44}/(C_{11} - C_{12})$ (Hirth and Lothe 1982). For an isotropic crystal, $A = 1$.

As an example, we consider a circular loop on the (111)-glide plane of an FCC crystal, with radius R and slip direction along $[\bar{1}10]$, see figure 7.24. A local coordinate is chosen as: the x- and z-axes are along the $[\bar{1}10]$ and $[111]$ directions, respectively. In the following figures, we will show the stress field induced by the circular dislocation loop in the slip systemIn the figures presented here, and the stresses are normalized/divided by $0.5(C_{11}-C_{12})b/R$, the ratio $C_{11}/C_{12}/\mu = 5:3:1$ is used throughout unless restated.

Figure 7.25 shows the shear stresses σ_{zx} and σ_{xy}, along the slip direction x-axis on the slip plane, for different anisotropy ratios. While the absolute value of the stress increases with A, the effects of elastic anisotropy are seen to be more salient inside the loop, as compared to the outside region. For $A \neq 1$, the crystal is not symmetric with respect to the slip direction any more, and there is a shear stress component σ_{xy} along the slip direction on the slip plane, see Figure 7.25-b.

The change in the stress magnitude and symmetry can be seen more clearly from the stress iso-

surfaces. For different anisotropy ratios $A = 1, 4, 0.25$, figures 7.26 and 7.27 show the stress iso-surfaces of σ_{zx} and σ_{xx}, respectively. The stresses are divided by $0.5(C_{11} - C_{12})b/R)$, the ratio $C_{11}/C_{12}/\mu = 5 : 3 : 1$, and local coordinate system is used, the length scale is R.

In the following examples, we choose dislocations crystals with real elastic constants. For fcc, we choose Al ($A = 1.21$), Cu ($A = 3.21$) and an isotropic material (with $A = 1$ and C_{11}, C_{12} choosing the same values as Cu). The slip system $(111)[\bar{1}10]$ and coordinates are the same as above. Figures 7.28-7.31 show the iso-surfaces of different stress components σ_{zx}, σ_{xx}, σ_{yy} and σ_{zz}, respectively. All stresses are divided by $10^{10}b/R$, and local coordinate system is used.

We give another example, dislocation loops in bcc materials, the slip system is $(110)[\bar{1}11]$, see figure 7.32. We choose Fe ($A = 2.36$), Nb ($A = 0.51$) and an isotropic material ($A = 1$, with C_{11} and C_{12} choosing the values as Nb). The iso-surfaces of σ_{zx}, σ_{xx} and σ_{zz} are shown in fig. 7.33-7.35, respectively. Stresses are divided by $10^{10}b/R$, and local coordinate system is used.

To show the effects of anisotropy on dislocation interactions, we first consider the Peach-Koehler force (interaction force) on a unit dislocation element of a straight dislocation on the same slip plane and along the $y-$ direction, induced by the glide circular dislocation loop. The Burgers vectors of the circular and straight dislocations are both along the slip direction, and their values are b and b_2 respectively. Similar to the tendency of stress components, the glide component of the Peach-Koehler force is shown to increase with A, as can be seen in Figure 7.36-a. It is interesting to note from Figure 7.36-b that, while a climb force is absent in an isotropic crystal (i.e. $A = 1$), we find that the lack of stress component symmetry about the glide plane introduces a climb force in anisotropic crystals.

In fig. 7.37, the self-forces along a circular glide loop are shown in materials with different anisotropy ratios. In the example, the loop radius is $R = 100\ b$. The self-force (divided by $0.5(C_{11} - C_{12})b^2/R$) is seen to increase with A. For strong elastic anisotropy (e.g. in Cu crystal), the variation of the self-force along the loop is found to be considerable and non-monotone. These examples clearly show that strong elastic anisotropy will not only change the magnitude and symmetry of the stress field, but it will also change interaction and self-forces, sometimes in a dramatic way. In fig. (7.38), we show the self forces for a circular dislocation loop in different materials, Al, Cu and Ni respectively. The radius of the loop is R, slip system is $(111)[\bar{1}10]$. The self force is normalized to $b^2R^{-1} \times 10^{10}$ (to which the unit magnitude of vector length equals).

7.5 Thin Films and Nanolayers

7.5.1 Introduction

The physics of strength in confined small volumes requires development of accurate methods for determination of dislocation interaction mechanisms. In particular, the influence of confining surfaces on dislocation motion, configuration, and force distribution as dislocations approach or cross interfaces needs precise quantification. Many recent technology applications are based on thin films or coatings that are composed of alternating layers of different materials. Other important systems where dislocation-interface interaction plays a significant role can be found in sandwiched interphases, nanolayered materials, quantum dots on substrates and fine precipitate dispersions in alloys. For these systems, free surfaces and interfaces have important effects on the stress field of dislocations and

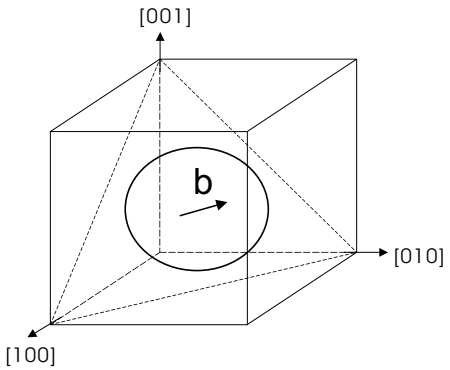

(a)

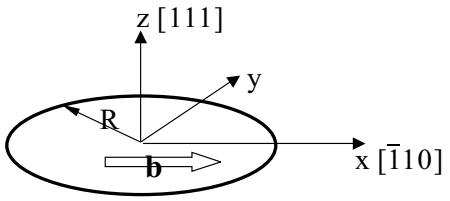

(b)

Figure 7.24: A circular dislocation loop on the (111) plane, with **b** along [$\bar{1}$10] direction (a) Global system, (b) Local coordinate system.

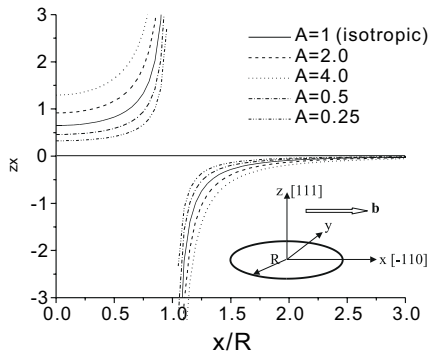

(a)

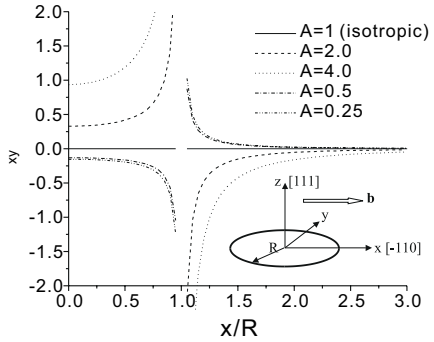

(b)

Figure 7.25: Stresses along x-axis (local coordinate system) (a)σ_{zx} and (b) σ_{xy}. With stresses divided by $0.5(C_{11} - C_{12})b/R$, $C_{11}/C_{12}/\mu = 5 : 3 : 1$.

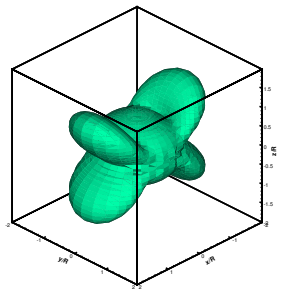

(a)

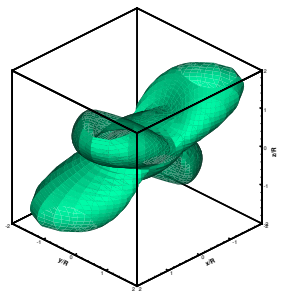

(b)

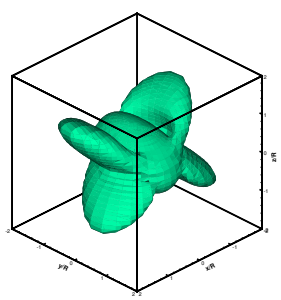

(c)

Figure 7.26: Stress Iso-surface for σ_{zx}(=0.08), with (a) $A = 1$, (b) $A = 4$ and (c) $A = 0.25$. Stresses divided by $0.5(C_{11} - C_{12})b/R$, $C_{11}/C_{12}/\mu = 5 : 3 : 1$, and local coordinate system is used.

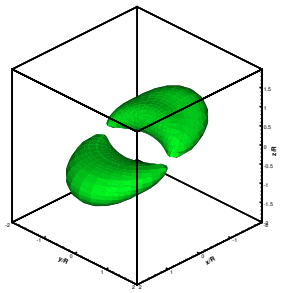

(a)

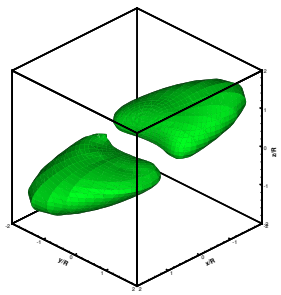

(b)

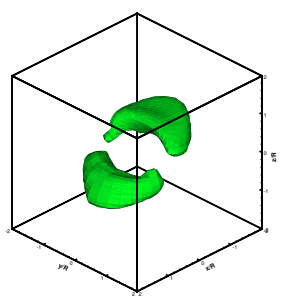

(c)

Figure 7.27: Stress Iso-surfaces for σ_{xx}(=-0.2), with (a) $A = 1$, (b) $A = 4$ and (c) $A = 0.25$. Stresses divided by $0.5(C_{11} - C_{12})b/R$, $C_{11}/C_{12}/\mu = 5 : 3 : 1$, and local coordinate system is used.

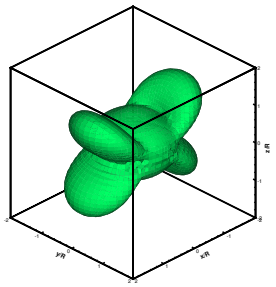

(a)

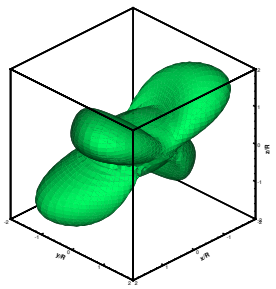

(b)

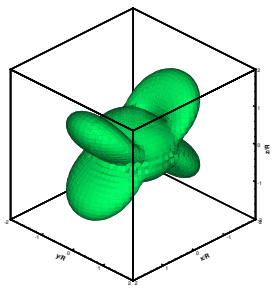

(c)

Figure 7.28: Stress Iso-surface for σ_{zx}(=0.2), dislocation loop in (a) Al ($A = 1.21$), (b) Cu ($A = 3.21$) and (c) Isotropic material ($A = 1$, with C_{11} and C_{12} choosing the values of Cu). Stresses divided by $10^{10}b/R$, and local coordinate system is used.

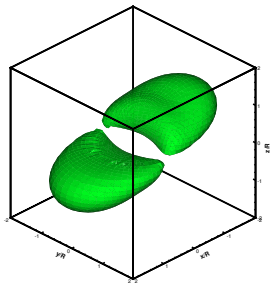

(a)

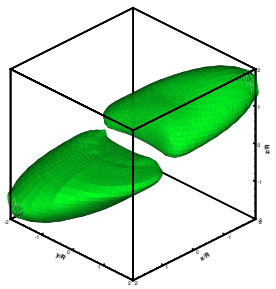

(b)

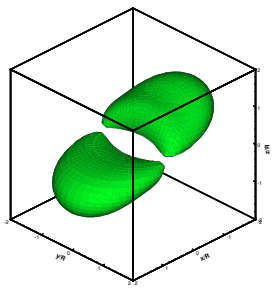

(c)

Figure 7.29: Stress Iso-surface for σ_{xx}(=-0.2), dislocation loop in (a) Al (A = 1.21), (b) Cu (A = 3.21) and (c) Isotropic material (A = 1, with C_{11} and C_{12} choosing the values of Cu). Stresses divided by $10^{10}b/R$, and local coordinate system is used.

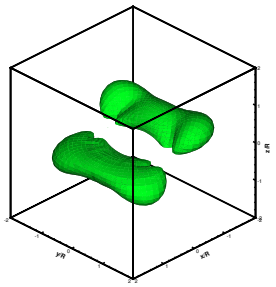

(a)

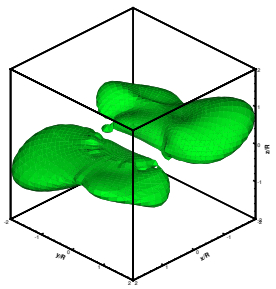

(b)

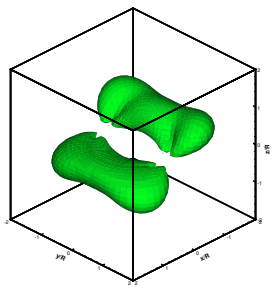

(c)

Figure 7.30: Stress Iso-surface for σ_{yy}(=-0.2), dislocation loop in (a) Al (A = 1.21), (b) Cu (A = 3.21) and (c) Isotropic material (A = 1, with C_{11} and C_{12} choosing the values of Cu). Stresses divided by $10^{10}b/R$, and local coordinate system is used.

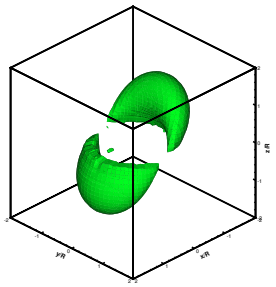

(a)

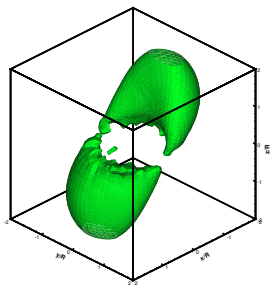

(b)

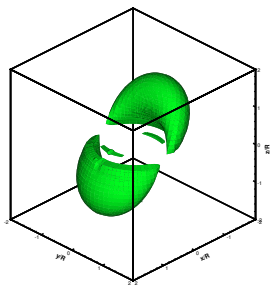

(c)

Figure 7.31: Stress Iso-surface for σ_{zz}(=-0.4), dislocation loop in (a) Al (A = 1.21), (b) Cu (A = 3.21) and (c) Isotropic material (A = 1, with C_{11} and C_{12} choosing the values of Cu). Stresses divided by $10^{10}b/R$, and local coordinate system is used.

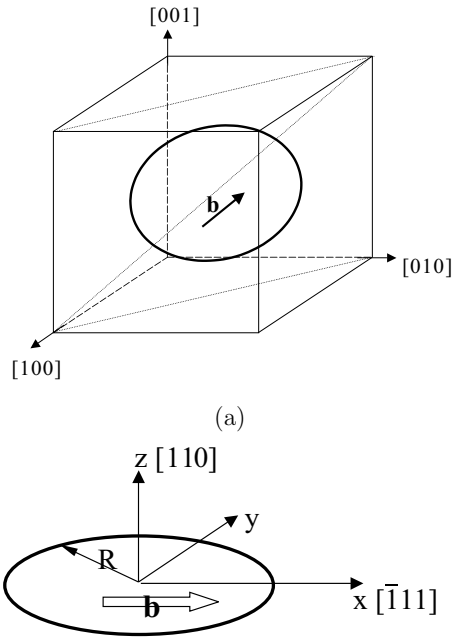

Figure 7.32: A circular dislocation loop on the (110) plane, with **b** along [$\bar{1}$11] direction (a) Global system, (b) Local coordinate system.

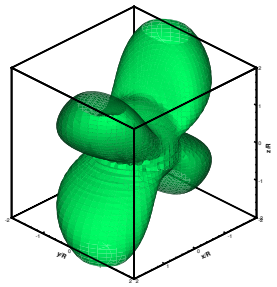

(a)

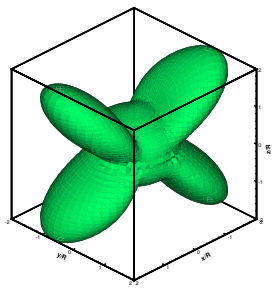

(b)

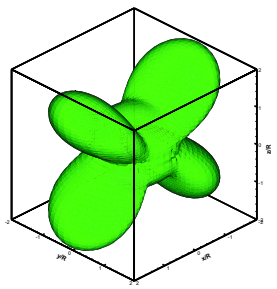

(c)

Figure 7.33: Stress Iso-surface for σ_{zx}(=0.2), dislocation loop in (a) Fe ($A = 2.36$), (b) Nb ($A = 0.51$) and (c) Isotropic material ($A = 1$, with C_{11} and C_{12} choosing the values of Nb). Stresses divided by $10^{10}b/R$, and local coordinate system is used.

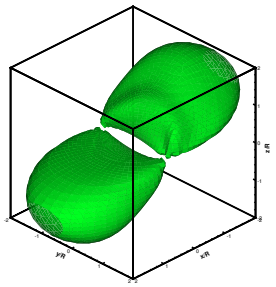

(a)

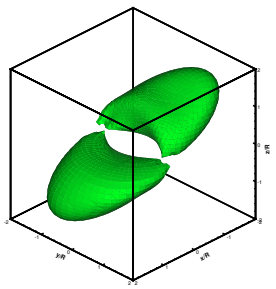

(b)

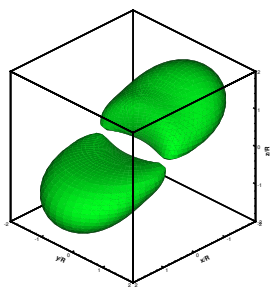

(c)

Figure 7.34: Stress Iso-surface for σ_{xx}(=-0.4), dislocation loop in (a) Fe (A = 2.36), (b) Nb (A = 0.51) and (c) Isotropic material (A = 1, with C_{11} and C_{12} choosing the values of Nb). Stresses divided by $10^{10}b/R$, and local coordinate system is used.

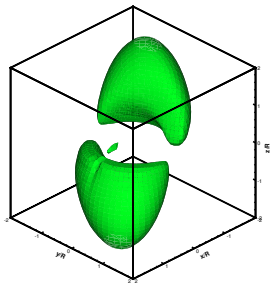

(a)

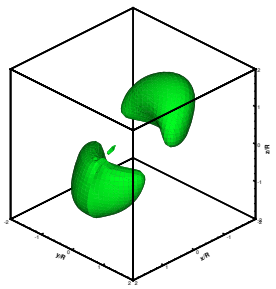

(b)

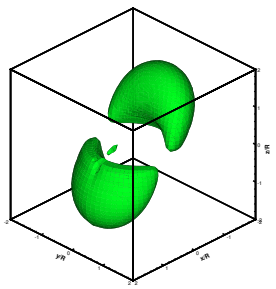

(c)

Figure 7.35: Stress Iso-surface for σ_{zz}(=-0.6), dislocation loop in (a) Fe (A = 2.36), (b) Nb (A = 0.51) and (c) Isotropic material (A = 1, with C_{11} and C_{12} choosing the values of Nb). Stresses divided by $10^{10}b/R$, and local coordinate system is used.

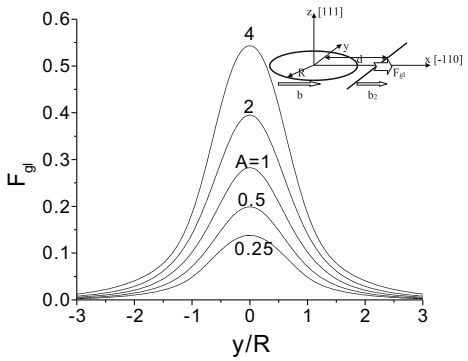

(a)

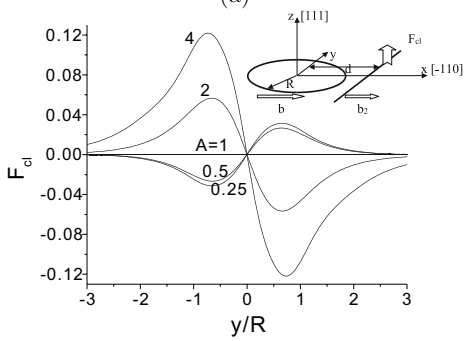

(b)

Figure 7.36: Peach-Koehler force (divided by $0.5(C_{11} - C_{12})bb_2/R$) of unit dislocation element on $z = 0$ plane and along y, with $d = 1.5R$, (a) glide component, (b) climb component

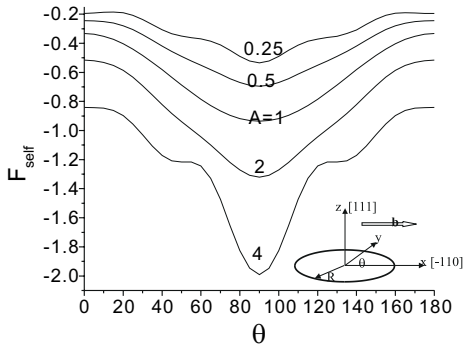

Figure 7.37: The self-force (divided by $0.5(C_{11} - C_{12})b^2/R$) along a slip circular loop, with $R = 100b$

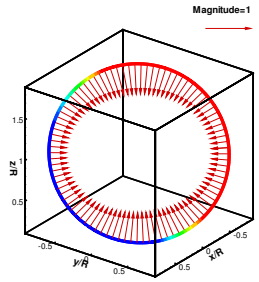

(a)

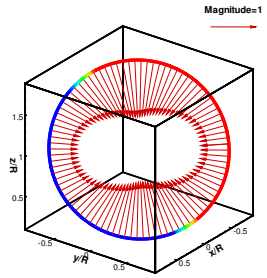

(b)

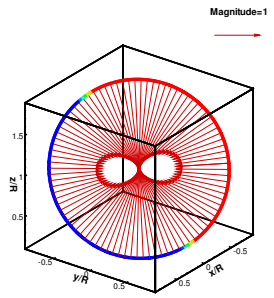

(c)

Figure 7.38: The self-force of a circular dislocation loop in different materials. (A) Al, (B) Cu, and (C) Ni. The self force is normalized to $b^2R^{-1} \times 10^{10}$.

hence on plastic deformation at the nano- and micro-scales. In nano-scale and micro-scale applications, the ratio of interface-to-volume becomes very large compared to bulk applications, and hence interfacial effects are expected to become dominant. Yield and post-yield properties of multi-layer nano-scale materials deviate from the properties of bulk materials, and cannot be explained by conventional plasticity theory. New mechanisms and relationships between the mechanical properties and interfacial properties (including structure) in nano-scale multilayer materials need to be explored with accurate theoretical methods.

The strength of multilayer materials is derived from the resistance of interfaces between layers to dislocation motion, as dislocations cross them from one layer to another. To design ultra-strong, yet ductile materials, one needs to understand how dislocations interact with interfaces. Resistance forces to dislocation motion can result from structural effects and/ or elastic moduli mismatches. The influence of interface structure is attributed to several sources: lattice constant mismatch that generates coherency strains, misfit interfacial dislocations in semi-coherent and incoherent interfaces, stacking fault energy mismatch of the incoming and outgoing slip planes, slip system mismatch that forces cross-slip of dislocations across the interface, and dislocation core spreading into the interface (Clemens, Kung and Barnett 1999, Rao and Hazzledine 2000, Anderson and Li 2001). Elastic moduli mismatch (discontinuity across the interface) induces dislocation image forces, which appear to be the dominant source of resistance (Clemens et al. 1999, Rao and Hazzledine 2000, Anderson and Li 2001). We will therefore focus our attention here on dislocation image forces in multilayer materials.

The computational framework of Dislocation Dynamics (DD) has been developed for fundamental descriptions of plasticity and fracture. The approach relies on direct numerical simulations of the collective motion of dislocation ensembles without ad hoc assumptions, e.g. (Kubin et al. 1992, Schwarz 1999, Zbib et al. 1998, Ghoniem et al. 2000a). However, most DD applications so far are for the deformation of bulk, isotropic materials. Very little attention has been paid to finding solutions for the elastic field of three-dimensional dislocations near interface, and no exact analytical solutions exist even for the simple case of a straight dislocation segment in two half-space materials. Using approximate methods or numerical calculations, a few recent studies have attempted to treat the influence of free surfaces (i.e. *image effects*) on the dynamics of dislocation systems. These are summarized as:

1. In the superposition method, combined with the finite element or boundary element methods, numerical techniques are utilized to satisfy traction equilibrium at free surfaces (Weigrand, Friedman, Van der Giessen and Needleman 2002, Martinez and Ghoniem 2002);

2. In the surface dislocation method, surface dislocation loop distributions are invoked so as to approximately satisfy interfacial or free surface traction conditions at specific surface collocation points (Khraishi, Zbib and de la Rubia 2001);

3. Approximate methods are based on Lothe's solution (Lothe, Indenbom and Chamrov 1982, Schwarz 1999), or assume rigid interfaces (Von Blanckenhagen, Gumbsch and Arzt 2001);

4. Elasticity methods for the solution of a dislocation segment near a free surface (Gosling and Willis 1994, Fivel, Gosling and Canova 1996), or the Boussinisque solution for a point force on a free surface (Verdier, Five and Groma 1998)

The approaches described above have their limitations. Numerical methods (the finite element (FEM) or the boundary element (BEM)), suffer from the necessity to re-calculate the super-posed FEM

or BEM solution every time step. As dislocations approach the surface or interface, the mesh must be refined, and the solution is not convergent if special care is not exercised with dislocation singularities. Other methods are limited to the simplest free surface boundary condition, and their extensions to anisotropic multilayered materials are not readily attainable, without ad hoc approximation. The numerous interfaces in multi-layer thin films pose particular difficulties for all existing methods. No solution for 3-D arbitrary shape dislocations in anisotropic multilayer materials is thus available.

The objective of the present work is to develop solutions for the elastic field of dislocation loops of arbitrary shape in anisotropic multilayer thin films, and to investigate interfacial image forces on dislocations. Methods for determination of the stress field and interface/free surface interaction forces will be considered for a number of cases, currently of practical interest:

1. A single thin film layer on a substrate. Here, we consider variations of hard/soft films on a substrate;

2. A capped thin film on a substrate, with variations of the thickness of the capped layer;

3. A dislocation loop crossing an interface between two adjacent layers.

The selected examples are intended to show features of the stress field and interaction forces of dislocations in anisotropic, multilayer thin films.

We will first utilize the method of Yang and Pan (Yang and Pan 2002a, Yang and Pan 2002b) to calculate Green's functions and their derivatives in anisotropic multilayers in Section **??**. The elastic field of dislocations in multilayer thin films is then presented in Section **??**, with numerical applications for infinitesimal and finite dislocation loops. Analysis of the effects of image forces due to free surfaces and interfaces will be presented for static dislocation loops in Section 9.3.6, where we consider dislocations in a film-on-substrate, capped film-on-substrate, and a dislocation crossing an interface. We finally present our conclusions in Section 9.5.5

7.5.2 Infinitesimal Dislocation Loop in Film-on-substrate

Here, we show results for a small (infinitesimal) dislocation loop in a thin film on top of a very thick substrate, which is approximated as half-space. The film-substrate system is shown in Figures **??** and 7.40, with a thin film (of thickness h) on top of a half-space substrate. The substrate material ($z < 0$) is copper, and the thin film is either aluminum or nickel. The materials selected for this example are all fcc cubic anisotropic crystals, with their crystallographic axes [100],[010] and [001] taken to coincide with the x, y and z directions, respectively. The elastic constants are taken from reference (Hirth and Lothe 1982). The anisotropic ratio $A = 0.5(C_{11} - C_{12})/C_{44})$ is 3.21, 1.21 and 2.52 for Cu, Al and Ni respectively ($A = 1$ for isotropic materials).

Assuming an infinitesimal dislocation is located at the middle of the thin film (i.e. $\mathbf{x}' = (0, 0, 0.5h)$), with its surface area δA lying on the (111) plane, and $\mathbf{b}$ along the $[\bar{1}10]$-direction. Figures 7.41 and 7.42 show contour lines for the out-of-plane stress σ_{32} and the in-plane stress σ_{12} on the plane $y = 0$, respectively. The stresses are normalized to $|\mathbf{b}|\delta A h^{-3} \times 10^{10}$. From these figures, it can be seen that the out-of-plane stresses are forced to decrease identically to zero at the surface to satisfy free traction boundary conditions. On the other hand, in-plane stresses are released at the free surface. At

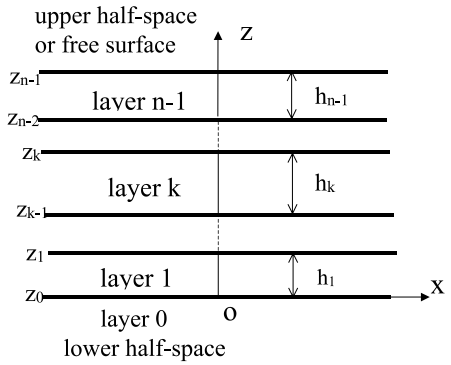

Figure 7.39: Geometry of a multilayered thin film system.

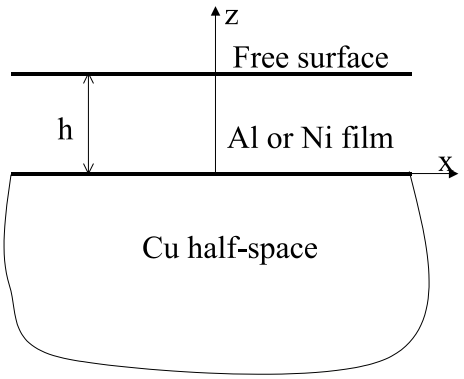

Figure 7.40: Geometry and coordinate system for the film-on-substrate arrangement.

the interface ($z = 0$), the out-of-plane stress components are continuous, while in-plane components experience jumps as a result of the discontinuity in the elastic properties. As one approaches the interface from a softer material to a harder one (e.g. Al to Cu), the stress fields, especially in-plane components, are arrested. Once one moves across the interface, in-plane components are released, and experience a jump. It is also observed that he stress fields usually are more complex for a source in a material with a high anisotropic ratio (e.g. Ni), while show smoother variations in nearly isotropic materials (e.g Al.)

7.5.3 Dislocation Loop in Film-on-substrate

To understand the effects of free surfaces and the interfaces on stress distributions around finite-size dislocation loops, we present here results for a circular loop. As an example, we choose the same (Al) film and (Cu) substrate, as shown in Figure **??**. The circular shear loop (radius, $R = 0.5h$) is located in

the middle of the film (0,0,0.5h), and lies on the (111)-plane, with $\mathbf{b}$ along the $[\bar{1}10]$-direction. Figure 7.43-(a) shows the $\sigma_{23} = 0.15$ iso-surface (normalized to $|\mathbf{b}|R^{-1} \times 10^{10}$). For comparison purposes, the same iso-surface in an Al infinite space is shown in Figure 7.43-(b). To satisfy the zero traction boundary condition at the top surface, the out–of-plane stress iso-surface is totally confined below it. The volume of the same iso-surface expands into the softer material across the interface. This means that the range of influence of a dislocation loop in a harder layer expands into neighboring softer layers, as compared to the infinite medium case.

7.5.4 Dislocation-Interface Interaction

So far, we determined the main characteristics of the elastic stress field induced finite size or infinitesimal dislocations in a multilayer material. However, an area of great interest, especially in relationship to DD simulations, is the distribution of configurational forces on dislocations as they move or change their shapes. A dislocations will experience a configurational force (so-called Peach-Koehler force), if it attempts motion or change in shape in a stress field, $\boldsymbol{\sigma}$. The force , $\mathbf{f}$, on a dislocation loop segment, $\mathrm{d}\mathbf{l}$, of a 3-D loop, of a burgers vector $\mathbf{b}$, can be determined by the Peach-Koehler formula:

$$\mathbf{f} = \boldsymbol{\sigma} \cdot \mathbf{b} \times \mathrm{d}\mathbf{l}. \tag{7.219}$$

We will divide the stress field induced by a dislocation into two parts: the full-space solution $\boldsymbol{\sigma}^{\infty}$ and the image contribution $\boldsymbol{\sigma}^{I}$. This separation will allow us to consider interface effects on dislocation forces, and to calculate the dislocation self-force without ambiguities. For a dislocation loop which is located totally whin a single material layer, the stress separation is clear. $\boldsymbol{\sigma}^{\infty}$ corresponds to the stress field induced by the dislocation in a homogeneous, infinite medium with a material that is identical to the layer where the dislocation is located. The stress field $\boldsymbol{\sigma}^{\infty}$ of a dislocation in an infinite anisotropic material can be expressed as a line integral along the dislocation loop by the formula of Mura (Mura 1968). $\boldsymbol{\sigma}^{\infty}$ will then induce a *self-force* on the dislocation, which can be obtained by the procedure of Gavazza and Barnett (1976), for details, see the work of Han et al. (2002). The force induced by the regular part of the stress field, $\boldsymbol{\sigma}^{I}$, is usually called *image force*, and can be calculated directly by applying the Peach-Koehler formula.

When a dislocation loop does not reside totally in one single layer, but crosses one or more interfaces and material layers, the separation of self-force from the image force is not so straightforward. In this case, we distinguish between them in the following way. Consider a point $\mathbf{P}$ on the loop, and assume that the whole loop is in a homogeneous, infinite medium, with a material identical to that in which the point $\mathbf{P}$ is located. This loop will induce a stress field $\boldsymbol{\sigma}^{\infty}$ and self-force on the unit dislocation segment where $\mathbf{P}$ located. Now, subtract $\boldsymbol{\sigma}^{\infty}$ from the total stress field to obtain the image stress $\boldsymbol{\sigma}^{I}$, which is regular. We use this part of the stress field to calculate, unambiguously, the image force on the dislocation segment at $\mathbf{P}$.

In the following, we focus our attention on image forces on dislocations in a variety of representative surface/interface conditions.

7.5.5 Film-on-substrate

Anisotropic thin films on extended substrates are common in many nano-scale and micro-scale applications. The distribution of image forces on dislocations in such systems determines how dislocations approach free surfaces or the interface between the film and substrate. We consider here the same film-on-substrate system with a representative circular dislocation loop, as in the previous section. The distribution of image forces on a circular dislocation loop in an Al and Ni film on top of an extended Cu substrate are shown in Figures 7.44-(a) and 7.44-(b), respectively. The force is per unit length, and is normalized to $|\mathbf{b}|^2 R^{-1} \times 10^{10}$. The free surface tends to attract the entire dislocation line. However, the closer a dislocation segment is to the free surface, and the harder the material is, the larger the surface image force. When a dislocation segment approaches an interface from a softer material to a harder one (Al to Cu), the interface tends to block it, while from a harder material to a softer side, the dislocation is attracted to the interface. It is noted from the figures that the image force is truly three dimensional, and that the distribution, magnitude and direction cannot be easily obtained from simple image constructions based only on 2-D analysis. This complexity presents significant computational challenges to the development of DD models that faithfully account for surface and interface effects. The other observation here is that while glide is the dominant component of surface and interface image forces, there is considerable contributions from climb as well.

7.5.6 Capped Film-on-substrate

A capping layer is often deposited on top of thin films for environmental protection, or to engender additional and desirable physico-chemical properties. Also, if the thin film is oxidizable, and is used at ambient conditions, a naturally-grown oxide capping layer will be present. We consider here the influence of capping layers on the behavior of dislocations confined within thin films. Strong interaction between the dislocation and a free surface or an interface results in its deformation, such that a large section of a dislocation loop is straight and parallel to the free surface or interface. We examine here interaction forces between dislocation loops and multiple interfaces and a free surface. We use a proto-typical dislocation loop to examine these interaction forces. We choose an Al film (width h) on a Cu substrate. However, the film here is capped with another thin Cu film, of width h_c. An oblong dislocation loop is located in the middle of the Al thin film. The oblong loop is composed of two straight segments parallel to the interfaces, and are connected by two half-circular segments, as shown in Figure 7.45. The length of the straight part, and the width of the oblong section of the loop, respectively, are L and D, with $L = 2D$ and $D = h$. The distribution of image forces on the loop are shown in Figures 7.45-a and 7.45-b, for various thicknesses of the capping layer. Image forces are normalized to $|\mathbf{b}|^2 h^{-1} \times 10^{10}$.

Numerical results show that image forces on the straight section of the loop near the capping layer display strong dependence on the layer thickness. Image forces vary rapidly with increasing the capping layer thickness, for $h_c < h$. However, the magnitude and direction of forces tend to those for $h_c \to \infty$. These conclusions mean that for thin capping layers (e.g. $h_c < h$), other nearby interfaces (e.g. the free surface of the capping layer) have strong coupling effects on force distributions of the dislocation. Thus, and in this case, the stress field and image force distributions are controlled by interacting nearby interfaces. For thicker capping layers, however, one may be able to use image forces resulting from an infinitely extended half-plane. We also consider image force variation, as the dislocation approaches the Al-Cu interface. When a dislocation segment is very close to an interface,

and distances to other interfaces are comparatively far, the image force exerted on this dislocation segment is dominated by the closest interface.

7.5.7 Dislocation loop across an interface

One of the most critical considerations in designing ultra-strong materials is the ability to confine dislocations in very thin layers, without allowing them to penetrate across interfaces. The strength of a nano-layered system is greatly enhanced, if interfaces can indeed offer the necessary resistance to their motion, even if high levels of stresses are applied. The maximum difference between the image force on a dislocation segment in one material and the corresponding force after the dislocation segment has crossed the interface into a neighboring material is known as the *Koehler barrier* (Koehler 1970). The applied stress must be large enough to overcome this barrier, in addition to other configurational resistance forces arising from structural effects of the interface itself. As such effects are outside the scope of the present investigation, and require atomistic simulations, we address here the behavior of dislocation segments in as much as the Kohler barrier is concerned. It is to be noted here that the origin of this barrier is the change in the stiffness of the interatomic potential (e.g. the curvature of the pair part of the potential), as dislocations cross from one material to another. In other words, sudden changes in the elastic constants across an interface are reflected in a jump in the magnitude of the image force on a dislocation segment. Since infinitesimal linear elasticity is used here, we would not expect that the results are rigorously accurate very near the interface, and some approximation is required. The original concept of Koehler was based on saturating (i.e. truncating) the image force, as the dislocation comes within a specified minimum distance of a dislocation core width of $2|\mathbf{b}|$ (Koehler 1970). We follow here the same model to deduce the resistance of an interface to dislocations crossing it. Image forces will be calculated with the methods outlined earlier, and assumed to be valid up to a cut-off distance of 1-2 atomic layers from the interface. This assumption is also consistent with evaluations of self-forces, using infinitesimal linear elasticity as well (Ghoniem et al. 2000a)

To examine the nature of the Koehler barrier, we choose here the case of a circular dislocation loop approaching an interface across two half-spaces. Figures 7.46-(a-c) show the force distributions, including the self-force and the image-force on the loop, as the loop is brought to closer proximity from the interface, and then finally cross the interface. In this example, the loop is on the (111)-plane with [$\mathbf{b}$ along $[\bar{1}10]$ and a radius $R = 200|\mathbf{b}|$. The Al-Cu interface is along the [001]-direction. The image force is very large only on the part of the loop that is close to the interface. The force is relatively small everywhere else, and decreases rapidly with distance away from the interface, as can be observed in Figures 7.46-(a-c).

Force variations, for the two points A and B (which are the closest points when the corresponding loop segment approaches the interface), are displayed in Figures 7.47-(a)&(b) respectively. Forces are plotted as functions of the distance of the point from the interface, and they include self and image contributions. They are also separated into glide and climb components. The 2D image force approximation (*Koehler barrier*), estimated for an infinite straight dislocation near the interface is calculated and shown in the figures as dashed lines (Koehler 1970). It can be seen that when the loop is in one material (not across the interface), only the glide component of the image force at the leading point (nearest to the interface) is close to the Koehler estimate. The climb component and other loop configurations show drastic differences

from the Koehler estimate as a result of the three dimensionality of the problem.

The direction of the in-plane curvature of the loop is chosen as the positive direction for the self- and glide- forces, while the positive direction of the climb force is defined along the plane normal to (111). It observed that when the distance between the leading point on the dislocation and the interface is less than $20|\mathbf{b}|$, image forces increase sharply and interface effects become dominant. If linear elasticity is taken as strictly valid, the force is singular at the interface. Here, however, we assume its validity up to a minimum approach distance on the order of the dislocation core width of $2|\mathbf{b}|$. The results displayed in Figures 7.47-(a)&(b) show the complexity of loop force variations in the close proximity of the interface. First, the jump in the self force is a result of the sudden change in the elastic constants of the medium, and the magnitude of the force scales with the stiffness of the material. What is interesting here to note is that while the climb component of the image force (including the Koehler barrier) is dominant on the closest segment when the loop crosses from the softer (Al) to the harder (Cu) material, as seen in Figure 7.47-(a), the situation is reversed when the loop crosses from Cu into Al (see Figure 7.47-(b)). This unique asymmetry is a result of the fact that the entire loop geometry determines the split between the climb ($\mathbf{f}_c$), and glide ($\mathbf{f}_g$) components of the force. Such detailed behavior can be critical to whether the dislocation segment would prefer to climb and cross-slip across an interface, or just simply continue gliding on the same glide plane if the orientation is favorable.

7.5.8 Summary and Conclusions

The interest in the mechanical behavior of ultra-strong materials, prepared by sputter deposition of multiple nano-layers, and in the reliability and failure of thin films in microelectronic and other applications, demands thorough understanding of dislocation behavior in such material systems. In these applications, interfaces play a prominent role in controlling dislocation motion, and hence, the strength and deformability. The present investigation provides a computational method by which one can assess forces and interactions amongst dislocations in anisotropic multi-layer materials. Future developments of DD, including applications in these systems, rely on understanding accuracy limits of approximate numerical methods. For example, the limits of existing methods for incorporation of free surface effects in DD simulations (e.g. FEM, BEM, surface dislocations, etc.) may be determined by detailed comparisons with the present method. We have shown here that the elastic field and configurational forces of dislocation loops of arbitrary geometry, and in any type of anisotropic layered thin film can be rigorously determined, if the thickness of the film is much less than its in-plane dimensions. Starting from the point force problem of Green's functions in a multi-layer thin film, the elastic field of dislocation loops is obtained by a surface integral. The key issue here is that 2D Fourier transforms can be used, together with the generalized Stroh's formalism to obtain the solution first in Fourier space, and then in real space by numerical inversion. To expedite the computational aspects of these steps, the approach recently proposed by Yang and Pan (2002b) is adopted.

Elastic field calculations of dislocations in anisotropic multilayer materials can be performed

with great accuracy, without any limits on the number of material layers, or dislocation shapes. However, direct implementation of this procedure in DD simulations may still be limited to systems containing few dislocations at present as a result of the heavy computational cost, despite efforts to expedite calculations of Fourier inversion integrals. Approximate methods to develop line rather than surface integrals will benefit from the present investigation, since numerical errors due to approximations can be readily determined.

Through a systematic numerical study of stress fields and forces induced by dislocations in multi-layered materials, we draw the following conclusions:

1. Stress fields and image forces on dislocations are greatly influenced by the presence of interfaces. Thus, interface image forces cannot be ignored or simply approximated without careful considerations. Generally, however, the nearest interface to a dislocation segment determines the majority of image effects. However, in layered systems where layer thicknesses are small (e.g. nano-layered materials), several neighboring interfaces ($\approx$ 2-4) simultaneously participate.

2. If applied forces on dislocations are large, the influence of interfaces on dislocation motion may be only significant very close to the interface, within less than 10 nm. In such cases, the closest interface becomes the most dominant.

3. When a dislocation segment is near an interface, the image force usually drives the segment towards a softer material and away from a harder one. Thus, when we consider events occurring near an interface, such as dislocation threading, or dislocation nucleation from interfaces, the force induced by the interface becomes very large and local. As an approximation, one may consider the effect from this interface only, and ignore interaction effects from other interfaces.

4. Stress fields emanating from dislocations are confined or released by a neighboring harder layer or softer layer, respectively.

5. Interfacial image forces are inherently 3-dimensional, since they cannot be simply determined by geometric image constructions, as is customary in some DD simulations. Both glide and climb components must be considered in the analysis of near-interface processes, such as nucleation and threading. The barrier to climb may be smaller than that for glide, and hence screw components may prefer to cross-slip rather than glide across an interface. Only the glide component of the image force at the leading point (nearest to the interface) is close to the 2-D Koehler estimate, when the loop is totally within one layer. The climb component and other loop configurations show drastic differences from the Koehler estimate.

6. Dislocation segments crossing interfaces display irreversibility of motion. When a dislocation crosses from a softer to a harder material, it may prefer to climb. If the same segment attempts to return from the harder to the softer material, however, its glide Koehler barrier is smaller, and will hence glide across rather than retrace its previous path. This mechanism cannot be explained by 2-D approximations, since it is a result of

the asymmetry created across the interface by the presence of the dislocation loop itself in two different media.

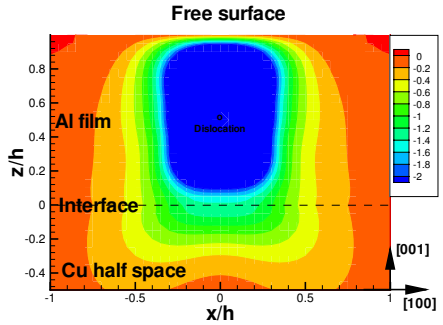

(a)

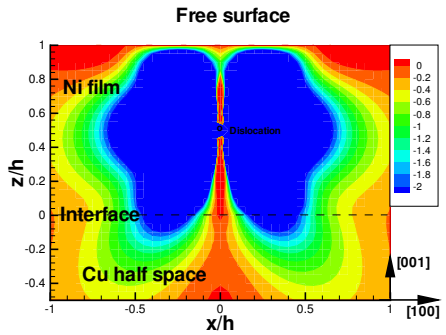

(b)

Figure 7.41: σ_{32} stress contours on the $y = 0$ plane due to an infinitesimal dislocation loop at $(0, 0, 0.5h)$ in (a) Al(film) on a Cu(substrate); (b) Ni(film) on a Cu(substrate).

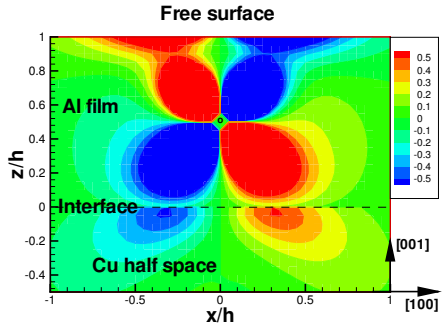

(a)

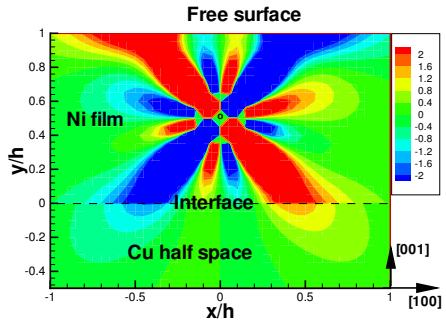

(b)

Figure 7.42: σ_{12} stress contours on the $y = 0$ plane due to an infinitesimal dislocation loop at $(0, 0, 0.5h)$ in (a) Al(film) on a Cu(substrate; (b) Ni(film) on a Cu(substrate).

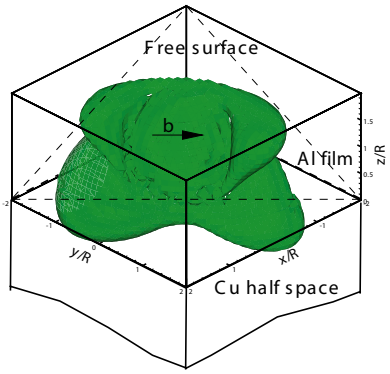

(a)

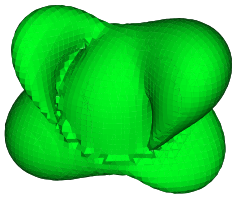

(b)

Figure 7.43: σ_{23} stress Iso-Surface for a circular shear dislocation loop in (a) Al(film) on a Cu(substrate); (b) Al infinite space.

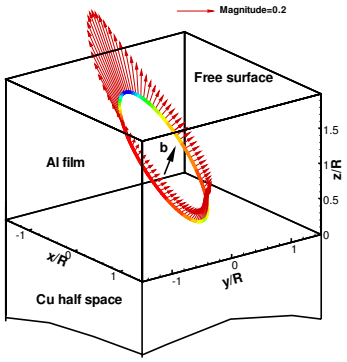

(a)

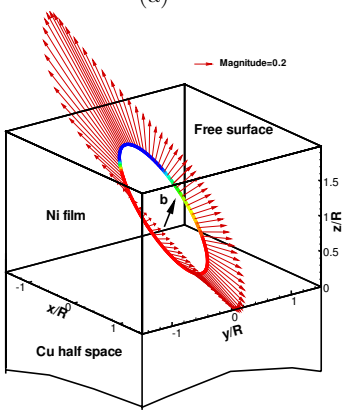

(b)

Figure 7.44: Free surface and interface image force distributions on a circular dislocation loop in (a) Al(film) on a Cu(substrate); (b) Ni(film) on a Cu(substrate).

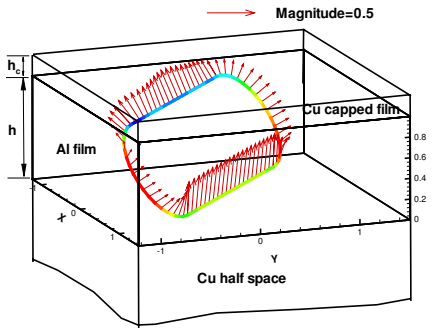

(a)

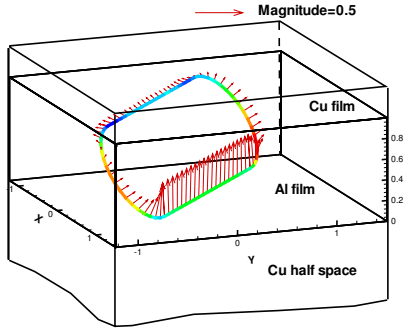

(b)

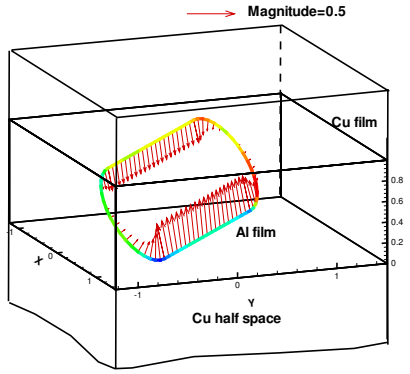

(c)

Figure 7.45: Image force of an oblong dislocation loop in an Al film on a Cu substrate. The Al film is capped by a Cu layer of thickness $h_c = 0.1h$ (a), $0.2h$ (b) and $0.5h$.

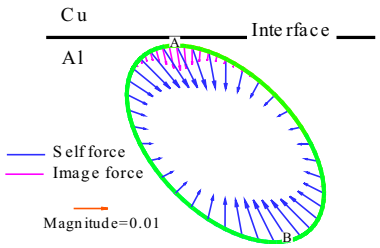

(a)

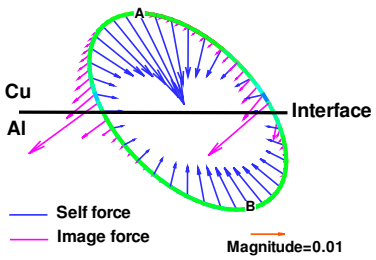

(b)

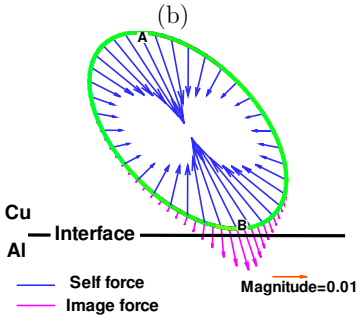

(c)

Figure 7.46: Force distributions on a dislocation loop : (a) as it approaches the interface, but is contained in a softer material of small elastic anisotropy; (b) as it straddles the interface (c) the loop is totally contained in a harder material of large elastic anisotropy.

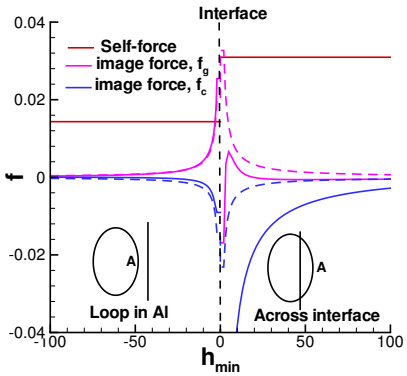

(a)

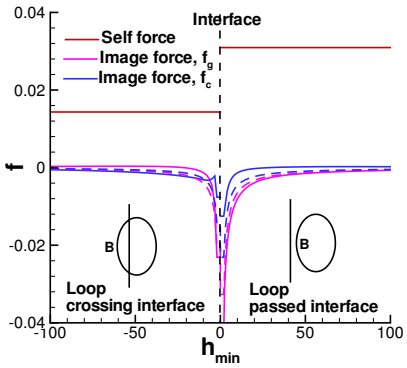

(b)

Figure 7.47: Dependence of force components on (a) the leading point A and (b) the trailing point B, as functions of their distance from the interface. Koehler's 2D solution is represented by dashed lines.

Chapter 8

Computational Methods

8.1 2D Dislocation Dynamics - Noronha

8.1.1 Basic Procedure

8.1.2 Multipole expansions

8.1.3 Applications

8.2 Variational Equations of Motion

In DD simulations of plastic deformation, the computational effort per time-step is proportional to the square of the number of interacting segments, because of the long-range stress field associated with dislocation lines. The computational requirements for 3-D simulations of plastic deformation of even single crystals are thus very challenging. It is therefore advantageous to reduce the total number of Equations Of Motion (EOM) during such calculations. Pioneering 3-D DD simulations of plasticity using straight segments are based on analytical solutions of the elastic field of pure screw and edge segments (**?**) -(**?**), or segments of mixed character (**?**)-(**?**). Zbib, Rhee and Hirth (**?**) have shown that the length of each straight segment is roughly limited to $\sim 50 - 200$ units of Burgers vector. Longer segments may have substantial force variations, thus limiting the usefulness of one single equation of motion for the entire segment. While Fig. 8.1 shows a schematic representation for the position of displaced segments, Fig. 9.56 illustrates force distributions on them. Singular forces and stresses arise at sharp intersection points of straight segments, which result in divergence of the average force over the straight segment as the segment length is decreased, as can be seen schematically from Fig. 9.56. When the dislocation loop is discretized to only screw or edge components, which move on a crystallographic lattice (**?**) -(**?**), the accuracy of strong dislocation interactions is compromised because line curvatures are crudely calculated. In addition, motion of dislocation segments on a fixed lattice

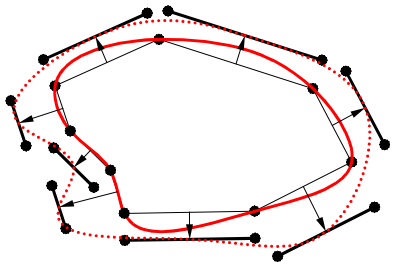

Figure 8.1: Discretization of a dislocation loop with linear segments leads to loss of connectivity when the equations of motion are developed only for mid-points.

produces inherent limitations to the accuracy of the overall dislocation dynamics. Recently, Schwartz (**?**) -(**?**) developed an adaptive method to reduce the segment size when dislocation interactions become strong. Using a modified form of the Brown formula (**?**) for the self-force on a segment, the field divergence problem for very short segments was circumvented . For closely interacting dislocations, substantial curvature and re-configuration of dislocations occur during the formation of a junction, dipole, or other configuration (**?**). However, the number of straight segments required to capture these processes is very large, and the segment size may have to be on the order of a few Burgers vectors. Most of these difficulties recognized from FIGS. (8.1) and (9.56) arise from the linear segment approximation, the *differential* treatment for their equations of motion, and the required curvature approximation for the self-force.

Dislocation loops in DD computer simulations are treated as dynamical systems, which can be described by the time dependence of specified coordinates. Obviously, if one attempts to solve the equations of dynamics for each atom within and surrounding the dislocation core, the number of equations is prohibitively large. On the other hand, if one knows that certain modes of motion for groups of atoms are closely-linked, many equations can be *adiabatically* eliminated, as is now conventional in the treatment of dynamical systems. Thus, instead of developing equations for the geometry of each single atom, one can find a much smaller set of geometric *generalized coordinates*, which would adequately describe the dynamical behavior of an entire dislocation loop. In Lagrangian descriptions, a number of generalized coordinates, q_r, is selected, where the subscript r represents a specific *Degree of Freedom (DF)* for the dynamical system. In a numerical computer simulation, however, the size of the system depends on available N_{DF}. Within the context of DD, one would expect that N_{DF} is relatively small in loops which conform to specific crystallographic or mobility constraints, while N_{DF} can be somewhat large in situations where strong interactions, cross-slip, or similar processes take place. In general, it is not of interest to follow every wiggle and bump on dislocation lines, unless such details develop into full-fledged instabilities. For specific applications, however, we intend to reduce N_{DF} as much as reasonable for the description of the physical situation at hand. This will be clarified by a number of examples, where physical constraints are imposed on dislocation motion.

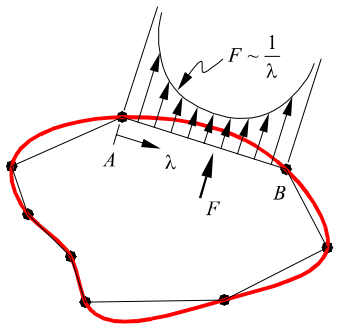

Figure 8.2: Force distribution on the straight segment AB from neighboring segments shows singular behavior at sharp corners. Force averaging over linear segments diverges as its length is decreased.

Our plan here is to describe the equations of motion for generalized coordinates in much the same way as in Lagrangian mechanics. Regardless of the dislocation loop shape complexity, we will develop an *integral* equation of motion for each curved segment within the loop, such that only relationships between global thermodynamic variables are obeyed. For concreteness, we focus the current approach on dislocation line representation by parametric dislocation segments, similar to the Finite Element Method (FEM). Thus, the equations of motion for the transport of atoms within the dislocation core should be consistent with the thermodynamics of irreversibility. A challenging prospect in such a description is the enormous topological complexity of materials containing dislocations. Dislocation lines assume complex shapes, particularly during heavy deformation and at high temperatures where they execute truly 3-D motion as a result of combined glide and climb forces. These dislocations can be highly curved because of their strong mutual interactions, externally applied stress fields, as well as other thermodynamic forces. It is apparent that whenever large curvature variations are expected, the accuracy of computing the dynamic shape of dislocation loops becomes critical.

The paper is organized as follows. First, irreversible thermodynamics of dislocation motion is presented in Sec. 8.2.1, in which we discuss energy components and entropy production during loop motion. This leads to an integral form of the variation in Gibbs energy in Sec. 8.2.2. A *weak* form of a variational procedure is pursued to formulate the equations of motion for the degrees of freedom based on the Galerkin approach. Computational *protocols* which are used to handle close-range interactions are then discussed in Sec. 8.2.3. To help illustrate the computational procedure, a simple example is also given. Applications of the present method to dislocation motion under physical constraints, and to several problems of loop-loop interaction and dislocation generation in fcc, bcc and diamond cubic (dc) Si crystals are given in Sec. 8.2.4 . Finally, conclusions and discussions follow in Sec. 9.5.5.

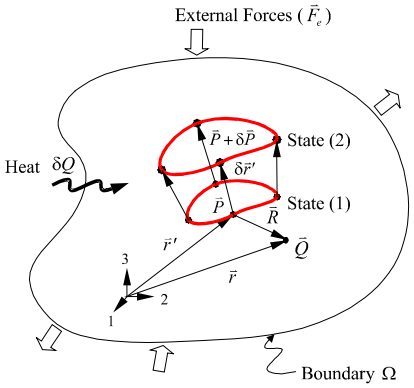

Figure 8.3: Representation of loop motion in an infinitesimal transition, illustrating thermodynamic variables

8.2.1 Irreversible Thermodynamics of Dislocation Motion

Consider a body, volume Ω and its boundary $\mathcal{S}$, in thermodynamic equilibrium, containing a dislocation loop in an initial position (1), as shown in Fig. 8.3. Under the influence of external mechanical forces ($\mathbf{F_e}$), and thermodynamic internal forces ($\mathbf{F_i}$), the dislocation loop will undergo a transition from the initial state to a new one designated as (2). Every point on the dislocation loop line is translated to a new position. In the meantime, material points in the body will deform elastically. During this transition of states, energy will be exchanged with the elastic medium, as given by the first law of thermodynamics:

$$\dot{U}^t + \delta E^t = \delta Q^t + \delta C^t + \delta W^t \tag{8.1}$$

where: δU^t is the change in internal energy, δE^t the change in kinetic energy, δQ^t the change in heat energy, δC^t the change in chemical energy by atomic diffusion, and δW^t the change in its mechanical energy. The left hand side of Equation (8.1) represents the total change in the energy of the body. We will ignore here changes in the kinetic energy, and restrict the applications of the present model to dislocation speeds less than approximately half of the transverse sound speed (see Refs. (**?**)-(**?**) for the effects of kinetic energy on the dynamics).

Now the total internal energy can be written as a volume integral: $\delta U^t = \int_\Omega \delta U d\Omega$, where δU is the specific (per unit volume) change of the internal energy. The mechanical power is composed of two parts: (1) change in the elastic energy stored in the medium upon loop motion under the influence of its own stress. This is precisely the change in the loop self-energy within a time interval δt, (2) the work done on moving the loop as a result of the action of external and internal stresses, excluding the stress contribution of the loop itself . These two components constitute the Peach-Koehler work. Thus: $\delta W^t = \int_\Omega \sigma_{ik} d\epsilon_{ik} d\Omega$. Care must be

exercised in evaluating the elastic field variables, as will be discussed later. The change in the total chemical energy can be written as a volume integral of the chemical potential μ_i, over the atomic concentration change dn_i, which is negative for mass transport out of the volume. Additionally, if loop motion produces geometric defects (e.g. jogs and vacancies), chemical energy is deposited. Thus: $\delta C^t = \int\limits_{\Omega} \left(dP_d - \sum\limits_i \mu_i dn_i \right) d\Omega$. Finally, the net change in the heat energy is composed of two parts: (1) heat energy (dH^*) generated by the loop as a result of atomic damping mechanisms (e.g. phonon and electron damping), and (2) heat transported across the boundary to the external reservoir, which is negative by convention. Hence, we have: $\delta Q^t = \int\limits_{\Omega} dH^* d\Omega - \int\limits_{\mathcal{S}} \mathbf{Q} \bullet d\mathbf{S}$. Here $\mathbf{Q}$ is the outgoing heat flux at the boundary. Using the divergence theorem for boundary integrals, we obtain:

$$\int\limits_{\Omega} \left[(dU - dH^* - dP_d) + (Q_{k,k} + \sum_i \mu_i dn_i - \sigma_{ik} d\epsilon_{ik}) \right] d\Omega = 0 \tag{8.2}$$

We will denote the enthalpy change $dH = dH^* + dP_d$, as the energy dissipated in defect generation and as heat. It is noted that in the special case where there is no heat or mass transport (i.e. $Q_{i,i} = dn_i = dP_d = 0$), no loop motion (i.e. $\delta W_{PK} = 0$), and under a hydrostatic stress field (i.e. $\sigma_{ik} = -P\delta_{ik}$), we get: $\sigma_{ik} d\epsilon_{ik} = -P\delta_{ik} d\epsilon_{ik} = -P d\epsilon_{ii} = -PdV$, for a unit initial volume. Thus, we recover the familiar relationship between enthalpy and internal energy: $dU = dH - PdV$. For an isothermal process, the Gibbs energy change is given by: $dG = dH - TdS$. Thus:

$$\delta G^t = \int\limits_{\Omega} \left[(dU - TdS) + (Q_{i,i} + \sum_i \mu_i dn_i - \sigma_{ik} d\epsilon_{ik}) \right] d\Omega \tag{8.3}$$

In addition to energy conservation, loop motion must result in a total increase in the entropy of the body and its surroundings. The Clausius-Duhem statement of the second law of thermodynamics can be phrased as (**?**): *"the total entropy production rate of the body and its surroundings must be positive for an irreversible process"*. Following Erringen (**?**), and Malvern (**?**), we construct the following entropy production inequality for the solid:

$$\delta \Phi^t = \delta S^t - B - \int\limits_{\mathcal{S}} \mathbf{\Xi} \bullet d\mathbf{S} \geq 0 \tag{8.4}$$

where $\delta \Phi^t \equiv \int\limits_{\Omega} \Phi d\Omega$ is the total *entropy production* during δt, δS^t the total change in entropy, b the *local entropy source* per unit volume with $B \equiv \int\limits_{\Omega} b d\Omega$, and $\mathbf{\Xi}$ the *entropy influx* due to heat input across the boundary $\mathcal{S}$. Utilizing the divergence theorem again in Equation (8.4), we obtain the following inequality per unit volume:

$$\Phi = \delta S - b - \Xi_{k,k} \geq 0 \tag{8.5}$$

Now, the entropy flux crossing the boundary is: $\mathbf{\Xi} = \frac{\mathbf{Q}}{T}$, and the flux divergence is given by:

$$\Xi_{k,k} = \left(\frac{Q_k}{T} \right)_{,k} = \frac{1}{T} Q_k (lnT))_{,k} - \frac{1}{T} Q_{k,k} \tag{8.6}$$

While the local entropy source is given by:

$$B = \int_{\Omega} \frac{dH}{T} = \int_{\Omega} \frac{1}{T} \left[dU + Q_{k,k} - \sigma_{ik} d\epsilon_{ik} + \sum_i \mu_i dn_i \right] d\Omega \tag{8.7}$$

Substituting Equations (8.6) and (8.7) into Equation (8.4), we obtain:

$$\int_{\Omega} \left\{ (dU - TdS) + Q_k (lnT)_{,k} - \sigma_{ik} d\epsilon_{ik} + \sum_i \mu_i dn_i \right\} d\Omega \leq 0 \tag{8.8}$$

Comparing the entropy production inequality (8.8) with Equation (8.3), we can immediately see that a consequence of irreversibility (i.e. entropy production) is a *decrease* in Gibbs free energy. Following arguments similar to Erringen (**?**), we write the internal energy in terms of entropy variations as:

$$\delta G^t = \int_{\Omega} \left[(\frac{\partial U}{\partial S} - T)\delta S + Q_k (ln(T))_{,k} - \sigma_{ik} d\epsilon_{ik} + \sum_i \mu_i dn_i \right] d\Omega \leq 0 \tag{8.9}$$

Since the inequality must be valid for all variations of δS, its coefficient must vanish (**?**),(**?**). Thus, the principle of entropy production results in the following statement:

$$\delta G^t = \int_{\Omega} \left[Q_k (lnT)_{,k} - \sigma_{ik} d\epsilon_{ik} + \sum_i \mu_i dn_i \right] d\Omega \leq 0 \tag{8.10}$$

Under conditions where heat generation during dislocation motion is significant (e.g. high-speed deformation), additional equations must be solved for the coupled point-defect and heat conduction. Thus, equations for point-defect conservation, as well as generalized forms of Fick's and Fourier laws must be added. These are expressed in the following:

$$C^{\gamma}_{,t} = J^{\gamma}_{k,k} \tag{8.11}$$

$$J^{\gamma}_{k} = -D^{\gamma}_{ik} C_{,i} - D_{ik} \left(\frac{Q^* C}{kT^2} \right) T_{,i} \tag{8.12}$$

$$Q_{\alpha,t} = -\kappa_{ik} T_{,i} - Q^* D_{i\alpha} C_{,i} \tag{8.13}$$

where $\kappa_{i\alpha}$ is the thermal conductivity tensor, D^{γ}_{ik} the diffusion tensor of defect γ, Q^* the corresponding heat of transport, and $Q_{k,t}$ the rate of change of the thermal energy.

We treat here the specific case where thermal effects are small (i.e. the first term in Equation (8.10) is ignored), and where climb motion of the dislocation loop is a result of point defect absorption (i.e. the third term in Equation (8.10) is summed over only vacancies and interstitials). In Equation (8.10), the volume integrals of the elastic term and the chemical term (osmotic) can be converted to line integrals over the dislocation loop. The stress tensor acting on any point is decomposed into a contribution resulting from the loop itself (i.e. self-stress $\sigma^{(s)}_{ik}$), and a contribution resulting from other dislocations, defects, Peierls stress, and the

applied stress field (i.e. external stress $\sigma_{ik}^{(e)}$). Thus, when the stress tensor in Equation (8.10) is written as: $\sigma_{ik} = \sigma_{ik}^{(s)} + \sigma_{ik}^{(e)}$, the elastic term results in two contributions to Gibbs energy, while the chemical term results in one additional contribution. We outline in the following how these three contributions can be converted to line integrals over the loop.

Now consider an infinitesimal variation in the position of a dislocation loop, depicted by the motion of the segments $\bigcup(AB, BC, CD, \cdot\cdot)$ in a time interval δt. During this motion, the dislocation core line length has changed from L to $L + \Delta L$. The dislocation line vector is denoted by $d\mathbf{s} = \mathbf{t} \mid \mathbf{s} \mid$, and the change in position for every atom on the dislocation line is described by the vector $\delta\mathbf{r}$. For the change in the amount of work done on the dislocation loop during its transition from state(1) to state(2) in Fig. 8.3 above, we assume that the stress field is uniformly acting on every surface element $\mathbf{dA} = \mathbf{b} \times d\mathbf{s}$. The associated element of virtual force is: $d\mathbf{F} = \mathbf{\Sigma} \bullet \mathbf{dA}$. During loop motion from state(1) to state(2), the variation in this Peach-Koehler work (**?**) obtained by integration along the path Γ is given by:

$$\begin{aligned} \int_{\Omega} [\sigma_{ik} d\epsilon_{ik}]^{(e)} d\Omega = \delta W_{PK} &= \oint_{\Gamma} d\mathbf{F} \bullet \delta\mathbf{r} = \oint_{\Gamma} (\mathbf{b} \times d\mathbf{s} \bullet \mathbf{\Sigma}) \bullet \delta\mathbf{r} \\ &= \oint_{\Gamma} (\mathbf{b} \bullet \mathbf{\Sigma} \times \mathbf{t}) \bullet \delta\mathbf{r} \mid d\mathbf{s} \mid \\ &= \oint_{\Gamma} (\in_{ijk} \sigma_{jm} b_m t_k \delta r_i) \mid d\mathbf{s} \mid \end{aligned} \tag{8.14}$$

The unit vector $\mathbf{t}$ is tangent to the dislocation line, and lies on its glide plane, while $\in_{ijk}$ is the permutation tensor. Ghoniem and Sun (**?**) -(**?**) showed that the stress tensor of a loop ensemble can be written as a fast numerical sum, given by:

$$\sigma_{ij} = \frac{\mu}{4\pi} \sum_{\gamma=1}^{N_{loop}} \sum_{\beta=1}^{N_s} \sum_{\alpha=1}^{Q_{max}} b_n w_\alpha \left[\frac{1}{2} R_{,mpp} \left(\in_{jmn} r_{i,u} + \in_{imn} r_{j,u} \right) + \frac{1}{1-\nu} \in_{kmn} \left(R_{,ijm} - \delta_{ij} R_{,ppm} \right) r_{k,u} \right] \tag{8.15}$$

In Equation (8.68) above, the fast sum is carried over the number of loops (N_{loop}), the number of parametric segments within each loop (N_s), and the number of quadrature points on each curved segment (Q_{max}). The third order tensor $R_{\alpha\beta\gamma}$ contains successive derivatives of the radius vector $\mathbf{R}$ connecting a point on the dislocation loop to a field point, and $r_{k,u}$ are parametric derivatives of the Cartesian components which describe the 3-D dislocation segment as a function of the parameter (u) (for details, see references (**?**) -(**?**)). The shear modulus is μ and w_α are weight functions at the quadrature point set $\{\alpha\}$ on the curved segment.

The total self- energy of the dislocation loop is obtained by double integrals along the contour Γ. Gavazza and Barnett (**?**) have shown that the first variation in the self- energy of the loop can be written as a single line integral of the form:

$$\int_{\Omega} [\sigma_{ik} d\epsilon_{ik}]^{(s)} \, d\Omega = \oint_{\Gamma} \left(\left[E(\mathbf{t}) - (E(\mathbf{t}) + E''(\mathbf{t})) \ln(\frac{8}{\varepsilon \kappa}) \right] \kappa - J(L, \mathbf{P}) \right) \mathbf{n} \bullet \delta \mathbf{r} \, |d\mathbf{s}| + [\delta U]_{core} \quad (8.16)$$

where $\mathbf{n}$ is normal to the dislocation line vector $\mathbf{t}$ on the glide plane, and $\varepsilon =\mid \mathbf{b}/2 \mid$ is the dislocation core radius (**?**). The first term results from loop stretching during the infinitesimal motion, the second and third are the *line tension* contribution, while $J(L, \mathbf{P})$ is a non-local contribution to the self-energy. The dominant contributions to the self- energy (or force) are dictated by the local curvature κ, and contain the pre-logarithmic energy term $E(\mathbf{t})$ for a straight dislocation tangent to the loop at point $\mathbf{P}$, and its second angular derivative E''. $[\delta U]_{core}$ is the contribution of the dislocation core to the self-energy. Defining the angle between the Burgers vector and the tangent as $\alpha = cos^{-1}(\frac{\mathbf{t} \bullet \mathbf{b}}{|b|})$, Gore (**?**) showed that a convenient computational form of the self- energy integral for an isotropic elastic medium of $\nu = \frac{1}{3}$ can be written as:

$$\int_{\Omega} [\sigma_{ik} d\epsilon_{ik}]^{(s)} \, d\Omega = \oint_{\Gamma} \left(-\kappa \;\; [E(\alpha) + E''(\alpha)] \ln(\frac{8}{\varepsilon \kappa}) + \mu b^2 [\kappa (\frac{21 + cos^2 \alpha}{64\pi}) + \bar{\kappa} (\frac{2 \;\; cos^2 \alpha - 1}{2\pi})] \right) \mathbf{n} \bullet \delta \mathbf{r} \, |d\mathbf{s}| \quad (8.17)$$

where the energy pre-factors are given by:

$$E(\alpha) = \frac{\mu b^2}{4\pi(1-\nu)} (1 - \nu \;\; cos^2 \alpha) \quad (8.18)$$

$$E''(\alpha) = \frac{\mu b^2 \;\; \nu}{2\pi(1-\nu)} cos \;\; 2\alpha \quad (8.19)$$

Accurate numerical calculations of the self-energy of any complex-shape loop have been performed by Ghoniem and Sun (**?**), where the double line integral is converted to a fast summation over the loop segments and quadrature points. However, a purely numerical method for evaluation of the self-energy requires intensive computations because of the need to use large quadrature order for good accuracy (**?**). Equation (8.17) is an alternate convenient approximation, in which the contributions of various terms are easily computed. Schwarz (**?**) conducted a numerical study to determine the effects of various terms on the self-force, and concluded that the major contribution results from the first two terms in Equation (8.17), which are the usual line tension approximation. However, the relative importance of the third term (which represents contributions from the dislocation core and dislocation line stretching) and fourth term (which is an approximation to non-local contributions from other parts of the loop) can be seen by a simple argument. The non-local term is obtained by approximating the loop as a pure shear loop at an average curvature of $\bar{\kappa}$. For a reasonable size loop of approximate radius in the range $1000 - 10000 \mid \mathbf{b} \mid$, it can be shown that the total contribution of non-local, core and stretch terms is on the order of less than 18%. The contribution of the non-local term is about half of this amount for purely edge components. Hence, a computationally efficient and very accurate method is obtained when all contributions are combined in Equation (8.17).

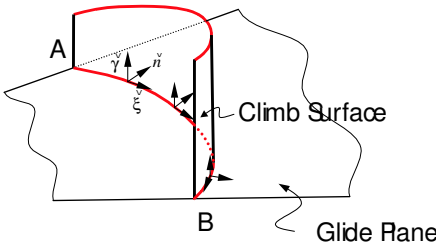

Figure 8.4: 3-D motion of a curved dislocation segment involving in-plane glide and out-of-plane climb.

Absorption of point defects by dislocation segments can be treated by considering the influence of the chemical term in Equation (8.10) on its motion. Incorporation of atomic defects into dislocation cores leads to dislocation climb. The thermodynamic force associated with this motion is referred to as the *osmotic* force. As illustrated in Fig. 8.4, during climb motion of atoms within the dislocation core, the number of vacancies (or interstitials) per unit length $\frac{dn_\gamma}{L}$, changes by the amount:

$$\frac{dn_\gamma}{L} = \frac{\mid \mathbf{b} \mid \mathbf{m} \bullet \delta\mathbf{r}}{\Omega_\gamma} \tag{8.20}$$

where Ω_γ is the vacancy (interstitial) volume, and $\mathbf{m}$ is a unit vector normal to the glide plane (see Fig. 8.4). The change in chemical potential per vacancy (interstitial) is given by:

$$\mu_\gamma = kT \ ln \ (\frac{C_\gamma}{C_\gamma^{eq}}) \tag{8.21}$$

Here C_γ is the non-equilibrium concentration of vacancies (or interstitials), which may result from quenching, a sudden change in temperature, irradiation or an externally applied stress (**?**), and C_γ^{eq} is the thermodynamic equilibrium concentration of the atomic defect. The corresponding contribution from point defect flow to the variation in Gibbs energy for the entire loop can now be obtained by line integration. Incorporating Equations [8.14,8.17,8.20,8.21] into inequality (8.10), we obtain:

$$\delta G^t = -\oint_\Gamma (\mathbf{f}_S + \mathbf{f}_O + \mathbf{f}_{PK}) \bullet \delta\mathbf{r} \mid d\mathbf{s} \mid \leq 0 \tag{8.22}$$

where we define the following generalized thermodynamic forces:

- $\mathbf{f}_{PK} \equiv$ the *Peach-Koehler force* per unit length $= \mathbf{b} \bullet \mathbf{\Sigma} \times \mathbf{t}$
- $\mathbf{f}_S \equiv$ the *self- force* per unit length $\Big(-\kappa \ \ [E(\alpha) + E''(\alpha)] \ln(\frac{8}{\varepsilon\kappa}) + \mu b^2[\kappa(\frac{21+cos^2\alpha}{64\pi}) + \bar{\kappa}(\frac{2 \ \ cos^2\alpha - 1}{2\pi})]\Big) \mathbf{n}$

- $\mathbf{f}_O \equiv$ the total *Osmotic force* (**?**) for defect γ per unit length $= -\sum_{\gamma} \gamma \ kT\frac{|\mathbf{b}|}{\Omega_\gamma} \ ln\left(\frac{C_\gamma}{C_\gamma^{eq}}\right) \ \mathbf{m}$ where $\gamma = (-1)$ for vacancies and$(+1)$ for interstitials

In compact tensor form, Equation(8.22) can be written as:

$$\delta G^t = -\oint_{\Gamma} f_k^t \delta r_k \mid d\mathbf{s} \mid \leq 0 \tag{8.23}$$

where f_k^t is the k-component of the total force: $\mathbf{f}^t = \mathbf{f}_S + \mathbf{f}_O + \mathbf{f}_{PK}$, and δr_k is the displacement of core atoms in the k-direction.

8.2.2 Variational Formulation

Governing Integral Equation of Motion

Inequality (8.10) suggests that the components of Gibbs energy can be written as *conjugate* pairs, representing the inner products of *generalized thermodynamic forces* and *generalized displacements*. The equations of motion can thus be obtained if one defines an appropriate set of generalized coordinates and conjugate generalized thermodynamic forces, in such a way as to result in entropy production and a corresponding decrease in δG during a virtual infinitesimal transition. Let's assume that atoms within the dislocation core are transported in some general drift force field, as a consequence of the motion of atomic size defects (e.g. vacancies, interstitials, kinks and jogs). The drift velocity of each atom is given by Einstein's mobility relationship: $\mathbf{V}_\lambda = \frac{1}{kT}\mathbf{D}\mathbf{f}_\lambda$, where $\mathbf{V}_\lambda$ is the drift velocity, $\mathbf{D}$ is a diffusion tensor, and $\mathbf{f}_\lambda$ is a generalized thermodynamic force representing process λ. Similarly, the flux resulting from a given process can be related to a corresponding thermodynamic force. We consider here three thermodynamic forces: (1) forces of mechanical origin (i.e. *Peach-Koehler forces*), as a result of variations in virtual work on the dislocation loop and variations in the stored elastic energy in the medium when the dislocation changes its shape, (2) gradients in point defect concentrations within the surrounding medium (i.e. *chemical forces*), and finally (3) temperature gradient forces associated with heat flow.

A generalization of the previous analysis can be accomplished if one postulates that near equilibrium, thermodynamic forces are sufficiently *weak* that we might expand the flux in a power series in $\mathbf{f}_\lambda$ (**?**). Let's denote $\mathbf{J}_k(\{\mathbf{f}_\lambda\}$ as type-k flux as a result of a generalized thermodynamic force λ, $\{\mathbf{f}_\lambda\}$. Thus, a generalization of Einstein's phenomenological transport relationship is given by:

$$\mathbf{J}_k(\{\mathbf{f}_\lambda\}) = \mathbf{J}_k(0) + \sum_{\lambda}\left(\frac{\partial \mathbf{J}_k}{\partial \mathbf{f}_\lambda}\right)_0 \mathbf{f}_\lambda + \frac{1}{2}\sum_{\lambda m}\left(\frac{\partial^2 \mathbf{J}_k}{\partial \mathbf{f}_\lambda \partial \mathbf{f}_m}\right)_0 \mathbf{f}_\lambda \mathbf{f}_m + \cdots \tag{8.24}$$

In the linear range of irreversible processes, Equation (8.24) is restricted to only the first two terms in the expansion. Moreover, at thermodynamic equilibrium in the absence of generalized

forces, all modes of atom transport vanish, and the first term, $\mathbf{J}(0)$, is identically zero. Taking the velocity of atoms on the dislocation line (i.e. representing the core) to be proportional to the atomic flux, and defining generalized mobilities via a mobility tensor $\mathbf{L}$ with components: $L_{ij} = \left(\frac{\partial \mathbf{V}_i}{\partial \mathbf{f}_j}\right)_0$, the phenomenological relationship (Equation (8.24)) is simplified to:

$$\mathbf{V}_\beta(\{\mathbf{f}_\lambda\}) = \sum_\lambda L_{\beta\lambda}\mathbf{f}_\lambda \tag{8.25}$$

As a consequence of the increase in entropy production Φ, or equivalently the decrease in Gibbs energyδG, Prigogine (**?**) showed that: $L_{\beta\lambda}\mathbf{f}_\beta\mathbf{f}_\lambda \geq 0$. This relationship gives a positive definite quadratic form, which imposes restrictions on the matrix of coefficients to be positive. The generalized *mobilities* L_{ij} are subject to additional temporal symmetries as a result of the principle of detailed balance, as shown by Onsager (**?**) : $L_{\beta\lambda} = L_{\lambda\beta}$. The mobility matrix relates the influence of an independent thermodynamic force of the λ-type to the partial flux of the k-type. In most applications of DD so far, the mobility matrix $L_{\lambda\beta}$ is assumed to be diagonal and independent of the type of thermodynamic force. However, we will assume that dislocation mobility is spatially anisotropic, since the speed of screw segments is usually smaller than edge segments as a consequence of the crystal structure. These simplifications lead to direct proportionality between the velocity and total force along each independent direction. Thus, we can denote $B_{\alpha k}$ as a diagonal resistivity (inverse mobility) matrix, and substitute in Equation (8.23) to obtain the following equivalent from of the Gibbs energy variation:

$$\delta G^t = -\oint_\Gamma B_{\alpha k}V_\alpha \delta r_k \mid d\mathbf{s} \mid \tag{8.26}$$

The resistivity matrix can have three independent components (two for glide and one for climb), depending on the crystal structure and temperature. It is expressed as:

$$[B_{\alpha k}] = \begin{bmatrix} B_1 & 0 & 0 \\ 0 & B_2 & 0 \\ 0 & 0 & B_3 \end{bmatrix} \tag{8.27}$$

Combining Equation(8.23) with Equation(8.26), we have:

$$\oint_\Gamma \left(f_k^t - B_{\alpha k}V_\alpha\right)\delta r_k \mid d\mathbf{s} \mid = 0 \tag{8.28}$$

The magnitude of the virtual displacement δr_k is not specified, and hence can be arbitrary. This implies that Equation(8.28) is actually a force balance equation on every atom of the dislocation core, where the acting force component f_k^t is balanced by viscous dissipation in the crystal via the term $B_{\alpha k}V_k$. However, this is not necessarily desirable, because one needs to reduce the independent degrees of freedom which describe the loop motion, yet still satisfies the laws of irreversible thermodynamics described here. To meet this end, we develop a general method, with greatly reduced degrees of freedom for the motion of dislocation core atoms.

The Galerkin Method

Assume that the dislocation loop is divided into N_s curved segments, as illustrated in Fig. 8.1 . The line integral in Equation (8.28) can be written as a sum over each parametric segment j, i.e.,

$$\sum_{j=1}^{N_s} \int_j \delta r_i (f_i^t - B_{ik} V_k) \mid d\mathbf{s} \mid = 0 \tag{8.29}$$

Note that in Equation (9.3.7), we sum over the number of segments j and follow the standard rules of 3-D tensor analysis. We now choose a set of generalized coordinates q_m at the two ends of each segment j. Then, the segment can be parametrically described as:

$$r_i = \sum_{m=1}^{N_{DF}} \mathcal{C}_{im}(u) q_m \tag{8.30}$$

where $\mathcal{C}_{im}(u)$ are shape functions, dependent on the parameter u ($0 \leq u \leq 1$). Equation (8.30) is a general parametric representation of the dislocation line for segment j. Possible convenient parameterization methods are discussed in Refs.(**?**)-(**?**). In Sec. 8.2.3 we introduce quintic splines as flexible and convenient parametric curves for complex dislocation loop geometry, while the applications in Sec. 8.2.4 illustrate the utilization of several types of parametric elements on the same loop. It is noted that the index m is assumed to be summed from 1 to N_{DF}, where N_{DF} is the number of total generalized coordinates at two ends of the loop segment. Accordingly, the three components of displacement vector are given by:

$$\delta r_i = \sum_{m=1}^{N_{DF}} \mathcal{C}_{im}(u) \delta q_m \tag{8.31}$$

On the other hand, we have for the velocity of any point on the dislocation line, within segment j:

$$V_k = r_{k,t} = \sum_{n=1}^{N_{DF}} \mathcal{C}_{kn} q_{n,t} \tag{8.32}$$

And the arc length differential for segment j is given by:

$$\mid d\mathbf{s} \mid = (r_{l,u} r_{l,u})^{\frac{1}{2}} du = \left(\sum_{p,s=1}^{N_{DF}} q_p \mathcal{C}_{lp,u} \mathcal{C}_{ls,u} q_s \right)^{\frac{1}{2}} du \tag{8.33}$$

An ensemble of dislocation loops is considered a continuous dynamical system, where every point on dislocation lines is subject to continuous displacement. The finite element process in continuum mechanics is based on approximating the continuous displacement field by a linear combination of piece-wise known shape functions over specified domains. To obtain the unknown coefficients in the linear combination, an integral form of the governing equation is formulated, and an element-by-element assembly is extracted. The result is a system of

equations for *standard discrete systems*, which can be handled by numerical methods. We will follow a similar approach here, in which the weight functions in the integral form are the same as the shape functions of the problem. Minimization of the weighted residuals results in symmetric matrices, which simplifies integration of the equations of motion. This variational approach is thus coincident with the Galerkin method as a special case of the method of weighted residuals. Recently, a number of investigators formulated microstructure evolution problems in a similar manner (see, for example Refs. (**?**) - (**?**)).

At this point, we may substitute Equations (8.31), (8.32), and (8.33) into the governing Equation (9.3.7), and obtain the following form:

$$\sum_{j=1}^{N_s} \int_0^1 \sum_{m=1}^{N_{DF}} \delta q_m \mathcal{C}_{im}(u) \left[f_i^t - B_{ik} \sum_{n=1}^{N_{DF}} \mathcal{C}_{kn} q_{n,t} \right] \left(\sum_{p,s=1}^{N_{DF}} q_p \mathcal{C}_{lp,u} \mathcal{C}_{ls,u} q_s \right)^{\frac{1}{2}} du = 0 \tag{8.34}$$

Appropriate collection of terms into more convenient functions can reduce the apparent complexity of this form of the equation of motion. We will define here two such functions: an effective force and an effective resistivity. A *generalized force*, f_m, is defined as:

$$f_m = \int_0^1 f_i^t \mathcal{C}_{im}(u) \left(\sum_{p,s=1}^{N_{DF}} q_p N_{lp,u} N_{ls,u} q_s \right)^{\frac{1}{2}} du \tag{8.35}$$

while a *resistivity matrix* element, γ_{mn}, is given by:

$$\gamma_{mn} = \int_0^1 \mathcal{C}_{im}(u) B_{ik} \mathcal{C}_{kn}(u) \left(\sum_{p,s=1}^{N_{DF}} q_p \mathcal{C}_{lp,u} \mathcal{C}_{ls,u} q_s \right)^{\frac{1}{2}} du \tag{8.36}$$

It is noted that $[\gamma_{mn}]$ is a symmetric matrix because of the structure of the above definition and symmetric mobilities. With these two parameters defined above, the variational integral form of the Gibbs energy equation is readily transformed to a discrete form, given by:

$$\sum_{j=1}^{N_s} \left[\sum_{m=1}^{N_{DF}} \delta q_m (f_m - \sum_{n=1}^{N_{DF}} \gamma_{mn} q_{n,t}) \right] = 0 \tag{8.37}$$

For the entire dislocation loop, we map all local degrees of freedom $q_i^{(j)}$ of each segment j onto a set of global coordinates, such that the global coordinates are equal to the local coordinates at each beginning node on the segment:

$$\{q_1^{(1)}, q_2^{(1)}, q_3^{(1)}, ..., q_1^{(2)}, q_2^{(2)}, q_3^{(2)}, ...\} = \{Q_1, Q_2, Q_3, ..., Q_N\}^T \tag{8.38}$$

where N is the total number of degrees of freedom of the loop. Similar to the finite element procedure, the local segment resistivity matrix $[\gamma_{mn}]$ is added into corresponding global locations in the global resistivity matrix $[\Gamma_{kl}]$, such that:

$$\sum_{j=1}^{N_s} \sum_{m=1}^{N_{DF}} \sum_{n=1}^{N_{DF}} [\delta q_m \gamma_{mn} q_{n,t}]^{(j)} = \sum_{k=1}^{N_{tot}} \sum_{l=1}^{N_{tot}} \delta Q_k \Gamma_{kl} Q_{l,t} \tag{8.39}$$

where $N_{tot} = N_s N_{DF}$ is the total number of degrees of freedom for the loop. The global resistivity matrix $[\Gamma_{kl}]$ is also symmetric and banded or sparse. The component Γ_{kl} is zero if the degrees of freedom k and l are not connected through a segment. In addition, the global force vector $\{\mathcal{F}_k\}$ can similarly be represented as

$$\sum_{j=1}^{N_s} \sum_{m=1}^{N_{DF}} [\delta q_m f_m]^{(j)} = \sum_{k=1}^{N_{tot}} \delta Q_k \mathcal{F}_k \tag{8.40}$$

Therefore, Equation (8.37) can be expressed as:

$$\sum_{k=1}^{N_{tot}} \delta Q_k \left(\mathcal{F}_k - \sum_{l=1}^{N_{tot}} \Gamma_{kl} Q_{l,t} \right) = 0 \tag{8.41}$$

Since the virtual displacements in the generalized coordinates are totally arbitrary, the previous equation can only be satisfied if:

$$\mathcal{F}_k = \sum_{l=1}^{N_{tot}} \Gamma_{kl} Q_{l,t} \tag{8.42}$$

Equation (9.60) represents a set of time-dependent ordinary differential equations which describe the motion of dislocation loops as an evolutionary dynamical system. Similar microstructure evolution equations have been derived by Suo (**?**) in connection with grain and void growth phenomena. Furthermore, the above spatially resolved equations can be discretized in time by the so-called *generalized trapezoidal family of methods* (**?**) as:

$$\sum_{l=1}^{N_{tot}} \Gamma_{kl}^{(n+\alpha)} Q_l^{(n+1)} = \sum_{l=1}^{N_{tot}} \Gamma_{kl}^{(n+\alpha)} Q_l^{(n)} + \Delta t \mathcal{F}_k^{(n+\alpha)} \tag{8.43}$$

where Δt is the time-step and n is the time-step index. In addition, α is a parameter, which determines explicit or implicit time-integration, taken to be in the interval [0,1] such that:

$\alpha = 0$ –for forward difference integration (Euler) ;

$\alpha = 1/2$ – for midpoint or trapezoidal integration;

$\alpha = 2/3$ – for Galerkin integration, and ;

$\alpha = 1$ –for backward difference (Euler) integration.

8.2.3 Computational Geometry of Dislocation Loops

Curved Spline Parametrization

A dislocation loop is divided into a set of curved segments connected at their end nodes, with each segment represented as an independent parametric space curve with parameter u varying

in the range 0 to 1. A general vector form of the dislocation line equation for segment (j) can be expressed as:

$$\mathbf{r}^{(j)}(u) = \sum_{i=0}^{n} \mathbf{A}_i^{(j)} \ u^i \tag{8.44}$$

where n is a polynomial order and $\mathbf{A}_i$ represent the associated vector coefficients. The value of n determines the segment type. Thus, when $n = 1$ the segment is a straight line, when $n = 3$ the segment is a cubic polynomial and when $n = 5$, the segment is a fifth-order (quintic) polynomial. The coefficients $\mathbf{A}_i$ are determined by boundary conditions imposed on beginning and end nodes. These boundary conditions can be described in terms of specified geometric properties, such as the nodal position, tangent, curvature, or torsion. To solve for the six coefficients $\mathbf{A}_0$ to $\mathbf{A}_5$ of a quintic spline segment, we have to assign six independent vectors, to be determined by six boundary conditions $\mathbf{r}^{(j)}(0)$, $\mathbf{r}^{(j)}(1)$, $\mathbf{r}_{,u}^{(j)}(0)$, $\mathbf{r}_{,u}^{(j)}(1)$, $\mathbf{r}_{,uu}^{(j)}(0)$, and $\mathbf{r}_{,uu}^{(j)}(1)$, where $\mathbf{r}_{,u}^{(j)} = d\mathbf{r}^{(j)}/du$ and $\mathbf{r}_{,uu}^{(j)} = d^2\mathbf{r}^{(j)}/du^2$. Geometrically, $\mathbf{r}^{(j)}(0)$ and $\mathbf{r}^{(j)}(1)$ are the position vectors of nodes j and $j+1$, i.e., $\mathbf{P}^{(j)}$ and $\mathbf{P}^{(j+1)}$. The vectors $\mathbf{r}_{,u}^{(j)}(0)$ and $\mathbf{r}_{,u}^{(j)}(1)$ are the tangent vectors of nodes j and $j+1$, i.e., $T_E^{(j)}\mathbf{t}^{(j)}$ and $T_B^{(j+1)}\mathbf{t}^{(j+1)}$, respectively, where $T_E^{(j)}$ and $T_B^{(j+1)}$ are magnitudes of tangent vectors at the end (E) and beginning (B) of each segment, while the unit vectors $\mathbf{t}^{(j)}$ and $\mathbf{t}^{(j+1)}$ are the dislocation sense vectors at nodes j and $j+1$, respectively. The vectors $\mathbf{r}_{,uu}^{(j)}(0)$ and $\mathbf{r}_{,uu}^{(j)}(1)$ are linear combinations of the tangent and normal vectors because they lie on the plane spanned by them. Because the resultant loop profile is a composite curve, dislocation line continuity may not be maintained at each node if boundary conditions on segments are arbitrarily assigned . In general, C^0(position) and C^1(tangent) continuity can be easily satisfied if we assign the same position and tangent vectors at each node. However, since self-forces on dislocation segments are proportional to the local curvature (see Equation (8.17), C^2 continuity will ensure the continuity of self-forces at segment nodes as well. The curvature of a general point on segment j can be expressed as

$$\kappa = \frac{\|\mathbf{r}_{,u}^{(j)}(u) \times \mathbf{r}_{,uu}^{(j)}(u)\|}{\|\mathbf{r}_{,u}^{(j)}(u)\|^3} \tag{8.45}$$

To maintain C^2 continuity at each node, we let the curvature of the end point of segment j be equal to the curvature at the beginning node of curved segment $j+1$.

$$\frac{\|\mathbf{r}_{,u}^{(j)}(1) \times \mathbf{r}_{,uu}^{(j)}(1)\|}{\|\mathbf{r}_{,u}^{(j)}(1)\|^3} = \frac{\|\mathbf{r}_{,u}^{(j+1)}(0) \times \mathbf{r}_{,uu}^{(j+1)}(0)\|}{\|\mathbf{r}_{,u}^{(j+1)}(0)\|^3} \tag{8.46}$$

From Equation (8.46), and the fact that $\mathbf{r}_{,uu}^{(j)}$ is a linear combination of $\mathbf{T}\&\mathbf{N}$, the tangent component of vector $\mathbf{r}_{,uu}^{(j)}$ does not influence the line curvature. Therefore, we can just assign the normal vectors $N_E^{(j)}\mathbf{n}^{(j)}$ and $N_B^{(j+1)}\mathbf{n}^{(j+1)}$ for $\mathbf{r}_{,uu}^{(j)}(1)$ and $\mathbf{r}_{,uu}^{(j+1)}(0)$, respectively, where N_E^j and $N_B^{(j+1)}$ represent magnitudes associated with the unit vectors $\mathbf{n}^{(j)}$ and $\mathbf{n}^{(j+1)}$. After substituting all boundary conditions into Equation (8.44) and rearranging terms, we obtain:

$$\mathbf{r}^{(j)}(u) = \mathcal{C}_1\mathbf{P}^{(j)} + \mathcal{C}_2\mathbf{P}^{(j+1)} + \mathcal{C}_3T_E^{(j)}\mathbf{t}^{(j)} + \mathcal{C}_4T_B^{(j+1)}\mathbf{t}^{(j+1)} + \mathcal{C}_5N_E^{(j)}\mathbf{n}^{(j)} + \mathcal{C}_6N_B^{(j+1)}\mathbf{n}^{(j+1)} \tag{8.47}$$

Note that the superscript on the LHS of Equation (8.47) refers to segment j, while on the RHS, it is associated with nodes j and $j+1$ on the same segment. The coefficients $\mathcal{C}_1$ to $\mathcal{C}_6$ are invariant shape functions, and can be expressed in terms of parameter ($0 \leq u \leq 1$) as:

$$\begin{aligned}
\mathcal{C}_1 &= -6u^5 + 15u^4 - 10u^3 + 1 \\
\mathcal{C}_2 &= 6u^5 - 15u^4 + 10u^3 \\
\mathcal{C}_3 &= -3u^5 + 8u^4 - 6u^3 + u \\
\mathcal{C}_4 &= -3u^5 + 7u^4 - 4u^3 \\
\mathcal{C}_5 &= -0.5u^5 + 1.5u^4 - 1.5u^3 + 0.5u^2 \\
\mathcal{C}_6 &= 0.5u^5 - u^4 + 0.5u^3
\end{aligned}$$

We can cast the parametric Equation (8.47) into a convenient matrix form for a single parametric quintic spline of a segment, if we re-organize the generalized coordinates q_m as:

$$\{q_m\} = \{q_1, q_2, q_3, ..., q_{18}\}^T \tag{8.48}$$

where the first nine components are for the beginning node of the segment; with $q_1 - q_3$ being three components of position, $q_4 - q_6$ three components of the tangent vector, and $q_7 - q_9$ three components of the normal vector. Correspondingly, q_{10} to q_{18} indicate all coordinates at the end of a segment. The shape functions for the quintic spline can also be organized in the following matrix form:

$$[\mathcal{C}_{im}] = \begin{bmatrix}
\mathcal{C}_1 & 0 & 0 & \mathcal{C}_3 & 0 & 0 & \mathcal{C}_5 & 0 & 0 & \mathcal{C}_2 & 0 & 0 & \mathcal{C}_4 & 0 & 0 & \mathcal{C}_6 & 0 & 0 \\
0 & \mathcal{C}_1 & 0 & 0 & \mathcal{C}_3 & 0 & 0 & \mathcal{C}_5 & 0 & 0 & \mathcal{C}_2 & 0 & 0 & \mathcal{C}_4 & 0 & 0 & \mathcal{C}_6 & 0 \\
0 & 0 & \mathcal{C}_1 & 0 & 0 & \mathcal{C}_3 & 0 & 0 & \mathcal{C}_5 & 0 & 0 & \mathcal{C}_2 & 0 & 0 & \mathcal{C}_4 & 0 & 0 & \mathcal{C}_6
\end{bmatrix} \tag{8.49}$$

With this notation, Equation (8.47) can be cast in the computational form of Equation (8.30). The total number of available degrees of freedom for a quintic spline segment is thus equal to the number of components in the Cartesian vector q_m, i.e. $N_{DF} = 6 \times 3 = 18$. However, because of geometric and physical restrictions on dislocation motion, N_{DF} can be greatly reduced, as we will discuss next.

Constrained Glide Motion and Reduced Degrees of Freedom

It is apparent that general dislocation motion would involve many degrees of freedom N_{DF} in the most general case. Fortunately, however, N_{DF} is small in practice. As a result of segment connectivity at common nodes, only half of the total DF's are required per segment, and $N_{DF} = 9$ for general 3-d motion, and $N_{DF} = 6$ for motion on a glide plane. The Peach-Koehler force on the glide plane imposes an additional constraints. As can be seen from Equations (8.14) and (8.17) , both external and self-forces on a dislocation node are along the normal direction $\mathbf{n}$. Also, because $\mathbf{n} \bullet \mathbf{t} = 0$, N_{DF} is reduced further from 6 to 4 for 2-d glide motion; that is one for the displacement magnitude, two for the tangent vector, and one for the magnitude of the normal. Furthermore, we introduce here two additional conditions, which simplify the loop

profile calculations even further. A *smoothness* condition is invoked such that rapid variations of curvature are avoided when two segments of vastly different lengths are connected via a composite spline. If the magnitude of the tangent is not related to nodal positions, undesirable *cusps* may develop on the dislocation line. Thus, we take the magnitude of the tangent vector to be estimated from the arc length between previous nodal positions on the segment. This criterion is exact when the parameter $u = s$, where s is the arc length itself. On the other hand, the line curvature can be independently computed from the dislocation configuration and nodal loading in a simple manner. If the forces at the node are not near equilibrium (i.e. the acting forces are much larger than the self-force), the curvature is determined from three neighboring nodes on the dislocation line. On the other hand, near equilibrium, the curvature of a node is readily computed from Equation (8.17), once the local external force is known. These approximations can lead to an additional reduction of two degrees of freedom, and we are left with solving for only two equations per node. These constraints can be relaxed, if one is interested in more complex details of dislocation motion. We will show later in Sec. 8.2.4 that dislocation glide motion can be adequately described in most cases with only two degree of freedom per node.

We derive here the constrained discrete equations of motion, when dislocation lines are confined to their glide plane. In this special case, there is six independent unknowns: $\Delta P_x, \Delta P_y, \Delta T_x, \Delta T_y, \Delta$ These correspond to incremental displacements, tangents, and normals in the x- and y-directions, respectively. Let us first consider the geometric constraints. Because the normal is always perpendicular to the tangent at the node, we have:

$$(\mathbf{T}^{(i)} + \Delta\mathbf{T}) \bullet (\mathbf{N}^{(i)} + \Delta\mathbf{N}) \quad (8.50)$$

$$\text{or, } \Delta T_x \Delta N_x + \Delta T_y \Delta N_y + N_x^{(i)} \Delta T_x + T_x^{(i)} \Delta N_x + N_y^{(i)} \Delta T_y + T_x^{(i)} \Delta N_y + T_x^{(i)} N_x^{(i)} + T_y^{(i)} N_y^{(i)} \quad (8.51)$$

where the symbols with superscript (i) refer to a previous time-step of known values (i.e. $\mathbf{T}^{(i+1)} = \mathbf{T}^{(i)} + \Delta\mathbf{T}$). Furthermore, from a geometric point of view, the curvature of the loop at a current time-step is related to the normal and tangent vectors as:

$$\kappa = \frac{||\mathbf{N}||}{||\mathbf{T}||^2} \quad (8.52)$$

where the curvature is assumed to be determined by local forces or nodal positions, as discussed earlier. The norm (magnitude) of the current tangent vector is proportional to the previous arc length of a segment. That is:

$$||\mathbf{T}|| = \eta \quad (8.53)$$

where η is determined by the arc length of the previous time-step. Finally, the displacement vector is perpendicular to the tangent direction of the considered node.

$$\frac{\Delta P_y}{\Delta P_x} = -\frac{T_x^{(i)}}{T_y^{(i)}} = \gamma \quad (8.54)$$

where γ is a constant determined by previous tangent components. Thus, by introducing an angle θ, which is the angle between the tangent vector and the x-direction, the six independent

unknowns can be reduced to only two: ΔP_x and θ, such that all constraints are automatically satisfied:

$$\begin{aligned}
\Delta P_x &= \Delta P_x \\
\Delta P_y &= \gamma \Delta P_x \\
\Delta T_x &= \eta cos\theta - T_x^{(i)} \\
\Delta T_y &= \eta sin\theta - T_y^{(i)} \\
\Delta N_x &= -\kappa \eta^2 sin\theta - N_x^{(i)} \\
\Delta N_y &= \kappa \eta^2 cos\theta - N_y^{(i)}
\end{aligned}$$

Moreover, a linearization technique can be used to approximate sine and cosine functions in terms of $\Delta\theta$, as long as the time-step is small, and hence the tangent angle variation is small between time-steps. Based on the above constraints, Equation (8.31) may finally be simplified with a reduced set of shape functions $\tilde{\mathcal{C}}$ as:

$$\{\delta x_i\} = \left[\tilde{\mathcal{C}}_{im}(u)\right] \{\delta q_m\} \tag{8.55}$$

where:

$$\{\delta r_i\} = \begin{Bmatrix} \delta x \\ \delta y \end{Bmatrix} \tag{8.56}$$

$$\{\delta q_m\} = \begin{Bmatrix} \delta P_{xB} \\ \delta \theta_B \\ \delta P_{yE} \\ \delta \theta_E \end{Bmatrix} \tag{8.57}$$

$$\left[\tilde{\mathcal{C}}_{im}(u)\right] = \begin{bmatrix} \mathcal{C}_1 & \mathcal{D}_1 & \mathcal{C}_2 & \mathcal{D}_2 \\ \gamma\mathcal{C}_1 & \mathcal{D}_3 & \gamma\mathcal{C}_2 & \mathcal{D}_4 \end{bmatrix} \tag{8.58}$$

and

$$\begin{aligned}
\mathcal{D}_1 &= -\eta_L \mathcal{C}_3 sin\theta_B - \kappa_B \eta_B^2 \mathcal{C}_5 cos\theta_B \\
\mathcal{D}_2 &= -\eta_E \mathcal{C}_4 sin\theta_E - \kappa_E \eta_E^2 \mathcal{C}_6 cos\theta_E \\
\mathcal{D}_3 &= \eta_L \mathcal{C}_3 cos\theta_B - \kappa_B \eta_B^2 \mathcal{C}_5 sin\theta_B \\
\mathcal{D}_4 &= \eta_E \mathcal{C}_4 cos\theta_E - \kappa_E \eta_E^2 \mathcal{C}_6 sin\theta_E
\end{aligned}$$

It is noted that the subscripts B and E refer to *Beginning* and *End* nodes of one segment of the dislocation loop.

Adaptive Protocols for Node and Time-step Assignments

Because of the evolving nature of dislocation line geometry as a result of strong interactions, it is highly desirable to develop adaptive methods which capture essential physics without

excessive computations. Control of the magnitude of the computational time-step, and nodal positions on each segment has a direct influence on the final accuracy of DD simulations. For node redistribution, we first compute a reference curvature $\bar{\kappa}$ for the entire loop, which is normally taken as the average curvature of all nodes. Then, we compare the curvature κ_i of each node with $\bar{\kappa}$, and classify nodes into high curvature groups ($\kappa_i > \bar{\kappa}$) and low curvature groups ($\kappa_i < \bar{\kappa}$). Finally, we increase the number of nodes for each high curvature group and decrease the number of nodes for each low curvature group. After adding or removing nodes, we redistribute the nodes evenly for that group. To prevent the number of nodes from increasing or decreasing too fast, we only add or remove one node at a time. If the number of nodes for a low curvature group is less than a specified minimum, we keep the current nodes because a prescribed minimum number of nodes is required to maintain the loop geometry. After redistributing nodes on each segment, we calculate the displacement and tangent angle of each new node based on the current loop geometry. The radius of curvature of each new node is determined by a linear interpolation from old nodes for open loops, or by circular arc approximations for closed loops. The highest curvature occurs always at fixed nodes or in the close proximity of other dislocations. In regions of high curvature, large self-forces occur and the curvature at the segment will be near its equilibrium value. Thus, the curvature in these special locations can be determined directly from the equilibrium condition on the segment. The entire geometry of the loop is finally determined by using Equation (8.47) at next time-step.

Time-step selection is determined by dislocation segment velocity and its adjacency to other segments. The time-step is selected such that, on average, dislocation-dislocation interaction is resolved within about 100 steps. If the dislocation density is ρ, the average distance between segments is on the order of $\rho^{-1/2} \sim 10^{-5} - 10^{-6}$ m. In fcc crystals, the dislocation resistivity is on the order of 5×10^{-5} Pa s, while it is about 8 orders of magnitude higher for screw segments in bcc crystals (**?**). These considerations lead to a time-step of $\sim 1ns$ for fcc crystals and $\sim 0.1s$ for bcc crystals at low temperatures. When two loop segments approach each other, a short-range reaction occurs, and the time-step must be reduced to determine whether the reaction will lead to annihilation or junction formation. In case of annihilation, two loops join together and form different new loops as a mode of plastic recovery. On the other hand, junction formation leads to hardening and stabilization of dislocation patterns. In either case, the minimum distance between segments on the loop itself, or on two adjacent loops is determined by calculating all local minimum distances from each node to a curved segment. By scanning all possible nodes of on a loop, we obtain the minimum distance d_{min} between two loops or between two segments on the loop itself. If this value is less than two times the maximum displacement, i.e. $2d_{max}$, then the time-step is adjusted to $0.25d_{min}/d_{max}$. This procedure is repeated until loop annihilation or junction formation is completed. After annihilation or junction formation is completed, the time-step is gradually increased to its maximum assigned value, as discussed above. During short-range encounters, local dislocation segment velocity can approach the sound speed, and inertial effects may have to be accounted for, if one is interested in the exact details of the short-range reaction (see (**?**)).

If new loops are generated during the short-range reaction, all nodes on the loop are rearranged. For loop junction formation, new loops are not generated, and the nodes are ordered to allow formation of straight junction segments. However, five possible cases for generating

new loops are considered during segment annihilation. On the glide plane, a full dislocation loop may be totally closed, or may have closure on other glide plane via sessile threading arms. Thus, we may have one of the following possibilities:(1) annihilation of two segments on the same open loop to produce one new open loop and one new closed loop; (2) annihilation of two segments on the same closed loop to produce two new closed loops; (3) annihilation of two segments on two different open-loops to produce two new open loops; (4) annihilation of two segments, one an open loop and the other on a closed one to produce one new open loop; (5) annihilation of two segments on two different closed loops to produce one new closed loop. In each case, the nodes on generated loops are reordered.

8.2.4 Applications of Parametric Dislocation Dynamics

Illustrative Example: Initial Bow-out of a Pinned Dislocation

To illustrate the computational procedure involved in the present method, we consider here a very simple example, where the equations of motion can be solved analytically for one time-step. Our purpose here is to highlight the essential features of the present computational method. More complex examples, which require extensive computations will be given in the next section. Assume that we are interested in determining the shape of a dislocation line, pinned at two ends and under the influence of pure shear loading on its glide plane. The glide mobility is assumed to be isotropic and constant, and the segments will be taken as linear for illustrative purp[oses only. The dislocation line is pinned at points L and R, with only two linear and equal segments connected at point A, as shown in Fig. 8.96. We will compute the shape of the line, advancing it from its initial straight configuration to a curved position. Under these simplifications, the variation in Gibbs free energy, δG for any one of the two segments is given by:

$$\delta G = -B \int_0^1 V \delta r \mid d\mathbf{s} \mid = -\int_0^1 f^t \delta r \mid d\mathbf{s} \mid \tag{8.59}$$

Now, we expand the virtual displacement and velocity in only two shape functions: $\mathcal{C}_1 = u, \quad \mathcal{C}_2 = 1 - u$. Thus:

$$\delta r_k = \delta q_{ik} \mathcal{C}_i \tag{8.60}$$

$$V_k = q_{ik,t} \mathcal{C}_i \tag{8.61}$$

Since we allow the displacement to be only in a direction normal to the dislocation line (y-direction), we drop the subscript k as well. For arbitrary variations of δq_{ik}, the following equation is applicable to any of the two segments (LA, AR).

$$-\int_0^1 \Delta t \times (f_{PK} + f_S) \mathcal{C}_i \mid ds \mid = -B \int_0^1 \Delta q_m \mathcal{C}_m \mathcal{C}_i \mid ds \mid \tag{8.62}$$

Equation (8.62) can be explicitly integrated over a short time interval Δt. The *resistivity matrix* elements are defined by: $\gamma_{im} \equiv B \int_0^1 \mathcal{C}_i \mathcal{C}_m \mid \mathbf{ds} \mid$, and the *force vector* elements by:

$f_i \equiv \int_0^1 \mathcal{C}_i \times (f_{PK} + f_S) \mid \mathbf{ds} \mid$. With these definitions, we have the following (2×2) algebraic system for each of the two elements:

$$\Delta q_m \gamma_{im} = f_i \times \Delta t \tag{8.63}$$

For any one linear element, the line equation can be determined by:

$$\begin{bmatrix} x \\ y \end{bmatrix} = \begin{bmatrix} u & 0 \\ 0 & (1-u) \end{bmatrix} \begin{Bmatrix} q_1 \\ \\ q_2 \end{Bmatrix} \tag{8.64}$$

And the resistivity matrix can the be simplified as:

$$[\gamma_{mn}] = \frac{Bl}{6} \begin{bmatrix} 2 & 1 \\ 1 & 2 \end{bmatrix} \tag{8.65}$$

Furthermore, as a result of the shear stress τ and the absence of self-forces during the first time-step only, the distributed applied force vector reads:

$$\{f_m\} = \frac{\tau bl}{2} \begin{Bmatrix} 1 \\ \\ 1 \end{Bmatrix} \tag{8.66}$$

Since the dislocation line is divided into two equal segments, we can now assmble the force vector, stiffness matrix and displacement vector in the global coordinates, and arrive at following equation for the global nodal displacements ΔQ_i:

$$\frac{Bl}{12} \begin{bmatrix} 2 & 1 & 0 \\ 1 & 4 & 1 \\ 0 & 1 & 2 \end{bmatrix} \begin{Bmatrix} \Delta Q_1 \\ \Delta Q_2 \\ \Delta Q_3 \end{Bmatrix} = \frac{\tau bl \Delta t}{4} \begin{Bmatrix} 1 \\ 2 \\ 1 \end{Bmatrix} + \Delta t \begin{Bmatrix} F_1 \\ 0 \\ F_3 \end{Bmatrix} \tag{8.67}$$

An important point to note here is that at the two fixed ends, we know the boundary conditions, but the reaction forces needed to satisfy overall equilibrium are unknown. These reactions act on the the fixed obstacles at $L\&R$, and are important in determining the overall stability of the configuration (e.g. if they exceed a critical value, the obstacle is destroyed, and the line is released). If $\Delta Q_1 = \Delta Q_3 = 0$ at both fixed ends, we can easily solve for the nodal displacement $\Delta Q_2 = \frac{3}{2}\frac{\tau b \Delta t}{B}$ and for the unknown reaction forces at the two ends: $F_1 = F_3 = -\frac{1}{8}\tau bl$. If we divide the dislocation line into more equal segments, the size of the matrix equation expands, but nodal displacements and reaction forces can be calculated similarly. Results of analytical solutions for successively larger number of nodes on the dislocation segment are shown in Fig. 8.96.

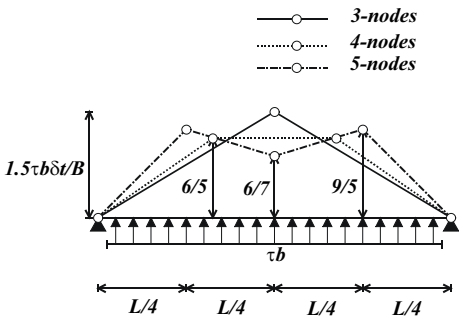

Figure 8.5: Nodal displacements for the first time-step of an initially straight segment.

Figure 8.6: Operation of the Frank-Read source for isotropic dislocation mobility on the glide plane.

Dislocation Loop Generation

Generation of new dislocation loops is an important process in determining the rate of hardening in materials under deformation. The basic mechanism involves the propagation of a dislocation segment from two immobile (fixed) ends under the action of applied stress. If the applied stress exceeds the resistance offered by the self-force, lattice friction, and additional forces from nearby dislocations, the segment length will increase. In fcc metals, the Peierls (friction) stress is very small, on the order of $10^{-5}\mu$, and is thus lower than typical applied stresses of $10^{-3}\mu$. Dislocation mobility is isotropic at all relevant temperatures because of the low value of Peierls stress in comparison to applied and self stresses on dislocation segments. Thus, the influence of the underlying crystal structure on dislocation generation is not pronounced. On the other hand, high anisotropic Peierls stresses in both fcc and diamond cubic (dc) materials (e.g. Si) imposes constraints on the shapes of generated dislocation loops in these systems, as discussed next.

Isotropic Mobility of Screw and Edge Segments

Fig. 8.7 shows the results of shape computations for the Frank-Read source in a bcc crystal at high temperature, where the dislocation segment mobility can be assumed to be isotropic on the $< 110 >$ glide plane. In this simulation, we use composite quintic spline segments to construct the loop after each time-step computation of the nodal displacement and tangent angle. The loop starts from an edge line segment with two fixed ends normal to the $< 11\bar{1} >$-direction, for which we assign only three nodes at the first time-step. The tangent vectors at the two end nodes are those of circular arcs constructed from three adjacent nodes. When the loop expands, more nodes are added around the two fixed end nodes (high curvature regions), while the number of nodes is automatically reduced in the low curvature region of the loop. After

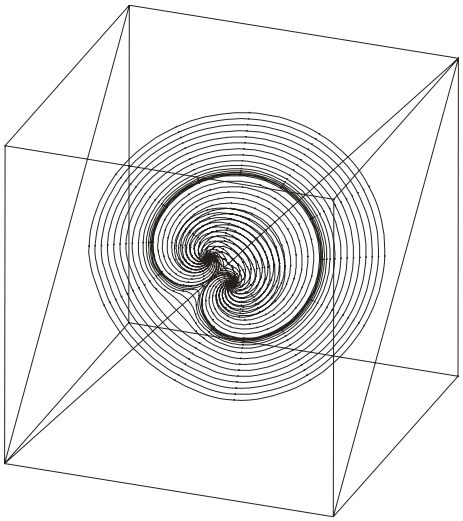

(a)

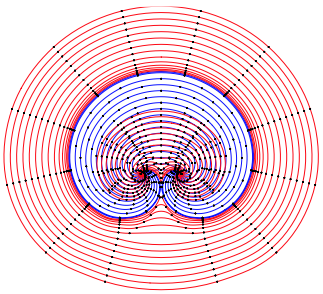

(b)

Figure 8.7: Operation of the Frank-Read source for isotropic dislocation mobility on the glide plane. (a) 3-d , (b) projection on the glide plane

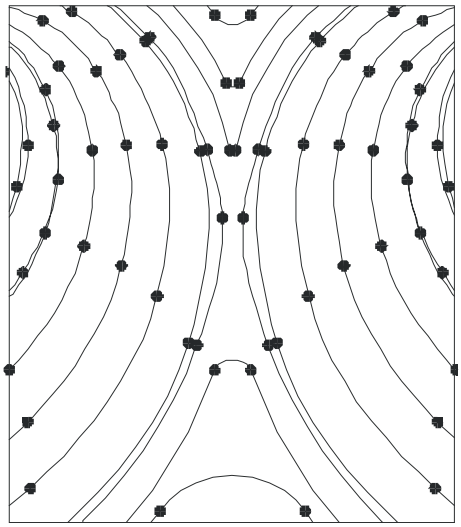

Figure 8.8: Details of nodal arrangements before annihilation of opposite-character segments.

each time-step, the minimum distance between loop segments is calculated. If the minimum distance is detected to be less than $6|\mathbf{b}|$, and $cos^{-1}(\mathbf{t}_1 \bullet \mathbf{t}_2) = (1. \pm 0.05)\pi$, the two segments are annihilated. Here, $\mathbf{t}_1 \& \mathbf{t}_2$ are the tangent vectors for segments 1 and 2, respectively. The value of $6|\mathbf{b}|$ for the critical annihilation distance in fcc is taken from experimental measurements on Cu (**?**) and Ni (**?**). Results of calculations are shown in Fig. 8.7, where nodal positions are indicated on each loop. Details of node rearrangement before and after an annihilation reaction between two curved segments on the Frank-Read source are shown in Fig. 8.8. The influence of the self-force on dislocation motion is significant, especially during short-range interaction of dislocation segments. In Fig.8.9, the angular distribution of the self-force on the glide dislocation loop, immediately after its formation by annihilation of opposite segments on the original dislocation line is shown. It is clear that the distribution of the self-force is negative everywhere on the loop, except for the small range of angles surrounding the newly formed dislocation segment. In this region, the self-force is positive, and thus it will assist the applied stress in expanding this curved region faster than others on subsequent time-steps. The action of applied and self-forces tend to even out curvature variations on the entire loop, once the short-range reaction is completed. The self-force is seen to be higher for the screw segments at $\theta = 90^o \& 270^o$, as compared to segments with a pure edge character.

Fig. 8.10 illustrates the operation of a single Frank-Read source on the $< 111 >$-plane in an fcc metal, where discrete barriers to dislocation motion are successively overcome by the expanding loop. The computational proptocol detects the existence of random barriers, such as other dislocations piercing the plane or defect clusters, and the loop is divided into two segments anchored at each barrier as a new node. The barrier strength is determined by a critical angle between the tangent to the dislocation and the normal to the node at the bottom

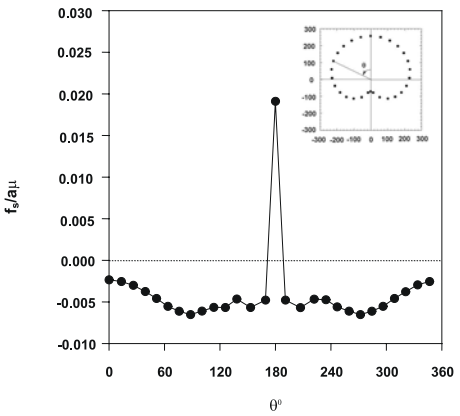

Figure 8.9: Angular variation of the self force (units of $\frac{\sigma}{\mu a}$) in copper for the Frank-Read source after segment annihilation. The angle θ is defined in the insert. All distances on the figure are in units of the lattice constant.

of the barrier. This critical angle has been determined to be $\sim 70^o$ for dislocation intersections in Cu by MD simulations (**?**).

BCC metals at low temperature

In bcc metals, the primary slip system is $\{110\} < 111 >$, although slip on secondary $\{112\}\&\{123\}$ planes are possible (**?**). Slip trace analysis at low temperature (**?**), (**?**) indicates that the main slip planes are $\{110\}$, and that dislocations are either of the screw or edge type. At temperatures below $T_a \sim 0.15T_m$, dislocations in bcc metals tend to move as straight lines, indicating that the mobility of the edge component is extremely high (**?**). The mobility of screw segments is controlled by double kink nucleation below the *athermal* temperature, T_a. Peierls lattice friction stress on screw components is very high, and the corresponding mobility is low. As the temperature increases, the influence of lattice friction on screw component mobility is reduced, and the mobility of screw and edge dislocations become comparable. It is expected, therefore, that dislocations become very straight at low temperatures, and that significant curvatures develop at higher temperatures. To adequately represent this physical picture, we use composite cubic spline curves joined with linear segments when necessary, and still maintain C^2 continuity at all nodes. In this case, the tangent directions of each curved segment are pre-determined by crystallography (i.e. $< 111 >$-directions for screw components), and only the magnitude of the tangent vector needs to be calculated from the condition of continuity. Additionally, nodes on expanding loops in this case are not re-distributed, but are selected to ensure construction of polygonal loop shapes, as is experimentally observed at low-temperature (**?**). The construction procedure of polygonal loop geometry is described as follows.

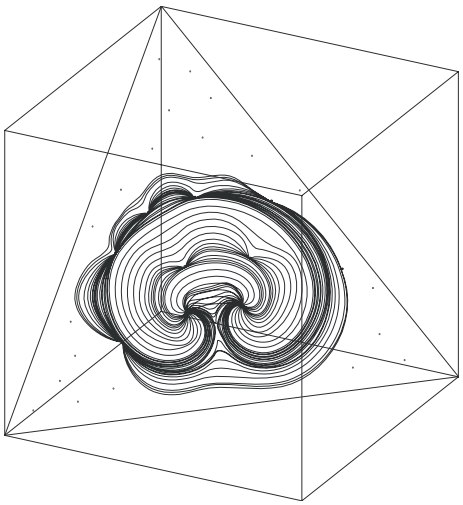

Figure 8.10: Interaction between a Frank-Read source and discrete barriers in fcc metals.

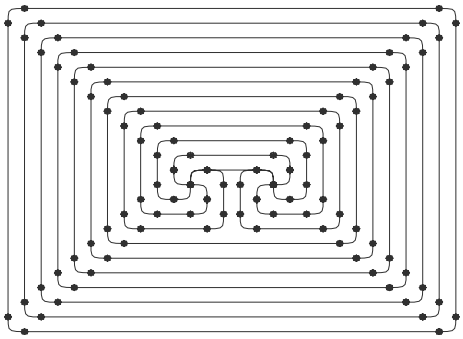

Figure 8.11: Double-ended Frank-Read source in bcc metals. The straight segments are either screw or edge, while the curved corners are of mixed type.

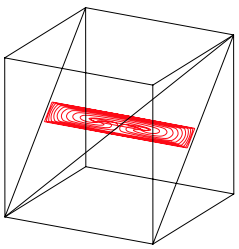

Figure 8.12: Dislocation loop generation by the Frank-Read mechanism for anisotropic mobility of screw and edge components.

First, straight linear segments are assigned parallel to specific crystallographic directions (i.e. $< 111 >$) for screw components. The displacement is computed for the entire linear segment in the normal edge direction. Then, two adjacent nodes at each corner of a the resulting rectangle are assigned, such that the distance of each node from the corner is proportional to the magnitude of the displacement, which is determined by the anisotropic mobility. Finally, after nodes are generated, the tangent direction of each node is aligned with the side of the polygon or is assigned a prescribed angle with the polygonal direction as an additional degree of freedom. For example, if the temperature is increased in bcc crystals, slight curvatures can be expected, and the tangent magnitudes can be solved for by applying the condition of C^2 continuity (Equation (8.46)). It is noted that at very low-temperatures in bcc metals, the mobility of edge components (kinks) is much higher than that of screw segments, and thus dislocation lines will be predominantly of the screw type. These features of adaptive shape computations are illustrated in Fig. 8.11 for low-temperature and Fig. 8.12 for higher temperatures.

Dislocation Sources in Si

Motion of dislocations on the glide plane of dc crystals, such as Si, occurs by breaking and reconstruction of strong covalent bonds. Thus, the resistance of the lattice to dislocation motion is significant up to very high temperatures (e.g 1200 K in Si). The dislocation must overcome a large energy barrier in the direction of maximum bond strength (i.e. the three $< 110 >$ close-

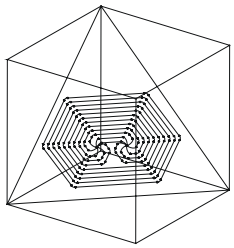

Figure 8.13: Dislocation generation in covalently-bonded silicon. The directions of the hexagon sides are along $< 111 >$-orientations for screw segments, and $\pm 60^o$ for mixed ones.

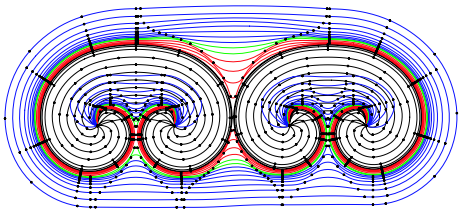

Figure 8.14: Coplanar dislocation loop interaction

packed directions on the {111}-family of slip planes), and a smaller one in directions $\pm 60^o$ to those primary ones. Dislocation segment mobility in Si is rather low, which leads to a time-step on the order of $0.01s$, similar to the situation in bcc metals (**?**).

When general cubic spline segments are used, we must solve for tangent vectors at each node, in addition to nodal displacements in order to generate the dislocation loop geometry at successive time-steps. However, for special polygonal loop geometries, additional constraints are needed to maintain accurate loop profiles. For this purpose, we use two types of segments: linear ones for the sides, and curved segments for polygonal corners. The curvature of all nodes is thus constrained to be zero, which guarantees the alignment of polygonal sides to crystallographic directions, as can be seen in Fig. 8.13. The procedure outlined above produces hexagonal loops with rounded corners, in agreement with the experimental observations on dislocation sources in Si by Dash (**?**).

Dislocation Loop Interactions

In this section, we illustrate the application of the present parametric method and its associated computational protocols to several problems involving the interaction of dislocation loops. In Fig. 8.14, two initial screw segments of equal length are assumed to be collinear, and of the same initial length on the [110]-slip plane of a bcc crystal at high temperature, and a high

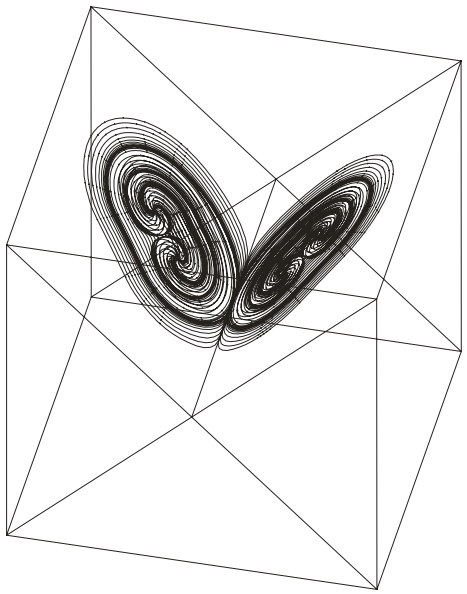

Figure 8.15: Formation of a dislocation junction in bcc metals

shear stress is applied on the slip plane. Bowing of the two segments is tracked with nodal displacements and tangent vector direction, and the loops are reconstructed by quintic spline segments after each time-step. The process is repeated till any two curved segments on the same loop, or on the two different loops, approach each other. The annihilation criterion is applied, leading to the loop profiles shown in Fig. 8.14. The applied stress is higher than the maximum value of the self energy after the two loops join one another, because the nodal curvatures are much smaller than corresponding values near the fixed ends of the each loop. Hence, further nodal displacements are not influenced as much with nodal curvatures, once the two loops join together as a single loop. Another illustration of loop-loop interaction is shown in Fig. 8.15, where two glide loops on different {111}-planes interact and form a sessile junction at the intersection between the two glide planes. In this case, the Burgers vector of the resulting junction does not lie on any of the two slip planes.

Figure (8.16) shows the results of computer simulations for the interaction between a slip dislocation on the $< 111 >$-glide plane in copper, after it is emitted from two fixed ends of a Frank-Read source with small defect clusters (Stacking Fault Tetrahedra (SFT)) in irradiated copper single crystals. The dislocation lines represent successive advancement stages under an applied shear stress. The corresponding values of the critical applied shear stress are: 93, 123, 154, and 185 MPa, respectively. A random distribution of SFT is introduced on the glide plane at an average spacing of $20nm$. The dislocation line seeks the nearest SFT and bends around it to a critical angle of $\sim 80^o$ before the obstacle is overcome. This critical angle is higher than the value attributed to dislocation-dislocation intersection in Cu, because the SFT is considered a

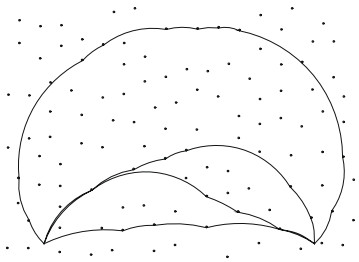

Figure 8.16: Computer simulation of forest hardening in Cu.

weak obstacle.

8.3 Numerical Accuracy & Convergence

The wide range of spatial and temporal scales involved in understanding the plastic deformation of materials at the nano-, micro-, single crystal, and polycrystalline levels necessitates the development of simulation methods of commensurate resolution and accuracy. While the details of dislocation configurations are relevant to resolving plasticity at the nano and micro-scales, they may not be of great impact at higher length scales. In addition, many physical mechanisms related to dislocations are inherently either stable or unstable. For example, above a critical applied stress value, it is known that the configuration of a Frank-Read source dislocation has no equilibrium solution. Most dislocation reactions have this *dynamic* feature, where junctions, dipoles, pileups, can all be either stable or unstable, depending on some critical stress level. It is therefore important to develop an understanding of the numerical accuracy, convergence and stability, so that one can actually resolve such critical reactions, without the effects of numerical artifacts. We plan to provide here an exposition of the numerical features of the PDD method when applied to the most significant dislocation interaction mechanisms.

The PDD methodology is based on two main principles that are often employed in modern numerical methods of continuum mechanics (e.g. the Finite Element Method **FEM**). The first is an energy-based variational principle, which allows derivation of the equations of motion (EOM) for a *reduced set* of Degrees Of Freedom (DOF). The second principle is a *kinematic* assumption regarding how the displacement or strain field varies in a specified region of the continuum. Thus, minimization of the Gibbs free energy of a single loop upon its virtual motion in the external and internal field results in the EOM, while assumed spline functions between fixed nodes on the dislocation loop corresponds to the kinematic assumption of continuum mechanics. The variational principle guarantees that the global energy is a minimum, but does not give specific information on the accuracy of dislocation configurations at every instant. Thus, the deviation of an assumed spline shape form (i.e. kinematic constraint), may actually lead to an erroneous configuration if that configuration is close to a critical state (e.g. Orowan stress, flow

stress for unlocking dislocations from cluster atmospheres, dipole and junction stability, etc.). The basic question here is, therefore, how crude can one be in imposing the kinematic shape constraint for a specified level of temporal or spatial resolution? It is fairly obvious that the answer will depend on the mechanism at hand, and the level of detail for our description of such mechanism.

The main objective of the present work is to determine the general limits of numerical accuracy and convergence of the PDD. This will be accomplished by analyzing specific dislocation mechanisms, and by determining the computational cost associated with desired levels of accuracy. Future large-scale computer simulations will be based on information generated from the present study, where the nodal densities and desired accuracy can be tailored for load balancing on parallel computational clusters. We plan to present systematic studies of two broad categories of dislocation mechanisms: generation (including Frank-Read (FR) sources, and pileups), and hardening (including finite size dipoles and junctions).

In section 8.3.1, we present a concise description of the PDD in a new dimensionless form. The temporal and spatial resolution of the PDD in a number of significant dislocation mechanisms will then be analyzed in section 8.3.2, for both generation in subsection 8.3.2, and hardening in subsection **??**. Finally, a discussion of these results and conclusions are given in section 9.5.5.

8.3.1 Dimensionless Equations of Motion for PDD

The method of PDD is described in sufficient detail in references (**?**)-(**?**), and we will attempt here to give only a brief description for completeness. The first step is to calculate the stress field of curved parametric segments. Let the Cartesian orthonormal basis set be denoted by $\mathbf{1} \equiv \{\mathbf{1}_x, \mathbf{1}_y, \mathbf{1}_z\}$, $\mathbf{I} = \mathbf{1} \otimes \mathbf{1}$ as the second order unit tensor, and $\otimes$ denotes out tensor product. Now define the three vectors ($\mathbf{g}_1 = \mathbf{e},\ \mathbf{g}_2 = \mathbf{t},\ \mathbf{g}_3 = \mathbf{b}/|\mathbf{b}|$) as a covariant basis set for the curvilinear segment, and their contravariant reciprocals as (**?**): $\mathbf{g}^i \cdot \mathbf{g}_j = \delta^i_j$, where δ^i_j is the mixed Kronecker delta and $V = (\mathbf{g}_1 \times \mathbf{g}_2) \cdot \mathbf{g}_3$ the volume spanned by the vector basis, as shown in Figure 9.51 . The parametric representation of a general curved dislocation line segment, shown in the figure, can be described by a parameter ω that varies from 0 to 1 at end nodes. The segment is fully determined as an affine mapping on the scalar interval $\{\omega \in [0, 1]\}$, if we introduce the tangent vector $\mathbf{T}$, the unit tangent vector $\mathbf{t}$, and the unit radius vector $\mathbf{e}$ as follows:

$$\mathbf{T} = \frac{d\mathbf{l}}{d\omega},\ \mathbf{t} = \frac{\mathbf{T}}{|\mathbf{T}|},\ \mathbf{e} = \frac{\mathbf{r}}{r}$$

Ghoniem, Huang and Wang (**?**) have shown that the elastic field of such a parametric segment can be obtained as an affine mapping transformation of the scalar parameter ω, and that the stress filed differential $d\sigma$ introduced by a parametric differential $d\omega$ are related as:

$$\frac{d\sigma}{d\omega} = \frac{\mu V|\mathbf{T}|}{4\pi(1-\nu)R^2}\left\{\left(\mathbf{g}^1\otimes\mathbf{g}_1+\mathbf{g}_1\otimes\mathbf{g}^1\right)+(1-\nu)\left(\mathbf{g}^2\otimes\mathbf{g}_2+\mathbf{g}_2\otimes\mathbf{g}^2\right)-(3\mathbf{g}_1\otimes\mathbf{g}_1+\mathbf{I})\right\} \tag{8.68}$$

Once the parametric curve for the dislocation segment is mapped onto the scalar interval $\{\omega \in [0,1]\}$, the stress field everywhere is obtained as a fast numerical quadrature sum from Equation 8.68 (**?**). To simplify the problem, let us define the following dimensionless parameters:

$$\mathbf{r}^* = \frac{\mathbf{r}}{a}, \qquad \mathbf{f}^* = \frac{\mathbf{F}}{\mu a}, \qquad t^* = \frac{\mu t}{B}$$

Here, a is lattice constant, $\mathbf{F}$ is resultant force which may consist of Peach-Koehler force (**?**) $\mathbf{F}_{PK}$ (generated by the sum of the external and internal stress fields), the self-force $\mathbf{F}_s$ generated by local curvature at the point of interest. μ is the shear modulus, t is time, and B is the isotropic dislocation mobility. Following (Ghoniem, Singh, Sun and Diaz de la Rubia 2000b), a closed dislocation loop can be divided into N_s segments. In each segment j, we can choose a set of generalized coordinates q_m at the two ends, thus allowing parametrization of the form:

$$\mathbf{r}^* = \mathbf{C}\mathbf{Q} \tag{8.69}$$

Here, $\mathbf{C} = \begin{bmatrix} C_1(\omega) & 0 & C_2(\omega) & 0 & \cdots & C_m(\omega) & 0 \\ 0 & C_1(\omega) & 0 & C_2(\omega) & & 0 & C_m(\omega) \end{bmatrix}$, $C_i(\omega), (i = 1,2,...m)$ are shape functions dependent on the parameter $(0 \le \omega \le 1)$, and $\mathbf{Q} = [q_1, q_2, ..., q_m]^\top$, q_i are a set of generalized coordinates. Substitute all these to the variational form of the governing equation of motion of a single dislocation loop (Ghoniem et al. 2000b), we obtain:

$$\sum_{j=1}^{N_s}\int_{\Gamma_j}\delta\mathbf{Q}^\top\left(\mathbf{C}^\top\mathbf{f}^* - \mathbf{C}^\top\mathbf{C}\frac{d\mathbf{Q}}{dt^*}\right)|d\mathbf{s}| = 0 \tag{8.70}$$

Let,

$$\mathbf{f}_j = \int_{\Gamma_j}\mathbf{C}^\top\mathbf{f}^*\,|d\mathbf{s}|, \qquad \mathbf{k}_j = \int_{\Gamma_j}\mathbf{C}^\top\mathbf{C}\,|ds|$$

Following a similar procedure to the FEM, we assemble the EOM for all contiguous segments in global matrices and vectors, as:

$$\mathbf{F} = \sum_{j=1}^{N_s}\mathbf{f}_j, \qquad \mathbf{K} = \sum_{j=1}^{N_s}\mathbf{k}_j$$

then, from EQN 8.70 we get,

$$\mathbf{K}\frac{d\mathbf{Q}}{dt^*} = \mathbf{F} \tag{8.71}$$

Equation 9.64 represents a set of ordinary differential equations, which describe the motion of an ensemble of dislocation loops as an evolutionary dynamical system. Generally, two numerical

time integration methods are available for solving this set of equations: the implicit and the explicit classes of procedures. We will later discuss the accuracy and stability issues associated with each scheme.

In the applications presented here, we specifically use cubic splines as shape functions, and confine dislocation motion to be on its glide plane(i.e. the climb speed is negligible). Thus, we end up with only 8 DOF for each segment with each node associated with 4 independent DOF. These cubic spline shape functions are given by:

$$C_1 = 2\omega^3 - 3\omega^2 + 1$$

$$C_2 = \omega^3 - 2\omega^2 + \omega$$

$$C_3 = -2\omega^3 + 3\omega^2$$

$$C_4 = \omega^3 - \omega^2$$

$$\mathbf{Q} = [\mathbf{P}_1, \mathbf{T}_1, \mathbf{P}_2, \mathbf{T}_2]^\top$$

Here, $\mathbf{P}_i$ and $\mathbf{T}_i$ $(i = 1, 2)$ correspond to the position and tangent vectors, respectively. In the following, we present results of studies for some of the main dislocation mechanisms to determine the effects of space and time discretization on the physical nature of the mechanism.

8.3.2 Spatial and Temporal Resolution of Dislocation Mechanisms

Dislocation Generation

F-R Source Symmetry and Stability

The Frank-Read mechanism of dislocation generation has been established as one of the primary processes which contribute to the increase in plastic strain upon application of a mechanical load. The main features of the mechanism have been documented in textbooks by hand sketches (e.g. references [(**?**)-(**?**)]). More recently, details of its evolution have been utilized as implicit test beds to validate the numerical procedures of 3-D DD [(**?**)-(**?**)]. Because of the existence of these extensive studies, we will apply the PDD to analyze the evolution of F-R sources, and show new aspects that are relevant to understanding the limitations of the PDD method in resolving spatial and temporal details. We examine in this section the following aspects of the F-R source evolution: symmetry of stable and unstable sources, stable/ unstable transition, shape accuracy as it depends on the number of segments (spatial resolution), solution stability (temporal resolution) and its dependence on time integration, adaptive nodal re-distribution techniques, and the accuracy of resolving dislocation annihilation and reconfiguration.

The influence of the Burgers vector direction on the evolution of F-R sources from an *initially straight* segment is determined in Figure **??**. A straight dislocation segment is pinned at two points ((-800,0) and (800, 0)) in the local coordinate system of the (111) glide plane of an FCC metal, and is divided into 20 cubic spline segments. Although the results can all be

given in dimensionless forms, it is instructive to use the properties of Cu for physical values. These are: $a = 0.36$ nm, $B = 10^{-4} Pa \cdot s$, $\mu \approx 50\ GPa$, and $\nu = 0.31$. These values show that when the dimensionless time is 1000, the physical time is 2 ps. The segment is subjected to a sudden uniaxial stress σ_{11}(corresponding to a critical resolved shear stress (CRSS) τ/μ). σ_{11} is represented by a step function in time. In Figure **??**, the initially screw segment has a Burgers vector of $\mathbf{b} = \frac{1}{2}[\bar{1}10]$, the edge has $\mathbf{b} = \frac{\sqrt{6}}{3}[\bar{1}\bar{1}1]$, while the initially mixed dislocation has $\mathbf{b} = \frac{1}{2}[\bar{1}01]$.

At the beginning, the curvature is almost zero everywhere and thus the effects of the self-forces are negligible. However, as the dislocation line bows out, the local curvature increases gradually, and then reaches its maximum value. In Figure**??**-a, the applied stress is relatively low ($\sigma_{11} = 80\ MPa$, or $\tau/\mu = 0.065\%$), thus the increase in the curvature everywhere eventually allows the self-force to balance the applied force and the F-R source achieves an equilibrium shape. It is noted that the shape of the F-R source is symmetric with respect to axis normal to its initial mid-point, for the initially pure screw and edge type of segments. The energy per unit length of a screw segment is lower than that for an edge segment. As a consequence, screw components tend to have higher self-forces (i.e. *stiffer*) than edge components. Figure **??** illustrates these features, where bowing out of initially screw dislocations is less pronounced than edge, both for the stable (Figure **??**-a) and unstable (Figure **??**-b) configurations. It is also noted that the F-R source *stretches* along the Burgers vector direction for the mixed character case, as it tries to minimize its total elastic energy by increasing the length of its line along the screw (Burgers vector) direction.

Since the overall curvature of the F-R source increases as it bows out, the applied stress must be increased to maintain successive equilibrium shapes. However, because the F-R source is pinned at the two ends only, other configurations of lower curvature are possible, and can pass through the same two fixed points. As a consequence, the average curvature of the F-R source reaches a maximum at a critical stress value (the Orowan stress), above which an unstable configuration of lower average curvature is reached. The transition from a stable F-R configuration to an unstable one is illustrated in Figure **??**-b, where the applied stress is high [$\sigma_{11} = 200$ MPa($\tau/\mu = 0.16\%$)], and the maximum self force cannot balance the external driving force. The dislocation will then continue expanding, which causes the curvature to decrease even further.

Resolution Limits of the F-R Shape

For large-scale computer simulations, there is an obvious need to reduce the computational burden without sacrificing the quality of the physical results. The smallest number of spline segments with the largest time step increment for integration of the EOM is a desirable goal. However, one must clearly identify the limits of this approach. We study here the influence of the nodal density on the dislocation line and the time integration scheme on the ability to satisfactorily resolve the shape of a dynamic F-R source. In order to estimate the error for different case, we define the absolute and relative errors, ϵ_a and ϵ_r, respectively, as follows:

$$\epsilon_a \quad = \quad \max \Delta r_i, i = 1, 2, ..., n$$

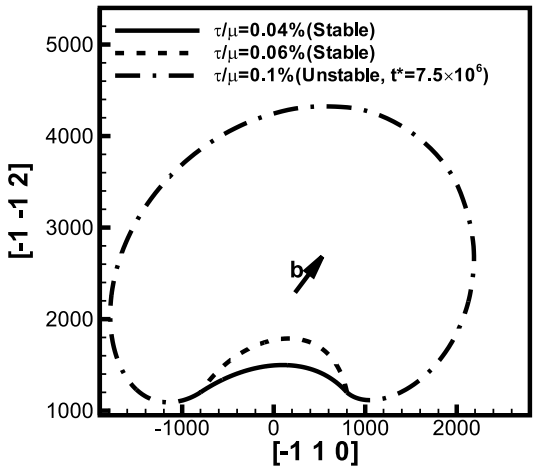

Figure 8.17: Effects of gradually increasing the applied stress on the evolution of an F-R source with $\mathbf{b} = \frac{1}{2}[\bar{1}01]$. When the Orowan stress is reached, the source is unstable

$$\epsilon_r = \left\{ \frac{1}{n} \sum_{i=1}^{n} \left(\frac{\Delta r_i}{r_i} \right)^2 \right\}^{1/2} \tag{8.72}$$

Here, $\Delta r_i = r_i - R_i$ is the error (difference) between the current position vector r_i at a sampling point i and a reference position vector at the same point, and n is the total number of sampling points on the dislocation line. The reference position vector R_i is that of a converged state (i.e. the highest resolution), since analytical solutions are not available.

In Figure 8.18, the dislocation line is divided into different number of segments, and the F-R source is evolved by numerical integration. Various levels of applied external stress are applied to the dislocation. Figure 8.18-a corresponds to low applied stress $\sigma_{11} = 80\ MPa(\tau/\mu = 0.065\%)$, resulting in a final stable configuration. It is shown that one can achieve very high precision

Table 8.1: Error Estimation for the stable state of a Frank-Read source.

No. of Segments	Absolute Error ϵ_a	Relative Error ϵ_r	CPU-time(sec)
2	6.06	0.17%	0.12
6	6.01	0.15%	0.42
15	1.32	0.018%	1.53
30	0	0	5.77

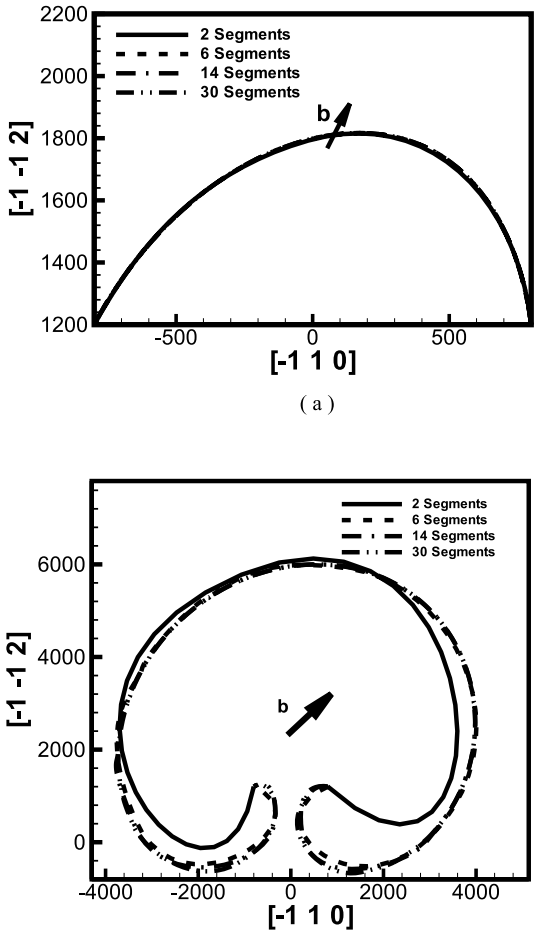

Figure 8.18: The influence of number of segments on the shape convergence of an F-R source with Burgers vector $\frac{1}{2}[\bar{1}01]$ at different stress levels: (a) stable state ($\sigma_{11} = 80\ MPa$, $\tau/\mu = 0.064\%$), (b)unstable state - same time: ($\sigma_{11} = 200\ MPa$, $\tau/\mu = 0.16\%$).

Table 8.2: Error Estimation for an unstable Frank-Read source at $t^* = 5 \times 10^6$.

No. of Segments	Absolute Error ϵ_a	Relative Error ϵ_r	CPU-time(sec)
2	1408.8	20.15%	0.02
6	191.1	5.04%	0.20
15	133.8	3.24%	2.53
30	142.0	2.93%	24.14
40	0	0	27.57

Table 8.3: Error Estimation for Different Integration Schemes. The implicit scheme is chosen as the reference configuration.

Integration Scheme	Absolute Error ϵ_a	Relative Error ϵ_r	CPU-time(sec)
Explicit ($\Delta t^* = 3000$)	168.4	6.11%	0.92
Explicit ($\Delta t^* = 1500$)	141.5	5.40%	1.82
Explicit ($\Delta t^* = 1000$)	56.90	2.34%	2.76
Explicit ($\Delta t^* = 500$)	0.06	0.003%	5.68
Implicit Integration	0	0	1.52

in describing the stable F-R shape with a very small number of segments. The dependence of the error on the number of segments is shown in Table 8.1. The reference configuration is chosen as that with 30 segments (thus the relative and absolute error is set to zero). It is found that as the number of segments increase, both the relative and absolute errors decrease sharply, while the CPU time (on a Pentium-III at 600 MHz) increases significantly. It is interesting to note that with only 2 segments, one can achieve almost the same resolution as that of 30 segments, with a relative error of less than 0.2%, while the CPU time is trivial compared with the case of 30 segments. However, when the F-R source becomes unstable, the variation of curvature is considerable between its middle section and the sections close to the pinning points. Figure8.18-b and Table 8.2 show the configuration and corresponding absolute error, relative error and CPU time, respectively, at higher applied stress $\sigma_{11} = 200MPa$ ($\tau/\mu = 0.16\%$). The dependence of the error on the number of segments is shown in Table 8.2 (the reference configuration in this case is chosen to be at 40 segments). It is found that with only 2 segments, poor shape accuracy is achieved, and a larger number of segments is needed for better accuracy. The curvature in this case is much higher near the fixed points. It is shown in Table 8.2 that with the increasing the number of segments, the accuracy is greatly increased, at the expense of a substantial increase in the CPU time.

The influence of the time integration method on the shape convergence of the F-R source is studied in Figure 8.19 and its corresponding error estimation at Table 8.3. The results of shape evolution for the explicit integration with different time steps are compared to those obtained with an implicit scheme. An one-step Euler forward integration explicit scheme is utilized. In the explicit scheme, it is noted that when the time step is larger than ≈ 3000,

a numerical shape instability sets in. For the parameters chosen here, this corresponds to a physical time step of ≈ 6 ps. The shape tends to diverge more along segments oriented near the screw direction. For a time step on the order of 1000 (i.e. $\Delta t \approx 2$ ps), the F-R shape is numerically stable, but not accurate. Finally, the F-R source shape converges (i.e. accurate and stable), when the explicit time step is less than 500 (i.e. $\Delta t \approx 1$ ps). Such small limit on the time step for high mobility crystals (e.g. FCC metals) can result in severe restrictions on the ability of current day computers to simulate plastic deformation of large volumes to realistic experimental times. An implicit integration method developed by C.W. Gear (**?**) is also used to test the same problem. The method is designed for the numerical integration of stiff, ordinary differential equations, with a variable time step that is automatically determined on the basis of the fastest variation of any of the DOF. A level of relative accuracy of 10^{-6} is selected as a convergence constraint. Since the time step is automatically adjusted to capture the specified level of accuracy, the overall scheme is stable and convergent. From Table 8.3, it is noted that the overall CPU time for explicit integration is much less than that for the explicit integration scheme to give comparable accuracy. This results from the ability to adjust the time step during explicit integration according to the stiffness of the equations, while the explicit Euler method has a fixed small time step to achieve the same level of accuracy.

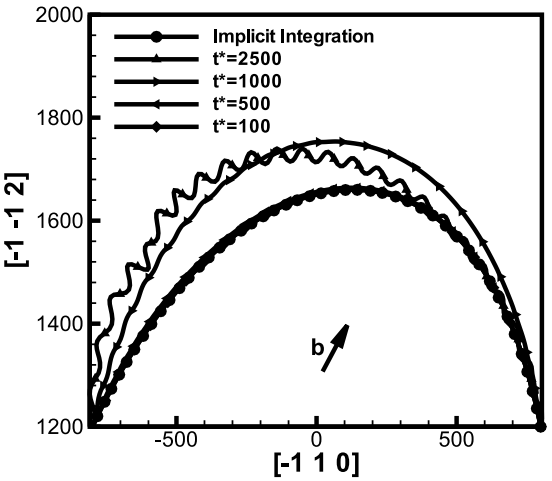

Figure 8.19: The influence of the time integration scheme on the shape convergence of an F-R source. Same conditions as in FIG. 8.18 .

Adaptive Node Redistribution

In small scale processes, such as the interaction between a dislocation and an atomic size defect cluster, or during the annihilation reaction between two dislocation segments of the same

Burgers vector and of opposite tangent vector direction, large variations of the local dislocation line curvature would be expected. To effectively resolve such mechanisms, we develop here a protocol for adaptively re-distributing the density of nodes on the dislocation line according to local curvature variation. The resolution level of this protocol is demonstrated by a study of the mechanism of dislocation segment annihilation during the expansion of an F-R source and the subsequent generation of a fresh dislocation loop. Figure 8.21 shows the details of the annihilation mechanism and the ensuing recovery process of a fresh closed loop, generated from an asymmetric F-R source. The simulation conditions are the same as in Figure 8.18, except that the applied stress $\sigma_{11} = 140$ MPa ($\tau/\mu = 0.112\%$), and the Burgers vector of the loop is $\mathbf{b} = \frac{1}{2}[0\bar{1}1]$.

The minimum distance between any two segments on the loop of opposite tangent vector directions is used to fully resolve the annihilation event. When this distance is less than a prescribed limit (e.g. 100), the time step is reduced and the integration proceeds further till the two segments are within a distance of 1-2 apart. The nodes are then re-distributed in the immediate region, resulting in two separate loops, as can be seen in Figure 8.21. After the annihilation event takes place, both new loops generate cusp regions, where the curvature is extremely high. To resolve such physical phenomena with sufficient accuracy, we develop here an adaptive node redistribution method.

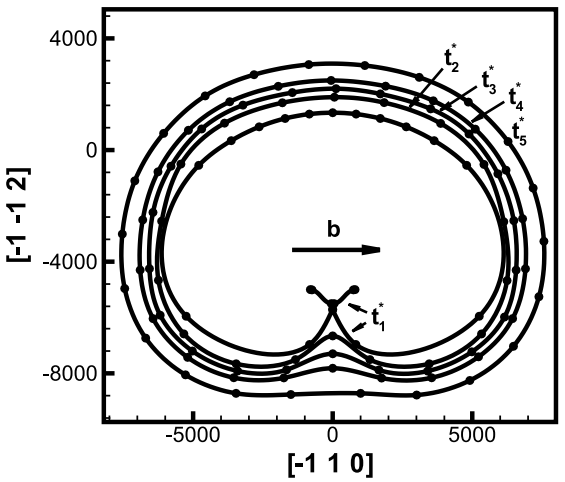

Figure 8.20: Expansion of an F-R source from an initially pure screw dislocation subjected to a step function stress $\sigma_{11} = 120$ MPa($\tau/\mu = 0.096\%$). The glide plane in Cu is (1 1 1), and the Burgers vector is $\mathbf{b} = \frac{1}{2}[0\bar{1}1]$. At the instant of annihilation the time is reset to $t_1^* = 0$. Subsequent dimensionless times are: $t_2^* = 1.0 \times 10^6$, $t_3^* = 1.5 \times 10^6$, $t_4^* = 2.0 \times 10^6$, $t_5^* = 3.0 \times 10^6$.

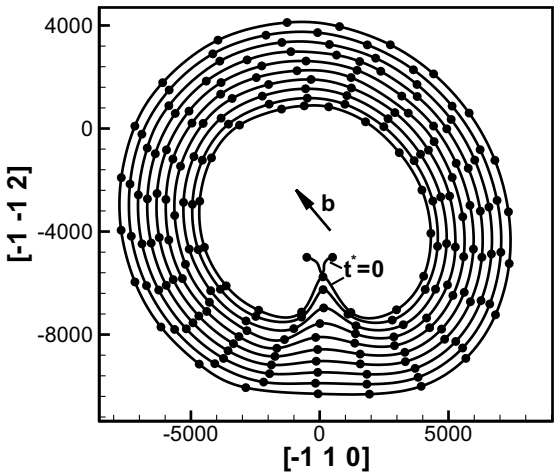

Figure 8.21: Expansion of an initially mixed dislocation segment in an F-R source under the step function stress of $\sigma_{22} = 140$ MPa($\tau/\mu = 0.112\%$). The F-R source is on the (1 1 1)-plane of a Cu crystal with Burgers vector $\mathbf{b} = \frac{1}{2}[0\bar{1}1]$. The time interval between different contours is $\Delta t^* = 5 \times 10^5$.

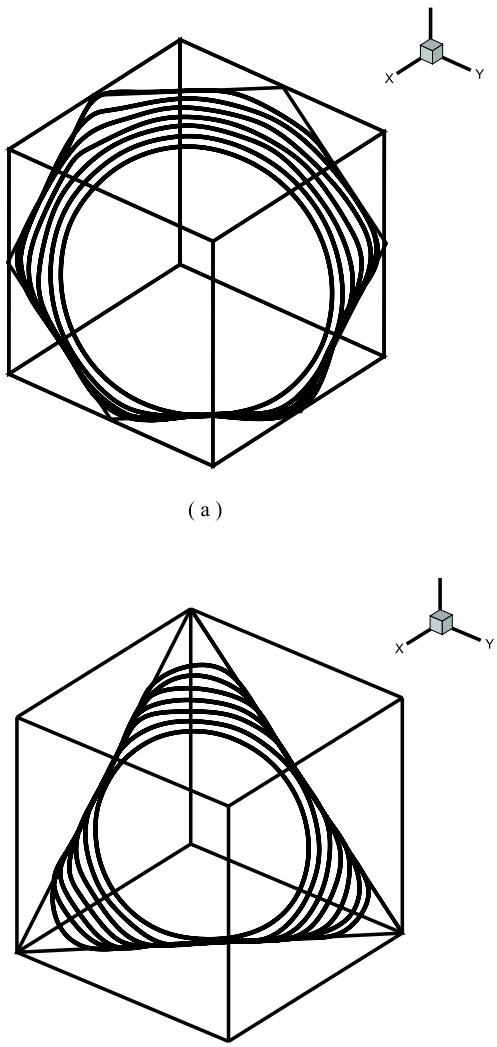

Figure 8.22: The effects of a rigid grain boundary in Cu on the evolution of a closed dislocation loop emanating from an F-R source. Conditions are the same as in FIG. 8.20, the time interval between successive positions $\Delta t^* = 1.5 \times 10^6$.

In the present algorithm, nodal redistribution is invoked at prescribed time intervals. Each cubic spline segment is divided into several sub-segments with equal arc length, and new ghost nodes are assigned. Thus, the entire loop is now filled with ghost nodes of equal nodal density per unit line length. The total number of DOF for the loop is not changed up till this point. The average loop curvature κ_{avg} is determined simply as the mean value of the maximum κ_{max}, and minimum κ_{min} curvatures of all ghost nodes. We then start from one end of the loop at a node of curvature κ (say CW), and skip a number of ghost nodes N_{skip} determined by the relation:

$$N_{skip} = C(\kappa_{avg}/\kappa) \tag{8.73}$$

where C is an adjustable constant. Thus, more nodes are added to high curvature zones, while in low curvature zones less nodes are introduced. In Figure 8.21, node re-distribution is shown in each closed loop. The total number of nodes in each loop at a given time is generally kept under 25.

Dislocation pileups

Dislocation generation by the F-R mechanism leads to an increase in the dislocation density, and hence the total strain. This process is however limited by dislocation interaction with various obstacles. Grain boundaries represent strong obstacles to dislocation motion, and have important effects on the subsequent dynamics of dislocation loops emitted from F-R sources. Strong grain boundaries can confine dislocations within the grain where they are emitted. If the F-R source continues to emit dislocations, new loops will interact with the immobilized leading dislocation, and as a result will form a *dislocation pileup*. In the following study, a single crystal is represented by a cube, 30000 (or 10 μm) in length. One F-R source of an initially mixed dislocation character, with Burger's vector $\frac{1}{2}[0\bar{1}1]$, under an applied uniaxial stress $\sigma_{22} = 140$ MPa ($\tau/\mu = 0.112\%$), is situated within the crystal to emit dislocation loops. For a rigid grain boundary, the leading loop nodes are assigned zero displacement condition once they reach the boundary. Figure 8.23 shows the formation of a 3-loop pileup from the same F-R source. The same nodal re-distribution strategy is used for each generated closed loop for higher accuracy.

8.4 O(N) Algorithms

8.4.1 Multipole Representation of Dislocation Fields

Although DD has been successfully applied to a wide range of physical problems, especially for problems involving length scales in the nano-to-micro range(**?**, **?**), the extension of the approach to larger length scales (e.g. for application in polycrystalline material deformation) is still a daunting task. The main impediment in this direction is the lack of methods for systematic and rigorous "coarse-graining" of discrete dislocation processes. Notable recent developments in this area have been advanced by LeSar and Rickman(**?**).

The main objective of the present work is to develop a "coarse-graining" approach for eval-

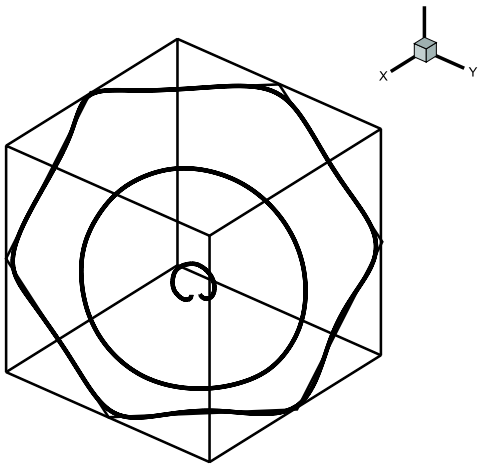

(a)

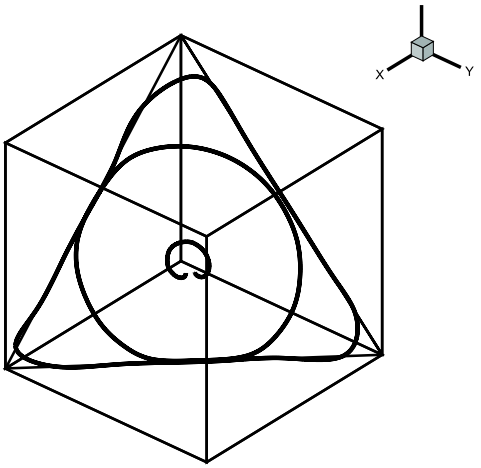

(b)

Figure 8.23: The effects of a rigid grain boundary of triangular cross-section in Cu on the evolution of a closed dislocation loop emanating from an F-R source. Conditions are the same as in FIG. 8.22.

uation of the elastic field of large dislocation loop ensembles of arbitrary geometric complexity. The method is an extension of the Lesar-Rickman multipole expansion of the elastic energy of dislocation ensembles(**?**). The broad "coarse-graining" objective of the present work is associated with a number of motivating reasons for this development, as given below.

1. To access the physics of plasticity through direct large-scale computer simulations of dislocation microstructure evolution. This is enabled by a substantial reduction of the speed of computation.
2. To remove the "cut-off" distance limitation in dislocation-dislocation interactions, and hence facilitate our understanding of microstructure evolution sensitivity to such computational limitation.
3. To allow efficient determination of the "effective" influence of dislocation arrays (e.g. in some representation of grain boundaries), or complex dislocation blocks (e.g. in dislocation walls and tangles) on the interaction with approaching dislocations.
4. To enable embedding into well established, $O(N)$, computational procedures for particle systems of long-range interactive force fields(**?**).
5. To shed more light on the connection between discrete dislocation dynamics, the Kröner-Kosevich continuum theory of dislocations(**?**), and moments of a basic local tensor that characterize the spatial distribution of dislocations.

In the following, we present the multipole expansion method (MEM) formulation in section **??**. In $O(N)$ methods for calculation of the effective fields in particle systems with long range interaction force fields, moments evaluated for smaller volumes are usually transferred or combined with moments defined in other volumes. This issue will be explained in section 8.4.2. Results for the far-field expansion of the stress field and interaction forces are given in section 8.4.2, while applications of the method to dislocation arrays in special boundaries or dislocation walls are presented in section 8.4.3. Finally conclusions of this work are presented in section **??**.

The stress field at any point from a single closed dislocation loop can be written as(Ghoniem, Huang and Wang 2002a):

$$\sigma_{ij} = \frac{\mu b_n}{8\pi} \oint [R_{,mpp}(\epsilon_{jmn} dl_i + \epsilon_{imn} dl_j) + \frac{2}{1-\nu} \epsilon_{kmn} (R_{,ijm} - \delta_{ij} R_{,ppm}) dl_k] \tag{8.74}$$

where $\mathbf{R} = \mathbf{Q} - \mathbf{P}$ is the vector connecting field point Q and source point P at dislocations (Figure 9.51 (a)). The stress field per unit volume of an ensemble of dislocation loops in a volume Ω, some of them may not be closed within Ω, is given by:

$$\begin{aligned} \sigma_{ij} \;=\; & \frac{\mu}{8\pi\Omega} \left\{ \sum_{\xi=1}^{N_L^{SSD}} \oint_{\xi} [R_{,mpp}(\epsilon_{jmn} dl_i + \epsilon_{imn} dl_j) + \frac{2}{1-\nu} \epsilon_{kmn} (R_{,ijm} - \delta_{ij} R_{,ppm}) dl_k] \right. \\ & \left. + \sum_{\xi=N_L^{SSD}+1}^{N_L} \int_{\xi} [R_{,mpp}(\epsilon_{jmn} dl_i + \epsilon_{imn} dl_j) + \frac{2}{1-\nu} \epsilon_{kmn} (R_{,ijm} - \delta_{ij} R_{,ppm}) dl_k] \right\} \end{aligned} \tag{8.75}$$

where N_L^{SSD} is the number of statistically stored dislocation(SSD) loops, which are closed within the volume Ω, N_L^{GND} is the number of geometrically necessary dislocation(GND) loops, which intersect the surfaces of the volume Ω, $N_L = N_L^{SSD} + N_L^{GND}$ is the total number of dislocation loops in the volume Ω.

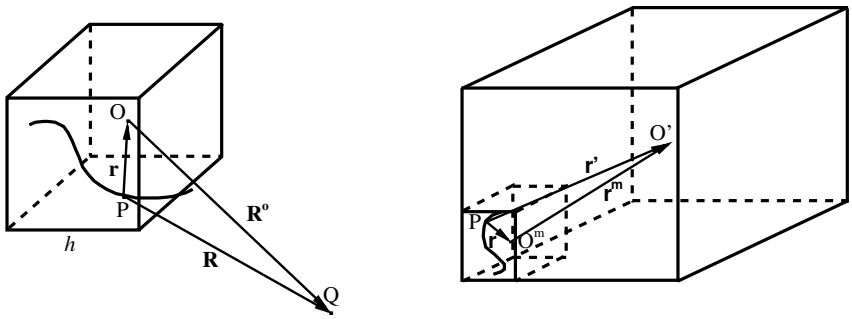

(a) (b)

Figure 8.24: Illustration of the geometries of (a) a single volume with center O containing dislocations, (b) a single volume (center $O^{'}$) containing many small volumes with centers O^m.

Suppose that the distance between point P on a dislocation and a field point Q is relatively larger than the size h of a certain volume that contains the dislocation loop, as shown in Figure 9.51. Point O is the center of the volume. Let us write the Taylor series expansion of the derivatives of vector $\mathbf{R}$ at point O as follows:

$$R_{,ijm} = R^o_{,ijm} + R^o_{,ijmk} r_k + \frac{1}{2!} R^o_{,ijmkl} r_k r_l + \frac{1}{3!} R^o_{,ijmkln} r_k r_l r_n + ... \tag{8.76}$$

where $\mathbf{r} = \mathbf{O} - \mathbf{P}$ and $\mathbf{R}^o = \mathbf{Q} - \mathbf{O}$.

Substituting these expansions in equation (8.75), and recognizing that $R^o_{,mpp}$, $R^o_{,ijm}$, $R^o_{,ppm}$ and their higher order derivatives depend only on $\mathbf{R}^o$, we find:

$$\begin{aligned}
\sigma_{ij} \;=\; & \frac{\mu}{8\pi} \Big\{ \Big[R^o_{,mpp}(\epsilon_{jmn}\alpha_{ni} + \epsilon_{imn}\alpha_{nj}) + R^o_{,mppq}(\epsilon_{jmn}\beta_{niq} + \epsilon_{imn}\beta_{njq}) \\
& + \frac{1}{2!} R^o_{,mppqs}(\epsilon_{jmn}\gamma_{niqs} + \epsilon_{imn}\gamma_{njqs}) \\
& + \frac{1}{3!} R^o_{,mppqst}(\epsilon_{jmn}\psi_{niqst} + \epsilon_{imn}\psi_{njqst}) + ... \Big] \\
& + \frac{2}{1-\nu} \epsilon_{kmn} \Big[R^o_{,ijm}\alpha_{nk} + R^o_{,ijmq}\beta_{nkq}
\end{aligned}$$

$$+\frac{1}{2!}R^o_{,ijmqs}\gamma_{nkqs}+\frac{1}{3!}R^o_{,ijmqs}\psi_{nkqst}+...\Big]$$
$$-\frac{2}{1-\nu}\delta_{ij}\epsilon_{kmn}\Big[R^o_{,ppm}\alpha_{nk}+R^o_{,ppmq}\beta_{nkq}$$
$$+\frac{1}{2!}R^o_{,ppmqs}\gamma_{nkqs}+\frac{1}{3!}R^o_{,ppmqst}\psi_{nkqst}+...\Big]\Big\} \tag{8.77}$$

where we define the dislocation moments of zeroth order within the volume Ω as:

$$\begin{aligned}\alpha_{ij} &= \frac{1}{\Omega}\sum_{\xi=1}^{N_L^{SSD}}\oint_\xi E^\xi_{ij}dl+\frac{1}{\Omega}\sum_{\xi=N_L^{SSD}+1}^{N_L}\int_\xi E^\xi_{ij}dl \\ &= \frac{1}{\Omega}\sum_{\xi=N_L^{SSD}+1}^{N_L}\int_\xi E^\xi_{ij}dl\end{aligned} \tag{8.78}$$

where $dl=|d\mathbf{l}|$ is an infinitesimal line length along the unit tangent $\mathbf{t}$. The Eshelby rational tensor E_{ij}, defined as $E^\xi_{ij}=b^\xi_i t^\xi_j(\mathbf{P})$, is a local tensor because it is defined at point $\mathbf{P}$ on a loop ξ, where t^ξ_i is the tangent vector at position $\mathbf{P}$ and $\mathbf{b}^\xi$ is the Burgers vector of the loop. It is clear that the only contribution to the tensor α_{ij} is from GNDs (i.e. the second term), since the contribution of SSDs is identically zero by virtue of the closed loop property. Equation 8.78 gives Nye's dislocation density tensor α_{ij}(**?**, **?**). This tensor is directly related to the lattice curvature tensor $\boldsymbol{\kappa}$ by(**?**):

$$\boldsymbol{\kappa}=\frac{1}{2}Tr(\boldsymbol{\alpha})\boldsymbol{I}-\boldsymbol{\alpha} \tag{8.79}$$

where $\mathbf{I}$ is the second-order unit tensor. Higher-order tensors $\boldsymbol{\beta}$, $\boldsymbol{\gamma}$, $\boldsymbol{\psi}$, ..., correspond to higher-order moments of the Eshelby rational tensor, and are defined as:

$$\begin{aligned}\beta_{ijk} &= \frac{1}{\Omega}\sum_{\xi=1}^{N_L}\int_\xi r_k E_{ij}dl \\ \gamma_{ijkl} &= \frac{1}{\Omega}\sum_{\xi=1}^{N_L}\int_\xi r_k r_l E_{ij}dl \\ \psi_{ijklq} &= \frac{1}{\Omega}\sum_{\xi=1}^{N_L}\int_\xi r_k r_l r_q E_{ij}dl \\ \zeta_{ijklq...p} &= \frac{1}{\Omega}\sum_{\xi=1}^{N_L}\int_\xi r_k r_l r_q \dots r_p E_{ij}dl\end{aligned} \tag{8.80}$$

We can write the stress field resulting from a dislocation ensemble within the volume Ω as:

$$\begin{aligned}\sigma_{ij} &= \frac{\mu\Omega}{8\pi}\sum_{t=0}^{\infty}\frac{1}{t!}\Big[R^o_{,mppa_1...a_t}(\epsilon_{jmn}\langle\zeta_{nia_1...a_t}\rangle+\epsilon_{imn}\langle\zeta_{nja_1...a_t}\rangle) \\ &\quad +\frac{2}{1-\nu}\epsilon_{kmn}R^o_{,ijma_1...a_t}\langle\zeta_{nka_1...a_t}\rangle-\frac{2}{1-\nu}\delta_{ij}\epsilon_{kmn}R^o_{,ppma_1...a_t}\langle\zeta_{nka_1...a_t}\rangle\Big]\end{aligned} \tag{8.81}$$

where $\langle \zeta_{ijk\ldots} \rangle$ represent the moments defined above of different orders, as α_{ij}, β_{ijk}, γ_{ijkl}, etc. These moments depend only on the selected center point O and the distribution of the dislocation microstructure within the volume. They can be evaluated for each volume independently. After the moments are determined, the stress field and interaction forces on other dislocations that are sufficiently well separated from the volume Ω are easily obtained.

8.4.2 Rules for Combination of Moments

For a fixed field point, if the distance of a volume to this point is larger than its characteristic size, we can utilize moments obtained from smaller sub-volumes to generate moments for the total volume. This procedure is similar to the "parallel axis theorem" for shifting moments of inertia for mass distributions in mechanics. Suppose that this large volume is composed of several sub-volumes and we have multipole expansions for each sub-volume, we develop here a procedure to obtain multipole expansion for the large volume from those for the sub-volumes instead of doing the calculations again for each dislocation loop. This idea is very suitable for hierarchical tree algorithms, such as the Greengard-Rokhlin method(**?**). We will describe formulations for combination of multipole expansions in this section.

Assume that a large material volume Ω centered at $\mathbf{O}^{'}$ contains M small sub-volumes centered at O^m, with their volumes as Ω^m, where m is an index(Figure 9.51 (b)). Here, $\mathbf{r}^m$ is the vector connecting O^m and $O^{'}$. The new vector connecting the center $O^{'}$ and a point on a dislocation is $\mathbf{r}^{'} = \mathbf{r} + \mathbf{r}^m$, where $\mathbf{r}^m = \mathbf{O}^{'} - \mathbf{O}^m$. With the dislocation moments for the m^{th} small material volume as α_{ij}^m, β_{ijk}^m, $\ldots$, we can write the moments of dislocations in the m^{th} sub-volume in the large volume as follows:

$$
\begin{aligned}
\alpha_{ij}^{m'} &= \frac{1}{\Omega} \sum_{\xi=N_L^{SSD^m}+1}^{N_L^m} \int_\xi E_{ij}^\xi dl = f^m \alpha_{ij}^m \\
\beta_{ijk}^{m'} &= \frac{1}{\Omega} \sum_{\xi=1}^{N_L^m} \int_\xi r_k^{'} E_{ij}^\xi dl \\
&= \frac{1}{\Omega} \sum_{\xi=1}^{N_L^m} \int_\xi (r_k + r_k^m) E_{ij}^\xi dl \\
&= \frac{1}{\Omega} \sum_{\xi=1}^{N_L^m} \int_\xi r_k E_{ij}^\xi dl + \frac{1}{\Omega} \sum_{\xi=1}^{N_L^m} \int_\xi r_k^m E_{ij}^\xi dl \\
&= f^m (\beta_{ijk}^m + r_k^m \alpha_{ij}^m) \\
\gamma_{ijkl}^{m'} &= \frac{1}{\Omega} \sum_{\xi=1}^{N_L^m} \int_\xi r_k^{'} r_l^{'} E_{ij}^\xi dl \\
&= f^m (\gamma_{ijkl}^m + r_k^m \beta_{ijl}^m + r_l^m \beta_{ijk}^m + r_k^m r_l^m \alpha_{ij}^m) \\
&\ldots
\end{aligned}
\tag{8.82}
$$

where $f^m = \frac{\Omega^m}{\Omega}$, N_L^m and $N_L^{SSD^m}$ are volume fraction, the number of total dislocation loops,

and SSDs in the mth volume, respectively.

Then, the total moments of dislocation loop distributions within the large volume are given by:

$$\begin{aligned}
\alpha_{ij} &= \sum_{m=1}^{M} \alpha_{ij}^{m'} = \sum_{m=1}^{M} f^m \alpha_{ij}^m \\
\beta_{ijk} &= \sum_{m=1}^{M} \beta_{ijk}^{m'} = \sum_{m=1}^{M} f^m \left(\beta_{ijk}^m + r_k^m \alpha_{ij}^m\right) \\
\gamma_{ijkl} &= \sum_{m=1}^{M} \gamma_{ijkl}^{m'} = \sum_{m=1}^{M} f^m \left(\gamma_{ijkl}^m + r_k^m \beta_{ijl}^m + r_l^m \beta_{ijk}^m + r_k^m r_l^m \alpha_{ij}^m\right) \\
&\dots
\end{aligned} \tag{8.83}$$

Equation (8.83) can be written in a compact form as:

$$\zeta_{ija_1\dots a_n} = \sum_{m=1}^{M} f^m \left\{ \sum_{p=0}^{n} \left[\sum_{q=1}^{C_n^p} \left[\left(r_{t_1}^m r_{t_2}^m \dots r_{t_p}^m\right) \langle \zeta_{ijt_{p+1}\dots t_n}^m \rangle \right] \right] \right\} \tag{8.84}$$

where $n = 0, 1, 2, \dots$ is the order of the moment. Here, $\sum_{q=1}^{C_n^p}$ means that r^m's sub-index group of $t_1 \dots t_p$ are selected from the n index group of a_n in a permutational manner, and group of indices $t_{p+1} \dots t_n$ are the corresponding $n-p$ indices of a_n after the selection.

Numerical Results

Based on the equations developed in the previous sections, we numerically implement here the multipole expansion for the stress field of a dislocation ensemble, expressed by equation (8.81). We consider here the results of the full calculation based on equation (8.75) as reference, and calculate relative errors from the MEM as $|\sigma_{MEM} - \sigma_{ref}|/\sigma_{ref}$. Tests are performed on a volume with h=10 μm for different expansion orders and different values of R/h. Dislocations are generated randomly inside the volume and with a density of 5×10^8 cm/cm^3. Numerical results are shown in figure (8.25). From these results, it is clear that the approximate moment solutions converge fast. For different values of R/h, the second order expansion gives a relative error less than 1%, while the fourth order expansion gives a relative error less than 0.05%.

8.4.3 Applications to dislocation boundaries and walls

Dislocation Interaction with A Tilt Boundary

An important consequence of heavy plastic deformation is the re-arrangement of dislocations into well-separated tangles or periodic arrays. Dislocation tangles evolve into walls that can act as sources of new dislocations, or stop approaching glide dislocations from neighboring volumes. On the other hand, some grain boundaries can be represented by dislocation arrays. The elastic field generated by grain boundaries in compatibility can thus be determined from the dislocation

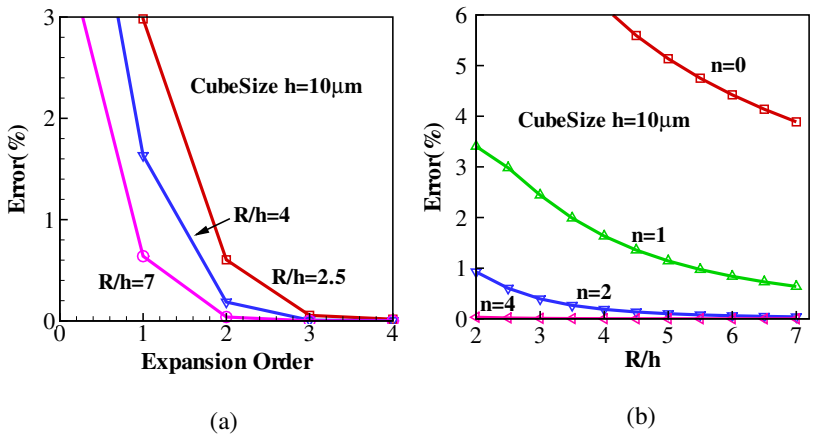

Figure 8.25: Relative error of the MEM vs (a) the expansion order, (b) the R/h value for a simulation volume with an edge length of 10 μm.

array representing its structure. Such dislocation microstructures have profound effect on the deformation characteristics of materials, and more often, some "effective" properties are needed. In this section, we investigate the feasibility of "effective" elastic representation of periodic dislocation arrays and dislocation walls utilizing the MEM derived earlier. We will first analyze the effective influence of a tilt boundary on the deformation of a dislocation emitted from a near-by Frank-Read source. We will then investigate the nature of the Peach-Koehler force on dislocations approaching a dense entanglement of dislocations within a dislocation wall. The following examples are for single crystal Cu, with the following parameters: shear modulus $\mu = 50$ GPa, lattice constant $a = 3.615 \times 10^{-10}$ m, Poisson's Ratio $\nu = 0.31$.

Figure 8.26 shows the geometry of a 1° tilt boundary containing 35 dislocations with $\frac{1}{2}[\bar{1}01]$ Burgers vector. A Frank-Read(FR) source is located 1 μm away from the tilt boundary. The source, which lies on the [111] glide plane, and emits dislocations with $[\bar{1}2\bar{1}]$ tangent vector and $\frac{1}{2}[\bar{1}01]$ Burgers vector as well. The initial length of the F-R source dislocation between pinned ends is 700 a. A constant uniaxial stress of 25 MPa is applied in the [100]-direction.

Dislocation motion under the influence of the externally applied stress and the internal stress generated by the tilt boundary is determined using the method of Parametric Dislocation Dynamics(PDD)(Ghoniem et al. 2000b, Ghoniem et al. 2002a). Interaction forces between the tilt boundary and the F-R source dislocation are calculated by two methods:(1) the fast sum method(**?**), which adds up the contributions of every dislocation segment within the boundary; (2) the current MEM up to second-order quadropole term. Dislocation configurations at different time steps are shown in figure 8.27(a). The relative error in the MEM in the position of the dislocation (at its closest point to the tilt boundary) is shown in Figure 8.27(b). The results of the simulation show that the MEM is highly accurate (error on the order of 0.4%), and that

the overall dislocation configuration is indistinguishable when evaluated by the two methods. However, the MEM is found to be 22 times faster than the full field calculation.

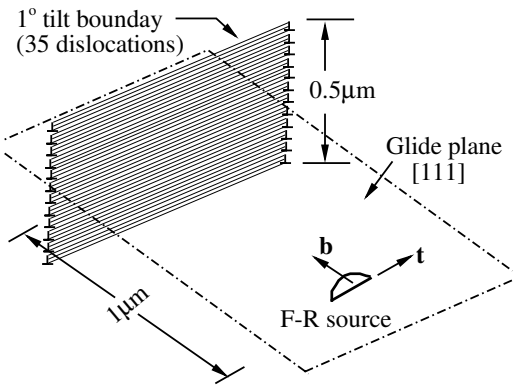

Figure 8.26: Illustration of a tilt boundary. A single dislocation from an F-R source lies on the [111] glide plane with Burgers vector $\frac{1}{2}[\bar{1}01]$ interacts with the tilt boundary.

Dislocation Interaction with a Dense Dislocation Wall

The physical role of dislocation walls in material deformation is recognized to be significant because they control the free path of mobile dislocations within subgrains(**?**). Dislocation walls generally contain high dislocation densities. Therefor, explicit large-scale simulation of the interaction between these walls and approaching dislocations can present computational difficulties. If the nature of decay of the elastic field away from the wall is determined, this would be helpful in studies of dislocation interaction with such walls without the excessive details.

A special algorithm was designed to implement the MEM in dense dislocation walls. The wall was divided into many small volumes, and a hierarchical tree structure was constructed on the bases of these small volumes. Each level of the hierarchical tree contains one or several nodes that correspond to specific volumes of the wall. Larger volumes correspond to higher levels of the tree. For each volume, we determine the properties: center, size, dislocation distribution and various moments. Dislocation moments for the lowest level volumes are first calculated. Then, by using Equation (8.84), dislocation moments for upper tree levels can be easily determined.

The procedure for calculations of the Peach-Koehler force on an approaching dislocation at point P is as follows:

1. The distance between the volume center and the point P is first evaluated. If the distance

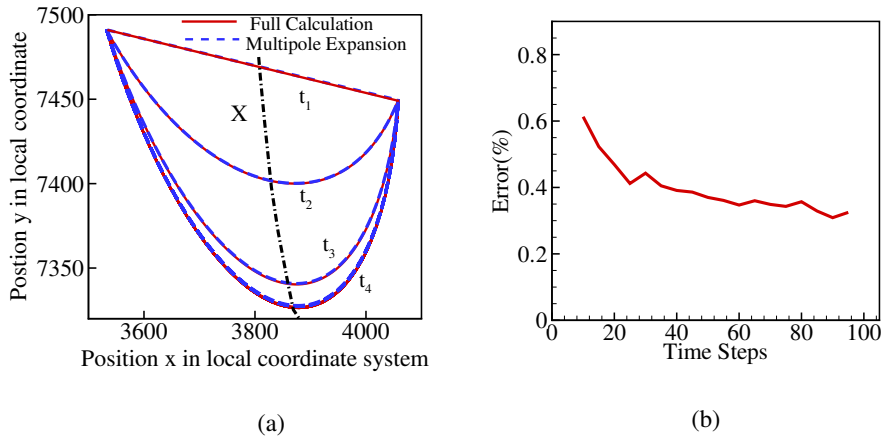

Figure 8.27: (a)Dislocation configurations at different simulation time steps: t_1=0 ns, t_2=0.31 ns, t_3=0.62 ns, t_4=1.23 ns, (b)Relative error of the dislocation position along the line X in (a).

is larger than the volume's size, MEM is used.

2. If the distance is smaller than the volume size and the volume does not have sub-volumes, the P-K force is determined by full calculation.

3. If the distance is smaller than the volume's size and the volume has sub-volumes, the algorithm checks on the distance between P and the center of each sub-volume, and the above procedures are repeated.

Figure 8.28 shows a dislocation wall structure with a density of 5×10^{10} cm/cm^3. The wall dimensions are 5 μm×5 μm×0.2 μm. The P-K force on a small dislocation segment, located at various positions along the center line X, with Burgers vector $\frac{1}{2}[10\bar{1}]$ was evaluated by both MEM and full calculations. The results of the P-K force and the relative errors are plotted in figure 8.29.

While the relative error using MEM of order 2 is very small (see Figure 8.29(b)), a great advantage in computational speed is gained. The results show that the CPU time (on a Pentium-4 CPU, 2.26GHz) increases almost linearly from 416 seconds to 3712 seconds for the full calculation, when the number of dislocations in the wall increases from 250 to 2200. However, the CPU time does not change much for the MEM (varying from 39 seconds to 40 seconds) for the same increase in the number of dislocations. For the case of 2200 dislocations within the wall, a speedup factor of almost 100 is achieved for the MEM. Recognizing that the CPU time for the MEM is almost constant and mostly dependent on the hierarchical tree structure, it is concluded that the method is very suitable for large scale simulations, which involve high dislocation densities.

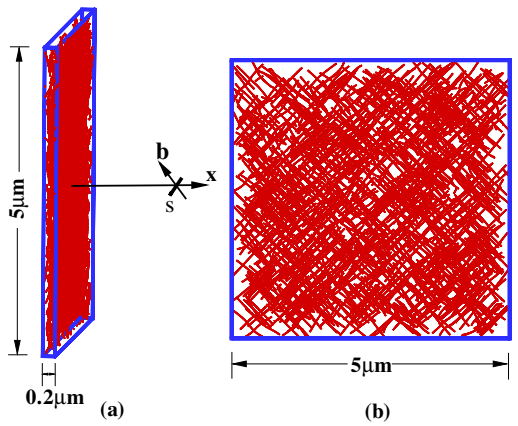

Figure 8.28: Dislocation wall structure with dislocation density 5×10^{10} cm/cm^3. A small dislocation segment S with Burgers vector $\frac{1}{2}[10\bar{1}]$ lies along x.

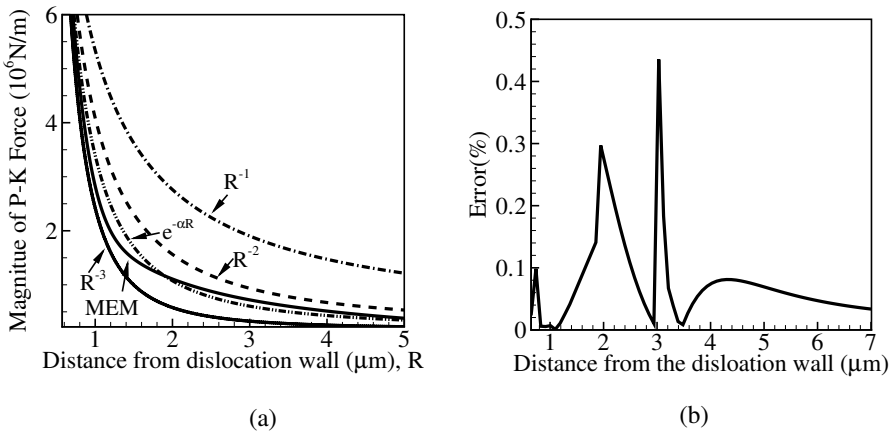

Figure 8.29: (a) P-K forces on a small dislocation segment at different positions along direction x, (b) Relative error of the P-K force from MEM with respect to that from full calculation.

It is of interest to determine the decay nature of the elastic field emanating from dislocation walls. Figure 8.29(a) shows a comparison between various forms of the spatial decay of the P-K force as a function of the distance R away from the wall, normalized to the force at $R_0 = 0.59$ μm. It is seen that the force decays faster than R^{-2}, and it can be simply represented by an exponential function of the form:

$$F(R) = F(R_0)e^{-\alpha(R-R_0)} \tag{8.85}$$

where $\alpha = 1.48$ μm^{-1}. Such simple exponential representation is a result of the self-shielding of the dislocations within the wall.

Conclusions

The MEM presented here shows a number of features that facilitate investigation into the physical and computational aspects of large dislocation ensembles in materials undergoing plastic deformation. The following conclusions are drawn from the present work:

(1) By re-expressing the elastic field of dislocation ensembles as a series solution of moments, the relative contributions of GNDs, dipoles, quadropoles, etc are easily separated out.

(2) The method results in significant computational advantages as compared to calculations performed in most dislocation dynamics simulation method. First, vast computational speed-up is achieved, especially in simulations of dense dislocation interactions. Second, the method offers a simple algebraic procedure for transfer of moments from one volume to another, in a manner similar to the parallel axis theorem for moments of inertia in the mechanics of distributed masses. This property is well-suited to algorithms based on hierarchical tree methods that are now efficiently used in $O(N)$ calculations.

(3) The zeroth order term in the MEM expansion is the Nye's dislocation density tensor, which is a direct measure of lattice curvature, and is affected only by GNDs within the ensemble. Diagonal components of this tensor describe screw dislocations, while off-diagonal components represent edge dislocations. On the other hand, higher order moments of the Eshelby tensor are associated with definite length-scale measures that may be useful in connections between discrete dislocation simulations and the continuum theory of dislocations.

(4) The analysis of dense dislocation walls indicates that the Peach-Koehler force has an exponential decay character as a result of mutual shielding effects of multipole dislocations within random ensemble constituting the walls.

8.4.4 R and Its Derivatives

$\mathbf{R}$ is the vector connecting field point Q and another point P on the dislocation or O, center of the volume (see Figure 9.51). $\mathbf{R}$ and its derivatives are used in expressions of displacements, strains, stresses and energies of dislocations(Ghoniem et al. 2002a). Here, we define a way to express $\mathbf{R}$ and its derivatives in compact tensor forms.

Define

$$\mathbf{R} = \{x_i\} \text{ and } \mathbf{g} = \left\{\frac{x_i}{R}\right\} \tag{8.86}$$

where $R = |\mathbf{R}|$. Thus,

$$\begin{aligned}
R_{,i} &= \frac{x_i}{R} = g_i && (8.87)\\
R_{,ij} &= \frac{\delta_{ij}}{R} - \frac{x_i x_j}{R^3} = -\frac{1}{R}(-\delta_{ij} + g_i g_j) && (8.88)\\
R_{,ijk} &= -\frac{\delta_{jk}x_i + \delta_{ik}x_j + \delta_{ij}x_k}{R^3} + \frac{3x_i x_j x_k}{R^5} \\
&= \frac{1}{R^2}\left[-\left(\delta_{jk}g_i + \delta_{ik}g_j + \delta_{ij}g_k\right) + 3g_i g_j g_k\right] && (8.89)\\
R_{,ijkl} &= -\frac{\delta_{ij}\delta_{kl} + \delta_{ik}\delta_{jl} + \delta_{il}\delta_{jk}}{R^3} \\
&\quad + \frac{3(\delta_{jk}x_i x_l + \delta_{ik}x_j x_l + \delta_{ij}x_k x_l + \delta_{kl}x_i x_j + \delta_{jl}x_i x_k + \delta_{il}x_j x_k)}{R^5} \\
&\quad - \frac{3 \cdot 5 x_i x_j x_k x_l}{R^7} \\
&= -\frac{1}{R^3}\left[(\delta_{ij}\delta_{kl} + \ldots) - 3\left(\delta_{jk}g_i g_l + \ldots\right) + 3 \cdot 5 g_i g_j g_k g_l\right] && (8.90)\\
&\ldots && (8.91)
\end{aligned}$$

Based on the above derivations and after careful analysis, we can write these derivatives as:

$$\begin{aligned}
R_{,a_1 a_2 \ldots a_n} &= \left(\frac{-1}{R}\right)^{n-1} \sum_{m=0}^{|\frac{n}{2}|} \{(-1)^m (2n-3-2m)!! \\
&\qquad \sum^{C_n^{2m}(2m-1)!!} \left(\delta_{t_1 t_2}\delta_{t_3 t_4}\ldots\delta_{t_{2m-1}t_{2m}} \cdot g_{t_{2m+1}} g_{t_{2m+2}} \ldots g_{t_n}\right)\}
\end{aligned} \tag{8.92}$$

where t_1, t_2, …, t_{2m} are a group of indices selected from a_n in a permutation manner, and t_{2m+1}, …, t_n are the other group of a_n after such a selection. The summation $\sum^{C_n^{2m}(2m-1)!!}$ means taking sum over all combinations.

By defining

$$\mathbf{1} = \{e_i\} \tag{8.93}$$

and,

$$\mathbf{R^{(n)}} = \{R_{,a_1 a_2 \ldots a_n}\} \tag{8.94}$$

we can write equation (8.92) as:

$$\mathbf{R^{(n)}} = \left(\frac{-1}{R}\right)^{n-1} \sum_{m=0}^{|\frac{n}{2}|} \left\{(-1)^m (2n-3-2m)!! \sum^{C_n^{2m} C_{2m}^2} \left[(\amalg \otimes^{n-2m} \mathbf{g})(\amalg \otimes^{2m} \mathbf{1})\right]\right\} \tag{8.95}$$

In this equation, m is the number of $\delta^{'}$s and is from 0 to $|\frac{n}{2}|$ which indicates the largest integer not larger than $n/2$. The symbol $\mathrm{II}\otimes^n$ indicates that there are a number of n items of $\mathbf{g}$ or $\mathbf{1}$ with the operation $\otimes$. The second summation $\sum^{C_n^{2m}C_{2m}^2}$ means doing summing in a permutation and combination manner, with the number of items $\mathbf{1}$ as $2m$ and the number of items $\mathbf{g}$ as $n-2m$. For example, with $m=1$ and $n=4$, we have:

$$\begin{aligned}\sum^{C_n^{2m}(2m-1)!!}\Big[(\mathrm{II}\otimes^{n-2m}\mathbf{g})(\mathrm{II}\otimes^{2m}\mathbf{1})\Big] &= \sum^{C_4^2}\Big[(\mathrm{II}\otimes^{2}\mathbf{g})(\mathrm{II}\otimes^{2}\mathbf{1})\Big]\\ = \;& \mathbf{1}\otimes\mathbf{1}\otimes\mathbf{g}\otimes\mathbf{g}+\mathbf{1}\otimes\mathbf{g}\otimes\mathbf{1}\otimes\mathbf{g}+\mathbf{1}\otimes\mathbf{g}\otimes\mathbf{g}\otimes\mathbf{1}\\ & +\mathbf{g}\otimes\mathbf{1}\otimes\mathbf{1}\otimes\mathbf{g}+\mathbf{g}\otimes\mathbf{1}\otimes\mathbf{g}\otimes\mathbf{1}+\mathbf{g}\otimes\mathbf{g}\otimes\mathbf{1}\otimes\mathbf{1}\end{aligned} \tag{8.96}$$

8.5 Coupling between the DD and FEM Computational Procedures

In the following, a uniaxial tensile stress is imposed on a cubic single crystal and its effect on the dislocation loop forces is calculated through the use of the Peach-Kohler formula. To evaluate image stresses due to crystal surfaces, first the elastic stress field in an infinite medium resulting from the dislocation loop is computed. The tractions that result at the surfaces of the finite crystal from this stress field are then determined, reversed, and placed on the FEM model as boundary conditions. The FEM model is then used to calculate the image stress field. From this stress field, the Peach- Kohler formula can again be used to detrmine image forces on the dislocation loop. This procedure follows the approach of Van der Giessen and Needleman (**?**), and extends it to 3-D DD applications.

Having described the general idea behind the coupled FEM-DD approach to the solution of the problem of a single dislocation loop in a finite crystal with external boundary conditions, we will now turn our attention to the details of the calculational method. The elastic field developed by the dislocation loop is evaluated at crystal spatial nodal positions defined by the FEM model of the ANSYS computer program. For the bulk of the present analyses, 10 divisions per cube side were employed for the FEM model. This resulted in 1,331 nodes and 3,990 degrees of freedom. Some analyses were run with a finer mesh generated by using 20 divisions per cube side, thus resulting in 9,261 nodes and 27,780 degrees of freedom. These FEM models have one node in the center of the crystal model with all degrees of freedom constrained to prevent rigid body motion. Once the ANSYS model is created, the coordinates of the nodes and the associated unit normals are introduced into UC-MICROPLASTICITY. Tractions are then calculated, with the unit normal vectors at the surface of the cell. The tractions, with their directions reversed, are then imported into the ANSYS computer program. After the FEM analysis is run and the stress field in the crystal interior computed to an intermediate file, which is then re-written into a format usable by UC-MICROPLASTICITY. The Peach-Kohler formula is then used to calculate the image forces on the loop nodes. Because the FEM analysis only calculates the stress field at specific positions, the stress on the loop nodes has to be estimated by a three-dimensional linear interpolation algorithm (**?**). To this end, a number of

subroutines were developed to perform the linear interpolation of the stress tensor components from FEM nodal positions to loop nodal positions. These subroutines determine the FEM field nodes that are closest to a specific loop node, and estimate the stress on the loop node by using a linear interpolation method described below.

8.5.1 Loop Node Stress Tensor Estimation

To estimate the stress on a specific loop node, the stress on the nearest FEM field points surrounding the loop node must be found. These field node values are found by comparing the FEM field node coordinate values to the loop node in question. The eight field nodes in a quadrilateral brick element closest to the loop node are thus selected. Another subroutine organizes the stress values and position coordinates so that the loop nodal stresses can be determined by appropriate weighting factors. The procedure used for estimating the stress on loop nodes from the stress that was calculated at the field nodes is taken from an extension of the quadratic quadrilateral used in finite element analysis, into three dimensions (**?**). The shape functions are given below.

$$N_1 = [(a-x)(b-y)(c-z)]/8V_e \quad (8.97)$$
$$N_2 = [(a+x)(b-y)(c-z)]/8V_e \quad (8.98)$$
$$N_3 = [(a-x)(b+y)(c-z)]/8V_e \quad (8.99)$$
$$N_4 = [(a+x)(b+y)(c-z)]/8V_e \quad (8.100)$$
$$N_5 = [(a-x)(b-y)(c+z)]/8V_e \quad (8.101)$$
$$N_6 = [(a+x)(b-y)(c+z)]/8V_e \quad (8.102)$$
$$N_7 = [(a-x)(b+y)(c+z)]/8V_e \quad (8.103)$$
$$N_8 = [(a+x)(b+y)(c+z)]/8V_e \quad (8.104)$$

In Eqns. (12.6-8.104), a, b and c are equal to half the length of a quadrilateral brick element, and V_e is the element volume. The variables x, y and z are the coordinates of the loop node with respect to element's local origin. The stress on the loop node is estimated through the following summation:

$$\sigma_{loopnode} = \sum_{i=1}^{8} N_i \, \sigma_i \quad (8.105)$$

Here, N_i is the shape functions and σ_i is the stress on the particular field node. Once the stress on the loop node is established, the image force is calculated using the Peach-Kohler equation. The applied stress is calculated in a similar fashion to that of the image force, and is then entered into UC-MICROPLASTICITY.

8.5.2 Peierls Forces

The applied resolved shear stress required to overcome the lattice resistance to movement by a dislocation loop is referred to as the Peierls-Nabarro stress. This stress is a consequence of the inter-atomic forces/displacement interaction between the dislocation loop and the surrounding crystal. This resistance to dislocation movement is due to the periodic variation in the misfit energy of atomic half planes above and below the slip plane with the dislocation loop. For high dislocation densities, the influence of the Peierls stress on the dynamics of the dislocation loop is comparable to the long-range interactions between the dislocation loops themselves. For low dislocation densities however, the contribution of the Peierls stress is significant. It is generally accepted that the Peierls stress is a dominant controlling factor in the plastic slip of BCC metals at low temperatures (**?**). Peierls and Nabarro calculated the dislocation energy per unit length as a function of position. This energy was found to oscillate with period $|\mathbf{b}|/2$, where $\mathbf{b}$ is the Burgers vector. This maximum value for the energy is given in the following equation.

$$E_p \;=\; \frac{\mu b^2}{\pi(1-\nu)}\, exp\left(\frac{-2\pi w}{b}\right) \tag{8.106}$$

The Peierls stress is the critical stress required to move a dislocation through the crystal. This is the maximum slope of the energy versus distance curve, divided by the Burgers vector.

$$\tau_p \;=\; \frac{2\mu}{(1-\nu)}\, \exp\left(\frac{-2\pi w}{b}\right) \tag{8.107}$$

In Eqns. (8.106) and (8.107), and w is the distance between the atoms immediately below the dislocation.

Values for E_p and τ_p are sensitive to the details of interatomic bonding. τ_p varies between (10^{-6} to $10^{-5}\mu$) for FCC metals, (10^{-2} μ) for covalent crystals, and is somewhere in between for BCC metals. The Peierls stress decreases with increasing temperature and with increasing dislocation width. It is also lower for edge dislocations as compared to screw dislocations (**?**). Based on the Peierls stress, the corresponding Peierls force can be found through the inner product of the Peierls stress with the Burgers vector.

The ratio of edge-to-screw velocities in Fe is estimated to be ≈ 2. By assuming that the ratio of Peierls forces associated with edge and screw dislocations are inversely proportional to the velocity ratio, the Peierls force in the direction of the Burgers vector was taken as $\frac{1}{2}$ that in the direction normal to the burgers vector. Other ratios were also explored to determine the variability in the deformed geometry with respect to this variable. The calculation of the Peierls force is given by the following formula.

$$\frac{\mathbf{F}}{L} = \tau_p \left(1 + \sin(\cos^{-1}\{\frac{\mathbf{b}\cdot\mathbf{u}}{|\mathbf{b}|\,|\mathbf{u}|}\}\right) \frac{\mathbf{u}}{|\mathbf{u}|} \tag{8.108}$$

The stress threshold value, τ_p is taken as (10^{-3} μ) for Fe, $\mathbf{u}$ is the displacement vector, and $\mathbf{b}$ is the Burgers vector.

8.5.3 A Shear Loop in a Finite Crystal

The displacement field for a shear dislocation loop with a radius of 4000 a is shown in the vector plot of Fig. 8.30. It is interesting to note that as a result of shearing the top plane with respect to the bottom along the dislocation line, a vortex-type displacement field is generated. Knowledge of this displacement field is important for Molecular Dynamics (MD) simulations, where the atomic positions around the shear loop can be determined. The stress field of the loop in an infinite crystal was calculated first by UC-MICROPLASTICITY, and the corresponding reversed tractions necessary for solving the FEM boundary value problem determined, as can be seen in Fig. 8.31. The stress iso-surfaces formed by the σ_{xx} stress component of the elastic stress field is added to the stress field formed by surface image stresses, and the results are shown in Fig. 8.32. The superposition of the image stress field onto the elastic stress field of the dislocation loop results in a total stress field with no normal components at the (x = 10,000 a) surface, as can be clearly seen in Fig. 8.32. The stress iso-surface appears to be repelled from the surface. These results, along with similar results for the shear components, show that the free surface boundary condition has been satisfied.

Force Distributions

Force distributions on a 4000 a-radius shear loop in the (101)- [111] slip system of an Fe single crystal with an applied load of 100 MPa were calculated. The applied, image, Peierls, self and resultant force distributions are all shown Fig. 8.33 below. The image, self and Peierls force distributions are all on the shear plane, while the applied and resultant force distributions are characterized by large out-of-plane components. The distribution of the applied force on the circular shear loop is similar to that proposed by Kroupa (**?**). Self forces seek to increase the length of screw components and decrease the length of edge components as a consequence of total energy minimization for the loop. The screw orientation has a lower energy per unit length as compared to the edge component, and hence is "stiffer" in opposing applied forces. Peierls forces are larger in the direction perpendicular to the Burgers vector, resulting in low mobility of the screw component as opposed to the edge component of the loop. Dislocation loops in BCC metals thus tend to have long, straight screw components, especially at lower temperatures.

Equilibrium of Shear Loops Near Crystal Surfaces

To complete the analysis of the influence of free crystal surfaces, a single dislocation loop was placed at different positions within the single crystal model, and the force distributions were calculated. In addition to loop position, other variables were evaluated including loop diameter, applied stress magnitude, and the number of FEM degrees of freedom. For all analyses, the material modelled is BCC Fe ($\mu = 36.4\ GPa, \nu = 0.25,$ and $a = 0.285\ nm$). An analysis was conducted with a fine mesh of 20 divisions per side and 60 nodes per loop. The loop is placed at 250 a from the crystal edge. The results of this analysis are illustrated in Fig. 8.34. As

the loop approaches the crystal corner, image forces increase, and on the portion of the loop closest to the boundary, they are characterized by attractive in-plane and attractive out-of-plane components. A deformation analysis was also conducted on this loop/boundary configuration. The results are displayed in Fig. 8.35. These results indicate that the loop advances away from the corner in the direction of the Burgers vector. It must however be noted that the motion of the loop is limited to the slip plane in the present numerical model. It is also obvious from Fig. 8.35 that large out-of-plane forces can induce cross-slip.

To better understand the qualitative relationship between the position of the shear loop and the crystal boundary forces, a loop with a radius of 2000 a was placed at different positions with respect to the top crystal surface. As the loop arrives at the surface, the magnitudes of image forces become very large. For a loop very close to the boundary, this force distribution becomes repulsive when projected onto the slip plane, and is characterized by large out-of-plane forces on the portion of the loop closest to the boundary. These forces should promote cross-slip toward the free surface for the screw components. Fig. 8.36 shows that forces on loop nodes not near the boundary evolve from a radial outward distribution at 250 a from the boundary, to a downward normal (from the slip plane) distribution at a distance of 10 a from the boundary. These results indicate that image force distributions are heavily dependent on the proximity of the loop to the the top crystal surface. Having established the distribution of forces, the deformed shape of the loop under an applied stress of 50 MPa was calculated (see Fig. 8.37). As predicted by the nodal force distribution, the loop is repelled by the surface due to the influence of image forces, as a result of constraining loop motion to be only on the glide plane. A final equilibrium loop geometry is achieved at a distance of 212 a from the free surface. If the model allowed for motion out of the slip plane, the loop would advance toward the boundary through cross-slip of its screw components. To understand why surface image forces become repulsive at close proximity to the boundary, the surface tractions were compared for this same configuration at 250 a and 10 a from the boundary. These tractions show that there are large shear forces acting on the surface of the crystal, and that these forces grow very large as the loop comes close to the boundary. Thus, the tendency of the loop to move out of its glide plane is driven by surface shear forces.

8.5.4 The Influence of Crystal Surfaces on the Deformation of Frank Reed Sources

Friedel concluded that a dislocation is attracted towards its image, and that it should arrive perpendicular to the free surface in order to achieve the most stable configuration (**?**). However, a dislocation in a medium that is separated from a free surface by a thin film of thickness h and shear modulus μ' behaves quite differently. A screw dislocation at a depth L from the interface will be drawn toward the free surface if $\mu' < \mu$. It will be repelled however, if $\mu' > \mu$ and $L << h$. For $\mu' > \mu$, and $L >> h$, the dislocation will be attracted toward the surface. This implies that there is an equilibrium position from the surface on the order of the film thickness h from the interface. In ionic crystals such as potassium chloride, evidence supports the conclusion that image forces repel dislocations from breaking the surface. Nabarro

also states that the image forces may induce cross slip (**?**). Gilman and coworkers conducted experimental studies involving the measurement of dislocation velocities in LiF single crystals (**?**), and proposed a mechanism of dislocation motion under the influence of surface forces in a single crystal. A variation on Gilman's model is illustrated schematically in Fig. 8.38. In this figure, an expanding Frank-Read (FR) source lies in the glide plane, which is at an angle θ with respect to the free surface. The fast-moving edge component of the loop intersects the surface first, as shown in Fig. 8.38-b. Through cross-slip of the screw component (which is readily achieved through out-of-plane forces), the screw segment bends to become normal to the crystal surface (**?**). This mechanism of cross-slip was assumed by Gilman to be the result of energy minimization through the reduction in the length of the dislocation along the slip plane. With the image force distribution observed in Fig. 8.37, it is obvious that this effect is the result of the large surface shear forces uncovered by the present analysis. Thus, we anticipate the creation of surface steps following the penetration of the edge component through the surface, as illustrated in the present extension of Gilman's mechanism.

The deformed geometry of a Frank Reed (FR) source in BCC Fe under the influence of an applied stress was then computed to determine the influence of surface image forces on the shape of the FR-source. In Fig. 8.39, a stress of 125 MPa was applied to a crystal containing a single FR source . The FR source is located on the slip plane with origin at(7500,5000,7500). The local coordinates of the fixed points on the FR-source are (-2000, 3000) and (2000,3000). The equilibrium shape of the FR-source is evolved, as it approaches the free crystal surface. The equilibrium position of the source is approximately 163 a from the surface of the crystal model, as can be seen in Fig. 8.39.

To study the effects of anisotropic Peierls forces on the deformation of FR-sources, the ratio of edge to screw Peierls forces were varied. Fig. 8.40 shows the deformation of an FR-source in a finite crystal with a screw to edge Peierls force ratio of 2 to 1, and a Peierls threshold shear stress of $1 \times 10^{-6}\mu$, and an applied stress of 200 MPa. This case may be representative of a crystal with a "low" screw to edge Peierls force ratio, such as an FCC crystal. The results depicted in Fig. 8.40 also show the deformation of an FR-source in a crystal with a screw to edge Peierls force ratio of 10 to 1, and Peierls shear stress threshold of $10^{-3}\mu$, typical of a BCC crystal and an applied stress of 700 MPa. Both cases indicate that the deformation for the high ratio case evolves with significantly less curvature than for the low ratio case, consistent with the observations of dislocation loop curvatures in FCC and BCC crystals, respectively.

8.5.5 Conclusions

The computer modelling and numerical results presented in this paper seek to determine the influence of free surfaces on dislocation motion in metallic single crystals. Much of the work in Dislocation Dynamics that is presented in the literature testifies to the importance of surface effects. However, little if any modelling has been completed which describes the precise nature of force distributions in 3-D geometry induced by the proximity of dislocation loops to crystal surfaces with specified boundary conditions. Based on the results of computer simulations for the elastic fields around static and dynamic dislocation loops and FR-sources in single crystals,

and the corresponding forces and deformation of these loops, the following conclusions can be drawn.

1. Imposed surface traction boundary conditions can be achieved through the use of a hybrid finite element method (FEM), coupled with Dislocation Dynamics (DD). Peierls and self-forces cause the loop to deform preferentially (stretch) in the direction of the Burgers vector, while surface image forces act to either attract or repel the loop, depending on its distance from the boundary, and the orientation of the slip plane with respect to the nearest free surface. For slip planes at an oblique angle to a free surface, the image forces on the closest screw-component portions of the loop are characterized by a large out-of-plane component, which acts to pull the loop toward the surface through the mechanism of cross-slip. For example, for loop model geometry characterized by 20 nodes, and 10 mesh divisions per side in the FEM model, the out of plane component became dominant at approximately 500 lattice constants.

2. For slip planes that are normal to the free surface, image force distributions on dislocation loops have negligible out-of-plane components. These image forces are directed along the slip plane regardless of the distance of the loop from the boundary. Furthermore, these image forces can either attract or repel portions of the loop closest to boundary depending on the distance between the loop and the boundary. For a 4000 lattice parameter diameter loop characterized by a 60 node geometry, and an FEM model with 20 mesh divisions per side, calculated image forces are attractive for a loop/free surface separation of 250 lattice parameters. For the same model, but with a separation of 10 lattice parameters between the loop and the free surface, the image forces are repulsive to the loop segment nearest to the surface.

3. Image forces dominate the resultant force distribution for orientations of the shear loop closest to the free surface. The distance from the boundary at which image forces become significant can be estimated based on the image force/self force ratio. This distance varies with respect to the loop radius. Loops with large radii are affected by image forces deeper into the single crystal than are loops with small radii. For small loops, self forces dominate and cause contraction. Thus, the expansion or contraction of the loop is dependent on a critical applied stress, radius of curvature, and proximity from the boundary.

4. Shear dislocation loops and FR-sources in similar slip systems under similar loading configurations close to the surface deform and evolve into similar geometric shapes. A dislocation loop (radius=2000 a, $\sigma_{xx} = 50$ MPa, initial loop surface separation of 10 a) and an FR-source of initial length= 4000 a, $\sigma_{xx} = 150$ MPa, initial separation from boundary = 535 a in the "oblique" orientation deform into similar shapes. The loop evolves into an equilibrium position 212 a from the surface, while the FR-source evolves to an equilibrium position approximately 163 a from the free surface.

5. Analysis and comparison of modelling results for FR-source deformation under the influence of an applied stress indicates that dislocation loops in BCC crystals deform into geometry with significantly less curvature than in FCC crystals under the same conditions.

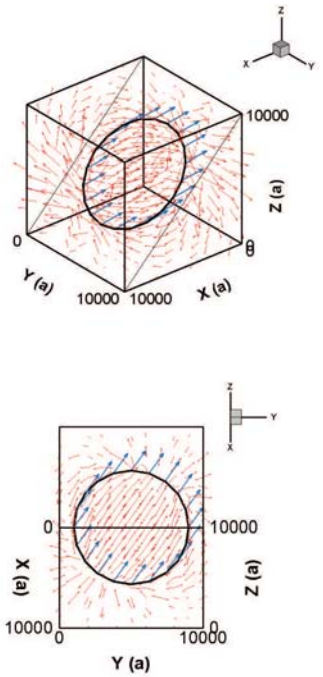

Figure 8.30: Two views of the displacement field induced by a 4000 a-radius shear loop in the (101)-[111] slip system. Burgers vectors are represented at loop nodes.

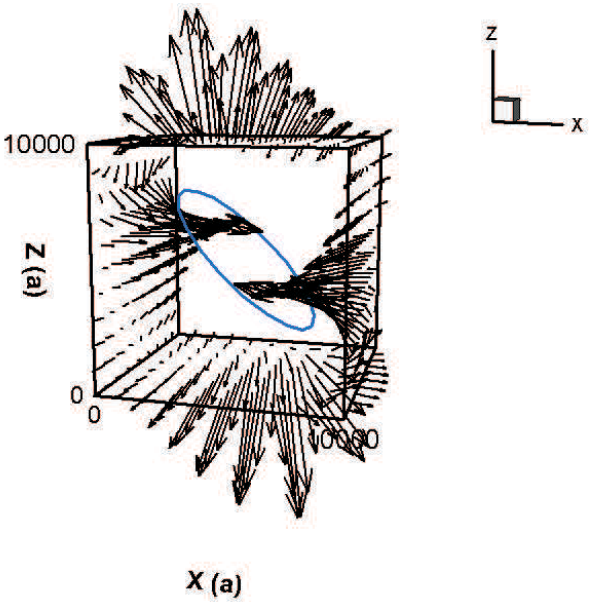

Figure 8.31: Vector plot for the tractions produced by the elastic stress field of a 4000 a radius shear loop

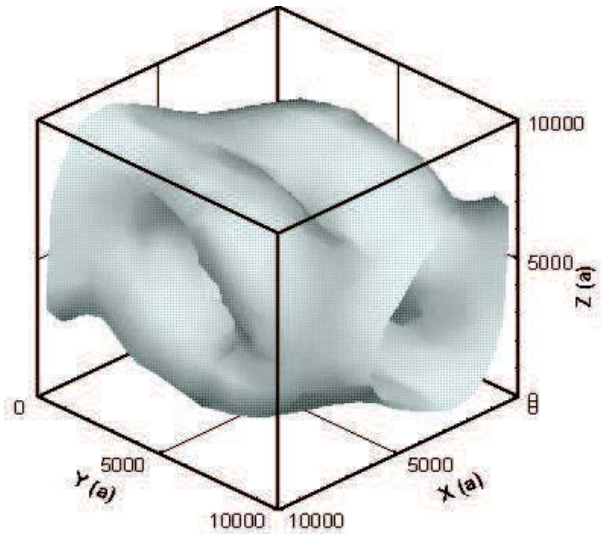

Figure 8.32: $\sigma_{xx} = 2000$ MPa stress iso-surface for the total dislocation plus image elastic field

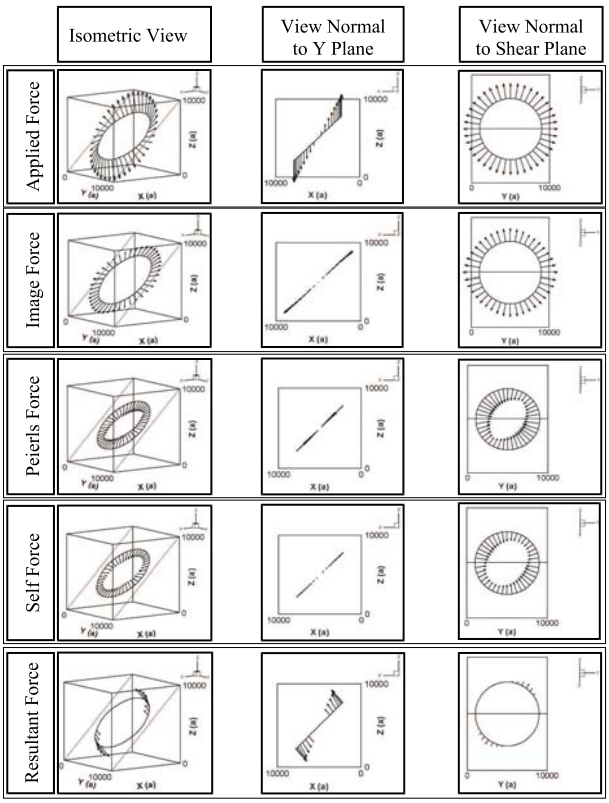

Figure 8.33: Force distributions on a 4000 a radius shear loop in the (101)-[111] slip system in Fe, applied stress $\sigma_{xx} = 100$ MPa. Vectors to scale except self and image with scale factors of 2 and 10, respectively

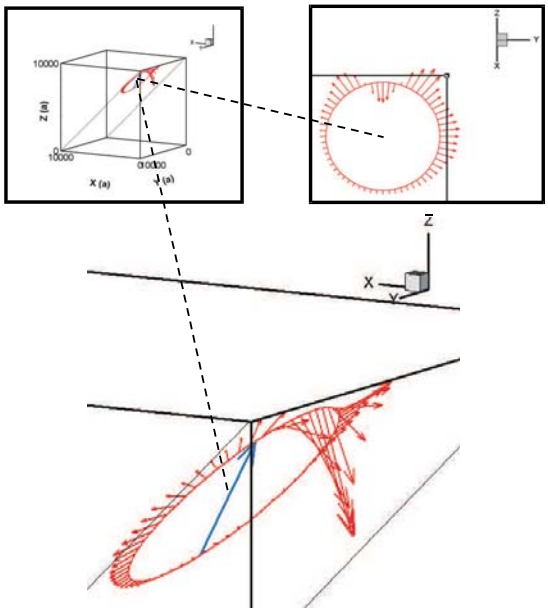

Figure 8.34: Two views of the image force distribution on a loop in the corner of the unit cell. The loop is 250 a from the edge of the cell. The Burgers vector direction is also represented.

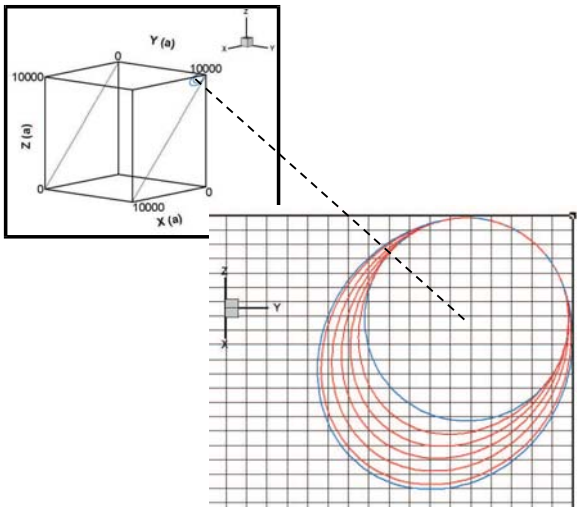

Figure 8.35: The 500 a radius loop and the deformation that results under an applied stress of 350 MPa.

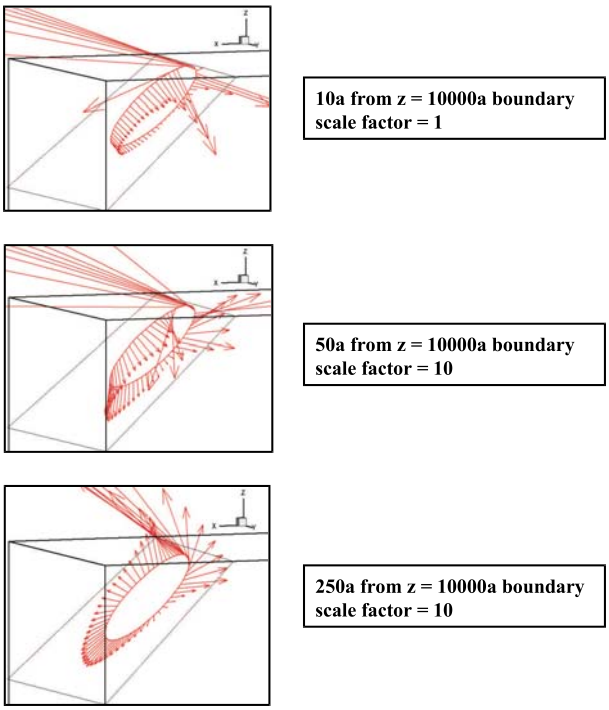

Figure 8.36: Image force distributions on a 2000 a radius shear loop in the (101)-[111] slip system, (A)1000 a, and (B) 10 a from z=10000 a surface. Vector scale factors: (A)100,(B) 1 .

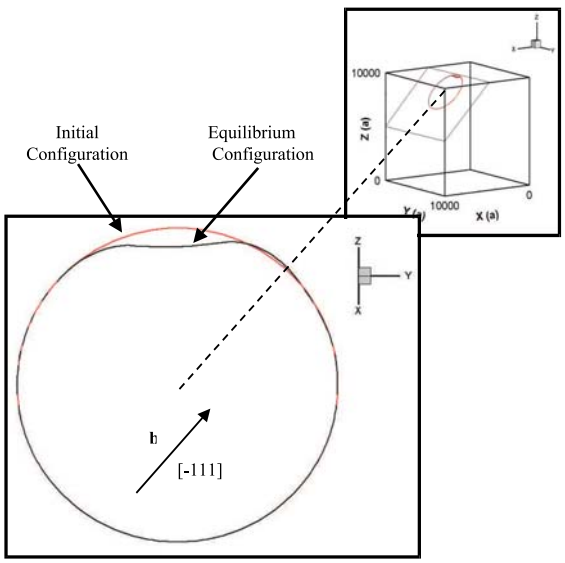

Figure 8.37: Deformation of a 2000 a radius shear loop in the (101) -[111] slip system. The loop is initially 10 a from the surface with applied stress: $\sigma_{xx} = 50$ MPa.

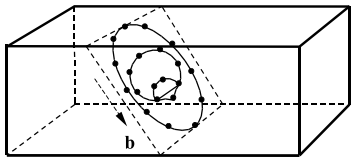

(a)

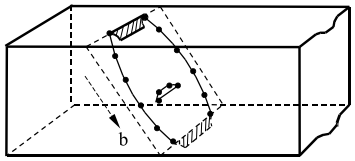

(b)

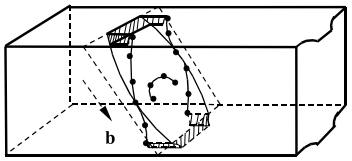

(c)

Figure 8.38: Schematic of cross-slip of a screw dislocation adjacent to a surface in a crystal.(a) Initial configuration of an expanding F-R source, (b) emergence of an incipient surface step by penetration of the edge component through the surface, and (c) the deformation of the dislocation line following cross-slip .
(after (**?**))

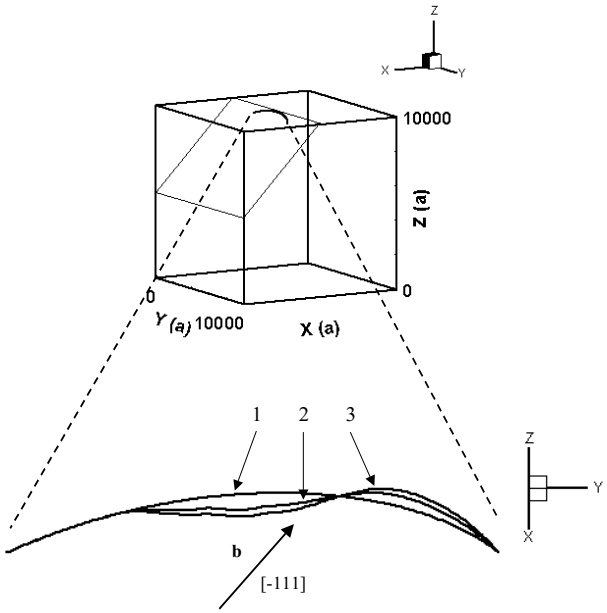

Figure 8.39: Isometric view of a crystal containing an FR-source, and a 2-d view of the deformed geometry as viewed normal to the (101)-plane. (1) Initial geometry, (2) Intermediate, and (3) Equilibrium. The applied stress $\sigma_{xx} = 125$ MPa.

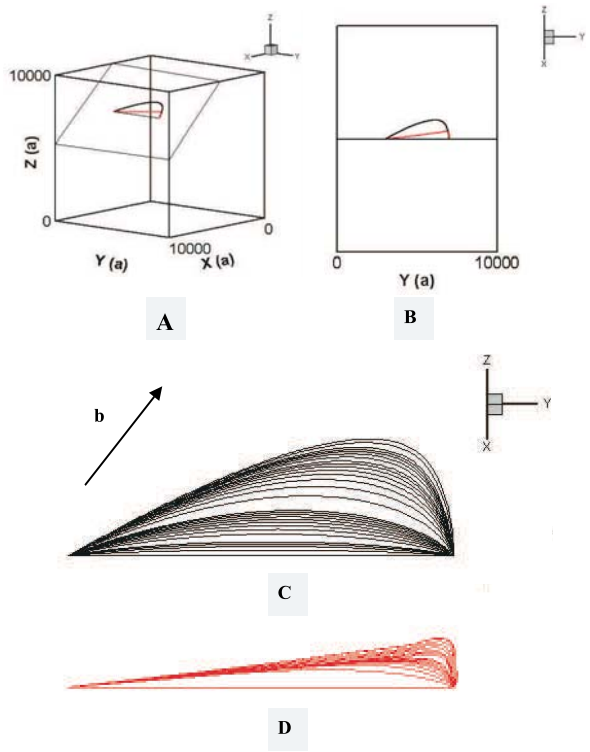

Figure 8.40: Isometric (A), and 2-d (B, C, and D) views of the evolution of an FR-source near a crystal surface. View C depicts the "low screw/edge force" ratio case, while D depicts the "high" ratio case. 4000 time steps.

Chapter 9

Applications

9.1 Fundamental Mechanisms

9.1.1 Finite-Size Dipole Formation and Destruction

In all previous applications of the PDD, strong interactions between different loops is not a major factor that determines the final outcome of each mechanism, although in the case of a dislocation pileup, moderate loop reconfiguration takes place as a result of loop-loop interaction. For large-scale computer simulations of dislocation ensembles(**?**), loop-loop and loop-obstacle interactions determine the rate of strain hardening or softening(Ghoniem et al. 2000b). We consider here several interaction mechanisms that are dominant in various stages of strain hardening. These are: dipole formation and breakup, dislocation unlocking from defect clusters, and the formation and destruction of dislocation junctions.

It has been pointed out(**?**) that the destruction of dislocation dipoles plays a significant role in the evolution of Persistent Slip Bands(PSB) under fatigue loading conditions. Dislocation dipoles play significant roles in a host of hardening mechanisms, and thus conditions for their formation and destruction must be worked out. The stability of very long dipoles has been determined from static equilibrium considerations, and the shear stress necessary to destabilize a dipole of a given width, h, is given by(**?**):

$$\tau_c = \frac{\mu b}{8\pi(1-\nu)}\frac{1}{h} \tag{9.1}$$

The more general dynamic stability conditions of infinite length dipoles have been determined by Huang et al.(**?**). Here, we focus on the resolution of the dynamics of formation and breakup of finite-size dipoles in FCC metals. Figure 9.1 shows a 2-D projection on the (111)-plane of the dynamic process finite-size dipole formation. Two initially straight dislocation segments with the same Burgers vector $\frac{1}{2}[\bar{1}01]$, but of opposite line directions are allowed to glide on nearby parallel {111}-planes without the application of an external stress. The two lines attract one

another, thus causing the two loop segments to move and finally reach an equilibrium state of a finite-size dipole. The two parallel dislocations are pined at both ends, the upper loop glides on the "upper" plane, while the "lower" one glides on the "lower" plane as shown in Figure 9.1. The mutual attraction between the two dislocations becomes significant enough to simultaneously reconfigure both of them only during the latter stages of the process. Because the two dislocations start with a mixed character, a straight and tilted middle section of the dipole forms. The length of this middle section, which we may simply ascribe as the dipole length, is only determined by the balance between the attractive forces on the middle straight section, and the self-forces on the two end sections close to the pinning points. The separation of the two planes is $25\sqrt{3}$, which is approximately 60 $|\mathbf{b}|$

Such finite-size dipoles will be stable on their own, so long as no perturbing external or internal stress field is present. It is immediately obvious from Figure 9.1 that the dipole configuration is *symmetric* with respect to the direction of an applied shear stress parallel to the two glide planes. Calculations of dipole dynamics under the influence of an externally applied stress show that it is much easier to *unzip* the dipole in the reverse direction than to destroy it in the forward direction. Figure 9.2 summarizes the relationship between the unzipping stress and the inverse of the inter-planar distance $1/h^*$. A comparison is also made in the same figure with stress values needed to destabilize an infinite dipole calculated by Equation 9.61, and the values needed to destroy it in the forward direction.

As a result of the self-forces generated by the curvature of the two end sections of the dipole, the unzipping strength is a factor of 2 smaller than the strength of an infinite dipole. In the forward destruction case, however, the self-forces tend to hold both dislocations back, thus a higher external stress is needed to break up the dipole . The present results are calculated for an initial horizontal separation of 350 for the two straight segments before the dipole forms. Increasing this distance results in smaller effects of the curved sections of the dipole, and hence both unzipping and forward destruction stresses approach the infinite dipole values. It is to be noted here that all these results are for static dipoles, or for initial dislocation velocities smaller than $\frac{1}{2}$ the transverse sound speed. The stability of the dynamic infinite dipole is treated in reference [(**?**)].

9.1.2 Dislocation interaction with defect clusters

Dislocation motion is effectively impeded by the elastic field of small defect clusters of various types, which can be generated during particle irradiation(**?**), rapid temperature changes (quenching), high speed deformation and cyclic fatigue conditions(**?**). Defect clusters are either glissile or sessile. One particular type of such clusters that is produced by particle irradiation is composed of a collection of self-interstitials, and its elastic field can be represented by a small prismatic dislocation loop. Experiments have shown that most dislocations in irradiated materials are decorated by sessile Self-Interstitial Atom (SIA) clusters. On this basis, a "Cascade Induced Source Hardening"(CISH) model has been proposed (**?**) to explain yield drop phenomena and the level of radiation hardening in irradiated materials. We present here results of PDD simulations for the problem of dislocation loop penetration through the elastic field of

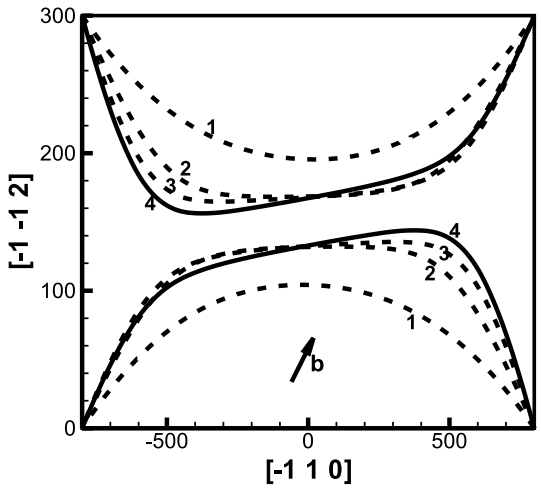

Figure 9.1: Two F-R source dislocations with the same Burgers vector($\mathbf{b} = \frac{1}{2}[\bar{1}01]$) but opposite tangent vectors gliding on two parallel (111)-planes (distance $h = 25\sqrt{3}a$ apart) form a short dipole in an unstressed state. The view is projected on the (111)-plane. Time intervals are: (1) 2.5×10^5, (2) 4.75×10^5, (3) 5×10^5 , (4) Equilibrium state

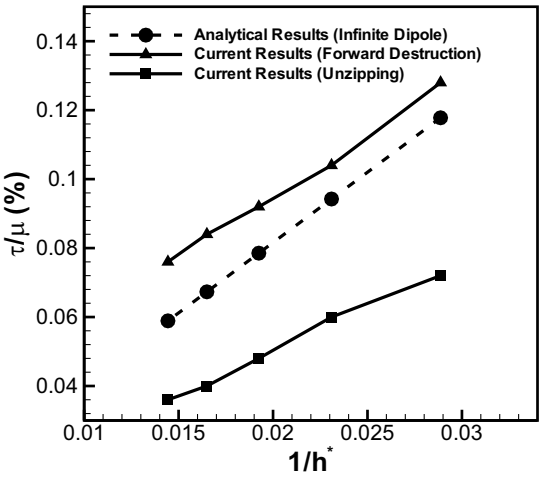

Figure 9.2: The relative shear stress(τ/μ) to break up a finite size dipole as a function of the relative inverse separation$1/h^*$, $h^* = h/a$. h is the distance between the two parallel planes. The distance between the pinning points of the two F-R sources $L = 1600a$, and they are originally separated by $350a$ horizontally.

sessile SIA clusters. SIA clusters are modelled as rigid, sessile prismatic loops, and their elastic field is computed from Kroupa's infinitesimal loop approximation(**?**).

First, we will use Kroupa's theory to obtain analytical estimates for the magnitude of the maximum stress required to free a rigid, straight dislocation of infinite length from the elastic field of a row of SIA clusters sitting above (or below) the glide plane. The average cluster diameter is d, and the inter-cluster distance is l. Consider the case when the Burgers vectors of all clusters are of the same magnitude and direction as that of the glide dislocation, as shown in Figure9.3-a. The glide dislocation is of an edge character and lies along the x_3 direction. The normal to the cluster habit plane is parallel to its Burgers vector. Utilizing the Peach-Koehler formula (Equation **??**) for the cluster force on the dislocation, and Kroupa's infinitesimal loop approximation(**?**), the force component on the glide plane that one cluster exerts on the dislocation per unit length is obtained.

For the particular case of Cu, with $\nu = 0.31$, the maximum value of the glide force per unit length can be easily shown to be:

$$F_{glide}^{max}/\mu = 0.0723 \left(\frac{bd}{y}\right)^2 \left(\frac{1}{y}\right) \tag{9.2}$$

When the cluster Burgers vector is orthogonal to that of the glide dislocation as shown in Figure9.3-b, this peak value is:

$$F_{glide}^{max}/\mu = 0.0258 \left(\frac{bd}{y}\right)^2 \left(\frac{1}{y}\right) \tag{9.3}$$

It is clear that the maximum force for the parallel case is greater than that for the orthogonal case by the factor $1/(1-\nu) \approx 2.8$. Since the dislocation is assumed to be rigid in this analytical approach, the dislocation will unlock from the collective cluster field when the external force integrated over the inter-cluster distance l just exceeds the force generated by a single cluster, integrated over the same distance. Ignoring the fact that the cluster force varies over the inter-cluster distance l, one obtains for the critical unlocking shear stress (CRSS) for Cu:

$$(CRSS)_{\parallel}/\mu \approx 0.0723 \left(\frac{d}{y}\right)^2 \left(\frac{b}{y}\right), \quad (CRSS)_{\perp}/\mu \approx 0.0258 \left(\frac{d}{y}\right)^2 \left(\frac{b}{y}\right) \tag{9.4}$$

By calculating the interaction energy between a cluster covering a a rigid dislocation segment l, Trinkaus, Singh and Forman(**?**) determined the critical stress to unlock a dislocation from a cluster atmosphere of parallel Burgers vectors as:

$$(CRSS)_{\parallel}/\mu \approx 0.1 \left(\frac{d}{y}\right)^2 \left(\frac{b}{l}\right) \tag{9.5}$$

Apart from the discrepancy in the numerical factor, Equations 9.4 and 9.5 show different scaling with the stand-off distance y. Agreement between the two equations is obtained if one considers

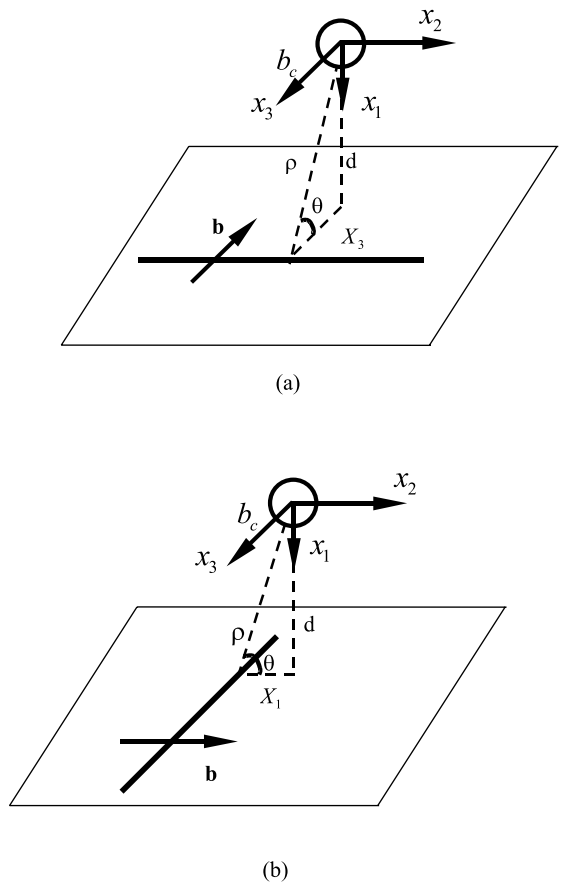

Figure 9.3: Geometry representation of the relationship between one cluster and a dislocation on its glide plane. (a) Burgers vector of the cluster is parallel to that of the F-R source. (b) the two Burgers vectors are normal to each other.

that the dislocation may break away from the cluster field at its weakest spot, mid-way between two clusters. If this is satisfied by assuming that the stand-off distance is on the order of the inter-cluster distance l, the $(\frac{b}{l})$ term in Equation 9.5 roughly replaces the $(\frac{b}{y})$ term in Equation 9.4.

Through numerical simulations, it will be shown next that dislocation reconfiguration by changing its curvature during the interaction process plays a major role in its ability to unlock from the stress field of defect cluster atmospheres. The analytical theory presented above is not suitable for analysis of the detailed mechanisms of dislocation unlocking from cluster atmospheres, because it neglects dislocation shape changes as it passes close to the cluster. Figure 9.4 shows the effects of a single cluster placed at different stand-off distances on the motion of a glide dislocation. A dislocation loop, pinned at the end points as shown in the figure ($\mathbf{b} = \frac{1}{2}[10\bar{1}]$) interacts with one SIA cluster ($\mathbf{b}_c = \frac{1}{2}[111]$). An external applied stress $\sigma_{11} = 120$ MPa($CRSS/\mu = 0.096\%$) is imposed as a step function in time. When the stand-off distance between the cluster and the glide plane y is 120, the stress field of the cluster is very weak. However, the dislocation line is very flexible, curving as it approaches the cluster, even though its field is very weak, as shown in Figure 9.4. At a normalized time of 4.0×10^6, the dislocation totally breaks through the influence of the cluster elastic field. In this case, the effect of the cluster is just to temporarily distort the dislocation configuration . After the dislocation breaks away from the cluster field, it can totally recover from this distortion as a result of the stabilizing effects of its self-force. However, when the same cluster is moved closer to the glide plane at a normalized distance of 80, the effect of the cluster elastic field is much stronger, and the dislocation is totally trapped. A permanent cusp distortion is generated near the cluster, and the dislocation splits into two portions, each achieving equilibrium with the applied field by its own self-force.

Now we will consider PDD numerical simulations for the interaction of an F-R source with a row a SIA clusters. As the glide dislocation comes close to the influence of the collective cluster filed, each segment will be subject to localized forces that quickly change from attractive to repulsive. The combined effects of cluster forces, the local self-force and the externally applied force then determine the dislocation's shape. Dislocation reconfiguration, in turn, dictates its ability to overcome the resistance of the cluster field to its motion.

In Figure9.5, a total of 15 SIA prismatic clusters, each with the same $\mathbf{b} = \frac{1}{2}[011]$, $d = 40$, $l = 100$, and $y = 80$, are shown to interact with an advancing dislocation on its glide plane. The external shear stress σ_{11}/μ or τ/μ is gradually increased from 0 at intervals of $\Delta\tau/\mu = 0.008\%$. At each stage, the dislocation reaches a new stable configuration, as shown in Figure 9.5a. As a result of the initial angle between the dislocation's Burgers and tangent vectors, its line becomes asymmetric, as can be seen in the figure. When the normalized applied stress is increased to 0.112%, the dislocation starts to break away from one side of the cluster atmosphere. Once this process of *unzipping* begins, it is further accelerated by the change in local curvature at the freed end of the dislocation, as can be ascertained form Figure 9.5-b.

To determine the spatial resolution of PDD in describing the instability phenomenon that leads to dislocation unlocking from clusters, we use different number of segments. Figure 9.6 shows the effects of using different nodal densities on the spatial resolution of the dynamic

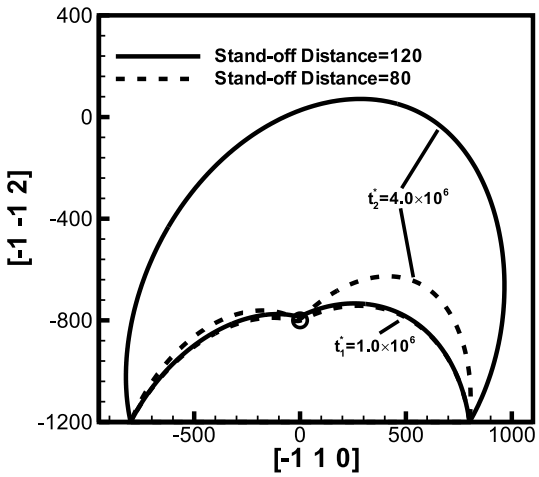

Figure 9.4: Interaction between an F-R source ($\mathbf{b} = \frac{1}{2}[10\bar{1}]$) in Cu on the (1 1 1)-plane with a single sessile prismatic interstitial defect cluster($\mathbf{b} = \frac{1}{2}[111]$), d=50 a, subjected to a step function stress σ_{11} = 120 MPa ($\tau/\mu = 0.096\%$). The cluster center has the local coordinate: (a)=(0 -800 80); (b)=(0 -800 120).

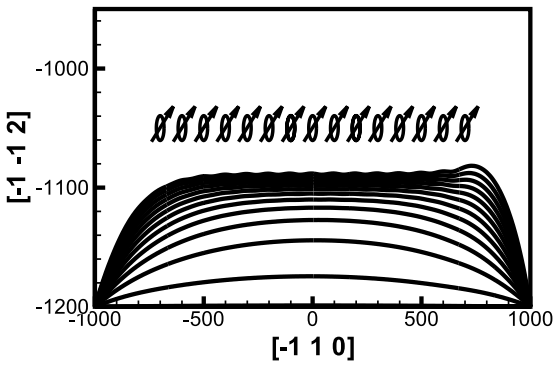

(a)

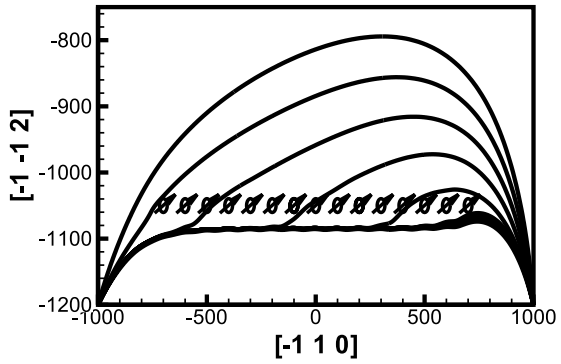

(b)

Figure 9.5: Dynamics of the *asymmetric unlocking* mechanism from a cluster atmosphere of 15 equally spaced sessile interstitial clusters ($d = 40,\ y = 80$ and $l = 100$). (a)Equilibrium state with equal shear stress interval of 4 MPa ($\Delta\tau/\mu = 0.008\%$). (b)Unlocking state at a stress $\sigma_{11} = 140$ MPa ($\tau/\mu = 0.112\%$), with equal time interval $\Delta t^* = 2 \times 10^5$.

dislocation shape, and on the critical unlocking stress. In Figure 9.6-a,b,c, the dislocation line is initially divided into 6, 18, 30 segments, respectively. It can be seen that as the nodal density is increased, the dislocation shows more variations in its local curvature. However, once the segment length is smaller than the inter-cluster distance, no more changes are observed, and a convergent shape is achieved. When the number of segments is decreased to only 6, the dislocation cannot sense the variation of the stress field of individual clusters, and only responds to their integrated effects. Consequently, it can not adjust its local curvature, since the present interpolation scheme is based on cubic shape functions. It is expected that quintic spline shape functions may be able to capture strong variations in dislocation curvature with a small number of segments. Comparing the spatial scales of FIGS. 9.5 and 9.6, one can see that convergent spatial resolution of the dynamic dislocation shape on the order of 1-2 atomic lattice spacings is obtained. To resolve smaller features, one may have to consider crystal anisotropy and non-linear displacement-force relationships in the analysis.

The results of scaling the CRSS with the inter-cluster and stand-off distances are shown In FIGS. 9.7 and 9.8, respectively. The analytical results of Trinkaus et al.(**?**) are also compared with the current numerical simulations. In Figure 9.7, 15 equally-spaced clusters interact with a glide edge dislocation with two pinned ends, $l = 80$ and $d = 40$, and $\mathbf{b} = \frac{1}{2}[\bar{1}10]$ for both dislocation and clusters. The figure shows that the CRSS decreases with the increase in the inter-cluster distance, in a manner consistent with the analytical estimates. The dislocation does not have a chance to *bulge out* in between the clusters, and thus breaks away in a rigid fashion from its middle section, where the cluster field decreases with the increase in l. It is very interesting, however, to note that the numerical simulations show two distinct regimes: regime A, where the $l \leq 2d$, and regime B, where $l \geq 2d$. In regime A, the cluster fields overlap, and the force distribution on the segment does not vary significantly to allow any *bulging out* during the unlocking process. Thus, the resistance to dislocation motion is globally produced by the collective field of all clusters. In regime B, however, once the inter-cluster separation is larger than twice its diameter, the force variation of clusters over the segment is large, and the dislocation prefers to *buckle* in between them. The radius of curvature of this bulge is on the order of $\frac{1}{2}$ the inter-cluster distance. Thus, the resistance to dislocation motion switches now to a local process, where its radius of curvature determines the CRSS. A sudden jump is clearly observed when we cross from regime A to B, as can be seen in Figure 9.7. As the inter-cluster distance increases in regime B, the resisting curvature decreases, and hence the decrease in the CRSS, albeit at a higher level than in regime B. This behavior represents *bistability* of the dislocation configuration as a function of the inter-cluster distance.

The dependence of the CRSS on the stand-off distance is likewise displayed in Figure 9.8, where a comparison with the analytical theory is also made. For the parallel Burgers vectors case, good agreement with analytical theory is obtained, because the behavior is mainly in regime A of Figure 9.7. The somewhat smaller values of the numerical simulations are a result of the self-forces close to the pinned ends reinforcing the applied stress field. However, when the clusters Burgers vectors are orthogonal to the dislocation's, the cluster field variations along the inter-cluster distance are very strong, and the dislocation prefers to *bulge out*, reverting to regime B behavior that is associated with higher resistance. The CRSS is higher by a factor of 2 in this case, as can be seen from Figure 9.8.

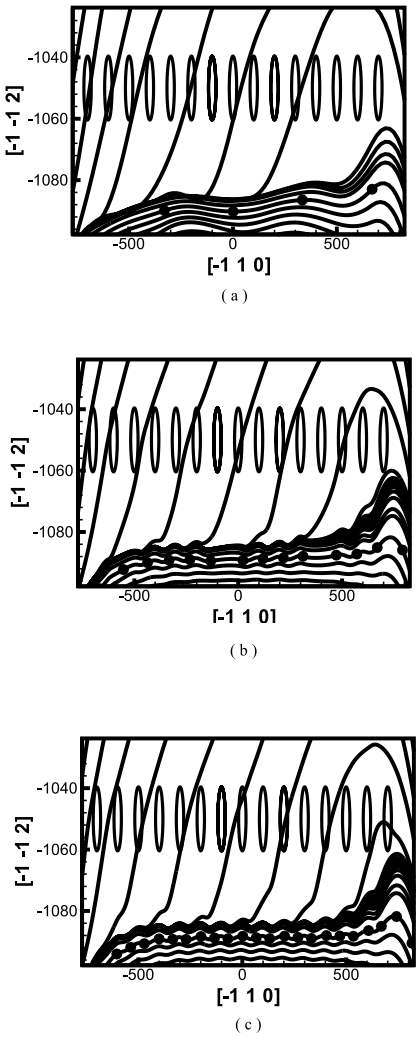

Figure 9.6: The influence of the number of segments on the resolution of the dislocation unlocking mechanism: (a) 6 segments; (b) 18 segments; (c) 30 segments.

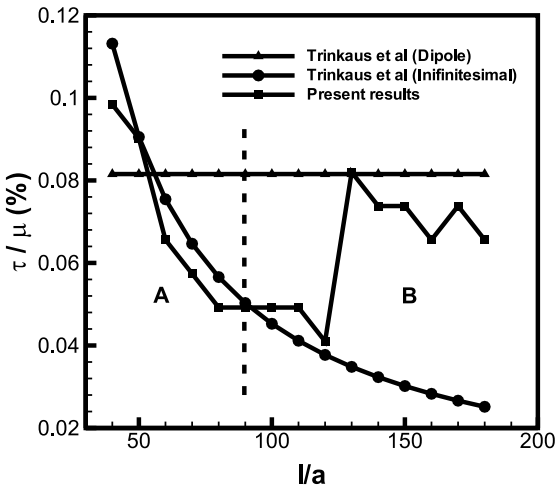

Figure 9.7: Comparison between the results of PDD simulations and the analytical results of Trinkaus et al. for the dependence of CRSS (τ/μ) on the inter-cluster distance.
(**?**)

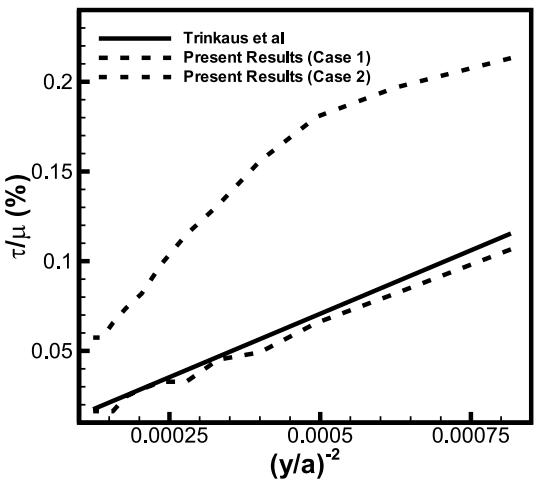

Figure 9.8: Comparison between the results of PDD simulations and the analytical results of Trinkaus et al.for the dependence of CRSS (τ/μ) on the inverse square stand-off distance. Case (1): Burgers vectors of clusters and the dislocation are parallel; Case(2): Burgers vectors of clusters is orthogonal to that of the dislocation.
(**?**)

9.1.3 Dislocation Junctions

Dislocation-dislocation interaction can result in either their attraction towards each other, or their repulsion from one another. The interaction of dislocations at close separation has been found to be associated with significant reconfiguration of their shapes(**?**)-(**?**). If dislocation interaction is attractive, the two closest segments are simultaneously pulled towards each other till a stable common part (junction) of the two dislocations is formed. However, when the segments repel one another, a stable crossed state can also form (**?**). The dynamics of dislocation junction formation and breakup have attracted recent attention(e.g. (**?**), (**?**), (**?**)), because of the importance of this mechanism in strain hardening and pattern formation(**?**). Especially in FCC metals of low stacking fault energy, dislocation junction structures are usually complex, since dislocation cores are dissociated into partials separated by stacking faults (**?**). Under these conditions, sessile Lomer-Cottrell junctions are generated. They significantly impede further dislocation motion resulting in strain hardening. Because of their stability, sessile junctions can also act as nucleation sites for dislocation cell walls(**?**). In the present PDD method, we introduce a critical length scale $r_c \approx |\mathbf{b}|$, where the two dislocation cores are not permitted to interpenetrate if they approach one another at smaller distances. In this simple fashion, complex atomic level simulation of the core structure is obviated(**?**), and no specific rules are further introduced.

First, we show in Figure9.9 the dynamics of attractive junction formation without any externally applied stress. Two initially straight dislocations of Burgers vectors and slip planes given by: $\mathbf{b}_1\mathbf{n}_1 = \frac{1}{2}[01\bar{1}](111)$ and $\mathbf{b}_2\mathbf{n}_2 = \frac{1}{2}[101](11\bar{1})$ are pinned at their ends, and allowed to move approaching each other until they are locked at equilibrium. Their locked equilibrium state can be understood to result from the balance between their mutual interaction at the close separation of r_c, and the respective self-forces of their curved arms that form close to the pinned ends. The length of the straight section (junction) that forms at the intersection of the two glide planes is approximately 200. Figure 9.9-a shows a 2-D projection view of the successive motion of $\frac{1}{2}[01\bar{1}](111)$, while the 3-D view of the junction structure is shown in Figure 9.9-b.

The intrinsic strength of junctions is the key factor in understanding strain hardening in crystals (**?**), thus it is important to study the process of junction destruction under an externally applied stress. Once an unstressed junction is formed, as shown earlier here, the binding forces on its middle straight section will be balanced by the self-forces on the four curved arms. However, if an applied stress is also introduced, the balance of forces is very delicate, because the dislocation curvature at both ends of the straight junction section changes considerably. The two ends of the junction act as pseudo pinning points, and the four arms start to behave as small F-R sources, bowing out considerably as the applied stress is gradually increased. Figure 9.10 shows the detailed dynamics of the junction unzipping process under an increasing applied stress σ_{11}/μ. When the applied stress is increased to 0.2%, the four arms of the two dislocations begin to curve, but the binding forces between the two dislocations in the junction are still very strong, and a final stable configuration is formed. When the applied stress is increased to 0.6%, the bowing out of the four arms achieves a high level of self forces at the two ends of the junction, overcoming binding forces in the immediate neighborhood. It is interesting to point out that, when the applied stress is gradually increased, the curvatures near the pseudo

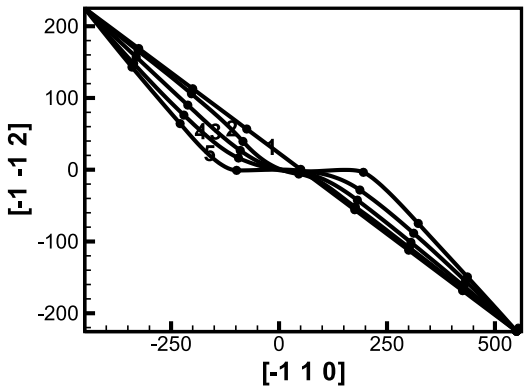

(a)

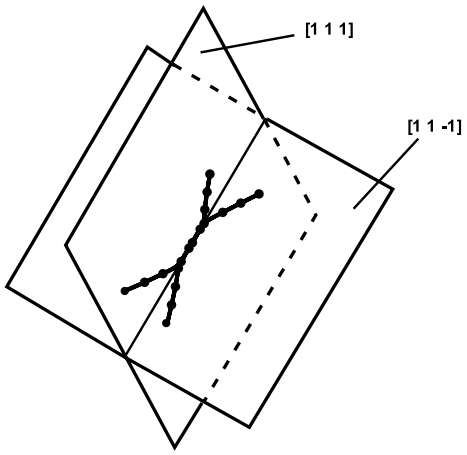

(b)

Figure 9.9: Dynamics of 2 unstressed F-R sources ($\frac{1}{2}[01\bar{1}](111)$ and $\frac{1}{2}[101](11\bar{1})$) forming a 3D junction along $(\bar{1}10)$, $\mathbf{b} = \frac{1}{2}[110]$. (a) 2D view for the motion of the F-R source $(\frac{1}{2}[01\bar{1}](111)\frac{1}{2}[\bar{1}01](1\bar{1}1))$ on its glide plane(111). Time intervals are (1) initial configuration, (2) 1.5×10^4, (3) 5.0×10^4, (4) 1.3×10^5, (5) Final configuration. (b) 3-D view of the junction

Table 9.1: Error Estimation for different nodal distributions during junction formation. The configuration with 12 segments for each dislocation is selected as reference.

No. of Segments	Absolute Error ϵ_a	Relative Error ϵ_r	CPU-time(sec)
3	27.8	20.05%	406.2
4	19.7	14.25%	841.1
6	16.0	8.75%	2932.6
8	4.97	1.00%	4902.4
12	0	0	8320.2

pinning points become very high, leading to high self-forces at the ends. Once the curvature at the two junction tips exceeds a critical value, the junction cannot sustain the high forces, and the "pinning" points themselves become unstable. In response, the two pseudo pinning points then move inward reducing the junction length. Once this process occurs, the length of the pseudo F-R sources gradually increases, causing the curvature near the "pinning" points to be even higher. A dynamically unstable *unzipping* process ensues at both ends of the junction till it totally breaks up, and the two dislocations are freed from one another. The high spatial and temporal fidelity of the PDD is clear in this example, since only 5-9 segments are used throughout the entire simulation. The simulation encompasses balance between binding forces as a result of interaction between straight segments within the junction separated by only one atomic distance with forces on the arms of the curved segments at much larger length scales with only a few segments. The results obtained here with a few degree of freedom for the dynamics of junction formation and destruction are in general agreement with the atomistic simulation of Rodney and Philips (**?**).

9.2 Work Hardening in Single Crystals

9.2.1 Introduction

It is now clear that microstructure at the microscale level controls the macroscale mechanical properties of metals. Such microstructures could be very heterogeneous like cells, persistent slip bands, and dislocation tangles. They are critical to the material properties. Dislocations are the carrier of plastic deformation of materials. The direct numerical simulation of dislocation motions is used to study the relation between microstructure and macroscale properties.

Work hardening of metals is a traditional problem that has been studied for decades. Because of the complex microstructure resulted from dislocation interactions, there is still not a single satisfactory theory that can be used to fully explain the underlying mechanism controlling the work hardening properties of materials.

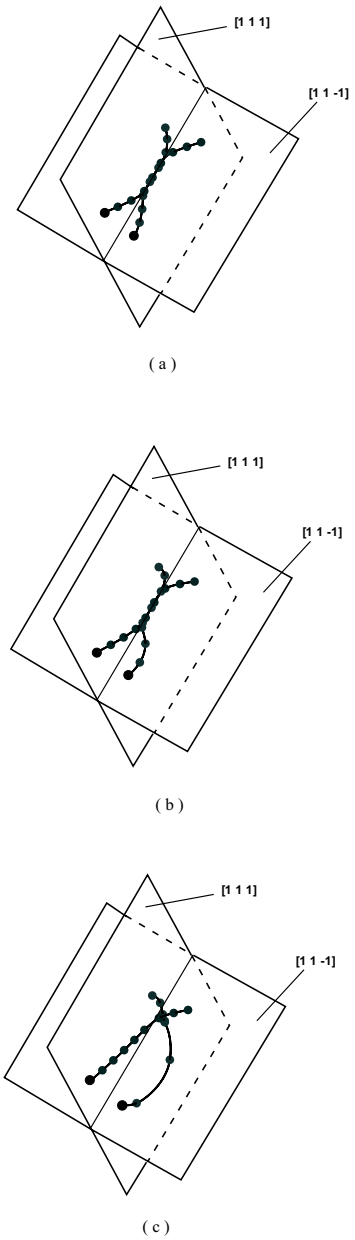

Figure 9.10: Dynamics of a *stressed* junction showing configurations at various stress levels: (a) Equilibrium, $\sigma_{11} = 100$ MPa (b) Equilibrium, $\sigma_{11} = 250$ MPa (c) Unstable, $\sigma_{11} = 300MPa$.

Work hardening of single crystals is generally divided into 3 or more stages. Each stage has a distinct work hardening rate ($d\epsilon/d\tau$). At the same time, specific microstructures form during the development of different stages. For example, cell structures are believed to form in stage III of work hardening. Cell sizes are believed to relate to the strength of materials.

To understand the work hardening and explore the underlying mechanisms, the UCLA-MICROPLASTICITY computer code is used to simulate dislocation microstructure evolutions during the material deformation.

9.2.2 Simulation Procedure

A simple one-dimension tension is applied to simulate the deformation of materials. The corresponding microstructure evolution and the stress-strain curve are obtained from the results.

The tension is applied through a constant strain rate. Define

$$c = \dot{\epsilon^e} + \dot{\epsilon^p} \tag{9.6}$$

as the applied strain rate, where ϵ^e is the elastic strain rate and ϵ^p the plastic strain rate. The plastic strain rate is obtained from the motion of dislocations as

$$\dot{\epsilon}^p = -\frac{1}{2V}\sum_{i=1}^{N} l_i v_i (\mathbf{n}_i \otimes \mathbf{b}_i + \mathbf{b}_i \otimes \mathbf{n}_i) \tag{9.7}$$

where l_i is the length of the dislocation segment, V is the volume of the simulated material, $\mathbf{n} = \mathbf{v} \times \xi$, $\mathbf{v}$ is the velocity of the dislocation segment and ξ is the tangent vector of the dislocation.

The elastic strain rate is defined as:

$$\dot{\epsilon}^e = \frac{\dot{\sigma}}{E} \tag{9.8}$$

where E is the Young's modules.

Substituting Eq. 9.7 and 9.8 into Eq. 9.6, we can obtain the expression of the relation of applied stress and strain rate as

$$\dot{\sigma} = E(c - \dot{\epsilon}^p) \tag{9.9}$$

Because of $\dot{\sigma} = \frac{\sigma^{t+1} - \sigma^t}{\delta t}$, Eq. 9.9 leads to

$$\sigma^{t+1} = \sigma^t + E\delta t(c - \dot{\epsilon}^p) \tag{9.10}$$

where δt is the time step.

In simulations, the plastic strain rate is calculated from the motion of dislocations. Using Eq. 9.10 we can obtain the strain-stress curves. The simulations will directly relate the dislocation motion at the microscale to the macroscale mechanical properties, which provides a way to study the material behaviors.

9.2.3 Simulation Results

We performed several simulations on different cases to study the dislocation microstructure evolution and the macroscopic mechanical behaviors (strain-stress curves). In our simulations, with the deformation increasing, dislocations deform into different microstructures like dislocation tangles, dislocation slip bands and cell structures. These microstructures interact with dislocations and the strain-stress curves reflect these underlying motions of defects.

The simulations are still in very low strain level. However, they provide us with the following:

1. Microstructure evolutions are directly simulated and it is clear that interactions between dislocations control the formation of different microstructure patterns.

2. The strain-stress curves are closely related to and are a direct result of the dislocation motions. For different dislocation motions (cases with different dislocation densities), there are some differences of the mechanical behaviors.

3. There are also some similarities. For example, with enough initial dislocations, dislocation densities for different cases have similar relations to the strains. This may help us in developing simulations to larger stain level.

Results for 5 μm and low density

In this case, the simulation volume is $5\mu m$, and the dislocation density is $5 \times 10^7 cm/cm^3$. The applied constant strain rate is $100s^{-1}$. The simulated results are shown in figures 9.11. Different microstructures at different strain levels are shown in figures 9.12 to 9.15. The different colors in the microstructure figures represent different glide systems as defined in figure 9.12(same for all the microstructure figures in the latter sections.

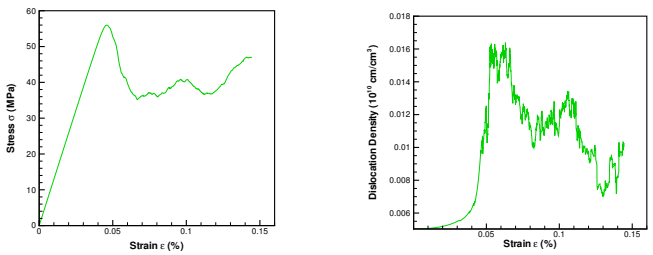

(a) (b)

Figure 9.11: (a) Simulated strain-stress curve; (b) Dislocation density vs strain simulated.(Result 1)

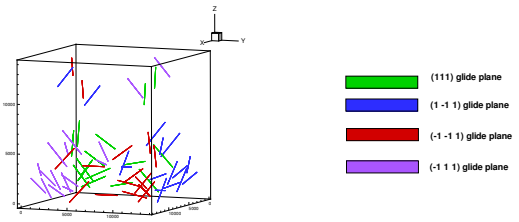

(a) (b)

Figure 9.12: (a) Initial simulated microstructure(Result 1); (b) Different colors represent different gliding systems.

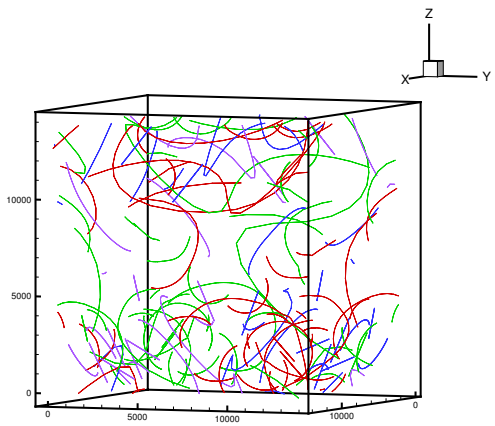

Figure 9.13: Simulated microstructure at time step 450.(Result 1)

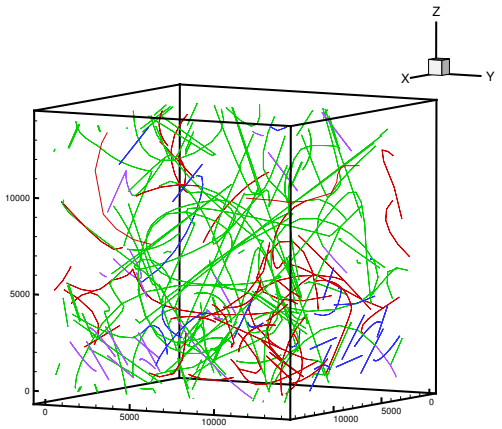

Figure 9.14: Simulated microstructure at time step 1200.(Result 1)

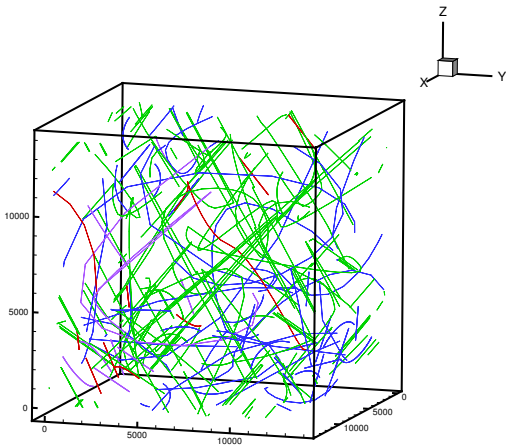

Figure 9.15: Simulated microstructure at time step 1800.(Result 1)

Results for 5 μm and intermediate density

In this case, the simulation volume is $5\mu m$, and the dislocation density is $4 \times 10^8 cm/cm^3$. The applied constant strain rate is $100s^{-1}$. The simulated results are shown in figures 9.16 and 9.17. Different microstructures at different strain levels are shown in figures 9.18 to 9.24

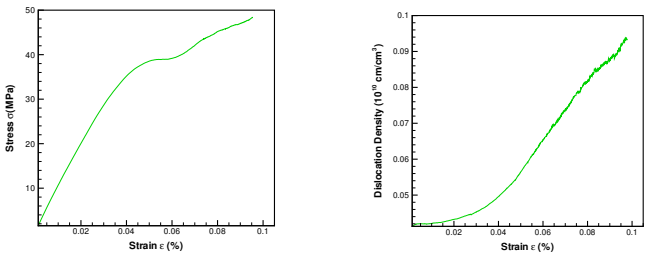

(a) (b)

Figure 9.16: (a) Simulated strain-stress relation; (b) Dislocation density vs strain.(Result 2)

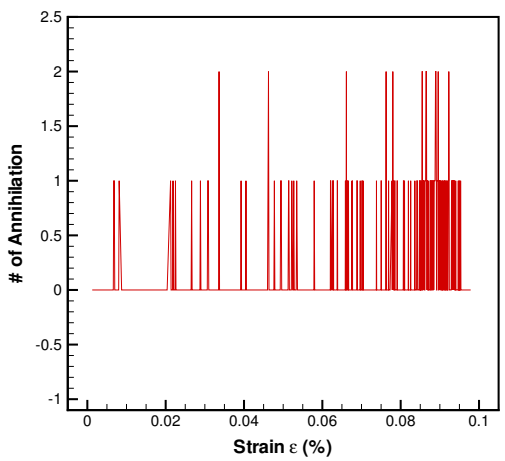

Figure 9.17: Frequency of annihilation vs strain simulated.(Result 2)

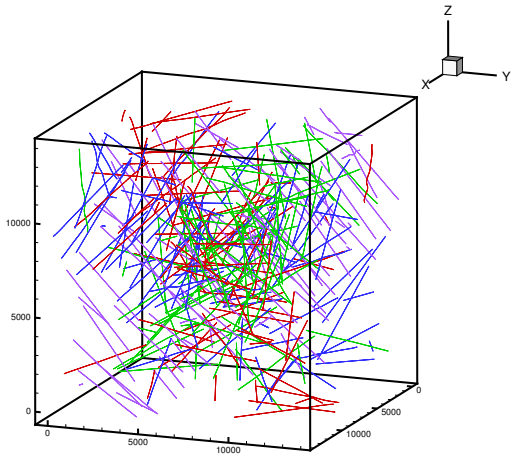

Figure 9.18: Initial simulated microstructure.(Result 2)

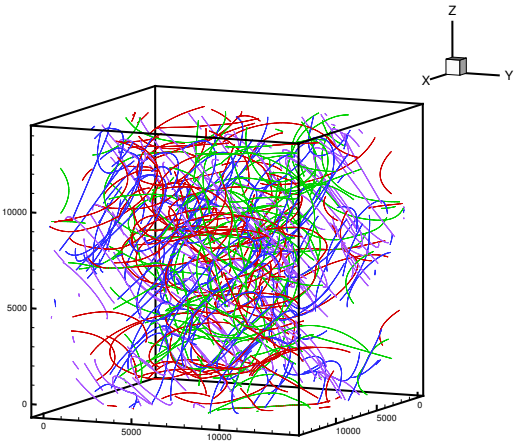

Figure 9.19: Simulated microstructure at time step 500.(Result 2)

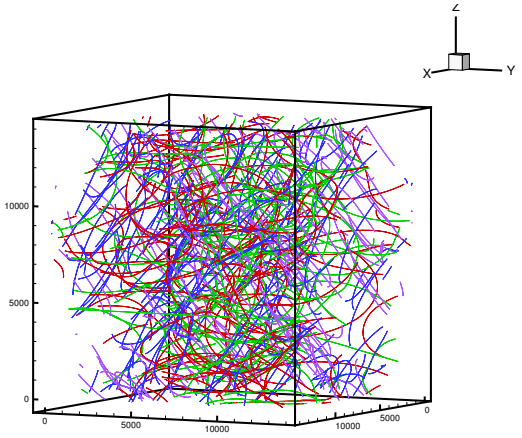

Figure 9.20: Simulated microstructure at time step 750.(Result 2)

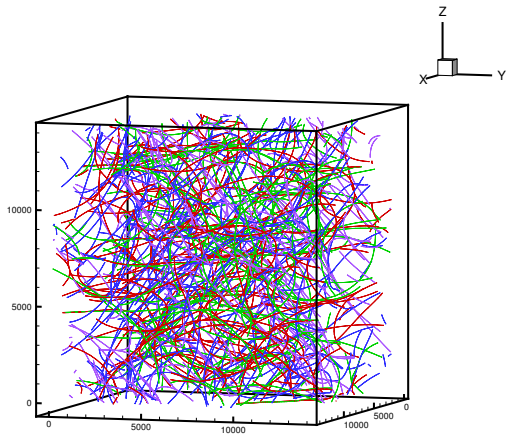

Figure 9.21: Simulated microstructure at time step 1000.(Result 2)

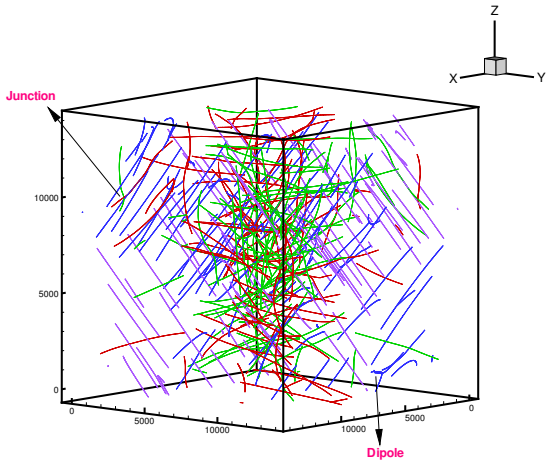

Figure 9.22: Simulated microstructure at time step 100. Short range interactions of junctions and dipoles are illustrated.(Result 2)

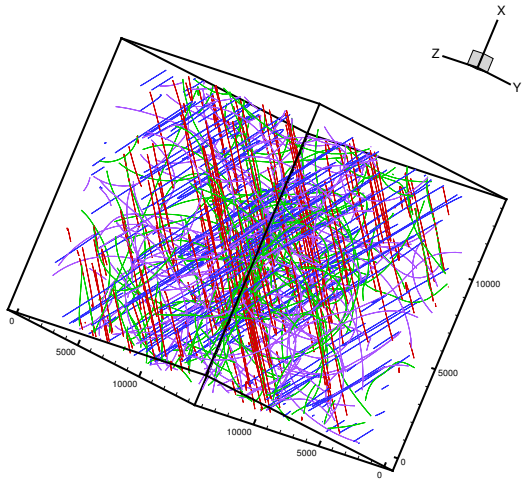

Figure 9.23: Simulated microstructure at time step 1000. Dislocations are forming into cell structures.(Result 2)

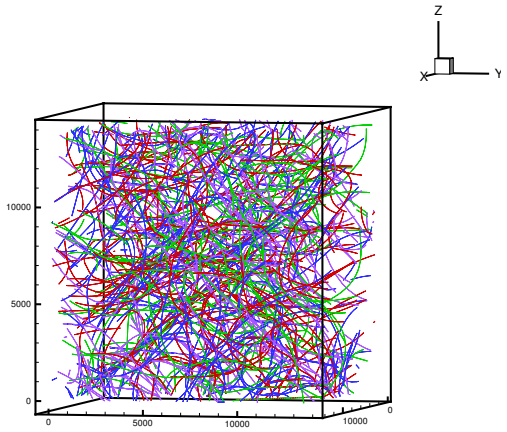

Figure 9.24: Simulated microstructure at time step 1000. Dislocation tangles are shown in the figure.(Result 2)

Results for 10 μm

In this case, the simulation volume is $10\mu m$, and the dislocation density is $1 \times 10^8 cm/cm^3$. The applied constant strain rate is $100s^{-1}$. Different microstructure at different strain levels are shown in figures 9.25 to 9.34.

Results for 5 μm and high density

In this case, the simulation volume is $5\mu m$, and the dislocation density is $1 \times 10^9 cm/cm^3$. The applied constant strain rate is $100s^{-1}$. Different microstructures at different strain levels are shown in figures 9.35 to **??**.

9.3 Thin Films & Nanolayers

Introduction

Transmission Electron Microscopy (TEM) offers the most direct method of comparison for DD simulations. However, few such comparisons have been made to date, and these have been qualitative examinations and not quantitative comparisons between experiment and modeling (**?**, **?**, **?**). Comparisons of DD simulations to static TEM images are necessarily indirect and qualitative since standard TEM images are two-dimensional thin foil projections of static mi-

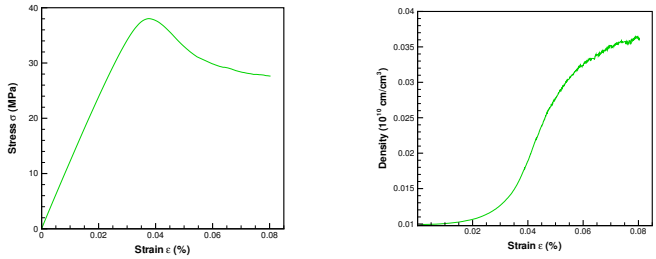

(a) (b)

Figure 9.25: (a) Simulated strain-stress relation; (b) dislocation density vs strain.(Result 3)

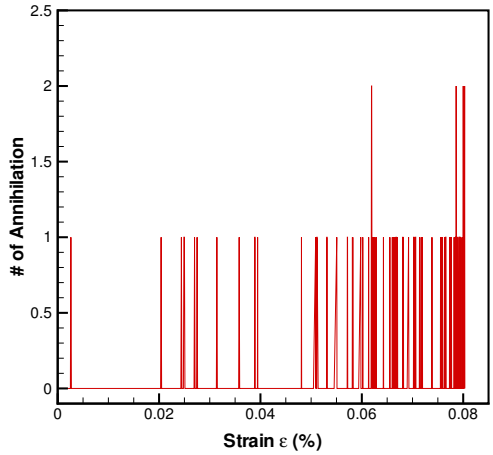

Figure 9.26: Frequency of annihilation vs strain.(Result 3)

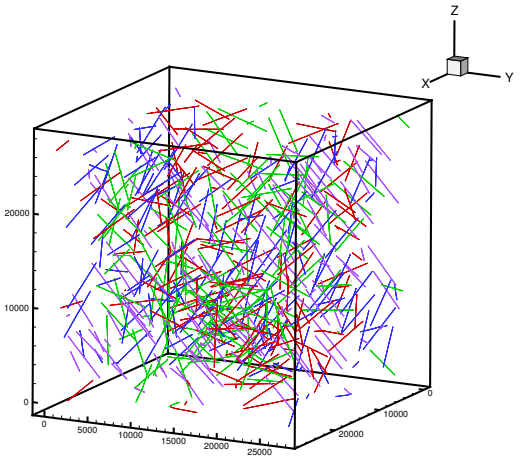

Figure 9.27: Initial simulated microstructure.(Result 3)

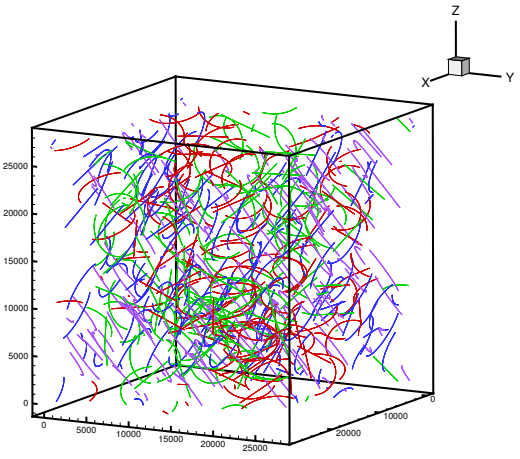

Figure 9.28: Simulated microstructure at time step 250.(Result 3)

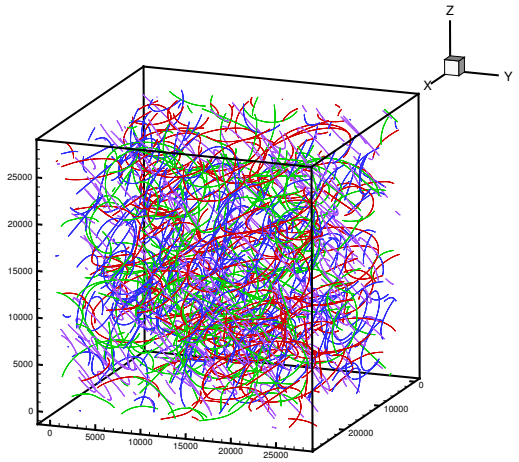

Figure 9.29: Simulated microstructure at time step 500.(Result 3)

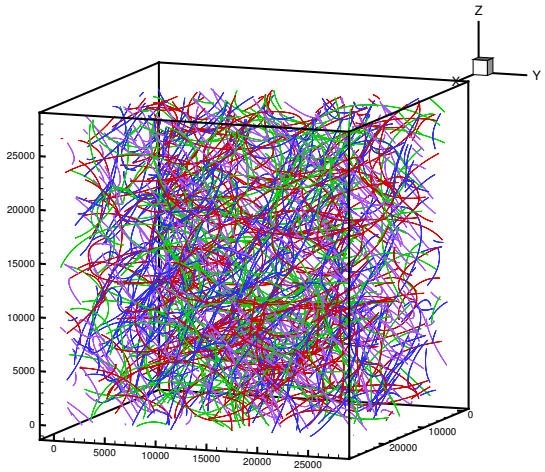

Figure 9.30: Simulated microstructure at time step 750.(Result 3)

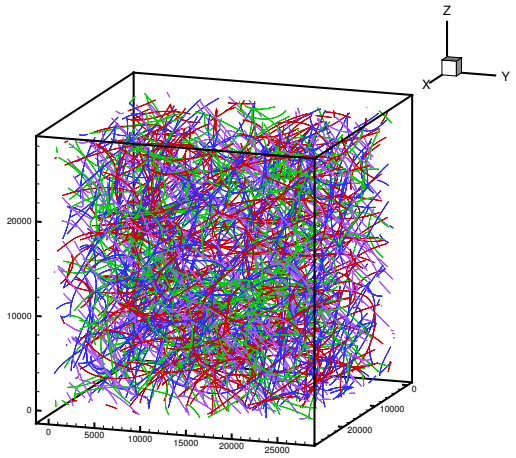

Figure 9.31: Simulated microstructure at time step 1000.(Result 3)

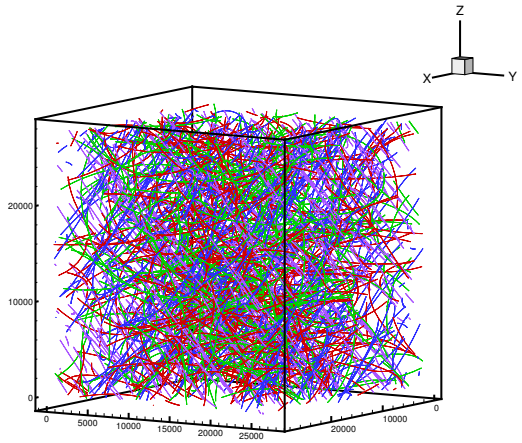

Figure 9.32: Simulated microstructure at time step 1350.(Result 3)

Figure 9.33: Simulated microstructure at time step 1000, junctions and dipoles are shown.(Result 3)

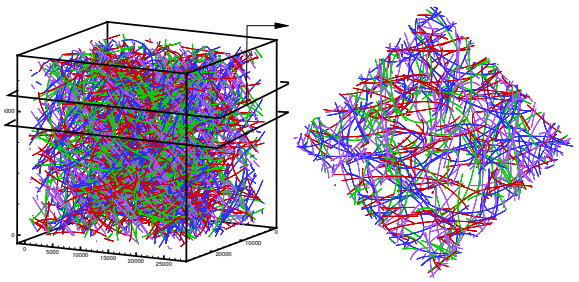

Figure 9.34: Simulated microstructure at time step 1350, dislocations form complex 3D structures.(Result 3)

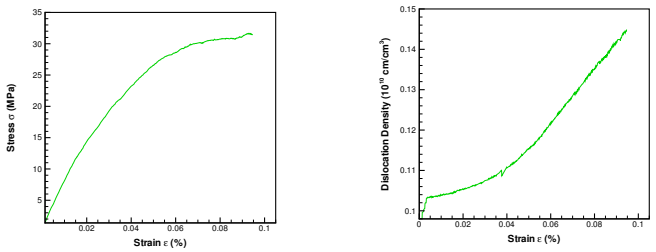

(a) (b)

Figure 9.35: (a) Simulated strain-stress curve; (b) dislocation density vs strain. (Result 4)

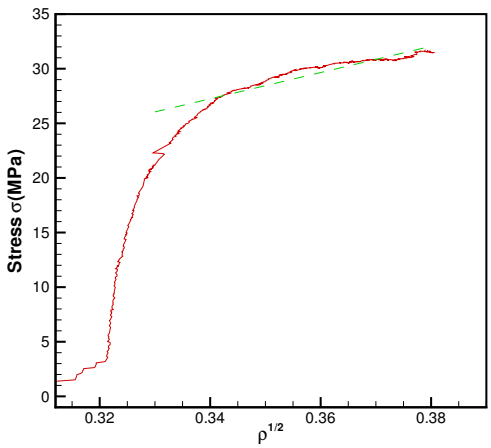

Figure 9.36: Relation of stress to the square-root of the dislocation density, the dashed line is the linear fit from least-square method.(Result 4)

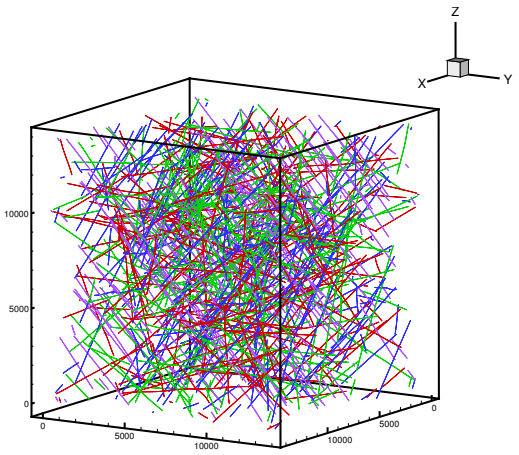

Figure 9.37: Initial simulated microstructure.(Result 4)

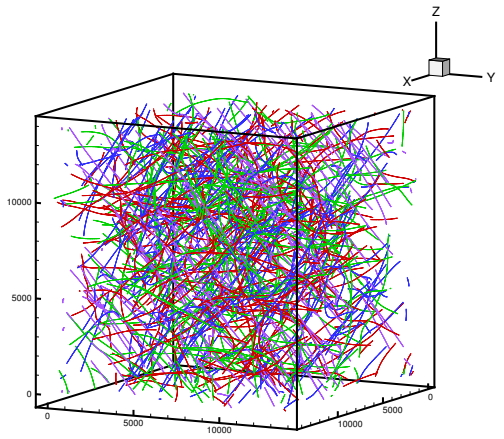

Figure 9.38: Simulated microstructure at time step 250.(Result 4)

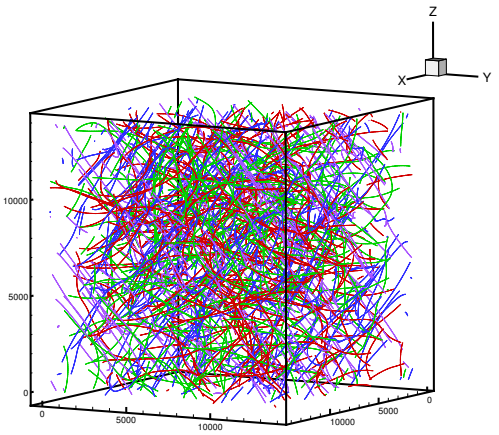

Figure 9.39: Simulated microstructure at time step 500.(Result 4)

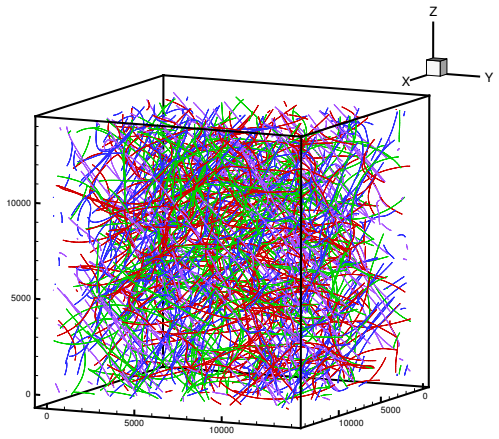

Figure 9.40: Simulated microstructure at time step 750.(Result 4)

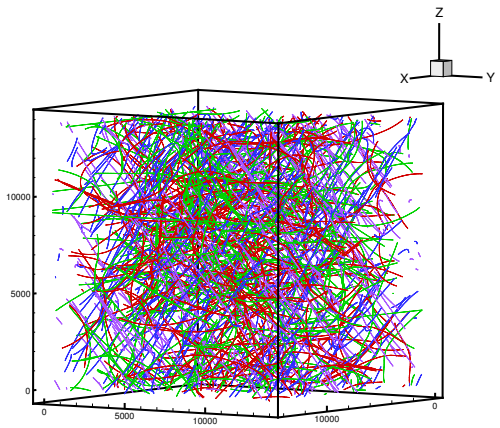

Figure 9.41: Simulated microstructure at time step 840.(Result 4)

crostructures. Dynamic dislocation behavior in thin foils can be observed by in-situ TEM, and several interesting experimental studies have been made using this technique(**?**, **?**). Some 3D information about dislocation motion can be ascertained if travelling dislocations leave a slip trace on the surface. However, information on the relative positions of dislocations is largely limited to 2D results, and without 3D information on dislocation configurations, the elastic interactions between dislocations cannot be accurately determined. A technique has been developed in which 3D dislocation configurations can be quantified before and during an in-situ straining TEM experiment (**?**). Although direct 3D observations of dislocation motion is not possible, knowledge of 3D configurations preceding and following deformation, along with 2D in-situ records of motion can be used to reconstruct the overall 3D behavior. Such information can also be used for direct validation of 3D DD simulations.

The present study details a direct comparison between experimental observations and computer simulations of dislocations in thin foils. The goal is to use these comparisons to ascertain the nature of forces on dislocations and the salient mechanisms that control their motion. The effects of the constrained geometry of the foil and the free surface on dislocation motion are explored. Simplified elasticity calculations of dislocation forces and motion are not reliable to correlate with experimental data because of the complex 3D structure of observed dislocations and the influence of surface image forces. Thus, utilization of 3D computer simulations, including surface image effects is necessary.

We specifically examine here two effects that are particular to dislocation behavior in thin foils. First, since dislocation loops may terminate at free surfaces, computer simulations must track the position of dislocation-free surface intersections. Thus, special boundary conditions

must be applied to the study of thin foil deformation. Second, the free surfaces of a thin foil may strongly influence dislocation behavior by introducing image stresses, which become significant when dislocations approach the surface. Strong image forces can influence dislocations by enhancing their out-of-plane motion through cross-slip and climb mechanisms.

Numerous experiments have shown that cross-slip, which is thermally activated, plays an important role during stage-III work hardening in FCC single crystals(**?**)-(**?**). Double cross-slip results in dislocation generation by expanding new Frank-Read sources on neighboring glide planes(**?**). Only segments of screw (or nearly screw) character may perform cross-slip, because they are able to move on any favorably-oriented glide plane. The probability of a dislocation segment to cross-slip onto a neighboring slip plane increases significantly when the resolved shear stress on that plane is high. Any large internal stress field, which may arise from inclusions and other obstacles to glide, surfaces, or interfaces, may induce cross-slip events.

Motion out of the glide plane can also be accomplished by climb (**?**, **?**, **?**). At low temperatures or in the absence of a non-equilibrium concentration of point defects, dislocation motion is restricted almost entirely to glide. However, at higher temperatures or owing to a locally-high stress, an edge dislocation can move out of its slip plane by climb.

The objective of this work is to utilize 3D stereo-TEM in conjunction with in-situ straining TEM to describe the evolution of the spatial topology of dislocations in thin foils. DD computer simulations are used to investigate the salient mechanisms that determine experimentally-observed dislocation shapes. In doing so, we explore the importance of image surface forces and their effects on out-of-plane dislocation motion by the cross-slip and climb mechanisms. We show that surface-force induced cross-slip greatly influences the structure and dynamics of the dislocation microstructure in thin foils, and that dislocation motion in thin foils may not be representative of bulk behavior. To our knowledge, this is the first direct comparison of experiment and simulation of moving dislocations.

9.3.1 Experimental Procedure and Results

Stereo-TEM was used in conjunction with in-situ straining to describe the evolution of the spatial distribution of dislocations in thin Cu foils. In-situ TEM experiments are generally used to develop an understanding of bulk material properties. However, the inference of bulk material properties from thin foil in-situ observations is often controversial due to the effects of free surfaces on dislocation configurations. We plan here to link direct experimental observations of dislocation motion and reconfiguration with computer simulations so as to discern dislocation mechanisms that are specific to thin films. Examining thin foil behavior is an advantage in that it includes surface effects, and can thus better gauge the fidelity of DD models.

TEM in-situ tensile specimens were cut, ground, and electro-polished from a well annealed copper sample. Tensile Cu foils were prepared with dimensions of 11.5 mm by 2.5 mm and a thickness of approximately 175 μm as shown in Fig. 9.42. Electrolytic polishing was used to thin the center of the specimen to perforation. The geometry of the thinned region can be approximated as two hemispherical dimples intersecting the top and bottom surfaces at 2

mm circles. Thinning produced a hole approximately 400 μm in diameter, and the specimen thickness at the edge of the hole is generally 10-20 nm. The experimental observations were made near the top edge of the hole at a position where the sample thickness is about 200 nm.

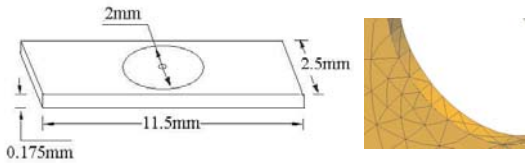

(a) (b)

Figure 9.42: (a) The solid model of the sample, and (b) FEM mesh around the central hole.

Deformation was carried out inside the TEM using a displacement control, single tilt, straining specimen holder. During in-situ straining TEM experiments, it is advantageous to pre-strain the specimen while viewing an area of interest until some dislocation activity begins. This is primarily to ensure that dislocation motion will occur in the area of interest before spending significant time doing stereo and Burgers vector analysis. However, once the specimen is pre-strained, there is potential for the specimen to relax somewhat while analysis is being performed, and some dislocations can change position or escape the region being observed.

The stereo-coupled in-situ experiments involve obtaining a 3D description of the dislocation configuration prior to and following in-situ straining in the microscope. 3D configurations are obtained using a modified stereo-TEM technique detailed elsewhere (**?**). Standard stereomicroscopy of crystalline materials is almost never possible with a single-tilt TEM holder making it unfeasible for all commercially available in-situ straining TEM holders. The modified approach is a weak beam technique involving changing the sign of $\mathbf{g}$ (the imaging beam) and/or s_g (how far the imaging beam deviates from the exact Bragg condition) between images while tilting across a Kikuchi band that is at less than approximately 10° to the tilting direction.

The stereo pair and diffraction pattern demonstrating the modified stereo technique for the initial dislocation configuration is shown in Fig.(9.43), with the tensile axis direction vertical (same as stereo tilt axis and specimen holder axis). The positions of the dislocations are measured using a computer program that allows the user to mark points along a dislocation line with a 3D cursor while viewing micrographs stereoscopically (**?**). The orientations of the tensile axis and specimen plane normal with respect to the grain are $[53(\bar{6}8)51]$ and $[(\bar{7}8)(1\bar{5})61)]$, respectively. Based on this geometry, Schmid factors for the common fcc slip systems obtained assuming a simple tension assumption are given in Table 9.5. Burgers vector analysis was performed on several key dislocations. Dislocations labeled 11, 13, and 22 in Fig. 9.43 have a Burgers vector of [101] and dislocation 12 has a Burgers vector of $[\bar{1}0\bar{1}]$.

During in-situ straining, dislocation motion was monitored in the TEM at 30 frames per second. Figure 9.44 shows dislocation configurations at various times during the in-situ straining. Comparing the first frame of Fig. 9.44 with the configuration seen in Fig. 9.43, it is evident

Table 9.2: Schmid factors for the Cu thin foil under simple tension.

(111)			$(11\bar{1})$		
$[0\ 1\ \bar{1}]$	$[10\bar{1}]$	$[1\bar{1}0]$	$[011]$	$[101]$	$[1\bar{1}0]$
0.174	0.003	0.177	0.046	0.279	0.325
(111)			$(11\bar{1})$		
$[0\ 1\ \bar{1}]$	$[101]$	$[110]$	$[011]$	$[10\bar{1}]$	$[110]$
0.339	0.296	0.043	0.119	0.014	0.105

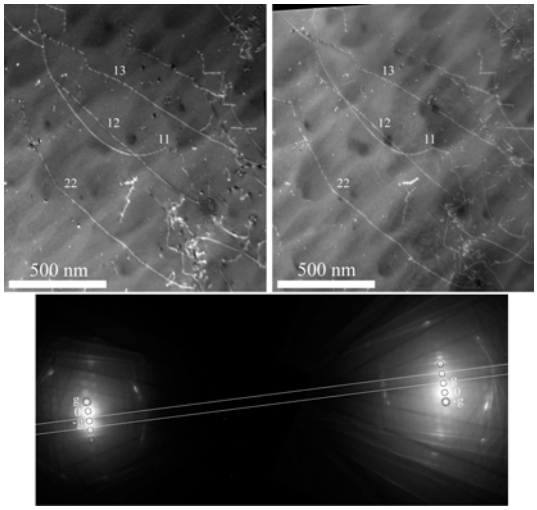

Figure 9.43: Stereo pair (top) and diffraction pattern demonstrating the modified stereo technique.

that dislocation 11 and 22 moved between the time when the stereo pair was taken and when the straining was continued and recorded. However, these two dislocations do not move during further straining. Three dimensional representations of the dislocation configuration before and after straining are given in Fig. (9.45). In the 3D representations and the DD calculations based on these configurations, the initial and final configurations of dislocation 11 are assumed to be the same, specifically the configuration given by the final stereo pair. This assumption is reasonable, since dislocations 11 and 22 do not react with one another in changing configuration, because the two dislocations have the same Burgers vector.

Dislocations 12 and 13 share the same primary glide plane, $(11\bar{1})$, and Burgers vector but have opposite signs. Hence, they move in opposite directions. One end of dislocation 13 is pinned at a node (point labeled (d) in the first frame) while the other end terminates at the foil surface (point labeled (a) in first frame). There is a jog, labeled (bc), along the length of

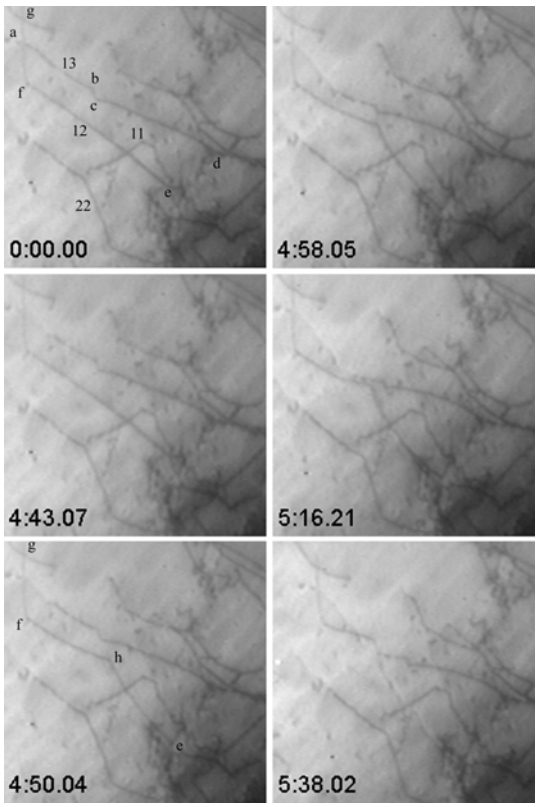

Figure 9.44: Time sequence of in-situ TEM measurements during straining. Time units are - min:sec:sec fraction

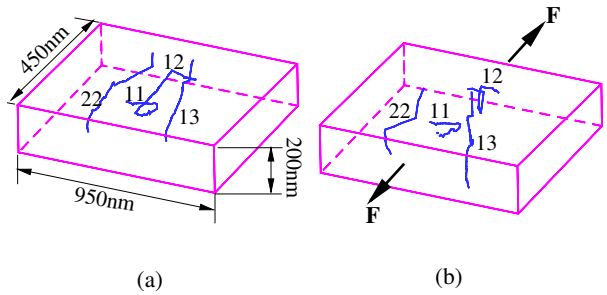

Figure 9.45: 3D rendering of experimentally-observed dislocation configurations in the Cu thin foil - (a) before deformation, and (b) after deformation.

dislocation 13 lying on the $(\bar{1}11)$ plane. During straining, the right end remains pinned at the node and the segment (ab) glides downward in the image. Dislocation 12 starts out pinned at a different node, labeled (e). A straight segment (labeled (ef)) of dislocation 12 extends from the node diagonally across the image towards the top left corner where it jogs upwards towards the free surface (segment labeled (fg)). During straining, unlike dislocation 13, dislocation 12 escapes from the pinning point (e) (third frame) first, only to be pinned again at another node directly below the first pinning point, labeled (e) in the third frame. The result is the formation of a jog along the length of dislocation 12 as seen in frame 3. The segment (he) appears to glide to the left, while insignificant movement of segment (hfg) was discerned up to frame 3. In frame 4-6, the segment (fh) glides upward in the image. This motion eventually leads to dislocation 12 escaping from the pinning point (e) and soon after that, a large portion of the dislocation segment (he) escapes to the surface. A key question not resolved from Fig. 9.44 is whether dislocations 12 and 13 intersect during glide (frames 4 and 5 appear to indicate a possible interaction). This is very difficult to discern from the 2D in-situ straining images, but the stereo imaging (Fig. 9.44) reveals that these dislocations do not intersect. Another question is the distance of the various dislocation segments from the free surfaces that can only be resolved from stereo imaging of the in-situ strained dislocation substructures. As shown later in this paper, having quantitative information of the dislocation positions in the in-situ straining experiment is crucial in modeling the dynamics of dislocations in thin foils.

The bowed out segment of dislocation 11 in Fig. 9.45 is not visible in the first frame of Fig. 9.44. This implies that this segment glided out to the free surface in the time between stereo imaging and the onset of further straining. Since the specimen is under strain during this time, beam heating may lead to escape of bowed out segments that are near the free surface. The

remaining segments seen in Fig. 9.44 are not on the glide plane, and hence no further motion is detected.

Dislocation 22 appears as a straight line in Fig. 9.43 but kinked in the first frame of Fig. 9.44. It is possible that it experiences a similar type of motion to that described above for dislocation 12 in frames 1-3. The kinked dislocation 22 may be strongly pinned at both ends (although the details of the pinning points are not discerned clearly in these images) and hence, no further motion is detected in the in-situ straining sequence shown in Fig. 9.44. Motion of dislocations motions shown in Fig. 2 appear to be more evident for dislocations that terminate at a free surface. The influence of surface forces on dislocation dynamics in thin films is discussed in more detail in the DD simulation section of this paper.

Based on slip trace analysis, dislocation glide has taken place on two glide planes: $(11\bar{1})$ and $(\bar{1}11)$. The resolved shear stresses for the $[101](11\bar{1})$ and $[101](\bar{1}11)$ dislocations are approximately the same, although slightly less than the highest stressed slip systems.

There is extensive discussion of the error involved in conventional and modified stereo-TEM given elsewhere (**?**). The experimental error in the third dimension (z) for standard stereo-TEM depends on the stereo angle and is around an order of magnitude greater than the measurement error in the other two dimensions. With the measurement error in the x and y directions being on the order of 1nm, the measurement error in the z direction is around 10 nm. The error for the modified technique is the same as for standard stereo provided both $\mathbf{g}$ and s_g change sign but not magnitude.(**?**) In the present case, these ideal imaging conditions were not obtained, likely resulting in a somewhat larger error in z. These errors are to be kept in mind during the direct comparison of the modeling results to the experimental data.

9.3.2 Dislocation Dynamics in Thin Foils

In the present study, we use the Parametric Dislocation Dynamics (PDD) method to simulate the motion and interaction of dislocations (**?**)-(**?**). We incorporate here additional forces on dislocations as a result of their interaction with the free surface. There are several models available to calculate the effects of surface forces, or to directly include the image stress field into DD simulations. These approaches include Lothe's energy theorem (**?**), Gosling and Willis' Green's function method (**?**), and the superposition method based on solution of the Boussinesq problem (**?**). For complex dislocation configurations and boundary conditions, image stresses due to surfaces and interfaces can now be computed by the finite element method (FEM) (**?**, **?**). In this work, we implemented Lothe's theorem for direct calculations of surface forces into the PDD code (**?**). For an isotropic medium, Lothe (**?**) determined the force per unit length induced by a free surface on a straight dislocation segment (**?**):

$$\mathbf{F} = \frac{\mu b^2}{4\pi\,(1-\nu)\,\lambda}\left[|(1-\nu\cos^2\beta)\tan\theta|\mathbf{n}_1 + |2\nu\cos\beta\sin\beta|\mathbf{n}_2\right] \quad , \tag{9.11}$$

where μ, ν are the material's shear modulus and Poisson's ratio, respectively. Parameters are

shown in Fig. 9.46. λ is the distance from point P, where the force is evaluated, to point O at which the dislocation line intersects the free surface. $\mathbf{n}_1$ is a unit vector on the plane OO'P, with direction perpendicular to the dislocation line, $\mathbf{n}_2$ is a unit vector on the plane containing OP and the Burgers vector, with direction perpendicular to the dislocation line on the glide plane. $\mathbf{n}_1$ represents the direction of the force component, which acts to rotate the dislocation line so that it is normal to the surface, while $\mathbf{n}_2$ represents the direction of the force component, which acts to align the dislocation along its Burgers vector. The angle θ is between the tangent and Burgers vectors, while β refers to the angle between the tangent vector and the surface normal. The surface force is then decomposed to a component on the glide plane, and added to be a part of the resolved glide forces, along with those dictated by the applied stress and interaction forces. Because curved dislocation segments are employed, the tangent vector is extended to its intersection with the free surface, and EQN. (9.11) is used to compute the force per unit length at any point on the dislocation line. This force is also integrated along the parametric curves to determine the nodal positions and coordinates, as described in reference (**?**).

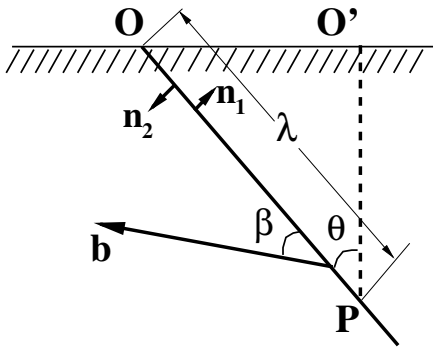

Figure 9.46: Illustration of Lothe's formula to calculate surface image force.

In the present model, dislocation loops are discretized into several curved segments that can glide on different glide planes (see Table 9.3). Internal nodes belonging to two different glide planes can only move along the intersection line of the two planes. Dislocations may end at the surface or at some joint nodes with other dislocations inside the material. Surface nodes can move along the intersection line of the glide and surface planes. Since the motion of surface nodes is associated with the creation of surface steps, the mobility of these nodes is assumed to be 20% of the bulk mobility (10^4 Pa^{-1} s^{-1})(**?**).

Because screw dislocation segments can move on different intersecting glide planes, cross-slip is possible (**?**). In the present simulations, the orientation of various segments are checked to determine if the average tangent vector on the segment is aligned within 15° of its Burgers vector orientation. If that is the case, another check is made on the resolved shear stress magnitude on

Table 9.3: Nodal segment distributions on dislocations, with corresponding Burgers vectors ($\boldsymbol{b}$), glide plane Miller indices. All segments are in mixed characters.

Dislo-cation	Seg. 1 Miller	Seg. 1 Nodes	Seg. 2 Miller	Seg. 2 Nodes	Seg. 3 Miller	Seg. 3 Nodes	$\boldsymbol{b}$
11	jog	1-15	$(11\bar{1})$	15-16	$(\bar{1}11)$	16-29	[101]
12	$(11\bar{1})$	1-7	$(\bar{1}11)$	7-24	$(11\bar{1})$	24-41	$[\bar{1}0\bar{1}]$
13	$(11\bar{1})$	1-27	$(\bar{1}11)$	27-28	$(11\bar{1})$	28-36	[101]
22	$(11\bar{1})$	1-18	$(\bar{1}11)$	18-37	$(11\bar{1})$	37-44	[101]

all glide planes on which the segment may glide. Following the Friedel-Escaig mechanism(**?**), the probability of a cross-slip event to occur is related to the activation energy and the resolved shear stress on any glide plane as(**?**, **?**):

$$P = \beta \frac{L}{L_0} \frac{\delta t}{\delta t_0} \exp(V \cdot \frac{\tau - \tau_{III}}{kT}) \tag{9.12}$$

where β is a normalizing coefficient that makes the probability ranging from 0 to 1, $\tau_{III} = 32$ MPa is the critical resolved shear stress at the onset of stage III of work hardening, $V = 300\ b^3$ is the activation volume, k is Boltzmann constant, T is the temperature, $L_0 = 1\ \mu m$ and $\delta t_0 = 1$ sec are respectively references to length and time, τ is the resolved shear stress on the cross-slip plane, L is the length of the screw segment, and δt is the discrete time-step(**?**).

After the probabilities of cross-slip on each plane are calculated, the plane with a larger probability of cross-slip is selected for dislocation to move. When the dislocation segment approaches the free surface, the resolved shear stress on possible glide planes increases dramatically, and the probability of cross-slip is enhanced. Further analysis of the experimental data also indicated the presence of many small jogs on dislocation lines. Such jogs can produce vacancies as they move towards the sample surface, which may result in additional out-of-plane motion due to climb of edge components as well. As a simple model of climb, comparison between the experimental and the computed dislocation structures was made and climb movement was attempted for segments that showed large differences. In summary, the simulations proceeded in the following way: (1) dislocation motion along glide planes only, (2) cross-slip motion, and (3) climb.

One uncertainty in the calculation is the stress state acting on experimentally-observed dislocations. The direction of the shear stress was determined by examining the dislocation bow out and motion. In the simulations, the applied stress was increased until the final position of the dislocations matched the experiment. A 3-D Finite Element Model (FEM) was also used to analyze the stress state in the sample. The model consisted of 7880 tetrahedral elements, corresponding to 16268 nodes. A displacement boundary condition was used, corresponding to sample straining by edge displacements in the range of (0-4) microns. A solid model for the sample is shown in Fig. 9.42. Results of the axial (normal) stress components along the tensile

axis (y-direction) and along its perpendicular (x-direction) are shown in Fig. (9.47). Also shown in Fig. 9.48 is the corresponding normal stress contour around the central perforation. Although large stress gradients are observed near the central hole region, the zone where dislocations are observed extend over a relatively small length (microns), and the axial stress level is estimated to be 150 MPa for the full 4 μm displacement. It is also found that the shear stress component in this zone is negligible, confirming that tensile stress state in our DD model is close to the correct value.

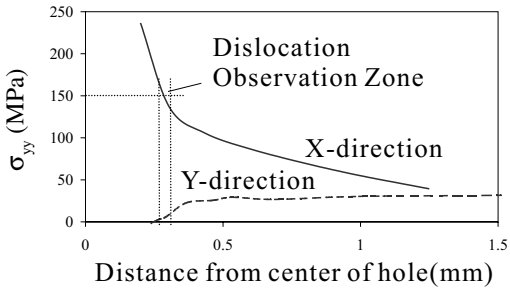

Figure 9.47: FEM results for normal stress distribution in the sample along the axial direction (y) and its normal (x).

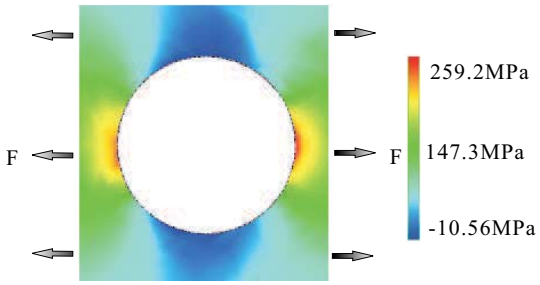

Figure 9.48: FEM results for σ_{yy} contour around the central hole.

9.3.3 PDD Simulations for Experimental Analysis

Initial PDD computer simulations of the experimental data restricted the motion of dislocations to movement on the glide plane. The initial results indicated that while the experimental dislocation motion on the glide planes is matched reasonably well in the simulations, motion in the direction normal to the TEM observation plane is greatly underestimated by the simulations. To be more concrete, with no climb or cross-slip mechanisms invoked, the difference between the simulations and experiments for dislocation 11 is approximately 16 nm within the observation plane and 12 nm out-of-plane, roughly within the experimental uncertainty. The

other dislocations were less well determined, with a difference in dislocations 22 and 13 within the observation plane of approximately 61 nm and an out-of-plane error of 80 nm. The motion of dislocation 12 is even more poorly modeled, with an in-plane difference of 200 nm and an out-of-plane error of 140 nm.

PDD simulations that include dislocation cross-slip and climb (using the methods described above) were thus performed. These simulation results are shown in Fig. (9.49) and are compared with experimental observations of Figs. (9.43) and (9.45). The results show that dislocation 22 undergoes cross-slip motion, dislocation 13 climbs, and dislocation 12 shows both climb and cross-slip motion. Details of the cross-slip mechanism of dislocation 22 are shown in Fig. (9.50), where we see that the segment reconfigures from the original slip plane to the neighboring one with a higher probability of cross-slip motion. The cross-slip probabilities of two screw segments are listed in table (9.4). It is obvious that cross-slip planes have larger probabilities. Although cross-slip does not have to happen on cross-slip plane, the dislocation segment will select the plane that has large a larger probability.

Table 9.4: Probabilities of cross-slip of screw segments at an applied stresses of 100MPa

Segment on Dislocation	Original Plane	Cross-slip Plane
segment 2 on Dislocation 12	P=0.44	P=1.0
segment 2 on Dislocation 22	P<0.01	P=0.63

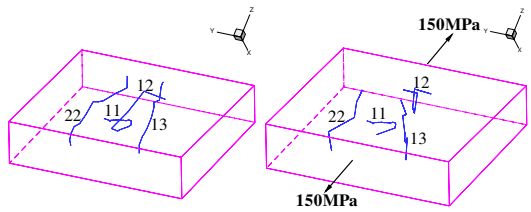

Figure 9.49: Initial and final dislocation configurations simulated by PDD

Image stresses play an important role in activating the cross-slip by changing the resolved shear stress on the cross-slip planes. For example, when cross-slip occurs, for dislocation 12, the resolved shear stresses resulting from image forces on the cross-slip plane$(11\bar{1})$ and on the original plane $(\bar{1}11)$ are 37.76 MPa and 20.15 MPa, respectively. The resolved shear stresses resulting from applied stress on the cross-slip plane and the original plane are 46.22 MPa and 48.18 MPa, respectively. The cross-slip plane has even a lower stress without the image effect. The average final resolved shear stresses on the cross-slip plane and the original plane are 81.98 MPa and 60.07 MPa, which shows that surface image forces greatly increase the cross-slip probability on the cross-slip plane. For climb, we calculated the climb stresses on dislocation

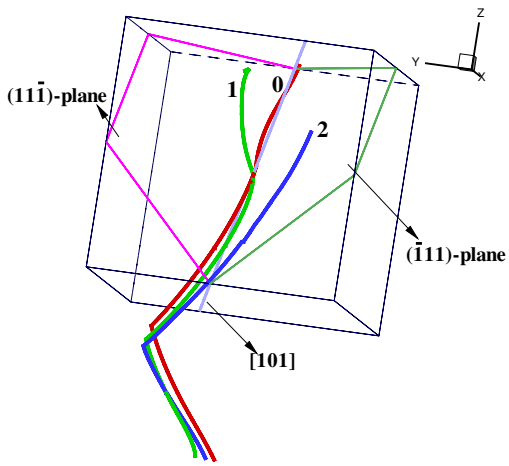

Figure 9.50: Dislocation 22 positions during cross-slip motion: (1) Final configuration without cross-slip, (2) Final configuration with cross-slip

12 and 13 as 208.3 MPa and 294.3 MPa at the end of straining. We believe that these high stresses can lead to pipe diffusion that results in dislocation climb(**?**, **?**). Careful analysis of node coordinates of the simulated and experimental configurations shows great reduction in the positional difference when cross-slip and climb motion are included, with the largest difference for any of the dislocations of about 13 nm in-plane and 17 nm out-of-plane. These uncertainties are well within experimental error.

Conclusions

Direct validation of DD simulations with experiments (in situ straining coupled with 3D imaging in TEM) allowed us to correctly model the motion of dislocations in thin, annealed Cu foils with a low initial dislocation density where surface image forces play a significant role in determining the dislocation dynamics. It is shown, through systematic comparison between experimental observations and PDD simulations, that dislocation configurations in thin copper foils acquire considerable 3-dimensional components that cannot be explained by glide events alone. The structure of dislocation lines is highly jogged, with non-planar components. Surface image forces in the thin copper foil appear to have two main effects: (1) they result in the inducement of cross-slip for screw components; (2) they also nucleate jogs on dislocation lines. Possibly through vacancy flow from the surface, the motion of these jogs may also result in additional out of plane displacement of edge dislocation segments as well.

Introduction to Nanolayer Mechanics

Nano-layered structures are candidates for applications requiring thin volumes (e.g. micro-electronics, opto-electronics, laser mirrors, etc.), or may be developed for more demanding structural applications (e.g. aircraft, rocket engines, transportation, advanced energy, etc.).

Table 9.5: Schmid factors for the common fcc systems under simple tension.

(111)			$(11\bar{1})$		
$[0\ 1\ \bar{1}]$	$[10\bar{1}]$	$[1\bar{1}0]$	$[011]$	$[101]$	$[1\bar{1}0]$
0.174	0.003	0.177	0.046	0.279	0.325
(111)			$(11\bar{1})$		
$[0\ 1\ \bar{1}]$	$[101]$	$[110]$	$[011]$	$[10\bar{1}]$	$[110]$
0.339	0.296	0.043	0.119	0.014	0.105

The mechanical behavior of these two types of structures can be vastly different as a result of geometry and structural constraints. Recent experimental research on the deformation behavior of multi-layer nanocrystal composites shows that very high strength and ductility can indeed be obtained, when plastic deformation is restricted to flow in confined small volumes (Mitchell, Lu, Griffin, Nastasi and Kung 1997, Misra, Verdier, Lu, Kung, Mitchell, Nastasi and Embury 1998, Anderson, Foecke and Hazzledine 1999, Misra, Verdier, Kung, Nastasi, Embury and Hirth 2000, Anderson and Hazzledine 2000). New material processing methods, such as wire drawing, sputtering or evaporation (Embury and Hirth 1994, Embury and Han 1999), have shown that nano-layered structures can be manufactured to be ultra-strong. The flow stress in nanolayered structures can approach to within 1/3 of the theoretical shear strength of order $\mu/30$, where μ is the shear modulus (Embury and Han 1999). This possibility raises a host of technological and fundamental considerations related to the maximum strength that can be attained in materials? In principle, plastic flow can be confined to small volumes by controlling the strength and spacing of *engineered* dislocation obstacles at the nanoscale (Anderson et al. 1999, Kung and Foecke 1999). The high strength, and the length scale of the nanostructure itself may result in new considerations in crystal plasticity (Embury and Hirth 1994).

In an effort to experimentally explore material parameters that control the strength of nanolayered composites, Cu-Nb, Cu-Cr and Cu-Ni layered structures were produced by cold-working (Spitzig, Pelton and Laabs 1987), evaporation or sputtering (Misra et al. 1998). In addition, aspects of fcc/bcc duplex structure deformation have been recently considered (Sinclair, Embury and Weatherly 1999). The strength increase associated with reduction of the bi-layer thickness has been explained by a variety of possible mechanisms, including the Hall-Petch model of dislocation pile-ups at interfaces, the Koehler model of dislocation image interactions, and the Orowan model of single dislocation bow-out between layers. Considering single dislocation behavior, Embury and Hirth (Embury and Hirth 1994) attempted to derive the strength and deformation mechanism maps, allowing for dislocation-dislocation and dislocation-interface interactions. A number of material *design knobs* can be used to impart high strength and control plastic slip in nanolayered structures, including nanolayer height in single crystals, grain size in polycrystals, lattice and interface Peierls stress levels, interface structure, coherency strain level, misfit dislocation structure and spacing, geometry of plastic slip transmission by shear transfer, and the co-deformation of incompatible slip systems (e.g. fcc/bcc, fcc/hcp, & hcp/bcc).

Plastic deformation of nanolayer materials is influenced by the existence of large interfacial areas, as compared to bulk polycrystalline materials. The first set of factors that affect strength is structural in nature, where forces on dislocations vary across an interface. The variation can be a result of: (1) lattice constant mismatch that generates coherency strains; (2) misfit interfacial dislocations in semi-coherent and incoherent interfaces; (3) stacking fault energy changes in incoming and outgoing slip planes; (4) slip system mismatch that forces cross-slip of screw dislocations across the interface; (5) and the effects of dislocation core spreading into the interface (Clemens et al. 1999, Anderson and Li 2001, Rao and Hazzledine 2000). The second factor is the mismatch across the interface of elastic properties (constants), which reflect changes in the strength of atomic forces as dislocations cross from one material to another. This *image force* effect places additional opposing forces as dislocations cross an interface, and is known as the *Koehler barrier* (see, for example Rao & Hazzledine (Rao and Hazzledine 2000)). Although the strength of nanolayer materials is dominated by the influence of interfacial image forces on dislocation motion (Clemens et al. 1999, Rao and Hazzledine 2000, Anderson and Li 2001), current theoretical estimates of image forces on dislocations often rely on approximate methods of analysis based on isotropic, infinitely extended materials. Accurate determination of nanolayer strength and plasticity require rigorous development of dislocation theory in layered media. The purpose of the present investigation is to establish a systematic theoretical and computational approach for 3-dimensional dislocation motion in anisotropic, nanolayer materials. Subsequently, we use the approach to calculate the strength of nano-layered materials.

The methodology of Dislocation Dynamics (DD) has been recently developed to describe plasticity on the basis of direct numerical simulations of the collective motion of dislocation ensembles, with successful applications to deformation problems at the nano- and micro-scales (e.g. (Kubin et al. 1992, Zbib et al. 1998, Schwarz 1999, Ghoniem et al. 2000a)). However, the majority of these approaches treat bulk materials, with a few investigations that treat free surfaces or strained layers (Schwarz 1999, Khraishi et al. 2001, Martinez and Ghoniem 2002, Weigrand et al. 2002) . In nanolayer materials that contain many interfaces, most of the present methods would either result in low accuracy, or have limitations on their applicability. Existing methods for dealing with dislocations near free surfaces or interfaces may be classified into a number of categories, as follows:

1. *The superposition method*, where regular solutions obtained by numerical methods (e.g. the finite element, boundary element (Weigrand et al. 2002, Martinez and Ghoniem 2002), or the Boussinesq point force solution on a free surface (Verdier et al. 1998)) are superposed on singular solutions for dislocations in infinite media to satisfy traction equilibrium at the free surface;

2. *Approximation methods*, based on Lothe's solution (Lothe et al. 1982), or by assuming that interfaces are rigid (Von Blanckenhagen et al. 2001);

3. *The surface dislocation method*, where a surface dislocation loop distribution is determined so as to satisfy interfacial or free surface traction conditions at collocation points (Khraishi et al. 2001);

4. *Elasticity methods*, based on solutions of a dislocation segment near a free surface (Gosling and Willis 1994, Fivel et al. 1996).

The approaches described above have limitations, either because they are restricted to the simple case of a planar free surface, or that they lack sufficient numerical resolution of the elastic field near interfaces and surfaces. For nanolayer materials, the density of interface area is high, and dislocations are expected to interact with many interfaces. It is desirable, therefore, to extend the methods of 3-dimensional DD that have been successfully developed for bulk materials, to treat nanolayer materials. However, solutions for the elastic field of 3D dislocations near free surfaces or interfaces are very few (e.g. see references (Bacon and Groves 1970, Salamon and Dundurs 1971, Comniou and Dundurs 1975, Lothe et al. 1982, Gosling and Willis 1994)), while solutions for the field of 3-D arbitrary shape dislocations in anisotropic multilayers are not available.

We first develop here a method for calculating the elastic field of an arbitrary 3D dislocation loop in a general multi-layered material. Theoretically, such an elastic field can be calculated through a surface integral (Mura 1968, Salamon and Dundurs 1971, Han and Ghoniem 2004), assuming that the Green's functions are known. It is desirable to determine the elastic field as a line integral so that faster computations can be performed, and at the same time allow the procedure to be incorporated into DD algorithms. For a dislocation in an infinite homogeneous medium, the stress field can be expressed as a line integral along the dislocation loop (Mura 1987). In addition to the special case of a dislocation loop in a homogeneous infinite space, a line integral representation of the elastic field due to a general dislocation loop is available only for an isotropic half-space (Gosling and Willis 1994).

In Section 9.3.4, we develop the essential formulas that govern the elastic field of an infinitesimal dislocation segment in an anisotropic multi-layered material by using the 2D Fourier transformation method. The elastic field of a general dislocation loop of arbitrary geometry is then evaluated through a line integral along the dislocation loop. Computational procedures are obtained for an anisotropic half-space, two half spaces, and for a multilayered material in Section 9.3.4, and the results are incorporated into line integrals for 3D dislocations of arbitrary shape in Section 9.3.5. Dislocation motion in multi-layered thin films is then investigated in Section 9.3.7 for incorporation into 3D dislocation dynamics computer simulations. The influence of elastic property mismatches on dislocation motion and interaction forces is finally discussed in section 9.5.5.

9.3.4 Basic Equations for Anisotropic Nanolayers

For a 3D dislocation loop of general geometry, the displacement vector can be expressed as (Mura 1968)

$$u_i(\mathbf{x}) = -\int_S C_{jlmn} b_m \frac{\partial}{\partial x'_l} G_{ji}(\mathbf{x}', \mathbf{x}) n_n(\mathbf{x}') \mathrm{d}S(\mathbf{x}') \tag{9.13}$$

where C_{jlmn} are the elastic moduli, $G_{ji}(\mathbf{x}', \mathbf{x})$ are the Green's functions at $\mathbf{x}'$ due to a point force applied at $\mathbf{x}$, S is an arbitrary surface capping the loop, n_n is a unit normal to S and b_m

is the Burgers vector.

The surface integral in Equation (9.13) is valid for a dislocation loop in either homogeneous or inhomogeneous materials, assuming that the elastic Greens functions for a particular geometry and elastic anisotropy are known. There are two main difficulties in using Equation (9.13). First, evaluation of surface integrals for dislocation loops of complex 3D geometry can be computationally demanding and intensive (Han and Ghoniem 2004). Second, elastic Greens functions are not explicitly known for inhomogeneous anisotropic materials.

For a dislocation loop in an infinite homogeneous space, the displacement gradient tensor can be reduced to a line integral along the dislocation as (Mura 1968, Mura 1987):

$$u_{i,j}(\mathbf{x})^{\infty} = \oint_L \beta^{\infty}_{jih}(\mathbf{x}-\mathbf{x}')\mathrm{d}l_h(\mathbf{x}') \tag{9.14}$$

where

$$\beta^{\infty}_{jih}(\mathbf{x}-\mathbf{x}') = C_{klmn}b_m\epsilon_{jnh}G^{\infty}_{ik,l}(\mathbf{x}-\mathbf{x}') \tag{9.15}$$

and L and $\mathrm{d}l_h$ are the dislocation line and line element, respectively. The superscript ∞ represents quantities in an infinite space, $f_{,l} = \partial f/\partial x_l$, and ϵ_{jnh} is the usual permutation tensor.

The stress field produced by the dislocation can then be expressed as:

$$\sigma_{ij}(\mathbf{x})^{\infty} = \oint_L S^{\infty}_{ijh}(\mathbf{x}-\mathbf{x}')\mathrm{d}l_h(\mathbf{x}') \tag{9.16}$$

where

$$S^{\infty}_{ijh}(\mathbf{x}-\mathbf{x}') = C_{ijkl}C_{pqmn}\epsilon_{lnh}b_m G^{\infty}_{kp,q}(\mathbf{x}-\mathbf{x}') \tag{9.17}$$

The kernel $S^{\infty}_{ijh}(\mathbf{x}-\mathbf{x}')$ in Equation (9.17) can be considered as the ij-stress component at $\mathbf{x}$ produced by a line element of dislocation lying in the h-direction at $\mathbf{x}'$, with Burgers vector $\mathbf{b}$ in an infinite space. While $\beta^{\infty}_{jih}(\mathbf{x}-\mathbf{x}')$ in Equation (9.15) can be considered as the corresponding displacement gradient.

For a finite space, the field produced by the elemental dislocation source in an infinite space is not guaranteed to satisfy prescribed boundary conditions. We therefore need to add a complementary solution (denoted as $S^{C}_{ijh}(\mathbf{x},\mathbf{x}')$ or $\beta^{C}_{jih}(\mathbf{x},\mathbf{x}')$) to the infinite medium solution ($S^{\infty}_{ijh}(\mathbf{x}-\mathbf{x}')$ or $\beta^{\infty}_{jih}(\mathbf{x}-\mathbf{x}')$), such that all boundary conditions can be satisfied. For example, on a free surface at $x_3 = 0$, we should have: $[S^{\infty}_{ijh}(\mathbf{x}-\mathbf{x}')+S^{C}_{ijh}(\mathbf{x},\mathbf{x}')]\,|_{x_3=0} = 0$. If a complementary solution (with a superscript C) can be obtained, then the elastic field due to a dislocation loop in the corresponding finite space can be evaluated through the line integral:

$$u_{i,j}(\mathbf{x}) = \oint_L \left[\beta^{\infty}_{jih}(\mathbf{x}-\mathbf{x}') + \beta^{C}_{jih}(\mathbf{x},\mathbf{x}')\right]\mathrm{d}l_h(\mathbf{x}') \tag{9.18}$$

$$\sigma_{ij}(\mathbf{x}) = \oint_L \left[S^{\infty}_{ijh}(\mathbf{x}-\mathbf{x}') + S^{C}_{ijh}(\mathbf{x},\mathbf{x}')\right]\mathrm{d}l_h(\mathbf{x}') \tag{9.19}$$

The first terms in Equations (9.18) and (9.19) are known infinite space solutions, and contain well-understood singularities. The second (complementary) terms, however, are regular, and need to be determined according to interface and boundary conditions. Now, assume that the displacement field of the complementary kernel is u^C_{kh}. The stress field it produces is then: $S^C_{ijh}(\mathbf{x},\mathbf{x}') = C_{ijkl}u^C_{kh,l}(\mathbf{x},\mathbf{x}')$, and the corresponding equilibrium equation is given by:

$$C_{ijkl}(\mathbf{x})u^C_{kh,lj}(\mathbf{x},\mathbf{x}') = 0 \tag{9.20}$$

For a layered medium, the general solution can be obtained by a Fourier transform with respect to the in-plane coordinates (x_1, x_2) as

$$\tilde{\mathbf{u}}(\xi_1,\xi_2,x_3;x_3') = \int_0^\infty\int_0^\infty \mathbf{u}(\mathbf{x};(0,0,x_3'))e^{\mathbf{i}\xi_\alpha x_\alpha}\mathrm{d}x_1\mathrm{d}x_2 \tag{9.21}$$

The equilibrium equation then becomes:

$$C_{i3k3}\tilde{u}^C_{kh,33} - \mathbf{i}(C_{i\alpha k3}+C_{i3k\alpha})\xi_\alpha\tilde{u}^C_{kh,3} - C_{i\alpha k\beta}\xi_\alpha\xi_\beta\tilde{u}^C_{kh} = 0 \tag{9.22}$$

where the Greek subscript α=1 or 2, whereas Roman subscripts range over 1,2,3.

The general solution of Equation (9.22) can be expressed in a compact form as (Yang and Pan 2002a):

$$\tilde{\mathbf{u}}^C(\xi_1,\xi_2,x_3;x_3') = \mathbf{i}\eta^{-1}(\bar{\mathbf{A}} < e^{-\mathbf{i}\bar{\mathbf{p}}\eta x_3} > \mathbf{V} + \mathbf{A} < e^{-\mathbf{i}\mathbf{p}\eta x_3} > \mathbf{W}) \tag{9.23}$$

where (η,θ) are the polar coordinates of (ξ_1,ξ_2) ($\xi_1 = \eta\cos\theta$, $\xi_2 = \eta\sin\theta$), $\mathbf{V}$ and $\mathbf{W}$ are unknown functions (of η, θ and x_3'), $< e^{-\mathbf{i}\mathbf{p}\eta x_3} >= \mathrm{diag}[e^{-\mathbf{i}p_1\eta x_3}, e^{-\mathbf{i}p_2\eta x_3}, e^{-\mathbf{i}p_3\eta x_3}]$. p_i ($\mathrm{Im}p_i > 0$) and $\mathbf{A} = (\mathbf{a}_1,\mathbf{a}_2,\mathbf{a}_3)$ are the eigenvalues and eigen-matrix of the generalized Stroh eigen-problem (Ting 1996):

$$[\mathbf{Q} + p_i\mathbf{R} + \mathbf{R}^T) + p_i^2\mathbf{T}]\mathbf{a}_i = 0 \tag{9.24}$$

$$Q_{ik} = C_{ijks}n_jn_s,\ R_{ik} = C_{ijks}n_jm_s,\ T_{ik} = C_{ijks}m_jm_s$$

with $\mathbf{n} = [\cos\theta,\sin\theta,0]^T$ and $\mathbf{m} = [0,0,1]^T$.

The displacement gradient for the complementary solution is:

$$\tilde{\mathbf{u}}^C_{,\alpha}(\xi_1,\xi_2,x_3;x_3') = n_\alpha(\bar{\mathbf{A}} < e^{-\mathbf{i}\bar{\mathbf{p}}\eta x_3} > \mathbf{V} + \mathbf{A} < e^{-\mathbf{i}\mathbf{p}\eta x_3} > \mathbf{W}) \tag{9.25}$$

The induced stress field will then be: $S^C_{ijh}(\mathbf{x},\mathbf{x}') = C_{ijkl}u^C_{kh,l}(\mathbf{x},\mathbf{x}')$. We will separate the field into two contributions: (1) out-of-plane stresses $\mathbf{t} = (S_{13h}, S_{23h}, S_{33h})$, and (2) in-plane stresses $\mathbf{s} = (S_{11h}, S_{12h}, S_{22h})$. In the transformed domain, these can be expressed as (Yang and Pan 2002a):

$$\tilde{\mathbf{t}}^C(\xi_1,\xi_2,x_3;x_3') = \bar{\mathbf{B}} < e^{-\mathbf{i}\bar{\mathbf{p}}\eta x_3} > \mathbf{V} + \mathbf{B} < e^{-\mathbf{i}\mathbf{p}\eta x_3} > \mathbf{W} \tag{9.26}$$

$$\tilde{\mathbf{s}}^C(\xi_1,\xi_2,x_3;x_3') = \bar{\mathbf{C}} < e^{-\mathbf{i}\bar{\mathbf{p}}\eta x_3} > \mathbf{V} + \mathbf{C} < e^{-\mathbf{i}\mathbf{p}\eta x_3} > \mathbf{W} \tag{9.27}$$

The matrices $\mathbf{B} = (\mathbf{b}_1, \mathbf{b}_2, \mathbf{b}_3)$ and $\mathbf{C} = (\mathbf{c}_1, \mathbf{c}_2, \mathbf{c}_3)$ are related to the Stroh eigen-matrix $\mathbf{A}$ as

$$\mathbf{b}_i = (\mathbf{R}^T + p_i\mathbf{T})\mathbf{a}_i, \qquad \mathbf{c}_i = \mathbf{D}_i\mathbf{a}_i \tag{9.28}$$

with $$D_{kli} = C_{1kl\alpha}n_\alpha + p_iC_{1kl3} \text{ for } k = 1, 2, \text{ and } D_{3li} = C_{22l\alpha}n_\alpha + p_iC_{22l3}.$$

Note that for a half space $x_3 \leq 0$, $V = 0$, while for $x_3 \geq 0$, $W = 0$.

In order to impose the appropriate boundary conditions for layered materials, the transformed Green's tensor in an infinite space is needed. This is given by:

$$\tilde{G}^\infty(\xi_1, \xi_2, x_3; x_3') = \mathbf{i}\eta^{-1} \begin{cases} \mathbf{A} < e^{-\mathbf{i}\mathbf{p}\eta(x_3 - x_3')} > \mathbf{A}^T, & x_3 < x_3' \\ -\bar{\mathbf{A}} < e^{-\mathbf{i}\bar{\mathbf{p}}\eta(x_3 - x_3')} > \bar{\mathbf{A}}^T, & x_3 > x_3' \end{cases} \tag{9.29}$$

Elastic Fields of Dislocations

We determine here the complementary terms necessary for obtaining full solutions for dislocation loops in half-space, bi-materials, and in general anisotropic layered media.

Dislocation in an Anisotropic Half-Space

Let's assume that a dislocation loop is situated in an anisotropic half-space, occupying $x_3 \leq 0$ and having a free surface on $x_3 = 0$. The surface equilibrium boundary condition is expressed as:

$$[S^C_{i3h}(\mathbf{x}, \mathbf{x}') + S^\infty_{i3h}(\mathbf{x} - \mathbf{x}')] \,|_{x_3=0} = 0 \tag{9.30}$$

In the transformed domain, we have:

$$\tilde{S}^C_{i3h}(\mathbf{x}, \mathbf{x}')|_{x_3=0} = \tilde{t}^C_{ih}|_{x_3=0} = \mathbf{BW} \,, \tag{9.31}$$

$$\begin{aligned} \tilde{S}^\infty_{i3h}(\mathbf{x} - \mathbf{x}') &= C_{i3kl}C_{pqmn}\epsilon_{lnh}b_m\tilde{G}^\infty_{kp,q}(\mathbf{x} - \mathbf{x}') \\ &= -\mathbf{i}\xi_\alpha C_{i3kl}C_{p\alpha mn}\epsilon_{lnh}b_m\tilde{G}^\infty_{kp} + C_{i3kl}C_{p3mn}\epsilon_{lnh}b_m\tilde{G}^\infty_{kp,3} \,. \end{aligned} \tag{9.32}$$

Substituting (9.29) (for $x_3' < x_3 \leq 0$) into (9.32), we obtain:

$$\tilde{S}^\infty_{i3h} \,|_{x_3=0} = \lambda_{ikhpq}\left[n_q(-\bar{\mathbf{A}} < e^{\mathbf{i}\bar{\mathbf{p}}\eta x_3'} > \bar{\mathbf{A}}^T)_{kp} + m_q(-\bar{\mathbf{A}} < e^{\mathbf{i}\bar{\mathbf{p}}\eta x_3'} >< \bar{\mathbf{p}} > \bar{\mathbf{A}}^T)_{kp}\right] \tag{9.33}$$

where $\lambda_{ikhpq} = C_{i3kl}C_{pqmn}\epsilon_{lnh}b_m$.

Substituting (9.31) and (9.33) into the free traction surface boundary condition (in the transformed domain): $\tilde{S}^C_{i3h}(\mathbf{x}, \mathbf{x}')|_{x_3=0} + \tilde{S}^\infty_{i3h}|_{x_3=0} = 0$, we get:

$$\mathbf{W} = \mathbf{B}^{-1}\lambda_{ikhpq}\left[n_q(\bar{\mathbf{A}} < e^{\mathbf{i}\bar{\mathbf{p}}\eta x_3'} > \bar{\mathbf{A}}^T)_{kp} + m_q(\bar{\mathbf{A}} < e^{\mathbf{i}\bar{\mathbf{p}}\eta x_3'} >< \bar{\mathbf{p}} > \bar{\mathbf{A}}^T)_{kp}\right] \tag{9.34}$$

The unknown coefficient $\mathbf{W}$ in the complementary solution is thus determined. Substituting (9.34) into Equations (9.23), (9.26) and (9.27) determines the complementary parts of the

displacement vector and stress tensor. These are complex explicit expressions, but can be written in the following forms:

$$\tilde{\mathbf{u}}^C = \mathbf{i}\eta^{-1}\mathbf{J_2} < e^{-\mathbf{i}\mathbf{r_1}\eta} > \mathbf{J_1} < e^{-\mathbf{i}\mathbf{r_0}\eta} > \mathbf{J_0} \tag{9.35}$$

for the displacement vector, and

$$\tilde{\mathbf{t}}^C = \mathbf{J_2} < e^{-\mathbf{i}\mathbf{r_1}\eta} > \mathbf{J_1} < e^{-\mathbf{i}\mathbf{r_0}\eta} > \mathbf{J_0} \tag{9.36}$$

for the traction tensor. The same expression is also obtained for the in-plane tensor $\tilde{\mathbf{s}}$. In Equations (9.35) and (9.36), the tensors $\mathbf{J_n}(\theta)$ and $\mathbf{r_n}(\theta)$ are independent of η, but are functions of θ. These solutions are in the transformed domain, and need to be transformed back to the physical domain by the inverse Fourier Transform:

$$f(x_1 - x_1', x_2 - x_2', x_3, x_3') = \frac{1}{(2\pi)^2}\int_0^\infty\int_0^{2\pi} \eta\tilde{f}(\eta, \theta, x_3, x_3')e^{-\mathbf{i}\eta[(x_1-x_1')\cos\theta+(x_2-x_2')\sin\theta)]}\mathrm{d}\theta\mathrm{d}\eta. \tag{9.37}$$

Carrying out the first integral over $(0 < \eta < \infty)$, the 2-D inverse transformation is reduced to a 1-D integral (Yang and Pan 2002a). The reduced integrals for the elastic fields are given by:

$$u_{ih}^C = \frac{1}{(2\pi)^2}\oint_0^{2\pi}\frac{H_{ih}}{s}\mathrm{d}\theta\ , \tag{9.38}$$

$$t_{ih}^C = -\frac{1}{(2\pi)^2}\oint_0^{2\pi}\frac{H_{ih}}{s^2}\mathrm{d}\theta\ , \tag{9.39}$$

with $H_{ih} = (J_{k_2})_2(J_{k_2k_1})_1(J_{k_1})_0$, and $s = (r_{k_2})_1 + (r_{k_1})_0 + (x_1 - x_1')\cos\theta + (x_2 - x_2')\sin\theta$. Note that s_{ih} has the same expression as that of t_{ih}, and that all these functions have their own H_{ih} (different from each other), but share the same s. Explicit expressions are given in Appendix **??**. Thus, the complementary parts of the elastic field of a dislocation in a half-space can be evaluated by line integrals over the interval $[0, 2\pi]$. The complementary parts plus the infinite-space solutions are the total elastic fields due to an infinitesimal dislocation segment, and the elastic field due to a dislocation loop is obtained through the line integrals (9.18) and (9.19).

Dislocation in Perfectly-Bonded, Anisotropic Two Half-spaces

Consider an anisotropic bi-material full space, where the lower half-space ($x_3 < 0$) is occupied by material (0), the upper half-space ($x_3 > 0$) by material (1), and quantities in them are denoted by the corresponding superscripts (0) and (1), respectively. Suppose now that the interface (at $x_3 = 0$) is perfectly bonded. This requires the continuity of the displacement and traction vectors across the interface, i.e.

$$\mathbf{u}^{(0)}|_{x_3=0^-} = \mathbf{u}^{(1)}|_{x_3=0^+} \qquad \mathbf{t}^{(0)}|_{x_3=0^-} = \mathbf{t}^{(1)}|_{x_3=0^+} \tag{9.40}$$

Instead of the displacement continuity condition (9.40), however, we will use an equivalent condition on the tangential displacement gradient, given by (Hill 1961):

$$\mathbf{u}^{(0)}_{,\alpha}|_{x_3=0^-} = \mathbf{u}^{(1)}_{,\alpha}|_{x_3=0^+} \tag{9.41}$$

Here, $\alpha = 1$ or 2, $\mathbf{u}_{,\alpha}$ is the in-plane component of the displacement gradient (or called tangential distortion).

Without loss of generality, we assume that we have an infinitesimal dislocation segment, located in material (0). We express the solution for the displacement gradient in material (0) as:

$$\tilde{\mathbf{u}}^{(0)}_{,j} = \tilde{\mathbf{u}}^{(0)\infty}_{,j} + \tilde{\mathbf{u}}^{(0)C}_{,j} = \tilde{\beta}^{(0)\infty}_{jih} + n_j \mathbf{A}^{(0)} < e^{-\mathbf{i}\mathbf{p}^{(0)}\eta x_3} > \mathbf{W} \tag{9.42}$$

The first term $\tilde{\mathbf{u}}^{(0)\infty}_{,j}$ corresponds to the homogeneous full-space solution, which is known from Equation (9.15), with the elastic properties of material (0). The second term corresponds to the complementary solution due to the interface. Correspondingly, the stress field is also separated into two components, and the traction vector can be expressed as:

$$\tilde{\mathbf{t}}^{(0)} = \tilde{\mathbf{t}}^{(0)\infty} + \tilde{\mathbf{t}}^{(0)C} = \tilde{S}^{(0)\infty}_{i3h} + \mathbf{B}^{(0)} < e^{-\mathbf{i}\mathbf{p}^{(0)}\eta x_3} > \mathbf{W} \tag{9.43}$$

where $S^{(0)\infty}_{i3h}$ is known from Equation (9.17), with the elastic properties of material (0).

Likewise, the solutions in material (1) due to the infinitesimal dislocation segment in material (0) can also be separated. Thus, the displacement gradient in material (1) is expressed as:

$$\tilde{\mathbf{u}}^{(1)}_{,j} = \tilde{\mathbf{u}}^{(0)\infty}_{,j} + \tilde{\mathbf{u}}^{(1)C}_{,j} = \tilde{\beta}^{(0)\infty}_{jih} + n_j \bar{\mathbf{A}}^{(1)} < e^{-\mathbf{i}\bar{\mathbf{p}}^{(1)}\eta x_3} > \mathbf{V} \tag{9.44}$$

The first term $\tilde{\mathbf{u}}^{(0)\infty}_{,j}$ is the known full-space solution, with the elastic properties of material (0), while the second term is the complementary solution (which is to be determined). The stress field in material (1) can be derived from $\tilde{\mathbf{u}}^{(1)}_{,j}$, giving the traction field as:

$$\tilde{\mathbf{t}}^{(1)} = \tilde{\mathbf{t}}^{(1)\infty} + \tilde{\mathbf{t}}^{(1)C} = \tilde{S}^{(1)\infty}_{i3h} + \bar{\mathbf{B}}^{(1)} < e^{-\mathbf{i}\bar{\mathbf{p}}^{(0)}\eta x_3} > \mathbf{V} \tag{9.45}$$

with

$$S^{(1)\infty}_{i3h} = C^{(1)}_{ijkl} C^{(0)}_{pqmn} \epsilon_{lnh} b_m G^{(0)\infty}_{kp,q}(\mathbf{x} - \mathbf{x}') \tag{9.46}$$

as the traction field in full-space material (1) due to the displacement field $\tilde{\mathbf{u}}^{(0)}$.

Substituting Equations (9.42)-(9.46) into the interface conditions, we have:

$$\mathbf{B^{(0)}}\mathbf{W} + \tilde{S}^{(0)\infty}_{i3h}|_{x_3=0} = \bar{\mathbf{B}}^{(\mathbf{1})}\mathbf{V} + \tilde{S}^{(1)\infty}_{i3h}|_{x_3=0} \tag{9.47}$$

$$n_\alpha \mathbf{A^{(0)}}\mathbf{W} + \tilde{\beta}^{(0)\infty}_{\alpha ih}|_{x_3=0} = n_\alpha \bar{\mathbf{A}}^{(\mathbf{1})}\mathbf{V} + \tilde{\beta}^{(0)\infty}_{\alpha ih}|_{x_3=0} \tag{9.48}$$

Finally, the full solution is obtained as:

$$\mathbf{W} = -(\bar{\mathbf{B}}^{(1)}\bar{\mathbf{A}}^{(1)-1}\mathbf{A}^{(0)} - \mathbf{B}^{(0)})^{-1}\Delta\tilde{S}^{\infty}_{i3h}, \quad \mathbf{V} = (\mathbf{B}^{(0)}\mathbf{A}^{(0)-1}\bar{\mathbf{A}}^{(1)} - \bar{\mathbf{B}}^{(1)})^{-1}\Delta\tilde{S}^{\infty}_{i3h} \tag{9.49}$$

with

$$\Delta\tilde{S}^{\infty}_{i3h} = \tilde{S}^{(1)\infty}_{i3h}|_{x_3=0} - \tilde{S}^{(0)\infty}_{i3h}|_{x_3=0} = (C^{(1)}_{ijkl} - C^{(0)}_{ijkl})C^{(0)}_{pqmn}\epsilon_{lnh}b_m\tilde{G}^{(0)\infty}_{kp,q}(\mathbf{x}-\mathbf{x}')|_{x_3=0},$$
$$\tilde{G}^{(0)\infty}_{kp,q}|_{x_3=0} = -n_q(\bar{\mathbf{A}}^{(0)} < e^{\mathbf{i}\bar{\mathbf{p}}^{(0)}\eta x'_3} > \bar{\mathbf{A}}^{(0)T})_{kp} - m_q(\bar{\mathbf{A}}^{(0)} < e^{\mathbf{i}\bar{\mathbf{p}}^{(0)}\eta x'_3} >< \bar{\mathbf{p}}^{(0)} > \bar{\mathbf{A}}^{(0)T})_{kp} \tag{9.50}$$

The displacement and stress (including displacement distortion) solutions have the same forms as Equations (9.35) and (9.36), respectively, and all real fields are obtained by 1D integrals, as in Equations (9.38) and (9.39).

Dislocation in an Anisotropic Multi-layer Material

Consider a laterally infinite composite thin film made of different layers. Each layer is homogenous, anisotropic and of uniform thickness. Interfaces between layers are assumed to be perfectly bonded. A coordinate system (x_1, x_2, x_3) is attached to the the thin film, with the x_3-axis perpendicular to all interfaces. A general layer n occupies the space $z_{n-1} \le x_3 \le z_n$, and quantities with its properties are denoted by corresponding superscripts (n). Assume now that an infinitesimal dislocation segment is located in layer k. The displacement gradient in layer n can be expressed as:

$$\tilde{\mathbf{u}}^{(n)}_{,j} = \tilde{\beta}^{(k)\infty}_{jih} + n_j[\bar{\mathbf{A}}^{(n)} < e^{-\mathbf{i}\bar{\mathbf{p}}^{(n)}\eta(x_3-z_{n-1})} > \mathbf{V}^{(n)} + \mathbf{A}^{(n)} < e^{-\mathbf{i}\mathbf{p}^{(n)}\eta(x_3-z_n)} > \mathbf{W}^{(n)}] \tag{9.51}$$

The first term is the full-space solution, given by Equation (9.15), with the elastic properties of material k. The other terms correspond to the complementary part of the solution. Accordingly, the out-of-plane traction vector is given by:

$$\tilde{\mathbf{t}}^{(n)} = \tilde{S}^{(n)\infty}_{i3h} + [\bar{\mathbf{B}}^{(n)} < e^{-\mathbf{i}\bar{\mathbf{p}}^{(n)}\eta(x_3-z_{n-1})} > \mathbf{V}^{(n)} + \mathbf{B}^{(n)} < e^{-\mathbf{i}\mathbf{p}^{(n)}\eta(x_3-z_n)} > \mathbf{W}^{(n)}] \tag{9.52}$$

with $S^{(n)\infty}_{i3h} = C^{(n)}_{ijkl}C^{(k)}_{pqmn}\epsilon_{lnh}b_m G^{(k)\infty}_{kp,q}(\mathbf{x}-\mathbf{x}')$, and the solution for the in-plane traction $\tilde{\mathbf{s}}^{(n)}$ is similar to that given by (9.52).

Perfectly bonded conditions along interfaces require that the traction and displacement (or tangential distortion) vectors are continuous. For interface n, this gives:

$$\begin{aligned}\bar{\mathbf{B}}^{(n)} < e^{-\mathbf{i}\bar{\mathbf{p}}^{(n)}\eta(z_n-z_{n-1})} > \mathbf{V}^{(n)} + \mathbf{B}^{(n)}\mathbf{W}^{(n)} + \tilde{S}^{(n)\infty}_{i3h}|_{x_3=0} \\ = \bar{\mathbf{B}}^{(n+1)}\mathbf{V}^{(n+1)} + \mathbf{B}^{(n+1)} < e^{-\mathbf{i}\mathbf{p}^{(n+1)}\eta(z_n-z_{n+1})} > \mathbf{W}^{(n+1)} + \tilde{S}^{(n+1)\infty}_{i3h}|_{x_3=0}\end{aligned} \tag{9.53}$$

$$\begin{aligned}\bar{\mathbf{A}}^{(n)} < e^{-\mathbf{i}\bar{\mathbf{p}}^{(n)}\eta(z_n-z_{n-1})} > \mathbf{V}^{(n)} + \mathbf{A}^{(n)}\mathbf{W}^{(n)} \ , \\ = \bar{\mathbf{A}}^{(n+1)}\mathbf{V}^{(n+1)} + \mathbf{A}^{(n+1)} < e^{-\mathbf{i}\mathbf{p}^{(n+1)}\eta(z_n-z_{n+1})} > \mathbf{W}^{(n+1)}\end{aligned} \tag{9.54}$$

With all interface, bottom and top layer (half-space or free surface) boundary conditions, a system of algebraic equations can be formed. Solving these equations, the elastic field is fully determined.

9.3.5 Peach-Koehler Forces in Layered Materials

Dislocation Loop Near an Interface

We give here an example of a 3-D dislocation loop of a simple circular geometry to verify the present line integral method, and to illustrate the main characteristics of dislocation fields near interfaces.

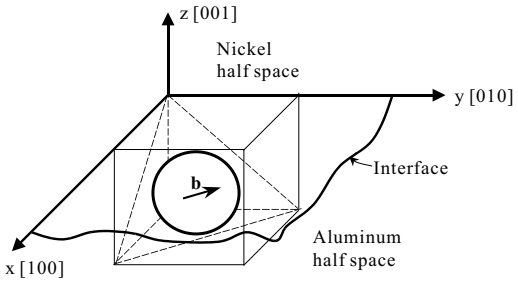

Figure 9.51: Schematic for the geometry of a 3-D circular dislocation loop near an interface or free surface

Consider a circular dislocation loop in a half-space substrate. The loop lies near a free surface or an interface, as shown in Figure (9.51). To be specific, we take the substrate material, which extends for all $z < 0$, to be an anisotropic aluminium crystal. The aluminum substrate is bound by a free surface or is perfectly bonded with an anisotropic nickel half-space along the surface $z = 0$. Both Al and Ni are fcc cubic anisotropic crystals, with their crystallographic axes [100],[010], and [001] lined up along the $x = 1$, $y = 2$, and $z = 3$ coordinate axes, respectively. The elastic constants needed for the present calculations are obtained from reference ((Hirth and Lothe 1982)). The circular dislocation loop lies on the (111) plane, its Burger's vector **b** is taken along the $[\bar{1}10]$ direction. The loop radius, R=200 b, and its center is located at z=-180 b, where b=$|\mathbf{b}|$ is the magnitude of the Burgers vector of aluminum. For verification of the present line integral results, we show in Figure (9.52) the results of stress field components for infinite space and the exact surface integral solutions. Calculations of surface integral, with Equation (9.13) as the starting point are performed using an evaluation of Green's functions and their derivatives in the corresponding materials (Han and Ghoniem 2004). We follow the procedure of Pan and coworkers for the numerical determination of Green's functions in anisotropic bi-materials and multilayered materials (Pan and Yuan 1999, Yang and Pan 2002b). Stress components along the z-axis, induced by the dislocation loop, are shown in Figure (9.52-a) for the case of free surface, and Figure (9.52-b) for the interface case. Because of symmetry, $\sigma_{11} = -\sigma_{22}$, $\sigma_{13} = -\sigma_{23}$, $\sigma_{12} = \sigma_{33} = 0$, and thus we only show the stress components σ_{22} and σ_{23}. It can be observed from the figures that the numerical results of the present line integral method are nearly identical to those obtained by the surface integration method (Han and Ghoniem 2004) for the case of a dislocation in half-space, and are in good agreement when

the dislocation loop is near the interface. As the dislocation loop approaches the free surface, the out-of-plane stress components are forced to decrease till they become identically zero at the surface. However, in-plane stresses increase in order to satisfy overall equilibrium. When the aluminum substrate is bonded to a harder half-space (e.g. nickel), out-of-plane stresses are continuous across the interface, and larger than their corresponding values in infinite space. In-plane stress components, on the other hand, experience jumps because of the discontinuity in the elastic properties across the interface. The magnitude of stress increases across the interface, moving from the softer (aluminum) to the harder substrate (nickel).

In general, the stresses near a free surface are larger than their corresponding values near an interface to a harder material. The influence of the interface on the disturbance of the elastic field is somewhat local, and is limited to within a distance of a few hundred lattice constants from the free surface or an interface.

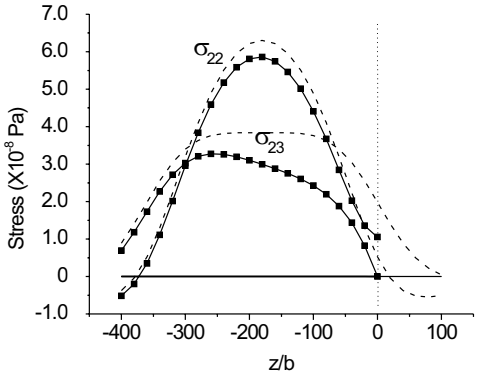

(a)

9.3.6 Dislocation-Interface Interaction

Dislocations move along the direction of the Peach-Koehler force exerted on them by the local elastic field, which of course includes image stresses due to interfaces in addition to applied and self-forces. The speed of the motion is controlled by the overall mobility, however, and that may include many contributions from interactions with electrons, phonons or other dispersed barriers. Complex DD simulations typically solve for the motion of interacting dislocation ensembles. In this section, we focus on understanding the influence of image forces due to interfaces or free surfaces on the magnitude and distribution of the Peach-Koehler force. This is given by: $\mathbf{f} = \boldsymbol{\sigma} \cdot \mathbf{b} \times d\mathbf{l}$, where the virtual force $\mathbf{f}$ is exerted on a line segment $d\mathbf{l}$ with the Burgers vector $\mathbf{b}$, and situated in the stress field $\boldsymbol{\sigma}$. The stress field may originate from various sources, such as applied forces, residual stresses, image stresses (due to boundary conditions), other dislocations, and even the dislocation loop itself (self-forces).

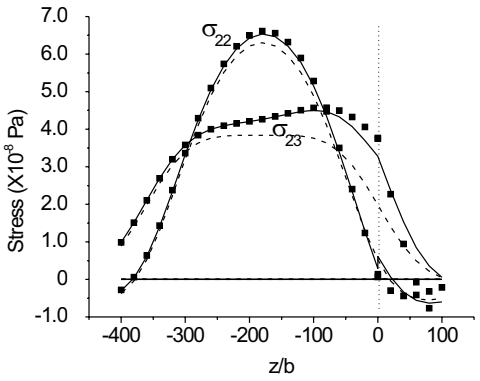

(b)

Figure 9.52: Stress components along the z-axis for a circular dislocation loop (see Figure (9.51)) in (a) Al half-space and (b) Al-Ni bi-material. Solid lines represent surface integral results, small square symbols: line integral results, and dashed lines: infinite space solutions.

When a dislocation resides in a finite medium, adjustments of the stress field to satisfy surface or interface boundary conditions result in local changes of the stress tensor close to the dislocation line. Thus, calculations of the self-force for this altered stress field, which requires integrals along the dislocation line, would also include the influence of the boundary adjustment. Thus, the self-force would subsume the image effects of the boundary, and would be geometry dependent. To remove such ambiguities, and to clearly determine the effects of the interface or boundary, the stress field induced by a dislocation is divided into two parts: the full-space stress $\boldsymbol{\sigma}^{\infty}$, and the image stress $\boldsymbol{\sigma}^{C}$. The stress $\boldsymbol{\sigma}^{\infty}$ corresponds to that induced by the dislocation in a homogeneous and infinite space, with elastic properties of the material where most of the dislocation resides. The stress field $\boldsymbol{\sigma}^{\infty}$ of a dislocation in an infinite anisotropic material can be calculated by the line integral given by Eq1uation (9.13), and will induce a *self-force* on the dislocation. Because of the singularity of $\boldsymbol{\sigma}^{\infty}$ along the dislocation line, an average field is obtained by the Brown procedure (Brown 1964), or alternatively through the Gavazza-Barnett limiting process (Gavazza and Barnett 1976). Details of the numerical procedure for the stress field and self-force of a dislocation loop in an infinite anisotropic material are found in our recent work (Han et al. 2002). The force induced by the complementary part of the stress field, $\boldsymbol{\sigma}^{C}$, which reflects the interface effect on modifying the infinite medium stress field of the dislocation, will be termed henceforth the *image force*, and is calculated directly by the Peach-Koehler formula.

We illustrate here the effects of free surfaces and interfaces on dislocation image forces for a typical dislocation configuration in an Al film, of width h, on a Cu substrate. The system will is modeled as a thin film that is perfectly bonded to a half-space. The Al film may have a

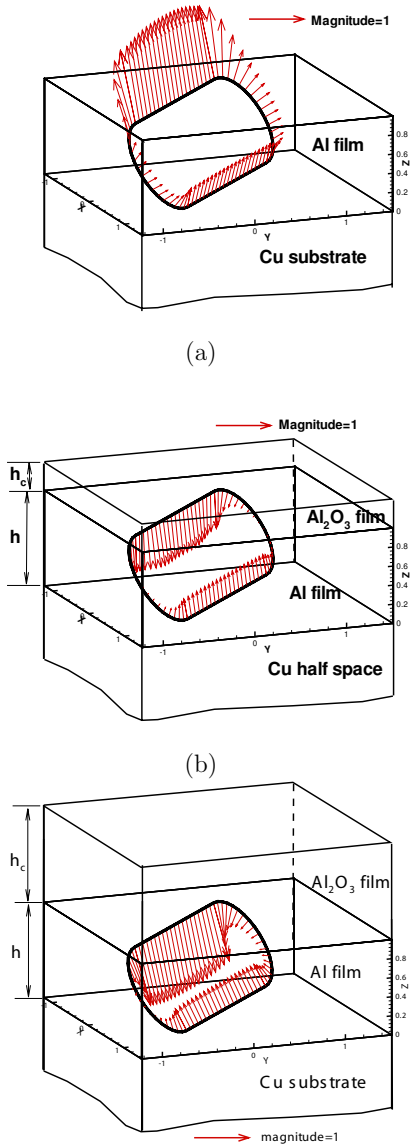

Figure 9.53: Image force distribution on an oblong dislocation loop in a thin Al layer on a Cu substrate with an additional aluminum oxide film on top (a) the layer is capped with an Al_2O_3 film of thickness h_c=0.1 h (b), and 1.0 h.

free surface (e.g. an un-oxidized film in vacuum), or is capped by a thin Al_2O_3 layer of width h_c. An oblong dislocation loop is located on the {111}-plane in the middle of the Al film, and has a Burgers vector of $\mathbf{b} = \frac{a}{2} < 1\bar{1}0 >$, and a is the lattice constant, as shown in Figure (9.53). The oblong loop is composed of two straight segments parallel to the interfaces, which typically result from interface image forces as will be shown later, and are connected by two half-circular segments. The length (straight section) and width of the oblong dislocation are L and D, respectively, with $L = 2D$ and $D = h$. The distribution of image forces on the loop is shown in Figures (9.53-a) through (9.53-c) for different thicknesses of the capped layer. The image force per unit length in these figures is normalized by $b^2 \times 10^{10}$ (Pa)/h.

The image force distribution on the straight dislocation segment closest to the free surface is attractive, as one expects. However, its magnitude and direction cannot be obtained through a simple geometric construction by reflecting the dislocation loop across the interface. It is seen from Figure (9.53-a) that the image force on the loop switches from attractive near the free surface to repulsive near the harder Cu substrate. When the Al film is capped by a harder oxide layer, the image force is found to have a strong dependence on the capping layer thickness, as long as it is less than the thickness of the thin film itself. Thus, for a thin film capped with several thinner layers, the image force would have major contributions from several neighboring interfaces. When the thickness of the capping layer is larger than the film thickness, as shown in Figure (9.53-c), the distribution of the image force tends to that generated by a semi-infinite medium. It is interesting to note that while the dislocation loop is attracted to the free surface, which would accelerate the formation of a surface step, it is repelled by the harder oxide film. A very thin oxide layer ($h_c = 0.1h$), as shown in Figure (9.53-b), almost balances the repulsive Cu interface forces on the middle curved sections of the loop rendering them force-free. This result cannot be expected from geometric image constructions as well.

9.3.7 Dislocation Dynamics in Layered Materials

A variational form of the governing equation of motion for a dislocation loop Γ has been developed for over-damped dislocation dynamics, where the work exerted on dislocation loop expansion is balanced by viscous dissipation (Ghoniem et al. 2000a), i.e. $\int_\Gamma (F_k^t - B_{\alpha k} V_\alpha) \delta r_k |\mathrm{d}\mathbf{s}| = 0$. Here, F_k^t is the total Peach-Koehler force induced by applied external forces, internal stress fields (such as dislocation interactions, interface image forces, and the self-force), $B_{\alpha k}$ is the resistance (inverse mobility) matrix, V_α is the velocity, r_k is the displacement of the dislocation line, and d$\mathbf{s}$ the dislocation line vector. Because the present formulation results in a line integral form of the force vector distribution, it can be readily incorporated into the PDD framework (Ghoniem et al. 2000a). In this section, we present computer simulation results for dislocation motion in nano-layered materials using the PDD methodology.

It has been experimentally established that the hardness (or strength) of multi-layer thin films is much higher than corresponding bulk materials. It is also shown by numerous experiments that the strength and hardness of the film increase as the thickness of constituent layers decreases (Shinn, Hultman and Barnett 1992, Misra et al. 1998, Clemens et al. 1999). Several underlying mechanisms have been proposed in recent years, although relying on approximate

treatments of dislocation fields in such systems. The objective here is to apply the present rigorous elasticity solutions for 3-D dislocation loops in anisotropic, multi-layer thin films to develop an understanding of plasticity and strength at the nano- to the micro-scale.

Experimental results and isotropic elasticity estimates show that the dominant mechanism that controls the strength and hardness of multi-layer thin films is the influence of the dislocation image force associated with a mismatch in elastic properties between adjacent film layers (Clemens et al. 1999). For layered materials with a large mismatch in elastic properties, a significant hardness enhancement was observed. On the other hand, for layered materials with small differences in their elastic properties, no measurable hardness enhancement was detected (Shinn et al. 1992, Clemens et al. 1999). Experiments on an Fe/Pt layered system (Daniels, Nix and Clemens 1995a, Daniels, Nix and Clemens 1995b) indicated that when the bilayer thickness ranges from few to tens of nano-meters, the hardness of this bilayer metal system exhibits a plateau. Over this bilayer period range, the interface structure, misfit dislocation density and coherency strains all change rapidly, so they are not likely to be the dominant mechanism. Hence, the mismatch in elastic moduli was concluded to be the most likely dominant factor determining hardness enhancements in these layered materials (Daniels et al. 1995a, Daniels et al. 1995b).

Two models are often used to explain the observed behavior of hardness (or flow stress) in thin films. In the threading dislocation model (Freund 1990, Nix 1998), the flow stress is determined by the energy balance between the threading glide dislocation segment and the misfit dislocation left behind at the interface. This model results in a flow stress that scales approximately with the inverse of the film/layer thickness. For a thin film/layer of thickness h, subjected to a uniform applied biaxial stress σ_a, the critical stress (σ_c^{th}) for threading dislocation motion is given by (Freund 1990)

$$\sigma_c^{th} \approx \frac{\mu b}{4\pi(1-\nu)h}[(4-\nu)\ln(h/r_0) - 1] \tag{9.55}$$

for an isotropic material with a shear modulus μ, Poisson's ration ν, and a dislocation core cut-off radius $r_0 \approx b$. In this model, interfaces are introduced as impenetrable planes for dislocations.

The second model is an extension of the well-known Hall-Petch effect. Here, dislocations are assumed to form a pile-up at a boundary until a critical stress is reached. This results in a flow stress which is inversely proportional to the square root of the layer thickness or grain size. Both models qualitatively explain the increase in the flow stress with decreasing film/layer thickness, but not the behavior as the layer thickness decreases below tens of nano-meters.

In the present work, we focus on simulation of dislocation motion in relatively thin layers, when the individual layer thickness is in the range of few nanometers to hundreds of nanometers. This is typically much smaller than the characteristic length scale of grains occupied by dislocation networks in bulk materials. Therefore, the number of dislocations needed in order to study thin layer plasticity is small. In many cases, plasticity and strength can be described through the behavior of a single dislocation loop.

Consider a Cu thin layer (thickness h), sandwiched between two semi-infinite harder Ni substrates. The dislocation is originally located within the thin layer. Cu and Ni are both fcc crystals with [001] out-of-plane orientations and $< 110 > \{111\}$ slip systems, and anisotropic elastic constants (Hirth and Lothe 1982). In Cu, $b = 0.361$ nm, and the dislocation mobility is taken to be isotropic ($M = 10^4$ Pa^{-1} s^{-1}). The system is subjected to a uniform applied biaxial stress σ_a. We will ignore here the stress due to lattice mismatch. We only consider the image force effect due to the modulus difference at the Cu-Ni interface. The value of image force increases as the dislocation segment approaches the interface, and is singular exactly at the interface. This is a consequence of the assumptions of linear elasticity, which has been successfully used in dislocation dynamics simulations including similar singular behavior of the dislocation self-force, energy and junction formation. If a cut-off radius is introduced for the dislocation, the results of infinitesimal linear elasticity for self-force, energy, and junction formation are in good agreement with more detailed atomistic simulations (Rodney and Phillips 1999). We assume also here that dislocations do not dissociate into partials, and take the cut-off radius to be $r_0 \approx b$ (Freund 1990, Nix 1998). Detailed atomistic simulations are required to ascertain the value of the cut-off distance. In the following simulations, we assume that there is one Frank-Read (F-R) source inside one of the layers, and that the source dislocation is initially straight and pinned from both ends.

9.3.8 Confined Layer Slip (CLS)

Figure (9.54) shows the propagation mode of a source dislocation in a Cu layer of thickness 144 nm at different loading levels. We choose the length L of the original dislocation to be longer than the layer thickness, h, i.e. L=4h. Under a small applied stress below a critical value (approximately estimated by Freund's formula, Equation (9.55)), the dislocation will bow out in the Cu layer towards the interface. As a result of the image force exerted by the harder Ni layer, the dislocation is repelled away from the interface and reaches an equilibrium configuration. If the applied stress is larger than the critical value, the dislocation first bows out towards the interface then it is blocked by the image force and is confined to propagate within the layer. The critical stress for the onset of confined layer slip is first estimated according to Equation (9.55) with equivalent isotropic values of μ and ν. This value is then refined by increasing (or decreasing) the applied stress until the dislocation cannot achieve its equilibrium configuration any more.

The influence of the dislocation source size is also considered. Below the critical stress for threading dislocation motionσ_c^{th}, dislocations cannot propagate in the layer. When the initial source size is approximately longer than the layer thickness, the dislocation bows out and reaches an equilibrium configuration. If the initial source size is smaller than the layer thickness, slip propagation is controlled by the Orowan mechanism, and the critical stress for bowing out can be estimated as: (Foreman 1967) $\sigma_c^O \approx \frac{\mu b}{2\pi L}\sqrt{6}\ln(L/r_0)$.

In comparing the critical stresses for a threading dislocation motion within a layer, σ_c^{th}, with that for the activation of an F-R source by the Orowan mechanism, σ_c^O, the two values are close when the layer thickness, h, is on the order of the initial F-R source length, L. In any

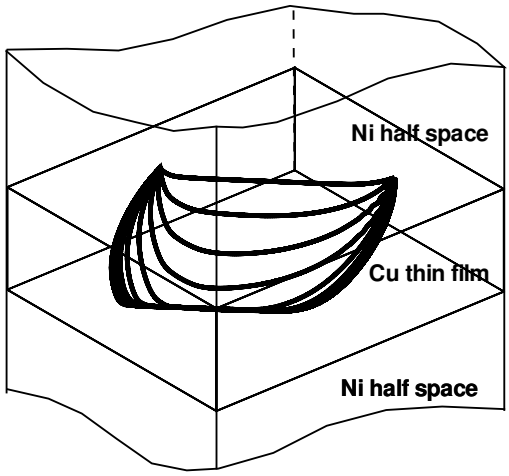

(a)

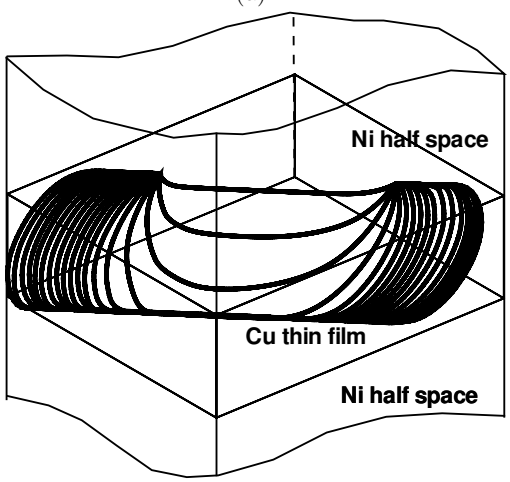

(b)

Figure 9.54: Dislocation motion in a thin layer with h=144 nm under different applied biaxial stress levels (a) $\sigma_a = 210$ MPa $< \sigma_c^{th} = 250$ MPa, and (b) $\sigma_a = 280$ MPa $> \sigma_c^{th} = 250$ MPa. Each line corresponds to a time increment of 0.1 ns.

thin layer, many F-R sources may exist with different sizes, locations and orientations. If the applied stress is smaller than the critical stress for threading dislocation motion, $\sigma < \sigma_c^{th}$, some dislocations will expend towards the interface, but none would be able to propagate within the layer. Once the applied stress is removed, F-R source dislocations will re-tract to their original length. This type of dislocation motion does not lead to permanent deformation of the thin film. We term this regime as *quasi-elastic*. When the applied stress reaches the critical value σ_c^{th}, longer dislocations with L>h will expand, but will still be confined within the layer. This regime of behavior is the so-called Confined Layer Slip (CLS)(Anderson and Li 2001). Finally, if the applied stress is increased further, $\sigma > \sigma_c^O > \sigma_c^{th}$, shorter dislocations L<h are gradually activated, first bowing out from stable shapes, then reach the interface, and finally propagate within the layer. Thus, dislocations emitted from longer F-R sources with L>h are controlled by the threading dislocation mechanism, while shorter ones by the Orowan mechanism.

9.3.9 Loss of Slip Confinement

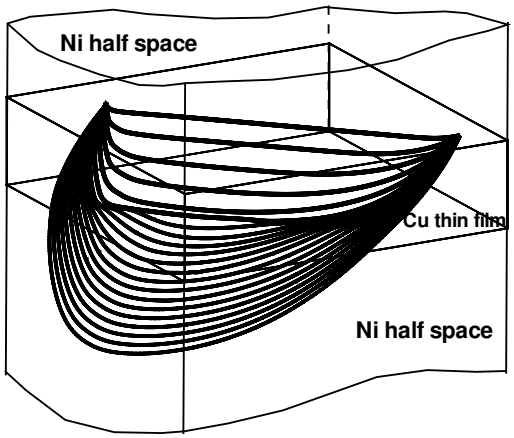

Figure 9.55: Dislocation motion in a thin layer with h=10.8 nm under an applied stress σ_a = 1.2 GPa $> \sigma_c^{th} = 1$ GPa. Each line corresponds to a time increment of 2 ps.

As individual layers become very thin (i.e. in the tens of nanometers), only single dislocations can propagate and expand upon the application of an externally applied stress. However, because the layer thickness is very small, the curvature of the dislocation loop in segments subtended between layers would be extremely high, and thus self-forces in these regions are very substantial. The externally applied stress would have to overcome such large self-forces if these curved segments are to expand. The applied P-K force on those segments that are parallel to the interface does not have to overcome self-forces because the curvature of these segments is small. Rather, the image force from neighboring and other interfaces would have to

be overcome by the applied P-K force. Since we regularized the solution by selecting a cut-off radius of one Burgers vector on either side of the interface, the dislocation will be repelled with a maximum image force on one side of the interface, and then attracted with a different maximum force once it crosses the interface. If the applied stress is high enough that the maximum P-K force on the straight dislocation segments close to the interface overcomes both repulsive and attractive forces, the dislocation will cross from one layer to the neighboring one, and CLS is finally lost. This mode of deformation is shown in Figure (9.55), where successive dislocation positions at 10 ns time intervals are shown for an F-R source dislocation, initially with a straight segment pinned at both ends, and is subjected to a suddenly applied bi-axial stress of magnitude 1.2 GPa. The dislocation, which lies on the (111)-slip plane, has an initial length of 43.2 nm, and its Burgers vector is $\frac{a}{2} < \bar{1}01 >$. After 15 ps, the leading edge of the bowed out dislocation reaches the interface. Since the applied P-K force is larger than both the attractive and repulsive components of the image force, the dislocation loses confinement within the copper layer and expands into the neighboring nickel layer.

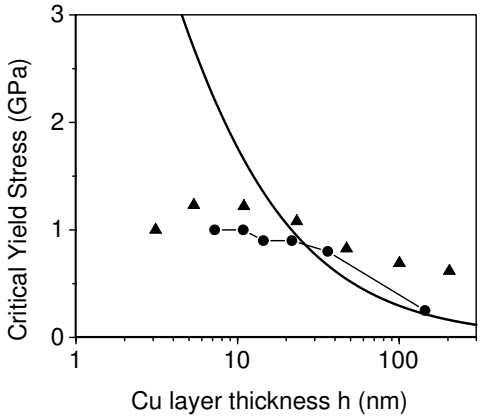

Figure 9.56: Yield strength of a Ni-Cu layered thin film as a function of the layer thickness. Solid line: Freund's formula , triangles: experimental results , and circles: current simulation results.

(Freund 1990, Misra et al. 1998)

Figure (9.70) shows results of our calculations for the maximum strength of a copper layer in a thin film of alternating Cu/Ni layers based on the activation of a single F-R source, as a function of the layer period. Experimental results for nano-indentation by Misra et al. (Misra et al. 1998) and Clemens et al. (Clemens et al. 1999) are also shown. Since Freund's formula is often used to estimate the strength of thin films, film strength using Equation (9.55) is also shown as a solid line on the same figure for comparison. For layers of thickness less than approximately 100 nm, a single F-R source will determine the overall strength of the layer as

a competition between confinement in the layer by image forces generated by elastic modulus mismatch, and resistance to deformation by self-forces on the curved ends of the dislocation loop. If the modulus mismatch is not too great, dislocation loops will cross from layer to layer rather than be confined within a layer. One would expect that the maximum strength is determined by the layer thickness and the ratio of elastic modulii as well. For thicker layers, F-R sources can operate many times leading to dislocation multiplication and the formation of a pile-up. In such case, the dominant deformation mode is the Hall-Petch mechanism.

Based on the present simulations, a strength-thickness map for Cu/Ni multi-layer materials is shown in Figure (9.57). Four regions representing different deformation mechanisms are shown, consistent with earlier investigations (see (Anderson et al. 1999, Misra, Verdier, Kung, Embury and Hirth 1999)). These are:

1. **Region I** - The applied P-K force is smaller than both the Koehler barrier and the self-force. Dislocation loops deform to an equilibrium shape, and regain their original shape upon removal of the applied stress. This is a *quasi-elastic* deformation mode;

2. **Region II** - The applied P-K force is larger than the Koehler barrier. Dislocation loops are no longer confined in this region, and *plastic instability* is manifest in loss of confinement;

3. **Region III** - The applied P-K force is less than the Koehler barrier but still greater than the maximum self-force anywhere on the loop. Loops are forced to propagate within one layer in this *Confined layer Slip* (CLS) mode of deformation;

4. **Region IV** - The layer thickness is so large that it can support several emitted dislocations from F-R sources within the layer, but the applied P-K force is such that the leading dislocation in the pile-up cannot overcome the Koehler barrier. This is the *classical Hall-Petch* mode of plastic deformation.

Conclusions

The development of a line integral form for the elastic field of dislocations in anisotropic, multi-layered materials has enabled an extension of the PDD method to the simulations of plasticity and strength in these material systems. Earlier efforts in this area rely on surface integrals for the derivatives of Green's functions, which complicates numerical implementation in DD computer simulation programs. The following conclusions can be drawn from applications of the developed method to a number of material deformation problems at the nano-scale to the micro-scale:

1. The influence of free surfaces or interfaces on dislocation motion through image forces extends into the material to several hundred lattice constants. Thus, for computer simulations of large material volumes (e.g. tens of microns), image forces can be neglected until the dislocation is within a few hundred lattice constants. Numerical resolution of any method (including the Finite Element) must be sufficient close the surface.

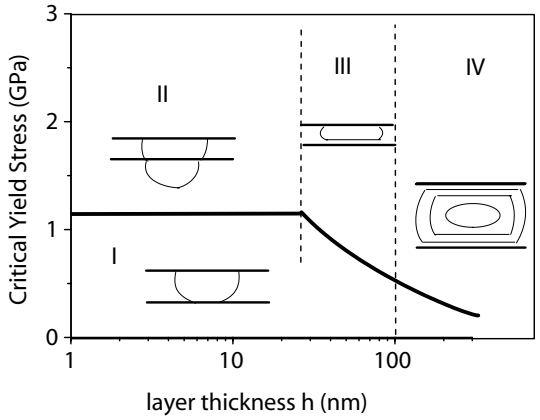

Figure 9.57: Plastic deformation mechanism and strength map for thin layered films.

2. In thin anisotropic films containing many layers of small thickness (i.e. in the tens to hundreds of nm), interaction between several interfaces contributes to the image force on dislocations. No simple geometric image construction can be found to yield accurate magnitude and direction of interface image forces.

3. To retain the original idea of the dislocation self-force in an infinite medium, the elastic field is separated into two components: one that yields the self-force in an infinite medium, while the second is due to the effect of interfaces (i.e. the image force).

4. In thin Al films on Cu substrates, it is shown that a small layer of aluminum oxide can reverse the surface image force from attractive to repulsive. Also, the interaction between the Al/Al_2O_3 interface and the Al/Cu interface can result in near zero image force on curved dislocation segments in the middle of the film. If the oxide film thickness is greater than the film thickness itself, its image force can be approximated by the semi-infinite half-space results.

5. Plastic deformation of very thin layers in the tens of nm thickness range is controlled by a competition between the resistance of curved segments due to high self-forces, and the maximum force to transmit nearly straight segments across the interface (i.e. the Kohler barrier). If the layer is too thin, this results in high curvatures and resistance to CLS. Depending on the ratio of the elastic modulii of adjacent layers, dislocations may find an easier path to move into adjacent layers, and thus CLS is lost. On the other hand, if the ratio of elastic modulii between adjacent layers is sufficiently high and the layer thickness is sufficiently large, dislocations are forced to be confined within one layer.

6. Strength calculations from the present model show reasonable agreement with experimental nano-indentation data on Cu/Ni nano-layered materials. Strength saturation below layer thicknesses of ~ 20 nm is a result of the near independence of the Koehler barrier strength on layer thickness. The present model is incapable of explaining the decrease in layer strength below ~ 10 nm, as shown in the experimental data. This limitation may be attributed to atomistic dislocation core effects not included in the model.

7. Four general deformation mechanisms are identified for layered thin films: quasi-elastic, plastic instability, Confined Layer Slip, and the Hall-Petch regime, consistent with recent literature (Anderson et al. 1999, Misra et al. 1999).

9.4 Ductile-to-Brittle Transition

9.5 Plastic Flow Localization

9.5.1 Introduction

Many experimental observations have shown that neutron irradiation of metals and alloys at temperatures below recovery stage V causes a substantial increase in the upper yield stress (radiation hardening), and beyond a certain dose level, induces a yield drop and plastic instability (see, for example, Smidt 1970, Dai 1995, Singh, Edwards & Toft 1996, and Baluc, Dai and Victoria 1999). Furthermore, the post-deformation microstructure of a specimen showing the upper yield point has demonstrated two significant features. First, the onset of plastic deformation is generally found to coincide with the formation of "cleared"channels, where practically all plastic deformation takes place. The second feature refers to the fact that the material volume in between cleared channels remains almost undeformed (i.e. no new dislocations are generated during deformation). In other words, the initiation of plastic deformation in these irradiated materials occurs in a very localized fashion. This specific type of plastic flow localization is considered to be one of many possibilities of plastic instabilities in both irradiated and unirradiated materials (e.g. Kocks 1981, Neuhäuser 1990 and Luft 1991). A theory of radiation hardening was proposed by Seeger (1958) in terms of dislocation interaction with radiation-induced obstacles (referred to as *depleted zones*). Subsequently, Foreman (1968) performed computer simulations of loop hardening, in which the elastic interaction between the dislocation and loops was neglected. The model is based on Orowan's mechanism, which assumes that the obstacles are indestructible. In this view of *matrix hardening*, the stress necessary to overcome localized interaction barriers represents the increase in the yield strength, while long-range elastic interactions are completely ignored. These *short-range* dislocation-barrier interaction models lead to an estimate of the increase of the critical resolved shear stress (CRSS) of the form: $\Delta\tau = \alpha\mu b/l$, where α is a numerical constant representing obstacle strength, μ the shear modulus, b the magnitude of the Burgers vector, and l is the average inter-obstacle distance. Kroupa (1966), and Kroupa and Hirsch (1964), on the other hand, viewed hardening to result from the *long-range* elastic interaction between slip dislocations and prismatic loops. In their model of *friction hardening*, the force necessary to move a rigid, straight dislocation on its glide plane past a prismatic loop was estimated. In these two classes of hardening models, *all* dislocation sources are assumed to be simultaneously activated at the yield point, and that plastic deformation is homogeneous throughout the material volume. Thus, they do not address the physics of plastic flow localization. Singh, Foreman & Trinkaus (1997) introduced the concept of "stand-off distance" for the decoration of dislocations with small SIA loops, and proposed the "Cascade Induced Source Hardening" (CISH) model , in analogy with *Cottrell atmosphere* (Cottrell 1948). The central question of the formation of dislocation decoration was treated analytically by Trinkaus, Singh & Foreman (1997a&b). Subsequent detailed elasticity calculations showed that glissile defect clusters that approach dislocation cores within the "Cascade Induced Source Hardening" are absorbed, while clusters can accumulate just

outside this distance (Ghoniem et al. 2000a). Trinkaus, Singh & Foreman (1997a&b) concluded that dislocation decoration is a consequence of defect cluster mobility and trapping in the stress field of grown-in dislocations. The CISH model was used to calculate the stress necessary to free decorated dislocations from the atmosphere of loops around them (upper yield, followed by yield drop), so that these freed dislocations can act as dislocation sources. The CRSS increase in irradiated Cu was shown by Singh, Foreman & Trinkaus (1997) to be given by: $\Delta\tau \sim 0.1\mu(b/l)(d/y)^2$, where μ is the shear modulus, b, l, d and y are the Burgers vector, inter-defect distance, defect diameter, and 'stand-off 'distance, respectively. Assuming that $y \sim d$, and that $l \sim 35b$, they estimated $\Delta\tau/\mu \sim 5 \times 10^{-3}$. The phenomenon of yield drop was proposed to result from the unpinning of grown-in dislocations, decorated with small clusters or loops of Self-Interstitial Atoms (SIAs). Fig.9.58 shows a set of stress-strain curves for annealed and cold-worked pure copper, copper containing a dispersion of aluminum oxide particles (also in cold-worked condition) and copper irradiated with fission neutrons at 320 K to dose levels of 0.01 and 0.2 dpa, and tensile-tested at 295 K (Singh, Edwards & Toft 1996). Neutron irradiation of pure copper at 320 K does not only lead to an increase in the upper yield stress, but it also causes a prominent yield drop and plastic flow localization. An example of localized plastic flow in irradiated CuCrZr alloy under low-cycle fatigue conditions is shown in Fig.9.59 (Singh, Stubbins & Toft 2000a). Note that cleared channels appear to be associated with relatively large inclusions (i.e. stress concentration). The objective of the present study is to assess the physical mechanisms, which are responsible for the initiation of plastic instability in irradiated FCC metals by detailed numerical simulations of the interaction between dislocations and radiation-induced defect clusters. Two distinct problems, which are believed to cause the onset of plastic instability are addressed in the present study. First, we aim at determining the mechanisms of dislocation unlocking from defect cluster atmospheres as a result of long-range elastic interaction between dislocations and sessile prismatic interstitial clusters situated just outside the *stand-off distance*. The main new feature of this analysis is that dislocation deformation is explicitly considered during its interaction with SIA clusters. Results of this study are presented in §9.5.3. Second, we investigate the mechanisms of structural softening in flow channels as a consequence of dislocation interaction with stacking fault tetrahedra (SFTs). Based on these numerical simulations, a new mechanism of channel formation is proposed, and the magnitude of radiation hardening is also computed in §9.5.4. Finally, summary and conclusions are given in §9.5.5.

9.5.2 Interaction Between Dislocations & Defects

The self-energy of a single dislocation loop can be calculated as $\frac{1}{2}$ the interaction energy between two identical dislocation loops separated by a distance r_0. The contribution to the self energy from the dislocation core can be estimated from atomistic calculations, and is usually on the order of 5-10% of the self energy (Kroupa 1966). However, the core contribution can be incorporated by adjusting the value of r_0. Using an infinitesimal loop approximation, Kroupa (1966) found the stress tensor of a prismatic loop to be of the form: $\sigma_{ij} = k_{ij}\mu b R^2/2\rho^3$, where k_{ij} is an orientation factor of on order of unity, R is the loop radius and ρ the distance from the loop center. The total force and its moment on an SIA cluster can be expressed respectively

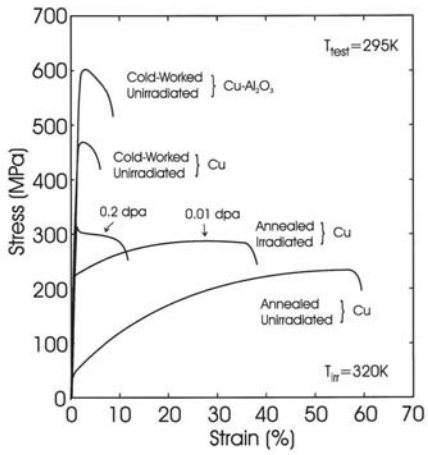

Figure 9.58: Experimental stress-strain curves for irradiated and unirradiated Cu. Specimens were irradiated in DR-3 reactor at RISO at 320 K, and tensile tested at 295 and 320 K (Singh, Edwards & Toft 1996).

as:

$$F_i = -n'_j \sigma_{jk,i} b'_k \delta A' \tag{9.56}$$

$$M_i = - \in_{ijk} n'_j b'_l \sigma_{lk} \delta A' \tag{9.57}$$

Where $n'_j, b'_k, \delta A'$ refer to the Cartesian components of the normal vector, the Burgers vector and the habit plane area of the cluster, respectively. As a mobile SIA dislocation loop moves closer to the core of the slip loop, the turning moment on its habit plane increases, as given by eqn. 9.57. When the mechanical work of rotation exceeds a critical value of $0.1\ eV$/crowdion (Foreman et al. 1992), we assume that the cluster changes its Burgers vector and habit plane, and moves to be absorbed into the dislocation core. Thus, the mechanical work for cluster rotation is equated to a critical value, (i.e. $\delta W = \int_{\theta_1}^{\theta_2} M_i d\theta_i = \Delta U_{crit}$), and used as a criterion to establish the *stand-off* distance (Ghoniem et al. 2000a). We describe dislocation motion by developing Equations Of Motion (EOM) for generalized degrees of freedom (DOF's) on the basis of a variational principle for Gibbs free energy, which is derived from irreversible thermodynamics. Inertial effects (i.e. the kinetic energy of moving dislocations) are not included in this work. We define the following:

1. $B_{\alpha k}$ as a diagonal friction (inverse mobility) matrix for phonon drag constants in two glide and one climb directions.

2. The sum of the Peach-Kohler force, self-force, Peierls lattice friction and climb forces (per unit dislocation line length) as: f_k^t

Figure 9.59: TEM picture of localized plastic flow emanating form internal inclusions in CuCrZr alloy, neutron-irradiated at 320 K to a dose level of 0.3 dpa and fatigue-tested at 320 K with a loading frequency of 0.5 Hz (Singh, Stubbins and Toft 2000a)

3. An effective *generalized force*, f_m on a curved segment defined as:

$$f_m = \int_0^1 f_i^t \mathcal{C}_{im}(u) \mid d\mathbf{s} \mid \tag{9.58}$$

4. A *phonon drag coefficient matrix* element, γ_{mn}, given by:

$$\gamma_{mn} = \int_0^1 \mathcal{C}_{im}(u) B_{ik} \mathcal{C}_{kn}(u) \mid d\mathbf{s} \mid \tag{9.59}$$

With these quantities calculated for each curved segment, Ghoniem, Tong & Sun (2000a) showed that the global *DOF's* for the entire loop, Q_l can be obtained by solving the set of differential equations given by:

$$\mathcal{F}_k = \sum_{l=1}^{N_{tot}} \Gamma_{kl} Q_{l,t} \tag{9.60}$$

Similar to the finite element procedure, the local segment phonon drag coefficient matrix $[\gamma_{mn}]$ is added into corresponding global locations in the global phonon drag coefficient matrix $[\Gamma_{kl}]$, while the force vector is mapped onto a corresponding global vector: $\mathcal{F}_k$. Here, the total number of *DOF's* for the loop are: $N_{tot} = N_s N_{DF}$. The global phonon drag coefficient matrix $[\Gamma_{kl}]$ is also symmetric and banded or sparse. The component Γ_{kl} is zero if the degrees of freedom k and l are not connected through a segment. Eqn. (9.60) represents a set of time-dependent ordinary differential equations which describe the motion of dislocation loops as an evolutionary dynamical system. The computational time-step is dictated by the dislocation mobility, which is quite high in FCC metals (the phonon drag coefficient (inverse mobility, eqn. 9.60) in Cu is taken as 5×10^{-5} *Pa s* (Kubin 1993)). Numerical integration of the equations of motion are performed by implicit iterative methods.

9.5.3 Unlocking of Dislocations from Defect Clusters

The two main aspects of dislocation interaction with defect clusters that affect both hardening and ensuing plastic flow localization are: (1) dislocation unlocking from defect cluster atmospheres; and (2) destruction of SFTs on nearby slip planes by gliding dislocations. The interaction between grown-in dislocations and trapped defect clusters has been shown to lead to unfaulting of vacancy clusters in the form of vacancy loops (Ghoniem, et al. (2000b)). It can also result in rotation of the habit plane of mobile SIA clusters (eqn. 9.57). Once either one of these two possibilities is realized for a vacancy or SIA cluster, it is readily absorbed into the dislocation core. Ghoniem, et al. (2000b) used these conditions to determine an appropriate *stand-off distance* from the dislocation core, which is free of irradiation-induced defect clusters. It is estimated (Ghoniem et al., 2000a) that clusters within a distance of 3-9 *nm* from the dislocation core in Cu will be absorbed, either by rotation of their Burgers vector or by unfaulting. We will use this estimate as a guide to calculations of long-range interactions of dislocations with sessile prismatic SIA clusters situated outside the stand-off distance in §9.5.3. While the experimentally-observed average SFT size is 2.5 *nm* for OFHC copper, the radius of a sessile

interstitial cluster, which results from coalescence of smaller mobile clusters, is assumed to be in the range: $\sim 4 - 20\ nm$. The local density of interstitial defect clusters at the stand-off distance is taken to be in the range $0.6 - 4 \times 10^{24}\ m^{-3}$, giving an average inter-cluster spacing of $\sim 18 - 35\ a$. In subsequent computer simulations, we use the following set of material data for Cu: lattice constant (a = 0.3615 nm), shear modulus ($\mu = 45.5\ GPa$), Poisson's ratio ($\nu = 0.35$), F-R source length (L=1500-2000 a).

Interaction between an F-R Source and a Single SIA Cluster

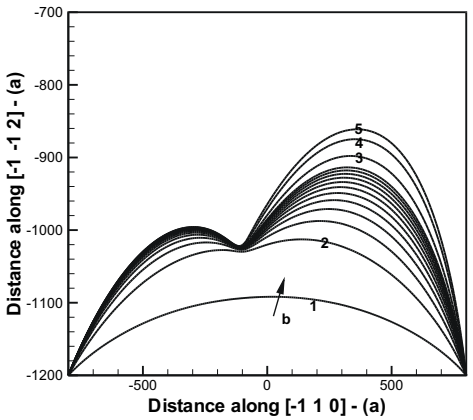

Figure 9.60: Dynamics of F-R source ($\mathbf{b} = \frac{1}{2}[\bar{1}01]$) interaction with a single sessile prismatic interstitial defect cluster very near the glide plane. The cluster has a radius of 50 a, and a Burgers vector of $\mathbf{b} = \frac{1}{2}[110]$ on the (111) glide plane. The cluster is located at (0, -1000 a, 40 a) in the local plane coordinates. Time intervals are: (1) 1 ps, (2) 2.5 ps, (3) 25 ps, (4) 50 ps, (5) 1200 ps.

To gain insight into the mechanism of dislocation unlocking from the random field of decorating clusters, we first consider the simpler situation for the interaction between an F-R source and one single sessile cluster (radius= 40 a) from the glide plane at a *stand-off* distance of 40 a. The original analysis of Kroupa (1966) of a similar problem considered the case of a single straight, infinitely long and rigid dislocation, interacting with another single circular dislocation loop. More recently, Kubin and Kratochvil (2000) have analyzed the interaction between an infinite dislocation and a rectangular dipolar loop. In the following, the defect cluster is assumed to be a circular prismatic dislocation loop situated above (or below) the glide plane of an F-R source. The Burgers vector of clusters is $\mathbf{b} = \frac{1}{2}[110]$ or $\mathbf{b} = \frac{1}{2}[\bar{1}\bar{1}0]$, while for the expanding F-R source: $\mathbf{b} = \frac{1}{2}[\bar{1}01]$. Other equivalent cluster orientations give redundant results. We also assume here that the dislocation loop is not dissociated into partials. A uniaxial stress

along [100] of $\sigma_{11} = 100$ MPa is suddenly applied. The equations of motion for position and tangent vectors are solved for 21 nodes on the expanding source, and the shape is re-computed by implicit iterative integration to ensure stability of the solution. Fig.9.60 shows the change in shape of the expanding F-R source dislocation, as it comes closer to the cluster location. After 1 ps, the advancement of the F-R source is nearly unaffected by the prismatic defect cluster off the glide plane, as shown in Fig.9.60. As the dislocation line of the F-R source come within 100 - 200 a from the cluster, the dislocation line is repelled, and starts to deform significantly by ~ 25 ps. Even though the cluster force is relatively small, the dislocation line is very flexible, thus achieving an equilibrium configuration in about 0.1 ns. When the same sessile SIA cluster is moved vertically away from the glide plane, the interaction dynamics is significantly changed, both quantitatively and qualitatively (see Fig.9.61). By ~ 10 ps, the F-R source dislocation clears itself from the influence of the cluster force field, which just distorts the dislocation line as it passes underneath it on the glide plane. The line deformation caused by the cluster is eventually erased as a result of the restoring dislocation self force. It is clear that the F-R source dislocation *unlocks* itself rather easily and quickly from the elastic field of one single SIA cluster at a distance of 80 a away from the glide plane.

Interaction between an F-R Source and a Row of SIA Clusters

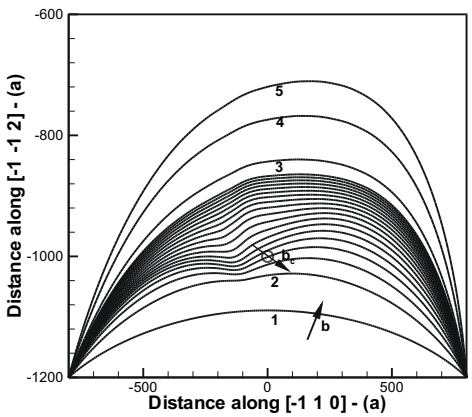

Figure 9.61: Dynamics of F-R source interaction with a single sessile prismatic interstitial defect cluster at a farther *stand-off* distance. All conditions are the same as in Fig.9.60, except that the cluster is located at (0, -1000 a, 80 a) in the local plane coordinate, and time intervals are: (1) 1 ps, (2) 2.5 ps, (3) 25 ps, (4) 50 ps, (5) 75 ps.

Consider now the more complex interaction between an expanding F-R source dislocation and the full field of multiple sessile SIA clusters (loops) present in a region of decoration. As

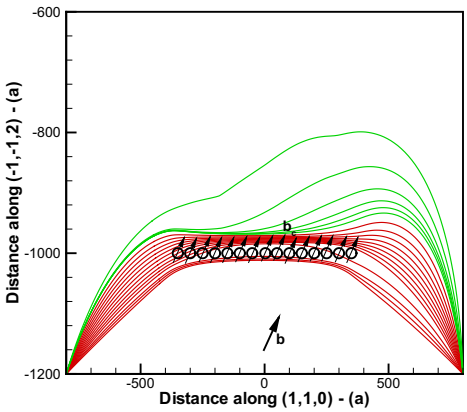

Figure 9.62: Dynamics of F-R source interaction with an attractive interstitial defect cluster atmosphere at the *stand-off* distance of 100 a. Clusters have parallel and identical Burgers vectors to the F-R source of $\mathbf{b} = \frac{1}{2}[\bar{1}01]$. The apllied stress, σ_{11} is gradually increased to 200 MPa before the dislocation line breaks free from clusters.

the F-R source expands in the elastic field of SIA clusters, each point on the dislocation line will experience a resistive (or attractive) force, which must be overcome for the dislocation to move further. The dislocation line curvature, and hence the local self force also change dynamically. To determine the magnitude of collective cluster resistance, systematic calculations for the dynamics of interaction between attractive (Fig.9.62) and repulsive (Fig.9.63) SIA clusters are presented. When the SIA clusters are all attractive, the dislocation line is immediately pulled into their atmosphere, but as the applied stress is increased, the dislocation remains trapped by the force field of SIA clusters. When the stress is increased to 200 MPa, the line develops an asymmetric configuration as a result of its Burgers vector orientation, and an *unzipping* instability eventually unlocks the F-R source from the collective cluster atmosphere, as shown in Fig.9.62. This asymmetric unlocking mode is characteristic of high linear cluster density on smaller sections of F-R source decorations, as shown in Fig.9.62, where the linear density of SIA clusters is $\sim \frac{1}{50}$ (cluster/ lattice constant). On the other hand, as the linear density of SIA clusters is reduced to $\sim \frac{1}{100}$ (cluster/ lattice constant), and the cluster coverage of the F-R source is extensive, another instability mode develops. Fig.9.63 shows the detailed dynamics of the collective cluster interaction with an expanding F-R source. The high fidelity of the current PDD method for space and time resolution of this interaction is clearly shown in the inset to Fig.9.63. A fluctuation in the line shape is amplified by the combined effects of the applied and self forces on the middle section of the F-R source, and the dislocation succeeds in penetrating through the collective cluster field at a critical tensile stress of $\sigma_{11} = 180MPa$ (or equivalently at CRSS of $\tau/\mu = 0.0015$). A summary set of results for similar calculations are shown as scaling graphs in Figs. 9.64 and 9.65. The critical shear stress (in units of the

shear modulus) is shown in Fig.9.64 as a function of the stand-off distance, for a fixed inter-cluster distance of 50 a. The results of current calculations are compared to the analytical estimates of Singh, et al. (1997) and Trinkaus, et al. (1997b). For farther stand-off distances, the current results show a *larger* critical stress as compared to the analytical estimates, while for stand-off distances smaller than $\sim 60\ a$, a *smaller* critical stress is required to unlock the F-R source. When the stand-off distance is large, the applied stress must overcome the self-force, which results from the finite length of the F-R source, in addition to the collective cluster elastic field. This aspect is not considered in the extension of Trinkaus, Singh & Foreman (1997b) of Kroupa's theory (1966), where the line is assumed to be rigid as it moves close to the clusters. At smaller stand-off distances, however, the dislocation easily unlocks by one of the two unzipping instability modes discussed earlier, and the predicted CRSS is smaller than analytical estimates. Similar features are displayed in Fig.9.65, where our calculations are again compared to the analytical scaling relationship developed by Trinkaus, Singh & Foreman (1997b). At inter-cluster distances smaller than 70 a, the dislocation shape instability reduces the CRSS from corresponding analytical results. It is estimated that the required CRSS is $\sim 0.001\mu$ ($\sim 50\ MPa$ for copper), for an average inter-cluster distance of $l \sim 50$ a, and a stand-off distance of $\sim 40\,a$. It is experimentally difficult to determine the local value of l in the decoration region of dislocations, which is likely to vary considerably, depending on the character of the dislocation Burgers vector. However, $l \sim 50\,a$ is an *upper bound*, while $l \sim 20 - 30\,a$ is more likely. Since the CRSS is roughly inversely proportional to l, the most likely value of the CRSS to unlock dislocations and start the operation of F-R sources would be $\tau_{CRSS} \sim 100 - 150\,MPa$. Depending on the local value of the Schmidt factor, the corresponding uniaxial applied stress is thus likely to be on the order of $200 - 300\,MPa$, under conditions of heavy decoration (i.e. at a displacement damage dose of ≥ 0.1 dpa). The current estimates for the unlocking stress are thus consistent with the experimental data of Fig.9.58, and indicate that the operation of F-R sources from decorated dislocations can be initiated by one (or both) of the following possibilities:

1. activated F-R sources are decorated with a statistically low linear defect cluster density;
2. dislocation sources are initiated at stress singularities in regions of internal stress concentration.

In either one of these two possibilities, the most likely orientation of plastic slip is along directions of maximum local Schmidt factors.

9.5.4 The Mechanism of Channel Formation

Once dislocation sources are unlocked from their decoration atmospheres causing a yield drop, they *additionally* interact with the surrounding random field of defect clusters (e.g. vacancy loops or SFTs). We investigate here the interaction between emitted F-R dislocations and vacancy-type defect clusters as a possible mechanism of *radiation softening* immediately beyond the yield point. Numerical computer simulations are performed for the penetration of

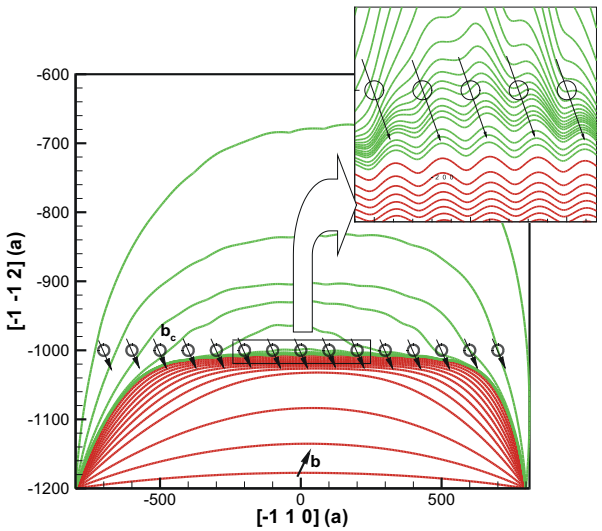

Figure 9.63: Dynamics of the *symmetric unlocking* mechanism, initiated by small fluctuations in the dislocation line as it passes near the cluster atmosphere. Conditions are the same as in Fig.9.62, except that the clusters are repulsive, and of a Burgers vector $\mathbf{b} = \frac{1}{2}[110]$.

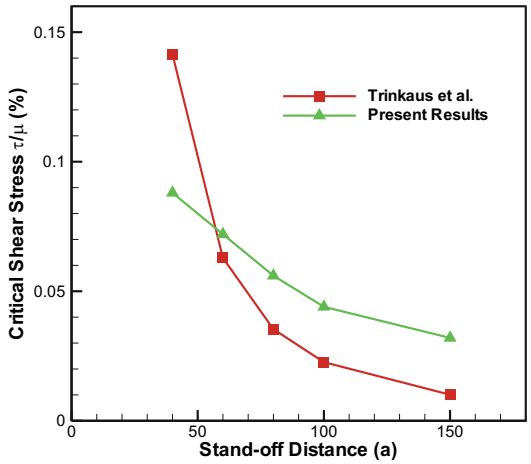

Figure 9.64: Scaling of the critical shear stress with the stand-off distance for a fixed inter-cluster spacing of 50 a

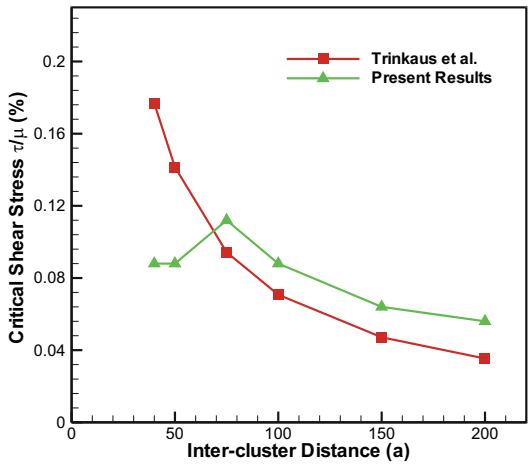

Figure 9.65: Scaling of the critical shear stress with the inter-cluster distance for a fixed stand-off distance of 40 a

undissociated slip dislocation loops emitted from active F-R sources (i.e. unlocked from defect decorations) against a random field of SFTs or sessile Frank loops of the type: $\frac{1}{3} < 111 > \{111\}$. At the present level of analysis, there is no distinction between SFTs and vacancy loops, since they are modeled as point obstacles to dislocation motion that can be destroyed once an *assumed* critical force on them is reached. The long-range elastic field of these small obstacles is ignored. The present computer simulations are extensions of Foreman's analysis (Foreman 1968) in the following respects: (1) dislocation sources are not *free* segments, and are emitted from pinned Frank-Read (FR) sources; (2) the simulations are fully 3-dimensional, and not on a single glide plane; (3) obstacles are *destructible*: a necessary condition for flow localization; (4) multiple, 3-D jogged and interacting dislocation loop pileups are simulated; and (5) dislocation segments in-between SFTs are *not* in equilibrium with the applied stress. The random distribution of SFTs is generated as follows: (1) the volumetric density of SFTs is used to determine the average 3-D position of each generated SFT; (2) a Gaussian distribution function is used (with the standard deviation being 0.1-0.3 of the average spacing) to assign a final position for each generated SFT around the mean value; and (3) the intersection points of SFTs with glide planes are computed by finding all SFTs that intersect the glide plane. For simplicity, we perform this procedure assuming that SFTs are spherical and uniform in size.

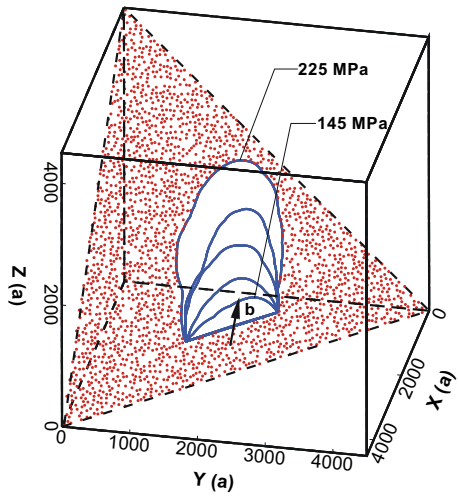

Figure 9.66: Propagation of plastic slip emanating from a single Frank-Read source in copper irradiated and tested at 100 ^oC. Displacement damage dose=0.1 dpa, STF's density= $4.5 \times 10^{23} m^{-3}$, size=2.5 nm. Simulated crystal size=4500 a (1.62 μm). Initial F-R source length=1600 a (576 nm). Stress is applied along [100]. "Unzipping" of curved dislocation segments is clear during the initial stages of deformation, where long segments can get "stuck" till they are unzipped by increasing the applied stress.

Interaction between Unlocked Dislocations and Matrix Defect Clusters (SFT's)

Initially, one slip dislocation loop is introduced between two fixed ends, as in section 3. A search is performed for all neighboring SFTs on the glide plane. Subsequent nodal displacements (governed by the local velocity) are adjusted such that a released segment interacts with only one SFT at any given time. The interaction scheme is a *dynamic* modification to Friedel statistics (Friedel 1956), where the asymptotic maximum plane resistance is found by assuming steady-state propagation of quasi-straight dislocation lines. While Friedel calculates the area swept as the average area per particle on the glide plane, we adjust the segment line shape *dynamically* over several time steps after it is released from an SFT. When a segment is within $5\,a$ from the center of any SFT, it is divided into two segments with an additional common node at the point of SFT intersection with the glide plane. The angle between the tangents to the two dislocation arms at the common node is then computed, and force balance is performed. When the angle between the two tangents reaches a critical value of Φ_c, the node is released, and the two open segments are merged into one. If the force balance indicates that the segment is near equilibrium, no further incremental displacements of the node are added, and the segment of the loop is temporarily stationary. However, if a net force acts on that segment of the loop, it is advanced and the angle re-computed. It is possible that the angle between tangents reach the critical value, even though the segment is out of equilibrium. Sun, Ghoniem and Wang (2000) have shown that the elastic interaction energy between a glissile dislocation and an SFT is not sufficient to transform the SFT into a glissile prismatic vacancy loop. They proposed an alternate mechanism for the destruction of SFTs by passage of jogged and/or decorated dislocations close to the SFT. The energy released from recombination of a small fraction of vacancies in the SFT was estimated to result in its local rearrangement. In the present calculations, we assume that vacancies in the SFT are absorbed in the dislocation core of the small contacting dislocation segment, forcing it to climb and form atomic jogs. With this mechanism, the entire SFT is removed from the simulation space, and jogged dislocations continue to glide on separate planes, thus dragging atomic-size jogs with them. Successive removal of SFTs from nearby glide planes can easily lead to channel formation and flow localization in the channel, because the passage of consecutive dislocation loops emitted from the F-R source is facilitated with each dislocation loop emission. The matrix density of SFTs in irradiated copper at low temperature (0.22-0.27 T_m) is taken from experimental data (Singh, Edwards & Toft 1996). Fig.9.66 shows the results of computer simulations for propagation of plastic slip emanating from a single Frank-Read source in copper irradiated and tested at 100 ^oC (Singh, Edwards and Toft 2000b). The density of SFTs is $4.5\times10^{23}\,m^{-3}$ and the average size is $2.5\,nm$. In this simulation, the crystal size is set at $\sim 1.62\,\mu m$, while the initial F-R source length is 1600 a ($\sim 576\,nm$). A uniaxial applied tensile stress along [100]- σ_{11} is incrementally increased, and the dislocation line configuration is updated till equilibrium is reached at the applied stress. Once full equilibrium of the dislocation line is realized, the stress is increased again, and the computational cycle repeated. At a critical stress level (flow stress), the equilibrium dislocation shape is no longer sustainable, and the dislocation line propagates till it is stopped at the crystal boundary, which we assume to be impenetrable. All SFTs interacting with the dislocation line are destroyed, and plastic flow on the glide plane is only limited by

dislocation-dislocation interaction through the pile-up mechanism. During the initial stages of deformation, small curved dislocation segments *unzip* forming longer segments, which are *stuck* till they are unzipped again by increasing the applied stress. It is noted that, particularly at higher stress levels, the F-R source dislocation *elongates* along the direction of the Burgers vector, as a result of the higher stiffness of screw dislocation segments as compared to edge components. The F-R source configuration is determined by (a) the character of its initial segment (e.g. screw or edge), (b) the distribution of SFTs intersecting the glide plane, and (c) any other dislocation-dislocation interactions. This aspect is illustrated in Fig.9.67, where two interacting F-R sources in copper are shown for a displacement dose of 0.01 dpa and an SFT density of $2.5 \times 10^{23}\, m^{-3}$ and with an average size of $2.5\, nm$. All other conditions are the same as in Fig.9.66. The two F-R sources are separated by 20 a ($\sim 7.2\, nm$). It is seen that the spread of the F-R dislocation line with an initial strong edge component of the Burgers vector is much faster than the F-R source with an initial pure screw component. Significant deformation of the two loops is also observed when corresponding segments meet, and a higher stress is required to overcome additional interaction forces.

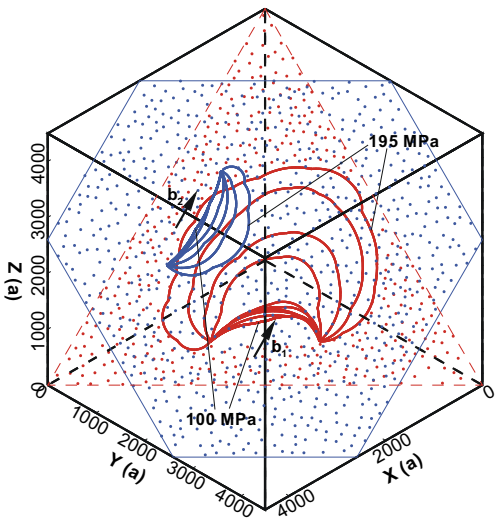

Figure 9.67: Spread of plastic slip emanating from two interacting Frank-Read sources in copper irradiated and tested at 100 ^oC. While the simulation conditions are the same in Fig.9.66, the two F-R sources are separated by 20 a (7.2 nm). Significant deformation of the two loops is observed when corresponding segments meet, and a higher stress is required to overcome the additional forces generated by each F-R source on the other one.

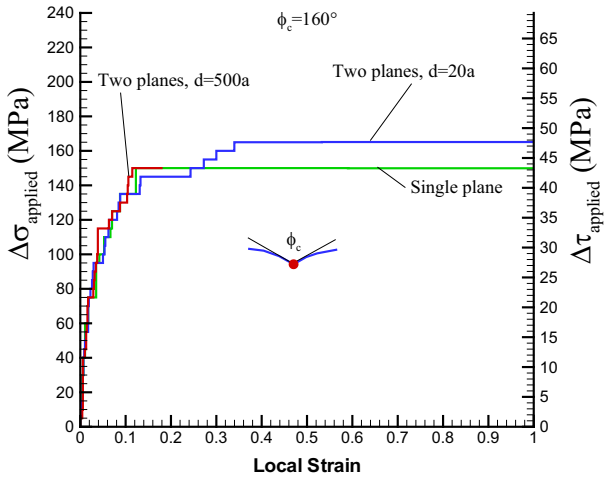

Figure 9.68: The effects of inter-planar F-R source interactions on the flow stress in copper irradiated and tested at 100 ^oC, and a displacement damage dose of 0.1 dpa. Local strain is measured as the fractional area of swept glide planes.

Matrix Radiation Hardening

Penetration of activated F-R sources into a 3-D field of destructible SFTs can be viewed as a percolation problem, first considered by Foreman (1968) on a single glide plane, and extended here to complex 3-D climb/glide motion. The critical stress above which an equilibrium dislocation configuration is unsustainable corresponds to the percolation threshold, and is considered here to represent the flow stress of the *radiation-hardened* material. Since activated F-R sources may encounter nearby dislocations, such interactions should be considered in estimates of the flow stress. The effects of inter-planar F-R source interactions on the flow stress in copper irradiated and tested at 100 ^oC is shown in Fig.9.68. A *plastic* stress-strain curve is constructed from the computer simulation data, where the local strain is measured in terms of the fractional area swept by expanding F-R sources on the glide plane. It is shown that while the majority of the increase in applied stress of irradiated copper can be rationalized in terms of dislocation interaction with SFTs on a single glide plane, dislocation-dislocation dipole hardening can have an additional small component on the order of 15 % for very close dislocation encounters on neighboring slip planes (e.g. separated by $\sim 20\,a$). For larger separation (e.g. $\sim 500\,a$) the additional effects of dipole hardening is negligible. Dislocation forest hardening does not seem to play a significant role in determination of the flow stress, as implicitly assumed in earlier treatments of radiation hardening (e.g. Seeger 1958, Makin and Minter 1960, and Foreman 1968). The influence of the irradiation dose on the local stress-strain behavior of copper irradiated and tested at 100 ^oC is shown in Fig.9.69. In the present calculations, we do not consider

strain-hardening by dislocation-dislocation interactions, and make no attempt to reproduce the global stress-strain curve of irradiated copper. Computed values of the flow stress are in general agreement with the experimental measurements of Singh, Edwards and Toft (2000b), as can be seen from Fig.9.70. A more precise correspondence with experimental data depends on the value of the critical interaction angle Φ_c, which is the only relevant adjustable parameter in the present calculations. In Fig.9.69, $\Phi_c = 165^o$. Determination of the two adjustable parameters (Φ_c and B) requires atomistic computer simulations beyond the scope of the present investigation. Additional calculations for the flow stress for OFHC copper, irradiated at 47 $^\circ C$ and tested at 22 $^\circ C$ are given in Table (2) below, and compared to the experimental data of Singh, Edwards and Toft (1996). The flow stress value at a dose of 0.001 dpa has been extrapolated from the experimental results of Dai (1995) for single-crystal copper irradiated with 600 MeV protons. It is noted that, while the general agreement between the computer simulations and the experimental data of irradiated Cu is reasonable at both 22 ^oC and 100 ^oC, the *dose-dependence* of radiation hardening indicates that some other mechanisms may be absent from the current simulations.

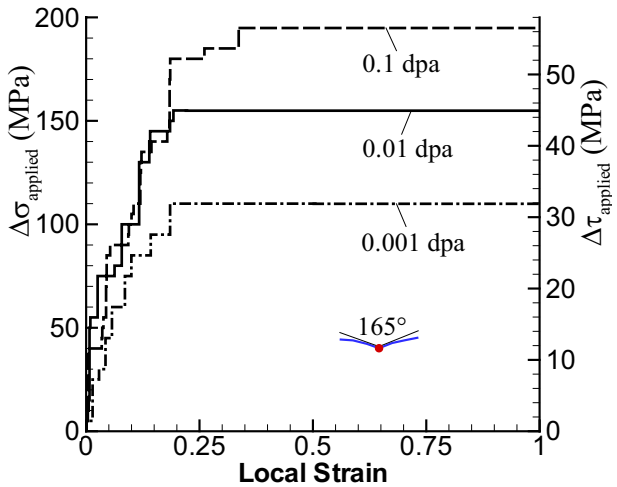

Figure 9.69: Dose dependence of the increase in flow stress in copper irradiated and tested at 100 ^oC. The displacement damage dose varies in the range 0.001 - 0.1 dpa, and conditions correspond to the experimental data of Singh, Edwards and Toft (2000b).

Table (2)
Experimental (Singh, Edwards and Toft 1996) and calculated tensile hardening parameters for OFHC copper, irradiated at 47 $^\circ C$ and tested at 22 $^\circ C$

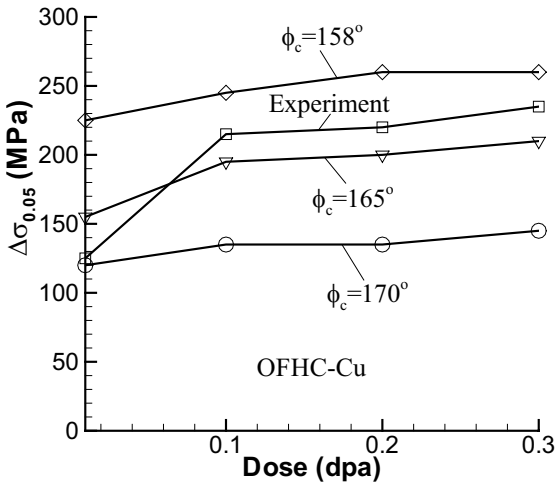

Figure 9.70: Comparison between the dose dependence of computed increase in flow stress values and the experimental measurements of Singh, Edwards and Toft (2000b).

Displacement Dose (dpa)	SFT density ($10^{23}m^{-3}$)	Planar inter-SFT distance (a)	Experimental $\Delta\sigma_{0.05}$ (MPa)	Calculated $\Delta\sigma$ (MPa) ($\Phi_c = 160^O$)	Calculated $\Delta\sigma$ (MPa) ($\Phi_c = 165^O$)
0.001	0.8	196	110 $^{(Dai1995)}$	145	110
0.01	5.3	76	134	240	205
0.1	6.7	67.5	238	250	210
0.2	6.6	68.5	249	245	205

Investigations of dislocation interaction with full or truncated SFTs considered recently by Sun, Ghoniem and Wang (2000) indicated that local heating may be responsible for the dissolution of SFTs by interacting dislocations, and that their vacancy contents are likely to be absorbed by rapid pipe diffusion into the dislocation core. The consequence of this event is dislocation climb out of its glide plane by formation of atomic jogs, followed by subsequent glide motion of jogged dislocation segments on a neighboring plane. In Fig.9.71, we present results of computer simulations of this glide/ climb mechanism of jogged F-R source dislocations. Fig.9.72 shows a side view of the glide/ climb motion of a dislocation loop pileup, consisting of three successive loops, by projecting dislocation lines on the plane formed by the vectors: [111] and $[\bar{1}\bar{1}2]$. SFTs have been removed for visualization clarity. It is noted that for this simulated three-dislocation pileup, the first loop reaches the boundary and is held there while the second and third loops expand on different slip planes. We assume that the simulation boundary is rigid, with no attempt to simulate slip transmission to neighboring grains. However, the force field of the first loop stops the motion of the second and third loop, even though the stress is sufficient

to penetrate through the field of SFTs. This glide/climb mechanism of jogged dislocations in a pileup can be used to explain two aspects of dislocation channel formation. As the group of emitted dislocations expand by glide, their climb motion is clearly determined by the size of an individual SFT. For the densities considered here, a climb step of nearly one atomic plane results from the destruction of a single SFT. The climb distance is computed from the number of vacancies in an SFT and the length of contacting dislocation segments. The jog height is thus variable, but is generally of atomic dimensions for the conditions considered here. The width of the channel is a result of two length scales: (1) the average size of an SFT ($\sim 2.5\,nm$); and (2) the F-R source-to-boundary distance ($\sim 1-10\,\mu m$). This aspect can be seen from Fig.9.59. Secondary channels, which are activated from a primary channel (i.e. source point), and which end-up in a nearby primary channel (i.e. boundary) are *thinner* than primary channels. Further detailed experimental observations of the channel width dependencies are necessary before final conclusions can be drawn. The second aspect of experimental observations (Fig.9.58), and which can also be explained by the present mechanism, is that a small degree of hardening occurs once dislocation channels have been formed. Dislocation-dislocation interaction within the non-coplanar jogged pileup requires a higher level of applied stress to propagate the pileup into neighboring grains.

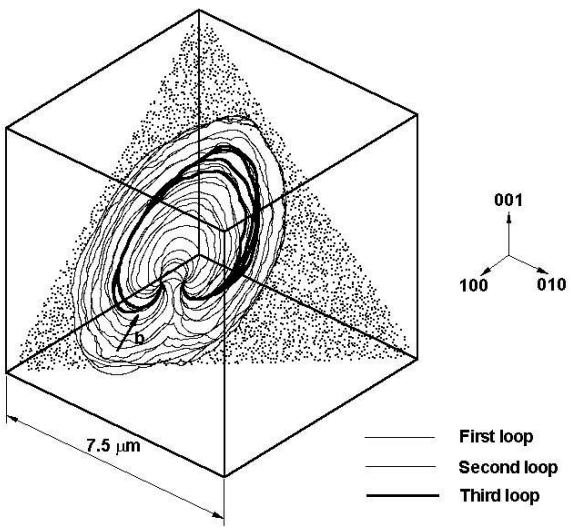

Figure 9.71: A front 3-D view of the glide/ climb mechanism of the jogged dislocation pileup. Note the gradual destruction of SFTs as the pileup develops.

While the initiation of a dislocation channel is simulated here, full evolution of the channel requires successive activation of F-R sources within the volume weakened by the first F-R source, as well as forest hardening within the channels themselves. The possibility of dislocation channel initiation on the basis of the climb/ glide mechanism is further investigated by computer

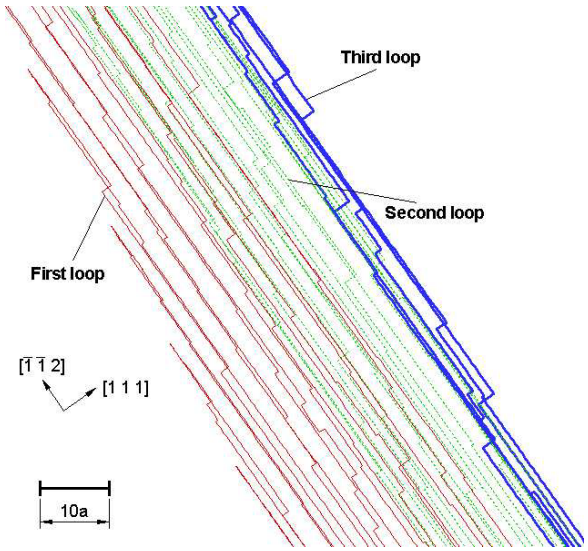

Figure 9.72: $< 1\bar{1}0 >$ projection for glide/ climb motion of a dislocation loop pileup, consisting of three successive loops. SFT's have been removed for visualization clarity.

simulation of OFHC copper irradiated to 0.01 dpa, and tested at 100 $^{\circ}C$, and is shown in Fig.9.73. Formation of clear channels is experimentally observed at this dose level (Singh, Edwards & Toft 2000b). The figure is a 3-D representation for the initial stages of multiple dislocation channel formation. For clarity of visualization, the apparent SFT density has been reduced by a factor of 100, since the total number of SFTs in the simulation volume is 3.125×10^7. The initial dislocation density is taken as $\rho = 10^{13}\, m^{-2}$. To show the importance of spatial SFT density variations, a statistical spatial distribution within the simulation volume has been introduced such that lower SFT densities are assigned near 10 glide planes. All dislocation segments are inactive as a result of high density of surrounding SFTs, except for those on the specified glide planes. Search for nearby SFTs is performed only close to active channel volumes, which in this case totals 174,846. It is observed that within a $5\,\mu m$ volume, the number of loops within a pileup does not exceed 5. It is expected that if the pileup continues across an entire grain (size $\sim 10\mu m$), a higher number of loops would be contained in a jogged dislocation pileup, and that the corresponding channel would be wider than in the present calculations. We have not attempted to initiate multiple F-R sources *within* the volume swept by the dislocation pile-up to simulate the full evolution of channel formation. As a result, the channel shape created by a single active F-R source is of a wedge nature. In future simulations, we plan to investigate the full evolution of dislocation channels.

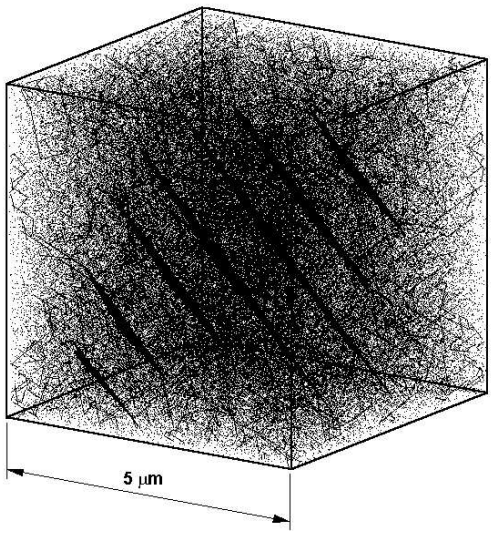

Figure 9.73: 3-D view for the formation of dislocation channels on glide planes which have low SFT density, for irradiated copper at a dose of 0.01 dpa. For clarity of visualization, the apparent SFT density has been reduced by a factor of 100. Note that other dislocation segments are inactive as a result of high density of surrounding clusters

9.5.5 Summary & Conclusions

The present investigations have shown that dislocation lines are highly flexible. For small inter-cluster or stand-off distances (which are typical of decorated dislocations), the unlocking stress can be a factor of two smaller than values obtained when one assumes rigid dislocation interactions. Two possible mechanisms of dislocation unlocking have been identified: (1) an asymmetric unzipping-type instability caused by partial decoration of dislocations; (2)a fluctuation-induced morphological instability, when the dislocation line is extensively decorated by defect clusters. Estimated unlocking stress values are in general agreement with experimental observations that show a yield drop behavior. It appears that unlocking of heavily decorated dislocations will be most prevalent in areas of stress concentration (e.g. precipitate, grain boundary, triple point junction, or surface irregularity). Computer simulations for the interaction between unlocked F-R sources and a 3-D random field of SFTs have been utilized to estimate the magnitude of radiation hardening, and to demonstrate a possible mechanism for the initiation of localized plastic flow channels. Reasonable agreement with experimental hardening data has been obtained with the critical angle Φ_c in the limited range of $158^o - 165^o$. Both the magnitude and dose dependence of the increase in flow stress by neutron irradiation at 50^o C and 100^o C are reasonably well predicted. In spatial regions of internal high stress, or on glide planes of statistically-low SFT densities, unlocked dislocation sources can expand and interact with SFTs. Dislocations drag atomic-size jogs and/or small glissile SIAs when an external stress is applied. High externally-applied stress can trigger point-defect recombination within SFT volumes resulting in local high-temperatures. A fraction of the vacancies contained in SFTs can therefore be absorbed into the core of a gliding dislocation segment producing atomic-size jogs and segment climb. The climb height is a natural length scale dictated by the near-constant size of the SFT in irradiated copper. It is shown by the present computer simulations that the width of a dislocation channel is on the order of (200-500 atomic planes), as observed experimentally, and is a result of a *stress-triggered* climb/ glide mechanism. The atomic details of the proposed dislocation-SFT interaction and ensuing absorption of vacancies into dislocations need further investigations by atomistic simulations. Finally, it should be pointed out that at relatively high neutron doses, dense decorations of dislocations with SIA loops, and a high density of defect clusters/ loops in the matrix are most likely to occur. As shown here, these conditions can lead to the phenomena of yield drop and flow localization. Solutions of these problems in the field of materials design may be sought, either to avoid dislocation decorations and channel formation, or to prevent propagation of dislocations through the channels (e.g. by providing closely-spaced indestructible obstacles on glide planes).

REFERENCES

Baluc, N., Dai, Y. and Victoria, M., 1999, 20^{th} *RISØ* Symposium Proc. on Materials Science, Bilde-Sorensen, et al., Eds. Cottrell, A.H., 1948, *Report of Conference on the Strength of Solids* (University of Bristol), England, Physical Society, London, **30**, 30.

Dai, Y., 1995, Ph.D. Thesis 1388, University of Lausanne, p.59. deWit, R., 1960, *Sol. State Phys.*, **10**, 269.

Friedel, J., 1956, Les Dislocations, Gauthiers-Villars, Paris, France. Foreman, A.J.E., 1968,

Phil. Mag., **17**, 353.

Foreman, A.J.E., English, C.A., and Phythian, W.J., 1992, *Phil. Mag.*, **66**, 655.

Ghoniem, N.M., and Sun, L.Z., 1999, *Phys. Rev. B*, **60**, 128.

Ghoniem, N.M., Singh, B.N., Sun, L.Z., & Diaz de la Rubia, T., 2000a, *J. Nucl. Mater*,

Ghoniem, N.M., Tong, S-.S.& Sun, L.Z., 2000b, *Phys. Rev. B*, **139(1)**, 913. **276**, 166.

Hirth, J.P., Rhee, M., and Zbib, H.M., 1996, *J. Computer-Aided Mater. Design*, **3**, 164.

Kocks, U.F., Argon, A.S., and Ashby, M.F., 1975, *Progr. Mat. Sci.*, **19**, 1.

Kroupa, F., and Hirsch, P.B., 1964, *Discuss. Faraday Soc.*, **38**, 49.

Kroupa, F., 1966, *Theory of Crystal Defects*, edited by B. Gruber (Academia Publishing House, Prague), p.275.

Kubin, L.P., and Canova, G., 1992, *Scr. Metall.*, **27**, 957.

Kubin, L. P., 1993, it Phys. Status Solidi (a), **135**, 433 .

Kubin, L.P., and Kratochvil, J., 2000, it Phil. Mag. A, **80(1)**, 201.

Luft, A., 1991, *Progr. Mater. Sci.*, **35**, 97.

Makin, M.J., and Minter, F.J., 1960, *Acta Met.*, **8**, 691. Neuhaüser, H., 1990, *Patterns, Defects and Materials Instabilities*, edited by D.

Walgraef and N.M. Ghoniem (NATO ASI Series E, Applied Sciences, Kluwer Academic Publishers, Dordrecht/Boston/London.), **183**, pp. 241-276.

Schwarz, K.W., 1997, *Phys. Rev. Lett.*, **78**, 4785.

Seeger, A., 1958, in *Proc. 2nd UN Int. Conf. on Peaceful Uses of Atomic Energy*, Geneva, **6**, 250.

Singh, B.N., Edwards, D.J., and Toft, P., 1996, *J. Nucl. Mater.*, **238**, 244.

Singh, B.N., Foreman, A.J.E., and Trinkaus, H., 1997, *J. Nucl. Mater.*, **249**, 103.

Singh, B.N., Stubbins, J.F., and Toft P., 2000a, *RISØ National Laboratory Report*, No. RISO-R-1128(EN).

Singh, B.N., Edwards, D.J., and Toft, P., 2000b, *RISØ National Laboratory Report*, No. RISO-R-1213(EN)., also *J. Nucl. Mat.*, to be published.

Smidt, Jr., F.R., 1970, "Dislocation Channelling in Irradiated Metals," NRL Report, NRL-7078, Naval Research Laboratory .

Sun, L.Z., Ghoniem, N.M., and Wang, Z., Q., 2000, Analytical and Numerical Determination of the Elastic Interaction Energy between Glissile Dislocations and Stacking Fault Tetrahedra in FCC Metals, *J. Mat. Sci. Engr.*, in the press. T

rinkaus, H., Singh B.N., and Foreman, A.J.E., 1997a, *J. Nucl. Mater.*, **249**, 91.

Trinkaus, H., Singh B.N., and Foreman, A.J.E., 1997b, *J. Nucl. Mater.*, **251**, 172.

9.6 Persistent Slip Bands in Fatigue

The spontaneous formation of dislocation patterns is one of the most striking features of plastic deformation of ductile crystalline solids at the micro scale. These patterns consist of alternating dislocation rich and dislocation poor regions usually in the μm range (e.g. dislocation bundles, veins, walls, channels, and dislocation cells). The formation of these patterns is widely believed to be a result of collective interactions between dislocations. Nonetheless, such collective phenomena play a prominent role in determining the general characteristics of plastic deformation, fatigue, and fracture properties of ductile materials.

The dislocation pattern formation process is a consequence of an overproduction of dislocations. Only a small fraction of them is needed to carry plastic deformation, while the rest is stored in the crystal. The deformed crystal, which is supersaturated with dislocations, tends to decrease the internal energy by mutual screening of their elastic fields. If dislocations possess sufficient maneuverability provided mainly by easy cross-slip, the leading mechanism is individual screening. Dislocations are stored in the form of dipoles, which are transformed to dipolar loops of prevailing edge character (i.e. prismatic). A sweeping mechanism was proposed to explain the pattern formation (Kratochvíl and Saxlova 1992). Loops are swept by glide dislocations, or may drift in stress gradients to clusters, and hinder the motion of fresh glide dislocations causing strain hardening. A homogeneous distribution of loops is thus unstable. The current understanding of the above scenario is still only intuitive. The theoretical predictions (Kratochvíl and Saxlova 1992) - (Kratochvíl 2001) are mostly qualitative, a fully quantitative description is hindered by lack of knowledge of the specific mechanisms outlined within this framework. The main objective of the present work is to utilize the dislocation dynamics approach (e.g. (Ghoniem and Amodeo 1990) - (Ghoniem et al. 2000a)), and provide quantitative data needed for continuum and statistical models of pattering.

During the initial stages of cycling at low plastic strain amplitudes (typically $<10^{-3}$), dislocation-rich regions form a pattern known as a matrix structure consisting of snake-like veins (tangles, bundles, loop patches) oriented on average along edge dislocation directions. The veins, which are loosely organized in quasi periodic patterns are surrounded by dislocation poor channels. It has been noted that the tangle (bundles) structure observed in cubic metals at the beginning of the second stage of hardening in tension tends to form an arrangement akin in morphology and size to the vein pattern. The veins (tangles) occupy approximately 50 % of the crystal volume and the density of stored dislocations in the veins increases with deformation. At a certain stage of cycling, the veins become saturated and start to be unstable. The saturation of the matrix structure is a prelude of localization of strain into thin lamellae called persistent slip bands (PSBs).

In the lamellae, the characteristic ladder structure of dipolar dislocation walls (cells) may

develop gradually from leftovers of the veins. The walls and veins contain predominantly narrow prismatic loops. The basic phenomena underlying the process of plastic deformation at the micro scale is the large difference between the internal energy of an ideal crystal and a crystal with dislocations strained by the same amount. This fact creates a thermodynamic driving force which is probably the reason for the highly non-correlated generation of dislocations by the bursts of activated dislocation sources. This process results in an overproduction of dislocations. Only a small fraction of them is needed to carry plastic deformation, while the rest is stored in the crystal. Deformed crystals supersaturated with dislocations tend to decrease the internal energy by mutual screening of their elastic fields. If dislocations possess sufficient maneuverability provided namely by easy cross-slip (solids with wavy slip), the leading mechanism is individual screening. The dislocations are stored in the form of dipoles, which are transformed to dislocation dipolar loops of prevailing edge character or such loops are directly formed. The loops hinder the motion of the fresh glide dislocations causing strain hardening. A homogeneous distribution of loops is unstable. Loops are swept by glide dislocations or are drifted by stress gradients to clusters and a dislocation pattern is formed. In the clusters (tangles, veins, walls) at a sufficient concentration, loops and dislocations start to annihilate, modify the dislocation pattern, and through strain hardening control strain localization.

An approximate analytical model of sweeping of a rigid prismatic loop by a straight glide dislocation has been studied analytically (Kratochvíl, Kroupa and Kubin 1999), and a quantitative criteria for the steady sweeping of the dipolar loop is obtained. Formulas for the stress field of a prismatic rectangular loop of an infinitesimal or finite width have been derived (Verecký, Kratochvíl and Kroupa 2002, Khraishi and Zbib 2002). Alternatively, the components of the stress tensor generated by a single loop has been evaluated by the numerical fast sum method (Ghoniem and Sun 1999a). As these stress fields are rather complex, an accurate method is needed to obtain reliable quantitative data on the sweeping process. For that reason, The parametric dislocation dynamics (PDD) method proposed by Ghoniem, Huang and Wang (Ghoniem, Tong, Huang, Singh and Wen 2002b, Huang and Ghoniem 2003) is employed here for the simulation. We study here the influence of forces between small dislocation dipoles on their individual and collective motion in stress gradients. We also investigate the basic mechanism of early clustering and pattering of dipolar loops that is experimentally observed under fatigue loading conditions.

In section 9.6.1, we develop a model used to simulate the dynamics of a glide dislocation and interacting dipolar loops. Results of the model are given in section 9.6.2, where we investigate the combined motion of a glide dislocation and a single dipolar loop, the behavior of two dipolar loops with and without their mutual interaction forces, and finally the collective motion of a group of dipolar loops under cyclic applied stress. Finally conclusions are given in section 9.6.3.

9.6.1 Dynamics of a Glide Dislocation and Dipolar Loops

We analyze here the dynamics of a single glide dislocation and interacting dipolar loops. There are basically four types of dipolar dislocation loops: vacancy and interstitial loops, each in two possible stable configurations (Verecký et al. 2002). In the analysis here, results for va-

cancy loops in one of the stable configurations are presented. For interstitial loops and other configurations, the results are similar, and will therefore not be presented.

Figure 9.74 shows the initial geometry of a glide dislocation and a single dipolar loop. The dislocation can glide on the (111) slip plane, while the dipolar loop can only move along its own glide cylinder, i.e. along the direction of the Burgers vector $[10\bar{1}]$. We assume here that the dipolar loop is a parallelogram. Its two long arms are parallel to the edge orientation $[1\bar{2}1]$ with a length of 60 nm and glide on (111) slip plane, while the two short arms glide on the $(1\bar{1}1)$ slip plane. The relative distance of the two long arms is chosen such that the dipolar loop plane and the glide plane (111) for the two long arms form an angle of 45° as shown in Figure 9.74-b. The height of the dipolar loop is taken as 4 nm (Tippelt, Bretschneider and Hahner 1997), which is measured by the distance between the two (111)glide plane. The originally straight glide dislocation with the same Burgers vector as the dipolar loop can have any orientation, and is pinned at both ends. We choose the glide plane normal as the z-axis, and the direction of the glide dislocation as the x-axis. The distance between the slip plane of the glide dislocation and the center of the loop is its stand-off distance, and is denoted by D, as shown in Figure 9.74-b. The distance of the projection of the center of the dipolar loop on the glide plane to the initial dislocation position is denoted by d. Thus the coordinates of the position of the dipolar loop in this local coordinate system can be written as (x,d,D). The geometric configuration and dimensions follow the experimental observations in reference (Tippelt et al. 1997).

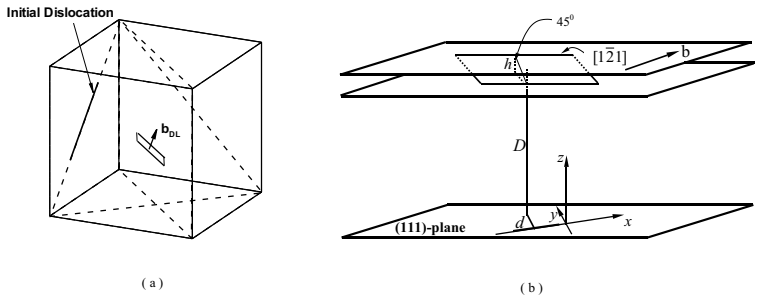

Figure 9.74: Geometry and initial configuration of a dipolar loop and a glide dislocation. (a) relative positions in 3D geometry. (b) representation of the dipolar loop and dislocation in the local coordinate system.

Figure 9.75 shows the deformation of a dipolar loop initially located at (0,30,20) under the influence of the glide dislocation and a shear stress $\tau = 4$ MPa. The glide dislocation and the four segments of the dipolar loop interact simultaneously under the influence of an external shear stress. It is shown that the deformation of the 2 short segments is very small, and they are almost straight. The maximum relative deflection of the two long arms is less than 1 % of their length. Thus the overall deformation of the dipolar loop is very small, and can be neglected. As a result, we will assume here that the dipolar loop shape is rigid under relatively low applied

shear stresses, and that it moves as a whole along the direction of its Burgers vector. The position of a loop is determined only by the coordinates of its center. A rigid approximation for the dipolar loop motion is thus possible. In all simulations, the material parameters are for Nickel (the shear modulus $\mu = 80$ GPa, Poisson's ratio $\nu = 0.33$, and $|\mathbf{b}|$=0.25 nm). We also assume that the effect of dislocation dissociation into partials in Nickel is small and can be neglected.

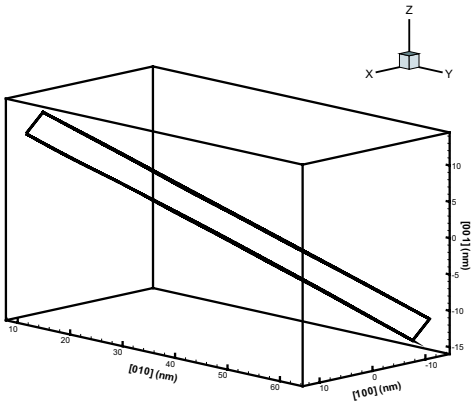

Figure 9.75: Configuration of the dipolar loop describe in Figure 9.74 under an external shear stress $\tau = 4$ MPa, with full interaction between its segments. The coordinates of the dipolar loop center are (0,30,20).

The equation of motion for the center of a loop in the rigid approximation can be written as:

$$\frac{dx_i^{DL}}{dt} = f^{dis} + \sum_{j \neq i} f_j^{DL} - f^{friction} \tag{9.61}$$

Here, x_i stands for the position of the ith dipolar loop center along the axis of its glide cylinder. f^{dis} and f_j^{DL} are force components along the glide direction generated by the stress fields of the glide dislocation and the interaction forces from other dipolar loops, respectively. $f^{friction}$ is the lattice friction, which introduces a threshold for the motion of the dipolar loop (Kubin and Kratochvíl 2000), it varies with the selection of specific material. The force components f^{dis} and f_j^{DL} have the general form:

$$f = \oint_{DL} (\boldsymbol{\sigma} \cdot \mathbf{b} \times \mathbf{t}) \cdot \mathbf{b}/b \, dl \tag{9.62}$$

where $\mathbf{b}$ stands for the Burgers vector, $\boldsymbol{\sigma}$ is the stress field of either the dislocation or of the j'th dipolar loop exerted on the i'th loop. The stress $\boldsymbol{\sigma}^{dis}$ is calculated by the fast sum method

as introduced in (Ghoniem and Sun 1999a). The stress of a loop $\boldsymbol{\sigma}_j^{DL}$ is easily computed by summing up the analytical solution (Devincre 1995) of the 4 straight segments of the dipolar loop. It is to be noted here that a spatially uniform stress field has no effect on the motion of a dipolar loop, as a result of the closed line integration giving a net zero force on the loop.

Once the parametric curve for the dislocation segment is mapped onto the scalar interval $\omega \in [0,1]$, the stress field everywhere is obtained as a fast numerical quadrature sum (Ghoniem and Sun 1999a). Let us define the following dimensionless parameters: $\mathbf{r}^* = \frac{\mathbf{r}}{a}, \quad \mathbf{f}^* = \frac{\mathbf{F}}{\mu a}, \quad t^* = \frac{\mu t}{B}$. Here, a is the lattice constant, μ the shear modulus, B the mobility and t is time. Following reference (Ghoniem et al. 2000a), a dislocation can be divided into N_s segments. In each segment Γ_j, we can choose a set of generalized coordinates q_m at the segment ends, thus allowing parameterization of the form: $\mathbf{r}^* = \mathbf{CQ}$. Here, $\mathbf{C} = [C_1(\omega), C_2(\omega), ..., C_m(\omega)]$, $C_i(\omega), (i = 1, 2, ...m)$ are shape functions dependent on the parameter $(0 \le \omega \le 1)$, and $\mathbf{Q} = [q_1, q_2, ..., q_m]^\top$.

Let, $\mathbf{f}_j = \int_{\Gamma_j} \mathbf{C}^\top \mathbf{f}^* \left|\mathbf{ds}\right|, \quad \mathbf{k}_j = \int_{\Gamma_j} \mathbf{C}^\top \mathbf{C} \left|\mathbf{ds}\right|$ be the total force vector on a curved segment Γ_j, and the corresponding stiffness matrix, respectively. Following a procedure similar to the Finite Element Method (FEM), the equations of motion for all curved segments can be assembled in global matrices and vectors, as:

$$\mathbf{F} = \sum_{j=1}^{N_s} \mathbf{f}_j, \qquad \mathbf{K} = \sum_{j=1}^{N_s} \mathbf{k}_j \tag{9.63}$$

and the equations of motion can be expressed as:

$$\mathbf{K} \frac{d\mathbf{Q}}{dt^*} = \mathbf{F} \tag{9.64}$$

EQN. 9.64 represents a system of ordinary differential equations, which describe the motion of an ensemble of interacting dislocations. Numerical integration of this system of coupled equations (EQN. 9.61 and 9.64) was carried out by the step forward Euler explicit integration method. The glide dislocation is typically discretized into 22 segments, and cubic splines are used to approximate the shape of each segment. The overall time step is controlled such that the maximum displacement of any dipolar loop or a node on the gliding dislocation is less than 0.01 nm within a time step.

9.6.2 Results

Conditions for the dislocation sweeping of dipolar loops proposed by Kratochvíl *et al.* (Kratochvíl et al. 1999), as the basic mechanism leading to the formation of Persistent Slip Bands (PSB), which was based on the assumptions of the interaction between straight rigid dislocation and dipolar loops, relies on a number of key processes. In this section, we present results that show quantitative assessments of some of the basic ingredients in the sweeping mechanism. First, we analyze the motion of a single dipolar loop that is simultaneously interacting with a glide dislocation. Then, we show results for two dipolar loops interacting with a glide dislocation to quantify the role of inter-dipolar forces on their coupled motion. And finally, the

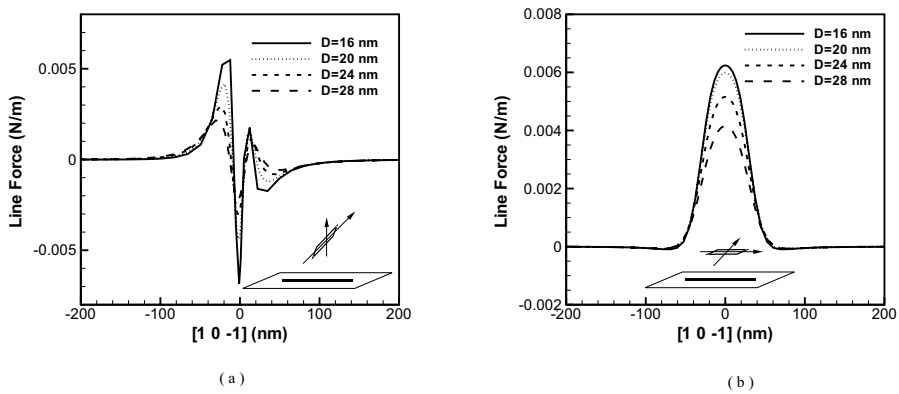

Figure 9.76: Distribution of line force per unit length generated on an initially straight dislocation line by a dipolar loop situated at various stand-off distances. The coordinates of the dipolar loop are (0,30,D). (a) The direction of the dislocation is normal to the loop's major axis. (b) The direction of the dislocation is parallel to loop's major axis.

collective motion of groups of dipolar loops is investigated as a pre-requisite for the initiation of PSBs during fatigue loading conditions.

Glide Dislocation and a Single Dipolar Loop

In the following calculations, the position of the dipolar loop relative to the glide plane is (0,30,D), and the glide dislocation is oriented along $[1\bar{2}1]$. Figure 9.76-a shows the distribution of the resolved shear force per unit length exerted by the dipolar loop on a straight glide dislocation, which lies along $[10\bar{1}]$, calculated for various stand-off distances. When the main loop axis is normal to the dislocation direction, the dipolar loop generates rapid asymmetric forces on the dislocation, as can be seen in Figure 9.76-a. The force distribution on the dislocation is shown in Figure 9.76-b, where the main axis of the dipolar loop is oriented along the dislocation line. The force distribution is symmetric in this configuration. The calculations clearly indicate that the range of the dipolar force on the dislocation is fairly localized, and is confined to about twice the larger dimension of the loop (i.e. $\sim$ 120 nm). As a result of such rapid dipolar force spatial variations, the method of PDD (Ghoniem et al. 2000a) is found to be very suitable.

Dipolar loop forces deform the dislocation line, and this in turn, produces stress gradients in the vicinity of the loop itself. Thus, the mere presence of a dipolar loop close to a straight dislocation generates forces on the loop tending to move it along. Once the effective total force on the dipolar loop exceeds the lattice friction force (the friction stress is assumed to be 8 MPa (Kubin and Kratochvíl 2000)), the loop moves along its glide cylinder, as governed by EQN. 9.61, and consequently changes the force distribution on the dislocation again. Figure

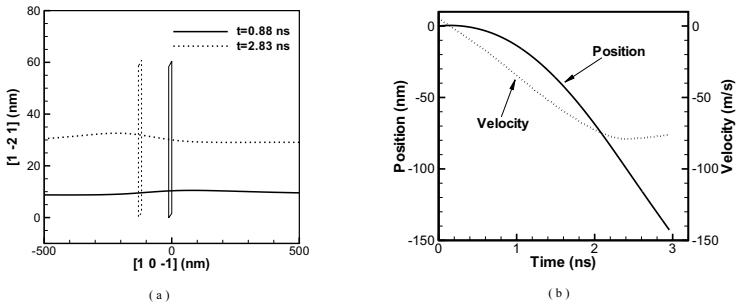

Figure 9.77: Interaction between a screw dislocation and a mobile dipolar loop under an external shear stress $\tau = 4$MPa. The initial condition of the dipolar loop is the same as that in Figure 9.76. Note that the scale on the axes is different. (a) Relative position of the dipolar loop and configuration of the dislocation at 0.88 ns and 2.83 ns, respectively. (b) Loop position and velocity as functions of time.

9.77 shows the simultaneous motion of a dipolar loop and the dislocation as obtained from the numerical integration of EQNs. 9.61 & 9.64. The projection of the configuration on the slip plane is shown in Figure 9.77-a, while the position of the dipole center along its glide cylinder is given in Figure 9.77-b.

The dipolar loop is swept away from its original location by the stress gradient generated from the curved dislocation. At the beginning of the process, the stress gradient is low, thus the velocity of the dipolar loop is low. After about 0.5 ns, the dipolar loop forces result in higher dislocation curvature. Thus, the loop is driven away faster with an increasing velocity. At about 2.5 ns, the loop reaches a terminal velocity of about 75 m/s, as shown in Figure 9.77-b. During the simulation, the two ends of the dislocation are pinned. In order to remove boundary effects of the glide dislocation, we choose a long dislocation with an initial length of 4 μm.

Under cyclic stress conditions, the applied stress is reversed within each cycle. We use here an applied shear stress with an amplitude of 4 MPa above the friction stress. The glide dislocation passes back and forth under the dipolar loop. However, the gradient vector of the stress field does not change its sign during stress reversals, because it depends only on the dislocation shape. Thus, the interaction force between the dipolar loop and the dislocation keeps the loop moving along the same initial direction with each oscillation. Figure 9.78 shows the position of the dipolar loop center as a function of the number of stress cycles.

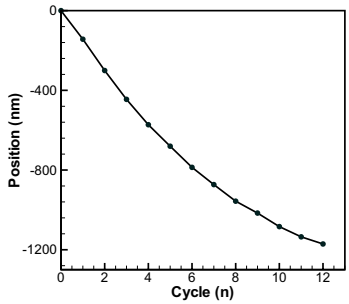

Figure 9.78: Change of position of the dipolar loop as a function of the number of stress cycles.

The Effects of Mutual Interaction Between Dipolar Loops

One important factor that controls the collective motion of dipolar loop groups is the influence of inter-loop forces. To study this effect, we examine here the interaction between two vacancy-type dipolar loops. The force as a function of the mutual position of the two loops is shown in Figure9.79. The stand-off distances of the loops are 12 nm and 20 nm, respectively. It is shown in Figure9.79-a that the inter-loop force is a complex function of their relative distance, and that the range of influence is rather small. This feature enables the introduction of a cut-off distance when we perform large-scale simulations. Figure9.79-b shows the mutual driving force when the relative $\Delta y = 0$ between loops (refer to Figure 9.74 for the coordinate system). Inter-dipole forces become small and negligible when the relative distance is larger than approximately twice the loop size.

Figure 9.80 demonstrates the interaction between a glide dislocation and two dipolar loops, initially located at (-5,30,24) and (5,30,24) respectively. The Burgers vector of the glide dislocation and the loops is $\mathbf{b}=\frac{1}{2}[10\bar{1}]$. The dislocation sweeps both loops away to the negative side, as shown in Figure 9.80-b. Due to their close distance, the mutual interaction between the two dipoles is very strong. Thus the second dipolar loop is pushed to the opposite direction until their relative distance is around 40 nm, where their mutual interaction decreases to around zero, They were then moved almost independently by the dislocation cusp, as shown in Figure 9.80-a. The stress state of the dipolar loops generated a cusp on the dislocation line. This cusp changes the stress state, and in this way modifies the motion of the dipolar loops.

The importance of inter-loop forces on the dynamics of dipole-dipole-dislocation interactions is demonstrated in Figure 9.81. The centers of two loops are initially located at (-10,30,24) and (10,20,24). In this configuration, the loops are bound together due to their mutual interaction. If mutual loop interaction is artificially switched off, the two dipolar loops move quite independently from one another, with the latter one moving a little bit faster than the leading one, as seen in Figure 9.81. On the other hand, if mutual interaction is included, inter-loop binding

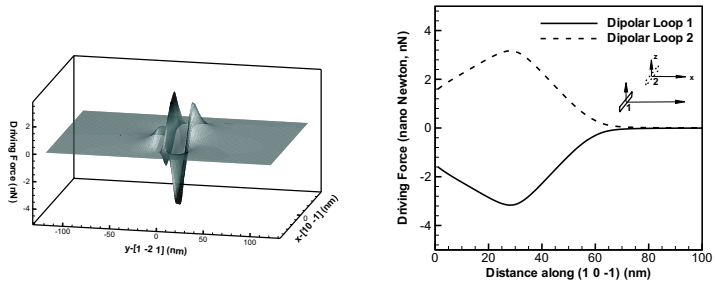

Figure 9.79: The effect of mutual interaction between two parallel dipolar loops. The stand-off distances are 12 nm and 20 nm, respectively. Both loops have the same Burgers vector $\mathbf{b}=[10\bar{1}]$. (a) Driving force generated by the first dipolar loop on the second. x & y stand for their relative horizontal distance. (b) The same driving force for $y = 0$. The dashed and solid lines stand for the forces of dipolar loop 1 and 2, respectively.

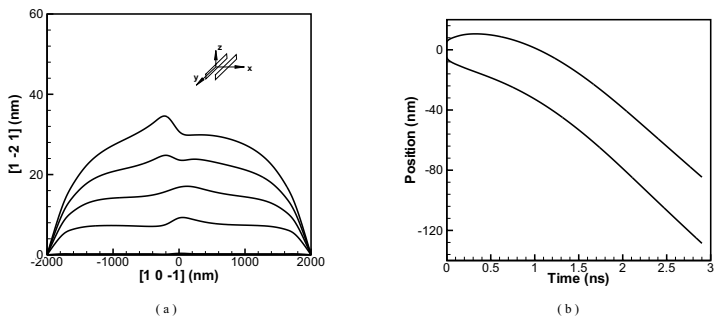

Figure 9.80: Interaction between a Frank-Read source with an initial screw orientation and two mutually interactive dipolar loops, initially located at(-5,30,24) and (5,30,24), respectively. Both dislocation and dipolar loops have $\mathbf{b}=\frac{1}{2}[10\bar{1}]$. (a) Dislocation configuration at different times (time interval Δt=0.7 ns). (b) Change of position for the two loops as a function of time.

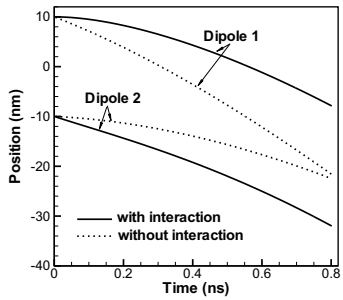

Figure 9.81: Comparison between the effects of including and excluding the mutual interaction of the two dipolar loops. The two dipolar loops are initially located at(-10,30,24) and (10,20,24) respectively.

forces are stronger than forces exerted by the glide dislocation. The loops move as a group, with their relative separation almost kept unchanged.

Collective Motion of Dipolar Loops

To demonstrate the collective sweeping of dipolar dislocation loops, the dynamics of interaction between a glide dislocation and 20 loops is simulated. The dislocation is pinned at its ends, representing a Frank-Read source, and is cycled by the applied stress. The loops are initially randomly distributed in the vicinity of the dislocation slip plane, in the range of distances -300 nm $\sim$ 300 nm, as shown in Figure 9.82-a. The dislocation line is very long (4 μm), so as to remove the effects of pinning boundary conditions on dipolar loop dynamics. Successive configurations of this system are shown in Figure 9.82-b through Figure 9.82-d. After a critical number of cycles, dipolar loops separate into two clusters, and both groups move in the negative direction. The dynamics of the interaction process is displayed in a *trajectory* plot, shown in Figure 9.83. Two well-separated loop clusters are formed after a number of cycles of the order of 20, as can be seen in Figure 9.82-d and Figure 9.83. Some loop pairs are strongly coupled together, retaining their relative positions throughout the entire simulation (see the trajectories of two loops at the lower end of Figure 9.83), while most others execute complex trajectories that cannot be predicted a priori. Nevertheless, the final configuration is represented by dipolar loop clusters swept into two well-separated groups. The glide dislocation then moves in the loop-free channel.

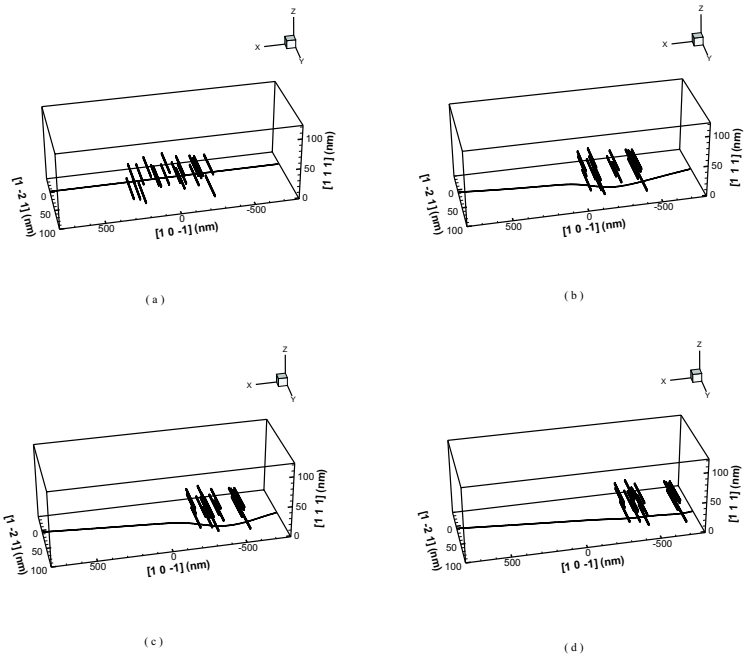

Figure 9.82: The relative configuration of 20 dipolar loops at the end of different cycles: (a)-initial, (b)-5^{th} cycle, (c)-10^{th} cycle, (d)-15^{th} cycle

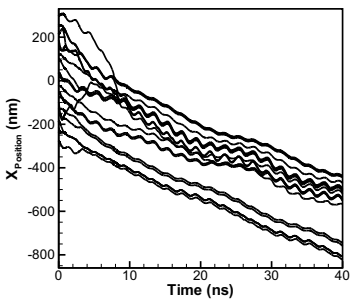

Figure 9.83: *trajectory* plot of the dynamics of 20 interacting dipolar loops, driven by an oscillating screw dislocation.

9.6.3 Conclusions

The results presented here show that the parametric dislocation dynamics method (Ghoniem and Sun 1999a, Ghoniem et al. 2002b) is a convenient tool for studies of elementary mechanisms of dislocation pattering caused by elastic interactions amongst defects. The method is accurate enough to deal with complex stress fields associated with the dynamic motion of dipolar dislocation loops and glide dislocations. The present investigation has demonstrated a number of physical processes involved in the sweeping mechanism:

1. The stress field of a dipolar loop forms a small cusp on the glide dislocation, which localizes high stress gradients in its vicinity, and the loop appears to be riding on that cusp.

2. Detailed investigation of loop-loop interaction forces show that such forces are critically important to the sweeping mechanism. The cusp on the dislocation line caused by one loop leads to indirect coupling with other loops, and this effect facilities loop cluster formation. On the other hand, when two loops are on different glide cylinders, and their inter-loop force barrier is overcome by the force exerted by the glide dislocation, loops trap one another in their mutual interaction field and move together. This self-trapping effect appears to be essential to the formation of loop clusters.

3. Dislocation dynamics simulations demonstrate that the loop clustering mechanism plays an important role in the process of sweeping, which results from the complex interaction between loops and glide dislocations. The sweeping process has been tested using fixed-ends of a glide dislocation that is about 4 μm long and 20 rigid dipolar loops.

Chapter 10

Continuum Dislocation Theory

Chapter 11

Kinetic Monte Carlo Simulation of Defects

11.1 Experimental Observations of Nano-defects

The microstructural evolution in both fcc and bcc metals produced by neutron irradiation has been studied for a long period of time. Under neutron irradiation, primary defect clusters, which are directly produced in displacement cascade, play an important role in microstructural evolution and changes in properties of irradiated materials. Evidence for the existence of self-interstitial atom (SIA) and vacancy cluster within the cascade volume has been provided by experimental methods as well as by computer simulations. For example, Diffuse X-ray scattering on fast neutron irradiated metals at temperatures below stage I provide evidence for spontaneous SIA cluster formation in cascades (von Guerard, Grasse and Peisl 1980, **?**, **?**). Molecular dynamics (MD) studies have also established the fact that SIA clusters are produced directly in high energy cascades without need for diffusion during the cooling down phase of the cascade (**?**, Foreman, English and Phythian 1992, **?**, **?**, Phythian, Stoller, Foreman, Calder and Bacon 1995, **?**, Osetsky, Victoria, Serra, Golubov and Priego 1997, Soneda and Diaz de la Rubia 1998, Bacon, Gao and Osetsky 2000). Small interstitial loops can further organize to make up patches or *rafts* at elevated temperature (Brimhall and Mastel 1970, Stiegler and Bloom 1971, **?**), and dislocations are often heavily decorated by SIA clusters in the form of small interstitial loops (Stiegler and Bloom 1971, Trinkaus, Singh and Foreman 1997, Singh et al. 1997). Under some conditions, say a high temperature for instance, a raft of small closely spaced loops becomes unstable due to easy proceeding of glide and climb, and can eventually result in a large dislocation loop (Brimhall and Mastel 1970).

Rafts of SIA loops and decoration of dislocations with loops have become a crucial issue that is concerned with the understanding of radiation hardening under cascade damage conditions. It has been experimentally observed that in the deformation process of metals and alloys under cascade damage conditions an increase of the upper yield stress without dislocation generation occurs and is followed by a yield drop and plastic instability (Singh et al. 1997). A 'cascade

induced source hardening' (CISH) model has been proposed by Singh et al. (Singh et al. 1997) and applied to explain the occurrence of yield drop, in which a dislocation decorated with interstitial loops is assumed to be confined by the surrounding atmosphere of interstitial loops and unable to move as supposed until the applied resolved stress reaches a high level so that the dislocation can be detrapped from cluster atmospheres in the vicinity of the glide plane. Huang and Ghoniem (Huang and Ghoniem 2002) investigated the interaction dynamics between sessile SIA clusters and dislocations in terms of elastic interactions with various SIA cluster densities, the spatial and size distributions of cluster, and the orientation distribution of individual Burgers vectors by using the method of parametric dislocation dynamics (PDD) simulations. A considerably smaller critical resolve shear stress (CRSS) was found comparing with the results of Kroupa's model (**?**) of dislocation–defect cluster interaction, and its extension by Trinkaus et al. (Trinkaus et al. 1997), which were based on calculations of elastic interaction forces between dislocations and defect clusters in rigid and static configurations.

Being associated with post-irradiation deformation behavior and post-deformation microstructures, properties of clusters of vacancies and SIAs have received considerable attentions because of their important effects on microstructural evolutions. The escalation of understanding the production, migration, and characters of the SIA clusters has lead to the development of dislocation- and production-bias (Woo and Singh 1992) theories to explain long-term damage accumulation and microstructural evolution in irradiated materials. Since these atomic-scale cluster processes like migration, agglomeration, recombination etc., are difficult to observe *in situ*, much of the understanding is extracted from modelling and simulation or inferred from experimental observations. In addition to the identification of defect cluster formation directly in cascades, MD simulations have demonstrated a significant character of these SIA clusters produced in the cascades that a large portion of them are highly glissile (Foreman et al. 1992). Computer simulation has also revealed that large SIA clusters in α-Fe can collapse to form perfect dislocation loops with Burgers vector $\mathbf{b} = \frac{1}{2} < 111 >$ that have $\{110\}$ habit planes and execute one-dimensional (1D) random motion in the slip direction (Wirth, Odette, Maroudas and Lucas 2000, Wirth, Odette, Maroudas and Lucas 1997, Soneda and de la Rubia 2001, Osetsky, Bacon and Serra 1999). The indirect experimental evidence for the intracascade clustering as well as for the 1D glide of SIA clusters have existed in the literature for quite some time (Trinkaus, Singh and Foreman 1993).

In the study of radiation damage, MD simulations using semi-empirical embedded-atom method (EAM) interatomic potentials have played a very important role in understanding the details of defect production in displacement cascades, and in helping to study the dynamics of point defect and defect cluster diffusion. Comprehensive reviews of recent development of MD simulations of radiation damage have been given by Diaz de la Rubia (**?**) and Osetsky et al. (**?**). Radiation damage, however, includes a vast range of irradiation effects, such as production and diffusion of point defects, and their interaction with microstructures, which take place over time and length scales than span many order of magnitude. MD techniques are inapplicable to deal with microstructural evolution in irradiated materials due to its limitation on time and length scales, or at least not solely capable to do so. Kinetic Monte Carlo (KMC) simulations, on the other hand, provide another option to perform atomic-level modellings of defect kinetics and microstructural evolution over relevant length and time scales. KMC

has been used to investigate the local short-term intracascade annealing of individual cascade (Heinisch and Singh 1997) as well as low dose defect accumulation (Heinisch and Singh 1999). In the present paper, KMC techniques are used to study a key aspect of microstructure evolution under irradiation: the inhomogeneity and segregation of point defects and damage accumulation by diffusion and interaction, and the resulting dislocation decoration and formation of rafts of interstitial clusters.

Using Foreman and Eshelby's (Foreman and Eshelby 1962) calculation of elastic interaction of prismatic dislocation loops, Barnes (Barnes 1963) presented a primary discussion on the migration of point defects by slip or climb or by both processes, and suggested a "rafts" configuration of loops which resulted from loops interacting elastically with others on neighbouring basal plane and thereby adjusting their positions and orientations to take up low energy positions. The experimental observation of rafts of loops was provided for graphite irradiated at 150^{O}C and subsequently annealed as well (Barnes 1963). A comprehensive and systematic investigation of the development of microstructure as a function of irradiation temperature was later executed by Brimhall and Mastel (Brimhall and Mastel 1970) for molybdenum in 1970. Even though the formation of rafts of small interstitial clusters/loops is one of the most striking features under cascade damage conditions and has been found for quite some time this phenomenon has not been investigated systematically in the past. Brimhall and Masterl's work still remains to be the most recognized on the mechanism of raft formation so far. They were the first to report the observation of raft formation in Mo. Through use of transmission electron microscopy (TEM), it was found that at low irradiation temperatures, ˜50 ^{O}C, existing small dislocation loops, presumably interstitial, grow by point defect addition; at intermediate temperatures, 400 to 600 ^{O}C, small interstitial loops can migrate and agglomerate into rafts; at high temperatures, 600 to 800 ^{O}C, the loops are highly mobile to form large loops, and eventually interact with each other to produce a coarse dislocation network. They discussed the possible mechanisms of formation of loops rafts and dislocation decoration by loops and attributed them to loop glide combine with self-climb, though their treatment was limited to higher temperatures where both prismatic glide and conservative climb were both operative. Eyre, Maher and Bartlett (Eyre, Maher and Bartlett 1971) have carried out experimental observations and theoretical calculations on the damage structures in molybdenum irradiated by neutrons, and concluded that the growth of interstitial loops during post-irradiation annealing also occurs by a combined glide and climb mechanism. Brimhall and Mastel (Brimhall and

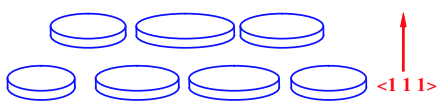

Figure 11.1: Idealized representation of an side view of prismatic edge dislocation loops comprising a raft

Mastel 1970) assumed that prismatic gliding of loops did not occur at 323 K. However, recent molecular dynamics simulations have demonstrated that small SIA loops glide rapidly via correlated diffusion of SIAs in the clusters/loops (Foreman et al. 1992), and furthermore, Trinkaus

et al. (Trinkaus et al. 1997) have shown that the decoration of dislocation and formation of rafts are attributed to the one-dimensional glide of SIA clusters to a great extent. An idealized configuration for a raft (Brimhall and Mastel 1970) was also proposed with using the elastic calculations by Foreman and Eshelby (Foreman and Eshelby 1962). The edge-on representation of the configuration for this idealized raft is shown in Figure 11.1. Elastic analysis shows that loops lying at 42.4^{O} with respect to one another render a minimum interaction energy and form a stable configuration. It was believed that rafts form by loops having identical Burgers vectors gliding together as a result of the elastic interaction between the loops, but being prevented from complete coalescence by the limiting process of self climb (**?**). Since then more subsequent experimental observation of raft formation in Mo and TZM (Mo-0.5Ti-0.1Zr) have been reported (Sikka and Moteff 1974, **?**, Evans 1980, Yamakawa and Shimomura 1988, **?**, Singh, Evans, Horsewell, Toft and Muller 1998). The formation of rafts of interstitial loops in the monocrystalline Mo was observed occurring at a relatively low dose level of 5.4×10^{-3} dpa (Singh et al. 1998). The segregation of the microstructure into rafts of loops and isolated loops eventually leads to a very heterogeneous microstructure at a dose level of 0.16 dpa. Eldrup and his co-workers (Eldrup et al. 2002) investigated the difference in defect accumulation behavior, mainly concerned about void nucleation and growth, between fcc Cu and bcc Fe under neutron irradiation to fluences in the range of 10^{-4} to 0.8 dpa. TEM observations show that the density of SIA clusters both in Fe and Cu first increases with dose. At doses higher than $\simeq 0.01$ dpa, the clusters begin to segregate and form rafts of SIA clusters. The formation of the rafts-like structures is significantly more efficient in bcc Fe than in fcc Cu. A TEM photograph of formation of rafts of loops in Fe irradiated to a dose of 0.72 dpa was presented, the engineering stress-strain curve by tensile test for the iron specimen irradiated to 0.72 dpa exhibited a strong yield drop as well. In their experimental observations on void formations in nickel 270 irradiated from 1×10^{18} to 1.5×10^{22} neutrons/cm^2 at various temperatures, Stiegler and Bloom (Stiegler and Bloom 1971) also reported rafts of small, perfect dislocation loops, which they presumed as interstitial, were dispersed throughout the specimens. Most experimental results suggest that a raft is made up of a bunch of clusters of small interstitial loops, all having the same Burgers vector, the raft as a whole having a clear $< 111 >$ habit plane identical to the Burgers vector of the loops. The size and distribution of rafts are heavily depended on the material purity, irradiation temperature and irradiation dose, and the size spectrum may range from ˜100 Å to more than 1000 Å (Brimhall and Mastel 1970, **?**).

In many microstructural studies of neutron irradiated metals and alloys segregation of small dislocation loops of SIA type is often observed in the vicinity of grow-in dislocations in form of a 'Cottrell-like' atmosphere (Cottrell 1953). Fig.11.2 shows the structure of a coarse dislocation network with a high concentration of small loops located on or near the dislocation lines in Nickel 270 irradiated to a fluence of 3.2×10^{19} neutrons/cm^2 (Stiegler and Bloom 1971). The phenomenon of decoration of dislocations by small interstitial loops under cascade damage conditions have been observed in a wide range of metals and alloys, for instance, pure nickel irradiated with 14 MeV neutrons at 300 K (**?**) and 560 K (**?**), Ni−2 at.% Cu and Ni−2 at.% Ge alloys irradiated with 14 MeV neutrons at 563K (**?**), pure copper and copper alloys irradiated with 14 MeV neutrons at 473 K (Satoh, Ishida, Yoshiie and Kiritani 1988), molybdenum irradiated at 500 $^{\mathrm{O}}$C to a fluence of 5.7 $\times 10^{19}$ neutrons/cm^2(Brimhall and Mastel 1970), and

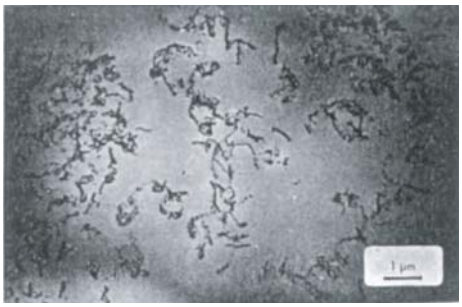

Figure 11.2: Dislocation structure in Nickel 270 irradiated to a fluence of $3.2\times10^{1}9$ neutron/cm^2 (Stiegler and Bloom 1971).

pure single crystal of molybdenum irradiated with fission neutrons to a dose level of 1.6×10^{-1} dpa at 320 K (Singh et al. 1998). The status of investigations on dislocation decoration has a similar situation as on raft formation. The available evidence on dislocation decoration could date back as early as the discovery of raft formation, but it is rather limited and scattered in literatures. No attempt was made to systematically study the phenomenon of dislocation decoration until Trinkaus, Singh and Foreman (Trinkaus et al. 1997) took the first leap on the mechanisms for decoration of dislocations by small SIA loops. Their model suggests that the trapping and accumulation of glissile SIA loops in terms of one-dimensional motion play a predominant role in the occurrence of dislocation decoration. Based on the analysis of experimental observations of plastic deformation in metals irradiated with fission neutron, as well as combining with dislocation decoration phenomenon, Singh, Foreman and Trinkaus (Singh et al. 1997) proposed the so-called 'cascade-induced source hardening' (CISH) model to explain the occurrence of yield drop and plastic instability.

Both raft formation and dislocation decoration heavily depend on an important process, the production and migration of SIA clusters. Theoretically, there are two main mechanisms which could result in the formation and growth of interstitial loops: (1) the acquiring single SIA one at a time, and (2) the migration and aggregation of interstitial clusters. In most of the cases reported, the first mechanism is supposed to play an inferior role on the basis of the fact that the coexistence and simultaneous growth of vacancy and interstitial clusters (Barnes 1963). If the first mechanism dominate the growth of clusters, it is necessary that an interstitial loop mainly acquires interstitial atoms and rejects vacancies. The efficiency of the growth process is predicably to be much lower than when the second mechanism of loops migration are involved. Barnes presented a primary discussion on the direction of migration, magnitude of the driving force, and migration distance by considering two interacting simple prismatic edge dislocation loops in aluminium (Barnes 1963). In reality the situation is much more complex than in the two-interacting-loops case. When it is considered that the vacancy and interstitial loops each have all the four possible Burgers vectors, are not simple edge dislocations, have various sizes, and in addition the interactions are not between two loops but with all those nearby, the situation is considerably complex. It is the intention of this paper to shed some lights

on the microstructural evolution, specifically dislocation decoration and raft formation, under displacement cascade conditions with considering interactions between defects.

11.2 Description of Point Defects by Force Multipoles

Most of the following considerations are reviewed from a book by Teodosiu (Teodosiu 1982). A nano-scale defect exerts forces on the atoms in its vicinity, which are different from those acting on these atoms in the perfect lattice. Let $\mathbf{P}^v$ denote the additional forces exerted by a nano-defect centred at $\mathbf{x}'$ on the atom situated at $\mathbf{x}'+\mathbf{l}^v$. According to the definition of Green's function, the force system $\mathbf{P}^v$ generates in an infinite elastic medium the displacement field

$$u_m(\mathbf{x}) = \sum_{v=1}^{N} G_{ms}(\mathbf{x}-\mathbf{x}'-\mathbf{l}^v)P_s^v \tag{11.1}$$

where $\mathbf{G}$ is Green's tensor function of the elastic medium, while N is the number of atoms on which extra forces are exerted. Theoretically, $N=\infty$, but, as $\mathbf{P}^v$ decays very rapidly when $\|\mathbf{l}^v\| \to \infty$, it is usually sufficient to take into account only the forces employed on the first and second nearest neighbors.

Expanding $\mathbf{G}(\mathbf{x}-\mathbf{x}'-l^v)$ in a Taylor series about $\mathbf{x}-\mathbf{x}'$ leads to

$$G_{ms}(\mathbf{x}-\mathbf{x}'-\mathbf{l}^{\mathbf{v}}) = \sum_{k=0}^{\infty} \frac{1}{k!} G_{ms,q_1'q_2'\ldots q_k'}(\mathbf{x}-\mathbf{x}')l_{q_1}^v l_{q_2}^v \ldots l_{q_k}' \tag{11.2}$$

$$= G_{ms}(\mathbf{x}-\mathbf{x}') + G_{ms,n'}(\mathbf{x}-\mathbf{x}')l_n^v + \frac{1}{2!}G_{ms,n'p'}(\mathbf{x}-\mathbf{x}')l_n^v l_p^v + \ldots, \tag{11.3}$$

where $(\cdot)_{,m'} = \frac{\partial(\cdot)}{\partial x_m'}$. Obviously, the expansion (11.2) converges only for sufficiently small values of $\|\mathbf{l}^v\|$, i.e. only if the application points of the forces $\mathbf{P}^v$ are sufficiently close to the investigated nano-defect.

By substituting (11.2) into (11.1), it yields

$$u_m(\mathbf{x}) = \sum_{k=0}^{\infty} \frac{1}{k!} G_{ms,q_1'q_2'\ldots q_k'}(\mathbf{x}-\mathbf{x}')P^{(k)}_{q_1q_2\ldots q_k s} \tag{11.4}$$

$$= G_{ms}(\mathbf{x}-\mathbf{x}')P_s^{(0)} + G_{ms,n'}(\mathbf{x}-\mathbf{x}')P_{ns}^{(1)} + \frac{1}{2!}G_{ms,n'p'}(\mathbf{x}-\mathbf{x}')P_{nps}^{(2)} + \ldots, \tag{11.5}$$

where

$$\mathbf{P}^{(0)} = \sum_{v=1}^{N} \mathbf{P}^v, \qquad P_s^{(0)} = \sum_{v=1}^{N} P_s^v \tag{11.6}$$

is the resultant force, and

$$\mathbf{P}^{(k)} = \sum_{v=1}^{N} \underbrace{\mathbf{l}^v\mathbf{l}^v\ldots\mathbf{l}^v}_{k}\mathbf{P}^v, \qquad P^{(k)}_{q_1q_2\ldots q_k s} = \sum_{v=1}^{N} l_{q_1}^v l_{q_2}^v \ldots l_{q_k}^v P_s^v \tag{11.7}$$

is the multipolar moment of k-th order, $k = 1, 2, ...$, of the system of additional forces $\mathbf{P}^v$ exerted by the nano-defect on its surroundings. In particular, it is called dipole moment, quadrupole moment, and octopole moment, respectively, for the tensors as follows

$$\mathbf{P}^{(1)} = \sum_{v=1}^{N} \mathbf{l}^v \mathbf{P}^v, \qquad P^{(1)}_{ns} = \sum_{v=1}^{N} l^v_n P^v_s \tag{11.8}$$

$$\mathbf{P}^{(2)} = \sum_{v=1}^{N} \mathbf{l}^v \mathbf{l}^v \mathbf{P}^v, \qquad P^{(2)}_{nps} = \sum_{v=1}^{N} l^v_n l^v_p P^v_s \tag{11.9}$$

$$\mathbf{P}^{(3)} = \sum_{v=1}^{N} \mathbf{l}^v \mathbf{l}^v \mathbf{l}^v \mathbf{P}^v, \qquad P^{(3)}_{npqs} = \sum_{v=1}^{N} l^v_n l^v_p l^v_q P^v_s \tag{11.10}$$

Equation (11.4) may be also given a somewhat different interpretation. Namely, it can be shown that Green's tensor function $\mathbf{G}$ satisfies the equilibrium equation

$$c_{ijmn} G_{ms,jn}(\mathbf{x} - \mathbf{x}') + \delta_{is}\delta(\mathbf{x} - \mathbf{x}') = 0 \tag{11.11}$$

in the sense of the theory of distributions. Applying on this equation the differential operator

$$\frac{1}{k!} P^{(k)}_{q_1 q_2 ... q_k s} \frac{\partial^k}{\partial x'_{q_1} \partial x'_{q_2} ... \partial x'_{q_k}} \tag{11.12}$$

and summing with respect to s, we obtain

$$c_{ijmn} \left\{ \frac{1}{k!} P^{(k)}_{q_1 q_2 ... q_k s} G_{ms,q'_1 q'_2 ... q'_k}(\mathbf{x} - \mathbf{x}') \right\} + \frac{1}{k!} P^{(k)}_{q_1 q_2 ... q_k i} \delta_{,q'_1 q'_2 ... q'_k}(\mathbf{x} - \mathbf{x}') = 0 \tag{11.13}$$

Finally, by comparing these relations with the equilibrium equations

$$c_{ijmn} u_{m,jn}(\mathbf{x}) + f_i(\mathbf{x}) = 0, \qquad i = 1, 2, 3 \tag{11.14}$$

we conclude that the body force

$$f_i(\mathbf{x}) = \frac{1}{k!} P^{(k)}_{q_1 q_2 ... q_k i} \delta_{,q'_1 q'_2 ... q'_k}(\mathbf{x} - \mathbf{x}') \tag{11.15}$$

produces the displacement field

$$u_m(\mathbf{x}) = \frac{1}{k!} G_{ms,q'_1 q'_2 ... q'_k}(\mathbf{x} - \mathbf{x}') P^{(k)}_{q_1 q_2 ... q_k s} \tag{11.16}$$

The body force (11.15) is called multipolar force of k-th order, and of strength

$$\tilde{P}^{(k)}_{q_1 q_2 ... q_k s} = \frac{1}{k!} P^{(k)}_{q_1 q_2 ... q_k s} \tag{11.17}$$

By making use of this terminology and comparing (11.4) with (11.16), we may say that the action of a nano-defect on the elastic medium is equivalent to that of a body force field which consists of force dipoles, quadrupoles, octopoles, etc. applied at the center of the defect, namely

$$f_i(\mathbf{x}) = \sum_{k=0}^{\infty} \tilde{P}^{(k)}_{q_1 q_2 ... q_k i} \delta_{,q'_1 q'_2 ... q'_k}(\mathbf{x} - \mathbf{x}') \tag{11.18}$$

the strengths of the multipolar forces being completely determined through (11.17) by the multipolar moments associated with the nano-defect. Kröner was the first to give a systematic description of point defects with the aid of multipolar moments or as multipolar forces of second and higher orders. It should be noted that the resultant force and couple exerted by a nano-defect on its surroundings are zero. Then, the equilibrium condition implies

$$\sum_{v=1}^{N} \mathbf{P}^v = \mathbf{0}, \qquad \sum_{v=1}^{N} \mathbf{l}^v \times \mathbf{P}^v = \mathbf{0} \tag{11.19}$$

The last relation may be rewritten as

$$\sum_{v=1}^{N} \epsilon_{kns} l_n^v P_s^v = \epsilon_{kns} P_{ns}^{(1)} = 0 \tag{11.20}$$

where ϵ_{kns} is so called replacement tensor, or Eddington tensor. It tells us that the dipole moment $\mathbf{P}^{(1)}$ must be a symmetric tensor. Hence, conditions (11.19) are equivalent with

$$\mathbf{P}^{(0)} = \mathbf{0}, \qquad \mathbf{P}^{(1)} = (\mathbf{P}^{(1)})^{\mathrm{T}} \tag{11.21}$$

By introducing (11.21) into (11.4) and taking into account that

$$G_{ms,n'}(\mathbf{x} - \mathbf{x}') = -G_{ms,n}(\mathbf{x} - \mathbf{x}'), \tag{11.22}$$

we obtain

$$u_m(\mathbf{x}) = \sum_{k=0}^{\infty} \frac{(-1)^k}{k!} G_{ms,q_1 q_2 \ldots q_k}(\mathbf{x} - \mathbf{x}') P^{(k)}_{q_1 q_2 \ldots q_k s} \tag{11.23}$$

$$= -G_{ms,n}(\mathbf{x} - \mathbf{x}') P_{ns}^{(1)} + \frac{1}{2!} G_{ms,np}(\mathbf{x} - \mathbf{x}') P_{nps}^{(2)} - \frac{1}{3!} G_{ms,npq}(\mathbf{x} - \mathbf{x}') P_{npqs}^{(3)} + \ldots, \tag{11.24}$$

Equation (11.23) shows that the elastic state produced by a nano-defect in an infinite elastic medium is completely determined by the multipolar moments $\mathbf{P}^{(k)}$, $k = 1, 2, \ldots$, provided Green's tensor function of the medium is known. For an isotropic material this function is

$$G_{ms}(\mathbf{x} - \mathbf{x}') = \frac{1}{16\pi\mu(1-\nu)} \left[\delta_{ms}(3 - 4\nu) \frac{1}{r} + \frac{(x_m - x'_m)(x_s - x'_s)}{r^3} \right] \tag{11.25}$$

where $r = \|\mathbf{x} - \mathbf{x}'\|$. By substituting (11.25) into (11.23), we see that $\mathbf{u}(\mathbf{x})$ is of the order $O(r^{-2})$ as $r \to \infty$, in agreement with the results obtained in modelling point defects by rigid spherical inclusions in an infinite isotropic medium. Assuming that the elastic medium is isotropic, we deduce from (11.25)

$$\frac{\partial G_{ms}(\mathbf{x} - \mathbf{x}')}{\partial x_s} = -\frac{1 - 2\nu}{8\pi\mu(1-\nu)} \frac{x_m - x'_m}{r^3} \tag{11.26}$$

As already mentioned, the elastic field of a nano-defect is characterized by its multipolar moments. The main procedure for evaluating these quantities is to solve the equation system (11.23) with the displacement field $\mathbf{u}(\mathbf{x})$ acquired by MD simulation. As a rough approximation, we can only consider the force system $\mathbf{P}^v$ exerted on the first nearest neighbors and the first term in the Taylor expansion (11.23).

The elastic interaction between nano-defects

In this section we will study the elastic interaction between nano-defects which are simulated by force multipoles acting in an infinite elastic medium. It should be noted that this description of nano-defects provides a good approximation only if the separation distance between defects is large enough. Otherwise, a semi-discrete or fully atomic model of the interacting defects must be adopted.

The elastic interaction energy between a nano-defect located at $\mathbf{x}$ and an elastic displacement field $\mathbf{u}$ is given, according to elastic theory, by the work done against the forces $\mathbf{P}^v$ exerted by the point defect on the neighboring atoms, i.e.

$$\Phi_{\text{int}} = -\sum_{v=1}^{N} \mathbf{P}^v \cdot \mathbf{u}(\mathbf{x} + \mathbf{l}^v) \tag{11.27}$$

By expanding $\mathbf{u}(\mathbf{x} + \mathbf{l}^v)$ in a Taylor series around $\mathbf{x}$, we obtain

$$u_m(\mathbf{x} + \mathbf{l}^v) = \sum_{n=0}^{\infty} \frac{1}{n!} u_{m,j_1 j_2 \ldots j_n}(\mathbf{x}) \mathbf{l}^v_{j_1 j_2 \ldots j_n} \tag{11.28}$$

$$= u_m(\mathbf{x}) + u_{m,i}(\mathbf{x}) l^v_i + \frac{1}{2!} u_{m,ij}(\mathbf{x}) l^v_i l^v_j + \frac{1}{3!} u_{m,ijk}(\mathbf{x}) l^v_i l^v_j l^v_k + \ldots \tag{11.29}$$

Substituting this expansion into (11.27) and considering (11.6), (11.7), and (11.21) yields

$$\Phi_{\text{int}} = -\sum_{n=0}^{\infty} \frac{1}{n!} u_{m,j_1 j_2 \ldots j_n}(\mathbf{x}) P^{(n)}_{j_1 j_2 \ldots j_n m} \tag{11.30}$$

$$= -\left\{ P^{(1)}_{im} u_{m,i}(\mathbf{x}) + \frac{1}{2!} P^{(2)}_{ijm} u_{m,ij}(\mathbf{x}) + \frac{1}{3!} P^{(3)}_{ijkm} u_{m,ijk}(\mathbf{x}) + \ldots \right\} \tag{11.31}$$

In a homogeneous strain field we have $u_{m,i}(\mathbf{x}) = \text{const.}$ and (11.31) reduces to

$$\Phi_{\text{int}} = -P^{(1)}_{im} u_{m,i} = -P^{(1)}_{im} E_{im} \tag{11.32}$$

i.e. only the dipole moments contribute to the interaction energy. Returning to the general case, we recall that the force employed on the nano-defects by the elastic state which generates the displacement field $\mathbf{u}$ is

$$\mathbf{F} = -\text{grad}_{\mathbf{x}} \Phi_{\text{int}} \tag{11.33}$$

Hence, by taking into account (11.31), we have

$$F_s = -\frac{\partial \Phi_{\text{int}}}{\partial x_s} = \sum_{n=1}^{\infty} \frac{1}{n!} u_{m,j_1 j_2 \ldots j_n s}(\mathbf{x}) P^{(n)}_{j_1 j_2 \ldots j_n m} \tag{11.34}$$

$$= P^{(1)}_{im} u_{m,is}(\mathbf{x}) + \frac{1}{2!} P^{(2)}_{ijm} u_{m,ijs}(\mathbf{x}) + \frac{1}{3!} P^{(3)}_{ijkm} u_{m,ijks}(\mathbf{x}) + \ldots \tag{11.35}$$

We can now easily derive the elastic interaction energy of two point defects situated at points $\mathbf{x}$ and $\mathbf{x}'$ in an infinite elastic medium and having the multipolar moments $\mathbf{P}^{(1)}, \mathbf{P}^{(2)}$, ..., and

respectively $\tilde{\mathbf{P}}^{(1)}, \tilde{\mathbf{P}}^{(2)}$, ..., by substituting the expression (11.23) of the displacement field produced by one of the defects into (11.31). The results reads

$$\Phi_{\text{int}} = -\sum_{n=0}^{\infty} \frac{1}{n!} P^{(n)}_{j_1 j_2 \dots j_n m} \sum_{k=1}^{\infty} \frac{(-1)^k}{k!} \tilde{P}^{(k)}_{q_1 q_2 \dots q_k s} G_{ms,q_1 q_2 \dots q_k j_1 j_2 \dots j_n}(\mathbf{x} - \mathbf{x}') \tag{11.36}$$

Since $\mathbf{G}(\mathbf{x} - \mathbf{x}') = O(r^{-1})$ as $r = \|\mathbf{x} - \mathbf{x}'\| \to \infty$, we see that the first three terms of the expression (11.36) decrease as r^{-3}, r^{-4},and r^{-5}, respectively, for sufficiently large values of the separation distance r between the defects.

Representation of nano-defects by force dipoles

Point defects are lattice imperfections having all dimensions of the order of one or more atomic spacing. The point defect may be a vacant sites in the atomic lattice, called a vacancy, a foreign atom replacing one atom of the lattice, called a substitutional atoms, or a atom situated between the normal sites of the lattice, called an interstitial atom. Sometimes, two or more point defects can build characteristic arrangements which are thermodynamically stable to form a point defect cluster. Our interest will be particularly focus on these nano-scalling point defect clusters. The collection of point defects produces viscous effects at a macroscopic scale, which are of great importance for many processes taking place in crystals. Moreover, the interaction of a nano-defect with other crystal defects is mostly of elastic nature. We will try to develop elastic models of nano-defects and methods for calculating the elastic interaction of a defect with other defects.

Firstly, let us consider now in detail the physical significance of the partial derivatives of first order of $\mathbf{G}(\mathbf{x})$. We can obviously write

$$G_{ij,k}(\mathbf{x}) = \lim_{h \to 0} \frac{1}{h} \{G_{ij}(\mathbf{x}) - G_{ij}(\mathbf{x} - h\mathbf{e}_k)\} \tag{11.37}$$

Consequently, the elastic state associated to the displacement field

$$u_i(\mathbf{x}) = G_{ij,k}(\mathbf{x}) \tag{11.38}$$

is the limiting value as $h \to 0$ of a sum of two elastic states: the first corresponds to the concentrated force $\mathbf{e}_j/h$ acting at the origin; the second corresponds to a concentrated load $-\mathbf{e}_j/h$ acting at the point with position vector he_k. A straightforward calculation shows that the resultant of the stress vectors acting on any sphere Σ_η with radius η and center at the origin is zero, while their resulting couple equals $-\mathbf{e}_k \times \mathbf{e}_j$. Following the terminology introduced by Love, we say that the elastic field corresponding to the displacement (11.38) is produced by a unit double force, which is statically equivalent to a directed concentrated couple or to $\mathbf{0}$ according as $j \neq k$ or $j = k$. In the latter case we say that the singularity at the origin is a unit double force without moment. The elastic state corresponding to the displacement field

$$u_i(\mathbf{x}) = G_{ij,j}(\mathbf{x}) \tag{11.39}$$

which is produced by three mutually orthogonal unit double forces without moment acting at the origin, is called a center of compression, whereas the elastic state corresponding to

the opposite of (11.39) is called a center of dilatation. It has been shown that the effects of a vacancy or an interstitial atom can be approximated by a spherical compression center of dilatation center.

In view of formula (11.38), we propose here that a nano-defect of arbitrary geometric shape can be described by a collection of double forces. Specifically, we have

$$u_i(\mathbf{x}) = G_{ij,k}(\mathbf{x} - \mathbf{x}')f_{kj}(\mathbf{x}') \tag{11.40}$$

where f_{jk} is a second order tensor of which the three diagonal components represents three mutually orthogonal force dipoles without moment, and the rest non-diagonal components are force dipoles with moment along $\mathbf{e}_j \times \mathbf{e}_k$. It should be noted that the resultant force and couple of these components consisting f_{jk} should be equal to zero. The condition of zero resultant force can be achieved in terms of the definition of force dipole. Then, the condition of zero net force couple implies that the tensor f_{jk} must be a symmetric tensor, i.e.

$$f_{kj}(\mathbf{x}') = f_{kj}^T(\mathbf{x}') \tag{11.41}$$

Suppose that we have already got the displacement of each and every lattice atom somehow, say by Molecular Dynamics simulation or experiments. We then can use the least square method to determine the point force dipolar system, i.e. f_{jk}, which are unknown and exerted on the center of the defect to characterize the elastic field of the defect. If the real displacement field is denoted by $\tilde{u}(\mathbf{x})$, we define the error function

$$\Pi = \sum_{m=1}^{N} \|\mathbf{u}(\mathbf{x}) - \tilde{\mathbf{u}}(\mathbf{x})\|^2 = \sum_{m=1}^{N} [\mathbf{u}(\mathbf{x}) - \tilde{\mathbf{u}}(\mathbf{x})] [\mathbf{u}(\mathbf{x}) - \tilde{\mathbf{u}}(\mathbf{x})] \tag{11.42}$$

where N is the number of points whose displacements are already known and we used to calculated the error. According to the method of least squares, the best fitting value of f_{jk} has the property that

$$\Pi = \text{aminimum}, \tag{11.43}$$

i.e.

$$\frac{\partial \Pi}{\partial f_{jk}} = 0 \tag{11.44}$$

By solving these six equations we would be able to define a force dipole tensor that can approximately describe the elastic field induced by the existence of the defect.

As far as the interaction energy between two nano-defects is concerned, it can be readily shown that

$$\Phi_{\text{int}} = -\mathbf{f} \cdot \text{grad}\tilde{\mathbf{u}}(\mathbf{x}) = -f_{ij}\tilde{u}_{j,i}(\mathbf{x}) \tag{11.45}$$

where f_{ij} is the force dipole used to represent the nano-defect at $\mathbf{x}$, and $\tilde{\mathbf{u}}(\mathbf{x})$ is the displacement field induced by the defect at $\mathbf{x}'$, which can also be described by a force dipole tensor $\tilde{\mathbf{f}}$. By substituting the expression (11.40) of the displacement field produced by one of the defects into (11.45), it results

$$\Phi_{\text{int}} = -f_{ij}\tilde{f}_{lk}G_{jk,li}(\mathbf{x} - \mathbf{x}') \tag{11.46}$$

Applications

For simplicity, we will choose the geometric center of the nano-defect as origin, i.e., $\mathbf{x}' = \mathbf{0}$.

Vacancy

$$G_{ij} = \frac{1}{16\pi\mu(1-\nu)r}\left[\delta_{ij}(3-4\nu) + \frac{x_i x_j}{r^2}\right] \tag{11.47}$$

$$G_{ij,k} = \frac{1}{16\pi\mu(1-\nu)r^3}\left[-(3-4\nu)\delta_{ij}x_k + \delta_{ik}x_j + x_i\delta_{jk} - \frac{3x_i x_j x_k}{r^2}\right] \tag{11.48}$$

$$u_i = G_{ij,k}f_{kj} = \frac{1}{16\pi\mu(1-\nu)r^3}\left[-(3-4\nu)f_{ik}x_k + f_{ij}x_j + x_i f_{jj} - \frac{3x_i x_j x_k}{r^2}f_{kj}\right] \tag{11.49}$$

At $r = r_0$, the displacement field $\tilde{\mathbf{u}}$ is known as

$$\tilde{u}_r(r_0) = Cr^{-2}, \quad \tilde{u}_\phi = \tilde{u}_\theta = 0 \tag{11.50}$$

where C is an arbitrary constant. Substituting (11.49) and (11.50) into (11.44) yields the equations designed to determine the values of f_{ij}. Actually, the derived equations are not completely mutually independent, and some other relations have to be introduced to help with solving equations. Due to the spherical symmetry of the deformation, only the components of dipolar forces whose indices occur in pairs of equal numbers are non-zero, i.e. $f_{12} = f_{13} = f_{23} = 0$. By solving equations, we obtain

$$f_{11} = f_{22} = f_{33} = 8\frac{(\nu-1)C\pi\mu}{1-2\nu} = -4\pi C(\lambda + 2\mu) \tag{11.51}$$

The field (11.51) represents three mutually orthogonal force dipoles without moment, having equal intensities, and acting at the centre of the point defect, and such distribution of concentrated loads is called a spherical dilatation centre. The values in (11.51) are exactly the same as the solutions given by the elastic theory with the assumption of point defect as rigid spherical inclusion.

Infinitesimal prismatic dislocation loop

Let us assume the loop is at the origin of the coordinate system on the x_1x_2 plane ($n_1 = n_2 = 0$, $n_3 = 1$) and suppose displacement field is given by Kroupa's formula. Namely, the displacements of a pure prismatic infinitesimal dislocation loop with an area δA, $b_1 = b_2 = 0$, $b_3 = b$ are as follows:

$$\begin{aligned}
\tilde{u}_1 &= \frac{K}{6}\frac{x_1}{r^3}\left[-(1-2\nu) + \frac{3x_3^2}{r^2}\right] \\
\tilde{u}_2 &= \frac{K}{6}\frac{x_2}{r^3}\left[-(1-2\nu) + \frac{3x_3^2}{r^2}\right] \\
\tilde{u}_3 &= \frac{K}{6}\frac{x_3}{r^3}\left[1-2\nu + \frac{3x_3^2}{r^2}\right]
\end{aligned} \tag{11.52}$$

where

$$r = \sqrt{x_1^2 + x_2^2 + x_3^2} \tag{11.53}$$

$$K = -\frac{3b_3}{4\pi(1-\nu)}\delta A \tag{11.54}$$

The displacements at $(x_1, 0, 0)$, $(0, x_2, 0)$, and $(0, 0, x_3)$ are

$$\begin{aligned}
\tilde{u}_1^{(1)} &= -\frac{K}{6}\frac{1}{x_1^2}(1-2\nu),\ \tilde{u}_2^{(1)} = \tilde{u}_3^{(1)} = 0, \\
\tilde{u}_2^{(2)} &= -\frac{K}{6}\frac{1}{x_2^2}(1-2\nu),\ \tilde{u}_1^{(2)} = \tilde{u}_3^{(2)} = 0, \\
\tilde{u}_3^{(3)} &= \frac{K}{3}\frac{1}{x_3^2}(2-\nu),\ \tilde{u}_1^{(3)} = \tilde{u}_2^{(3)} = 0,
\end{aligned} \tag{11.55}$$

respectively, However, the displacements at these three points given by (11.49) are

$$\begin{aligned}
u_1^{(1)} &= \frac{1}{16\pi\mu(1-\nu)x_1^2}\left[-4(1-\nu)f_{11} + f_{22} + f_{33}\right],\ u_2^{(1)} = -\frac{(1-2\nu)f_{12}}{8\pi\mu(1-\nu)x_1^2}, \\
u_3^{(1)} &= -\frac{(1-2\nu)f_{13}}{8\pi\mu(1-\nu)x_1^2} \\
u_1^{(2)} &= -\frac{(1-2\nu)f_{12}}{8\pi\mu(1-\nu)x_2^2},\ u_2^{(2)} = \frac{1}{16\pi\mu(1-\nu)x_2^2}\left[-4(1-\nu)f_{22} + f_{11} + f_{33}\right], \\
u_3^{(2)} &= -\frac{(1-2\nu)f_{23}}{8\pi\mu(1-\nu)x_2^2} \\
u_1^{(3)} &= -\frac{(1-2\nu)f_{13}}{8\pi\mu(1-\nu)x_3^2},\ u_2^{(3)} = -\frac{(1-2\nu)f_{23}}{8\pi\mu(1-\nu)x_3^2}, \\
u_3^{(3)} &= \frac{1}{16\pi\mu(1-\nu)x_3^2}\left[-4(1-\nu)f_{33} + f_{11} + f_{22}\right]
\end{aligned} \tag{11.56}$$

Substituting (11.55) and (11.56) into (11.42) results

$$\Pi = \sum_{m=1}^{3}\sum_{i=1}^{3}\left[u_i^{(m)} - \tilde{u}_i^{(m)}\right]^2 \tag{11.57}$$

By solving the equations given by (11.44) we obtain

$$f_{12} = f_{13} = f_{23} = 0, \quad f_{11} = f_{22} = -\lambda b_3 \delta A, \quad f_{33} = -(\lambda + 2\mu)b_3 \tag{11.58}$$

It can shown that (11.58) are exactly the same as those given by Kroupa. It implies that the displacement field produced by force dipoles (11.58), as well as the strain and stress field will be the same as the results derived by Kroupa.

11.3 The Kinetic Monte Carlo (KMC) Method

11.3.1 The n-fold way algorithm

In Metropolis MC methods we decide whether to accept a move by considering the energy difference between the states. In KMC methods we use rates that depend on the energy

difference between the states. The term "Kinetic Monte Carlo" was initiated by Horia Metiu, Yan-Ten Lu and Zhenyu Zhang in a 1992 Science paper (Metiu, Lu and Zhang 1992). The paper first pointed out the demands on atomic level control of modern electronic and photonic devices and the importance of *in situ* STM observations of small atomic "clusters" to a theorist who wants to understand growth and segregation; it then elaborated upon the usefulness of KMC simulations in reproducing these experimental observations. The basic feature of their model was to move atoms site-to-site on a square lattice terrace. They postulated rates for all of the elementary processes involved, such as the site-to-site jumps, the jumps to leave or join a step or an existing adsorbate cluster, and so forth. The atoms were deposited on the surface and moved from site to site with a frequency proportional to the rate of the respective move: if the rate constant of the i-th kinetic process was r_i, the largest rate was chosen as a reference and denoted r_r. The probability $P_i = r_i/r_r$ was then used in a MC program as the probability that the atom performed a jump i. The work used Voter's transition state theory (Voter and Doll 1985) to monitor the simulation time. The essence through the references can be traced to Bortz, Kalow, and Lebowitz's n-fold way algorithm (**?**, Lu, Petroff and Metiu 1990, Kang and Weinberg 1988).

The n-fold way idea was created to replace the standard MC algorithm in generating new configurations in simulating Ising spin systems. In or near the equilibrium state, the standard MC scheme using a Boltzmann kinetic factor, exp(-$\Delta E/kT$), (where ΔE is the system energy change, k is the Boltzmann constant and T the absolute temperature) becomes very inefficient since the Boltzmann factor is usually very small in comparison with a random number over the interval $[0, 1]$ (**?**). On the other hand, the n-fold way chooses a spin site from the entire ensemble based upon its probability of flipping. Once a site was selected, the flipping was guaranteed and could be immediately performed. The n-fold way also provided a new simulation time concept. At each flip, the time was incremented by a stochastic variable, Δt, whose expectation value is proportional to Q^{-1} (where Q is the number of spins times the average probability that an attempt will produce a flip for a given configuration). Mathematically, $\Delta t = -(\tau/Q)\ln\xi$, where ξ is a random fraction and τ a system dependent time. This choice reflects properly the distribution of time intervals between flips for a reasonable physical model. The cumulative time thus summed is approximately proportional to real time. The n-fold way reduced computation time by an order of magnitude or more for many applications (**?**). A similar concept was used in Voter's 1987 transition state theory (Voter and Doll 1985).

11.3.2 Simulation Procedure

Molecular dynamics is probably the most accurate atomistic simulation technique. However, due to the fact that it simulates all the lattice atoms and, most importantly, that it uses an almost constant time step on the order of femtosecond (10^{-15} s), it cannot simulate the time scales involved in typical technological processing steps (seconds to hours). The kinetic Monte Carlo method, on the contrary, is an event-driven technique, i.e., simulates events at random with probabilities according to the corresponding event rates. In this way it self-adjusts the time step as the simulation proceeds, depending on the fastest event present at that time.

If Arrhenius-like relationship is assumed to describe the diffusional processes of clusters, the jump frequency (or the probability per unit time) for a possible jump of a cluster, i, to take place is given by:

$$r_i = \omega_0 \exp(-\frac{E_i}{k_B T}) \tag{11.59}$$

where ω_0 is the pre-exponential factor of the defect cluster, k_B the Boltzmann constant, E_i the 'effective' activation energy for jumps of the cluster, and T is the absolute temperature. Although the values of E_i for interstitials and vacancies are well known from experiments, the values of E_i for small clusters and glissile dislocation loops and of ν_0 for all kinds of defects have not been obtained experimentally. In the present work, we will use results of MD calculations for these values.

In many applications of the MC method, such as the equilibration of atomic positions in a defected crystal, the space of possible configurations that the system can assume is continuous. Therefore, there exists (in theory) an infinite number of new configurations available to the system at any MC step. However, since we are simulating defects in a volume of *finite* size which evolves according to a *finite* set of physical or mechanical mechanisms, the number of new configurations available at any MC step is *finite* and *enumerable*. This configuration space is discrete. In other words, at each MC step, we can determine all of the potential changes that the system can possibly undergo. Therefore, instead of attempting a random change to the system at each simulation step and then accepting or rejecting that change based on some criterion, we choose and execute one change from the list of all possible changes at each simulation step. The choice is made based on the relative rates at which each change can occur (i.e., the probability of choosing one particular reaction instead of another is proportional to the rate at which the reaction occurs relative to the rates of the other reactions).

Thus the microstructure evolution of the cascade-induced defect clusters is accomplished by a KMC procedure in which one reaction is executed at one site during each time step. The first step in KMC simulations is to tabulate the rate at which an event (i) will take place anywhere in the system, r_i. The probability of selecting an event is simply equal to the rate at which the event occurs relative to the sum of all possible event rates. Once an event is chosen, the system is changed appropriately, and the list of events that can occur at the next KMC step is updated. Therefore, at each KMC step, one event denoted by m is randomly selected from all possible M events, as follows:

$$\frac{\sum_{i=0}^{m-1} r_i}{\sum_{i=0}^{M} r_i} < \xi_1 < \frac{\sum_{i=0}^{m} r_i}{\sum_{i=0}^{M} r_i} \tag{11.60}$$

where r_i is the rate at which event i occurs ($r_0 = 0$) and ξ_1 is a random number uniformly distributed in the range [0, 1]. The way in which the M events are labelled (i.e., by specifying which events correspond to $i = 1, 2, 3, \ldots, m, \ldots, M$) is arbitrary. After an event is chosen and executed, the total number of possible events, M, and the sequence in which the events are labeled, will change.

The reciprocal of an atomic jump probability per unit time is a residence time for a defect

cluster that moves by that specific type of jump. Since the jump probabilities of all the different types of jumps are independent, the overall probability per unit time for the system to change its state by any type of jump step is just the sum of all the possible specific jump type probabilities, and so the residence time that would have elapsed for the system in a specific configuration is the reciprocal of this overall jump probability

$$\Delta t = \frac{1}{\sum_{i=0}^{M} r_i} \tag{11.61}$$

which is independent of the chosen transition. It may also be important to include the appropriate distribution of escape times. For random uncorrelated processes, this is a Poisson distribution. If ξ_2 is a random number from 0 to 1, the elapsed time for a particular transition is given by

$$\Delta t = \frac{-\ln \xi_2}{\sum_{i=0}^{M} r_i} \tag{11.62}$$

The system is then advanced to the final state of the chosen transition and the process is repeated. By following the ensuing discrete jump path for the system, accumulating the residence time of the system along the path, and linking this history to the cascade arrival interval (or the damage rate), the diffusion process can be realistically simulated. The expression for Δt in Eqn. 11.62 is rigorous(**?**), and a derivation is also provided by Battaile(Battaile and Srolovitz 1997).

11.3.3 Elastic Interaction between Point Defects

The interaction between the atoms can be obtained from an (approximate) solution of the Schrödinger equation (Ballone, Andreoni, Car and Parrinello 1988) describing electrons, or from a potential energy function determined in some empirical way (for example, MD simulations (Osetsky, Bacon, Serra, Singh and Golubov 2000a)), but they are computationally expensive. Most often, it is sufficient to treat the interactions between atoms in terms of the analysis of elastic interactions. However, so far, all KMC computer simulations for microstructure evolution under irradiation have not considered the influence of the internal and applied stress fields on defect motion (for example (Heinisch, Singh and Diaz de la Rubia 1994, **?**, Soneda and Diaz de la Rubia 1998, Caturla, Soneda, Alonso, Wirth, Diaz de la Rubia and Perlado 2000)). We propose here a KMC simulation, where the elastic interactions between SIA/vacancy clusters themselves, SIA and vacancy clusters, and SIA/vacancy clusters and dislocations are explicitly accounted for.

Recently, a new computational method has been developed (Ghoniem 1999, **?**) for accurate evaluation of the elastic field of dislocation aggregates in complex 3-D geometry. The method extends the capabilities of 2-D estimates of elastic field variables in realistic material geometry, and enables calculations of displacements, strain, stress, interaction and self-energies, and finally, the work associated with rotation and translation of defect clusters. In the following

sections, the numerical method developed by Ghoniem (Ghoniem 1999) and Ghoniem and Sun (**?**) to examine the mechanisms of interaction between small defect clusters and slip dislocation loops is introduced, followed by the calculation needed to develop an specific elastic interaction energies between defects for use in this thesis.

For the specific case of parametric dislocation loop representation, the elastic field tensors (strain ε_{ij} and stress σ_{ij}) of a dislocation loop are given by line integrals over the dislocation loop line vector as follows (Ghoniem et al. 2000b)

$$\begin{aligned}\varepsilon_{ij} &= \frac{1}{8\pi}\oint_C \Big[-\frac{1}{2}(\epsilon_{jkl}b_i R_{,l} + \epsilon_{ikl}b_j R_{,l} - \epsilon_{ikl}b_l R_{,j} - \epsilon_{jkl}b_l R_{,i})_{,pp} \\ &\quad + \frac{1}{1-\nu}\epsilon_{kmn}b_n R_{,mij}\Big]\, dl_k \end{aligned} \tag{11.63}$$

where $R = \|\mathbf{R}\| = \|\mathbf{x} - \hat{\mathbf{x}}\|$.

Since the linear stress-strain relationship is $\sigma_{ij} = 2G\varepsilon_{ij} + \lambda\varepsilon_{rr}\delta_{ij}$, the stress tensor is also obtained as a line integral, of the general form

$$\sigma_{ij} = \frac{Gb_n}{4\pi}\oint_C \Big[\frac{1}{2}R_{,mpp}(\epsilon_{jmn}dl_{i'} + \epsilon_{imn}dl_{j'}) + \frac{m}{m-1}\epsilon_{kmn}(R_{,ijm} - \delta_{ij}R_{,ppm})dl_{k'}\Big] \tag{11.64}$$

where G is the shear modulus, b_n the components of Burgers vector, $R_{,ijk}$ are derivatives of the radius vector norm between a loop point at $\hat{\mathbf{x}}$ and a field point $\mathbf{x}$, $dl_{i'}$ are differential line elements along the dislocation line vector, and ϵ_{ijk} is the permutation tensor (or Eddington tensor). Ghoniem (Ghoniem 1999) developed explicit forms for the integrals of general parametric dislocation loops. An efficient numerical integration scheme has also been developed for calculations of the stress field, as a fast summation by Ghoniem and Sun (**?**). Their results read

$$\begin{aligned}\sigma_{ij} &= \frac{G}{4\pi}\sum_{\gamma=1}^{N_{\text{loop}}}\sum_{\beta=1}^{N_{\text{s}}}\sum_{\alpha=1}^{Q_{\max}} b_n w_\alpha \Big[\frac{1}{2}R_{,mpp}(\epsilon_{jmn}\hat{x}_{i,u} + \epsilon_{imn}\hat{x}_{j,u}) \\ &\quad + \frac{1}{1-\nu}\epsilon_{kmn}(R_{,ijm} - \delta_{ij}R_{,ppm})\hat{x}_{k,u}\Big] \end{aligned} \tag{11.65}$$

where N_{loop}, N_{s}, and $Q_{\max}$ are the total number of loops, segments, and Gaussian quadrature, respectively. w_α is the quadrature weight, and $\hat{x}_{j,u}$ are parametric derivatives of the Cartesian components of the vector $\hat{\mathbf{x}}$, which describes the loop geometry. The interaction energy of two dislocation loops over the volume V of the material is expressed by

$$E_I = \int_V \sigma_{ij}^{(1)}\varepsilon_{ij}^{(2)}dV \tag{11.66}$$

in which $\sigma_{ij}^{(1)}$ is the stress arising from the first dislocation and $\varepsilon_{ij}^{(2)}$ the strain originating in the other. For the present study, if the second loop (defect cluster) is assumed to be infinitesimal, the interaction energy can be simplified to (**?**)

$$E_I = \delta A^{(2)} n_i^{(2)} \sigma_{ij}^{(1)} b_j^{(2)} \tag{11.67}$$

where $n_i^{(2)}$ is the unit normal vector to the defect cluster habit plane of area $\delta A^{(2)}$. By substituting Eqn. 11.65 into Eqn. 11.67 with $N_{\text{loop}} = 1$, we can readily compute the interaction energy of the cluster, designated with the superscript (2), and the slip loop, of Burgers vector $b_n^{(1)}$, as

$$\begin{aligned} E_I &= \frac{G\delta A^{(2)} n_i^{(2)} b_j^{(2)}}{4\pi} \sum_{\beta=1}^{N_s} \sum_{\alpha=1}^{Q_{\max}} b_n^{(1)} w_\alpha \left[\frac{1}{2} R_{,mpp} (\epsilon_{jmn} \hat{x}_{i,u} + \epsilon_{imn} \hat{x}_{j,u}) \right. \\ &\quad \left. + \frac{1}{1-\nu} \epsilon_{kmn} (R_{,ijm} - \delta_{ij} R_{,ppm}) \hat{x}_{k,u} \right. \end{aligned} \tag{11.68}$$

In the above equation, we assume that the stress tensor of the grown-in (slip) dislocation loop is constant over the cross-section of a small point-defect cluster. In case we treat one single vacancy or interstitial atom as a center of dilatation, the interaction energy simplifies to

$$E_I = -\frac{4}{9} \pi r_0^3 \varepsilon_{ii}^{(2)} \sigma_{jj}^{(1)} \tag{11.69}$$

where $\varepsilon_{ii}^{(2)}$ is the dilatation and r_0 is the effective radius of a point defect. The above equation does not reveal dependence of the interaction energy surface on the orientation of the cluster Burgers vector, unlike Eqn. 11.68.

Kroupa (**?**) obtained the formulae for the displacement and stress field around an infinitesimal dislocation loop by extending the derivation used by Eshelby (**?**). The stress tensor σ_{ij} is

$$\begin{aligned} \sigma_{ij} &= \left\{ -\frac{k_0 G}{4\pi(1-\nu)R^3} \left[\frac{3(1-2\nu)}{R^2} b_k \rho_k n_l \rho_l + (4\nu - 1) b_k n_k \right] \delta_{ij} \right. \\ &\quad + (1-2\nu)(b_i n_j + n_i b_j) + \frac{3\nu}{R^2} \left[b_k \rho_k (n_i \rho_j + \rho_i n_j) + n_k \rho_k (b_i \rho_j + \rho_i b_j) \right] \\ &\quad \left. + \left[\frac{3(1-2\nu)}{R^2} b_k n_k - \frac{15}{R^4} b_k \rho_k n_l \rho_l \right] \rho_i \rho_j \right\} \delta A \end{aligned} \tag{11.70}$$

where $\rho_i = x_i - \hat{x}_i$ is the radius vector between the loop center at point $\hat{\mathbf{x}}$ and a field point at $\mathbf{x}$. $\mathbf{n}$ is the the unit normal vector to the defect cluster habit plane of area δA, and $\mathbf{b}$ Burgers vector. By applying Eqn. 11.67, the elastic interaction energy between two infinitesimal loops can also be obtained.

Main Model Features

The cascade-induced defect distribution process consists of several distinct steps, introduction of defects associated with one high-energy displacement cascade, interaction between defects resulting in instant (intracascade) recombination of defects of opposite types and agglomeration of defects of the same type, diffusion incorporated with interactions between dislocations, impurities and point defects leading to defect annihilation at a sink, trapping of defects by impurities, decoration slip dislocations with defect clusters. To simulate the defect distribution process, all of the process should be incorporated. Although interaction may not be important

at a dilute defect density or very large apart distance and can be approximated accordingly using ALSOME (**?**, Heinisch and Singh 1996, Heinisch 1990, Heinisch et al. 1994, Heinisch and Singh 1997) or BIGMAC (Soneda and Diaz de la Rubia 1998, Caturla et al. 2000) code, in most practical situations the interactions between dislocations and point defects play a key role in determining the effects of radiation on mechanical properties. This interaction effects must therefore be taken into account. The methodology should also address the many diffusional pathways available. It should also connect with the temperature and damage rate these control the available time for microstructure evolution processes before the defect densities reach a dynamic equilibrium state (saturated densities).

In section two the main idea of KMC scheme has been described. We present here a computer simulation method which explicitly incorporates the effects of the elastic interactions between SIA and vacancy clusters themselves (cluster-cluster type), and between defect clusters and dislocations (dislocation-cluster type). SIA clusters are directly produced on the periphery of neutron collision cascades, and they may contain from a few atoms up to tens of atoms in the near vicinity of the cascade (Bacon and Diaz de la Rubia 1994). Such clusters are extremely mobile, and migrate predominantly along highly-packed crystallographic directions, with migration energies of less than 0.1 eV (Bacon and Diaz de la Rubia 1994, Soneda and Diaz de la Rubia 1998). Small SIA clusters may also spontaneously change their Burgers vector, and thus have the flexibility to translate along various crystallographic directions if their motion is not obstructed by internal strain fields. Since MD simulations have shown that the majority of SIA clusters have the form of mobile (glissile) perfect dislocation loops, in this work, we represent SIA clusters as small prismatic, rigid and circular dislocation loops. As for vacancies, small spherical voids are employed to approximate single vacancies and vacancy clusters. The effective radius of void has been defined as

$$r_v = \sqrt[3]{\frac{3N\Omega}{4\pi}} \tag{11.71}$$

where Ω is the atomic volume and N the number of defects in the cluster. The temperature dependence of the jump frequency of defect clusters diffusion has been given as 11.59. In our KMC simulation, the elastic interaction is incorporated. The influence of other defects and the external stress on one SIA or vacancy cluster is given by the stress field σ_{ij}. By applying the infinitesimal dislocation loop approximation for SIA clusters , the work necessary to form the loop characterized by normal n, Burgers vector b and area δA in the stress field σ_{ij} is SIA cluster interaction energy E_{int}, and is given by Eqn. 11.67. Similarly, we have vacancy cluster interaction energy shown as Eqn. 11.69 where it need to be noted that,

$$\varepsilon_{jj} = \frac{q}{K} = \frac{G\delta V}{\pi a_0^3 K} \tag{11.72}$$

where $3K = 3\lambda + 2G$ called the volume modulus.

The total cluster activation energy is then given by:

$$\tilde{E}_m = E_m + \Delta E_{\text{int}} \tag{11.73}$$

where E_m is the activation energy in a perfect crystal structure and can be obtained by either experiments or MD simulations, and ΔE_{int} the difference in the interaction energy of an defect cluster placed at two neighboring equivalent position in the crystal. This includes the effects of forces and moments on the virtual loop or microvoid motion.

Displacement Cascade Simulations

In this section, we study the evolution of cascade-induced defect clusters in BCC Fe at 300 K using KMC simulations. The input data necessary for these simulations, namely defect migration energies and the initial defect configurations produced by displacement cascades are all obtained by MD simulations. Based on intensive MD simulations, Osetsky *et al*. (Osetsky et al. 2000a) developed a generalized size dependence of cluster jump frequency to describe the one-dimensional diffusional transport behavior of SIA clusters

$$\omega^n = \omega_0 n^{-S} \exp\left(-\frac{\langle E_m \rangle}{k_B T}\right) \tag{11.74}$$

where $\langle E_m \rangle$ is the averaged effective activation energy, n the number of SIAs in the cluster, and ω_0 is a new, size-independent, pre-exponential factor. The value of $\langle E_m \rangle$ is estimated from the MD simulations as 0.023 ± 0.003 eV for $\frac{1}{2}\langle 111 \rangle$ clusters in BCC Fe. By fitting to the simulation results of various cases, the values $\omega_0 = 6.1 \times 10^{12}$ s^{-1}, $S = 0.66$ for Fe describe the MD data very well and are used in our KMC simulations. There are also a large number of vacancies produced in displacement cascade. The vacancies are allowed to execute random 3-D diffusion jumps with a probability proportional to their diffusivity. The temperature dependence of the defect diffusivity is written as (Caturla et al. 2000)

$$D = D_0 \exp(-\frac{E_m}{k_B T}) \tag{11.75}$$

where D is the defect diffusivity, D_0 the pre-exponential factor, E_m the migration energy of vacancy. The migration rates are defined as

$$r = \frac{6D}{\delta^2} \tag{11.76}$$

where δ is the jump distance and equal to the magnitude of Burgers vector in our simulations. Eqn. 11.76 has a similar form to Eqn. 11.59, and is used in some other KMC simulations (e.g., (Soneda and Diaz de la Rubia 1998, Soneda and de la Rubia 2001, Caturla et al. 2000)). The values of the migration energy and prefactors obtained from MD simulations for vacancies are 0.87 eV and 1.15×10^{-2} cm^2/s, respectively(Soneda and Diaz de la Rubia 1998). The jump rates of vacancies are almost 10˜12 orders of magnitude larger than that of SIAs in room temperature. Therefore, vacancies can be treat as immobile when we consider the microstructure evolution during the first few nanoseconds in cascade. By now, cascades of primary-knock-on-atom (PKA) energy, E_{PKA}, up to 100 keV have been simulated in BCC metals over a wide temperature range(Stoller 2002, Bacon et al. 2000). We present here the KMC simulations using the initial defect configurations produced by cascade of 100 keV PKAs (Stoller 2002). Fig. 11.3 is a typical defect configuration resulting from a 100 keV cascade. The size of the KMC computation box

is 1 μm^3. The starting defect microstructure is introduced at a random position of the KMC simulation box according to the spatial configuration obtained by the MD simulations of the corresponding cascade. Then, the system runs for a certain time period at a given temperature ($T = 100$ K), and a fixed boundary condition is employed (defects that are able to reach the edge of the KMC simulation box are counted to escape away). MD study of interactions between glissile interstitial clusters and small dislocation loops in α-Fe and Cu has been carried out by Osetsky *et al.*(Osetsky, Serra and Priego 2000b). As a result of the inter-cluster interactions both glissile and sessile clusters can be obtained and this depends on the metal, reaction type and size of the clusters. In our simulations, when two big clusters ($>$ 37 SIAs) of differently oriented Burgers vectors approach to each other, they keep their own orientations and the complex formed becomes sessile. Otherwise, one cluster changes its Burgers vector to be parallel to the other, so that a bigger glissile cluster is formed.

Our simulations show that a large portion of the interstitials and vacancies are lost in a very short time (˜50 ps) by recombination. This is consistent with the results of MD modeling in which an extensive amount of recombination of SIAs and vacancies occurs during the cooling stage of HEDCs. Fig. 11.4 shows a close view of the microstructure at $t = 94$ ps. It can be seen that some SIAs has coalescence into bigger clusters. The result is supported by MD simulations in which one of the most significant findings is the occurrence of intracascade clustering. Most of the recombination and clustering take place within 10 ns. Most of the glissile interstitials and interstitial clusters escape away from the cascade center within around 60 ns. The value of freely migrating defects(FMDs) production efficiency η obtained by our KMC simulation is $\eta \approx 0.1$ (i.e. 10%). The cases of incorporating with internal dislocations are also studied. Since the density of glissile SIAs is rather low (˜10^{18} m^{-3}), no visible dislocation decorations have been observed.

Dislocation Decoration

The effects of displacement damage on the physical and mechanical properties of metals and alloys have been extensively investigated for many years. Much interest has been shown in the role of cascade-induced defect clusters on the process of damage accumulation and changes in mechanical behavior of metal and alloys. Evidence for the direct formation of clusters of vacancies and self-interstitial atoms within the displacement cascade volume during the cooling down phase of the cascade have existed in the literature for some time (see review (Trinkaus et al. 1993)). A large number molecular dynamics simulation studies have also shown a significant fraction of defects formed in the high-energy displacement cascades (HEDCs) is in the form of clusters (e.g. (**?**, Bacon, Calder, Gao, Kapinos and Wooding 1995, Phythian et al. 1995, Stoller 1996, Wirth et al. 1997)). The properties of clusters of SIAs have extremely important effects on further evolution of defect microstructure for they are highly stable(Osetsky et al. 1997, Osetsky, Serra, Singh and Golubov 2000c) and exhibit fast motion by thermally-activated one-dimensional (1-D) glide(Osetsky et al. 2000c, Osetsky et al. 1999, Wirth et al. 2000). In addition, ferritic steel (α-Fe) are considered to be candidate materials for the blanket and first wall of fusion reactors due to their law activation under 14MeV neutron irradiation (Kohyama, Hishinuma, Gelles, Klueh, Dietz and Ehrlich 1996). To characterize and predict the degradation of these materials during prolonged exposure to an irradiation environment, a

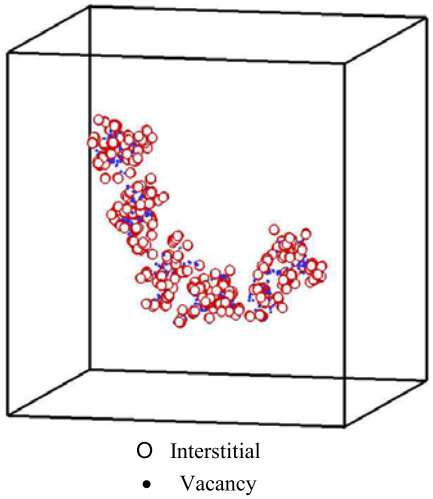

Figure 11.3: Primary damage state at 17 ps for a 100 KeV cascade: (◯) interstitials; (•) vacancies.

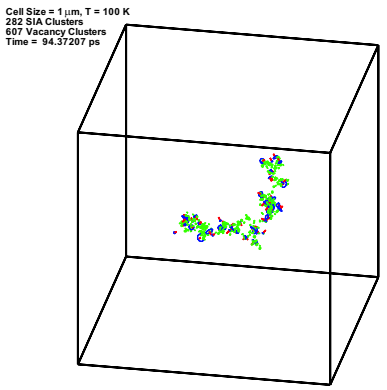

Figure 11.4: A close view of the structure of one single cascade at $t = 94$ ps. Small circular loops represent SIA clusters, and solid points represent vacancies.

understanding of the fundamental processes of the defects properties, production due to neutron irradiation, and of the role of these defects in the resulting microstructural evolution is required (Soneda and Diaz de la Rubia 1998). It was recognized, however, that the complexity of the microstructure in these alloys make mechanistic studies considerably difficult. It was therefore decided to focus the investigations first on pure iron.

The fact that SIA and vacancy clusters are produced directly in HEDCs has significant effect on damage accumulation behavior, and thus physical and mechanical properties of materials under cascade damage conditions. The 1-D motion of small SIA clusters is especially important. Since the formation of glissile SIA clusters results in the creation of a vacancy supersaturation, which leads to void swelling. In addition, another consequence may be the creation of specific microstructural features in neutron-irradiated metals, such as decoration of dislocations by SIA loops (Stiegler and Bloom 1971, Singh, Horsewell, Toft and Edwards 1995) and formation of rafts of dislocation loops (**?**), which contribute significantly to change of mechanical properties. In addition, the restriction of diffusion of SIA clusters to 1-D leads to a reduction in the reaction rate with other defects because one dimensionally moving clusters are able to travel in the atmosphere of randomly distributed lattice defects through larger distances than those 3-D moving ones, and consequently the possibility that such SIA clusters annihilate at extended sinks such as pre-existing dislocations and grain boundaries increase. At the same time lattice defects affect the motion of one dimensionally diffusing clusters in a more substantial way than they influence the motion of vacancies since one dimensionally moving clusters have less chances to avoid obstacles by changing their direction of diffusion (Dudarev 2000). As a consequence, a diffusion bias is established during steady-state irradiation whereby the vacancy concentration can greatly exceed that of SIAs. In addition to the 1-D diffusion of SIA clusters, the motion of a single SIA is also of interest. Guinan et al. presented one-dimensional motion of a single SIA in the $\langle 111 \rangle$ direction in BCC tungsten (W) in MD simulations for the first time. Similar result for BCC Fe was also shown in MD simulations by Soneda and Diaz de la Rubia, which is consistent with the fact that no reorientation is observed in experiments during stage I_D annealing in electron-irradiated pure BCC Fe (Soneda and Diaz de la Rubia 1998). All such information will be used as the basis for a kinetic model of SIA diffusion.

In view of the symmetry of BCC structure and the description above, it is reasonable to assume that all defects move along the close-packed direction, namely the $\langle 111 \rangle$ direction. There is a total of eight equivalent $\langle 111 \rangle$ slip directions for defects in BCC Fe. Thus, there are eight equivalent choices for each defect at each KMC step. Therefore, there is a total of $8N$ possible events for the N active (mobile) clusters at each KMC step. However, the restriction of SIA diffusion to 1-D motion implies that these eight possibilities are not equal, which means the possibility of reorientation for an SIA cluster is rather small, and the migration energy of a preferred $\langle 111 \rangle$ direction is much lower than that of all other seven equivalent directions. We use the frequency of a defect jumping along a $\langle 111 \rangle$ orientation, r which has the form shown in Eqn. 11.59, as the rate at which an event occurs in our KMC model. Some meta-positions between the current position and the next possible position can be used to obtain a better estimation for the activation energies of a candidate in Eqn. 11.73. In our simulations, the activation energy for a cluster to rotate and jump to a neighboring site is calculated as follows. First we move the cluster from initial site 1 to a neighboring site 2 along the direction of the

original orientation. Then it is moved in small step along a line connecting site 2 and final position 3, and at the same time it is rotated by a small angle such that its orientation is parallel to the vector pointing from 1 to 2. After each movement and rotation, the interaction energy at the current position is calculated. The maximum value of these interaction energies is used to calculate the activation energy in Eqn. 11.73.

Due to the significance of the effects of glissile SIA clusters on damage evolution, our concentration will firstly put on the dynamics of SIAs. The value of the migration energy, pre-factors, and other input parameters for SIA diffusion used in this work are list in Table 11.1. A computation cell of $400a \times 400a \times 400a$ ($a = 2.867$ Å is the lattice constant) is taken with periodic boundary conditions. In order to take the 1-D migration mechanism of SIAs into account, we introduced a factor f which is the ratio of activation energies for direction change to the 1-D migration energy. Fig. 11.5(a) shows the trajectories of the centres of mass of a SIA cluster for diffusion at 300 K, where $f = 8.0$. Clearly, the one-dimensional characteristic can be observed. The same value of f is used in all our simulations. For the purpose of studying dislocation-cluster interaction, a dislocation loop lying on the $\langle 101 \rangle$ plane, with Burgers vector $\mathbf{b} = \frac{1}{2}\langle \bar{1}11 \rangle$ is introduced into the simulation box. The loop is generated by using the parametric method developed by our group (Ghoniem 1999, **?**). The dislocation loop consists of two curved segments and two straight junction segments that are normal to the loop's Burgers vector. An initial number of SIA clusters with the same size (1.7 nm diameter) are first randomly distributed in the simulation box, and their initial jump directions are also randomly specified. The SIA cluster density is varied in the range $5 \times 10^{22} - 2 \times 10^{23}$ m^{-3}. The orientation of each cluster's Burgers vector is kept the same as the jump direction, because clusters are represented as small prismatic dislocation loops. A schematic view of the KMC calculations of microstructure evolution is shown in Fig. 11.5(b). When a cluster approaches the dislocation loop at distances closer than the standoff distance (taken as 1.5 nm), the cluster is stopped, and all the events related to it are removed from the event table. Another consideration included in our simulations is the capture radius for defect interaction. In the followed cases the interaction radius between defects has been defined as

$$R = R_s + a \tag{11.77}$$

where R_s is the defect radius. Two small Clusters will combine to form a bigger one when they get inside the capture radius.

Table 11.1: Migration Energy E_m, lattice constant a, initial cluster radius R, Temperature T, pre-exponential factor ω_0, ratio of migration energy of 1-D motion relative to reorientation energy f, shear modulus μ, and Poisson's ratio ν for BCC Fe.

E_m(eV)	a(Å)	$R(a)$	T(K)	ω_0(s^{-1})	f	G(GPa)	ν
0.02	2.867	3.0	300.0	2.5×10^{13}	8.0	81.8	0.29

Plastic behavior of metals is primarily determined by the mechanisms that control dislocation motion. In unirradiated metals, dislocation-dislocation interactions play a very significant

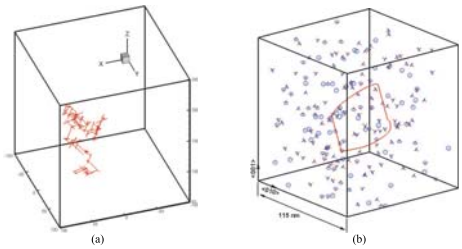

Figure 11.5: (a) Center-of-mass trajectories of a SIA cluster migration for 10000 consecutive KMC steps at 300K with a reorientation activation energy ration $f = 0.8$. The unit are in lattice constant. All the straight line segments are oriented along the $\langle 111 \rangle$ directions. (b) Schematic view of the computational box for the KMC simulations. The small circles represent randomly distributed SIA clusters. The Burgers vector directions as well as the normal directions of loop planes are shown as small line segments.

role in determining the characteristics of plastic deformation, where the impedance of dislocation motion is associated with the formation of sessile junctions or dipoles. In BCC metals (for example, α-Fe), however, the flow stress and the presence of an upper yield point can be drastically changed by small additions of impurities. Also, in some alloyed FCC metals (e.g. copper crystals containing zinc), the upper yield point has also been observed. To explain this effect, Cottrell (Cottrell 1948) showed that the flow stress at the upper yield point is a consequence of dislocation detrapping from impurity clouds, which are attracted to dislocations because of their elastic interaction with dislocations. It has thus long been recognized that interactions between dislocations and impurities, extrinsic and intrinsic lattice defects play a vital role in determining the mechanical properties of materials. During irradiation, glissile SIA clusters are produced and migrate very quickly, interact with other features of the microstructure including dislocations. The motion of dislocation and thereby the initiation of plastic yield in irradiated metals are then significantly affected by the interactions with these SIA clusters.

The specific goal of the present work is to study the influence of elastic field of dislocations on the motion of SIA clusters. The cluster-cluster interactions amongst SIAs themselves are excluded in current simulations in order to stress the effect of internal dislocation fields. The starting defect microstructure is introduced as described before (see Fig. 11.5(b)). Since there are no cluster-cluster interactions considered, the clustering will not occur even one cluster approach to another within the capture radius. As can be seen in Fig. 11.6, the mobility and spatial distribution of SIA clusters are significantly changed as a result of the dislocation-cluster interactions. Just after around 1.5 nanoseconds, the majority of the initially glissile clusters stick around the main dislocation loop (nearby the edge components) and become nearly virtually immobile. In effect, these clusters re-orient themselves by rotation of their Burgers vectors to respond to the elastic field of internal dislocations. Thus, their migration is forced towards internal stress fields, and not random, as implied by MD simulations. This high concentration of SIA loops result in a extremely inhomogeneous spatial distribution in simulation box. Due to the effect of dislocation fields, the trapped SIA loops change their Burgers vectors to be

consistent with the Burgers vector of the main dislocation loop. Ending up near the core of grown-in dislocations, the SIA clusters form what is known as a cluster atmosphere, similar to the well-known Cottrell impurity atmosphere around dislocations in unirradiated BCC metals.

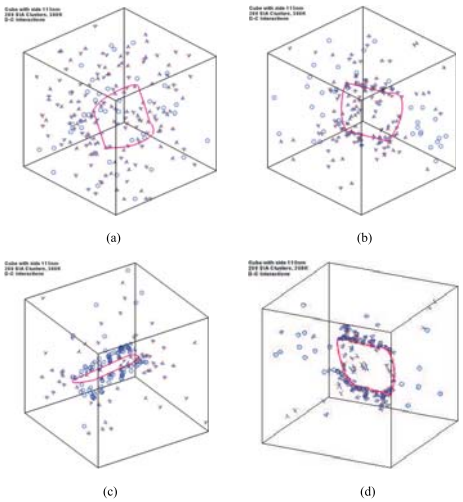

Figure 11.6: KMC simulation of 200 SIA clusters diffusion in the stress field of a 3-D dislocation loop. SIA loops are clearly observed to accumulate along edge components of the loop. (a) 0 ns; (b) 0.1 ns; (3) 0.3 ns; (d) 0.4 ns.

One of the most striking features in the evolution of dislocation microstructures under cascade damage conditions, first observed about thirty years ago is the decoration of grown-in dislocations by loops(Stiegler and Bloom 1971, Singh et al. 1995) which may even extend to form dislocation walls (Singh et al. 1995). Most dislocations are observed to be heavily decorated by small, sessile interstitial clusters (Singh et al. 1997). Fig. 11.7 shows a TEM micrograph of pure single crystal Molybdenum irradiated with fission neutrons at 320 K (Singh et al. 1997). Grown-in (slip) dislocations are clearly decorated with small defect clusters. To explain the experimentally observed yield drop, and to understand the relationship between dislocation decoration and the yield behavior of irradiated materials, the Cascade Induced Source Hardening (CISH) model has been proposed (Trinkaus et al. 1997, Singh et al. 1997, Ghoniem et al. 2000b). In this concept, a dislocation decorated with loops, like a Cottrell atmosphere of impurities (Singh et al. 1997), is assumed to be locked so firmly that it cannot play as dislocation source until the applied stress reaches a very high level. SIA cluster mobility and trapping in the stress field of grown-in dislocations therefore become the main reason behind experimental observations of dislocation decoration, and the corresponding presence of an upper yield point in irradiated metals and alloys. Our simulations show a clear picture of how SIA clusters attract to dislocations to decorate and lock them in place, and have a good agreement with experimental observations qualitatively.

Pinning and Small Rafts

Figure 11.7: A TEM micrograph of pure single crystal Mo irradiated with fission neutrons at 320 K to a displacement dose level of 0.16 dpa (Singh et al. 1997).

In this section we put our effort to investigate the cluster-cluster interactions amongst SIA clusters, and the dislocation is temporarily removed from the simulation box. The simulation was begun with 200 SIA clusters of the same initial size, which are generated in the computational cell, randomly in space and orientation. The diffusion of SIA clusters is extremely fast, and within a few nanoseconds (ns) at room temperature, clusters migrate along close-packed crystallographic directions over microstructurally-significant distances (see Fig. 11.5(a)). Previous MD simulations of isolated SIA clusters have also indicated this fast diffusion feature of their migration along $\{111\}$ in BCC metals, as a result of their rather low migration energies (˜0.02 eV)(Osetsky et al. 2000a). Our KMC simulations reveal that their mutual elastic interactions affect their distribution and motion drastically. Because of their mutual interaction fields, two clusters that are oriented along non-parallel crystallographic orientations will either coalesce forming larger ones, or just pin one another at a short distance with having their Burgers vectors in parallel direction and move along that direction together. Once two clusters pin together, they have less chance to change the orientation such that their motion becomes almost pure one-dimensional. As this process moves on, some additional clusters may be trapped into this *pin* structure by changing their Burgers vectors. This self-organizing course eventually results in the occurrence of so-called $rafts$ which consist of a number of small dislocation loops with same diffusion direction. This feature has been experimentally observed for some time(Trinkaus et al. 1997). As shown in Fig. 11.8, along with the progress of the simulations, the number of glissile SIA clusters is decreasing , while their average size are increasing. Moreover, due to the influence of the mutual elastic interactions, the frequencies of direction change are considerably dropped as well. More and more SIAs will move along a fairly regular route. Similar results are also obtained for the cases of 50 SIA clusters and temperature $T = 600$ K.

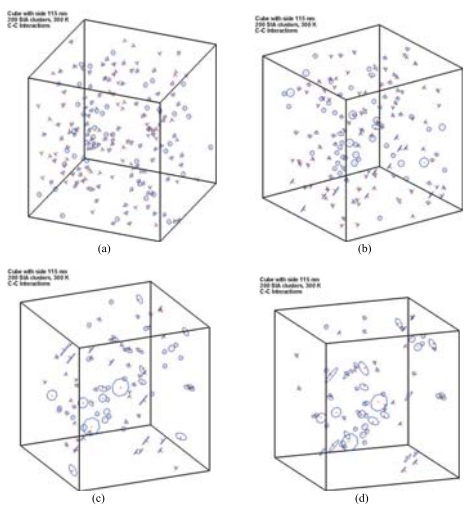

Figure 11.8: KMC simulation of SIA cluster diffusion and agglomeration. SIA loops are self-pinned, and rafts are clearly observed as the simulation progresses.

It is now well established that in displacement cascades a substantial fraction of SIAs are produced in the form of clusters (**?**) and that some of these clusters are glissile. Such an interstitial cluster may perform a thermally activated random glide motion until it gets trapped in the strain field of another defect clusters or a dislocation (Trinkaus et al. 1993). As an extension of the investigation described in two last sections, we present here a study of cluster motion integrating the influence of the internal stress field created by grown-in dislocations as well as the clusters themselves.

Fig. 11.9shows a typical defect evolution time sequence views of 200 SIA clusters at 300 K. The initial microstructure configuration is taken as same as the case of dislocation decoration (see Fig. 11.9(a)). Compared with the result of dislocation-cluster interaction case, it is shown that the inhomogeneity of loops spatial distribution is higher in the present case. Principally, there are two mechanisms which could result in such a effect: (1) the decreasing of the number of glissile loops due to cluster-cluster interactions, and (2) the accumulation of clusters enhancing the influence of the strain fields of the internal dislocation loop. In both cases quoted above, the cluster-cluster interactions play an essential role. The effects of internal dislocation fields, aided by their mutual elastic interactions, render most of these clusters virtually immobile and accumulating in the vicinity of the internal dislocation. The progress of the decoration process may even lead to dislocation 'walls'; an experimental evidence of such a wall has been reported in literature (**?**). The dislocation decoration has a profound influence on the plastic deformation of irradiated metals. It may be one of the main issues contributing to the occurrence of an upper yield point followed by a drop in the yield strength observed in some metals and alloys(e.g., FCC Cu). The resistance of the sessile SIA clusters to dislocation motion could be the main reason for the tremendous increases in yield strength. Once dislocations are released from localized SIA clusters, they will undoubtedly move very fast under the same applied stress that unlocked them, and unless their motion is further hindered, strain softening may occur. This may give a reasonable explanation to the followed yield drop phenomenon. Computer simulations using PDD for the process of dislocation unlocking from coalesced and immobilized SIA clusters have been presented by Huang and Ghoniem (Huang and Ghoniem 2002).

All these three types of interactions have been studied for cases of 50 SIA clusters and 600 K as well to account for the variations of cluster densities and temperatures. A comparison of the evolution time is given in Table 11.2. It can be seen that SIA cluster density seems to have greater influence on reaction time than temperature. Under higher temperature conditions it may took less time for the occurrence of remarkable dislocation decoration phenomenon than in lower temperature. The high temperature increases the thermal activities of clusters, which makes clusters have more chance to approach to reaction range of internal dislocations. The simulations also show that the $rafting$ structure can be more easily to appear in lower temperature and higher cluster density cases.

Input Parameters to KMC Simulation

The calculation begins by determining a time interval between cascade arrivals based on the damage rate. From the view point of energy transfer, Kinchin and Pease(Kinchin and Pease 1955) proposed the first clear theoretical assessment of defect production in displacement cascades by deriving a simple relationship between the number, N_{KP}, of SIA-vacancy pairs, i.e.

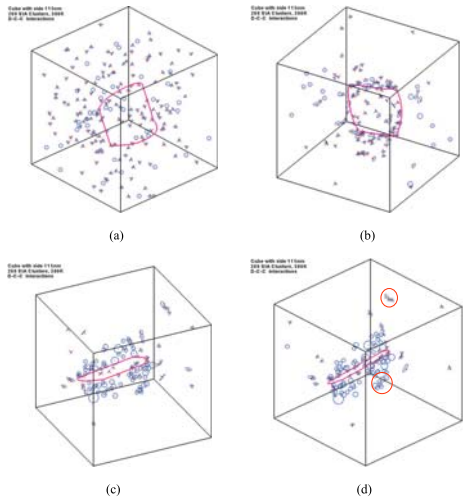

Figure 11.9: KMC simulation of 200 SIA clusters diffusion and clustering in the stress field of a 3-D dislocation loop. Dislocation decoration and SIA loop $Rafts$ are clearly observed in the circled region in (d). (a) 0 ns; (b) 0.4 ns; (3) 0.7 ns; (d) 1.0 ns.

Table 11.2: Evolution time for Running 800,000 KMC Steps (in ns).

Number of SIA Clusters	D-C Interactions		D-C-C Interactions	
	300 K	600 K	300 K	600 K
50	1.95	1.28	3.29	3.14
200	0.416	0.237	1.04	0.79

Frenkel defects, created by a cascade and the kinetic energy, E_{PKA}, of the primary knock-on atom (PKA).

$$N_{KP} = \frac{E_{PKA}}{2E_d} \tag{11.78}$$

where E_d is the displacement threshold energy, and a round value is suggested in the ASTM standard as Fe - 40 eV. It was subsequently revised by Norgett et al. (Norgett, Robinson and Torrens 1975) (the NRT model) to give the standard formula for estimating the displacements per atom (dpa) in irradiated metals

$$N_{NRT} = K\xi(E)N_{KP}(E) \tag{11.79}$$

where the factor K is defined as the displacement efficiency, the function $\xi(E)$ is defined as the damage efficiency. Both are less than unity, and an acceptable value for K is 0.8. All the MD simulations show that defect production by displacement cascades in metals is not as efficient as predicted by the NRT formula. In fact, typically only $20-40\%$ of N_{NRT} for a given cascade energy can survival at the end of the cascade process. Therefore, the number of displaced atoms takes the form:

$$N_F = \gamma_C N_{NRT} = \gamma_C K\xi(E)N_{KP}(E) \tag{11.80}$$

where γ_C is defined as the *cascade efficiency*, and less than unity. We use Lindhard's enery-partitioning theory to evaluate the damage efficiency, $\xi(E)$

$$\xi(E) = \frac{1}{1 + 0.13(3.4\epsilon^{1/6} + 0.4\epsilon^{3/4} + \epsilon)} \tag{11.81}$$

where ϵ is a reduced PKA energy:

$$\epsilon = \frac{E_{PKA}}{2Z^2e^2/a} \tag{11.82}$$

e is the electronic charge ($e^2 = 14.4$ eV$\cdot$ Å), and a is the screening radius, given by

$$a = \frac{\sqrt{2}\lambda a_B}{\sqrt{Z_1^{2/3} + Z_2^{2/3}}} \tag{11.83}$$

where a_B (= 0.5291772083 Å) is the Bohr radius, λ (= 0.88) is a constant of order unity, Z_1 and Z_2 are the atomic numbers of two collision atoms. The parameters used in the calculation of N_{NRT} in BCC iron are summarized in the following

K	Z, Z_1, Z_2	a_B (Å)	e^2(eV$\cdot$ Å)	λ	E_d(eV)
0.8	26	0.5291772083	14.4	0.88	40

Therefore, for $E_{PKA} = 40$ KeV and 100 KeV we have $N_{NRT} = 280$ and 635, respectively. In view of the cascade efficiency, the theoretical predictions of the number N_F, of SIA-vacancy pairs, i.e. Frenkel defects are 112 and 254 for PKA energy 40 KeV and 100 KeV, respectively,

with $\gamma_C = 0.4$. Bacon et al. ((Bacon et al. 2000)) have shown a new empirical relationship between N_F and E_{PKA} by fitting MD-generated N_F data for several metals

$$N_F = A(E_{PKA})^m \tag{11.84}$$

where A and m are constants which are weakly dependent on the material and temperature. For E_{PKA} up to 40 KeV for α-Fe the above equation gives a good fit to MD simulation results with $A = 5.57$ and $m = 0.83$. Actually, by applying A, m to Eqn. 11.84 PKA energy of 40 KeV case, we get $N_F = 119$, which is quite close to the value computed by Eqn. **??**. Even for PKA energy up to 100 KeV, the predictions made by Eqn. **??** (= 254) and Eqn. 11.84 (= 255) are still in a very good consistence.

On the other hand, since dpa has been extensively used as a measure of damage accumulation in irradiated materials, the number of displaced atoms can then be written as

$$N_P = PN_t \tag{11.85}$$

where P is the displacement dose (dpa), and N_t the total number of atoms in the system. Therefore, the displacement dose level corresponding to one cascade can be readily calculated by

$$P = \frac{N_F}{N_t} = \frac{\gamma_C K \xi(E) N_{KP}(E)}{N_t} \tag{11.86}$$

The interstitial clusters considered in our simulations were assumed to be created in cascades of 40 KeV at 300 K. For a simulation box of $(100\ \text{nm})^3$, one cascade will produce $N_F = 112$ Frenkel defects, and the corresponding dose level is 1.306×10^{-6} dpa. With the relationship between cascade and damage dose, we can design the number and frequency of cascades required for producing a certain mount of damage at certain displacement dose rate by pumping corresponding cascades into the simulation box.

There are some very important input parameters of interstitials and vacancies, such as the number and size distribution of defects created in one cascade, and properties especially mobility of these clusters, which are used in KMC simulations and have to be quantitatively identified. MD simulations using interatomic potentials fitted to many of the equilibrium and defect properties of metals offer us a quite realistic description of all stages of the cascade process. Bacon, Gao and Osetsky (Bacon et al. 2000) carried out an analysis of the MD simulations results on the primary damage state due to displacement cascades in fcc, bcc and hcp metals. The cluster statistics of cascades of 40 KeV in energy in α-Fe was provided and used as input parameters in our KMC simulations. In order to emphasize the effect of interstitial clusters on the microstructural evolution, we ignored single interstitials and small interstitial clusters (containing less than 4 interstitial atoms) and mainly focused on bigger clusters although most SIAs are created in the form of single defects, di- or tri-SIA clusters (about 77% of the SIAs created in cascades of 40 KeV at 100 K in α-Fe were single defect or in clusters of size two or three (**?**)). A supportive argument is for to do so that, Soneda and Diaz de la Rubia (Soneda and Diaz de la Rubia 1998) have shown that two third of the defects that escape from the parent cascade region are in form of small SIA clusters which migrate in one dimension. Therefore,

monodefects as well as relatively smaller clusters can be ignored for a simulation addressed on the effect of clusters on the evolution of microstructure because of their minority population and insignificant three-dimensional motion property. Room temperature irradiation of iron by neutron was simulated with a flux of 40 KeV cascades containing interstitial clusters (size > 4).

As far as the mobility of interstitial clusters are concerned, computer simulations have demonstrated that the majority of SIA clusters formed during the cascade process are highly mobile, a property that is intimately associated with their atomic structure. MD simulations have also confirmed a striking feature of the motion of interstitial clusters that small SIA clusters and loops preferentially perform thermally-activated, one-dimensional glide along close-packed direction of the crystal lattice. For example, the one-dimensional random glide motion of a planar SIA cluster consisting of four SIAs has been observed in a MD study (Foreman et al. 1992, **?**). It has been shown in this study that small loops consisting of four, five and six atoms transform spontaneously from the faulted into the highly glissile unfaulted configuration. In addition, the change in the Burgers vector of a cluster consisting of four SIAs has been observed to occur in these studies. From the lifetime of one configuration a value of 0.4 eV is estimated for the barrier against this transformation. The height of the barrier of orientation change is expected to increase significantly with increasing cluster size. In fact, the idea of changes between crystallographically equivalent 1D direction has been supported by experimental evidences, such as the saturation of void growth in void lattices, which can be rationalized in terms of 1D diffusion of SIA clusters only if direction changes in the 1D diffusion and/or some transversal diffusion (for instance, by random self-climb of small dislocation loops) is included (**?**). The MD studies show that small, strongly bounded interstitial clusters (two to about five-SIA clusters) exhibit long-range, three-dimensional (3D) diffusion, which occurs by reorientation of the constituent $< 111 >$ dumbbells from one $< 111 >$ to another (Wirth et al. 2000, Soneda and de la Rubia 2001). As cluster size increase, thermal-activated reorientation from one Burgers vector to another becomes increasingly more difficult to achieve, no 3D motion is observed even at very high temperatures. This is another reason that we exclude interstitial cluster of less than four SIAs in our simulations in order to address the effect of 1D motion of SIA clusters and loops on the development of heterogenous and segregated accumulation of defects.

The value of the migration energy and pre-factors for defect diffusivity (11.37) used in this work were collected from MD simulations. Based on extensive MD simulations, Osetsky *et al.* (Osetsky et al. 2000a) developed a generalized size dependence of cluster jump frequency to describe the one-dimensional diffusional transport behavior of SIA clusters

$$\omega^n = \omega_0 n^{-S} \exp\left(-\frac{\langle E_m \rangle}{k_B T}\right) \tag{11.87}$$

where $\langle E_m \rangle$ is the averaged effective activation energy, n the number of SIAs in the cluster, and ω_0 is a new, size-independent, pre-exponential factor. The value of $\langle E_m \rangle$ was found not depending on size and close to that of the individual crowdion. It was estimated for clusters containing up to 91 SIAs in iron that $\langle E_m \rangle = 0.023 \pm 0.003$ eV for $\frac{1}{2}\langle 111 \rangle$ clusters in bcc iron. By fitting to the simulation results of various cases, the values $\omega_0 = 6.1 \times 10^{12}$ s^{-1}, $S = 0.66$ for Fe describe the MD data very well and were used in our KMC simulations. As

we mentioned before, there is another crucial quantity that has to be determined, the barrier against the change in Burgers vectors of clusters. However, to date, there are only very limited information on the activation energy for direction change of interstitial clusters, and systematic MD simulations for this vital parameter like what has been done for migration energies and diffusion pre-factors of clusters is yet to come.

Soneda and Diaz de la Rubia (Soneda and Diaz de la Rubia 1998) studied the direction change frequency of 2-SIA and 3-SIA clusters in α-Fe using MD simulations and obtained the activation energies for direction change were 0.09 eV and 0.27 eV for the 2-SIA and 3-SIA clusters respectively. Gao et al. (Gao, Henkelman, Weber, Corrales and Jonsson 2003) investigated possible transition states of interstitials and small interstitial clusters in SiC and α-Fe using the *dimer method* (**?**) . The transition states of defects in α-Fe have been studied as a function of cluster size, and the saddle points generally increase in magnitude with increasing clusters. The migration energies of interstitial clusters along the $< 111 >$ direction range from 0.0022 to 0.039 eV, which is consistent with those obtained using MD simulations (Osetsky et al. 2000a). The activation energies of directional change are 0.163, 0.133 and 0.342 eV for 1-, 2-, and 3-SIA clusters, respectively, which are smaller than the migration energy of a single vacancy. The value for a cluster of size 4 and 5 is about 1 eV.

In our work, we assumed that the relationship between the activation energy of directional change for a interstitial cluster and the size of the cluster is linear, and is equal to 0.05 eV per interstitial atom. In fact, MD simulations have shown that the motion of small SIA clusters and loops is the result of the motion of individual crowdions (Bacon et al. 2000, Osetsky et al. 2000a) and the reorientation may occur in a one-by-one fashion (Osetsky et al. 2000b), so that it is perhaps acceptable to assume a size-dependence of the probability of reorienting all the crowdions to the same new direction. The value of 0.05 eV/atom is probably an underestimation for the energy barrier for direction change of a small cluster, say size less than four, but for bigger clusters it dose reflect the characteristic of preferentially one-dimensional motion of interstitial clusters. Fig. (11.10) show the trajectories of the centres of mass of a 6-SIA cluster for diffusion at 300 K with respect to different energy barriers for directional change.

In addition to interstitials, there are also a large number of vacancies produced around the core of displacement cascades. Both experimental observations (**?**, **?**) and MD simulations (see a review by Bacon et al.(Bacon et al. 2000)) have as well confirmed the intracascade clustering of vacancies in bcc iron. Small clusters of vacancies are metastable in the form of planar or 3-D, void-like configurations, and during high temperature annealing transform into cloud-like complexes. Although such loose clusters are mobile in the bcc structure, the diffusivity of vacancies (migration energy is about 0.8 eV for the single vacancy) is much lower than that of interstitial clusters. Therefore, instead of introducing randomly located vacancies of various sizes as an initial configuration into the simulation box and making them mobile and capable of agglomerating, we use immobile, compact (in other word, spherical micro-voids) configurations of vacancy clusters. In fact, MD simulations revealed that the defect structure of the cascade is characterized by a vacancy-rich core surrounded by a shell of SIAs. The formation of small SIA clusters results in the creation of a vacancy supersaturation, which leads to void swelling. Our model is actually taking this vacancy-rich core region as a spherical recombination center.

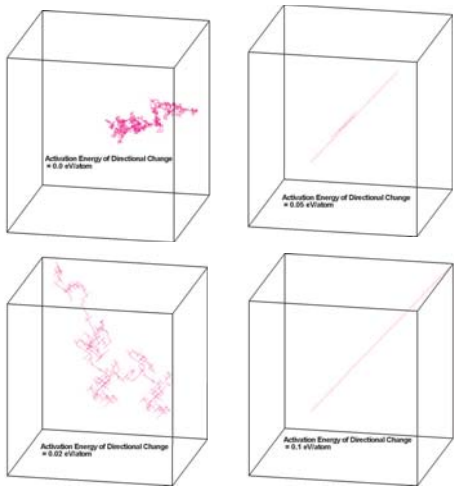

Figure 11.10: Centre-of-mass trajectories of a 6-SIA cluster migration for 10000 consecutive steps.

The size of a recombination center or micro-void is given by an equivalent diameter, i.e. the diameter of a sphere with a volume equal to the number of vacancies, which varies in terms of a Gaussian distribution with mean 100 and standard deviation 8 according to the number of Frenkel pair created in one cascade summarized in Eqn. (11.84).

11.4 Comparison of KMC model with Experiments

Doses up to 5.21×10^{-3} dpa were simulated at a damage rate of 5×10^{-8} dpa/s, and the damage accumulation was observed as a function of dose. Fig. 11.11 shows the interstitial cluster density as a function of dose up to 5.21×10^{-3} dpa with considering recombination, as well as of dose up to 1.48×10^{-3} dpa without recombination centers. In addition, SIA clusters containing more than 100 interstitial atoms (diameter > 3 nm) are counted as visible clusters, and the corresponding cluster density is calculated and compared with the experimental results for bcc Fe irradiated at $\simeq$ 70 °C in the HFIR rector at Oak Ridge National Laboratory to displacement dose levels in the range of 10^{-4} to 0.72 dpa (Eldrup et al. 2002). At initial stage (dpa ¡ 10^{-4} dpa), the cluster density increases almost linearly with damage dose; the increasing of cluster density is then slow down when the dose level is higher than 10^{-4} dpa and lower than about 3×10^{-3} dpa; and the cluster density approaches to a saturated value and does not change much beyond the dose level of 3.5×10^{-3}. When the simulation started, the cluster densities of both interstitials and vacancies are rather low, and the chance that one interstitial cluster could get close enough to another interstitial or vacancy cluster so that they can feel each other in terms of elastic interaction is rather small as well. Because of the 1D motion of SIA

clusters, the recombination cross section with vacancy clusters produced in the cascade core as well as the agglomeration cross section with other interstitial clusters are small. Theoretically, there are only two mechanisms by which a SIA cluster could change its diffusion direction: either thermal activation or the interaction with other defects or microstructures. The effect of thermal activation can be rule out here because our simulation is carried out at constant room temperature. At low damage dose level, the big distance between clusters makes interaction between them weak and can hardly affect the migration of SIA clusters, which results in the density of clusters increasing linearly with dose.

When the damage builds up to a certain level, say 10^{-4} dpa in our simulations, the simulation box becomes crowd, the newly introduced interstitial clusters as well the mobile existing clusters would have more possibilities encountering one another and interacting with each other. The events of recombination and agglomeration would occur more frequently than the early stage. Consequently, these reactions slow down the increasing of the number of SIA clusters in the simulation box. Once the damage accumulated to some extent, 3.5×10^{-3} dpa in our simulation, the number of disappeared interstitial clusters due to annihilation and clustering and the number of clusters produced by new cascade reach to a dynamic equilibrium, and the density of clusters in the simulation box thereby reaches to saturation. The vacancy cluster, micro-voids in our simulation, had a significant influence on the density of interstitial clusters. As we can see in Fig. 11.11, at dose level lower than 5×10^{-4} dpa the difference between the cases of including micro-voids and no micro-voids is not distinct. But the difference was broadened as the dose increasing, at a dose of 1.5×10^{-3} dpa, the cluster density of the micro-voids free case is about 50% higher than the case with micro-voids. It indicates that the existence of vacancy clusters considerably reduces the density of mobile interstitial clusters and recombination plays an important role in the microstructural evolution.

Although the number density of SIA clusters reached a steady state after 3.5×10^{-3} dpa, the sizes of clusters are still evolving with dose increasing. More clusters with bigger size were developed at high dose level, for example, clusters consisting of more than 180 SIAs were observed in our simulations. In order to compare the results from our simulations with the experimentally measured cluster densities, it is necessary to assume a minimum size that can be resolved in the experiments. A value between 1.5 and 2 nm in diameter is quoted in the literature as the minimum size resolved by TEM (Singh and Zinkle 1993). For the infinitesimal dislocation loop approximation adopted here, the relationship between radius of the loop (R) and the number of defects (N) is $N = 2^{\frac{1}{2}}\pi R^2/a_0^2$ for a bcc material, where a_0 is the lattice parameter. For a radius of 1.4 nm that corresponds to approximately 100 defects in bcc iron. Considering visible interstitial clusters as those with more than 100 interstitial atoms, we extracted the total 'visible' cluster density from the simulations, as we show in Fig. 11.11 as well. We can see that the fraction of 'visible' interstitial clusters obtained in the simulations presented here is bigger than the experimental measurement in high dose level, but still in good agreement. The number of SIA clusters as a function of cluster size at dose of 5.2×10^{-3} dpa is demonstrated by the histogram in Fig. 11.12. More than half of the total interstitial clusters consist of more than 30 defects though small clusters consisting of less than 10 SIAs still have the highest value for one single section. It can expected that distribution of Fig. 11.12 will shift towards the bigger cluster size as damage accumulating.

We would like to spend a bit more discussion on the size of interstitial clusters because it brings up another very important issue for KMC simulations, to determine the size at which SIA clusters may be considered mobile, i.e., which clusters are glissile dislocation loops and which are not. MD simulations have shown that even though the activation energy for migration of clusters is constant with size, the cluster diffusivity decreases as the cluster size increases (see a review by Osetsky et al. (**?**)). Due to the same reason the clusters measured in experiments as often referred as immobile or sessile because of their low mobility. For bcc iron, the large stacking fault energy makes the occurrence of faulted loops very unlikely, and therefore all interstitial clusters in the KMC simulation are considered to be mobile loops. The only mechanism that a mobile interstitial cluster could turn into an immobile cluster is either getting trapped by a dislocation or getting locked with another cluster on the condition that both clusters are big (> 37 SIAs) and have different Burgers vectors. Due to the low temperature, the re-arrangement of a cluster so that it can become glissile cannot happen in our simulations. However, a cluster of large size is virtually immobile in KMC simulations due to the small pre-factor. Therefore, it would be more meaningful to compare the density of large clusters with the experimental observation.

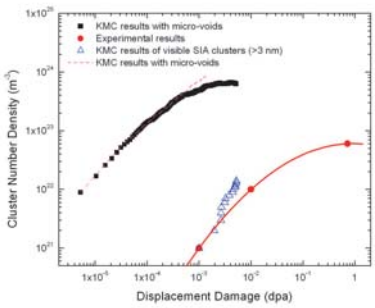

Figure 11.11: SIA cluster densities as a fuction of accumulated dose for bcc iron irradiated at 300 K under cascade irradiation at 5×10^{-8} dpa/s. Simulation results are compared to experimental data from TEM observation of iron irradiated in HFIR ((Eldrup et al. 2002)).

Characteristics of Decoration and Raft Formation

As we mentioned before, the main character of the presented KMC simulations different from other authors' work is that the elastic interaction between defects and microstructures has been included and thereby some distinct features of damage accumulation under cascade irradiation, such as dislocation decoration and raft formation, can actually be studied.

The accumulation and absorption of radiation induced defects in the vicinity of dislocations is controlled by the interaction between the two components. To dislocation decoration occur, except for a direct encounter of a mobile SIA cluster with a dislocation, the cluster will generally be trapped in a region of strong attractive elastic interaction between it and the dislocation. As expected, at very low dose level (¡ 10^{-4} dpa) the probability that a dislocation finds a

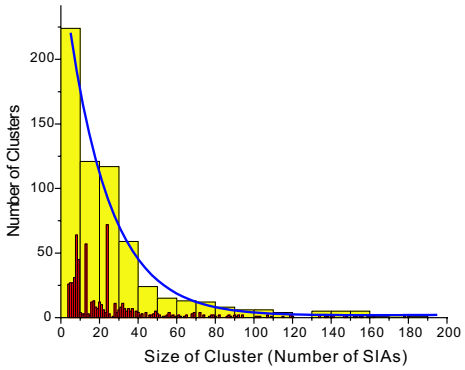

Figure 11.12: Size distribution of SIA clusters at a dose level of 5.21×10^{-3} dpa. The red slim bar is the number of clusters of a certain size, and the yellow thick bar are the total number of clusters within a certain range of sizes.

cluster in the attractive region and can then affect the motion of the cluster is rare, so that the decoration phenomenon does not occur in the early stage of irradiation. The decoration process builds up quickly with dose increasing, and at 3×10^{-4} dpa the dislocation has already got a bunch of interstitial clusters trapped in its neighbouring area. The micro-structural configuration of interstitial clusters at 1.3×10^{-3} dpa is shown in Fig. 11.14 where the decoration by interstitial clusters along dislocation line has become very significant. The accumulation of glissile interstitial clusters near the dislocation is further intensified at dose of 5.2×10^{-3} dpa as shown in Fig. 11.15. Generally, when an extremely mobile one-dimensionally migrating interstitial cluster passes through the neighbourhood of a pre-existing dislocation it will feel the influence of the strain field of the dislocation. As long as the defect/dislocation interaction is attractive and the distance is small enough, the interaction of the defect with the stress field of the dislocation could be so strong that the cluster cannot escape from within the attractive zone by thermally-activated random walk. Once a interstitial cluster is trapped into the strain field of a dislocation, it will rotate its Burgers vector to accommodate to the strain field of the dislocation and tend to migrate along the direction of lowest energy barrier.

Using dislocation dynamics simulation, Ghoniem et al. (Ghoniem et al. 2000b) investigate the elastic interaction between nano-size prismatic loops and grown-in dislocation loops in bcc-Fe and fcc-Cu. Their calculation shows that the iso-energy surface for bcc iron has a maximum width around the edge component of the dislocation. Our simulations show a good agreement with their result. It can be clearly seen in Fig. 11.15 that the pure edge components of the slip dislocation gets more SIA clusters trapped in its vicinity than the mixed character segments. Due to the influence of the strain field of the dislocation, the majority of the decorating clusters has change their Burgers vector to parallel to the Burgers vector of the dislocation. The trapped clusters can still serve as sinks for the glissile clusters and increasing their size in terms of agglomeration before they take Burgers change and finally get absorbed by dislocations. With the accumulating of clusters along the dislocation line a repulsive force field is then gradually

building up against further cluster trapping. Fig. 11.13(a) shows contours of the interaction energy between an interstitial defect cluster of Burgers vector $a/2 < \bar{1}\ 1\ 1 >$ and an edge dislocation on the $< \bar{1}\ \bar{2}\ 1 >$ -plane in bcc iron; and Fig. 11.13(b) shows contours of the interaction energy between an interstitial defect clusters of Burgers vector $a/2 < \bar{1}\ 1\ 1 >$ and a pre-existing same type cluster and an edge dislocation on the $< \bar{1}\ \bar{2}\ 1 >$ -plane. As can be seen, the shielding effect of the decorating defect cluster is clearly illustrated.

When the attractive stress field of the leading dislocation is fully compensated by the existing clusters, the SIA content in the primary trapping region accumulation achieve saturation and the decoration process stops. Although the decoration of the leading dislocation is no long proceeding, the primary region of cluster trapping virtually shifts the stress field of the dislocation and cluster trapping occurs only ahead of the existing dislocation/loop structure where the interaction remains attractive (Trinkaus et al. 1997). Cluster trapping process whereby continuous away from the leading dislocation and results in a dislocation wall formation. As seen in Fig. 11.9(d), our simulations have already shown the extension of cluster trapping and the formation of dislocation wall.

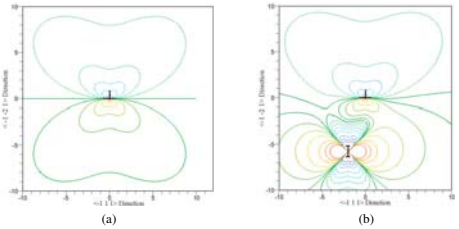

Figure 11.13: (a) Local iso-energy contours for the interaction energy of an interstitial cluster of Burgers vector $a/2 < \bar{1}\ 1\ 1 >$ with an edge dislocation on the $< \bar{1}\ \bar{2}\ 1 >$ -plane in bcc iron; (b) local iso-energy contours of the interaction energy of an interstitial defect clusters of Burgers vector $a/2 < \bar{1}\ 1\ 1 >$ with a pre-existing same type cluster and an edge dislocation on the $< \bar{1}\ \bar{2}\ 1 >$ -plane.

In addition to dislocation decoration, the formation of rafts is another major striking feature of microstructural evolution of cascade induced irradiation damage. Fig. 11.16 shows a configuration of rafts of interstitial clusters formed at dose level of 1.8×10^{-3} dpa. The Burgers vectors of the clusters making up of a raft are parallel to each other, which is in agreement with the experimental observation. When an interstitial cluster approaches to another one, they are inevitably subject to the influence of the strain field of each other. If the interaction between them is attractive and strong enough to overcome the energy barrier for directional change, the clusters will comply with the interaction between them in terms of adjusting the relative positions and orientations. This scenario is similar to the pinning of clusters which has been demonstrated in the previous section. The nature of the configuration of pinning clusters is still glissile, which has been observed in our simulations. The development of this pinning procedure eventually leads to formation of an extended stable complex that consists of a bunch of SIA clusters lying on parallel planes. As the number of clusters within a complex

increases, the mobility of the complex as a whole decreases. Using MD simulations Osetsky et al. investigated the mobility of complexes of glissile SIA clusters and demonstrated that the complex of a compact set of five clusters of size 19, 19, 37, 61 and 91 SIAs separated by a mean distance equal to the average cluster diameter was immobile (**?**). The decreasing of mobility of individual clusters can be attribute to the elastic interaction between the member clusters within one complex, which prevents a cluster from breaking the strain field of the others and jumping away. The complex of clusters can grow further, attracting more glissile cluster with the same Burgers vector, thereby creating a raft of SIA clusters.

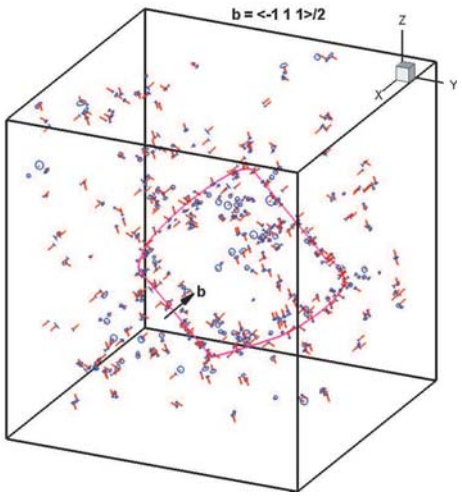

Figure 11.14: A snap-shot of the micro-structure of interstitial clusters at 1.3×10^{-3} dpa, where the decoration by interstitial clusters along dislocation line can be clearly seen.

General Conditions for Decoration and raft Formation

There are two key issues that play important roles in the process of damage accumulation and resultant dislocation decoration and raft formation: (1) the one-dimensional motion of glissile SIA clusters created in displacement cascades, and (2) the interaction between defects and microstructure. The restriction of diffusion of SIA clusters to 1-D leads to a reduction in the reaction rate with other defects because one dimensionally moving clusters are able to travel in the atmosphere of randomly distributed lattice defects through larger distances than those 3-D moving ones, and consequently the possibility that such SIA clusters annihilate at extended sinks such as pre-existing dislocations and grain boundaries increase. At the same time lattice defects affect the motion of one dimensionally diffusing interstitial clusters in a more substantial way than they influence the motion of vacancies since one dimensionally moving clusters have less chances to avoid obstacles by changing their direction of diffusion. Heinisch, Singh and Golubov (**?**, **?**, **?**) investigated the effects of one-dimensional, three-dimensional and mixed one-dimensional/three-dimensional migration (one-dimensional diffusion with direction changes) on defect reaction kinetics by using Kinetic Monte Carlo simulations. Significant

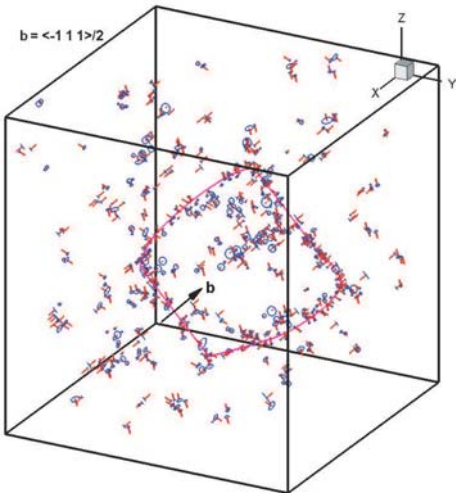

Figure 11.15: A snap-shot of the micro-structure of interstitial clusters at 5.2×10^{-3} dpa, where the accumulation of glissile interstitial clusters near the dislocation is further intensified.

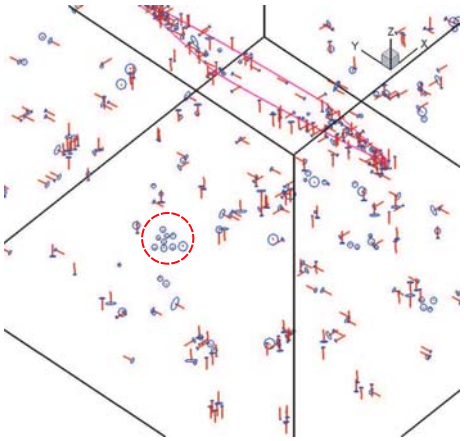

Figure 11.16: A close view of the configuration of a raft of interstitial clusters formed at dose level of 1.8×10^{-3} dpa.

effects of Burgers vector changes on the reaction kinetics of the diffusing interstitial clusters were demonstrated. The functional relationships between the sink strength, the size of sinks and the average distance between direction changes during mixed one-dimensional/three-dimensional migration were explored. Trinkaus et al. (Trinkaus et al. 1997) have shown that a grown-in dislocation would have a large drainage area for accumulating one-dimensionally migrating glissile loops in its neighborhood. Our simulation also demonstrates that even at a fairly low dose of 1.3×10^{-3} dpa a quit clear decoration phenomenon has already occurred in the vicinity of the pre-existing dislocation loop. A detailed analysis of the conditions for the accumulation of glissile SIA clusters near dislocations as well as the dose and temperature dependencies of this phenomenon can be found has been carried out by Trinkaus et al. (**?**) and will not be repeated here.

The energy barrier for directional change is a crucial quantity in controlling when, how and in what extend the dislocation decoration and raft formation occur. It determines the maximum ranges for the elastic interaction that could be strong enough to surpass the barrier and thereby lead to Burgers vector change, as well as the trapping region in the vicinity of dislocations and clusters. In other words, the interaction between defects and microstructure contributes to the dislocation decoration and formation of rafts in terms of changing the diffusivity and the characteristics of mixed 1D/3D migration. Brimhall and Mastel (Brimhall and Mastel 1970) proposed that loops move through the lattice by a combination of prismatic glide and self-climb and form the rafts. Our present simulations, however, suggest that raft formation could be achieved just by prismatic glide of glissile interstitial clusters under the condition of one-dimensional migration combined with strain-field-induced Burgers vector changes. A necessary condition for an undelayed and pronounced formation of rafts of glissile clusters is that the group of clusters having the same Burgers vector is big enough to trapping a single glissile cluster in the strain field formed by the group and prevent any trapped cluster from detrapping or Burgers vector change before it is immobilized by other clusters in the same group. Our simulations indicate that small patches containing two or three clusters is still mobile; more specifically, these small patches still perform one-dimensional migration. With the size of a patch increasing the mobility of the patch decreases, and a raft consisting of more than five clusters is literally immobile. Due to thermal activation or interaction with other defects, a interstitial cluster trapped in the outer region of a raft may break loose the constrain of the strain field of the raft and detrap from the raft.

Chapter 12

Dislocation Representation of Cracks

Instead of solving Equation (**??**) which needs an FEM method or other complicated techniques (**?**), we here propose another discrete method based on the Parametric Dislocation Dynamics.

According to **Bueckner's Principle** (**?**), the stress state around a general 3-D crack in an elastic body subjected to general external loading is identical to the summation of the following two parts:

1. The stress generated if the same external loading acting on the same solid but assuming the crack plane is welded
2. The stress from the same crack in the body subjected only to the internal pressure, or the the counterforce generated in previous step, acting on the same plane.

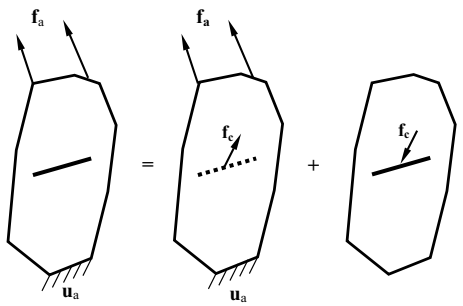

Figure 12.1: Illustration of the solution to general crack problem according to Bueckner's Principle.

Thus, the problem can be divided into two steps for the solution of a general crack problem in an elastic solid. First, under the applied load $\mathbf{f}_a$ and displacement constraint $\mathbf{u}_a$ as shown in

Figure (12.1), and assume the original crack is welded, obtained the stress distribution $\boldsymbol{\sigma}_1$, and then the force vector along the crack plane $\mathbf{f}_c$. The second step is to apply $-\mathbf{f}_c$ on the crack plane and solve for the stress distribution $\boldsymbol{\sigma}_2$. The final stress distribution is thus obtained by summing up $\boldsymbol{\sigma}_1$ and $\boldsymbol{\sigma}_2$ together. We here try to use the discrete dislocation representation method in the second step.

Following Bibly and Eshelby's ideas, the general 3D crack surface is assumed to be filled with layers of material strips. The crack is then welded , and the load is applied, thus producing a group of dislocation loops along the crack surface. The stress state in this solid, $\boldsymbol{\sigma}^t$, is the combination of the applied load and stress from these dislocations. Note that the acting force along the original crack plane can be adjusted to zero by way of adjusting the position or thickness of these dislocation loops. When the welded surface is cut, the overall stress state in the solid will not be changed, since the boundary condition is not changed. According to the uniqueness theorem, the stress distribution of the crack system is the same as $\boldsymbol{\sigma}^t$ produced by the previous steps. In this way, the problem is now to solve the distribution function for the dislocation loops.

By minimization of the total elastic energy of the whole system, a variational form of the governing equations of motion of dislocation loops can be derived, and the spatial distribution is easily obtained. Thus, one can obtain the final configuration of the crack when each dislocation loop reaches its equilibrium state, with the whole system reaching a minimum free energy. Due to the complexity of the stress field and the shape of the crack, an accurate method is needed to obtain reliable quantitative data on the process of the energy minimization. For that reason, the parametric dislocation dynamics (PDD) method is employed here for the simulation.

Note that either solving for the length of the Burgers vector or the loop position, one can achieve force balanced. To simplify the problem, we here set the value of the Burgers vector $\mathbf{b}$ of each dislocation loop as:

$$\mathbf{b} = \alpha \mathbf{f}_c \tag{12.1}$$

Where, α is a constant related to the selection of the length of the Burgers vector. $\mathbf{f}_c$ is the force acting on the crack plane, as defined in Figure (12.1). It is interesting to point out that $\mathbf{f}_c$ is not uniform on the crack plane especially under general 3-D loading. Hence the Burgers vector along the representation dislocations are different. We call here the dislocation on the crack surface as Somigliana dislocation, while the dislocation inside the material as Volterra dislocation, since the Burgers vector is usually the same along the dislocation line inside the material.

We here develop a dynamic addition-deletion strategy for the numerical simulation to obtain the final distribution of dislocation loops. For a given crack, an initial distribution of three equally separated dislocation loops are placed on the crack plane. The shape is chosen according to the crack outer boundary shape with the outermost one chosen as the crack outer boundary, and outermost one is fixed during the whole simulation (Here we assume that there is no crack propagation.). Under the combined effect of their mutual interactions, stress from the applied load and their self-force, these Somigliana dislocations will either move and stretch towards the outermost boundary if the effect of the applied load is dominant, or shrink if the self-force

is dominant, until they reach an equilibrium state. In the simulation process, new loops are continuously added to the simulation, and loops that collapse are taken out of the simulation.

In the adjusting process, once the innermost loop expands when the repulsive force from other loops is less than the applied load, its characteristic length r will be larger than a critical value r_0, and a fresh new loop is generated in the center. r_0 can be given by the equilibrium position of the loop under the applied load and self-force, or a very small set value. The new loop has the same property as the old one, except that its Burgers vector is chosen locally by Equation (12.1). The total number of Somigliana dislocations is thus increased by one. If the repulsive force on the innermost loop is too large, making its characteristic length r smaller than r_0, its self-force makes the loop contract and finally collapse to zero. This loop is taken out of the simulation. Thus, the total number of Somigliana dislocations on the crack plane is then decreased by one. With this dynamic addition-deletion process, a final equilibrium distribution of dislocation loops is obtained.

12.1 Numerical Simulations of General 3-D Cracks

We analyze here the stress field of different shape cracks under either mode-I or mode-II loading, and check the numerical precision of the developed method.

12.1.1 Penny-shaped Crack

The stress distribution in an infinite solid containing a penny-shaped crack under arbitrary loading has been extensively studied in the past. Sack (**?**) and Sneddon (**?**) first solved the problem of a penny-shaped crack opened by pressure applied over its surface in an infinite elastic solid. Collins (**?**) later investigated the stress distribution of a penny-shaped crack in a thick plate. Kassir and Sih (**?**) studied elliptical cracks under arbitrary loading, and compared the results of the stress intensity factor under shear loading with different loading directions. A comparison between the dislocation distribution method and the analytical results will be given here to ascertain the numerical accuracy of the present method.

Pure Shear Loading

Consider a penny-shaped crack with diameter of $2\,r_0$, as shown in Figure (12.2)a, under constant pure shear loading $\sigma_{xz} = \tau$. We construct the local coordinate system on the crack plane as shown in the figure. An initial distribution of dislocations is put inside the crack surface, with 3 equally spaced circular dislocation loops, including the outermost static one which prevents all others moving outside. The applied load generates a uniform shear stress field σ_{xz}. According to Equation (12.1), the Burgers vector of the Somigliana dislocations can be chosen uniformly as:

$$\mathbf{b} = b\mathbf{i}$$

Here, b is constant number since τ is constant.

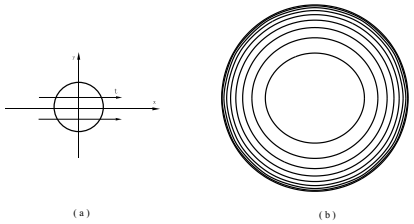

Figure 12.2: Distribution of crack dislocation loops of penny-shaped crack under mode-II loading with $\tau/\mu = 0.004$. (a) illustration of local coordinate system. (b) Final distribution of crack dislocations.

Figure (12.2)b illustrates the final equilibrium distribution of dislocation loops under the applied shear load $\tau/\mu = 0.004$. In the simulation, the constant b is chosen as $b/r_0 = 4 \times 10^{-4}$, the shear modulus $\mu = 50$ GPa, Poisson's ratio $\nu = 0.31$, and crack radius $r_0 = 1000$ a. As shown in the figure, 9 dislocation loops are fitted in the crack plane by using the addition-deletion strategy. The energy of a screw segments is lower than that of a edge one per unit length, as self-force of screw component tends to be higher or *stiffer* than that of a edge one. Thus the edge component tends to stretch more than the screw one, as shown in the figure, and a slightly oval configuration is generated for each loop. Due to the effect of the outmost circular loop, the ratio of the long to short axis of the oval loop decreases from the inner to the outer, as the effect of the outer dislocation loop becomes stronger. It is shown in the figure that the minimum distance of the two outermost loops is within 10 b. In order to capture their mutual interaction with high precision, more Gaussian quadrature points are used in the line integral for stress calculation.

Figure (12.3)a shows the distribution of σ_{xz} as a ratio of the applied shear load τ, compared with the analytical solution obtained by Kassir and Sih (**?**). The relative error along the y-direction is shown in Figure (12.3)b. Within a small range of distances from the tip (≈ 2 % of r_0), the stress drops quickly, and tends to a saturated value which is equal to the applied stress. When the distance is far from the crack tip, the stress is not proportional to $r^{-1/2}$, as in two dimensional cracks. When the distance is less than 0.5% of r_0, the relative error is larger than 10%. The main error comes from the the Fast Sum Method which is used in the stress calculation. As mentioned in (**?**), the relative error of the stress tends to be higher when the field point approaches the dislocation loop. More segments or Gaussian quadrature points are needed for higher precision. In our simulation, when the distance is extremely small (i.e. within a distance of 0.5 % of the radius from the crack tip), the error is inevitably high, since only 16 points are used for the integration for saving CPU time. When the distance increased to 1% of the radius r_0, the relative error is decreased to 5% which is acceptable in numerical simulation.

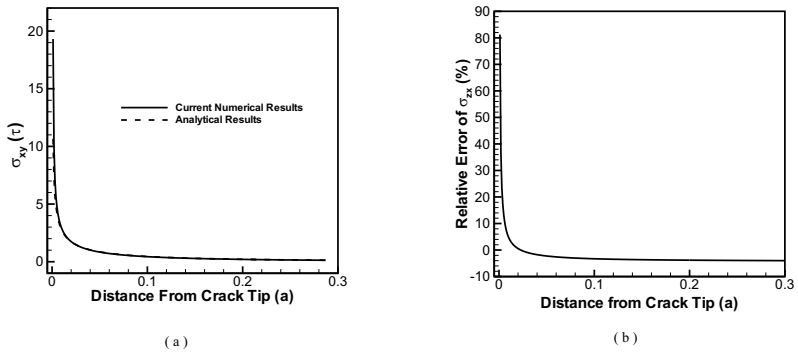

Figure 12.3: Comparisons of the stress component σ_{xz} along y-direction from the final dislocation distribution between current numerical results and analytical results. All the other loading conditions are the same as that in Figure (12.2) (a) The distribution of σ_{xz}. (b) The relative error of σ_{xz}.

Pure Tensile Loading

In the previous section, when shear loading is applied to the penny-shaped crack, the only motion of crack dislocations is glide along the glide plane. But when the same crack is subjected to tensile loading, $\mathbf{b}$ is chosen uniformly according to Equation (12.1) as follows:

$$\mathbf{b} = b\mathbf{k}$$

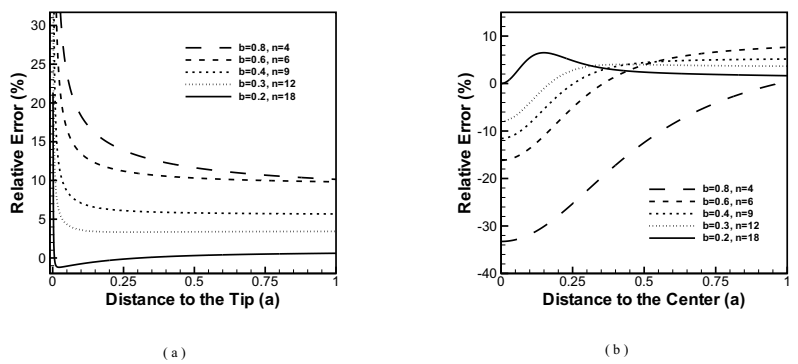

Figure 12.4: Comparisons of relative error of σ_{zz} for penny-shaped crack under external load $\sigma_{zz}/\mu = 0.004$. (a) along radial direction, (b) along the vertical direction from the center

The direction of the Burgers vector is chosen normal to the glide plane, thus it is the climb part of the force that drives the motion of the dislocation loops. With the same addition-deletion

strategy, Figure (12.4) shows the relative error of σ_{zz} along both the z and x directions, when compared with analytical results (**?**). The external loading is chosen as $\sigma_{zz}/\mu = 0.004$. With the increase of the length of the Burgers vector, the mutual repulsive force is increased, and a smaller number of dislocation loops are required in the final distribution. As a result, there is a higher relative error in stress computations. When the length is 0.08% of radius r_0, a relative lower number of dislocation loops (4) is enough for the representation of the crack, but the relative error is high, 91% relative error along the radial direction at 0.005 r_0. When b is decreased to 0.02% of the radius, 18 dislocations are needed. As a result, the error is lowered to 7.65%, and the error along the vertical direction at the crack center is only around 0.1 %. When the length of the Burgers vector is decreased, more dislocations enter into the computation, and when it approaches zero, a continuous distribution of dislocations can be obtained. The error can be lowered to a negligible value, but the price for smaller b is sharp increase in the CPU time. As discussed in (**?**), CPU time for the interaction is proportional to N^2, where N is the total number of segments in dislocations.

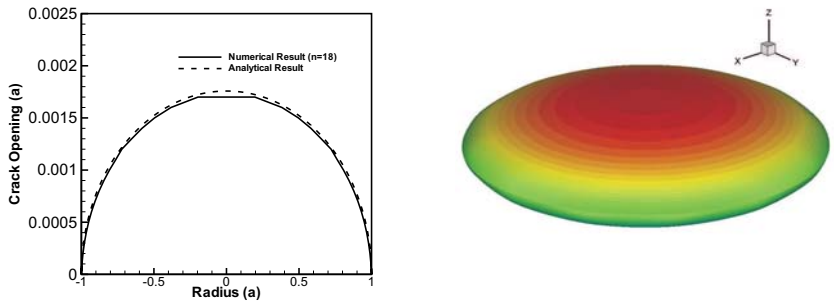

(a) (b)

Figure 12.5: Comparisons of crack opening displacement(COD) with the same condition as in Figure (12.4) except the density of crack dislocation n=18. (a) The COD along diameter. (b) Recover of the crack opening shape in three dimension.

Since each dislocation stands for a displacement jump, which equals to the length of its associated Burgers vector, the byproduct of this simulation is that we can reconstruct the crack opening shape according to the distribution of dislocation loops. The outermost loop stands for zero displacement, since its function is to confine the motion of the dislocation. When we count inwardly, the displacement increases one level for each crack dislocation, with a value of **b**. Figure (12.5)b shows the final reconstructed crack shape. A comparison of crack opening obtained by present method with analytical results along the diameter direction is shown in Figure (12.5)a. When $b = 2.0 \times 10^{-4} r_0$, the number of dislocations is 18, and the maximum relative error is 3.3 % at the center. Since in the simulation scheme, the distribution is discrete, due to the self-force of each loop, no loop can exist in the center except when the length of the Burgers vector is chosen as zero, which means that we have a continuous distribution. But

with decreasing b, the maximum relative error for crack opening displacement(COD) can be decreased to an acceptable level. The crack shape is more like an ellipsoid.

12.1.2 Effect of a Non-uniform Stress Field

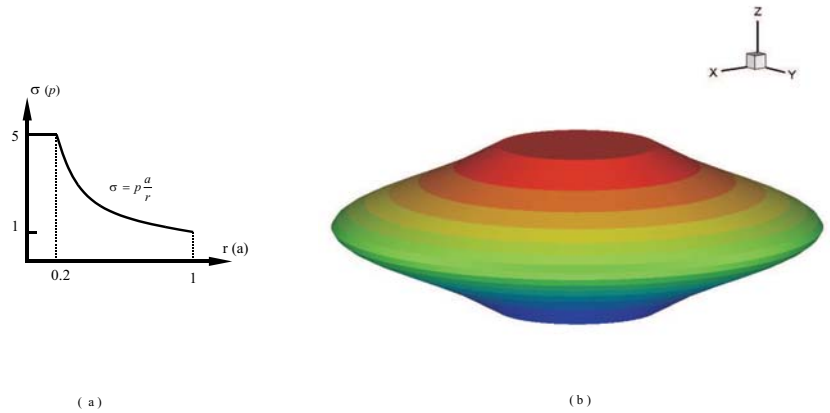

Figure 12.6: A penny-shaped crack is subjected to a normal stress inside the crack surface with a decreasing gradient. (a) the applied stress. (b) correponding crack opening shape

When a non-uniform applied stress directly acts on the surface of the same penny-shaped crack, the shape no longer preserves an ellipsoid configuration. Both Figure (12.6) and Figure (12.7) show different crack shapes obtained by the present method. Decreasing normal stress from the center is applied along the radial direction as shown in Figure (12.6)a, when the stress is chosen as $\sigma = pr_0/r$, where p is a constant value, r is the distance from the center, and r_0 is the crack radius. To avoid a singularity in the center, a cut-off distance of 0.2 r_0 is chosen here. An increasing normal stress chosen as $\sigma = pr/r_0$, is applied in Figure (12.7). In these two cases, the Burgers vector of each crack dislocation is different, and changes according to its position. Since a higher stress is applied in the center, the central part of the crack penning shape is more obtrude as shown in Figure (12.6), and more flat with a lower stress as shown in Figure (12.7).

12.1.3 2-D Straight Crack

Two dimensional cracks have been extensively used in Ductile-to-Brittle transition simulations. Hence it is important to obtain crack dislocation distributions under different loading conditions. Notice that once the ratio of the crack length to its width is very large, stress field of the central

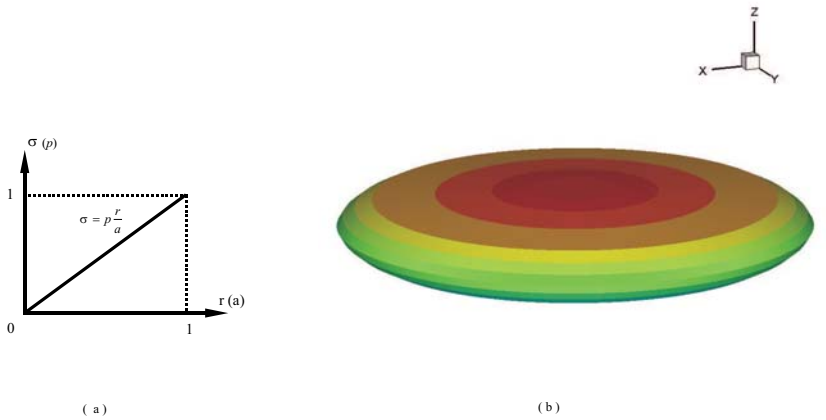

Figure 12.7: A penny-shaped crack is subjected to a normal stress inside the crack surface with an increasing gradient. (a) the applied stress. (b) crack opening shape

part can be viewed as that of a 2-D crack. We will therefore use the same method to re-construct the stress field of 2D cracks.

Simple Loading

Considerer a straight crack with a length $2r_0$ in the x-direction, but with a finite width $20r_0$ in y-direction. The normal of the crack plane is chosen along z-direction as illustrated in Figure (12.8)a.

Unlike the penny-shaped crack, the boundary of the crack surface is a rectangle, and the two ends in the y-direction are open. Dislocations are assumed to be dipolar loops, with the two long arms as F-R source type dislocations with opposite line directions, and their ends moving along the x-direction. The Burgers vector of the two short arms are assumed to be zero, since there are no displacement jumps at the two end boundaries.

The distribution of dislocation loops on the crack surface is shown in Figure (12.8)b for $r_0 = 200\ a$ and a uniform applied tension $\sigma_{zz}/\mu = 0.004$. The shear modulus μ is chosen as 50 GPa, and Poisson's ratio $\nu = 0.31$. The Burgers vector of the Somigliana dislocations is chosen uniformly in the format of $\mathbf{b} = b\mathbf{k}$. The middle part ($-2r_0 \leq y \leq 2r_0$) of the dislocation is perfect straight, and stress field in this region can be viewed as that of a 2-D crack. As a result of the distribution, the crack opening shape can also be recovered as shown in Figure (12.8)c. The relative error of σ_{zz} in the center along the x-direction from the crack tip is shown in Figure (12.9). With the increase in the number of dislocation pairs, the relative error drops significantly. With only 7 dislocation loop pairs, the relative error is less than 2 % when the distance is larger than $0.025r_0$.

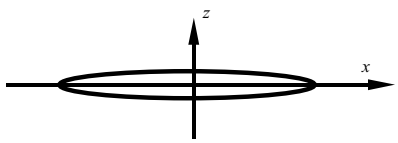

(a)

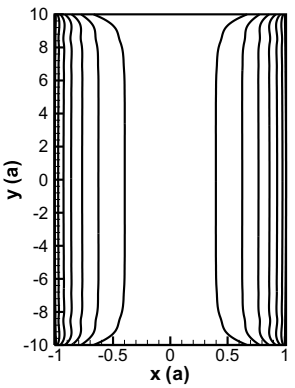

(b)

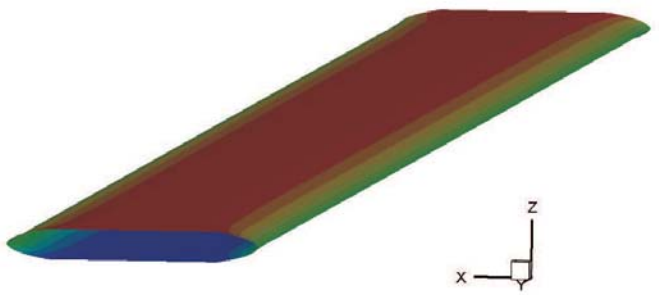

(c)

Figure 12.8: Distribution of crack dislocations of a straight crack under mode-I loading with an applied tension of $\sigma_{zz}/\mu = 0.004$ along the z-direction. (a) the projection view of the crack. (b) Distribution of crack dislocations, the length of the Burgers vector is chosen as $b/r_0 = 7.5\times10^{-4}$. (c) The crack shape in three dimension

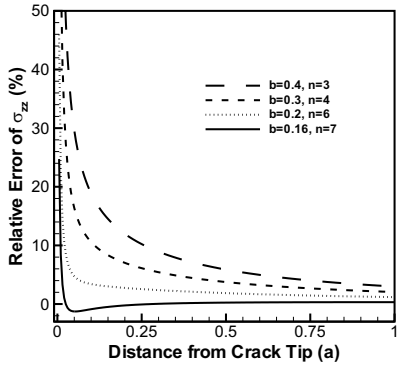

Figure 12.9: Comparison of relative error of σ_{zz}. The same condition as in Figure (12.8)

Mixed Mode Cracks

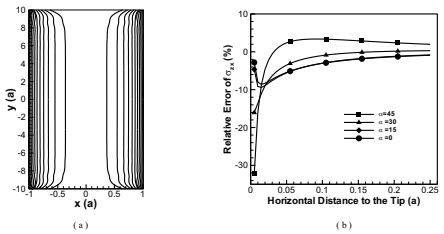

Figure 12.10: Straight crack under mixed model I & II loading. (a) Crack dislocation distribution. (b) Comparison of the relative error of σ_{zx} with different inclination angle.

When the same crack is subjected to mixed mode I & II loading, the results are shown in Figure (12.8)a. The applied tension is chosen as $\sigma/\mu = 0.004$, and shear stress $\tau/\mu = 0.002$, thus the stress tensor on crack surface is:

$$\boldsymbol{\sigma} = \begin{pmatrix} 0 & 0 & 0.002 \\ 0 & 0 & 0 \\ 0.002 & 0 & 0.004 \end{pmatrix} \mu$$

thus the Burgers vector of each Somigliana dislocation loop is then selected of the form:

$$\mathbf{b} = \begin{pmatrix} 2.5 \\ 0 \\ 5.0 \end{pmatrix} \times 10^{-4} r_0$$

The Burgers vector has both in-plane and out-of-plane components. Thus the motion of the dislocation is a mixture of climb and glide.

The final distribution of dislocation loops is shown in Figure (12.10)a, where there are 11 crack dislocation pairs to represent the crack. Figure (12.10)b shows a comparison of the relative error for σ_{zx} with different inclination angles α to the crack plane. As shown in the figure, when the distance is larger than 0.05 r_0, the relative error decrease to less than 5%.

12.2 Three Dimensional Dislocation Interaction with Cracks

A free crack surface results in additional forces (image forces) on dislocations nucleated close to the crack tips. On the other hand, such image forces decrease the crack tip stress intensity factor. Many analytical models have been proposed to study the shielding of a pure edge or screw dislocation of a two dimensional crack (**?**, **?**). Analytical estimation of shielding effect of single dislocation (i.e. Equation (**??**)) has been well utilized in previous 2-D simulations (e.g. (**?**)). Devincre and Roberts (**?**) provided an estimation of the local fracture toughness that is based purely on crack opening or closing stress components of the dislocation stress field at the crack tip. In their estimation, if the crack extends into the z-direction, and the crack is on the y=0 plane, the σ_{yy} component of the stress tensor causes crack opening. Then, the local stress intensity factor is written as

$$\mathrm{k}^{tip}(z) = \mathrm{K}^{app} + \sum_{i=1}^{N} \sqrt{\mu b \mid \sigma^i_{yy}(zz) \mid} \mathrm{sign}(\sigma^i_{yy}(zz)) \tag{12.2}$$

where N is the total number of dislocation segments and $\sigma^i_{yy}(zz)$ is the yy-component of the stress field of the i-th dislocation segment at position z along crack tip. This formula gives a crude estimation for the shielding of general 3-D dislocations. The effects of crack surface changes due to the applied load and the existence of the dislocation itself are not taken into consideration. Other methods based on Boussinesq problem of point loading in a half space (**?**), or the weight function method (**?**, **?**, **?**), have been attempted, but both are painstaking and not practical in real computations.

A new method based on the 3D discrete dislocation representation method is proposed here. Recall in Chapter **??** that, when we solve a 3D crack problem, the external load is the only applied stress, but when there are dislocation loops inside the material, their collective field can be added to the applied load. The Burgers vector of the dislocation loops on the crack surface is thus modified as:

$$\mathbf{b} = \alpha(\mathbf{f}_a + \mathbf{f}_d) = \mathbf{b}_a + \mathbf{b}_d \tag{12.3}$$

Here, $\mathbf{f}_a$ and $\mathbf{f}_d$ are the counterforces of force vectors generated by the applied load and dislocations inside the material respectively, as depicted in Figure (12.1). $\mathbf{b}_a = \alpha\mathbf{f}_a$ is the contribution to the Burgers vector by the applied load, which is usually constant on the crack surface. $\mathbf{b}_d = \alpha\mathbf{f}_d$ is the part contributed by the Volterra dislocations, which is usually not uniform on the crack surface, and it decreases with the increase of the distance to the Volterra dislocation. Since the stress field of the dislocation decreases quickly, the effective contribution to the Burgers vector of the crack dislocation is very small.

With the same procedure of obtaining the final distribution as that in Chapter **??**, one can obtain the overall stress field under both the external load and the Volterra dislocations. The stress field from such a distribution can be divided into two parts, one is the original stress from the crack under external loading, and the other is the extra part due to the crack free surface, and this part is the so-called image stress.

The local stress intensity factor $\mathrm{K}(x)$ at each point x along the crack tip can be easily obtained from this stress distribution by:

$$\mathrm{K}(x) = \lim_{r\to 0} \sigma(r)\sqrt{2\pi r} \tag{12.4}$$

Thus the shielding effect of the dislocation K^d can be obtained by

$$\mathrm{K}^d = \mathrm{K}^a - \mathrm{K}^t \tag{12.5}$$

Here K^t is the total stress intensity factor obtained by the Somigliana dislocation distribution, and K^a is the applied stress intensity factor. When K^d is larger than zero, the overall stress intensity factor is decreased, hence the dislocation has shielding effect on the crack, on the contrary, when $\mathrm{K}^d < 0$, the dislocation can have anti-shielding effect on the crack.

As a comparison, we here use the 3-D model to simulate the shielding effect on a 2D straight edge dislocation ahead of a finite crack, and compare that with the analytical results obtained by Wang and Lee (**?**). Suppose that a finite crack with a length $2r_0 = 1000$ a, a width of $20r_0$, its tip along [010]-direction, and (001)-plane is the crack plane. Now a straight edge dislocation with $\mathbf{b} = 1/2[101](\bar{1}01)$ is introduced close to the crack. It sits on the slip plane $(\bar{1}01)$ with a distance d to the crack tip. Before the introduction of the edge dislocation, the crack plane is already filled with equilibrium state Somigliana dislocations at the applied stress $\sigma/\mu = 0.004$ as shown in Figure (12.11)a. With the existence of the edge dislocation, the equilibrium state is broken, and distributed dislocations will re-adjust their configuration till a new equilibrium state is achieved. From this new equilibrium distribution of Somigliana dislocations, the image stress as well as its shielding effect can be obtained.

It is shown in Figure (12.11) that with the increase of the distance to the tip, the shielding effect decreases. The numerical results show that the shielding effects of a dislocation is stronger by a factor of 2, compared to analytical estimation. This difference can be attributed to the effect of the extra crack surface deformation due to combination effect of the shear and tension force from the dislocation itself. While in the analytical results of Wang and Lee (**?**), the two effects of the Volterra dislocation is treated separately, leading to two independent groups of Somigliana dislocations, the shielding effects is the summation of the effect from these two groups. During the simulation, the applied tension σ/μ is chosen as 0.004, and μ=50 GPa, $\nu = 0.31$, $r_0 = 200$ a.

Under the same conditions as in Figure (12.11), when the straight dislocation is replaced by a circular dislocation loop with $\mathbf{b} = 1/2[101]$, the shielding effect is shown in Figure (12.12). The distance of the center of the loop to the crack tip is chosen as $d/r_0 = 0.2$, and $r_0 = 500$ a. The variation of the stress intensity factor of the loop along the crack tip is shown in Figure (12.12)b. The contour plot of the $\{33\}$ component of the stress tensor (σ_{33}) on the crack surface

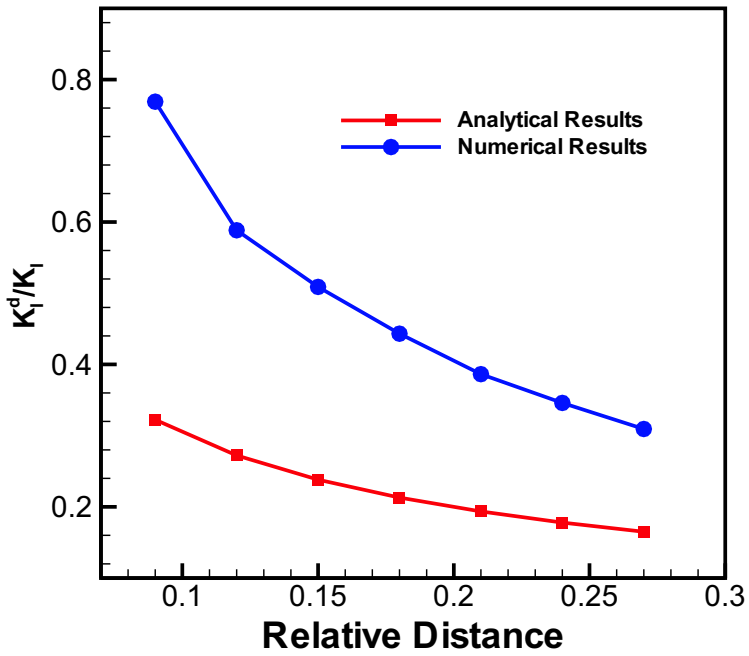

Figure 12.11: Interaction of an edge dislocation and a straight crack in 2D. (a) relative position of crack and the edge dislocation, r_0 is the half width of the crack. (b) comparison of the numerical simulation in the stress intensity factor (solid line) with the analytical results (dashed line).

is shown in Figure (12.12)a, when the loop radius R_0 is chosen as $0.5d$. σ_{33} is always negative, having a tendency to close the crack, thus it has a shielding effect to the crack. When the radius is increased, the shear loop is more close to the tip, thus it has a higher shielding effect. And since the stress field of the loop can only affect a small area, the shielding effect is within a small zone. The effective shielding area is within $-5d \sim 5d$ as shown in the figure when the loop radius $R_0 \leq d$.

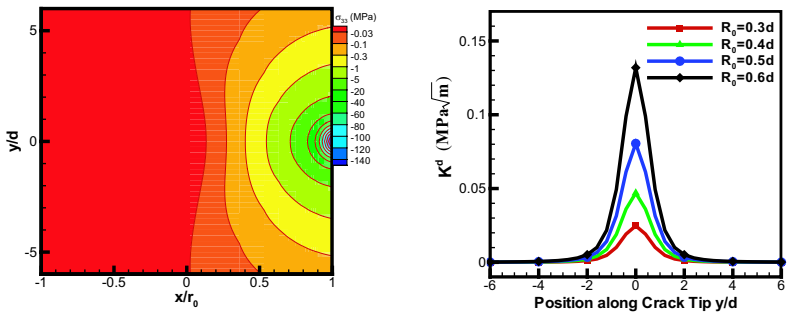

(a) (b)

Figure 12.12: Shielding effect of a shear dislocation loop ahead of crack tip. (a) contour of the σ_{33} generated by the loop when its radius R_0 is $0.5d$. (b) comparison of the stress intensity factor for different initial source sizes.

12.3 Motion of Dislocations ahead of Crack Tips

Dislocation motion ahead of crack tips is quite complicated, and is a key issue to the understanding of the change in the effective stress intensity factor. Assume that a straight dislocation is emitted from a finite crack tip in Tungsten single crystal, and starts to move away from the tip. Figure (12.13) shows its configuration and the corresponding shielding effect on the crack. The size of the crack is chosen as $2r_0 = 1000$ a, and (100) is its plane. The uniaxial applied stress is $\sigma_{11} = 3.0$ GPa (or $K^a = \sigma_{11}\sqrt{\pi r_0} = 2.11$ MPa$\sqrt{\text{m}}$). The Burgers vector of the dislocation is chosen along $(11\bar{1})$-direction with length 0.274 nm and its glide plane is (101) with an angle of 45° to the crack plane. The length of the loop is initially chosen as 400 a, with its two ends at (-200 a, 15 b), (200 a, 15 b) respectively. The two ends are confined to slide along the crack tip direction. We choose the stress exponent m as 2 and the temperature 450 K, all the other constants are chosen according to Table **??**. The force-velocity relation Equation (**??**) is rewritten as:

$$v = M\left(\tau/\tau_0\right)^2 \tag{12.6}$$

Here, M is the effective mobility and $M = 2.47 \times 10^{-3}$ sec/a, v is the nodal velocity.

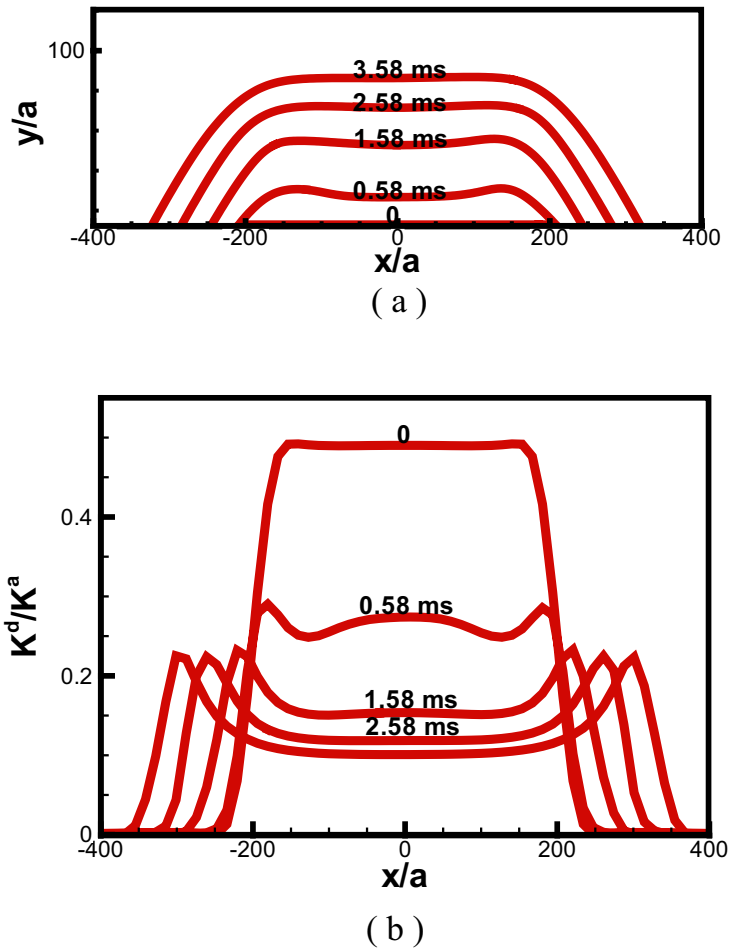

Figure 12.13: Motion of dislocation a half loop ahead of a crack tip in Tungsten single crystal. The initial size of the loop is chosen as 400 a. (a) configuration of the dislocation at different times. (b) the corresponding shielding effects of the dislocation along the crack.

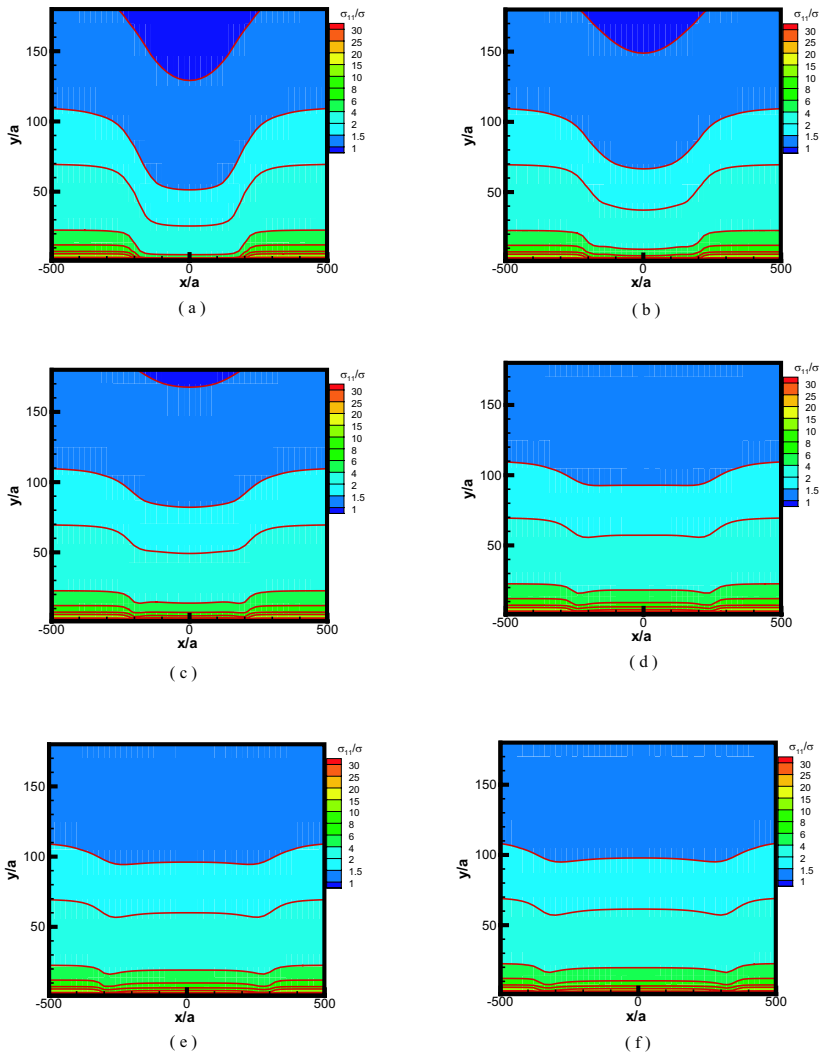

Figure 12.14: Contour of the $\{11\}$ component of the stress tensor from crack tip due to the applied stress and image stress. (a) t=0, (b) t=0.29 ms, (c) t=0.58 ms, (d) t=1.58 ms, (e) t=2.58 ms, (f) t=3.58 ms

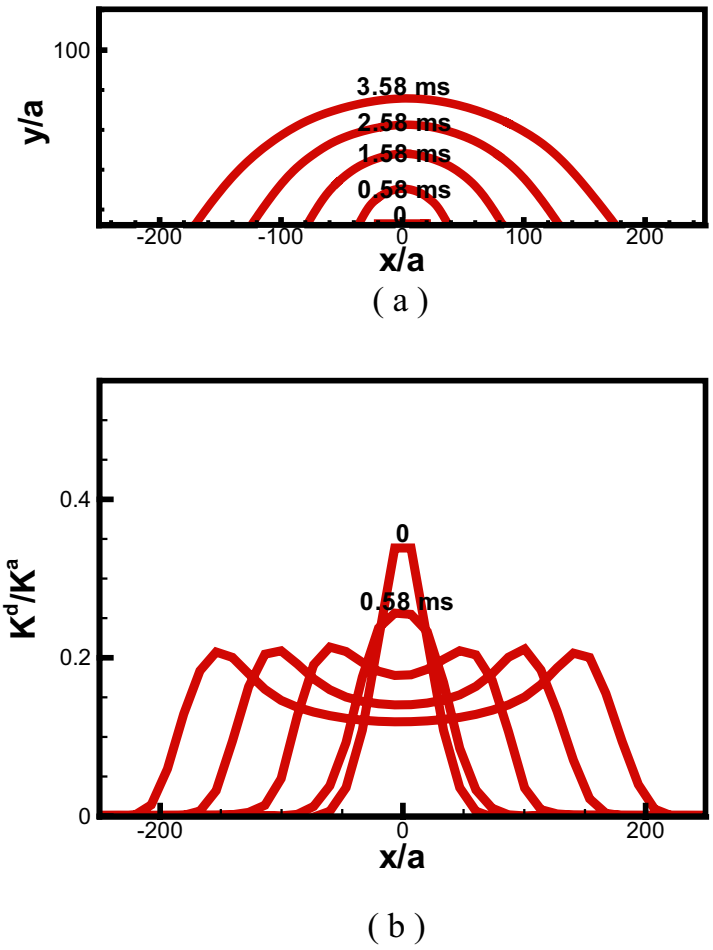

Figure 12.15: Motion of dislocation half loop ahead of crack tip. The initial size of the loop is chosen as 40 a. (a) configuration of the dislocation at different times. (b) the corresponding shielding effects of the dislocation on the crack.

The free surface of the crack tends to pull the dislocation back to the crack. In order to avoid being pulled back and absorbed into the crack, the initial distance of the dislocation to the crack tip is chosen as 15 b. Under the driving force of the crack, the dislocation starts to move away from the tip. At its early stages, when t<2.58 ms, due to the image stress, the total stress applied on the dislocation in the central part is much lower than that at the two ends. Thus, its speed is much lower, and a concave configuration is generated. With the dislocation continually moving away from the tip, the effect of the image stress decreases, and the concave configuration gradually disappear as shown in Figure (12.13)a at t=2.58 ms. Due to the fast decay of the crack stress, the speed of the nodes in the central part is still lower than that at the two sides. Thus a flat top is generated, and the flat top becomes longer during the motion. The shielding effect, expressed as the dislocation stress intensity factor K_d, is shown in Figure (12.13)b. K_d initially has a maximum value, reaching around 50 % of K^a at the center, but after 0.58 ms, the shielding of the center is only 27 % of K^a. Due to the dislocation loop stretch along the crack tip, it can cover larger region of the crack tip field, thus more areas of the crack tip stress intensity factor is lowered. Figure (12.14) shows a contour plot for σ_{11} produced by the loaded crack in the presence of the expanding dislocation loop. The influence of the dislocation is clear in the zone close to the crack tip. Contour plots are shown for t=0, 0.29 ms, 0.58 ms, 1.58 ms, 2.58 ms, 3.58 ms respectively. It can be seen that as the dislocation moves away from the crack, its influence on the crack field itself becomes small.

Figure (12.15) shows the motion of a dislocation loop and its corresponding shielding effect, when the initial size of the source is only 40 a. The initial influence range of the dislocation is very narrow, as can be seen from Figure (12.15)b, when t<0.01 ms. Because the two ends are confined to slide along the crack tip direction, the concave configuration is very small as compared to Figure (12.13), A convex shape is easily recovered around t=0.02 ms. At the time of recovery, the difference between the maximum distance at the central part and the minimum distance at the two sides is only around 5 a. Thus when compared with the corresponding value 83 a in Figure (12.13), variation of the nodal speed in the dislocation is not very large, and there is no flat top in its configuration, as shown in Figure (12.15)a.

12.4 Conclusion

Representation of cracks with 2D distributions of dislocation pileups has been extensively studied analytically and numerically by previous work. In the continuous method, cracks are assumed to be a distribution of loops with an infinitesimal length of Burgers vector. Solving singular (in 2D) or hyper-singular (in 3D) integral equations, one can obtain the distribution function of dislocations. In this work, we assume that the crack surface is filled with discrete dislocation loops with a finite Burgers vector. Minimization the system Gibbs free energy, the PDD is utilized to obtain the final equilibrium distribution and the configuration of dislocation loops under an applied load. The outer dislocation of the distribution is assumed to represent the crack boundary, and is fixed, while the rest dislocation loops are determined by a dynamic addition-deletion process. The crack opening displacement is easily obtained from the distribution, since each dislocation loop stands for one layer of displacement jump, and hence the

crack opening shape can also be easily reconstructed. It is shown that for the penny-shaped crack under mode-I loading, the maximum relative error of the crack opening displacement can be lowered to 3.3 % when 18 dislocation loops are used. High accuracy can be obtained in mode I & II loading in penney-shaped and slit cracks with the decreasing of the length of Burgers vector of the Somigliana dislocation loops. The relative error of the stress field tends to be higher when the field point is near to the crack tip, and more nodal points and Gaussian Quadrature points are needed for the same accuracy. The Burgers vector is chosen to be proportional to the applied load, such that the changes of the applied load will not affect the dislocation distribution significantly.

Chapter 13

The Dislocation Core

Many demanding applications e.g. microelectronics, optoelectronics, aerospace, rocket engines and fuel cells, requires synthesis of structures, such as intermetallic compounds, layered semiconductors etc. made of improved electronic, corrosion resistance, high-temperature intermetallic alloys. The nucleation and mobility of dislocations play a central role in understanding the mechanical and physical properties of these materials. While the continuum elasticity theory predicts well the long range elastic field of a dislocation, it suddenly breaks down within a few atomic spacings surrounding the dislocation center, known as dislocation core. As a consequence, there has been a resurgence of interest to understand the core structure due to its primary importance in controlling many phenomena of crystalline plasticity. In spite of the significant progress that has been made with atomistic models of the dislocation core, the analytical insights into the role of the core remain largely inadequate. In this section, we review and expand the analysis of the disloctaion core in the scope of the Peierls-Nabarro (PN) model to develop a better understanding of this phenomenon.

13.1 The Peierls-Nabarro (PN) Model

13.1.1 The Edge dislocation

Let us consider a cubic crystal with an interplanar spacing d. It is convenient to regard the dislocation of burgers vector b as constructed by slicing the material along the slip plane $x0x'$ that forms two semi-infinite planes and inserting an extra plane of atoms along the cut $0y$ in the lower plane (see fig.). The initial disregistry in displacement in the x direction across the plane $y = 0$ of the bottom half plane with respect to the top half is given by

$$\phi_x^0 = b/2 \quad x > 0 \tag{13.1}$$

$$\phi_x^0 = -b/2 \quad x < 0 \tag{13.2}$$

The two planes are then joined together along $x0x'$, the upper one being extended and lower

one compressed, such that there is a perfect alignment of corresponding atoms at infinity. The system is now in equilibrium under the action of forces applied at the boundaries $PP^{'}$ and $QQ^{'}$. The upper half is said to be in equilibrium by the action of shear stresses acting away from the origin along the the boundary PP'. Similarly, the shear stresses acting along the boundary $QQ^{'}$, being equal and opposite to the shear stresses in $PP^{'}$, maintain the equilibrium of the lower half. It is clear that the relative displacement of an atom at the point x in $PP^{'}$ to the corresponding atom in $QQ^{'}$ is given by

$$\phi_x(x) = 2u_x(x) + b/2 \quad x > 0 \tag{13.3}$$
$$\phi_x(x) = 2u_x(x) - b/2 \quad x < 0 \tag{13.4}$$

where the displacement, $u(x)$, of an atom at the point x in $PP^{'}$ will be equal and opposite to the displacement of the corresponding atom in $QQ^{'}$ in the slip direction, i.e., $u(x)$ is antisymmetric about the plane $y = 0$ with the boundary conditions,

$$u_x(\infty) = -u_x(-\infty) = -b/4 \tag{13.5}$$

It is now convenient to consider that at each point a distance $x^{'}$ from the dislocation line, the displacement ,$u_x(x)$, of the upper boundary with respect to the lower boundary results from the continuous distribution of infinitesimal dislocations with burgers vectors density $b^{'}(x^{'})dx' = -2(du_x/dx)dx^{'}$, so that

$$b = \int_{-\infty}^{\infty} b^{'}(x^{'})dx^{'} = -2\int_{-\infty}^{\infty}(du_x/dx)dx^{'} \tag{13.6}$$

On the basis of classical elasticity theory (see edge dislocation in infinite isotropic media), this distribution of dislocation produces a shear stress, σ_{xy}, at (x,0), given by

$$\sigma_{xy}(x,0) = \frac{\mu}{2\pi(1-\nu)}\int_{-\infty}^{\infty}\frac{b^{'}(x^{'})dx^{'}}{x-x'} = -\frac{\mu}{\pi(1-\nu)}\int_{-\infty}^{\infty}\frac{(du_x/dx)dx^{'}}{x-x^{'}} \tag{13.7}$$

which is balanced by the corresponding component of the periodic restoring force stress $F_b(u_x)$, i.e. $\sigma_{xy}(x,0) = F_b(u_x)$, acting between atoms on either side of the interface mentioned earlier. The original PN model assumes this restoring force stress as a sinusoidal function of bond disregistry $\phi(x)$ with period b and alternatively positive and negative in each half period. Furthermore, it has a limiting form $F_b = \frac{\mu\phi_x}{d}$ for small relative displacements. A simple function of this type takes the form

$$F_b(u_x) = \frac{\mu b}{2\pi d}\sin\frac{2\pi\phi_x}{b} \tag{13.8}$$
$$= -\frac{\mu b}{2\pi d}\sin\frac{4\pi u_x}{b} \tag{13.9}$$

Equating (13.5) and (13.7), we obtain the integro-differential equation known as the PN equation,

$$\frac{b(1-\nu)}{2d}\sin\frac{4\pi u_x}{b} = \int_{\infty}^{\infty}\frac{(du_x/dx)dx'}{x-x'} \tag{13.10}$$

As may be verified by substitution, a solution of (13.8) which satisfies boundary conditions (13.3), and which represents a single dislocation, is given by

$$u_x(x) = -\frac{b}{2\pi}\tan^{-1}\frac{x}{\xi}, \quad \xi = \frac{d}{2(1-\nu)} \tag{13.11}$$

wherein 2ξ is found convenient to define the width of a dislocation, since the $u_(x)$ is numerically less that $b/8$, i.e half of its limiting value. This gives us a rough estimation of the extent of the core region that cannot be prescribed by linear elasticity. From (13.9) and (13.5), the distribution of shear stress which maintains the equilibrium is

$$\sigma_{xy}(x,0) = -\frac{\mu b}{2\pi(1-\nu)}\frac{x}{x^2+\xi^2} \tag{13.12}$$

and the corresponding Burgers vector distribution from (13.4) is

$$b'(x') = \frac{b}{\pi}\frac{\xi}{x'^2+\xi^2} \tag{13.13}$$

The stress field due to such distribution of Burgers vector can be calculated as

$$\sigma_{xx} = \frac{\mu b}{2\pi(1-\nu)}\{\frac{3y+2\xi}{x^2+(y+\xi)^2} - \frac{2y(y+\xi)^2}{[x^2+(y+\xi)^2]^2}\} \tag{13.14}$$

$$\sigma_{yy} = \frac{\mu b}{2\pi(1-\nu)}\{\frac{y}{x^2+(y+\xi)^2} - \frac{2x^2y}{[x^2+(y+\xi)^2]^2}\} \tag{13.15}$$

$$\sigma_{xy} = -\frac{\mu b}{2\pi(1-\nu)}\{\frac{x}{x^2+(y+\xi)^2} - \frac{2xy(y+\xi)}{[x^2+(y+\xi)^2]^2}\} \tag{13.16}$$

$$\sigma_{zz} = \nu(\sigma_{xx}+\sigma_{yy}) = \frac{\mu b\nu}{\pi(1-\nu)}\frac{y+\xi}{x^2+(y+\xi)^2} \tag{13.17}$$

Comparing the stress field with that for a straight edge dislocation, it can be seen that the parameter ξ in the PN model removes the singularity at the origin (x,y), (0,0). Hence the PN model substitutes continuum theory to deal with the dislocation core. However, it is questionable whether Hooke's law applies since the strains are way high at the core region. Thus certain corrections need to be introduced.

13.1.2 The Screw dislocation

The analysis for screw dislocation follows exactly in a similar manner as that for an edge dislocation. Let us assume that the created disregistry in displacement in the z direction is

given by

$$\phi_z^0 = b/2 \quad x > 0 \tag{13.18}$$
$$\phi_z^0 = -b/2 \quad x < 0 \tag{13.19}$$

The two planes are then stitched together along yz plane so that the relative displacement between the atoms can be written in terms of the displacement $u_z(x)$ of the crystal as

$$\phi_z(x) = 2u_z(x) + b/2 \quad x > 0 \tag{13.20}$$
$$\phi_z(x) = 2u_z(x) - b/2 \quad x < 0 \tag{13.21}$$

subjected to the boundary condition

$$u_z(\infty) = -u_z(-\infty) = -b/4 \tag{13.22}$$

The displacement are assumed to be produced by a continuous distribution of dislocation $b^{'}(x^{'})dx' = -2(du_z/dx)dx^{'}$, so that

$$b = \int_{-\infty}^{\infty} b^{'}(x^{'})dx^{'} = -2\int_{-\infty}^{\infty}(du_z/dx)dx^{'} \tag{13.23}$$

This distribution of dislocation produces a shear stress, σ_{yz}, at (x,0), given by

$$\sigma_{yz}(x,0) = \frac{\mu}{2\pi}\int_{-\infty}^{\infty}\frac{b^{'}(x^{'})dx^{'}}{x-x'} = -\frac{\mu}{\pi}\int_{\infty}^{\infty}\frac{(du_z/dx)dx^{'}}{x-x^{'}} \tag{13.24}$$

The restoring force stress takes the same form as that of an edge dislocation (see eqn. 13.7), as a consequence, the integro-differential can be expressed as

$$\frac{b}{2d}\sin\frac{4\pi u_x}{b} = \int_{\infty}^{\infty}\frac{(du_z/dx)dx^{'}}{x-x^{'}} \tag{13.25}$$

The solution of (13.8) is given by

$$u_z(x) = -\frac{b}{2\pi}\tan^{-1}\frac{x}{\eta}, \quad \eta = \frac{d}{2} \tag{13.26}$$

The distribution of shear stress caused by the misfit is

$$\sigma_{yz}(x,0) = \frac{\mu b}{2\pi}\frac{x}{x^2+\eta^2} \tag{13.27}$$

and the distribution of Burgers vector

$$b'(x') = \frac{b}{\pi}\frac{\eta}{x'^2+\eta^2} \tag{13.28}$$

The stress field induced anywhere can be shown to be

$$\sigma_{yz} = \frac{\mu b}{2\pi} \frac{x}{x^2 + (y \pm \eta)^2} \tag{13.29}$$

$$\sigma_{xz} = -\frac{\mu b}{2\pi} \frac{y \pm \eta}{x^2 + (y \pm \eta)^2} \tag{13.30}$$

It is interesting to note that $\eta = (1 - \nu)\xi$. Thus the width of the screw dislocation, 2η, is less than the width of the edge dislocation, 2ξ.

13.2 Modifications of the PN Model

The original PN model predicts very narrow core width which is not probable in actual crystals. One obvious reason for this narrowness is due to the assumed restoring force stress law (13.6) which, in general, does not exist for real crystals. Several attempts have been made over the decades to rectify the force stress law and enhance the PN model to achieve comparable results with experiments. They are summarized below:

1. Foreman et al. (1950) suggested a modification by introducing a parameter, namely 'a', in the displacement function, $u_x(x)$, that controls the width of the dislocation as follows:

$$u_x(x) = -\frac{b}{2\pi} \tan^{-1} \frac{\beta}{a}, \quad \beta = \frac{2(1-\nu)x}{d} \tag{13.31}$$

where 'a' is a parameter greater than unity. When $a = 1$, this becomes the solution 13.9. Hence the width of the dislocation is given by $w = \frac{ad}{1-\nu}$ and is a linear function of a. The corresponding stress distribution and PN restoring force is found to be

$$\sigma_{xy}(x, 0) = -\frac{\mu b}{\pi d} \frac{\beta}{a^2 + \beta^2} \tag{13.32}$$

and

$$F_b(u_x) = \frac{\mu b}{2\pi a d} \sin \frac{2\pi \phi_x}{b} = -\frac{\mu b}{2\pi a d} \sin \frac{4\pi u_x}{b} \tag{13.33}$$

respectively. The force stress law, however, has an incorrect initial slope, except when $a = 1$. A modified $u_x(x)$ is introduced to ensure correct initial slope of the form $\mu\phi_x/d$ for small ϕ_x/d:

$$u_x(x) = -\frac{b}{2\pi} \{\tan^{-1} \frac{\beta}{a} + (a-1) \frac{\beta}{a^2 + \beta^2}\} \tag{13.34}$$

The resulting stress distribution is then

$$\sigma_{xy}(x, 0) = -\frac{\mu b}{\pi d} \{\frac{\beta}{a^2 + \beta^2} + 2a(a-1) \frac{\beta}{(a^2 + \beta^2)^2}\} \tag{13.35}$$

As dislocation widens, that is as a increases, the maximus stress decreases and its position move outwards. The sharp rise of stress that occurs when $a = 1$ simply disappears and gives smoother type of curve. The restoring force stress can be written conveniently in the parametric form

$$\frac{2\pi d}{\mu b}F_b = \frac{1}{2a^2}2(2a-1)\sin\theta - (a-1)\sin 2\theta \tag{13.36}$$

$$\frac{2\pi\phi_x}{b} = \theta - \frac{a-1}{a}\sin\theta \tag{13.37}$$

where θ is given by $\xi = a\cot\theta/2$. It can be found that the slope of the F_b curves remain constant for all values of a, but the amplitudes decrease as a increases, i.e. as the core width increases.

2. Another method of solving the PN integro-differential equation was proposed by Lejcek (1976) and was used later by Freeman et al. (1996).

$$\frac{1}{\pi}\int_{-\infty}^{\infty}\frac{b^{'}(x^{'})dx^{'}}{x-x^{'}} = \frac{2(1-\nu)}{\mu}F_b(u) = -g(x) \tag{13.38}$$

The restoring force law can be derived from the stacking fault energies $\gamma(u)$ using the relation

$$F_b(u) = \frac{d\gamma}{du}. \tag{13.39}$$

The solution (13.30) can also be obtained using Hilbert transformation. Let the function $\phi(z)$ be chosen in the form

$$\phi(z) = \sum_{k=1}^{N}\sum_{n=1}^{p_k}\frac{A_{nk}}{(z-z_k)^n} \tag{13.40}$$

where $A_{nk} = a_{nk} + ib_{nk}$ are complex parameters and $z = x + iy$. The function $\phi(z)$ must carry the following properties: (i) in the upper half plane $\phi(z)$ has N poles of the order p_k in the points $z_k = x_k + i\xi_k$, $(k = 1, ...N)$, (ii) $\phi(z) \to 0$ for $|z| \to \infty$; (iii) the function $\phi(x)$ defined on the real axis by the relation $\phi(x) = \lim_{y\to 0}\phi(z)$, has the following useful for investigation of Hilbert pairs:

$$\frac{1}{\pi}\int_{-\infty}^{\infty}\frac{\phi(x^{'})dx^{'}}{x-x^{'}} = i\phi(x) \tag{13.41}$$

Equation (13.33) can be proved using the relation

$$\sum_{k=1}^{N} res_{z=z_k}\left(\sum_{n=1}^{p_k}\frac{A_{nk}}{(x-z)(z-z_k)^n}\right) = \phi(x) \tag{13.42}$$

If $b^{'}$ and g denote the Hilbert pairs of the function $\phi(x)$, i.e. $\phi(x) = b^{'}(x) + ig(x)$, then the real part of equation (13.33) gives equation (13.30) and the imaginary part has the form

$$\frac{1}{\pi}\int_{-\infty}^{\infty}\frac{g(x^{'})dx^{'}}{x-x^{'}} = b^{'}(x) \tag{13.43}$$

Thus $b'(x)$ and $g(x) = -\frac{2(1-\nu)}{\mu} F_b(u)$ can be written explicitly in terms of x as

$$b'(x) = \sum_{k=1}^{N} \sum_{n=1}^{p_k} b'_{nk}(x) \tag{13.44}$$

$$\frac{2(1-\nu)}{\mu} F_b(u(x)) = -\sum_{k=1}^{N} \sum_{n=1}^{p_k} g_{nk}(x) \tag{13.45}$$

where

$$b'_{nk} = \frac{1}{2}\left[\frac{A_{nk}}{(x-z_k)^n} + \frac{\overline{A}_{nk}}{(x-\overline{z}_k)^n}\right] \tag{13.46}$$

$$g_{nk} = -\frac{i}{2}\left[\frac{A_{nk}}{(x-z_k)^n} - \frac{\overline{A}_{nk}}{(x-\overline{z}_k)^n}\right] \tag{13.47}$$

From the relation between $F_b(u)$ and $b'(x)$ given by the PN equation it can be concluded that the number N of poles of function $\phi(z)$ can be interpreted as the number of partial dislocations into which a total dislocation with burgers vector b dissociates. The positions of partials are determined by the parameters x_k and their widths by ξ_k. The parameters A_{nk} must satisfy the condition

$$u(-\infty) = 0; \quad u(-\infty) = 0 \tag{13.48}$$

$$F_b = 0 \quad for \quad u = 0, \quad u = b \tag{13.49}$$

and both z_k and A_{nk} have to be determined in such a way that the function on the right-hand side of (13.36b) fits the prescribed force law $F_b(u)$. The number p_k which determines the order of the poles of $\phi(z)$ gives an approximation for fitting the prescribed $F_b(u)$. Explicit form of $b'_{nk}(x)$, $g_{nk}(x)$ and $u_{nk}(x)$ can be found for various p_k in Lejcek(1976) and will not be repeated here.

3. Later Medvedeva and Freeman (1996) used this to configure the core structure of NiAl and FeAl. They used two types of dislocations with burgers vector <111> and <100>. It is sufficient to use parameters $N = 1$ and $p_k = 3$ in the case of <100> dislocations, and $N = 2$ and $p_k = 2$ for <111> dislocations. Using 3.36(a)-3.37(b) one can obtain expressions for displacements $u(x)$ and restoring forces $F_b(u(x))$ in convenient parametric forms:

(a) for <111> dislocations

$$\frac{2\pi(\theta)}{b} = \frac{1}{2}\left[\theta_1 + \theta_2 - \frac{\alpha-1}{\alpha}(\sin\theta_1 + \sin\theta_2)\right] \tag{13.50}$$

$$\frac{2\pi d}{\mu b} F_b(u) = \frac{1}{2\alpha}\left[\sin\theta_1 + \sin\theta_2 + 2\frac{\alpha-1}{\alpha} \times \left(sin^2\frac{\theta_1}{2}\sin\theta_1 + sin^2\frac{\theta_2}{2}\sin\theta_2\right)\right] \tag{13.51}$$

(b) for <100> dislocations

$$\frac{2\pi u(\theta)}{b} = \theta - \frac{\alpha-1}{\alpha}\sin\theta - \beta\sin\theta \tag{13.52}$$

$$\frac{2\pi d}{\mu F_b(u)} = \frac{1}{\alpha}\left[\sin\theta + 2\frac{\alpha-1}{\alpha}\sin^2\frac{\theta}{2}\sin\theta + 2\sin^3\frac{\theta}{2}\beta\cos\frac{3\theta}{2}\right] \tag{13.53}$$

where,

$$\theta_1(\theta) = 2\cot^{-1}\frac{x-\delta}{\xi}; \quad \theta_2(\theta) = 2\cot^{-1}\frac{x+\delta}{\xi}; \quad \theta = 2\cot^{-1}\frac{x}{\xi} \tag{13.54}$$

It was assumed that superpartial dislocations are at $\pm\delta$ and have the same core width $\xi = \alpha d/2(1-\nu)$. It can be seen that for $\delta = 0$ and $\theta_1 = \theta_2$ we obtain expressions similar to Foreman et al.(1950) solution, in addition, for $\alpha = 1$ expression 13.39,40 give original solution of the PN model. The parameter α, β and δ are determined from the fit to plots of stacking fault energy (γ).

13.3 The Peierls Stress

The magnitude of the Peierls stress, σ_p, may be determined if one assumes that the field of the displacements $u(x-l)$ does not depend on the position of the center of the dislocation l. In the absence of a dislocation the spacing of atomic planes in the direction of x is defined by a'. When the dislocation is introduced at the position l , the planes, in the upper half of the crystal at a position na' in a direction perpendicular to the dislocation line, will be displaced w.r.t the lower half by $u(na'-l)$, along b. The misfit energy can be considered as the sum of misfit energies between pairs of atomic planes, and can be written as (Joos and Duesbery, 1997)

$$W(u) = \sum_{n-\infty}^{\infty} \gamma(u(na'-l))a' \tag{13.55}$$

Then the Peierls stress σ_p, the maximum stress required to overcome the periodic barrier in $W(u)$,

$$\sigma_p = max[\sigma] = max\left[\frac{1}{b}\frac{dW}{du}\right] \tag{13.56}$$

Assuming the restoring force to be of the form

$$F(u(x)) = \tau_{max}\sin\frac{2\pi u(x)}{b}, \tag{13.57}$$

the misfit energy can be calculated after integrating (13.43) as

$$W(u) = \sum_{n-\infty}^{\infty}\frac{\tau_{max}a'b}{2\pi}\left[\cos\left(2\tan^{-1}\left(\frac{na'-l}{\xi}\right)\right)+1\right] \tag{13.58}$$

After some manipulation, it finally takes the form

$$W(y) = \frac{Kb^2}{4\pi} \frac{\sinh 2\pi\Gamma}{\cosh 2\pi\Gamma - \cos 2\pi y}. \tag{13.59}$$

In (13.44) and (13.45) $\xi\tau_{max} = Kb/4\pi$, $\Gamma = \xi/a^{'}$, $y = u/a^{'}$, $K = \mu/(1-\nu)$ and $K = \mu$. To get the Peierls stress we first have to compute the stress associated with the misfit energy variation.

$$\sigma(y) = \frac{1}{b}\frac{dW}{du} = -\frac{Kb}{2a'} \frac{\sinh 2\pi\Gamma \sin 2\pi y}{(\cosh 2\pi\Gamma - \cos 2\pi y)^2}. \tag{13.60}$$

Maximizing (13.46) yields the Peierls stress

$$\sigma_p = \sigma(y_m), \quad 2\cos 2\pi y_m = -\cosh 2\pi\Gamma + \sqrt{(}9 + \sinh^2 2\pi\Gamma) \tag{13.61}$$

Observe that for narrow dislocations ($\Gamma \leq 1$) and for wide dislocations ($\Gamma \geq 1$). Hence the Peierls stress for these two extreme cases can be obtained as: (a) for narrow dislocations

$$\sigma_p = \frac{3\sqrt{(}3)}{8}\tau_{max}\frac{a^{'}}{\pi\xi} \tag{13.62}$$

(a) for wide dislocations

$$\sigma_p = \frac{Kb}{a^{'}} e^{-2\pi\xi/a^{'}} \tag{13.63}$$

In the original PN model discussed earlier, τ_{max} was chosen so that, for small displacements, the elastic limit is recovered. This approximation, however, no longer valid for real crystals since dislocation cores rely more on the value of the small displacement. Hence, more realistic approximation for τ_{max} is to take the maximum slope of the generalized stacking fault energy surface, in the appropriate direction for the dislocation under study.

Chapter 14

Surface Defects and Atom Clusters

14.1 Surface Defects and Surface Atoms

Deposited adatoms on the substrate can be treated as an atomic defect. Similar to the case of bulk defects, the stress field of surface defects can be calculated from the response of the material to a force density on the surface. If the force density is given as T_i, the elastic relaxation energy E^s_{el} can be written as:

$$E^s_{el} = -\int d\vec{\rho} \cdot T_i\left(\vec{\rho}\right) u_i\left(\vec{\rho}\right) \tag{14.1}$$

where $\rho_i = (x, y)$ is the position vector on the surface and u_i is the displacement field of the underlying substrate. Note that this E^s_{el} is the *surface* relaxation energy. The complete elastic energy should be $E_{el} = E^V_{el} + E^S_{el}$.

In terms of Green's Function $G_{ij}(\rho - \rho', z)$, u_i, this can be written as:

$$u_i\left(\vec{\rho}, z\right) = \int d\vec{\rho} \cdot T_j\left(\vec{\rho}\right) G_{ij}\left(\vec{\rho} - \vec{\rho}', z\right) \tag{14.2}$$

Thus, the elastic strain energy becomes:

$$E^s_{el} = -\iint d\vec{\rho} d\vec{\rho}' \cdot T_i\left(\vec{\rho}\right) T_j\left(\vec{\rho}'\right) G_{ij}\left(\vec{\rho} - \vec{\rho}', 0\right) \tag{14.3}$$

The interaction energy of two defects E_{int} may be determined by the following equation:

$$E^s_{\text{int}} = -\tfrac{1}{2}\iint d\vec{\rho} d\vec{\rho}' \left[T^{(1)}_i\left(\vec{\rho}\right) T^{(2)}_j\left(\vec{\rho}'\right) G_{ij}\left(\vec{\rho} - \vec{\rho}', 0\right) + T^{(2)}_i\left(\vec{\rho}\right) T^{(1)}_j\left(\vec{\rho}'\right) G_{ji}\left(\vec{\rho}' - \vec{\rho}, 0\right)\right] \tag{14.4}$$

For Green's function, as shown before, we have:

$$G_{ij}\left(\vec{R},0\right)=\frac{1+\nu}{\pi E}\left[(1-\nu)\frac{\delta_{ij}}{R}+\nu\frac{R_iR_j}{R^3}\right] \tag{14.5}$$

For anisotropic crystal surfaces, the *explicit* expressions of surface Green tensor functions in the Fourier space are known only for hexagonal crystals (Dobrzynski and Maradudin 1976) and cubic crystals (Portz and Maradudin 1977).

By expressing the force density T in the following different cases, we can obtain the general form of the interaction energy.

14.2 Bulk Point Defects

Details of solutions for point defects in the crystal bulk can be found in (Kossevich 1999). Physically, an interstitial atom in a crystal material can be treated as a point defect in the bulk. If the equivalent forces exerted on the system have three pairs of forces with *equal* value between each pairs applied to that point, we can always describe the system by a spatial distribution of forces:

$$T_i\left(\vec{r}\right)=-K\Omega_0\frac{\partial}{\partial x_i}\delta\left(\vec{r}\right) \tag{14.6}$$

where K is the total compression modulus. In a cubic crystal or an isotropic medium, Ω_0 equals to the increase in the crystal volume caused by one interstitial atom, which is the product of dilatation and volume.

If the deformation by the point defect is equivalent to three pairs of forces with different values of each pairs, we call it as a dipole-type point defects and the force densities has to be written by:

$$T_i\left(\vec{r}\right)=-K\Omega_{ik}\frac{\partial}{\partial x_k}\delta\left(\vec{r}\right) \tag{14.7}$$

In an isotropic case, the dilatation volume tensor Ω_{ik} has the symmetric form: $\Omega_{ik}=\Omega\delta_{ik}$.

Another way to get a better understanding about the equation (14.7) is to follow Mura's way, that is the total strain induced by a defect is composed of elastic strain (ε^{el}) and eigenstrain ($\varepsilon^{\dagger}$). Ignoring the boundary terms, we can make the simple derivation as the following:

$$\begin{aligned}E_{el} &= \frac{1}{2}\int\limits_V d\vec{r}\varepsilon_{ij}\sigma_{ij}=\frac{1}{2}\int\limits_V d\vec{r}\left(\varepsilon_{ij}^{el}+\varepsilon_{ij}^{\dagger}\right)C_{ijkl}\varepsilon_{kl}^{el}\\ &= \frac{1}{2}\int\limits_V d\vec{r}\varepsilon_{ij}^{el}C_{ijkl}\varepsilon_{kl}^{el}+\frac{1}{2}\int\limits_V d\vec{r}\left(\nabla_l u_k\right)C_{ijkl}\varepsilon_{ij}^{\dagger}\end{aligned}$$

$$= \frac{1}{2}\int_V d\vec{r}\varepsilon_{ij}^{el}C_{ijkl}\varepsilon_{kl}^{el} + \int_V d\vec{r}\cdot u_k\nabla_l\left(-\tfrac{1}{2}C_{ijkl}\varepsilon_{ij}^{\dagger}\right) \tag{14.8}$$

If the point defect is considered, in general case we have $\varepsilon_{ij}^{\dagger}(\vec{r}) = \varepsilon_{ij}^{0}\delta(\vec{r})$ and the force density becomes the equation (14.7).

Single Surface Adtom

A single adatom on the surface is represented as a dipole-type. Consider one single atom as a point defect, the force density of point defects is then given by:

$$T_i(\vec{\rho}) = A_{ij}\frac{\partial}{\partial x_j}\delta(\vec{\rho}) \tag{14.9}$$

where A_{ij} is the symmetric dipole force tensor. In the elastically isotropic case, we have $A_{ij} = A\delta_{ij}$.

Substituting equation (14.9) and (14.5) into equation (14.4), we obtain the elastic interaction energy between two single adatoms in a simple form:

$$E_{\text{int}}^{s} = \frac{1-\nu^2}{\pi E}\frac{A^2}{\rho^3} \tag{14.10}$$

We can see here that identical defects repel one another. Shilkrot and Srolovitz calculated the numerical value of the dipole force $A = 0.62$ eV by atomistic simulations (Shilkrot and Srolovitz 1997). Thus an order of magnitude estimate for the strength of the interaction can be evaluated as 0.1 meV for two adatoms within 5 atomic units apart, which is much smaller than the value reported in (Lau and Kohn 1977).

14.3 Surface Atom Clusters

A direct way to obtain the interaction energy of two monolayer clusters is to consider adatoms as point defects. Without considering the capillary effect, we can rewrite the equation (14.9) as:

$$T_i(\vec{\rho}) = A_{ij}\nabla_j c(\vec{\rho}) \tag{14.11}$$

where c is the density of adatoms at a position $\vec{\rho}$.

Doing the same operation as for a single atom, we can find in the isotropic case:

$$E_{\text{int}}^{s} = \iint d\vec{\rho} d\vec{\rho}' \frac{(1-\nu^2)}{\pi E} \frac{A^2}{R^3} c\left(\vec{\rho}\right) c\left(\vec{\rho}'\right) \tag{14.12}$$

However, owing to the new surface formed by a monolayer of atoms, the capillary phenomena will bring an important effect and the different surface domains will interact with each other by discontinuous intrinsic surface stresses. This, in turn, can be used express the force density. As defined in references (Marchenko and Parshin 1980) and (Andreev and Kosevich 1981), the surface force density T_i can be represented by a divergence of the intrinsic surface stress tensor τ_{ik}:

$$T_i\left(\rho\right) = \frac{\partial \tau_{ik}}{\partial x_k} \tag{14.13}$$

The change in the surface stress tensor (τ_{ik}) can be estimated by the formula:

$$\delta \tau_{ik} = \varepsilon_{ik}^{(a)} n_a \tag{14.14}$$

where ε^a is the energy of atoms in the a^{th} clusters, n_a is the number of atoms per unit surface area. Here, the key assumption is that the surface monolayer clusters are treated as a collection of *point defects*. Substituting Equations (14.13) and (14.14) into Equation (14.4), and assuming that the boundary term vanishes, we can obtain:

$$E_{\text{int}} = -\tfrac{1}{2} \iint d\vec{\rho} d\vec{\rho}' n_a\left(\vec{\rho}\right) n_b\left(\vec{\rho}'\right) \varepsilon_{il}^{(a)} \varepsilon_{k'm'}^{(b)} \nabla_l \nabla_{m'} \left[G_{ik}\left(\vec{R}\right) + G_{ki}\left(-\vec{R}\right)\right] \tag{14.15}$$

In the isotropic case, we can set $\varepsilon_{ik}^{(a,b)} = \varepsilon_{xx}^{(a,b)}$. By applying Green's Tensor equation (14.5), the interaction energy assumes the following simple form:

$$E_{\text{int}} = \iint d\vec{\rho} d\vec{\rho}' \frac{(1-\sigma^2)}{\pi E} \frac{\varepsilon_{xx}^{(a)} \varepsilon_{xx}^{(b)}}{R^3} n_a\left(\vec{\rho}\right) n_b\left(\vec{\rho}'\right) \tag{14.16}$$

To make an estimation of the order of magnitude of E_{int}, we know that $\varepsilon \sim 0.035$ eV/$\mathring{A}$ (Alerhand, Vanderbilt, Meade and Joannopoulos 1988). For two planar islands, each of which have 10 atoms, the interaction energy is about ~ 0.1 eV when they are 5 atomic distance apart.

14.3.1 Interaction between a line defect and a point defect

As we mentioned in the preceding section, the elastic source of monolayer islands is induced by the discontinuity of the intrinsic surface stress along the boundary, which means that the surface cluster can be viewed as a line defect (dislocation). In fact, if we write down the correct force density of line-type defects, we can do the exactly same thing as we did for point defects. For example, considering the interaction energy between a single adatom and a surface step,

since the derivative of the δ function along the direction of the step is replaced by a constant, we have:

$$E^s_{\text{int}} = \frac{2\,(1-\nu^2)}{\pi E}\frac{D_x A}{\rho^2} \tag{14.17}$$

where D_0 is the force dipole strength of a surface step. Compared with the relation of $1/\rho^3$ in Equation (14.10), we can find that the interaction energy of the line defect to be proportional to $1/\rho^2$.

14.3.2 Interaction between periodic line defects

A special solution for the equation (14.3) can be obtained in the case of periodic surface domains. In the isotropic case, it is found that the energy of the periodic structure has a logarithmic dependence on the period l (Alerhand et al. 1988, Marchenko 1981), that is:

$$E_{el} \sim \frac{1}{l}\ln\left(\frac{l}{a}\right) \tag{14.18}$$

Since l is always found to be larger than the lattice parameter a by at least an order of magnitude, the continuum elastic approach is justified. It should be noted that in this case, the interaction between domains is a monopole-monopole interaction.

Different types of interaction energy between periodic line defects are completely reviewed by Shshukin et al. (Shchukin and Bimberg 1999). For example, for periodically faceted surfaces or periodic arrays of macroscopic step bunches, this is: $E \sim 1/l - 1/l\ln(l/a)$.

Islands with shapes and lattice mismatches

In reality, as deposition continues, surface islands will involve from planar domains into tilted shapes. If the material system is a heterostructure, the lattice mismatche can also play an important role in the energy. Thus, and as summarized by Shchukin et al. , the elastic energy of an island including both bulk and surface contributions is given by 4 terms (Shchukin and Bimberg 1999):

- The first one is the strain-mismatch elastic energy in a planar film
- The second one is the volume elastic energy by the tilted facets of islands
- The third one is due to the surface stress discontinuity at the edges.
- The last one comes from the interaction between tilted facets and surface stress discontinuity.

Expressing these four terms using Green's tensor functions, we can write the complete formula for elastic interaction:

$$\begin{aligned} E_{el} &= \lambda\varepsilon_0^2 V \\ &\quad -\frac{1}{2}\left(c_{11}+2c_{12}\right)\varepsilon_0 \oint dA \int dA' m_i\left(\vec{r}\right) G_{i\alpha}\left(\vec{r},\vec{r}'\right) \widetilde{\sigma_{\alpha\beta}} m_\beta\left(\vec{r}'\right) \\ &\quad -\frac{1}{2}\int dl \int dl' T_i\left(\vec{r}\right) G_{ij}\left(\vec{r},\vec{r}'\right) T_j\left(\vec{r}'\right) \\ &\quad -\int dl \int dA' T_i\left(\vec{r}\right) G_{i\alpha}\left(\vec{r},\vec{r}'\right) \widetilde{\sigma_{\alpha\beta}} n_\beta\left(\vec{r}'\right) \end{aligned} \tag{14.19}$$

where $\vec{m}$ is the local normal to the facet of islands, V is the volume of the equivalent planar, uniform film, $G_{ij}(\vec{r},\vec{r}')$ is the static Green's tensor defined for a semi-infinite crystal with a stress-free surface of a given profile, $\widetilde{\sigma_{\alpha\beta}} = -(c_{11}+2c_{12})(c_{11}-c_{12})c_{11}^{-1}\varepsilon_0\delta_{\alpha\beta}$ is the stress tensor in a planar heteroepitaxial film, $\oint dA$ is defined over both the side facets of the island and the interface between the island and the wetting layer, $\int dA'$ contains nonvanishing contributions from side facets of the island only and $\int dl$ and $\int dl'$ are carried out over the edges of the island.

Instead of the complicated details of calculation, Shchukin et al. gave us a hint of estimating the relation between the energy and two islands' distance by evaluating the second term only. They obtained the following formula:

$$E_{\text{int}}^{(2nd)} = \frac{\left(c_{11}+2c_{12}\right)^2\left(c_{11}-c_{12}\right)^2 c_{11}^2}{4\pi c_{11}^2}\varepsilon_0^2 V^2 \frac{B_1 + 15B_2\left(1-8m_x^2 m_y^2\right)}{R^3} \tag{14.20}$$

where B_1 and B_2 are two interpolated coefficients of angular dependence of the exact Green's tensor by the lowest-order angular polynomial having cubic symmetry. For an isotropic medium, $B_2 = 0$.

Chapter 15

Computer Programs & Architecture

15.1 Basic DD Program

```
      module variables

 implicit none
 double precision::norm,pi,nu,m1,m2,m3,x_elp,y_elp,f1,f2,f3,core,
+seg_size,s0,r_cluster,G_shear,a_thick,T_temp

 integer :: max_quad, n_points1,n_points2,inside,n_loops,
+n_segments,n_nodes
 integer :: k_ref,k_1,k_2,i_loop, i_node
 integer, dimension(3)::i_max

 character (len=20):: segment_type,mesh
 character (len=200):: title

 double precision,dimension(3):: mil,burg,b_loc,b_test,center,
+delta,t_vec,QL,QG,R,r_small,r_prime,dr_prime,dr,e_1,e_2,e_3,grid,
+normal,displace,force,zero,mil2,burger2

 double precision, dimension(3,3) :: EG,EP,ES,LG1,LPG,LGP,sig_loc,
+sig_glo,delta_loc, sig

 double precision, dimension(20) :: mod_R,R3,R5,R111,R112,R113,
+R221,R222,R223,R331,R332,R333,R123,t,w,theta
 double precision, dimension(3,20) :: X,DX
```

```
 double precision,allocatable,dimension(:,:):: PL,PG,tangent,
+r_local,angle,burger


       END module variables
 !=================================================================

     program microplasticity

 use variables
 double precision, dimension(3)::trans
 integer:: k_abs,j_segment,ix,iy,iz,time1,time2,start1,start2,
+finish1,finish2
 integer, dimension(8):: values
 character (len=8):: today; character (len=10)::time
 character (len=5)::zone

 call date_and_time(today,time,zone,values)
  print *, "date", today
  print *, "time=", time
  start1 = values(7)
  start2 = values(8)

 namelist /input/mil,burg,b_test,center,x_elp,y_elp,f1,f2,f3,delta,
+          grid,mil2,burger2,r_cluster,G_shear,a_thick,T_temp
 namelist /limits/max_quad,n_loops,n_segments,n_nodes,segment_type,
+      n_points1,n_points2,inside,title,mesh,i_max

 OPEN (UNIT=1, FILE="data")
 OPEN (UNIT=3, FILE="loop_coord.txt")
 OPEN (UNIT=4, FILE="diagnostics.txt")
 OPEN (UNIT=7, FILE="local_stress.txt")
 OPEN (UNIT=8, FILE="global_stress.txt")
 OPEN (UNIT=9, FILE="field_coord.txt")
 OPEN (UNIT=10,FILE="surface_mesh.txt",action="read")
 OPEN (UNIT=11,FILE="surface_tractions.txt")
 OPEN (UNIT=12,FILE="int_energy2.txt")

   !  Read Data, and prepare basic parameters

   call defaults
   read (1,input); read (1,limits)
   print *,title; write(7,*)title; write(8,*)title
```

```
      ! write(12,*)title

       ! Allocate dimensions

       allocate(PL(3,n_segments+1),PG(3,n_segments+1),burger(3,n_loops),
     +          tangent(3,n_segments+1),angle(n_loops,n_segments+1),
     +          r_local(n_loops,n_segments+1))

      ! Calculate initial conditions

        call initial

        ! Global and Plane Basis Vectors

        call base_vectors

    !Find local Burgers vector

    call transform (EG,zero,burg,EP,zero,b_loc,LGP)

     !Generate full dislocation loops

        do i_loop=1,n_loops
      x_elp=f1*x_elp;y_elp=f2*y_elp
           do j_segment=0,n_segments
             call loop_generator (j_segment)
       end do
       seg_size= dsqrt ((PG(1,1)-PG(1,2))**2+(PG(2,1)-PG(2,2))**2
     +        +(PG(3,1)-PG(3,2))**2)

    end do

    if (segment_type=="spline")then; call tangent_vec; end if

    select case (mesh)

    ! Uniform Cartesian Mesh (i_max(1)*imax(2)*imax(3))

    case ("global")

    do ix=0,i_max(1)
        do iy=0,i_max(2)
            do iz=0,i_max(3)
               QG(1) = ix*grid(1)
```

```
            QG(2) = iy*grid(2)
            QG(3) = iz*grid(3)
            call transform(EG,zero,QG,EP,center,QL,LGP)
            call stress_calcs
            call int_energy2
            call inner_product(sig_glo,b_test,t_vec)
            write (11,fmt=101)QG,t_vec
         end do
      end do
   end do

   case ("local")

   !Generate (n_points1*2n_points2*n_nodes*n_loops) local points
   ! & calculate stress

      do i_loop=1,n_loops
         do i_node=0,n_nodes-1
       QL(2)=0
         do k_2=-n_points2,n_points2,1
           QL(1)=0;QL(3)=0;
           k_abs = abs(k_2)
           if (k_abs==0)then; k_abs=1;end if
           QL(2) = core*(k_2/k_abs)*k_abs**f3
             do k_1=0,n_points1
             call transform(EP,center,QL,EG,zero,QG,LPG)
             call stress_calcs
             end do
         end do
     end do
   end do

   case ("surface")

   !Calculate tractions on a surface mesh

   read (10,fmt=*)QG,normal

      call transform(EG,zero,QG,EP,center,QL,LGP)
      call stress_calcs
      write (*,101) sig_glo
      call inner_product(sig_glo,normal,t_vec)
      write (*,102) QL,QG,t_vec
   write (11,fmt=101)QG,t_vec
```

```
    case ("nodes")

    !Calculate force at all loop nodes

        do i_loop=1,n_loops
           do i_node=0,n_nodes-1
        do m=1,3
          QL(m)=PL(m,i_node)
          displace (m) = burger(m,i_loop)
        end do
        call stress_calcs
            call inner_product(sig_glo,displace,force)
       end do
    end do

    end select

        call date_and_time(today,time,zone,values)
       print *, "time=", time
       finish1 = values(7)
       finish2 = values(8)

       time1 = finish1 - start1
       time2 = finish2 - start2

        print *,  "cpu_time=     seconds"
    write(unit=*,fmt=103)time1
        print *,  "cpu_time=     milli-seconds"
    write(unit=*,fmt=103)time2

101     format(6(2x,es12.5))
102     format(9(2x,es12.5))
103     format(I6)

        end program microplasticity
      !=====================================================================

            subroutine initial

    use variables
    integer:: i,n

      call quadrature(max_quad,t,w)
```

```
  pi    = 2.*dasin(1.d0)
  nu    =0.34d0
  m1    =2*nu/(1-nu)
  m2    =m1/nu
  m3    =(1+nu)/(1-nu)
  s0    = 1./(4.*pi*(1-nu))
  norm  = dsqrt(mil(1)**2+mil(2)**2+mil(3)**2)
  delta_loc =0
  sig_loc   =0
  sig_glo   =0
  zero  =0

    do i=1,3
    e_2(i)=-mil(i)/norm
    end do

                end subroutine initial

    !=============================================================

        subroutine defaults

    use variables

    mil(1)  =1;     mil(2)  =1;     mil(3)  =0
    burg(1) =1; burg(2) =1;     burg(3) =1
    dr(1)   =2;  dr(2)  =0;     dr(3)   =2
    max_quad=16;     n_nodes=10;    n_loops =1
    x_elp       =200;       y_elp   =200
    n_segments  =10;        core    =1.5
    center      =1000;      delta   =0
    i_max   =10;    grid    =100
    segment_type ="loop"

    end subroutine defaults
!=================================================================

    subroutine quadrature(n,pos,wt)

intent(in):: n; intent(out)::pos, wt
integer::n; double precision, dimension(20)::pos,wt
select case (n)
```

```
case (2)

 pos(1)= -0.577350269189626;    wt(1)= 1.000000000000000
 pos(2)=  0.577350269189626;    wt(2)= 1.000000000000000

case (3)

 pos(1)=-0.774596669241483; wt(1)=  0.555555555555556
 pos(2)= 0.000000000000000; wt(2)=  0.888888888888889
 pos(3)= 0.774596669241483; wt(3)=  0.555555555555556

case(4)

 pos(1)=-0.861136311594053; wt(1)=  0.347854845137454
 pos(2)=-0.339981043584856; wt(1)=  0.652145154862546
 pos(3)= 0.339981043584856; wt(3)=  0.652145154862546
 pos(4)= 0.861136311594053; wt(4)=  0.347854845137454

case(5)

 pos(1)=-0.906179845938664; wt(1)=  0.236926885056189
 pos(2)=-0.538469310105683; wt(2)=  0.478628670499366
 pos(3)= 0.000000000000000; wt(3)=  0.568888888888889
 pos(4)= 0.538469310105683; wt(4)=  0.478628670499366
 pos(5)= 0.906179845938664; wt(5)=  0.236926885056189

case(6)

 pos(1)=-0.932469514203152; wt(1)=  0.171324492379170
 pos(2)=-0.661209386466265; wt(2)=  0.360761573048139
 pos(3)=-0.238619186083197; wt(3)=  0.467913934572691
 pos(4)= 0.238619186083197; wt(4)=  0.467913934572691
 pos(5)= 0.661209386466265; wt(5)=  0.360761573048139
 pos(6)= 0.932469514203152; wt(6)=  0.171324492379170

case(7)

 pos(1)=-0.949107912342759; wt(1)=  0.129484966168870
 pos(2)=-0.741531185599394; wt(2)=  0.279705391489277
 pos(3)=-0.405845151377397; wt(3)=  0.381830050505119
 pos(4)= 0.000000000000000; wt(4)=  0.417959183673469
 pos(5)= 0.405845151377397; wt(5)=  0.381830050505119
 pos(6)= 0.741531185599394; wt(6)=  0.279705391489277
 pos(7)= 0.949107912342759; wt(7)=  0.129484966168870
```

```
case(8)

 pos(1)=-0.960289856497536; wt(1)=  0.101228536290376
 pos(2)=-0.796666477413627; wt(2)=  0.222381034453374
 pos(3)=-0.525532409916329; wt(3)=  0.313706645877887
 pos(4)=-0.183434642495650; wt(4)=  0.362683783378362
 pos(5)= 0.183434642495650; wt(5)=  0.362683783378362
 pos(6)= 0.525532409916329; wt(6)=  0.313706645877887
 pos(7)= 0.796666477413627; wt(7)=  0.222381034453374
 pos(8)= 0.960289856497536; wt(8)=  0.101228536290376

case (9)

 pos(1)=-0.968160239507626; wt(1)=  0.081274388361574
 pos(2)=-0.836031107326636; wt(2)=  0.180648160694857
 pos(3)=-0.613371432700590; wt(3)=  0.260610696402935
 pos(4)=-0.324253423403809; wt(4)=  0.312347077040003
 pos(5)= 0.000000000000000; wt(5)=  0.330239355001260
 pos(6)= 0.324253423403809; wt(6)=  0.312347077040003
 pos(7)= 0.613371432700590; wt(7)=  0.260610696402935
 pos(8)= 0.836031107326636; wt(8)=  0.180648160694857
 pos(9)= 0.968160239507626; wt(9)=  0.081274388361574

case (10)

 pos(1)=-0.973906528517172; wt(1)=  0.066671344308668
 pos(2)=-0.865063366688985; wt(2)=  0.149451349150581
 pos(3)=-0.679409568299024; wt(3)=  0.219086362515982
 pos(4)=-0.433395394129247; wt(4)=  0.269266719309996
 pos(5)=-0.148874338981631; wt(5)=  0.295524224714753
 pos(6)= 0.148874338981631; wt(6)=  0.295524224714753
 pos(7)= 0.433395394129247; wt(7)=  0.269266719309996
 pos(8)= 0.679409568299024; wt(8)=  0.219086362515982
 pos(9)= 0.865063366688985; wt(9)=  0.149451349150581
 pos(10)=0.973906528517172; wt(10)= 0.066671344308668


case (11)

 pos(1)=-0.978228658146057; wt(1)=  0.055668567116174
 pos(2)=-0.887062599768095; wt(2)=  0.125580369464905
 pos(3)=-0.730152005574049; wt(3)=  0.186290210927734
 pos(4)=-0.519096129206812; wt(4)=  0.233193764591990
```

```
 pos(5)=-0.269543155952345; wt(5)=  0.262804544510247
 pos(6)= 0.000000000000000; wt(6)=  0.272925086777901
 pos(7)= 0.269543155952345; wt(7)=  0.262804544510247
 pos(8)= 0.519096129206812; wt(8)=  0.233193764591990
 pos(9)= 0.730152005574049; wt(9)=  0.186290210927734
 pos(10)=0.887062599768095; wt(10)= 0.125580369464905
 pos(11)=0.978228658146057; wt(11)= 0.055668567116174

case (12)

 pos(1)=-0.981560634246719; wt(1)=  0.047175336386512
 pos(2)=-0.904117256370475; wt(2)=  0.106939325995318
 pos(3)=-0.769902674194305; wt(3)=  0.160078328543346
 pos(4)=-0.587317954286617; wt(4)=  0.203167426723066
 pos(5)=-0.367831498998180; wt(5)=  0.233492536538355
 pos(6)=-0.125233408511469; wt(6)=  0.249147045813403
 pos(7)= 0.125233408511469; wt(7)=  0.249147045813403
 pos(8)= 0.367831498998180; wt(8)=  0.233492536538355
 pos(9)= 0.587317954286617; wt(9)=  0.203167426723066
 pos(10)=0.769902674194305; wt(10)= 0.160078328543346
 pos(11)=0.904117256370475; wt(11)= 0.106939325995318
 pos(12)=0.981560634246719; wt(12)= 0.047175336386512

case (13)

 pos(1)=-0.984183054718588; wt(1)=  0.040484004765316
 pos(2)=-0.917598392222975; wt(2)=  0.092121498837728
 pos(3)=-0.801578090733310; wt(3)=  0.138873510219787
 pos(4)=-0.642349339440340; wt(4)=  0.178145980761946
 pos(5)=-0.448492751036447; wt(5)=  0.207816047536889
 pos(6)=-0.230458315955135; wt(6)=  0.226283180262897
 pos(7)= 0.000000000000000; wt(7)=  0.232551553230874
 pos(8)= 0.230458315955135; wt(8)=  0.226283180262897
 pos(9)= 0.448492751036447; wt(9)=  0.207816047536889
 pos(10)=0.642349339440340; wt(10)= 0.178145980761946
 pos(11)=0.801578090733310; wt(11)= 0.138873510219787
 pos(12)=0.917598392222975; wt(12)= 0.092121498837728
 pos(13)=0.984183054718588; wt(13)= 0.040484004765316

case (14)

 pos(1)=-0.986283808696812; wt(1)=  0.035119460331752
 pos(2)=-0.928434883663574; wt(2)=  0.080158087159760
 pos(3)=-0.827201315069765; wt(3)=  0.121518570687903
```

```
 pos(4)=-0.687292904811685; wt(4)=  0.157203167158194
 pos(5)=-0.515248636358154; wt(5)=  0.185538397477938
 pos(6)=-0.319112368927890; wt(6)=  0.205198463721296
 pos(7)=-0.108054948707344; wt(7)=  0.215263853463158
 pos(8)= 0.108054948707344; wt(8)=  0.215263853463158
 pos(9)= 0.319112368927890; wt(9)=  0.205198463721296
 pos(10)=0.515248636358154; wt(10)= 0.185538397477938
 pos(11)=0.687292904811685; wt(11)= 0.157203167158194
 pos(12)=0.827201315069765; wt(12)= 0.121518570687903
 pos(13)=0.928434883663574; wt(13)= 0.080158087159760
 pos(14)=0.986283808696812; wt(14)= 0.035119460331752

case (15)

 pos(1)=-0.987992518020485; wt(1)=  0.030753241996117
 pos(2)=-0.937273392400706; wt(2)=  0.070366047488108
 pos(3)=-0.848206583410427; wt(3)=  0.107159220467172
 pos(4)=-0.724417731360170; wt(4)=  0.139570677926154
 pos(5)=-0.570972172608539; wt(5)=  0.166269205816994
 pos(6)=-0.394151347077563; wt(6)=  0.186161000015562
 pos(7)=-0.201194093997435; wt(7)=  0.198431485327112
 pos(8)= 0.000000000000000; wt(8)=  0.202578241925561
 pos(9)= 0.201194093997435; wt(9)=  0.198431485327112
 pos(10)=0.394151347077563; wt(10)= 0.186161000015562
 pos(11)=0.570972172608539; wt(11)= 0.166269205816994
 pos(12)=0.724417731360170; wt(12)= 0.139570677926154
 pos(13)=0.848206583410427; wt(13)= 0.107159220467172
 pos(14)=0.937273392400706; wt(14)= 0.070366047488108
     pos(15)=0.987992518020485; wt(15)= 0.030753241996117

case (16)

 pos(1)=-0.989400934991650; wt(1)=  0.027152459411754
 pos(2)=-0.944575023073233; wt(2)=  0.062253523938648
 pos(3)=-0.865631202387832; wt(3)=  0.095158511682493
 pos(4)=-0.755404408355003; wt(4)=  0.124628971255534
 pos(5)=-0.617876244402644; wt(5)=  0.149595988816577
 pos(6)=-0.458016777657227; wt(6)=  0.169156519395003
 pos(7)=-0.281603550779259; wt(7)=  0.182603415044924
 pos(8)=-0.095012509837637; wt(8)=  0.189450610455068
 pos(9)= 0.095012509837637; wt(9)=  0.189450610455068
 pos(10)=0.281603550779259; wt(10)= 0.182603415044924
 pos(11)=0.458016777657227; wt(11)= 0.169156519395003
 pos(12)=0.617876244402644; wt(12)= 0.149595988816577
```

```
 pos(13)=0.755404408355003; wt(13)= 0.124628971255534
 pos(14)=0.865631202387832; wt(14)= 0.095158511682493
 pos(15)=0.944575023073233; wt(15)= 0.062253523938648
 pos(16)=0.989400934991650; wt(16)= 0.027152459411754

end select

    end subroutine quadrature

!=================================================================

    subroutine stress_calcs

use variables
integer::i,j_seg

    if(segment_type=="loop")then
    n_segments=1
end if

if (mesh=="local") then
call point_generator
end if


        do i=1,n_loops
           do j_seg =0,n_segments-1

             if (segment_type=="analytic") then
             call Hirth(j_seg)
             else
             call green(j_seg)
             end if

          sig_loc= sig_loc+delta_loc
    if (mesh=="local") then
          sig_glo=matmul(matmul(LPG,sig_loc),transpose(LPG))
else
          sig_glo=matmul(matmul(transpose(LGP),sig_loc),LGP)
end if


           end do
       end do
```

```
  call writer
  sig_loc=0

        end subroutine stress_calcs

 !=============================================================

    subroutine green(k_seg)

use variables
integer::i

delta_loc=0

  do i=1,max_quad

 call parametric (i,k_seg)

R111(i)=(-3*X(1,i)/R3(i))+(3*X(1,i)**3                  /R5(i))
R112(i)=(-  X(2,i)/R3(i))+(3*X(1,i)**2*X(2,i)           /R5(i))
R113(i)=(-  X(3,i)/R3(i))+(3*X(1,i)**2          *X(3,i) /R5(i))
R221(i)=(-  X(1,i)/R3(i))+(3*X(1,i)   *X(2,i)**2        /R5(i))
R222(i)=(-3*X(2,i)/R3(i))+(3          *X(2,i)**3        /R5(i))
R223(i)=(-  X(3,i)/R3(i))+(3          *X(2,i)**2*X(3,i) /R5(i))
R331(i)=(-  X(1,i)/R3(i))+(3*X(1,i)           *X(3,i)**2/R5(i))
R332(i)=(-  X(2,i)/R3(i))+(3          *X(2,i) *X(3,i)**2/R5(i))
R333(i)=(-3*X(3,i)/R3(i))+(3                  *X(3,i)**3/R5(i))
R123(i)=(                 3*X(1,i)   *X(2,i)   *X(3,i) /R5(i))

call stress(i)
delta_loc=delta_loc+sig*w(i)

  end do

    end subroutine green

  !=================================================================

    subroutine stress(i)

use variables
double precision, dimension(3,3,3)::g
integer::k,m,n,i
```

```
      g = 0; sig = 0

     g(1,1,1)=+b_loc(2)*(-2*R113(i)+m1*(R223(i)+R333(i)))+
    *b_loc(3)*(2*R112(i)-m1*(R222(i)+R332(i)))
     g(1,1,2)=-b_loc(1)*m2*(R223(i)+R333(i))+b_loc(3)*m2*
    +(R221(i)+R331(i))
     g(1,1,3)=+b_loc(1)*m2*(R222(i)+R332(i))-b_loc(2)*m2*
    +(R221(i)+R331(i))

     g(1,2,1)=+b_loc(1)*(R113(i)+R223(i)+R333(i))-b_loc(2)*m2*R123(i)+
    *b_loc(3)*(+m3*R221(i)-R111(i)-R331(i))
     g(1,2,2)=+b_loc(1)*m2*R123(i)-b_loc(2)*(R113(i)+R223(i)+R333(i))+
    *b_loc(3)*(-m3*R112(i)+R222(i)+R332(i))
     g(1,2,3)=m2*(-b_loc(1)*R221(i)+b_loc(2)*R112(i))

     g(1,3,1)=-b_loc(1)*(R112(i)+R222(i)+R332(i))+b_loc(2)*
    +(R111(i)+R221(i)- m3*R331(i))+b_loc(3)*m2*R123(i)
     g(1,3,2)=m2*(+b_loc(1)*R331(i)-b_loc(3)*R113(i))
     g(1,3,3)=-b_loc(1)*m2*R123(i)-b_loc(2)*
    +(-m3*R113(i)+R223(i)+R333(i))+b_loc(3)*(R112(i)+R222(i)+R332(i))

     g(2,2,1)=+b_loc(2)*m2*(R113(i)+R333(i))-b_loc(3)*m2*
    +(R112(i)+R332(i))
     g(2,2,2)=+b_loc(1)*(-m1*(R113(i)+R333(i))+2*R223(i))+
    *b_loc(3)*(+m1*(R111(i)+R331(i))-2*R221(i))
     g(2,2,3)=+b_loc(1)*m2*(R112(i)+R332(i))-b_loc(2)*m2*
    +(R111(i)+R331(i))

     g(2,3,1)=-b_loc(2)*m2*R332(i)+b_loc(3)*m2*R223(i)
     g(2,3,2)=+b_loc(1)*(-R112(i)-R222(i)+m3*R332(i))+
    *b_loc(2)*(R111(i)+R221(i)+R331(i))-b_loc(3)*m2*R123(i)
     g(2,3,3)=+b_loc(1)*(R113(i)+R333(i)-m3*R223(i))+
    *b_loc(2)*m2*R123(i)-b_loc(3)*(R111(i)+R221(i)+R331(i))

     g(3,3,1)=+b_loc(2)*m2*(R113(i)+R223(i))-b_loc(3)*m2*
    +(R112(i)+R222(i))
     g(3,3,2)=-b_loc(1)*m2*(R113(i)+R223(i))+b_loc(3)*m2*
    +(R111(i)+R221(i))
     g(3,3,3)=+b_loc(1)*(m1*(R112(i)+R222(i))-2*R332(i))+
    *b_loc(2)*(-m1*(R111(i)+R221(i))+2*R331(i))

   do m=1,3
       do n=m,3
```

```
          do k=1,3
      sig(m,n)=sig(m,n)+g(m,n,k)*DX(k,i)/(8*pi)
          end do
      end do
  end do

  do n=1,3
      do m=n,3
      sig(m,n) = sig (n,m)
      end do
   end do

          end subroutine stress
    !=====================================================================

      subroutine Hirth (j_seg)

  use variables
  integer::j_seg,m
  double precision:: z2
  double precision, dimension(3)::T1,es_1,es_2,es_3,v_s1,v_s2,QS
      double precision, dimension(3,3)::sig_z1,sig_z2,LPS

    do m=1,3
      v_s1(m) = PG(m,j_seg)
      v_s2(m) = PG(m,j_seg+1)
      es_3(m)=(v_s1(m)-v_s2(m))/seg_size
      T1(m)=(v_s2(m)+v_s1(m))/2.
    end do

  es_2 = e_2
  call cross_product(es_2,es_3,es_1)
  do i=1,3
   ES(1,i)=es_1(i);ES(2,i)=es_2(i);ES(3,i)=es_3(i)
  end do

  call transform (EP,center,QL,ES,T1,QS,LPS)
  call analytic_sig(QS,-seg_size/2,sig_z2)
  call analytic_sig(QS,seg_size/2,sig_z1)

  delta_loc = sig_z2 - sig_z1
  delta_loc = matmul(matmul(transpose(LPS),delta_loc),LPS)

      end subroutine Hirth
```

```
!=============================================================

    subroutine analytic_sig(QS,z2,s_z2)

use variables
double precision::RR2,RR,RR3,lambda,R_lam,c2,bx,by,bz,
 +  xs,xy,xz
double precision, intent(in):: z2
double precision, dimension(3), intent (in):: QS
double precision, dimension(3):: b_s
    double precision, dimension(3,3)::LGS
double precision, dimension(3,3), intent(out):: s_z2

call transform (EG,zero,burg,ES,zero,b_s,LGS)

xs = QS(1); ys=QS(2); zs=QS(3)
RR2 = xs**2+ys**2+(zs-z2)**2
RR  = dsqrt (RR2)
RR3 = RR*RR2
lambda = z2 - zs
R_lam = RR+lambda
c2 = RR*R_lam
bx = b_s(1); by=b_s(2); bz=b_s(3)

s_z2(1,1) =s0*(bx*ys*(1+xs*xs/RR2+xs*xs/c2)/c2+
 +           by*xs*(1-xs*xs/RR2-xs*xs/c2)/c2)
s_z2(2,2) =s0*(-bx*ys*(1-ys*ys/RR2-ys*ys/c2)/c2-
 +           by*xs*(1+ys*ys/RR2+ys*ys/c2)/c2)
    s_z2(3,3) =s0*(bx*(2.*nu*ys/c2+ys*lambda/RR3)+
 +           by*(-2.*nu*xs/c2-xs*lambda/RR3))
    s_z2(1,2) =s0*(-bx*xs*(1-ys*ys/RR2-ys*ys/c2)/c2+
 +           by*ys*(1-xs*xs/RR2-xs*xs/c2)/c2)
    s_z2(1,3) =s0*(-bx*xs*ys/RR3+by*(-nu/RR+xs*xs/RR3)+
 +          bz*ys*(1.-nu)/c2)
s_z2(2,3) =s0*(bx*(nu/RR-ys*ys/RR3)+by*xs*ys/RR3-
 +          bz*xs*(1.-nu)/c2)

s_z2(2,1) = s_z2(1,2)
s_z2(3,1) = s_z2(1,3)
s_z2(3,2) = s_z2(2,3)

    end subroutine analytic_sig
!=============================================================
```

```
          subroutine parametric (i,k)

      use variables
      integer::i,k,j,m
      double precision::u
      double precision, dimension(3)::a0,a1

      r_small=QL

      select case (segment_type)

      !Select parametric representation

      case ("loop")

      !Elliptic polar curve
      theta(i)=pi*t(i)+pi
r_prime(1) = x_elp*dcos(theta(i))
r_prime(2) = 0.
r_prime(3) =-y_elp*dsin(theta(i))

dr_prime(1) = -pi*x_elp*dsin(theta(i))
dr_prime(2) = 0.
dr_prime(3) = -pi*y_elp*dcos(theta(i))

case ("linear")

    ! linear parametric curve
do j=1,3
a0(j) = 0.5*(PL(j,k) + PL(j,k+1)); a1(j)=0.5*(PL(j,k+1)-PL(j,k))
r_prime(j) = a0(j)+a1(j)*t(i)
dr_prime(j)= a1(j); end do

case ("spline")

   !Composite Cubic Spline Curve
  u = (t(i)+1)/2
      do j=1,3
       r_prime(j)=(2*u**3-3*u*u+1)*PL(j,k)+(-2*u**3+3*u*u)*PL(j,k+1)
 +      +(u**3-2*u*u+u)*tangent(j,k)+(u**3-u*u)*tangent(j,k+1)
       dr_prime(j)=((6*u**2-6*u)*PL(j,k)+(-6*u**2+6*u)*PL(j,k+1)
 +      +(3*u**2-4*u+1)*tangent(j,k)+(3*u**2-2*u)*tangent(j,k+1))/2
      end do
```

```
  end select

do m=1,3
   DX(m,i)=dr_prime(m)
   R(m) = r_small(m) - r_prime(m)
   X(m,i)=R(m)
end do

mod_R(i)=dsqrt(R(1)**2+R(2)**2+R(3)**2)
R3(i)=mod_R(i)**3 ; R5(i)=mod_R(i)**5

    end subroutine parametric

!=================================================================

    subroutine tangent_vec

use variables
double precision::c,e
    double precision, dimension(2)::a,f

    n = n_segments
    do j=1,3
    PL(j,0)=PL(j,n)
    PL(j,n+1)=PL(j,1)
    end do

  !Solve the tangent vectors at each data point
  c=4
  a(1)=(-c+sqrt(c*c-4))/2; a(2)=(-c-sqrt(c*c-4))/2
  DO j=1,3
    DO m=1,2
    e=1;f(m)=0
       do i=0,n-1
      f(m)=f(m)+3*e*(PL(j,n+1-i)-PL(j,n-1-i))
      e=e*a(m)
       end do
      f(m)=f(m)/(1-e)
    END DO

  !Calculate tangent vectors
    tangent(j,1)=(a(1)*f(1)-a(2)*f(2))/(a(1)-a(2))
    tangent(j,n)=(f(1)-f(2))/(a(1)-a(2))
```

```
      END DO

           DO j=1,3
            tangent(j,0)=tangent(j,n)
            tangent(j,n+1)=tangent(j,1)
           END DO
      do j=1,3
          DO ii=2,n-1
          tangent(j,ii)=3*(PL(j,ii)-PL(j,ii-2))-4*tangent(j,ii-1)
     +          -tangent(j,ii-2)
          END DO
      end do

        end subroutine tangent_vec

    !=============================================================

        subroutine point_generator

    use variables
    integer::i,j

    i = i_loop
    j = i_node

    if (k_1==inside) then
    QL(1)=(r_local(i,j)-core)*dcos(angle(i,j))
    QL(3)=(r_local(i,j)-core)*dsin(angle(i,j));dr=0
    elseif (k_1>inside) then;
    dr(1) =2.*(k_1-inside)**f3*core*dcos(angle(i,j))
    dr(3) =2.*(k_1-inside)**f3*core*dsin(angle(i,j))
    elseif (k_1==0) then; dr=0
    else
    dr(1) = r_local(i,j)*dcos(angle(i,j))/(k_1+4)
    dr(3) = r_local(i,j)*dsin(angle(i,j))/(k_1+4)
    end if

    QL(1)   =  QL(1)+dr(1); QL(3)=QL(3)+dr(3)
    write(4,fmt=101)i_loop,i_node,k_1,inside,r_local(i,j)
  101   format(5x,4(1x,I5),1(1x,es12.5))

            end subroutine point_generator

        !=============================================================
```

```
          subroutine loop_generator (j)

      use variables
      integer::i,j,m

      i   =  i_loop
      angle(i,j)  = 2*pi*j/n_segments
  QL(1)   =i*delta(1)+x_elp*dcos(angle(i,j))
  QL(2)   =i*delta(2)
      QL(3)   =i*delta(3)-y_elp*dsin(angle(i,j))

  call transform (EP,center,QL,EG,zero,QG,LPG)

   do m=1,3; PL(m,j)=QL(m); PG(m,j)=QG(m);end do
   r_local(i,j)=dsqrt(QL(1)**2+QL(3)**2)

  write(3,fmt=102)i,j,QL,QG,r_local(i,j)
102   format (2(1x,I5),7(1x,es12.5))

          end subroutine loop_generator

      !=================================================================

      subroutine base_vectors

  use variables
  integer:: i,j

  do i=1,3
      do j=1,3
          if(i==j)then
          EG(i,j)=1
          end if
      end do
  end do

      e_1(1)=1.0/1.414213562
      e_1(2)=-1.0/1.414213562
      e_1(3)=0.0

      call cross_product(e_1,e_2,e_3)

  do i=1,3
```

```
EP(1,i)=e_1(i);EP(2,i)=e_2(i);EP(3,i)=e_3(i)
end do

    END subroutine base_vectors
  !=====================================================================

    subroutine transform (E2,T2,v2,E1,T1,v1,L21)

! subroutine for coordinate transformations
! v1= translation + rotation (L21*v2) .. all measured in sys_1
use variables
intent (in) :: E2,T2,v2,E1,T1; intent(out) :: v1,L21
double precision, dimension(3) :: v1,v2,T1,T2,T21
double precision, dimension(3,3) :: E1,E2,L12,L21

L21     = matmul(E1,transpose(E2))
LG1     = matmul(E1,transpose(EG))
T21     = T2 - T1

v1  = matmul(LG1,T21)+matmul(L21,v2)

        END subroutine transform
  !=====================================================================

    subroutine inner_product(a,b,c)
implicit none
intent(in)::a,b; intent(out)::c
double precision, dimension(3)::b,c
double precision, dimension(3,3)::a
integer:: m,i

    do i=1,3
      c(i)=0.0
        do m=1,3
              c(i) =c(i)+a(i,m)*b(m)
        end do
    end do

    end subroutine inner_product
!=============================================================

    subroutine cross_product(v1,v2,v3)

intent (in) :: v1,v2; intent(out) :: v3
```

```
    double precision,dimension(3) :: v1,v2,v3

        v3(1)=v1(2)*v2(3)-v1(3)*v2(2)
        v3(2)=v1(3)*v2(1)-v1(1)*v2(3)
        v3(3)=v1(1)*v2(2)-v1(2)*v2(1)

        end subroutine cross_product
      !=====================================================================

        subroutine writer

    use variables
    double precision:: polar_r

    polar_r = dsqrt(QL(1)**2+QL(3)**2)

         write(7,fmt=101)QL,sig_loc(1,1),sig_loc(1,2),
     +       sig_loc(1,3),sig_loc(2,2),sig_loc(2,3),sig_loc(3,3)
             write(8, fmt=101)QG,sig_glo(1,1),sig_glo(1,2),
     +       sig_glo(1,3),sig_glo(2,2),sig_glo(2,3),sig_glo(3,3)
         write (9, fmt=102)QG,i_loop,i_node,k_1,k_2

  101   format (9(1x,es12.5))
  102   format (3(1x,es12.5),4(1x,I5))

         end subroutine writer

    !=============================================================

             subroutine int_energy2

      use variables
      integer:: i,j,k,l
      double precision:: norm2,int_energy,mid1,mid2,mid3,mid4,
     +                   tr_sig,e_sia,e_vac,Moment_all,workdone
      double precision, dimension(3):: normal2,Moment_C
      double precision, dimension(3,3,3):: permu

      norm2=dsqrt(mil2(1)**2+mil2(2)**2+mil2(3)**2)
      normal2(1)=mil2(1)/norm2
      normal2(2)=mil2(2)/norm2
      normal2(3)=mil2(3)/norm2

      int_energy=0.0
```

```
      mid1=0.0

        do j=1,3
          do k=1,3
          int_energy=normal2(j)*burger2(k)*sig_glo(j,k)+
     +               int_energy
          end do

          mid1=mid1+normal2(j)*burger2(j)
        end do

      mid2=1.6d-19*mid1*T_temp*8.617065e-5
      int_energy=int_energy*0.25*G_shear*a_thick**3/mid2

      mid3=3.0*1.6d-19*T_temp*8.617065e-5
      tr_sig=sig_glo(1,1)+sig_glo(2,2)+sig_glo(3,3)
      e_sia=-0.1*a_thick**3*tr_sig*G_shear/mid3
      e_vac=-0.5*e_sia

      mid4=1.6d-19*mid1

        do i=1,3; do j=1,3; do k=1,3
          permu(i,j,k)=0.0
        end do; end do; end do

        permu(1,2,3)=1.0
        permu(2,3,1)=1.0
        permu(3,1,2)=1.0
        permu(1,3,2)=-1.0
        permu(3,2,1)=-1.0
        permu(2,1,3)=-1.0

        do i=1,3
          Moment_C(i)=0.0
          do j=1,3
            do k=1,3
              do l=1,3
                Moment_C(i)=Moment_C(i)-permu(i,j,k)*normal2(j)*
     +                      burger2(l)*sig_glo(l,k)
              end do
            end do
          end do
          Moment_C(i)=Moment_C(i)*0.25*G_shear*a_thick**3/mid4
        end do
```

```
        Moment_all=Moment_C(1)**2+Moment_C(2)**2+Moment_C(3)**2
        workdone=dsqrt(Moment_all)*0.5*pi/0.1d0

      write(12,fmt=1002)QG,int_energy,e_sia,e_vac,workdone
1002  format (7(1x,es12.5))

            end subroutine int_energy2

      !=====================================================================
```

15.2 2D Simulations - Noronha

15.3 Isotropic DD - Jianming

15.4 Anisotropic DD - Han

15.5 DD in Nanolayers - Han

15.6 Large-Scale DD - Zhiqiang

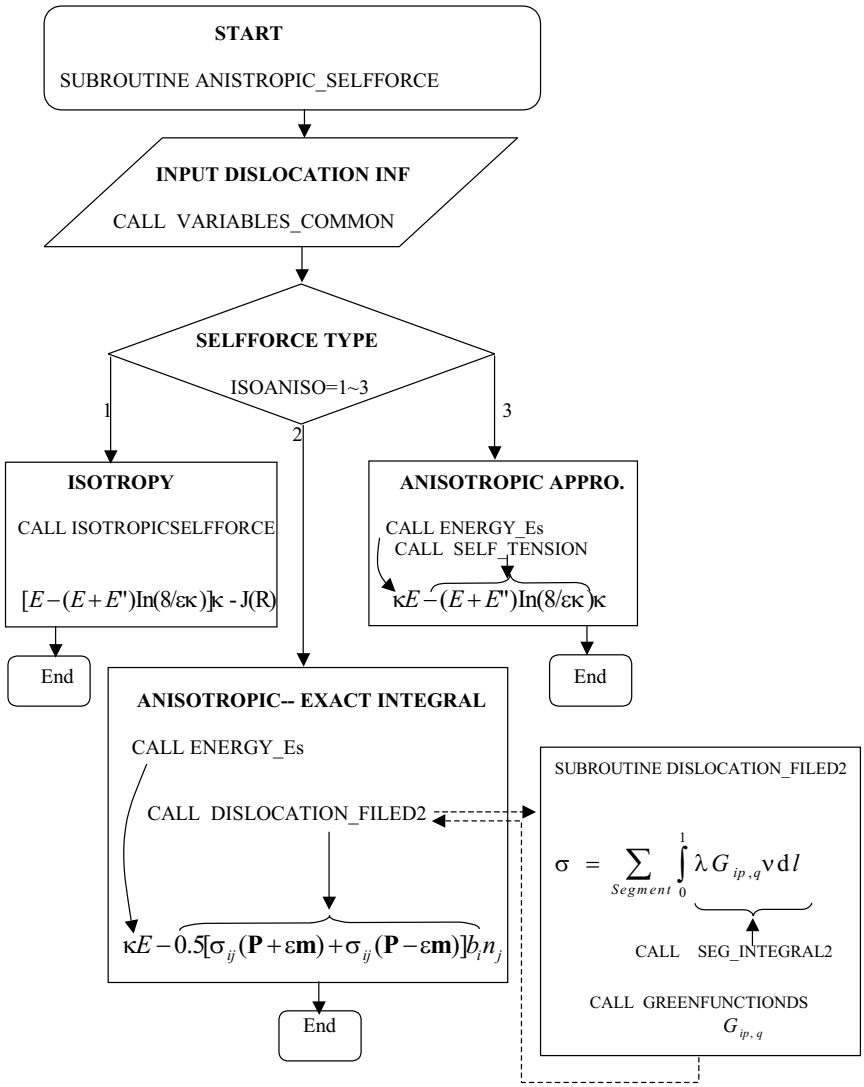

Figure 15.1: Self force calculation of a dislocation loop in anisotropic or isotropic materials.

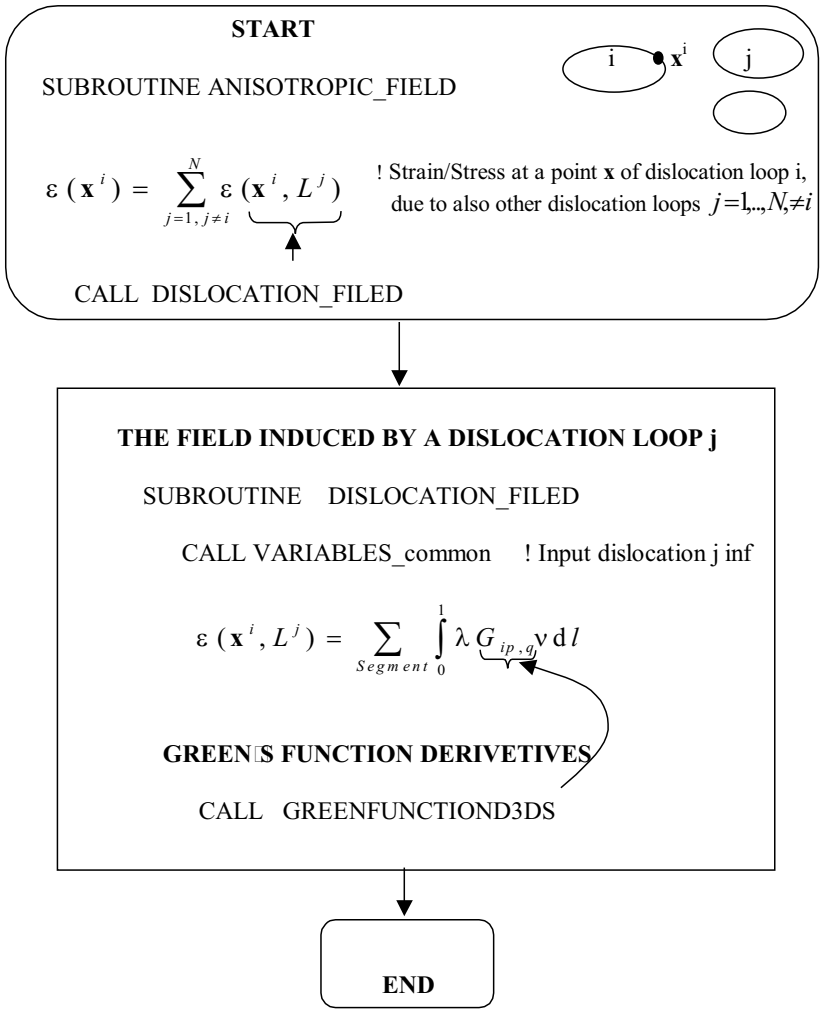

Figure 15.2: The stress field induced by dislocation loops and their interactions.

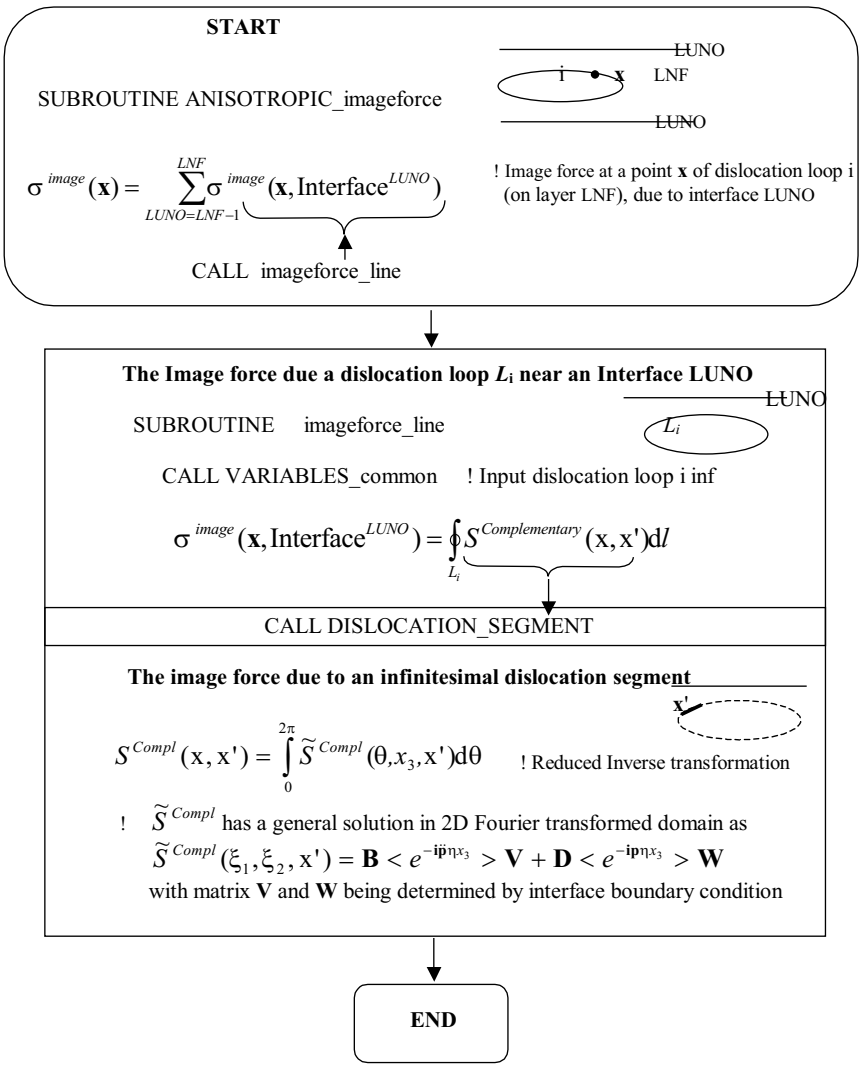

Figure 15.3: Image force calculation in multilayers, using line integration method.

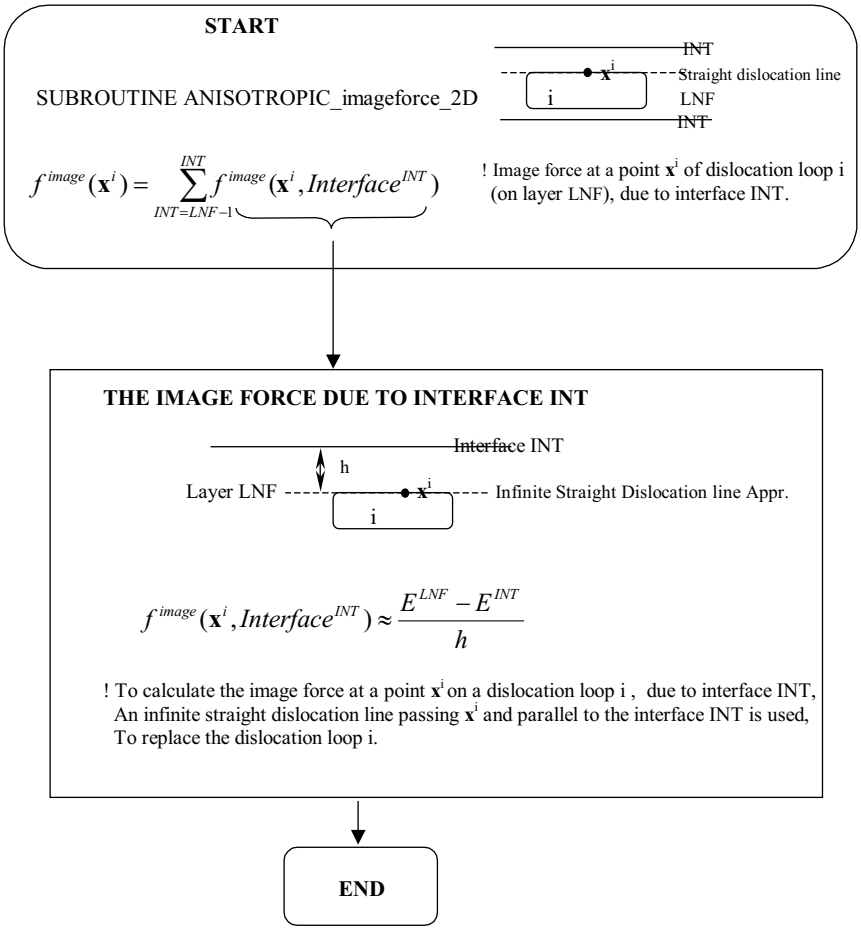

Figure 15.4: Image force calculation in multilayers, using straight line approximation method.

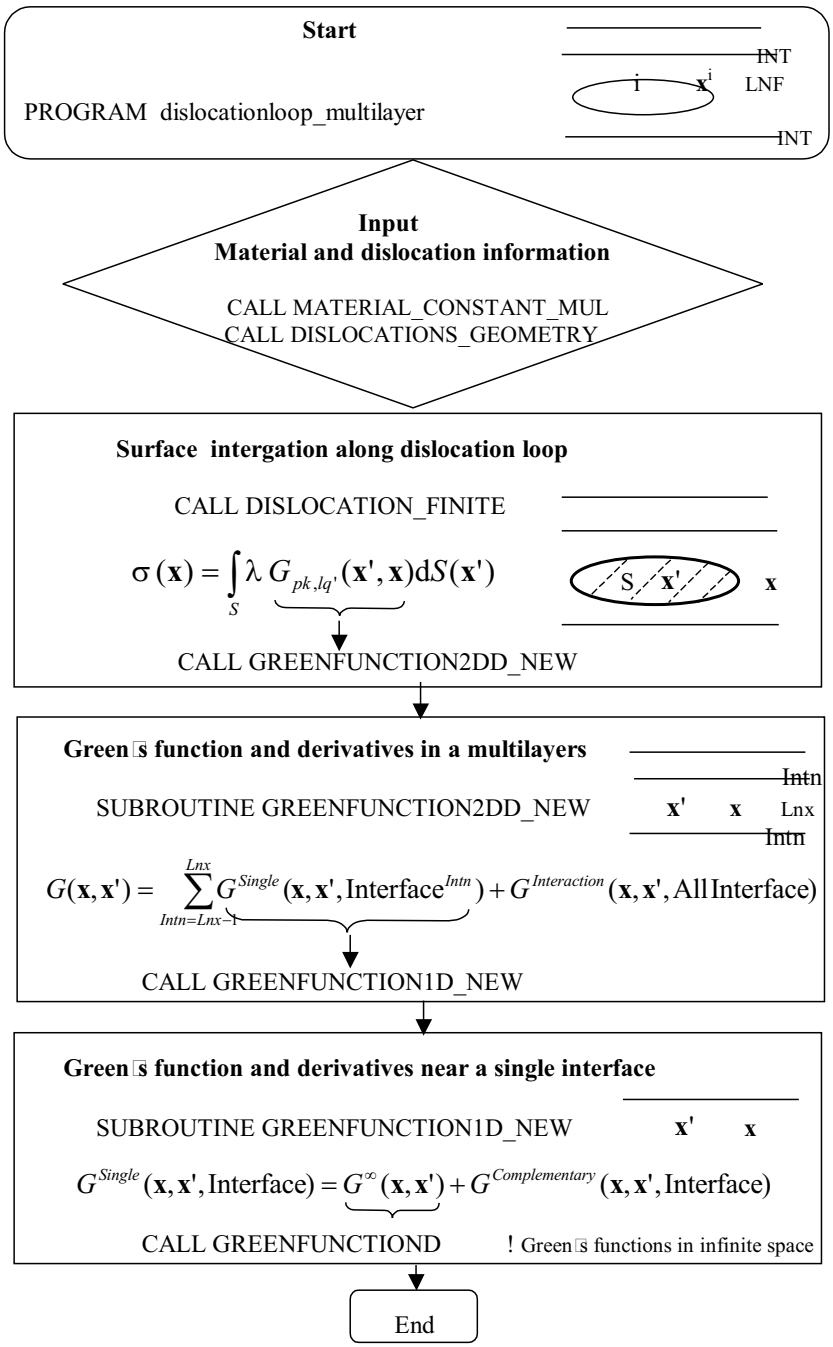

Figure 15.5: Green's functions and dislocation image force calculation in multilayers, using Green's functions and surface integral method.

Acknowledgements
Contribution to this work by UCLA was supported by the US Department of Energy, Office of Fusion Energy, through Grant DE-FG02-03ER54708, by the National Science Foundation (NSF) through grant DMR-0113555, by the Air Force Office of Scientific Research (AFOSR) grant number F49620-03-1-0031, and by Los Alamos National Laboratory grant number UCLANSL/USDOE5428000103.

Bibliography

Alerhand, O., Vanderbilt, D., Meade, R. and Joannopoulos, J. (1988). Spontaneous formation of stress domains on crystal surfaces, *Physical Review Letters* **61**(17): 1973–6.

Amodeo, R. J. and Ghoniem, N. M. (1990a). Dislocation dynamics ii: Applications to the formation of persistent slip bands, planar arrays, and dislocation cells, *Phy. Rev.* **41**: 6968.

Amodeo, R. J. and Ghoniem, N. M. (1990b). Dislocation dynamics i: A proposed methodology for deformation micromechanics, *Phys. Rev.* **41**: 6958.

Anderson, P.M., R. S. C. Y. and Hazzledine, P. (2000). Critical stress for transmission of a dislocation across an interface: results from peierls and embedded atom models., *presented at Interfacial Engineering for Optimized Properties II, Boston, MA*.

Anderson, P. and Li, Z. (2001). A Peierls analysis of the critical stress for transmission of a screw dislocation across a coherent, sliding interface., *Materials Science and Engineering* **A319-321**: 182–187.

Anderson, P., Foecke, T. and Hazzledine, P. (1999). Dislocation-based deformation mechanisms in metallic nanolaminates., *MRS Bulletin 24* **2**: 27–33.

Andreev, A. and Kosevich, Y. (1981). Capillary phenomena in the theory of elasticity, *Sov. Phys. JETP* **54**(4): 761–5.

Asaro, P., Hirth, J., Barnett, D. and Lothe, J. (1973). A further synthesis of sextic and integral theories for dislocations and line forces in anisotropic media., *Phys. Stat. Sol.(b)* **60**: 261–271.

Bacon, D. and Diaz de la Rubia, T. (1994). Molecular dynamics computer simulations of displacement cascades in metals, *J. Nucl. Mater.* **216**: 275.

Bacon, D. and Groves, P. (1970). The dislocation in a semi-infinite isotropic medium, *in* J. Simmons, R. de Witt and R. Bullough (eds), *Fundamental Aspects of dislocation Theory, NBS spec. pub. 317*, Vol. 1, U.S. National Bureau of Standards, Washington, pp. 35–45.

Bacon, D., Barnett, D. and Scattergodd, R. (1980). Anisotropic continuum theory of lattice deffects., *in* C. J. M. T. Chalmers, B (ed.), *Progress in Materials Science Vol. 23*, Pergamon Press, Great Britain, pp. 51–262.

Bacon, D., Calder, A., Gao, F., Kapinos, V. and Wooding, S. (1995). Computer simulation of defect production by displacement cascades in metals, *Nucl. Instrum. Meth. B* **102**(1-4): 37.

Bacon, D. J., Gao, F. and Osetsky, Y. N. (2000). The primary damage state in FCC, BCC and HCP metals as seen in molecular dynamics simulations, *J. Nucl. Mater.* **276**(2): 1–12.

Ballone, P., Andreoni, W., Car, R. and Parrinello, M. (1988). Equilibrium structures and finite temperature properties of silicon microclusters from ab initio molecular-dynamics calculations, *Phys. Rev. Lett.* **60**(4): 271.

Barnes, R. S. (1963). The migration of large clusters of point defects in irradiated materials, *J. Phys. Soc. Japan* **18, Suppl. III**: 305–311.

Barnett, D. M. and Lothe, J. (1973). Synthesis of the sextic and the integral formalism for dislocations, greens function and sur-face waves in anisotropic elastic solids, *Phys. Norv.* **7**: 13–19.

Barnett, D. M. and Lothe, J. (1974). An image force theorem for dislocations in bicrystals, *J. Phys. F.* **4**: 1618C1635.

Barnett, D. M. and Lothe, J. (1975). Line force loadings on an-isotropic half-spaces and wedges, *Phys. Norv.* **8**: 13–22.

Barnett, D. M. and Lothe, J. (1995). Mutual attraction of a dislo-cation to a bi-metallic interface and a theorem on proportional anisotropic bimaterials, *Int. J. Solids Structures* **32**: 291–301.

Barnett, D. M. and Swanger, L. A. (1971). The elastic energy of a straight dislocation in an infinite anisotropic elastic medium, *Physica Status Solidi B* **48**: 419–428.

Barnett, D. (1972). The precise evaluation of derivatives of the anisotropic elastic green's functions., *Phys. Status Solidi (b)* **49**: 741–748.

Barnett, D. (1976). The singular nature of the self-stress field of a plane dislocation loop in an anisotropic elastic medium., *Phys. Status Solidi (a)* **38**: 637–646.

Battaile, C. C. and Srolovitz, D. J. (1997). A kinetic monte carlo method for the atomic-scale simulation of chemical vapor deposition: application to diamond, *J. Appl. Phys.* **82**(12): 6293.

Boussinesq, J. (1885). *Applications des Potentiels*, Gauthier-Villars, Paris.

Brimhall, J. L. and Mastel, B. (1970). Neutron irradiated molybdenum-relationship of microstructure to irradiation temperature, *Radiat. Effects* **3**: 203–215.

Brown, L. (1964). The self-stress of dislocations and the shape of extended nodes., *Phil. Mag.* **10**: 441–466.

Brown, L. (1967). A proof of Lothe's theorem., *Phil. Mag.* **15**: 363–370.

Canova, G., Brechet, Y. and Kubin, L. P. (1992). 3D dislocation simulation of plastic instabilities by work-softening in alloys, *in* S. I. Anderson et al. (ed.), *Modeling of Plastic Deformation and its Engineering Applications*, RISØNational Laboratory, Roskilde, Denmark.

Caturla, M., Soneda, N., Alonso, E., Wirth, B., Diaz de la Rubia, T. and Perlado, J. (2000). Comparative study of radiation damage accumulation in cu and fe, *J. Nucl. Mater.* **276**: 13.

Chadwick, P. and Smith, G. D. (1977). Foundations of the theory of surface waves in anisotropic elastic materials, *Adv. Appl. Mech.* **17**: 303–376.

Choi, S. and Earmme, Y. (2002). Elastic study on singularities interacting with interfaces using alternating technique, *Int. J. Solids and Structure* **39**: 943–957.

Clemens, B., Kung, H. and Barnett, S. (1999). Structure and strength of multilayers., *MRS Bulletin 24* **2**: 20–26.

Comniou, M. and Dundurs, J. (1975). The angular dislocation in a half space., *J. Elasticity* **5**: 203–313.

Cottrell, A. H. (1953). *Dislocations and Plastic Flow in Crystals*, Oxford University Press, London.

Cottrell, A. (1948). Report of conference on the strength of solids, *Technical Report 30*, University of Bristol, England, Physical Society, London.

Daniels, B., Nix, W. and Clemens, B. (1995a). *in* P. T. C. V. S.P. Baker, C.A. Ross and P. Borgesen (eds), *Thin Films:Stress and Mechanical Properties V*, Mater. Res. Soc. Symp. Proc. 356, Pittsburgh, pp. 373–378.

Daniels, B., Nix, W. and Clemens, B. (1995b). *in* B. C. S. S. K. S. T.D. Nguyen, B.M. Lairson (ed.), *Structure and Properties of Multilayered Thin Films*, Mater. Res. Soc. Symp. Proc. 382, Pittsburgh, pp. 373–378.

Dederichs, P. H. and G., L. (1969). *Physical Review* **188**: 1175–1183.

Devincre, B. and Kubin, L. P. (1994a). Simulations of forest interactions and strain hardening in fcc crystals., *Mod. Sim. Mater. Sci. Eng.* **2, (3A)**: 559.

Devincre, B. and Kubin, L. (1994b). The Japan Institute of Metals, pp. 179–189.

Devincre, B. (1995). *Solid State Communications* **93**: 875–878.

Devincre, B. (1996). Kluwer Academic Publishers, Netherlands, Dordrecht, pp. 309–323.

Dikici, M. (1986). Green's tensor for a cubic material, *Acta Crystallographica, A* **42**: 202–203.

Dobrzynski, L. and Maradudin, A. A. (1976). Surface contribution to the low-temperature specific heat of a hexagonal crystal, *Physical Review B* **14**(6): 142200–10.

Dudarev, S. (2000). Inhomogeneous nucleartion and growth of cavities in irradiated materials, *Phys. Rev. B* **62**(14): 9325.

Dundurs, J. and Hetenyi, M. (1965). Transmission of force between two semi-infinite solids, *J. Appl. Mech.* **32**: 671–674.

Dundurs, J. and Sendeckyj, G. P. (1965a). Behavior of an edge dislocation near a bimetallic interface, *J. Appl. Phys.* **36**: 3353–3354.

Dundurs, J. and Sendeckyj, G. P. (1965b). Edge dislocation inside a circular inclusion, *J. Mech. Phys. Solids* **13**: 141–147.

Dundurs, J. (1969). Elastic interaction of dislocations with inhomogeneities, *in* T. Mura (ed.), *Mathematical Theory of Dislocations*, ASME, New York, pp. 70–115.

Dunn, M. L. and Wienecke, H. A. (1996). Green's functions for transversely isotropic piezoelectric solids, *Int. J. Solids Structures* **33**: 4571–4581.

Dunn, M. L. and Wienecke, H. A. (1999). Half-space green's functions for transversely isotropic piezoelectric solids, *J. Appl. Mech. ASME* **66**: 675–679.

Eldrup, M., Singh, B. N., Zinkle, S. J., Byun, T. S. and Farrell, K. (2002). Dose dependence of defect accumulation in neutron irradiated copper and iron, *J. Nucl. Mater.* **307-311**: 912–917.

Elliott, H. A. (1948). Three-dimensional stress distributions in hexagonal aeolotropic crystals, *Proc. Camb. Phil. Soc.* **44**: 522C533.

Embury, J. and Han, K. (1999). Dislocation accumulation at large plastic strains-an approach to the theoretical strength of materials., *presented at Eighth International Conference on the Mechanical Behavior of Materials, Victoria, Canada.*

Embury, J. and Hirth, J. (1994). On dislocation storage and the mechanical response of fine scale microstructures., *Acta Metall. Mater.* **42**: 2051–2056.

Eshelby, J. D., Read, W. T. and Shockley, W. (1953). Anisotropic elasticity with applications to dislocation theory, *Acta Metall.* **1**: 251–259.

Evans, J. H. (1980). Void swelling and irradiation-induced void shrinkage in neutron irradiated molybdenum and TZM, *J. Nucl. Mater.* **88**: 31–41.

Eyre, B. L., Maher, D. M. and Bartlett, A. F. (1971). Neutron irradiation damage in molybdenum part v. mechanisms of vacancy and interstitial loop growth during post-irradiation annealing, *Phil. Mag. A* **24**: 767–797.

Fivel, M., Gosling, T. and Canova, G. (1996). Implementing image stresses in a 3d dislocation simulation., *Modeling Simul. Mater. Sci. Eng.* **4**: 581–596.

Foreman, A. J. E. and Eshelby, J. D. (1962). Atomic energy research establishment report, *Technical Report R4170*.

Foreman, A. J. E., English, C. A. and Phythian, W. J. (1992). Molecular dynamics calculations of displacement threshold energies and replacement collision sequences in copper using a many body potential, *Phil. Mag. A* **66**(5): 655–669.

Foreman, A. (1967). The bowing of a dislocation segment., *Phil. Mag.* **15**: 1011–1021.

Fournet, R. and Salazar, J. (1996). *Physical Review* **53**: 6283–6290.

Fredholm, I. (1900). Sur les equations de l'equilibre d'un corps solide elastique., *Act. Math.* **23**: 1–42.

Freund, L. (1990). The driving force for glide of a threading dislocation in a strained epitaxial layer on a substrate., *J. Mech. Phys. Solids* **58**: 657–679.

Gao, F., Henkelman, G., Weber, W. L., Corrales, L. R. and Jonsson, H. (2003). Finding possible transition states of defects in silicon-carbide and alpha-iron using the dimer method, *Nucl. Instr. and Meth. B* **202**: 1–7.

Gavazza, S. and Barnett, D. (1976). The self-force on a planar dislocation loop in an anisotropic linear-elastic medium., *J. Mech. Phys. Solids* **24**: 171–185.

Ghoniem, N. and Amodeo, R. (1990). Kluwer Academic Publishers, Netherlands, Dordrecht, p. 303.

Ghoniem, N. and Sun, L. Z. (1999a). *Phys. Rev. B* **60**(1): 1.

Ghoniem, N., Huang, J. and Wang, Z. (2002a). A new covariant-contravariant vector forms for the elastic field of parametric dislocations in isotropic crystals, *Phil. Mag. Lett.* **82**(2): 55.

Ghoniem, N. M. and Amodeo, R. J. (1988). Computer simulation of dislocation pattern formation., *Solid State Phenomena* **3 &** 4: 377.

Ghoniem, N. M. and Sun, L. Z. (1999b). Fast sum method for the elastic field of 3-d dislocation ensembles, *Phy Rev B* **60, (1)**: 128–140.

Ghoniem, N. M., Huang, J. and Wang, Z. (2001). Affine covariant-contravariant vector forms for the elastic field of parametric dislocations in isotropic crystals, *Phil. Mag. Lett.* **82, (2)**: 55–63.

Ghoniem, N. M., Tong, S.-H. and Sun, L. Z. (2000a). Parametric dislocation dynamics: A thermodynamics-based approach to investigations of mesoscopic plastic deformation, *Phys. Rev.* **61, (2)**: 913–927.

Ghoniem, N. M. (1999). Curved parametric segments for the stress field of 3-d dislocation loops, *Transactions of the ASME, J. Eng. Mater. Tech.* **121**(2): 136.

Ghoniem, N., Singh, B., Sun, L. and Diaz de la Rubia, T. (2000b). Interaction and accumulation of glissile defect clusters near dislocations, *J. Nucl. Mater.* **276**: 166.

Ghoniem, N., Tong, S., Huang, J., Singh, B. and Wen, M. (2002b). Mechanisms of dislocation-defect interactions in irradiated metals investigated by computer simulations., *J. Nuclear Materials* **307**: 843–851.

Glazov, M. and Laird, C. (1995). *Acta metall. mater.* **43**: 2849–2857.

Glazov, M., Llanes, L. M. and Laird, C. (1995). *phys. stat. sol. (a)* **149**: 297–321.

Gosling, T. and Willis, J. (1994). A line-integral representation for the stresses due to an aritrary dislocation in an isotropic half-space., *J. Mech. Phys. Solids* **42**: 1199–1221.

Hanson, M. T. and Wong, Y. (1997). Concentrated ring loadings in a full space or half-space: Solutions for transverse isotropy and isotropy, *Int. J. Solids Structures* **34**: 1379–1418.

Han, X. and Ghoniem, N. (2004). Stress field and interaction forces of dislocations in anisotropic multilayer thin films., *Phil. Mag.*

Han, X., Ghoniem, N. and Wang, Z. (2002). Parametric dislocation dynamics of anisotropic crystals., *Phil. Mag.* **83 (31-34)**: 3705.

Head, A. K. (1953). Interaction of dislocations and boundaries, *Phil. Mag.* **44**: 92–94.

Head, A. K. (1965). The dislocation image force in cubic polycrystals, *Physica Status Solidi* **10**: 481–484.

Heinisch, H. and Singh, B. (1996). Stochastic annealing simulation of differential defect production in high energy cascades, *J. Nucl. Mater.* **232**(2-3): 206.

Heinisch, H. L. and Singh, B. N. (1997). Stochastic annealing simulation of intracascade defect interactions, *J. Nucl. Mater.* **251**: 77–85.

Heinisch, H. L. and Singh, B. N. (1999). Simulation of the kinetics of defect accumulation in copper under neutron irradiation, *J. Nucl. Mater.* **271-272**: 46–51.

Heinisch, H., Singh, B. and Diaz de la Rubia, T. (1994). Calibrating a multi-model approach to defect production in high energy collision cascades, *J. Nucl. Mater.* **212-215**: 127.

Heinisch, H. (1990). Computer simulation of high energy displacement cascades, *Radiat. Eff. Def. Solids* **113**: 53.

Hill, R. (1961). *in* I. Sneddon and R. Hill (eds), *Progress in Solid Mechanics 2*, North-Holland, Amsterdam, pp. 245–276.

Hirth, J. and Lothe, J. (1982). *Theory of dislocations*, John Wiley & Sons, New York.

Hirth, J. P., Rhee, M. and Zbib, H. (1996). Modeling of deformation by a 3D simulation of multi pole, curved dislocations, *J Comp-Aided Mat. Design* **3**: 164.

Huang, J. and Ghoniem, N. M. (2002). the dynamics of dislocation intercation with sessile self-interstitial atom (SIA) defect clusters atomospheres, *J. Comp. Mater. Sci.* **23**: 225–234.

Huang, J. and Ghoniem, N. M. (2003). *Modelling Simul. Mater. Sci. Eng.* **11**: 21–39.

Indenbom, V. and Orlov, S. (1968). Construction of green's function in terms of green's function of low dimension., *J. Appl. Math. Mech.* **32**: 414–420.

Kang, H. and Weinberg, W. (1988). Kinetics of precursor-mediated ordering of two-dimensional domains, *Phys. Rev. B* **38**(16B): 11543.

Kausel, E. and Roesset, J. (1981). Stiffness matrices for layered soils, *Bull. Seism. Soc. Am.* **71**: 1743–1761.

Khraishi, T. and Zbib, H. (2002). *Phil. Mag. Letters* **82**: 265–277.

Khraishi, T., Zbib, H. and de la Rubia, T. (2001). The treatment of traction-free boundary condition in three-dimensional dislocation dynamics using generalized image stress analysis ., *Materials Science and Engineering A* **309-310**: 283–287.

Kinchin, G. and Pease, R. (1955). The displacement of atoms in solids by radiation, *Rep. progr. phys.* **18**: 1.

Kirchner, H. and Alshits, V. I. (1987). Elastically anisotropic angularly inhomogeneous media ii, the green's function for piezoelectric, piezomagnetic and magnetoelectric media, *Phil Mag.* **74**: 861–885.

Koehler, J. (1970). Attempts to design a strong solid, *Philosophical Magazine* **2**: 547.

Kohyama, A., Hishinuma, A., Gelles, D., Klueh, R., Dietz, W. and Ehrlich, K. (1996). Low-activation ferritic and martensitic steels for fusion application, *J. Nucl. Mater.* **233-237**: 138.

Kossevich, A. (1999). *The Crystal Lattice: Phonons, Solitons, Dislocations*, number in , 1st edn, Wiley-VCH, Berlin.

Kratochvíl, J. and Saxlova, M. (1992). *Scripta Metallurgica et Materialia* **26**: 113–116.

Kratochvíl, J. and Saxlova, M. (1993). *Physica Scripta* **49**: 399–404.

Kratochvíl, J., Kroupa, F. and Kubin, L. (1999). *in* J. Blide-Sorensen, J. Carstensen, N. Hansen, D. J. Jensen, T. Leffers, W. Pantleon, O. Pedersen and G. Winther (eds), *Proceedings of the 20th Riso international symposium on materials science: Deformation-induced Microstructures: Analysis and Relation to Properties.*, Riso National Laboratory, Roskilde, Denmark, pp. 387–392.

Kratochvíl, J. (2001). *Materials Sci. Eng. A* **309-310**: 331–335.

Kroner, E. (1953). Das fundamentalintegral der anisotropen elastischen differentialgleichungen, *Zeit. Phys.* **136**: 402C410.

Kroupa, F. (1960). Circular edge dislocation loop., *Czech, J. Phys. B* **10**: 284–293.

Kubin, L. and Kratochvíl, J. (2000). *Philosophical Magazin A* **80**: 201–218.

Kubin, L. P., Canova, G., Condat, M., Devincre, B., Pontikis, V. and Brechet, Y. (1992). Dislocation microstructures and plastic flow: a 3d simulation, *Diffusion and Defect Data - Solid State Data, Part B (Solid State Phenomena)* **23-24**: 455.

Kung, H. and Foecke, T. (1999). Mechanical behavior of nano structured materials., *MRS Bulletin* **24**: 14–15.

Kuo, C. and Keer, L. (1995). Three-dimensional analysis of cracking in a multilayered composite, *J. Appl. Mech.* **62**: 273–278.

Landau, L. and Lifshitz, E. (1959). *Theory of elasticity*, Vol. 7 of *Course of Theoretical Physics*, Pergamon Press.

Lau, K. and Kohn, W. (1977). Elastic interaction of two atoms adsorbed on a solid surface, *Surface Science* **65**: 607–18.

Lee, N. (1979). Elastic green's function for an infinite half-space of a hexagonal continuum with its basal plane as surface, *Int. J. Eng. Sci.* **17**: 681C689.

Lejcek, L. (1969). The green function of the theory of elasticity in an anisotropic hexagonal medium, *Czech. J. Phys. B* **19**: 799–803.

Lepinoux, J. and Kubin, L. P. (1987). The dynamic organization of dislocation structures: a simulation., *Scripta Met.* **21, (6)**: 833.

Lie, K. C. and Koehler, J. S. (1968). The elastic stress field produced by a point force in a cubic crystal, *Advances in Physics* **17**: 421–478.

Lifshitz, I. M. and Rozenzweig, L. N. (1947). On the construction of the green's tensor for the basic equation of the theory of elasticity of an anisotropic infinite medium, *Zh. Eksp. Teor. Fiz.* **17**: 783–791.

Lin, W. and Keer, L. (1989). Analysis of a vertical crack in a multilayered medium, *J. Appl. Mech.* **56**: 63–69.

Lothe, J., Indenbom, V. and Chamrov, V. (1982). Elastic field and self-force of dislocations emerging at the free surfaces of an anistropic halfspace., *Phys. Stat. Sol. (b)* **11**: 671–677.

Lu, Y.-T., Petroff, P. and Metiu, H. (1990). Growth-kinetics simulation of the al-ga self-organization on (100) gaas vicinal surfaces, *Appl. Phys. Lett.* **57**(25): 2683.

Malen, K. (1971). A unified six-dimensional treatment of elastic green's functions and dislocations, *Physica Status Solidi B* **44**: 661–672.

Malygin, G. (1995). *Solid State Physics* **37**: 3–42.

Malygin, G. (1999). *Progress in Physics* **169**: 979–1010.

Mal, A. (1988). Guided waves in layered solids with interface zones, *Int. J. Eng. Sci.* **26**: 873–881.

Marchenko, V. and Parshin, A. (1980). Elastic properties of crystal surfaces, *Sov. Phys. JETP* **52**(1): 129–31.

Marchenko, V. (1981). Theory of the equilibrium shape of crystals, *Sov. Phys. JETP* **54**(3): 605–7.

Martinez, R. and Ghoniem, N. (2002). The infuence of crystal surfaces on dislocation interactions in mesoscopic plasticity: A combined dislocation dynamics- finite element approach., *J. Comp. Meth. Engr. Science, CMES* **3(2)**: 229–243.

Metiu, H., Lu, Y.-T. and Zhang, Z. (1992). Epitaxial-growth and the art of computer-simulations, *Science* **255**(5048): 1088.

Mindlin, R. D. (1953). Force at a point in the interior of a semi-infinite solid, *Proc. Midwest. Conf. Solid Mech.* pp. 56–59.

Misra, A., Verdier, M., Kung, H., Nastasi, M., Embury, J. and Hirth, J. (2000). Strengthening mechanisms in ultra-fine scale metallic multilayers., *presented at Ultrafine Grained Materials, Nashville, TN*.

Misra, A., Verdier, V., Kung, H., Embury, J. and Hirth, J. (1999). Deformation mechanism maps for polycrystalline metallic multiplayers., *Scripta Materialia* **41**: 973–979.

Misra, A., Verdier, V., Lu, Y., Kung, H., Mitchell, T., Nastasi, M. and Embury, J. (1998). Structure and mechanical properties of cu-x (x = nb,cr,ni) nanolayered composites., *Scripta Materialia* **39**: 555–560.

Mitchell, T., Lu, Y., Griffin, A., Nastasi, M. and Kung, H. (1997). Structure and mechanical properties of copper/niobium multilayers., *Journal of the American Ceramic Society* **80**: 1673–1676.

Mura, T. and Kinoshita, N. (1971). Green's functions for anisotropic elasticity, *Physica Status Solidi B* **47**: 607C618.

Mura, T. (1968). *in* H. Herman (ed.), *Advances in materials research*, Vol. 3, Interscience Pub., New York, pp. 1–108.

Mura, T. (1987). *Micromechanics of defects in solids*, Martinus Nijhoff, Dordrecht.

Nix, W. (1998). Yielding and strain hardning of thin metal films on substrates., *Scripta Materialia* **39**: 545–554.

Norgett, M., Robinson, M. and Torrens, I. (1975). A propsed method of calculating displacement dose rates, *Nucl. Eng. Des.* **33**(1): 50.

Osetsky, Y., Bacon, D. and Serra, A. (1999). Thermally activated glide of small dislocation loops in metals, *Phil. Mag. Lett.* **79**(5): 273.

Osetsky, Y. N., Bacon, D. J., Serra, A., Singh, B. N. and Golubov, S. I. (2000a). Stability and mobility of defect clusters and dislocation loops in metals, *J. Nucl. Mater.* **276**: 65–77.

Osetsky, Y. N., Serra, A. and Priego, V. (2000b). Interactions between obile dislocation loops in Cu and α-Fe, *J. Nucl. Mater.* **276**: 202–212.

Osetsky, Y., Serra, A., Singh, B. and Golubov, S. (2000c). Structure and properties of clusters of self-interstitial atoms in fcc copper and bcc iron, *Phil. Mag. A* **80**(9): 213.

Osetsky, Y., Victoria, M., Serra, A., Golubov, S. and Priego, V. (1997). Computer simulation of vacancy and interstitial clusters in bcc and fcc metals, *J. Nucl. Mater.* **251**: 34.

Pan, E. and Yuan, F. (1999). Three-dimensional Green's functions in anisotropic bimaterials., *Int. J. Solids Struct.* **37**: 5329–5351.

Pan, E. (1989). Static response of a transversely isotropic and layered half-space to general dislocation sources, *Physics of the Earth and Planetary Interior* **58**: 103–117.

Pan, E. (1997). Static Green's functions in multilayered half spaces., *Applied Mathematical Modelling* **21**: 509–521.

Pan, Y. C. and Chou, T. W. (1971). Point force solution for an infinite transversely isotropic solid, *J. Appl. Mech.* **43**: 608C612.

Pan, Y. C. and Chou, T. W. (1979a). Green's functions for two-phase transversely isotropic materials, *J. Appl. Mech.* **46**: 551C556.

Pan, Y. C. and Chou, T. W. (1979b). Green's function solutions for semi-infinite transversely isotropic materials, *Int. J. Eng. Sci.* **17**: 545C551.

Phythian, W., Stoller, R., Foreman, A., Calder, A. and Bacon, D. (1995). A comparison of displacement cascades in copper and iron by molecular dynamics and its application to microstructural evolution, *J. Nucl. Mater.* **223**(3): 245.

Portz, K. and Maradudin, A. A. (1977). Surface contribution to the low-temperature specific heat of a cubic crystal, *Physical Review B* **16**(8): 163535–40.

Qu, J. (1991). Green's functions in anisotropic bimaterials, *in* T. C. T. T. J. J. Wu and D. M. Barnett (eds), *Modern Theory of Anisotropic Elasticity and Applications*, SIAM Proceedings Series, SIAM, Philadelphia, p. 62C73.

Rao, S. and Hazzledine, P. (2000). Atomistic simulations of dislocation-interface interactions in the Cu-Ni multilayer system., *Phil. Mag. A* **80**: 2011–2040.

Rhee, M., Zbib, H., Hirth, J., Huang, H. and Diaz de la Rubia, T. (1998). Models for long-/short-range interactions and cross slip in 3d dislocation simulation of bcc single crystals., *Model. Simul. Mater. Sci. Eng.* **6**: 467–492.

Rodney, D. and Phillips, R. (1999). Structure and strength of dislocation junctions: an atomic level analysis, *Phys. Rev. Lett.* **82**: 1704–1707.

Rongved, R. (1955a). *J. Appl. Mech.*

Rongved, R. (1955b). Force interior to one of two joined semi-infinite solids, *Proc. 2nd Midwest. Conf. Appl. Mech.*, pp. 1–13.

Salamon, N. and Dundurs, J. (1971). Elastic field of a dislocation loop in a two-phase material., *J. Elasticity* **1**: 153–164.

Satoh, Y., Ishida, I., Yoshiie, T. and Kiritani, M. (1988). Defect structure development in14 mev neutron irradiated copper and copper dilute alloys, *J. Nucl. Mater.* **155-157**: 443–448.

Saxlova, M., Kratochvíl, J. and Zatloukal, J. (1997). *Materials Science and Engineering* **A234-236**: 205–208.

Schwarz, K. V. and Tersoff, J. (1996). Interaction of threading and misfit dislocations in a strained epitaxial layer, *App. Phys. Lett.* **69, (9)**: 1220.

Schwarz, K. (1999). Simulation of dislocations on the mesoscopic scale., *J. Appl. Phys.* **85**: 108–129.

Seale, S. and Kausel, E. (1989). Point loads in cross-anisotropic, layered halfspaces, *J. Eng. Mech.* **115**: 509–524.

Shchukin, V. and Bimberg, D. (1999). Spontaneous ordering of nanostructures on crystal surfaces, *Reviews of Modern Physics* **71**(4): 1125–1171.

Shilkrot, L. and Srolovitz, D. (1997). Adatom-step interactions: Atomistic simulations and elastic models, *Physical Review B* **55**(7): 554737–44.

Shinn, M., Hultman, L. and Barnett, S. (1992). Growth, structure, and microhardness of epitaxial tin/nbn., *J. Mater. Res.* **7**: 901–911.

Sikka, V. K. and Moteff, J. (1974). Damage in neutron-irradiated molybdenum : (I). characterization of as-irradiated microstructure, *J. Nucl. Mater.* **54**: 325–345.

Sinclair, C., Embury, J. and Weatherly, G. (1999). Basic aspects of the co-deformation of bcc/fcc materials., *Materials Science and Engineering A* **272**: 90–98.

Singh, B. N. and Zinkle, S. J. (1993). Defect accumulation in pure fcc metals in the transient regime: a review, *J. Nucl. Mater.* **206**: 212–229.

Singh, B. N., Evans, J. H., Horsewell, A., Toft, P. and Muller, G. V. (1998). Effects of neutron irradiation on microstructure and deformation behaviour of mono- and polycrystalline molybdenum and its alloys, *J. Nucl. Mater.* **258-263**: 865–872.

Singh, B. N., Foreman, A. J. E. and Trinkaus, H. (1997). Radiation hardening revisited: role of intracascade clustering, *J. Nucl. Mater.* **249**(2-3): 103–115.

Singh, B. N., Horsewell, A., Toft, P. and Edwards, D. J. (1995). Temperature and dose dependencies of microstructure and hardness of neutron irradiated ofhc copper, *J. Nucl. Mater.* **224**(2): 131.

Singh, S. (1970). Static deformation of a multilayered half-space by internal sources, *J. Geophys. Res.* **75**: 3257–3263.

Singh, S. (1986). Static deformation of a transversely isotropic multilayered half-space by surface loads, *Phys. Earth Planet. Inter.* **42**: 263–273.

Soneda, N. and de la Rubia, D. (2001). Migration kinetics of the self-interstitial atom and its clusters in bcc Fe, *Phil. Mag. A* **81**(2): 331–343.

Soneda, N. and Diaz de la Rubia, T. (1998). Defect production, annealing kinetics and damage evolution in α-Fe: an atomic-scale computer simulation, *Phil. Mag. A* **78**(5): 995–1019.

Spitzig, W., Pelton, A. and Laabs, F. (1987). Characterization of the strength and microstructure of heavily cold-worked cu-nb composites., *Acta Metall.* **35**: 2427–2442.

Stiegler, J. O. and Bloom, E. E. (1971). Void formation in irradiated nickel 270, *Radiat. Eff.* **8**: 34–41.

Stoller, R. (1996). Point defect survival and clustering fractions obtained from molecular dynamics simulations of high energy cascades, *J. Nucl. Mater.* **233-237**: 999.

Stoller, R. (2002). priviate communication.

Stroh, A. N. (1958). Dislocations and cracks in anisotropic elasticity, *Phil. Mag.* **3**: 625–646.

Synge, J. L. (1885). *The Hypercircle in Mathematical Physics*, Cambridge Univ. Press.

Teodosiu, C. (1982). *Elastic Models of Crystal Defects*, Editura Academiei, Bucuresti; Springer-Verlag, New York.

Tewary, V. K., Wagoner, R. H. and Hirth, J. P. (1989a). Elastic green's function for a composite solids with a planar interface, *J. Mater. Res.* **4**: 113–123.

Tewary, V. K., Wagoner, R. H. and Hirth, J. P. (1989b). Elastic green's function for a composite solids with a planar crack in the interface, *J. Mater. Res.* **4**: 124C136.

Tewary, V. K. (1995). Computationally efficient representation for elastostatic and elastodynamic green's functions, *Physical Review B* **51**: 15695–15702.

Ting, T. C. T. and Barnett, D. M. (1993). Image force on line dislocations in anisotropic elastic half-spaces with a fixed boundary, *Int. J. Solids Structures* **30**: 313–323.

Ting, T. C. T. and Lee, V. (1997). The three-dimensional elastostatic green's function for general anisotropic linear elastic solids, *Q. J. Mech. Appl. Math.* **50**: 407–426.

Ting, T. C. T. (1992a). Anatomy of green's functions for line forces and dislocations in anisotropic media and degenerate materials, *Physica Scripta T* **44**: 137–144.

Ting, T. C. T. (1992b). Image singularities of green's functions for anisotropic elastic half-spaces and bimaterials, *Q. J. Mech. Appl. Math.* **45**: 119–139.

Ting, T. (1996). *Anisotropic Elasticity: Theory and Applications*, Oxford University Press, New York.

Tippelt, B., Bretschneider and Hahner, P. (1997). *Phys. stat. sol. (a)* **163**: 11–26.

Tonon, F., Pan, E. and Amadei, B. (2001). Green's functions and boundary element method formulation for 3d anisotropic media., *Compt. and Struct.* **79**: 469–482.

Trinkaus, H., Singh, B. N. and Foreman, A. J. E. (1993). Impact of glissile interstitial loop production in cascades on defect accumulation in the transient, *J. Nucl. Mater.* **206**(2-3): 200.

Trinkaus, H., Singh, B. N. and Foreman, A. J. E. (1997). Mechanisms for decoration of dislocations by small dislocation loops under cascade damage conditions, *J. Nucl. Mater.* **249**(2-3): 91–102.

Tucker, M. O. (1969). Plane boundaries and straight dislocations in elastically anisotropic materials, *Phil. Mag.* **19**: 1141–1159.

Verdier, M., Five, M. and Groma, I. (1998). Mesoscopic scale simulation of dislocation dynamics in fcc metals: Principles and applications., *Model. Simul. Mater. Sci. Eng.* **6**: 755–770.

Verecký, S., Kratochvíl, J. and Kroupa, F. (2002). *phys. stat. sol. A* **191**: 418–426.

Volterra, V. (1907). Sur l'équilibre des carps élastiques multiplement connexes, *Annal. Sci. de l'École Norm. Super., Paris* **24**: 401–517.

Von Blanckenhagen, B., Gumbsch, P. and Arzt, E. (2001). Dislocation sources in discrete dislocation simulations of thin-film plasticity and the hall-petch relation., *Modeling Simul. Mater. Sci. Eng.* **9**: 157–169.

von Guerard, B., Grasse, D. and Peisl, J. (1980). Structure of defect cascades in fast neutron irradiated alumium by diffuse X-ray scattering, *Phys. Rev. Lett.* **44**(4): 262–265.

Voter, A. and Doll, J. (1985). Dynamical corrections to transition state theory for multistate systems: Surface self-diffusion in the rare-event regime, *J. Chem. Phys.* **82**: 80.

Wang, C. (1997). Elastic fields produced by a point source in solids of general anisotropy, *J. Engr. Math.* **32**: 41–52.

Wang, H. Y. and LeSar, R. (1995). O(N) Algorithm for dislocation dynamics, *Phil. Mag. A* **71, (1)**: 149.

Wang, Y., Jin, Y., Cuitino, A. M. and Khachaturyan, A. G. (2001). Nanoscale phase field microelasticity theory of dislocations: Model and 3D simulations, *Acta Mat.* **49**: 1847.

Weigrand, D., Friedman, L., Van der Giessen, E. and Needleman, A. (2002). Aspects of boundary-value problem solutions with three-dimensional dislocation dynamics., *Modeling Simul. Mater. Sci. Eng.* **10**: 437–468.

Willis, J. R. (1966). Hertzian contact of anisotropic bodies, *J. Mech. Phys. Solids* **14**: 163C176.

Willis, J. (1970). Stress fields produced by dislocations in anisotropic media., *Phil. Mag.* **21**: 931–949.

Willis, J. (1975). The interaction of gas bubbles in an anisotropic elastic solid., *J. Mech. Phys. Solids* **23**: 129–138.

Wirth, B., Odette, G., Maroudas, D. and Lucas, G. (1997). Energetics of formation and migration of self-interstitials and self-interstitial clusters in alpha-iron, *J. Nucl. Mater.* **244**(3): 185.

Wirth, B., Odette, G., Maroudas, D. and Lucas, G. (2000). Dislocation loop structure, energy and mobility of self-interstitial atom clusters in bcc iron, *J. Nucl. Mater.* **276**: 33.

Woo, C. H. and Singh, B. N. (1992). Production bias due to clustering of point defects in irradiation-induced cascades, *Phil. Mag. A* **65**(4): 889–912.

Wu, K. C. (1999). Generalization of the stroh formalism to three-dimensional anisotropic elasticity, *J. Elasticity* **51**: 213–225.

Yamakawa, K. and Shimomura, Y. (1988). Defects in fission-neutron irradiated Mo at high temperature in the JOYO reactor, *J. Nucl. Mater.* **155-157**: 1211–1216.

Yang, B. and Pan, E. (2002a). Efficient evaluation of three-dimensional Green's functions in anisotropic elastostatic mulitlayered composites., *Engng Analysis Boundary Element* **26**: 355–366.

Yang, B. and Pan, E. (2002b). Three-dimensional Green's functions in anisotropic trimaterials., *Int. J. Solids Struct.* **39**: 2235–2255.

Yuan, F., Yang, S. and Yang, B. (2003). Three-dimensional Green's functions for composite laminates., *Int. J. Solids Struct.* **40**: 331–342.

Yu, H. Y. and Sanday, S. C. (1994). Dislocations anddisclinations in transversely isotropic elastic solids, *Phil. Mag. A* **70**: 725–738.

Zbib, R. M., Rhee, M. and Hirth, J. P. (1998). On plastic deformation and the dynamics of 3d dislocations., *In. J. Mech. Sci.* **40 (2-3)**: 113.